THE UNIVERSITY
of EDINBURGH

MULTIPHASE FLOW MODELLING FOR ENHANCED OIL & GAS DRILLING AND PRODUCTION

Emmanuel I. Epelle

Doctor of Philosophy Thesis

University of Edinburgh

2020

Declaration

I declare that this thesis was composed by myself and that the work contained herein is my own, except where explicitly stated otherwise in the text.

(*Emmanuel I. Epelle*)

Acknowledgements

Firstly, I would like to thank God, Almighty, for the wisdom, strength, and courage to complete this project.

I also thank the following persons and entities, without whom this would not have been possible.

Dr Dimitrios I. Gerogiorgis for his technical guidance, encouragement, and continuous motivation throughout the entire duration of the project. His remarkable foresight, persistence, rigour, and attention to detail have made my PhD journey an excellent, albeit intensive learning experience.

Dr Nicholas Polydorides for his support and advice during the PhD.

Professor Michael Fairweather and Professor Kenneth McKinnon, my viva examiners, for the insightful feedback towards improving the final version of this thesis.

The School of Engineering, University of Edinburgh, for the PhD studentship.

My mother (Mrs. Ihuoma Lois Epelle), who although passed on during my PhD studies, continues to inspire me by her dedication and hard work during her lifetime. I also thank my family (Mr Benjamin Epelle, Ms Blessing Epelle, and Ms Winifred Obande) and my colleagues (Dr Samir Diab and Dr Alistair Rodman) for their support.

Abstract

From the exploration to the abandonment of an oil and gas discovery, operators and engineers are constantly faced with the challenge of achieving the best commercial potential of oil fields. Although the petroleum engineering community has significantly contributed towards maximising the potential of discovered prospects, the approach adopted so far has been compartmentalised with little (heuristics-based) or no quality integration. The highly interconnected nature of the decision factors affecting the management of any field requires increased implementation of Computer-Aided Process Engineering (CAPE) methods, thus presenting a task for which chemical engineers have the background to make useful contributions. Drilling and production are the two primary challenging operations of oilfield activities, which span through different time horizons with both fast and slow-paced dynamics. These attributes of these systems make the application of modelling, simulation, and optimisation tasks difficult. This PhD project aims to improve field planning and development decisions from a Process Systems Engineering (PSE) perspective via numerical (fluid dynamics) simulations and model-based deterministic optimisation of drilling and production operations, respectively. Also demonstrated in this work is the importance of deterministic optimisation as a reliable alternative to classical heuristic methods. From a drilling operation perspective, this project focuses on the application of Computational Fluid Dynamics (CFD) as a tool to understand the intricacies of cuttings transport (during wellbore cleaning) with drilling fluids of non-Newtonian rheology. Simulations of two-phase solid-liquid flows in an annular domain are carried out, with a detailed analysis on the impact of several drilling parameters (drill pipe eccentricity, inclination angle, drill pipe rotation, bit penetration rate, fluid rheology, and particle properties) on the cuttings concentration, pressure drop profiles, axial fluid, and solid velocities. The influence of the flow regime (laminar and turbulent) on cuttings transport efficiency is also examined using the Eulerian-Eulerian and Lagrangian-Eulerian modelling methods. With experimentally validated simulations, this aspect of the PhD project provides new understanding on the interdependence of these parameters; thus facilitating industrial wellbore cleaning operations. The second part of this project applies mathematical optimisation techniques via reduced-order modelling strategies for the enhancement of petroleum recovery under complex constraints that characterise production operations. The motivation for this aspect of the project stems

from the observation that previous PSE-based contributions aimed at enhancing field profitability, often apply over-simplifications of the actual process or neglect some key performance indices due to problem complexity. However, this project focuses on a more detailed computational integration and optimisation of the models describing the whole field development process from the reservoir to the surface facilities to ensure optimal field operations. Nonlinear Programs (NLPs), Mixed-Integer Linear Programs (MILPs), and Mixed-Integer Nonlinear Programs (MINLPs) are formulated for this purpose and solved using high-fidelity simulators and algorithms in open-source and commercial solvers. Compared to previous studies, more flow physics are incorporated and rapid computations obtained, thus enabling real-time decision support for enhanced production in the oil and gas industry.

Lay Summary

Oil and natural gas remain the world's leading energy sources, accounting for approximately 60% of global energy consumption. Natural gas, in particular, is projected to be an integral part of the low carbon energy transition and decarbonisation goals in decades to come. This demand represents a challenge for the oil and gas industry concerning its adaption to the changing investment landscape and the global pressure to decarbonise the energy system. Thus, the industry continuously seeks the development of technologies that revolutionise drilling and production activities in comparison to the currently applied, intuitive-based, and suboptimal methods. This PhD thesis addresses this challenge by developing sound mathematical-oriented methods that improve drilling and production activities for safer, more profitable, and environmentally friendly operations. Specifically, advanced numerical tools such as Computational Fluid Dynamics (CFD) and mathematical optimisation are employed for this purpose. As drilling progresses, rock particles of different sizes evolve, and these must be removed using a fluid with complex flow characteristics. CFD techniques implemented in this work allow drilling engineers to understand the fluid-particle interactions, thus avoiding problematic deposition of these particles in the wellbore; if this deposition persists, expensive drilling equipment could get stuck, kilometres beneath the earth surface and operational time is lost. Furthermore, the increased insight provided into this operation (in this thesis) allows the adequate selection of pumping requirements, and desirable fluid properties necessary for problem-free operations. Moreover, the application of mathematical optimisation, ensures that a field's profitability is enhanced while satisfying constraints on the pressures and flow rates of the subsurface reservoir, wells, pipelines, and processing facilities, respectively. Specifically, the framework proposed in this research seeks to address the following questions. How much oil and gas should be produced? Where should wells be placed? In what way should the wells be connected to other components at the surface? How much water or gas (such as CO_2) can be injected back into the reservoir to minimise environmental impact while sustaining production? With reliable projections of the increased demand for oil and gas in the far future, this resource will arguably be needed for electricity generation, transportation, powering our process plants, and other aspects of our lives. This research has provided novel methodologies for ensuring long-term sustainability and economic viability.

Contents

List of Figures

List of Tables

PART I: INTRODUCTION & MOTIVATION

Chapter 1 Introduction

The annual increase in global energy demand and the diverse applications of oil and gas resources (conventional and unconventional) are indicative of the fact that these energy resources will continuously remain relevant to humanity in the far future. With increasing climate change concerns, natural gas already provides a promising transition between some oil-based fuels and renewables in the long run, despite its well-known transportation difficulties (Tavallali et al., 2016a; b). It can be further argued that natural gas represents an economically attractive option for electricity generation (particularly in the US where shale gas is naturally abundant) with significantly reduced greenhouse gas emissions compared to coal, thus increasing its market demand (Zhang et al., 2014). These reasons have warranted advancements in technologies of varying sophistication for larger-scale development of complex hydrocarbon reservoirs, over the past ten decades.

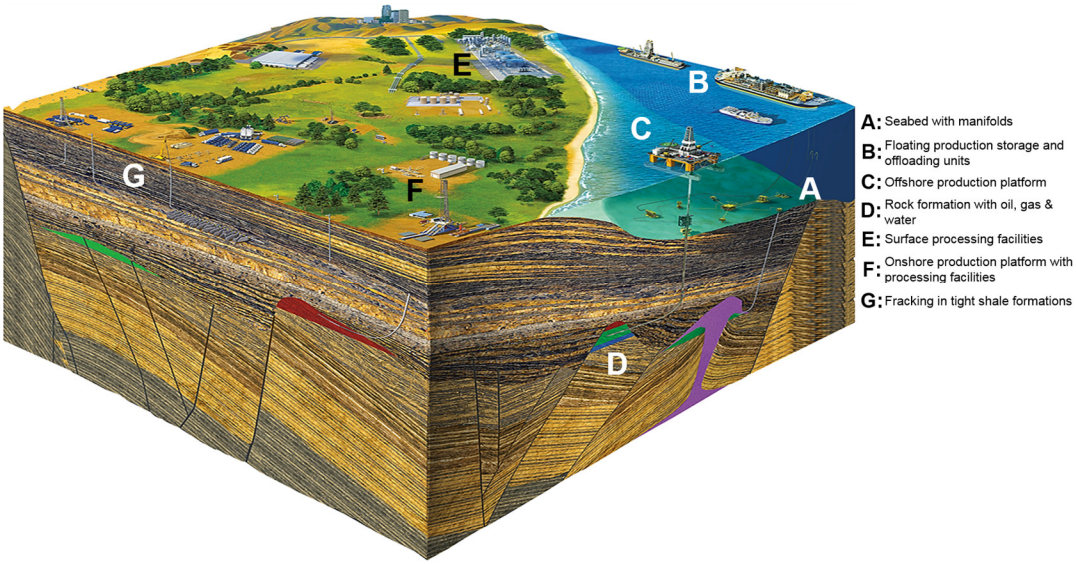

Figure 1.1. Illustration of onshore and offshore drilling and production (Schlumberger, 2019).

Oil field development projects (Fig. 1.1) aim to locate, characterise, and extract oil and gas resources in a safe and profitable way over the field's lifetime. These processes can be systematically classified into exploration (searching for oil and gas deposits), appraisal (investigating the volume of reserves), development (installing oilrig & processing equipment), production (fluid extraction) and abandonment (uninstalling facilities) phases (Fanchi and Christiansen, 2017). Well drilling and production are the main activities that take place throughout a field's lifetime. Only by drilling a well, can a field's prospect be

validated after many geological and geophysical interpretations in the exploration phase. Furthermore, production technologies enable reservoir fluids to be delivered safely to the surface facilities at the required pressure over long operation periods (typically, tens of years).

The average capital cost of constructing a well (drilling, completion, and facilities) in US onshore basins could be as high as $8.3 million. Drilling alone translates to approximately 31% of the total well development costs (EIA, 2016). In 2015, Shell abandoned drilling activities in the Arctic (northwest coast of Alaska – USD 7 billion worth of investment) after finding disappointing results from a well in the Chukchi Sea. Huge drilling and development costs were the main reasons leading to this decision. The Macondo oil well blowout during production activities by British Petroleum (BP) in the Gulf of Mexico, was an industrial disaster that resulted in fatalities and an oil spill that lasted 87 days (Paris et al., 2012; Wilson and Stammler, 2016; Gulas et al., 2017). These examples demonstrate the challenges of field development in difficult-to-access, environmentally unfriendly, and highly uncertain and risky regions, which oil companies must address to maintain global energy relevance.

1.1 Process Modelling and Systems Engineering of Drilling and Production Operations

The complicated economics, technical operational challenges, and the overall multifaceted nature of industrial drilling and production activities have rendered it open to multiscale modelling, robust simulation methodologies, optimisation, control and even state-of-the-art experimentation techniques for the accurate understanding of the flow scenarios and optimal parameters necessary for problem-free operation (Carlsen et al., 2013; Epelle and Gerogiorgis, 2019a; Pastusek et al., 2019). Steady-state and dynamic modelling, multiphase flow complexities, model nonlinearities and convexities, and the highly uncertain parameters and models describing the drilling and production operations are challenges for which process engineers have the right background to tackle. Computer-aided process engineering tools are increasingly becoming powerful, and they play an essential role in the development of the oil and gas industry. Notably, the applications of mathematical optimisation and Computational Fluid Dynamics (CFD) to solve drilling and production problems have continued to grow. The potential for computer-aided tools has also been recognised by the industry, as demonstrated by the recent increase in the

use of terms such as *Digital oilfields*, *intelligent oilfield*, *Integrated Field Management (IFM)* and *Closed Loop Reservoir Management*. These denote the extensive use of computers and communication-based systems for enhanced workflows of drilling and production systems (Nikolaou, 2013; Epelle and Gerogiorgis, 2019b, c; Petex, 2019). Over the past decades, both fields have attracted numerous successful contributions from the chemical, petroleum, and mechanical engineering communities for the modelling and optimisation of different aspects of drilling and production activities, respectively. These contributions are presented in the subsequent sections of this chapter.

1.2 Computational Fluid Dynamics

Contributions from the field of fluid dynamics have been mainly targeted towards cuttings removal and the rheological performance of drilling muds at unfavourable downhole conditions. The development of good rheological designs and an accurate understanding of mud shearing behaviour has been aided by advancements in multiphase flow description using physics-based phenomenological models (Akhshik et al., 2016; Epelle and Gerogiorgis, 2018). Due to the profound economic implications of inadequate/late rheological planning, drilling engineers are constantly faced with several intricate questions, some of which include: what flow properties are associated/expected with a given drilling mud? Can the level of downhole blockage (due to accumulated cuttings) be inferred from the flow rate and pressure drop data? In the worst scenario of severe cuttings accumulation, what is the optimal/critical flow rate to lift cuttings back into full suspension (Larsen et al., 1997; Bizhani et al., 2016)? Furthermore, the occurrence of dense fluid-particle flows (granular flows) in which inter-particle collisions are a dominant feature in drilling operations (Sun et al., 2017) is challenging to model; these flows can be very different to single-phase flows of drilling muds. An accurate understanding of different forms of granular flow has been made possible by the use of robust particle collision models (hard and soft particle models) embedded in state of the art computer simulators (Fluent, 2017), thus making it possible to describe slow and rapid granular flows effectively. The methods used to describe suspended and segregated flows depend on the flow regime, the accuracy level desired, and the spatial and temporal resolution required.

1.2.1 Direct Numerical Simulations

Direct Numerical Simulations (DNS), which fully resolve microscopic flow scales around particles, rely on the Navier Stokes equations to calculate the stresses acting on the particles and thus require little empirical modelling. Induced forces on the particle and the corresponding particle trajectories are obtained by the solution of the Newton equations of motion and the integration of the stresses on the particle surfaces (Liu, 2014; Tersa, 2015). Based on the continuous phase discretisation methods, several DNS techniques have been proposed in the literature; they include, front tracking, level set, immersed boundary, shock capturing, marker particle, simple line interface calculation (SLIC) volume of fluid, and piecewise linear interface construction (PLIC) as documented in Sommerfield et al. (2009). DNS methods are computationally expensive and are mostly applied to solve fundamental research problems on a small scale (for example, calibrating turbulence and particle force models). Hence, their implementation to model the cuttings removal in drilling systems involving millions of particles is extremely difficult. Fluid-particle simulations using DNS methods can be found in several published studies (Deen et al., 2012; Pan et al., 2002). Large Eddy Simulations (LES) and the Reynolds Averaged Navier Stokes (RANS) equations are computationally less expensive methods for describing various flow phenomena (such as turbulence) at different levels of accuracy. The ANSYS Fluent theory guide (Fluent, 2017) provides further details of their implementation.

1.2.2 Lagrangian-Eulerian (LE) Methods

This multiphase flow representation approach denotes a family of techniques in which particles are represented in a Lagrangian frame of reference (such as in the Discrete Phase Model – DPM and the Discrete Element Method – DEM); whereas the fluid flow field (carrier phase) is represented in an Eulerian frame. In contrast to DNS methods, LE methods require closure equations to describe interphase and momentum transfer forces. The coupling of the fluid and particle phases is a crucial aspect of LE methods. This is achieved through the volume fraction field variable of the momentum transfer terms. With computed particle positions and trajectories in the computational domain (i.e., in each control volume), the volume fraction can be determined. Besides, the coupling of the Lagrangian tracking of particles with the fluid flow description based on DNS methods, it is also possible to do this with the RANS equations and LES methods.

Statistical descriptions of multiphase flows have been readily applied to describe the positional variability of particles in a continuous phase; these descriptions are dependent on the level of closure in the statistical theory. The LE method can be likened to the point process description as presented by Subramaniam (2013), in which the dispersed phases are represented as a stochastic point process in the Lagrangian frame and the continuous phase represented as a random field in the Eulerian frame.

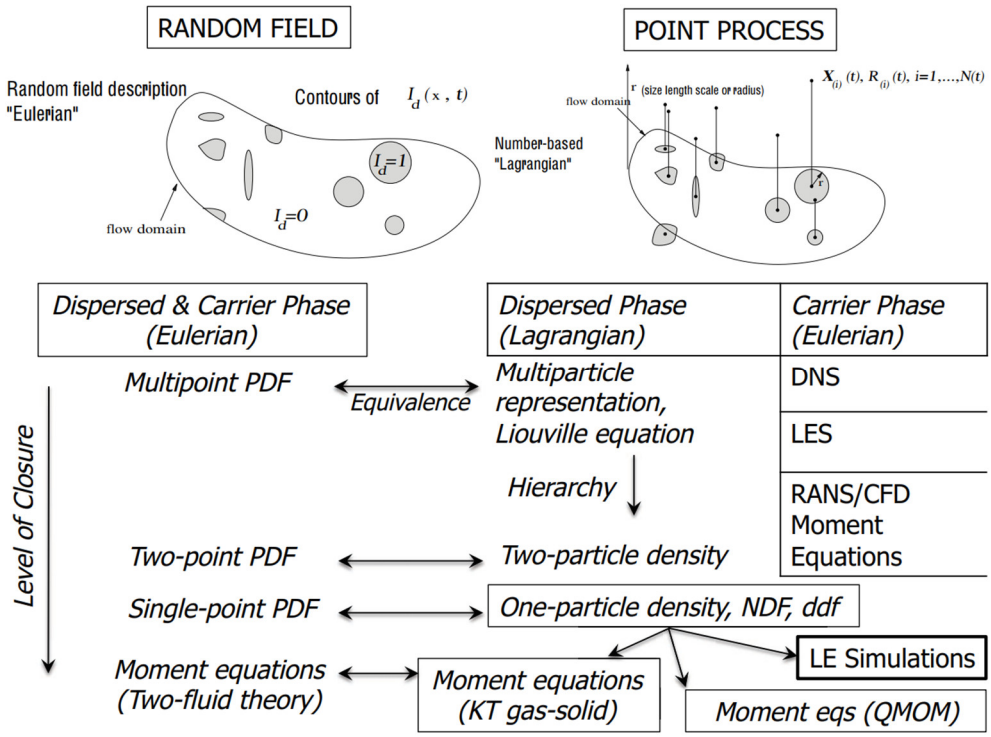

Figure 1.2. Random field and point-process approaches for representing multiphase flows (Subramaniam, 2013).

1.2.3 Eulerian-Eulerian (EE) Methods

Otherwise referred to as the two-fluid model or the multi-fluid model (if more than 2 phases are involved), this method involves the treatment of both particle and fluid phases as continuous media interpenetrating each other, and the macroscopic conservation equations are valid throughout the entire computational domain (Fluent, 2017). As shown in Fig. 1.2, in this method, statistical information only at a single space-time location (x, t) of the random field representation is considered. This model utilises several averaging techniques (such as time-averaging, volume-averaging, or ensemble averaging) for every variable involved. Although computational less intensive compared to the LE method, the discrete behaviour of the particles is lost due to the averaging procedures employed and thus must be regained through robust closure correlations. Drag, lift, and virtual mass

forces are some of the applied closures in this framework. To further describe solid properties, the Kinetic Theory of Granular Flow (KTGF) is usually employed, as documented in the work of Gidaspow (1994). The kinetic theory modelling for interparticle collisions, extended from the kinetic theory of gases, applies to dense particulate systems where the transport of the particle phase is dominated by inter-particle collisions (Fan and Zhu, 2005).

One of the advantages of the EE model is that the numerical simulation scheme of the continuous phase is also applicable to the discrete phase, and they follow the same discretisation procedure. Since the computational cost is independent of the number of particles, dense granular flows can be readily simulated with this scheme compared to the more expensive LE methods. However, the rheological description of the solid phase in the EE method can be challenging, thus limiting its accuracy (Crowe et al. 2011; Tersa, 2015).

1.2.4 CFD Tools and Software

The fluid dynamics community has witnessed the development of commercial software packages such as ANSYS Fluent™, ANSYS CFX™, Star CCM+™, (mainly for cuttings transport and drilling mud analyses) with ANSYS Fluent being the predominantly applied software in CFD related studies. Other open-source codes such as Gerris™, OpenFOAM™, SU2 code™, and Simscale™ have also gained popularity. Pre-processing, visualisation, and post-processing of CFD results are also paramount for successful interpretation of computations and have been carried out using software like GAMBIT™, AUTOCAD™, SpaceClaim™, and Paraview™, respectively. Recent studies that couple CFD computations with DEM models for the detailed resolution of particle contacts, have applied EDEM™ and LIGGGHTS™.

1.2.5 Research Contributions on CFD Applications for Cuttings Transport Modelling

One of the earliest CFD studies conducted to understand cuttings transport phenomena was that of Bilgesu et al. (2002). In their study, the impact of particle size and mud rheology on cuttings removal efficiency was determined using a solid-liquid multiphase flow model. Both water and a non-Newtonian power-law fluid were used in horizontal and vertical flow geometries. The results of the simulations showed that annular velocity

plays a vital role in hole cleaning. In a subsequent study of Bilgesu et al. (2007), steady-state CFD simulations were carried out to determine the effects of fluid velocity, cuttings size, drill pipe rotation and inclination angle in deviated wells using the Eulerian model. They observed that the drill pipe rotation aids cuttings removal, especially with smaller particles. CFD studies using foam as the circulating fluid have shown that the power-law model performs better than the Herschel-Bulkley model in predicting cuttings transport phenomena. (Rooki et al. 2014; Rooki et al., 2015). The authors examined the effect of foam quality, foam velocity, drill pipe rotation, and wellbore inclination on the cuttings transport efficiency and concluded that cuttings removal is enhanced by increasing foam quality and pipe rotation. In their study, the cuttings transport efficiency was examined as a function of the Cuttings Transport Ratio – (CTR, the ratio of annular solids velocity to fluid axial velocity). However, studies conducted by Tomren et al. (1986) showed that the use of CTR as an index of cuttings removal efficiency could be misleading when particle buildup occurs in inclined or horizontal annuli.

Pereira et al. (2007) studied single-phase non-Newtonian fluid flow in an annulus using CFD techniques. Their study demonstrates the effectiveness of the adopted simulation strategy in replicating experimental data of velocity profiles from literature (as illustrated in Chapters 3-6). Pereira et al. (2010) also analysed multiphase (solid-liquid) flow phenomena in an annulus using the Discrete Phase Model (DPM) with special consideration to particle trajectory as a function of drill pipe rotation. Although their model had good agreements with experimental data, not many drilling variables were considered in their work. Mishra (2007) studied the impact of fluid velocity, cuttings size, ROP, drill pipe rotation, and inclination angle on cuttings removal using the Eulerian–mixture model. The findings of Mishra's investigations substantiate the results of Bilgesu et al. (2007), which illustrate that the impact of drill pipe rotation is greater with particles of smaller sizes. It was also shown that fluid flow rate, hole inclination angle, and ROP have a major impact on transport efficiency. Ofei et al. (2014) implemented the Eulerian-Eulerian multiphase model to predict cuttings concentration and pressure losses at different diameter ratios in eccentric horizontal annuli. According to their results, drilling mud had superior transport capabilities compared to water at low diameter ratios; however, the performance of both fluids can be similar at a high diameter ratio of 0.9. Wang et al. (2009) examined cuttings transport in extended reach wells under the

influence of drill pipe rotation. Their CFD simulations showed that drill pipe rotation causes an asymmetric deposition of cuttings in the annulus. Sorgun (2010) studied the cuttings transport phenomena using experimental and CFD modelling approaches. It was discovered that drill pipe rotation improves cuttings removal and also decreased the critical fluid velocity required to suspend particles in the flow stream. Pang et al., (2018a) conducted a numerical study on cuttings transport behaviour using the Kinetic Theory of Granular Flow (KTGF) and a power-law non-Newtonian fluid. In their study, the swaying motion of the cuttings due to drill pipe rotation was observed. They particularly observed that a critical rotational speed exists for which there is no additional contribution of drill pipe rotation to the cuttings transport phenomena. In another similar study of Pang et al., (2018b), a Herschel-Bulkley model, was adopted for the rheological property description of the drilling mud. It was discovered that the flow behaviour index in the HB model is the most influential factor on the annular pressure drop computed. Sun et al. (2017) analysed the cuttings transport behaviour in a slim hole inclined annulus using a CFD-DEM model. They analysed the effects of annular fluid velocity, inclination angle, feed cuttings concentration, and drill pipe rotation on the cuttings concentration. With the obtained results, they proposed a correlation for the critical cuttings deposition velocity in the annulus.

The work of Yilmaz (2012) involved the development of a CFD model to investigate cuttings bed height and velocities in deviated wellbores using DPM simulations for particle tracking. The one-way Lagrangian-Eulerian (LE) coupling scheme implemented by Yilmaz was found to reasonably represent the transport phenomena of liquid and solid phases, given the low volume fractions involved. Demiralp (2014) focused on the effects of drill pipe whirling motion on cuttings transport performance in eccentric horizontal annuli. His work featured a two-way coupling of the particle-fluid interactions using the Discrete Element Method (DEM) and consequently discovered a corresponding increase in pressure with an increase in the whirling speed. The application of CFD-DEM models to three-phase multiphase flow description during unbalanced drilling with an aerated mud has been investigated by Akshik and Rajabi (2018). In their coupled approach, they implement the VOF model for capturing the gas-liquid interphase in the annulus. Several validation tests were performed, and the obtained results showed good agreement with experimental results. They further observed that an increased gas injection rate causes a

reduction in the cuttings volume fraction; hence the gas-liquid ratio is an important factor that determines the wellbore cleaning efficiency. While much attention has been given to drill pipe rotation by most CFD campaigns, very few research efforts have addressed the impact of changing hole eccentricity along the wellbore, which constitutes a major cause of downhole pressure fluctuations during drilling. This thesis addresses this challenge. The length of the computational domain considered, mesh skewness, orthogonality, and the number of nodes are qualities, which make the herein developed model more robust, and accurate compared to others. These important properties that determine the quality of the solution obtained are not often reported.

Many researchers have demonstrated via experiments that cuttings transport is affected by drilling variables such as pipe rotation, hole inclination and many other factors (Tomren et al. 1986; Capo et al. 2004; Chen et al. 2007a; b; Duan et al. 2006; Duan et al. 2010; Han et al. 2010; Osgouei, 2010; Ozbayoglu et al. 2010; Xu et al. 2013). It is worth mentioning that a majority of these works have analysed cuttings transport phenomena as a function of the cuttings concentration and pressure drop, which are relatively easy to measure physically. However, only a few studies exist in the literature that analyse the velocities of particles due to the difficulties earlier mentioned. The Positron Emission Particle Tracking (PEPT) technique has been implemented in analysing particle transport velocity profiles with a non-Newtonian fluid under laminar conditions in a pipe (Barigou, 2004; Eesa and Barigou 2008; Eesa and Barigou 2009). Similarly, cuttings slip velocity has been determined by Garcia-Hernandez et al. (2007) through optical measurements of specially marked cuttings in a transparent annulus. The effects of flow rate, pipe rotation, and loop inclination were investigated using a moving camera system with water and a polymer-based drilling fluid. However, CFD techniques possess great potential for the elucidation of these complexities. Furthermore, the impact of changing hole eccentricity has also not been extensively studied by these experimental methods. Several one–dimensional (across the wellbore) and two-dimensional (across cross-sectional flow area) mechanistic modelling studies on cuttings transport with a variety of drilling fluids have also been conducted (Guckes, 1975; Nguyen and Rahman, 1996; Ozbayoglu et al., 2005; Osunde and Kuru, 2006; Zaisha et al., 2012). The impact of particle shape on cuttings transport is an important phenomenon that has hardly been studied experimentally and also using CFD methods.

Comer and Kleinstreuer (1995) specifically reported that the assumption of a spherical shape could result in the underestimation of the drag coefficient by 30% for some spheroids. This discrepancy could be widened, when the particle's orientation with respect to the bulk fluid motion plays an important role due to irregularities in particle shape. Just as most research endeavours on the motion of solid particles in a fluid consider mainly spherical particles (Ofei et al., 2014; Rooki et al., 2015; Epelle and Gerogiorgis, 2017a; Heydari et al., 2017), most investigations accounting for particle sphericity are concerned with Stokes flow at low particle Reynolds number (Karnis et al., 1963; 1966; Ding et al., 2000; Mandø et al., 2007). Adjustments of the drag coefficient for higher Reynolds numbers significantly depend on empirical data and sometimes the particle orientation. The dominating and crucial role of the drag force in determining particle behaviour in a fluid is the rationale behind several modifications of the drag coefficient compared to other forces acting on a particle moving in a fluid. It is also important to note that most of the studies in the literature that account for the impact of particle shape on fluid-solid multiphase flows have been carried out for single-particle flow or multi-particle flow systems in fluidised bed applications; during which the carrier fluid is mostly a gas or a Newtonian fluid (Qi and Luo, 2003; Reuge, 2008; Sobieski, 2009; Sobieski, 2010; Hua et al., 2015). Very little attention has been paid to oil and gas drilling systems.

The works of Al-Kayeim et al. (2010), Yilmaz (2012), Akhshik et al. (2016), and Mohammadzadeh et al. (2016) appear to be the primary studies channelled towards drilling operations with sphericity considerations. Akhshik et al. (2016) evaluated the fluid-particle flow patterns, particle velocity and concentration profiles for non-spherical particles using a coupled CFD-DEM model and discovered that particle sphericity plays a significant role in fluid-solid interaction. Yilmaz (2012) used the Discrete Phase Model (DPM) with the Rosin-Rammler size distribution to study the moving bed velocity of particles with a sphericity of 0.1. By using particles of three different sphericities and the Eulerian-Eulerian model, Al-Kayeim et al. (2010) observed a slight improvement in cleaning performance as the sphericity increased. In the work of Mohammadzadeh et al. (2016), the Particle Transport Ratio (PTR) was analysed as a function of the viscosifier content of a drilling fluid using spherical and non-spherical particles. Their implementation of the EE model produced a significant influence of the sphericity on the PTR.

In the work of Cayeaux et al. (2014), a new approach for monitoring annular cuttings deposition via a transient cuttings-transport model was presented; this model incorporated closure laws for cuttings transport into a transient drill string model for the real-time evaluation of wellbore cleaning conditions. Their model was calibrated against field data by parameter adjustment and provided real-time monitoring of the drilling process. They were able to observe the positional annular velocity variation in different sections of the well, thus predicting regions prone to deposition. This positional variation is also demonstrated in this thesis using CFD. The consideration of deviated wellbore geometry in most numerical studies is very scarce; however, Naganawa et al. 2017 proposed a 1D two-layer transient cuttings model for directional and extend-reach drilling applications. They validated their model against ECD field data obtained during LWD operations.

1.3 Simulation-Based Optimisation

Mathematical programming or numerical optimisation methods, tools and software have been applied in the upstream oil and gas industry to support production activities and decisions which include: production system/facility design, infrastructural planning, fluid flow, and resource scheduling, history matching in the context of closed-loop reservoir management, well placement and control, fluid recovery maximisation and production parameter tuning (Gerogiorgis et al., 2009; Tavallali et al., 2013; 2014; Epelle and Gerogiorgis, 2017; Khor et al., 2017). Accurate description of physical flow phenomena, advanced mathematical techniques, and high-performance computing are important components embedded in these tools, which have led to lower operational cost and increased process efficiency when they are systematically applied (Epelle and Gerogiorgis, 2018a; b; c). However, it is essential that optimisation is considered in the early stages of design and model development by production engineers for maximum benefits (Eason, 2018). A typical oil and gas production system is a collection of interconnected components, which include: reservoirs, wells (with an attached surface choke), manifolds, and pipelines for routing the fluids to a separator where the respective phases (oil, gas, and water) are split. Each component requires a set of complicated models (sometimes embedded in simulators) for the accurate description of critical physical phenomena. Since optimisation algorithms require compatible explicit mathematical models,

collectively handling these systems of models for optimisation purposes is a challenging task.

1.3.1 Surrogate-Based Optimisation

High-fidelity simulators employed in the petroleum industry can be very complex due to size, the type of physical phenomena modelled and accompanying model uncertainty; thus, the runtime for these simulators can be high, especially if high accuracy is required (Epelle and Gerogiorgis, 2018b; 2018c). The number of network components and hence the number of equations describing each component, their physical interactions and interdependencies, further imply that numerous equations and unknown variables are necessary to characterise the entire production system. The challenges faced from an optimisation viewpoint can be attributed to the type of problems solved (Linear Programs, LPs, Mixed Integer Linear Programs, MILPs, Nonlinear Programs, NLPs, Mixed-Integer Nonlinear Programs MINLPs and Stochastic Programs) by available robust algorithms (commercial and open-source). Optimisation formulations can also be classified based on the presence and type of constraints (equality and inequality), the amount of information provided by the model (derivative-free, first-order, second-order), the presence of nonlinearities and non-convexities, and the presence of discrete decisions in the problem (Kosmidis et al., 2004; 2005; Codas et al., 2012; Gunnerud et al., 2012). Leveraging the power of simulation within an optimisation framework often requires the development of equation-based approximations (surrogate or proxy models – polynomial interpolation, kriging and neural networks) from the outputs of black-box simulators. The development of accurate proxy models is an active area of research that has received contributions from statistics, machine learning and engineering (Eason, 2018). When these models are to be used for optimisation purposes, the functional form and validation procedures are essential concepts to consider in their construction.

1.3.2 Gradient-Based and Derivative-Free Optimisation

Production optimisation methods can generally be classified into stochastic/derivative-free methods and gradient-based methods. The application of mathematical optimisation to production-related problems suffers from the lack of gradient information, because of the prevalence of complex models within simulators. Thus, optimising a production system requires numerous calls to these simulators (black-box), which is computationally inefficient and requires access to the simulator's source code (this is hardly available since

these simulators are mostly commercial). This has warranted the development of derivative-free optimisation methodologies (Awotunde, 2014). Some of these methods include Hooke-Jeeves direct search (HJDS), Generalised Pattern Search (GPS), Genetic Algorithms (GA), Mesh Adaptive Direct Search (MADS), Particle Swarm Optimisation (PSO), Simultaneous Perturbation Stochastic Algorithm (SPSA) and Simulated Annealing techniques (Ciaurri et al., 2010). Although these methods aim at providing a global optimum, they do not guarantee a monotonic improvement of the objective function with successive iterations and usually fail to scale properly as the optimisation problem increases (Li et al., 2013). Probability constrained models, especially when geological uncertainty is involved, is another area of production optimisation that has witnessed increased usage of derivative-free methods.

However, gradient-based methods can be efficient when gradients are available, for example, through adjoint methods. Production optimisation problems can be very rough and non-convex; thus resulting in discontinuous gradients and numerous optima. This results in the difficulty of finding a global solution when gradient-based methods are employed. Furthermore, adjoint methods for computing gradients are invasive with respect to the subsurface flow simulator. Their implementation requires a detailed knowledge/full access to the simulator source code, compared to the non-invasive technique of derivative-free methods which treat the simulator as a black box (only values of the cost functions are required). This treatment is also made possible by using special constraint handling techniques such as penalty functions and filter-based methods (Datta-Gupta et al., 1995; Wang et al., 2012; Bellout et al., 2012; Gildin et al., 2013; Beykal et al., 2018; Narasingam et al., 2018; Jesmani et al., 2020).

Since the explicit form of the simulators for each system component (reservoir, wells, and pipelines) can be approximated via surrogate modelling methods, other gradient-based methods for nonlinear programming can be used. Unlike the derivative-free methods, these methods guarantee a monotonic improvement in the objective function as the number of iterations increases and thus follow the local convergence theory (Proinov, 2009). Some of these methods include Sequential Quadratic Programming (SQP) and Interior Point Methods. Details of these algorithms can be found in Eason (2018).

1.3.3 Optimisation Solvers & Software

A survey of popular software packages and algorithms for solving production optimisation problems and the general properties of these problems are presented in Tables 1.1 and 1.2. It is worth mentioning that most of the solvers implement more than one algorithm for solving the corresponding formulation type; thus increasing their versatility and performance. Similarly, some of the algorithms in Table 1.2 have several variants (for example, variants of the Branch and Bound algorithm include depth-first and best-first algorithms depending on how the optimisation search tree is progressively developed). Significant advances in optimisation (particularly, in the field of Mixed Integer Programming – MIP) have been made over the past three decades. Presolving, coefficient tightening, reformulation techniques and heuristic procedures are some of the technological advances characterising solver development which have enabled tighter relaxations, faster convergence and globally optimal results.

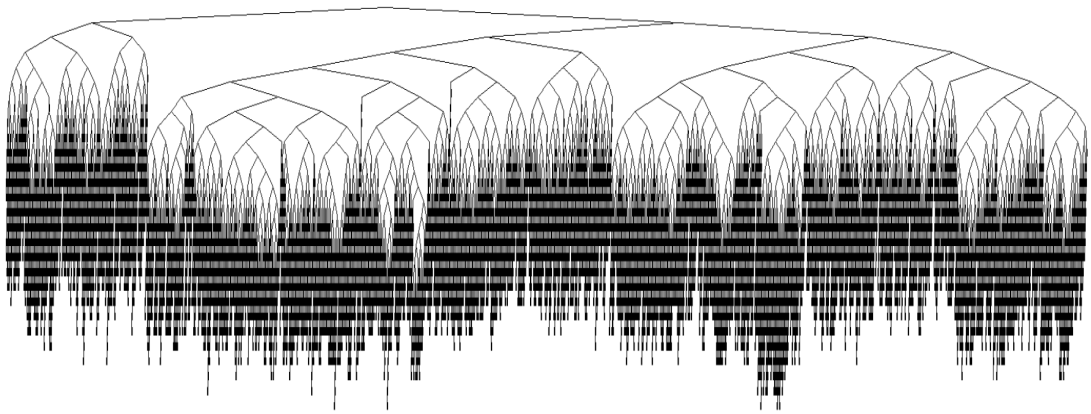

Figure 1.3: Evolution of a Branch and Bound tree with thousands of nodes required for an optimal solution (Belotti et al., 2012).

Presolving includes problem reduction methods (LP-presolve reduction or MIP specific reduction), which are applied to reduce the problem size and to tighten the formulation. Without techniques such as these, a significant increase in the tree size (Fig. 1.3) within a few seconds of starting the optimisation computations could ensue depending on the problem complexity. Furthermore, the speed of convergence to an optimal solution is dependent on how fast an incumbent solution is found; many solvers apply several heuristic measures to simultaneously probe different nodes of a search tree for the extraction of a feasible integer solution. Parallelisation of MIP algorithms is another critical feature that has enhanced solver performance; high-dimensional models with a

large search space can be configured to efficiently exploit processing cores, with a significant reduction in computational time (Gurobi, 2020).

Table 1.1. Methods applied for production optimisation (adapted from Grimstad, 2015).

Characteristics	**LP**	**MILP**	**NLP**	**MINLP**	**DFO**
Objective	Linear	Piecewise Linear	Nonlinear	Piecewise Nonlinear	Any
Constraints	Linear	Piecewise Linear	Nonlinear	Piecewise Nonlinear	Possible for some DFO methods
Achievable Accuracy	Low	Intermediate - High	Intermediate - High	High	High
Discrete Decisions	No	Yes	No	Yes	Possible for some DFO methods
Derivatives Required	Yes	Yes	Yes	Yes	No
Complexity Class	P	NP-Hard	P (NP-Hard)	NP-Hard	–
Expected Speed	Fast	Fast or Slow	Fast or Slow	Slow	Slow
Convergence	Global	Global	Global**	Global**	Local*

* Not guaranteed for all DFO methods; ** Global solver required for non-convex problems; favourable properties are highlighted blue.

These solvers (Table 1.2) have been implemented in different programming languages, available as standalone executables or readily accessible libraries from algebraic modelling software (e.g. GAMS, AMPL and AIMMS). The direct implementation of other solvers in programming languages like MATLAB and Python also enables their accessibility and interoperability. The differences in the optimisation platform make it difficult to simultaneously harness the computational capabilities of these solvers within a single platform like MATLAB. However, OPTI Toolbox, an object-oriented, flexible interface makes this possible. The implementation of this toolbox (within MATLAB) in this thesis allows seamless integration with several optimisation solvers written in languages like C, C++, GAMS, and Java within the Windows operating system. Table 1.1 illustrates the characteristics of the different formulations used in production optimisation problems.

Table 1.2. Summary of the formulations, algorithms and solvers applicable to production optimisation problems.

Linear Programs (LPs)	**Mixed-Integer Linear Programs (MILPs)**	**Nonlinear Programs (NLPs)**	**Mixed-Integer Nonlinear Programs (MINLPs)**	**Stochastic Programs**
$\min_x F^T x$ Subject to $Ax \leq b$ $A_{eq}x \leq b_{eq}$ $l_b \leq x \leq u_b$	$\min_x F^T x$ Subject to $Ax \leq b$ $A_{eq}x \leq b_{eq}$ $l_b \leq x \leq u_b$ $x_i \in \mathbb{Z}$ $x_j \in \{0,1\}$	$\min_x f(x)$ Subject to $Ax \leq b$ $A_{eq}x \leq b_{eq}$ $l_b \leq x \leq u_b$ $c(x) \leq d$ $c_{eq}(x) \leq d_{eq}$	$\min_x f(x)$ Subject to $Ax \leq b$ $A_{eq}x \leq b_{eq}$ $l_b \leq x \leq u_b$ $c(x) \leq d$ $c_{eq}(x) \leq d_{eq}$ $x_i \in \mathbb{Z}$ $x_j \in \{0,1\}$	$\min_x f_1(x) + E\{f_2(x), w\}$ $g_1(x) \leq 0, \ldots g_m(x) \leq 0,$ $h_1(x, y(w)) \leq 0, \forall\ w \in W$ ... $h_p(x, y(w)) \leq 0, \forall\ w \in W$ $w \in W, y(w) \in Y$
Algorithms applied to solve these optimisation formulations				
• Simplex • Ellipsoid • Interior Point • Siedel	• Branch and Bound • Gomory Cuts • Benders Partitioning	• Interior Point • Trust Region Reflective • SQP	• Branch and Bound • Extended cutting plane • Extended supporting hyperplane • Outer Approximation • Generalised Benders Decomposition • LP/NLP-based Branch and Bound	• GA • PSO • SPSA • Cooperative Stochastic Approximation
Open source and commercial optimisation solvers applicable to the respective formations				
CLP, CPLEX, Xpress, SCIP, CBC, MOSEK, GUROBI	CPLEX, Xpress, SCIP, CBC, MOSEK, GUROBI	CONOPT, filterSQP, IPOPT, Knitro, LANCELOT, LOQO, MINOS, NPSOL, SNOPT, NOMAD, GUROBI	AlphaECP, ANTIGONE, AOA, BARON, BONMIN, Couenne, DICOPT, Juniper, Knitro, LINDO, Minotaur, SHOT, SCIP, SBB, Pavito, Muriqui, NOMAD, GUROBI	GUROBI, GAMS, FortSP, NEOS, DECIS, Infanger, OptiRisk, MSLiP

F is an $n \times 1$ vector containing the linear objective function; **f** is a scalar function containing the nonlinear objective function; **A** is an $m \times n$ sparse matrix; **b** is an $m \times 1$ vector; **Aeq** is a $k \times n$ sparse matrix; **beq** is a $k \times 1$ vector; $\mathbf{l_b}$ is the lower bound on **x**; $\mathbf{u_b}$ is the upper bound on continuous decision variables **x**; $\boldsymbol{x_i}$ are decision variables which must be integers; $\boldsymbol{x_j}$ are decision variables which must be binary; **c** is a $u \times 1$ vector of functions containing nonlinear inequality constraints; **d** is a $u \times 1$ vector; $\mathbf{c_{eq}}$ is a $v \times 1$ vector of functions containing nonlinear equality constraints; $\mathbf{d_{eq}}$ is a $v \times 1$ vector; **y(w)** is a vector of decisions that represents new actions or consequences of **x**; **E** is the expected value; $\mathbf{h_1 \ldots h_p}$ describe the links between first-stage decisions **x** and second stage decisions **y(w)**; **w** represents the possible outcomes of **y**; $\mathbf{f_1}$ and $\mathbf{f_2}$ are the objective functions.

1.3.4 Research Contributions on the Application of Mathematical Optimisation for Enhanced Production Operations

The highly diverse range of research efforts targeted towards field production optimisation from a reservoir to surface facility perspective can be generally grouped into short-term and long-term optimisation scenarios. A further classification could comprise field studies undergoing primary production and others with some secondary enhancement. Furthermore, some studies consider production optimisation by only analysing hydrocarbon flow from the reservoir to the wellbore without constraints on processing facilities. It is also possible to classify existing studies based on the type of problem tackled, which include: well placement, rate allocation/production planning and scheduling, pipeline and surface facility routing, drilling and drill rig scheduling, infrastructure installation under geological and economic uncertainty. Recently, Tavallali et al. (2016) evaluated the differences in research contributions (relating to production optimisation) from both petroleum and process systems engineering perspectives. In doing this, they grouped research endeavours from both perspectives into 3 main classes: oil field design, oil field operations and integrated field design and operations. In their discussion of this broad classification, subcategory problems such as rig scheduling (Iyer and Grossmann, 1998; van den Heever and Grossmann, 2000; van den Heever et al., 2000; 2001), flow scheduling (Kosmidis, 2005; Gunnerud et al., 2012), field planning (Gupta and Grossmann, 2012b; Tavallali et al., 2014; 2016a; b; Humphries and Hayes, 2014), surface network design and well placement (Wang et al., 2012; Li et al., 2013) were also discussed. A major highlight from this review was the fact that contributions from the petroleum engineering community have primarily focused on the subsurface, whereas, the process systems engineering community has paid more attention to the surface networks. Given the highly interconnected nature of a production system, more work is needed to address the challenges of integrated field design and operation; thus capturing surface and subsurface complexities. A range of previous contributions is however presented, with emphasis on the advancements developed in this thesis in comparison to these contributions.

Barragan-Hernandez et al. (2005), formulated a model for the simulation and optimisation of oil and gas production systems. A one-day operating period was considered in their work. Important phenomena such as reverse flow and critical flow in valves were also modelled using a set of differential-algebraic equations and thermodynamic state

calculations in their adopted case study. Simulators (depending on complexity) could be viewed as functions whose explicit forms are unknown but compute outputs based on some input parameters. Furthermore, the inability of most black-box simulators to compute gradients necessary for the speedy performance of an optimisation algorithm is an additional difficulty. To address this problem, the work of Gunnerud et al., (2013) proposed a disaggregated framework for optimising an entire production network over a short-term horizon at steady-state conditions (a simulation-based optimisation method that incorporates the complex behaviour of production system components via simulator data approximation). This was based on a trust region approach coupled with an MINLP formulation. They demonstrated the superior performance of their approach (in terms of solution quality and runtime) to a standard industry approach where derivative-free optimisation methods (which directly call the black box simulator at each iteration) are used. However, their approach requires in-depth knowledge of the simulator, especially when large production networks with complicated nonlinear behaviours of the components are to be optimised. This framework, which is adopted in this thesis, analyses the entire system as a combination of wells, pipelines and separators. Several rigorous model approximation methods, such as linear interpolation, spline interpolation, algebraic proxy modelling and SOS2 approximations have been implemented in similar works (Gunnerud and Foss, 2010; Gunnerud et al., 2012; Gunnerud et al., 2013; Kosmidis et al., 2004; Kosmidis et al., 2005). Silva and Camponogara (2014) addressed the optimisation of gas lifted wells under facility, routing and pressure constraints. Single-dimensional and multidimensional piecewise approximations for pipelines and wellbores were used to compute pressure drops. As demonstrated by Codas et al., (2012), integrated production optimisation problems can be solved speedily for real-time application. Their optimisation framework considered a production system with complex routing, capacity and pressure constraints with wells exhibiting gas coning behaviour. Despite these proposed developments, little attention is given to fields undergoing secondary production.

Tavallali et al., (2013; 2014; 2015), tackled a well placement, production planning, and facility allocation optimisation problem using an open box approach that involved a problem-specific modification of the outer approximation algorithm proposed by Grossmann and co-workers (Duran & Grossmann, 1986; Kocis & Grossmann, 1987; Viswanathan & Grossmann, 1990). Furthermore, long-term infrastructure planning and

production scheduling challenges have also been addressed in several works of Grossman via complex MILP and MINLP formulations (Iyer and Grossmann, 1998; van den Heever and Grossmann, 2000; van den Heever et al., 2000; 2001; Gupta and Grossmann, 2012). Although the productivity index of wells in a field is bound to change with time in practical field operations, the work of Iyer and Grossmann, (1998) assumed a constant productivity index (PI) for all the wells across a long-term horizon. A time-dependent PI approach is thus adopted in this thesis as an improvement strategy. An adaptive simulated annealing algorithm was employed in the work of Azamipour et al., (2017) for the production optimisation of a field undergoing water injection. Optimisation time reduction was attained by sequentially implementing coarse and fine grids without considerable loss in model accuracy. In a subsequent work of theirs (Azamipour et al., 2018), they improved the optimisation approach by using a hybridised Genetic Algorithm. As part of their improvements, streamline simulation was also adopted for the determination of good initial guesses for the water injection rates. However, they (Azamipour et al., 2018), do not account for the surface facilities in their optimisation study. Furthermore, multiphase flow complexity in deviated well geometries is generally not considered.

Decline Curve Analysis (based on real production data) has also been combined with production optimisation for fast prediction of future operating rates in the work of Kritsadativud et al. (2015). The motivation for this approach was to eliminate the enormous time requirements in developing detailed numerical reservoir models, and the difficulty of using such models for optimisation purposes. Although their method does not adequately capture the underlying flow physics, they argue that it could provide reasonable initial solutions for subsequent large-scale optimisation problems with full reservoir simulation. Despite the widespread application of ESP artificial lift systems in petroleum field operations, production optimisation studies, which consider these well types, are very scarce. To the best of our knowledge, only the work of Hoffmann and Stanko (2016) addresses this kind of wells in the context of production optimisation. They formulated a Mixed Integer Linear Program (MILP via piecewise linearisation), which determines the ESP performance characteristics for the different wells in their production network. The fast solution times they reported, demonstrated the real-time applicability of their formulation. However, representing the exact model characteristics via nonlinear

constraints is an important attribute of this thesis; hence the formulation of a solvable Mixed-Integer Nonlinear Program (MINLP).

A multiperiod MINLP formulation was established by Gupta and Grossmann (2012) for the optimal planning of oilfield (offshore) infrastructural development over a 20-year production horizon. The resulting formulation yielded good solutions when solved with MINLP solvers, DICOPT, SBB and BARON. They also presented a reformulation strategy of their MINLP problem into an MILP via binary reduction and elimination of bilinear terms; thus obtaining globally optimal solutions. Epelle and Gerogiorgis (2019a) presented an MINLP formulation for real-time optimisation of a production system with wells of different types. They considered gas lift, ESP-assisted and naturally flowing wells of complex geometries with the potential for sand production. They obtained rapid computations using the BONMIN solver. An integrated approach for production optimisation from multiple offshore reservoirs in the Santos Basin of Brazil was presented by Camponogara et al. (2017). Their approach relied on a reformulation of an MINLP problem to an MILP via piecewise linear approximations which served as proxy models for each production unit.

Silva et al. (2015) modelled flow splitting of well fluids to multiple headers and embedded this model in an MILP formulation via piecewise linearisation for production optimisation purposes. Piecewise reformulations of MINLPs have also been applied in several other studies (Gerogiorgis et al., 2009; Kosmidis et al., 2005; Aguiar et al., 2014; Codas et al., 2012; Gunnerud et al., 2012; Silva and Camponogara, 2014). Rodrigues et al. (2016) developed a new formulation called the Multicapacitated Platforms and Wells Location Problem (MPWLP) and solved it as an MILP using the CPLEX solver. The solution to this model provides the number and locations of production platforms, wells and manifolds, the capacities of the production platforms, the interconnections between platforms, manifolds and wells, and which sections of each well should be vertical or horizontal. Zhang et al. (2017) developed a unified MILP formulation for obtaining the best possible topological structure in a production gathering network consisting of wells and pipelines under operational constraints. Their model (solved using MINLP solvers in GUROBI) facilitates the development of field planning schedules.

The application of mathematical optimisation to well placement problems has generally been carried out using gradient-based approaches (based on adjoint methods and finite differencing), mixed integer programming (MILPs/MINLPs), simulated annealing, genetic algorithms, cat swarm optimisation and particle swarm optimisation (Bangerth et al., 2006; Onwunalu and Durlofsky, 2010; Tavallali et al., 2013; Isebor et al., 2014; Hongwei et al., 2019; Tavallali et al., 2016b). Simultaneous parametric optimisation of well patterns, well types and location have received considerable attention in the past decades (Yeten et al., 2003; Onwunalu and Durlofsky, 2010; Yasari et al., 2013; Fan et al., 2018). In these studies, the well arrangements are constrained by repeated patterns which are common in industrial field operations (5-spot pattern, 7 spot pattern, and 9 spot pattern). Ciaurri et al. (2011) applied a PSO algorithm for perturbing well locations within four pre-defined patterns in a repeated manner. Although this procedure may force some wells that were initially within the reservoir boundary to be shifted out, thus leading to suboptimal results. However, this approach was shown to be more computationally tractable than an exhaustive approach. A 22% increment in NPV was attained by performing a well-by-well perturbation compared to well placement optimisation via well pattern description.

Ciaurri et al. (2010) performed a computational analysis of non-invasive derivative-free optimisation methods to some production optimisation problems of practical relevance. Their findings indicate that the Hooke-Jeeves direct search (HJDS) is the recommended approach when distributed computing resources are unavailable. They also highlighted that a rigorous iterative process is often required when handling constraints using the penalty function method; a filter-based method was proposed as a reliable alternative when hybridised with a generalised pattern search procedure. It was shown in the work of Onwunalu and Durlofsky, (2010), that the PSO algorithm (with fewer function evaluations) represents a viable alternative to the widely adopted GA algorithm for well placement problems. A benchmarking study by Minton (2012) arrived at a similar conclusion for the PSO algorithm (in comparison to GA). Other methods, such as the simulated annealing and hill-climbing algorithms, showed poor performance.

Jesmani et al. (2016) introduced a decoder method for handling constraints in well placement optimisation problems. The decoder procedure maps the feasible search space onto a cube; thus avoiding repeated parameter tuning. When compared with the penalty

function method, it was shown in most cases that the decoder method outperforms the penalty function method. A joint approach for well placement and control optimisation was proposed by Bellout et al. (2012). Derivate-free (pattern search) methods were adopted for the well placement problem, whereas, sequential programming using adjoint-computed gradients was implemented for determining optimal well controls. They realised up to 20% increment compared to sequential methods, although with an order of magnitude increase in the number of function evaluations. A hybrid algorithm that utilises PSO and GPS was applied for the simultaneous optimisation of well placement and controls in the work of Humphries and Haynes (2014). They compared the quality of solutions obtained using a joint approach and a decoupled/sequential approach. They discovered that in 3 out of 5 experiments, the decoupled approach found better solutions than the joint method. Isebor et al. (2014) developed a hybrid PSO-MADS algorithm that outperforms standalone MADS and PSO procedures and a relaxed Branch and Bound method (B&B) when solving a well placement optimisation problem formulated as an MINLP. The B&B method was the computationally least efficient (with the highest number of iterations required).

The reduction of computational complexity using proxy models in well placement optimisation problems has also received some attention, with crucial contributions from Guyaguler (2002) and Pouladi et al. (2017). Kriging and fast marching methods were respectively applied. Furthermore, several studies (Bouzarkouna, 2012; Wang et al., 2012; Li et al., 2013) have accounted for uncertainty using stochastic optimisation techniques, such as GA, PSO, Covariance Matrix Evolution Strategy (CMA-ES) and Simultaneous Perturbation Stochastic Approximation (SPSA). Uncertainty reduction (selection of a subset of geological realisations from a superset) has also been applied for computational time reduction in the work of Rahim and Li (2015). Their well placement optimisation problem was formulated as an MILP and solved using the NOMADS optimiser (Nonlinear Optimisation with MADS algorithm).

Research contributions that tackle well placement optimisation problems using gradient-based optimisation methods are scarce. Zandvliet et al. (2008) introduced an adjoint method for computing gradients using pseudowells. The main advantage of this algorithm over previous approaches is that, improved directions for all wells are computed only in one forward and backward simulation. It was discovered that the algorithm converges to

similar optimal NPV values with different initial well locations. This gradient-based method was extended by Wang et al. (2007); in their algorithm, the optimisation problem is initialised by adding an injection well to every grid block that does not contain a production well. This number of injection wells is successively reduced by assigning a drilling cost to each well and constraining the total maximum injection rate that should be allocated to all injection wells remaining at each iteration.

By developing a continuous functional approximation to an original discrete-parameter well placement problem, Sarma et al. (2008) applied gradient-based algorithms to determine optimal well locations efficiently. Kourounis et al. (2014) developed adjoint procedures for general compositional problems (which are more challenging than oil-water systems). They successfully applied these procedures with a new heuristic method of handling constraints in a gradient-based optimisation framework to optimise well controls using different real field examples. More recently, Volkov and Bellout (2018) introduced a novel gradient-based approach, which utilises finite difference approximation of augmented Lagrangian derivatives. They coupled their adjoint formulation with a Sequential Quadratic Programming (SQP) solver, which enabled fast convergence and efficient constraint handling. A more comprehensive summary of key research contributions on drilling and production modelling and experimentation is presented in Tables C.1 to C.5.

Chapter 2 PhD Project Motivation

Drilling and production are multi-billion dollar investments which constitute a significant fraction of a field's entire operating and capital expenditure. This chapter discusses several operational problems that arise during drilling and production activities; thus motivating the work herein. It is also worth mentioning that these problems often occur at subsurface locations (kilometres downhole) away from the physical reach of field engineers. This has led to the development of sophisticated remedial technologies which must be implemented from afar. In this chapter, not only are these operational difficulties presented, the scope for improvement in a variety of experimental and computational techniques adopted by the oil and gas industry is also evaluated.

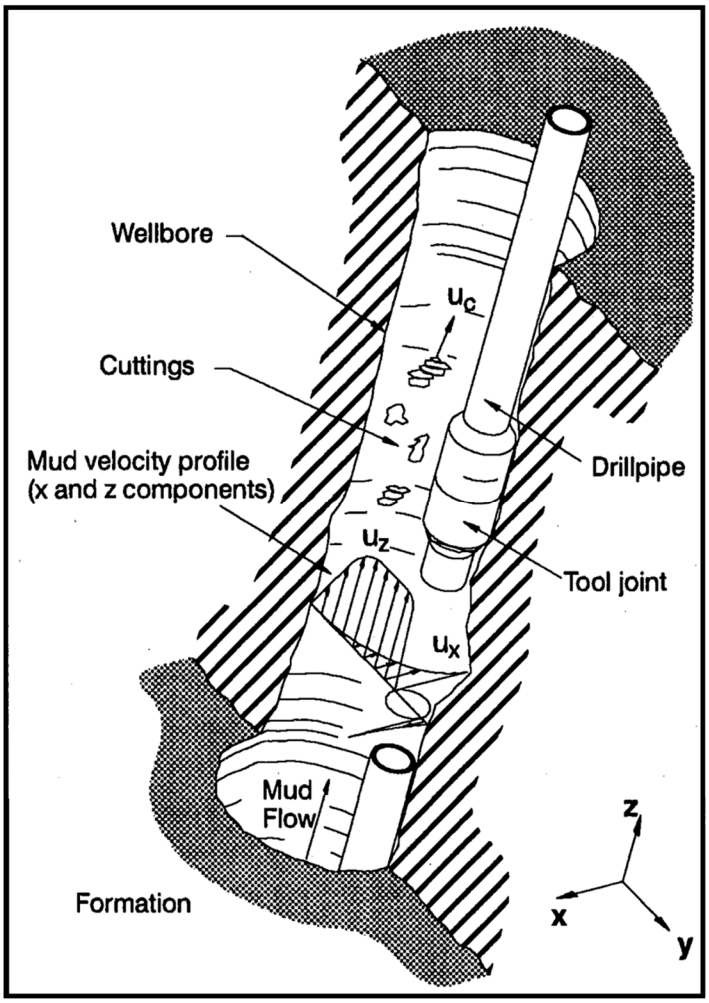

Figure 2.1. Particle transport in the presence of a mainstream non-Newtonian fluid during drilling operations (Clark and Bickham, 1994).

2.1 Challenges of Drilling Operations

Excessive drill pipe torque, slow drilling rates, pressure instabilities, stuck drill pipe (Fig. 2.1) and lost circulation are some of the operational challenges faced by drilling engineers (Sorgun, 2010; Caenn et al., 2011). These problems culminate to an increased overall cost, reduced efficiency of the drilling process, unwanted fluid influx, a severe interruption for days and sometimes an entire abandonment of the well. In the following section, a detailed discussion of these problems is presented with some real field observations.

2.1.1 Stuck Drill Pipe and Slow Drilling Rates

Well drilling in the oil and gas industry is usually done with a highly flexible rotating drill string (to which the drill bit is attached), and this produces a trajectory that is never perfectly vertical. This implies that the drill pipe makes contact with the walls of the wellbore (Fig. 2.1) at numerous positions several meters downhole (Caenn et al., 2011). Thus, frictional resistance generated may require extra torque than otherwise required to turn the drill pipe and the bit; this translates to unacceptable power consumption.

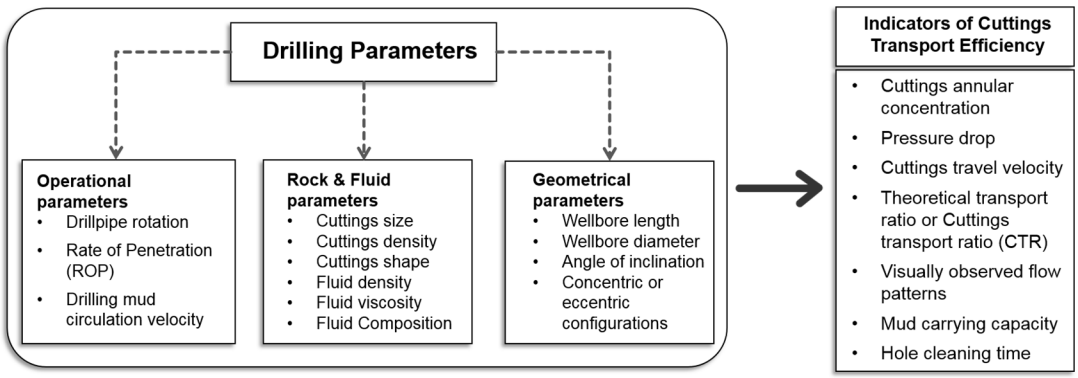

Figure 2.2. Factors affecting drill cuttings transport efficiency.

Similarly, the drill string's tripping (lowering into and pulling out of the wellbore) movements often causes a differential sticking effect on the mud cake (residue generated from drilling mud due to pressure difference between the formation and the wellbore) deposited around the borehole wall. This causes the drill string to be trapped, and the pulling power of the rig is unable to release the string from the mud cake (Bailey et al., 2000). Loosely compacted and fractured formations and gravels may also collapse into the wellbore as drilling progresses, thus forming a bridge around the drill string or jamming the drill string. The clay swelling effect of certain reactive formations in contact with water-based muds may also constrict the wellbore. Poor hole cleaning, which causes

cuttings accumulation, may also cause stuck pipe problems (Epelle and Gerogiorgis 2017; 2018a). Understanding the interdependence between several drilling parameters (Fig. 2.2) is necessary for the prevention of this problem.

Due to the complex geological properties of most reservoirs, it is expected that the layers of rock formations will vary in their hardness. This translates to different penetration rates of the drill bit through these layers. The mechanical performance of the drilling machinery as typically indicated by the quality of drill bit and extent of penetration attainable will primarily affect the overall efficiency of the operation. Furthermore, since drilling muds, cool, lubricate, and transmit hydraulic energy to the drill bit, the rheological properties of these fluids largely affect the bit penetration rate. In 1993, the Dutch petroleum company (Nederlandse Aardolie Maatschappij – NAM) reported several significant cost overruns due to stuck drill pipe problems (Hopkins and Leicksenring, 1995; Massie et al., 1995). According to the report, the cost incurred to handle stuck equipment incidents amounted to US$15 million (5% of entire drilling capital expenditure). These problems are likely to increase despite technological advancements over the last decade. This is because of the ever-growing complexity of exploration activities (large diameter wellbores with high inclination angle, extended-reach and multilateral structures) in challenging offshore environments with very harsh conditions such as the Arctic.

2.1.2 Complex Wellbore Geometries

Drilling wells with deviated/horizontal geometries and multiple branches to improve recovery from multiple reservoir zones by commingling production have become common in the oil and gas industry. A successfully designed and implemented multilateral well that replaces several vertical wells may drastically reduce the overall completion costs; thus enhancing field profitability. However, the accompanying complexities of these well types increase the risks of failure (Economides and Nikolaou, 2011). Compared to vertical wells, sophisticated mechanical steering tools are required to ensure the planned trajectory is attained. Hence, correctly positioning and maintaining the horizontal well section within the target reservoir (layer) thickness is of utmost concern to drilling engineers (Bosworth et al., 1998; Gravdal et al., 2010). Furthermore, ensuring proper zonal isolation in each of the well sections is also a major challenge with horizontal and multilateral wells. If the drilling crew fails to maintain zonal isolation, downhole annular pressure control becomes extremely difficult, and blowouts may occur. Depending on the well perforation intervals

adopted, these wells may be subsequently exposed to production-related problems such as water and gas coning and sand production. Hence, challenges of deviated well drilling are influenced mainly by the expected fluid delivery rates of the well.

2.1.3 Lost Circulation

Lost circulation is the migration of drilling fluids through the pores, fissures and high permeability zones in rock formations. The loss of drilling fluids and its accompanying problems represent a major fraction of the total drilling cost in most fields. Calcada et al. (2015) reported that drilling fluids of varying compositions represent 15-18% of the total drilling cost. In turn, 10-20% of the total cost of production and exploration wells can be attributed to lost circulation. It is estimated that over 2 billion USD is spent annually in combating and mitigating the problem of lost circulation (Arshad et al., 2015).

According to Waldmann et al. (2012), 1 out of 3 wells drilled by PETROBRAS have lost circulation problems. This generates additional net costs and in extreme cases, compromises completion integrity, operational safety and the environment, thus increasing non-productive time. Palsson et al. (2014) described a series of lost circulation events in the drilling of a geothermal well in the Krafla field in Iceland (designed to reach a depth of 4500 m). Over 60 L/s of mud losses occurred at a depth of 2,043 m; the drilling team could not stop this, and the remedy was to replace the mud with water. Breakage of the bottomhole assembly occurred at 2,101 m; due to unsuccessful fishing, the well was eventually sidetracked and terminated.

2.1.4 Wellbore Stability Challenges

During drilling, several process disturbances that could cause pressure fluctuations might occur, and drilling operators must ensure that a safe operating pressure window is maintained for the avoidance of formation fracturing and unwanted fluid influx/kicks. The small tolerance between pore pressure and fracture pressure gradients is of paramount concern to drilling engineers (Zhou et al., 2009; Zhou et al., 2010; Aarsnes et al., 2016a). As drilling progresses, the well length increases and the wellbore is exposed to more of the formation's high pressure. This gradual-to-rapid exposure (depending on the penetration rate) constitutes a disturbance to the overall system's stability that must be controlled. Another complication is that downhole measurements are usually unavailable, and mostly topside measurements (such as the inlet pressure at the well choke and

standpipe) can be utilised for control purposes (Breyholtz and Nikolaou, 2012; Hauge et al., 2013).

Since the Macondo catastrophe, the level of automation in the oil and gas industry has continued to evolve due to severe economic implications and stringent health and safety standards/constraints. This has paved the way for the advancements and implementation of control methods in the oil and gas industry, given the highly complex extended-reach and multilateral wells the industry must drill to access oil and gas in harsh environmental and climatic conditions. Event detection (e.g. kicks) and post-drilling data analysis require the application of sophisticated downhole sensors. Challenges such as repeated rigorous calibration, sensor drift, poor-quality data at extreme downhole conditions, high cost and false alarms that exist in real field operations provide opportunities for performance improvements of these devices.

2.1.5 Hydrate Bearing Zones

Hydrate bearing zones and sediments are occasionally encountered during operations (Østergaard et al., 2000; Jiang et al., 2011; Golmohammadi and Nakhee, 2015). If this is the case, gas hydrate dissociation occurs, and gas released erodes the drilling pipe, thus increasing the risk of mechanical failure. In addition to this risk, the mud density is reduced, and there could be uncontrolled flow (potentially leak to the seafloor) and ultimately a blowout of the well (Zhang et al., 2019). A comprehensive geotechnical investigation was carried out by Shell to evaluate the potential of drilling difficulties due to gas hydrates in the Gumusut-Kakap offshore development in Malaysia (McConnell et al., 2012). This was done using logging while drilling (LWD) techniques coupled with rigorous seismic interpretations. The presence of hydrates was observed from the abnormal LWD responses and the gas bubbles produced at the wellhead during drill pipe connections.

2.1.6 Modelling and Simulation Challenges

Drilling fluids or drilling muds generally have many functions (cooling and cleaning the drill bit, maintaining wellbore stability and cuttings removal) and also contain many performance-enhancing substances (such as polymers and nanoparticles) as shown in Fig. 2.3. This complicates their overall rheological behaviour, thus making them non-conformant to Newtonian fluid behaviour.

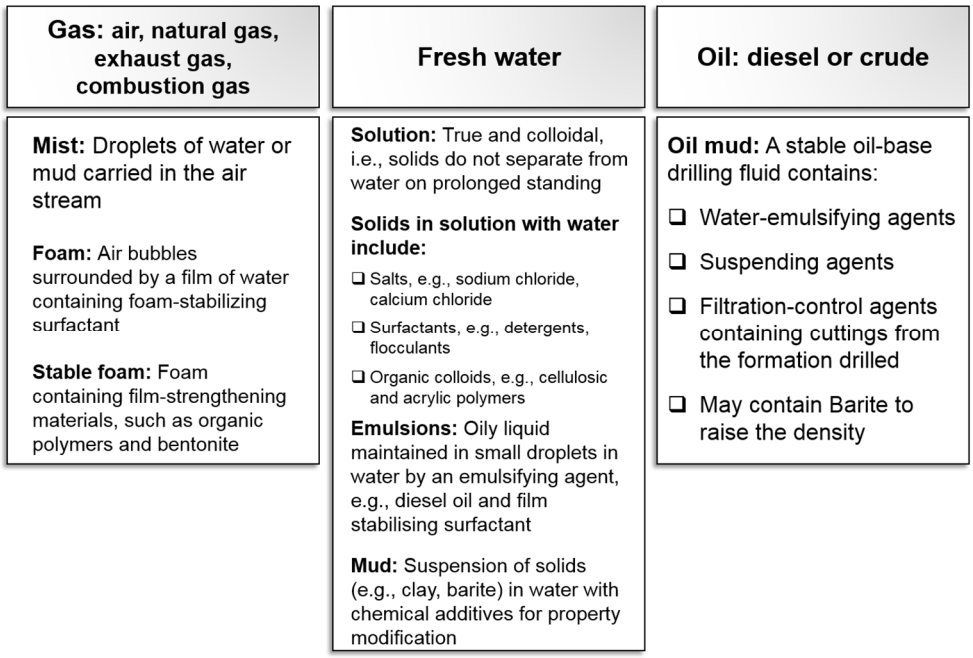

Figure 2.3. Classification of drilling fluids according to their principal constituent (Caenn et al., 2011).

Although the performance of these fluids is mostly understood through experimental measurements of their shearing behaviour, non-Newtonian rheological models such as the Power Law, Herschel Bulkley and Bingham Plastic models may also provide useful insights if well parameterised. This is in itself an optimisation problem that must be solved for the development of validated CFD models. The industrial application of supercritical fluids and nanoparticles at harsh (high pressure and high temperature) operating conditions with performance deterioration tendencies also represents a formidable challenge for these models.

Several one- and two-dimensional models have been developed to study multiphase flow phenomena during drilling (mainly cuttings transport) with a few successes obtained on comparing results of these models with experiments. However, the application of three dimensional CFD methods to drilling operations is still an emerging field with some vital flow phenomena not yet studied (such as the effect of particle shape, size, polydispersity and complex well geometries on multiphase annular flow). The accompanying spatiotemporal visualisations obtainable via this approach also make it possible for direct qualitative comparisons with experimental observations. 4-way coupling between fluid and particles and the inclusion of particle-particle interactions via DEM models is also an area needing further investigations. Particle sizes employed thus far in most modelling

studies also fail to cover the range obtainable in real-field operations. The interpretation of flow phenomenon based on volume averaged analysis of flow properties across the entire domain also pave the way for region-specific analysis for better insight as demonstrated in this work.

Although 3D approaches have the potential for increased accuracy, their applicable for real-time decision support is still a significant challenge. 1D calibrated methods (based on drilling data) have the potential for enhancing drilling operations. Other model reduction strategies that retain high-fidelity model accuracy are paramount for real-time evaluation of drilling operations and thus motivate the work herein. Furthermore, enhanced experimental procedures with sophisticated instrumentation are needed to capture flow effects in hardly-accessible regions for validation purposes to increase model fidelity.

2.2 Challenges of Managing Complex Decisions during Production Operations

Daily production activities are typically faced with a variety of challenges that require intelligent systems engineering techniques integrated with intuitive engineering judgement. This project is thus motivated by the prevalence of sub-optimal heuristic-based methods for enhancing production operations in the upstream oil and gas industry and aims to address this by developing robust process systems engineering methods.

2.2.1 Reservoir Deliverability and Uncertainty

Reservoir deliverability is generally dependent on the reservoir pressure, permeability, porosity, well radius, fluid properties, pay zone thickness, near-wellbore conditions and the nature of the reservoir boundary and distance. Since it is difficult to know the exact spatiotemporal variation or distribution of the reservoir properties over a particular region, geological uncertainty becomes an inherent challenge of petroleum production. For example, the existence of a sealing fault might be unknown to the reservoir and production engineering team; thus leading to poorly placed wells and consequently, reduced production rates (below the estimated productive potential). Water and gas coning due to poorly perforated completions are some of the many flow mechanisms that may also negatively impact production. Unfortunately, the engineer's understanding of the field at its early life is limited due to scarce production data. However, as more data becomes available, history matching can be performed with a reduction in the field's

uncertainty; thus leading to more reliable forecasts of the field's production. Ensuring excellent reservoir deliverability in the presence of this inevitable uncertainty constitutes a research gap that warrants the presented contributions in this project.

2.2.2 Liquid Loading and Artificial Lift

A field's fluid deliverability is not only dependent on favourable reservoir properties (permeability and porosity), but also on the well's capability to lift the produced fluids to the surface. The accumulation of reservoir fluids in the tubing, due to gravity and fluid density is called liquid loading. If not addressed promptly, the production rates from such a well can be severely hampered and the well, eventually killed. Artificial lift methods such as gas lift (which aerates the fluid) and pumping mechanisms, can be installed downhole to reduce the hydrostatic head in the liquid column; thus increasing production. However, the main question to answer here is: how much gas should be injected and what should the pump specifications be? These questions are vital because excessive gas injection could cause a prohibitively high-pressure loss in the tubing; thus overcoming the hydrostatic pressure again. Furthermore, Electrical Submersible Pumps are expensive and require proper selection for optimum results.

2.2.3 Flow Assurance

Flow assurance evaluates the potential of hydrocarbons to disrupt field operations due to deposition and instabilities in a flow system. This problem occurs in many forms and may significantly impact production rates, sometimes causing full blockage of flow conduits. Impeded hydrocarbon flow could occur in the form of hydrates, wax, asphaltenes and scale deposits including phenomenon like slugging, corrosion, sand production and erosion in wellbores, subsea risers, flowlines, pipelines, and other process equipment. Multiphase flow modelling under these conditions is indeed challenging considering the unconventional flow geometries created once these flow restrictions are in place. Analytical methods developed for quick assessment of flow efficiency are mostly appropriate for circular geometries and thus become inapplicable under these conditions (Chin, 2001). Consequently, engineers are often faced with questions like: how much production is lost due to these obstructions? What pump pressures are required to maintain production? Can flow blockage be inferred from flowrate versus pressure drop data? How fast can we obtain solutions for the flow field and productivity indexes for the respective wells? Some of these questions are addressed in this project.

2.2.4 Finding Optimal Field Settings

The decisions that characterise the operation of a petroleum field are highly interconnected. How much oil should be produced to guarantee long-term sustainability and profitability? Which wells should be allocated the highest injection rates? What is the optimal choke setting? What are the best well-to-manifold and pipeline-to-separator connections? Where should new wells be drilled? These questions represent some of the challenging decisions to be made on a daily, monthly and yearly basis. The answers to these questions have mainly been provided through heuristic-based approaches, which yield solutions that are mostly field-specific. Furthermore, as operating conditions change, the production strategy becomes outdated and must be updated to reflect the dynamic behaviour of the entire production system (Ursin-Holm et al., 2014). This motivates the development of a robust and flexible framework for determining optimal field settings in real-time; such a method would have an increased potential for its implementation across fields with very different properties.

2.2.5 A Computational Perspective: Coupling Production System Components Operating at Different Time Scales & Dimensionality Problems

It could take months for significant flow changes (in terms of the gas-oil ratio and water cut) to occur in a reservoir. Conversely, flow in the wellbore and pipelines are prone to changes over a shorter time frame (hours, days, or weeks). Thus, it can be stated that a production system consists of components with both fast-paced and slow-paced dynamics. It is safe to assume that the flow conditions are constant over a short-term optimisation horizon. However, coupling the dynamic responses of these components within a single optimisation framework over a long-term production horizon is a formidable task. This problem of handling components that operate at multiple time scales is under continuous development in literature and motivates the work in this project. These systems often involve a broad range of variable types (continuous, discrete and random) for their mathematical description, thus resulting in highly non-convex MINLPs. This class of optimisation formulations have the capability of modelling discrete decisions, and highly nonlinear and challenging flow phenomena (such as coning). Despite this advantage, MINLP problems are challenging to solve because they integrate all the complexities of their subclasses: the combinatorial nature of mixed-integer problems and the difficulty of solving highly non-convex nonlinear programs (Bussieck

and Pruessner, 2003). Furthermore, the number of system components and the variables describing the respective components, make production systems optimisation prone to combinatorial explosion; otherwise termed – the curse of dimensionality. This is the rapid increase in problem complexity due to the interdependencies (increasing number of possible combinations) of the system inputs, constraints and bounds. The nature of the optimisation formulation affects the magnitude of this problem. For example, Reformulated MILPs (via special ordered sets) based on original MINLPs often suffer more from this problem when the system size increases compared to the equivalent MINLP formulations.

2.3 Thesis Aims and Objectives

Sustained wellbore cleaning and production optimisation constitute longstanding objectives within the petroleum industry, with only incremental advances observed over the past decades (as highlighted in Chapter 1). Furthermore, the operational and mathematical modelling challenges described in this chapter indicate that the industry is still in search for new technologies, capable of providing viable and sound solutions for improved understanding of flow phenomena and optimal decision making in its operations. Thus, this research aims to improve field planning and development decisions from a process systems engineering perspective via fluid dynamics simulations and model-based deterministic optimisation of drilling and production operations, respectively. In addition, the potential for this optimisation methodology to outperform classical heuristic methods currently adopted in the industry is also demonstrated. The specific objectives outlined next, illustrate the systematic workflow adopted to fulfil the project aims from both drilling and production perspectives.

2.3.1 Drilling Perspective

2.3.1.1 Annular Geometry Design and Rheological Analysis

Before performing CFD computations in this project, it is essential to screen candidate flow geometries (vertical, inclined and horizontal) to ascertain the flow regimes which are prevalent and the peculiar transport phenomenon they provide. Cuttings transport along complex geometries with bends (which are typical in deviated drilling operations) has been scarcely studied; this also provides an incentive to examine cuttings transport under this condition further. Furthermore, the determination of the annular flow performance of non-Newtonian fluids is essential in the planning and design of the hydraulic program of

a wellbore. Thus, determining the appropriate rheological model and accompanying parameters of the drilling fluid is essential to this PhD project.

2.3.1.2 Test of Grid/Mesh Independent Solutions

Depending on the adopted meshing style (hexahedral or tetrahedral), ensuring that CFD solutions are mesh-independent is a vital step that yields increased accuracy. Although the application of high-resolution meshes, depends on the availability of High-Performance Computing (HPC) facilities, a trade-off between solvability and accuracy has to be maintained if useful results must be produced in a reasonable time. This project strikes a balance between these two concepts by implementing the HPC facility of the University of Edinburgh (Eddie mark 3) for developing accurate models and generating grid-independent results.

2.3.1.3 Experimental Data Acquisition for Model Validation

This work also conducts several experimental validation tasks to justify the choice of the fluid and particle treatment methods in the simulation workflow. Published experimental findings that analyse the impact of a wide variety of drilling parameters are utilised for this purpose. By testing different submodels in the CFD framework, the best performing combinations of models for describing particle transport can be employed to gain a new understanding of the transport phenomena.

2.3.1.4 Sensitivity Analysis for Novel Insights

Based on the validated grid-independent models, sensitivity analyses that capture multi-parametric combinations (not considered before) and their effects on the overall cuttings transport efficiency can be performed. New post-processing methods are developed to analyse fluid-particle transport in critical regions of the annular domain. The prevalence of dense and dilute granular flows and their interdependencies on drilling parameter of interest are also analysed in detail.

2.3.2 Production Perspective

2.3.2.1 Complexity Reduction for Fast Optimisation

In this project, novel insights and improvements of a field's operation are provided by formulating and solving a long-term, multi-period production optimisation problem via simultaneous consideration of production and injection wells with both vertical and deviated geometries. The tools of multiphase flow and reservoir simulation are utilised

for the flow rate and pressure drop evaluation in wellbores and flow lines of the considered production network; extra measures are taken in the adopted simulation methodology to ensure that all flow lines are free from hydrates at the prevalent temperature and pressure conditions. The problem is solved as a nonlinear program (NLP) comprising an economic objective function and several constraints to ensure operational feasibility. The potential of the proposed computational approach for enhancing profitability via production and water injection optimisation is evaluated, thus demonstrating the efficiency and value of the proposed method towards exploring and securing economic benefits.

2.3.2.2 Optimisation of Different Operational Modes

This PhD project also addresses the optimisation of a realistic field with operationally distinct well behaviours (including gas lift and ESP-assisted wells) with potential for sand production. This problem is complicated by the presence of binary routing variables which result in an MINLP formulation with an NPV objective function. The dependence of the obtained solutions on the supplied initial guess is determined, and the scope for global optimisation presented.

2.3.2.3 Enhanced Optimisation via Problem Reformulation

The merits and demerits of MINLP reformulation to MILPs for production optimisation are explored in this PhD project. Piecewise linear approximations (via Special Ordered Sets of Type II) are employed for this purpose. A comparative assessment of both formulation types examines the impact of linearisation breakpoints and problem size on the solution quality, robustness and ease of automation. Several optimisation solvers are implemented and quality assessment provided in terms of the number of nodes, solution time and optimality gap. The computational efficiency of a newly developed optimisation framework by Schlumberger Limited (in PIPESIM®) is also compared against the optimisation approach adopted in this project. Water coning, a rarely-studied multiphase flow phenomenon, is incorporated into the optimisation formulation.

2.3.2.4 Adjoint-Based Methods for Optimal Well Placements

In combination with operational optimisation methods developed herein, this work also addresses an infrastructural planning problem (that of well placement optimisation). A modification to an existing adjoint-based well placement optimisation algorithm is

proposed, with considerations of geological uncertainty. This modification improves the algorithm's versatility to handle both injection and production wells, and also shows potential for increased solution speeds in comparison to other evolutionary-based algorithms. This framework is applied to 2 separate real fields including the popular Norne field in the Norwegian Sea consisting of 30 wells.

PART II: CUTTINGS TRANSPORT MODELLING IN DRILLING OPERATIONS USING COMPUTATIONAL FLUID DYNAMICS

Chapter 3 Steady State Modelling and Multiparametric Analysis of Multiphase Annular Laminar Flows

In this chapter, cuttings transport phenomena in different annular configurations (Fig. 3.1) is investigated using Computational Fluid Dynamics. This is based on the analysis of cuttings concentration, pressure drop profiles, axial fluid and solid velocities as a function of several drilling parameters: hole eccentricity, inclination, ROP, circulation velocity and fluid rheology. A non-Newtonian fluid (power-law) with clearly-defined flow parameters and spherical cuttings of 3 mm diameter are used in the commercial CFD software, (ANSYS FLUENT™ 17.1).

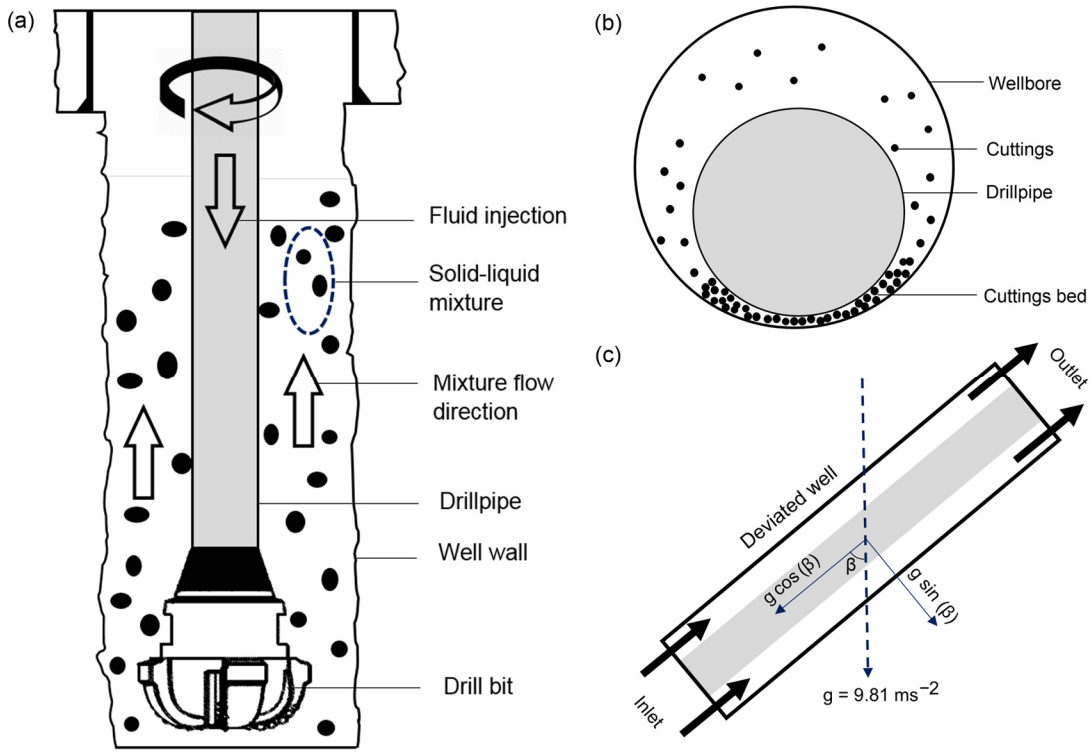

Figure 3.1. Wellbore cleaning operation during drilling.

3.1 Equations of the Eulerian-Eulerian Model

The choice of a multiphase flow-tracking model significantly depends on the governing particle driving force during flow (drag, lift or collision). As earlier shown (Section 1.2), the nonlinearity of these multiphase interactions yields a variety of flow phenomena, which are modelled using two major approaches: the Lagrangian tracking of computational particles coupled with the Eulerian flow description of the continuous

phase and the Eulerian-Eulerian description in which the solid particles are represented as a random field in the Eulerian reference frame (Subramaniam, 2013). The accuracy of mathematical representation, consistency of accompanying closure models and numerical stability are the attributes that make these techniques very applicable. However, the limitation of the Lagrangian-Eulerian (DPM) approach in handling flow systems involving high solids concentration (>12%) makes the Eulerian-Eulerian approach more suitable for the present study. The Eulerian model describes multiphase flows as interpenetrating continua and incorporates the concept of phasic volume fractions represented as α_q. The annular space occupied by each phase is termed the volume fraction, and conservation laws of mass and momentum are respectively satisfied by each phase (Fluent, 2017). The volume fraction of phase q, V_q is given by:

$$V_q = \int_V \alpha_q dV \tag{3.1}$$

where:

$$\sum_{q=1}^{n} \alpha_q = 1 \tag{3.2}$$

The effective density of phase 'q' can be written as:

$$\hat{\rho}_q = \alpha_q \rho_q \tag{3.3}$$

3.1.1 Conservation of Mass

The continuity equation for phase 'q' can be written as:

$$\frac{\partial}{\partial t}\left(\alpha_q \rho_q \vec{v}_q\right) + \nabla \cdot \left(\alpha_q \rho_q \vec{v}_q\right) = \sum_{p=1}^{n} \left(\dot{m}_{pq} - \dot{m}_{qp}\right) + S_q \tag{3.4}$$

3.1.2 Conservation of Momentum

The momentum balance for phase 'q' gives:

$$\begin{aligned} &\frac{\partial}{\partial t}\left(\alpha_q \rho_q \vec{v}_q\right) + \nabla \cdot \left(\alpha_q \rho_q \vec{v}_q \vec{v}_q\right) \\ &\qquad = -\alpha_q \nabla p + \nabla \cdot \bar{\bar{\tau}}_q + \alpha_q \rho_q \vec{g} + \sum_{p=1}^{n} \left(\vec{R}_{pq} + \dot{m}_{pq} \vec{v}_{pq} - \dot{m}_{qp} \vec{v}_{qp}\right) \\ &\qquad + \left(\vec{F}_q + \vec{F}_{lift,q} + \vec{F}_{wl,q} + \vec{F}_{vm,q} + \vec{F}_{td,q}\right) \end{aligned} \tag{3.5}$$

where:

$$\bar{\bar{\tau}}_q = \alpha_q \mu_q \left(\nabla \vec{v}_q + \nabla \vec{v}_q^T\right) + \alpha_q \left(\lambda_q - \frac{2}{3}\mu_q\right) \nabla \cdot \vec{v}_q \bar{\bar{I}} \tag{3.6}$$

$$\vec{R}_{pq} = -\vec{R}_{pq}; \vec{R}_{qq} = 0 \tag{3.7}$$

$$\sum_{p=1}^{n} \vec{R}_{pq} = \sum_{p=1}^{n} K_{pq} (\vec{v}_p - \vec{v}_q) \tag{3.8}$$

3.1.3 Closure Models

Due to the continuum assumption and the averaging property of the Eulerian-Eulerian model, the stress tensor of the solid phase is not explicitly accounted for, and the discrete character of the dispersed phase is often lost; hence, the Kinetic Theory of Granular Flow (KTGF) is used to obtain the solid phase kinematic properties. By so doing, additional closure models are required to re-capture essential aspects of particle behaviour (Shah et al., 2015; Liu, 2014).

Interphase drag and granular viscosity are the main phenomena, which are often considered to obtain solutions, which are well representative of the actual flow physics. In addition, the stress tensor of the solid phase contains shear and bulk viscosities arising from particle momentum exchange due to translation and collision (Fluent, 2017). The frictional viscosity component can also be included to accurately model conditions of very high solid volume fraction. Hence, the total viscosity of the solid phase is calculated as:

$$\mu_S = \mu_{S,col} + \mu_{S,kin} + \mu_{S,fr} \tag{3.9}$$

3.1.3.1 Collisional Viscosity

The collisional component of the shear viscosity proposed by Gidaspow (1994) is modelled as:

$$\mu_{S,col} = \frac{4}{5} \alpha_S \rho_S d_S g_{0,SS} (1 + e_{SS}) \left[\frac{\Theta_S}{\pi}\right]^{1/2} \alpha_S \tag{3.10}$$

3.1.3.2 Kinetic Viscosity

According to Gidaspow (1994):

$$\mu_{S,kin} = \frac{10\rho_S d_S \sqrt{\Theta_S \pi}}{96\alpha_S(1+e_{SS})g_{0,SS}}\left[1+\frac{4}{5}g_{0,SS}\alpha_S(1+e_{SS})\right]^2 \alpha_S \quad (3.11)$$

3.1.3.3 Bulk Viscosity

The bulk viscosity accounts for the resistance the particles possess against compression and expansion during flow. Lun et al. (1984) described this effect as:

$$\lambda_S = \frac{4}{3}\alpha_S^2 \rho_S d_S g_{0,SS}(1+e_{SS})\left[\frac{\Theta_S}{\pi}\right]^{1/2} \quad (3.12)$$

3.1.3.4 Frictional Viscosity

The frictional component of the total solids viscosity applies to dense flows at low shear, in which the solids volume fraction approaches the packing limit and is calculated using the model proposed by Schaeffer (1987).

$$\mu_{S,fr} = \frac{p_S \sin\phi}{2\sqrt{I_{2D}}} \quad (3.13)$$

3.1.3.5 Particle Drag Model

The model proposed by Gidaspow (1994) combines the Wen and Yu (1966) model and the Ergun (1952) equation for accurate solutions. The Gidaspow interphase drag model can also be used for large volume fractions, especially at high ROPs. This flexibility is not offered by the Wen and Yu drag model.

When $\alpha_l > 0.8$, the fluid-solid exchange coefficient, K_{sl}, is calculated as:

$$K_{sl} = \frac{3}{4}C_D \frac{\alpha_S \alpha_l \rho_l |\vec{v}_s - \vec{v}_l|}{d_s}\alpha_l^{-2.65} \quad (3.14)$$

where:

$$C_D = \frac{24}{\alpha_l Re_s}[1+0.15(\alpha_l Re_s)^{0.687}] \quad (3.15)$$

When $\alpha_l \leq 0.8$,

$$K_{sl} = \frac{150\alpha_S(1-\alpha_l)\mu_f}{\alpha_l d_s^2} + 1.75\frac{\alpha_s \rho_l |\vec{v}_s - \vec{v}_l|}{d_s} \quad (3.16)$$

3.1.3.6 Particle Lift Model

The Saffman-Mei lift force model was adopted in ANSYS-FLUENT (Saffman, 1965; Mei and Klausner, 1994). Its applicability to spherical and slightly distorted particles makes it more robust compared to the Moraga (1999) lift force model.

$$C_l = \frac{3}{2\pi\sqrt{Re_\omega}} C'_l \tag{3.17}$$

$$C'_l = 6.46 \; and \; 0 \leq Re_p \leq Re_\omega \leq 1 \tag{3.18}$$

Mei and Klausner (1994) extended the model to a higher range of particle Reynold numbers (Re_p). Hence, the Saffman-Mei model can be empirically represented as:

$$C_l = \frac{3}{2\pi\sqrt{Re_\omega}} C'_l \tag{3.19}$$

$$C'_l = \begin{cases} 6.46 \times f\left(Re_p, Re_\omega\right) & Re_p \leq 40 \\ 6.46 \times 0.0524(\tilde{\beta} Re_p)^{1/2} & 40 < Re_p < 100 \end{cases} \tag{3.20}$$

where:

$$\tilde{\beta} = 0.5(Re_\omega / Re_{p)} \tag{3.21}$$

$$f\left(Re_p, Re_\omega\right) = \left(1 - 0.3314\tilde{\beta}^{0.5}\right)e^{-0.1Re_p} + 0.3314\tilde{\beta}^{0.5} \tag{3.22}$$

$$Re_p = \frac{\rho_q \left|\vec{V}_q - \vec{V}_p\right| d_p}{\mu_q} \tag{3.23}$$

$$Re_\omega = \frac{\rho_q \left|\nabla \times \vec{V}_p\right| d_p^2}{\mu_q} \tag{3.24}$$

3.1.3.7 Frictional Pressure

According to Johnson and Jackson (1987)

$$P_{friction} = Fr \frac{(\alpha_s - \alpha_{s,\min})^{\boldsymbol{n}}}{(\alpha_{s,max} - \alpha_s)^{\boldsymbol{p}}} \tag{3.25}$$

Where coefficient $Fr = 0.05$, $\boldsymbol{n} = 2$ and $\boldsymbol{p} = 5$

3.1.3.8 Solids Pressure

Lun et al. (1984) proposed the following equation for the solids pressure:

$$p_s = \alpha_s \rho_S \Theta_S + 2\rho_S(1 + e_{SS})\alpha_S^2 g_{0,SS}\Theta_S \tag{3.26}$$

Where e_{SS} is the coefficient of restitution for particle collisions; $g_{0,SS}$ is the radial distribution function and Θ_S is the granular temperature.

3.1.3.9 Radial Distribution

The radial distribution function as developed by Lun et al. (1984) is given in Eq. 3.27

$$g_{0,SS} = \left[1 - \left(\frac{\alpha_s}{\alpha_{s,max}}\right)^{\frac{1}{3}}\right]^{-1} \tag{3.27}$$

3.1.3.10 Collisional Dissipation of Energy

The collisional dissipation of energy was also proposed by Lun et al. (1984):

$$\gamma_{\Theta_S} = \frac{12(1 - e_{ss}^2)g_{0,SS}}{d_S\sqrt{\pi}}\rho_S\alpha_S^2{\Theta_S}^{3/2} \tag{3.28}$$

3.1.3.11 Granular Temperature Transport Equation (Algebraic Formulation)

$$\Theta_s = \frac{1}{3}(v_{s,i} \cdot v_{s,i});\ 0\ = \left(-p_S\bar{\bar{I}} + \bar{\bar{\tau}}_s\right): \nabla\vec{v}_s - \gamma_{\Theta_S} + \phi_{ls} \tag{3.29}$$

Θ_s is the granular temperature, $\left(-p_S\bar{\bar{I}} + \bar{\bar{\tau}}_s\right): \nabla\vec{v}_s$ is the generation of energy by the solid stress tensor; γ_{Θ_S} is the collisional dissipation of energy and ϕ_{ls} is the energy exchange between the fluid and solid phases.

Particle concentration is vital for calculating the effective fluid-particle suspension viscosity, which is affected by momentum exchange contributions due to both translation and collision. Moreover, the collisional energy dissipation term within the solid phase due to inter-particle momentum exchange ($\gamma_{\Theta s}$) was derived by Lun et al. (1984) and is adopted in our CFD simulations (Eq. 3.28). For granular flow in the compressible regime (particle concentration is less than the maximum allowable value), a solids pressure can be calculated using Eq. 3.26 and included in the pressure gradient term of the solid phase momentum equation for improved accuracy. A correction factor ($g_{0,ss}$), which modifies the inter-particle collision probability in dense granular flow conditions (Eq. 3.27) is

introduced into the Eulerian model; its physical significance can be thought of as the dimensionless distance between spherical particles. A Maxwell particle velocity distribution is considered, with a granular temperature term, introduced into the solids pressure equation. This granular temperature of the solid phase (Θ_s) is proportional to the kinetic energy of the cuttings random annular motion and is given by Eq. 3.29. The application of the Johnson and Jackson (1987) friction pressure equation (Eq. 3.25) enables accurate prediction of frictional viscosity in dense granular flow conditions (when the particle concentration is near the packing limit).

The finite volume technique was implemented for the discretisation of the flow equations in the ANSYS-FLUENT solver (version 17.1). The capability of this discretisation scheme in ensuring the conservation of mass and momentum at the elementary control volume and the global level (over entire flow geometry), makes it physically consistent and hence more suitable compared to other discretisation schemes. Pressure-Velocity coupling was effected using the Phase Coupled Semi-Implicit Method for Pressure Linked Equations (SIMPLE scheme), and the momentum equations were discretised using the Quadratic Upstream Interpolation for Convective Kinematics (QUICK) routine due to its excellent performance on hexahedral grids (Pereira et al., 2007).

Numerical solutions of the discretised equations and accompanying initial and boundary conditions were obtained after several iterations. The parallel computing feature of the software was activated for faster convergence on four processing cores. A computer with the following specifications was used to run all simulations in this study: (Windows 7, 64-bit operating system, with 16GB RAM, and Quad-Core-i7 processor at 3.40GHz). The tolerance factor was set to 10^{-3} for the continuity and 10^{-4} for all other equations. Fig. 3.3 explains the numerical simulation procedure required to replicate experimental data and obtain fully converged results.

3.2 Fluid Rheology and Annular Flow Geometry

The drilling fluid adopted is a mixture comprising of 350 ml Water, 22.5 g of Bentonite and 2.5 g of Xanthan gum. Experimental flow properties of the non-Newtonian drilling fluid were obtained from the work of Al-Kayiem et al. (2010). The power-law model was used to describe the fluid rheology using the least-squares curve fitting method, as shown in Eq. 3.30. Water is also tested comparatively with the drilling mud for a few case studies

to demonstrate the effectiveness of a non-Newtonian fluid in particle transport during drilling operations.

$$\tau = K\gamma^n \tag{3.30}$$

Table 3.1 summarises the fluid and particles properties used as simulation input parameters; some of which are based on experimental studies of Chen et al. (2007a) and Duan et al. (2010). The flow system considered in this study consists of an inner rotating drill pipe with a diameter of 3.5 in (0.0889 m), and a stationary outer pipe, representing the wellbore with diameter 5.76 in (0.1463 m). A pipe length of 14 m was selected after calculating the hydrodynamic entrance length - L_e (the length required for fully developed flow for all fluid circulation velocities). Shook and Roco (1991) proposed a correlation for calculating the entrance length in the case of single-phase laminar flow as:

$$\frac{L_e}{D} = 0.062Re_t \tag{3.31}$$

where:

$$Re_t = \frac{\rho_f \tilde{u}_m D}{\mu_f} \tag{3.32}$$

No correlation for predicting L_e exists for solid-liquid flow, however, Eq. (3.31) can be used as an approximation of the required entrance length, where D becomes the difference between the drill pipe diameter and the hole diameter. Three separate flow configurations are studied with eccentricities of 0, 0.4 and 0.8, respectively (concentric, moderately eccentric and highly eccentric annuli – Fig. 3.2).

$$e = \frac{2\delta}{D_{hole} - D_{drillpipe}} \tag{3.33}$$

3.3 Mesh Independence Study

Structured hexahedral meshes (Fig. 3.2) were adopted in all flow configurations comprising of approximately 0.93 - 4.5 × 10^6 elements. Edge sizing and face meshing methods were implemented at the inlet and outlet boundaries, thus providing an excellent resolution capable of capturing boundary conditions. It was essential to ensure high orthogonality and low skewness in the mesh; thus, the number of external pipe divisions

were the same as those of the internal pipe. Table 3.2 shows the mesh quality parameters for the different flow configurations studied.

Table 3.1. Simulation input parameters.

	Drilling Mud	**Water**
Geometry		
Drill pipe diameter (m)	0.0889	0.0889
Hole diameter (m)	0.1463	0.1463
Computational Length (m)	14	14
Particle properties (spherical)		
Cuttings diameter (m)	0.003	0.003
Cuttings density ($kg.m^{-3}$)	2,610	2,610
Fluid properties		
Density ($kg.m^{-3}$)	1,036.5	998.5
Consistency index, K ($Pa.s^n$)	22.52	0.00103
Flow behaviour index (n)	0.151	1
Drilling variables		
ROP ($ft.hr^{-1}$)	50, 75, 100	50
Fluid circulation velocity ($ft.s^{-1}$)	2, 3, 4, 5	4
Flow regime	Steady-state laminar	Steady-state laminar
Drill pipe rotation (rpm)	0, 70, 140	0, 70, 140
Hole eccentricities (e)	0, 0.4, 0.8	0, 0.4, 0.8
Hole inclination from vertical (degrees)	0, 20, 40, 60, 90	90

To determine the optimum number of elements for which an accurate solution can be obtained at the expense of least computational resources, a mesh/grid independence study was necessary for all pipe eccentricities considered (Fig. 3.4). Flow simulations were carried out in a horizontal annulus without pipe rotation at a fluid velocity of 1.22 $m.s^{-1}$. The study was carried out at different total face divisions while keeping the number of axial divisions constant.

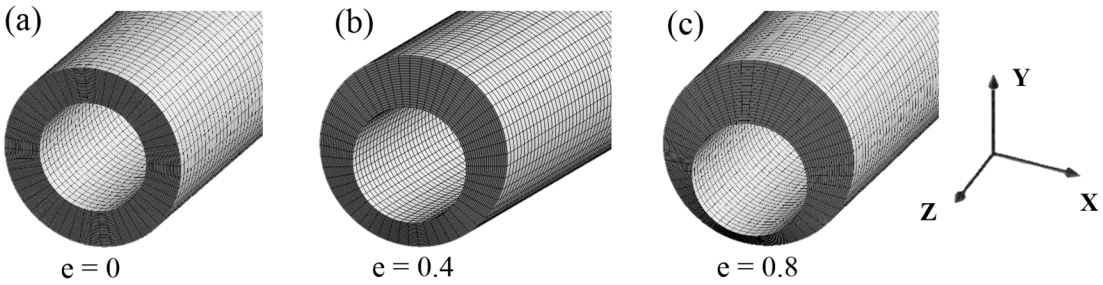

Figure 3.2. Computational mesh for the different flow configurations (a) concentric (b) moderately eccentric (c) highly eccentric.

The total number of face divisions is calculated by multiplying the number of edge divisions by radial face divisions. Figs. 3.2a-c and Table 3.2 show that the concentric flow configuration requires more elements compared to the eccentric annuli for a solution independent of the grid size.

Table 3.2. Computational mesh properties.

	Concentric Hole **e = 0**	**Eccentric Hole - 1** **e = 0.4**	**Eccentric Hole - 2** **e = 0.8**
Edge divisions	50	50	50
Radial face divisions	30	20	20
Total face divisions	1500	1000	1000
Number of elements	2,842,500	1,952,280	2,109,400
Number of nodes	11,658,850	8,105,124	8,757,296
Minimum skewness	0.0391	0.0333	0.0352
Maximum skewness	0.0451	0.1443	0.2091
Average skewness	0.0407	0.0896	0.1001
Minimum orthogonality	0.9981	0.9751	0.9041
Maximum orthogonality	0.9987	0.9988	0.9987
Average orthogonality	0.9985	0.9897	0.9713

Besides the flow physics, the under-relaxation factors are major determinants of the speed of convergence and stability of steady-state CFD simulations. These were carefully tuned until most appropriate values were obtained. In all cases except when water was used as the drilling fluid, each simulation converged within 30 mins. The difficulties observed with water resulted in double the run time required for the non-Newtonian drilling fluid cases.

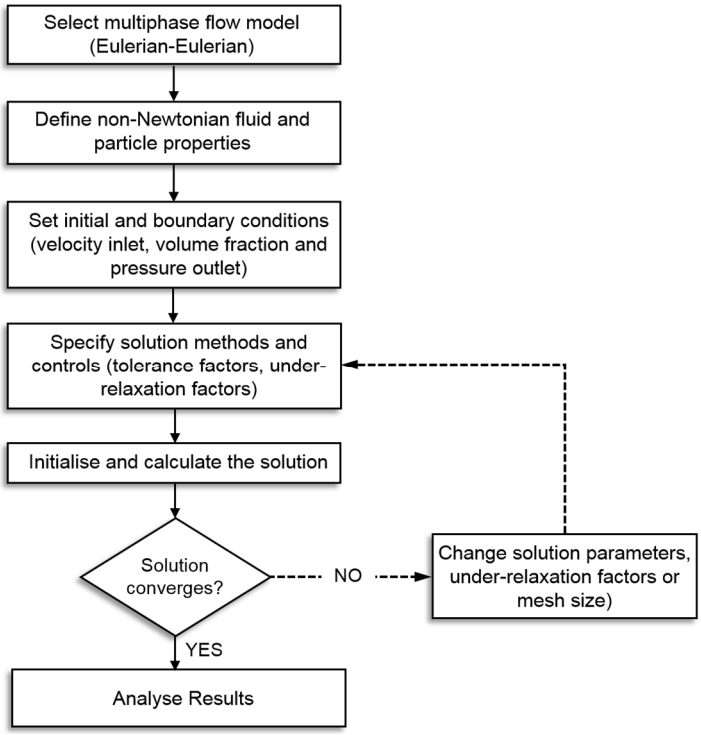

Figure 3.3. Simulation procedure using the Eulerian-Eulerian Multiphase flow model.

3.4 Model Validation

To validate the CFD model, several experimental observations were compared with the cuttings concentrations, cuttings velocity and pressure losses predicted. Table 3.3 summarises the simulation input parameters for all three experimental studies. The inlet cuttings concentration was determined using the methods of Larsen et al. (1997) and Ozbayoglu et al. (2010) for experiments in which cuttings bed porosity was measured (Eq. 3.34; Rooki et al., 2014a; b) and when it was ignored (Eq. 3.35).

$$c_p = \frac{ROP\ (1-\varphi)}{\left[1-\frac{D_{pipe}}{D_{hole}}\right]^2 v_{cut}} \tag{3.34}$$

$$c_p = \frac{ROP}{\left[1-\frac{A_{pipe}}{A_{hole}}\right] v_{cut}};\ \text{also calculated as}\ C = \frac{ROP(A_{bit})}{CTR \times Q} \tag{3.35}$$

where:

$$c_p = \frac{\text{Net volume occupied by particles}}{\text{Total volume of the annulus}} \times 100 \tag{3.36}$$

Figs. 3.5a-d show results of CFD predictions for the pressure losses, cuttings concentration and cuttings velocity in the annulus with average percentage errors between 2% and 11% for all cases considered. The predictive ability of the CFD model used in the present study is thus confirmed by its congruence with experimental data. Cuttings lag velocity was the most difficult parameter to predict using the Eulerian model (Figs. 3.5e and 3.6c).

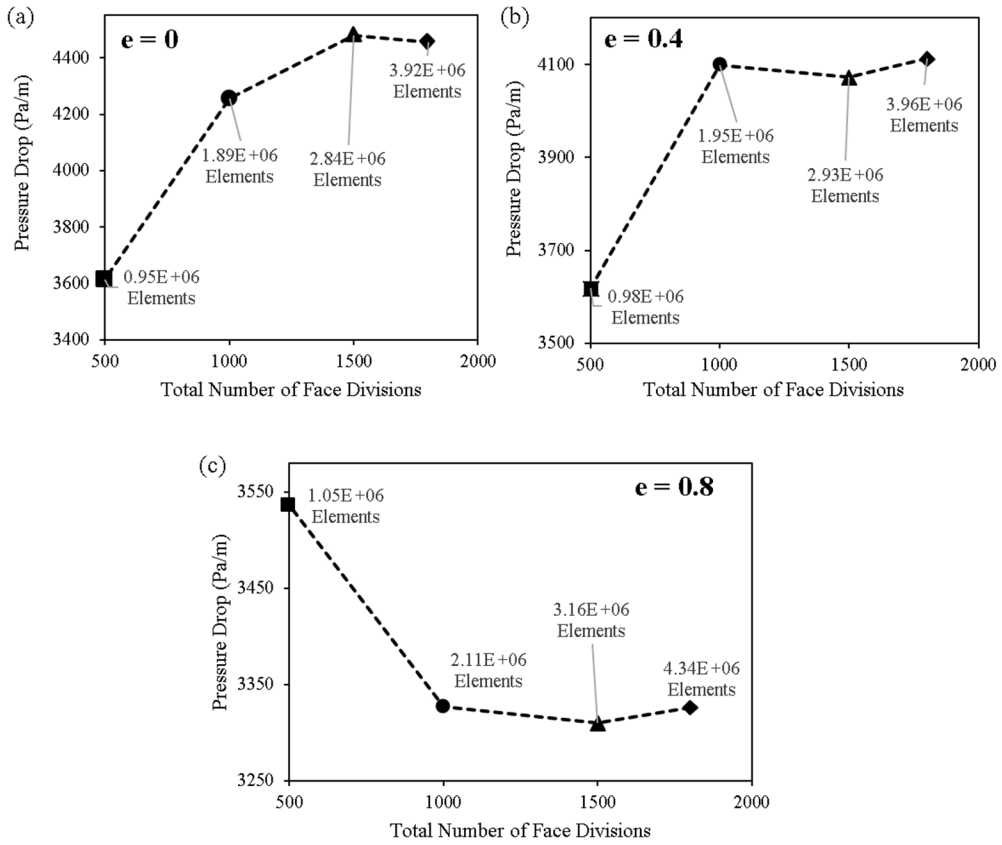

Figure 3.4. Grid Independence Study (a) e = 0, (b) e = 0.4, (c) e = 0.8 at 0 rpm, 1.22 $m.s^{-1}$ fluid velocity in a horizontal annulus.

Yilmaz (2012) also predicted the experimental results of cuttings bed velocity (Garcia-Hernandez et al., 2007) using the DPM one-way coupling of the particle-fluid interactions. The mean absolute error obtained was 8.5%. A lower error of 4.2% was obtained in the work of Demiralp (2014) in which interparticle collisions were accounted for, using the DEM technique. The present work, however, produced a mean error of 10.8% using the Eulerian model. The relatively higher error observed in this work can be attributed to the inherent approximation of the discrete phase as a continuum phase in the Eulerian-Eulerian model. Thus, interparticle collision using the Discrete Element Method (DEM)

could be adopted with the Discrete Phase Model for better predictions; however, this is bound to prohibitively increase the computational run time considering the relatively large flow domain implemented in this work.

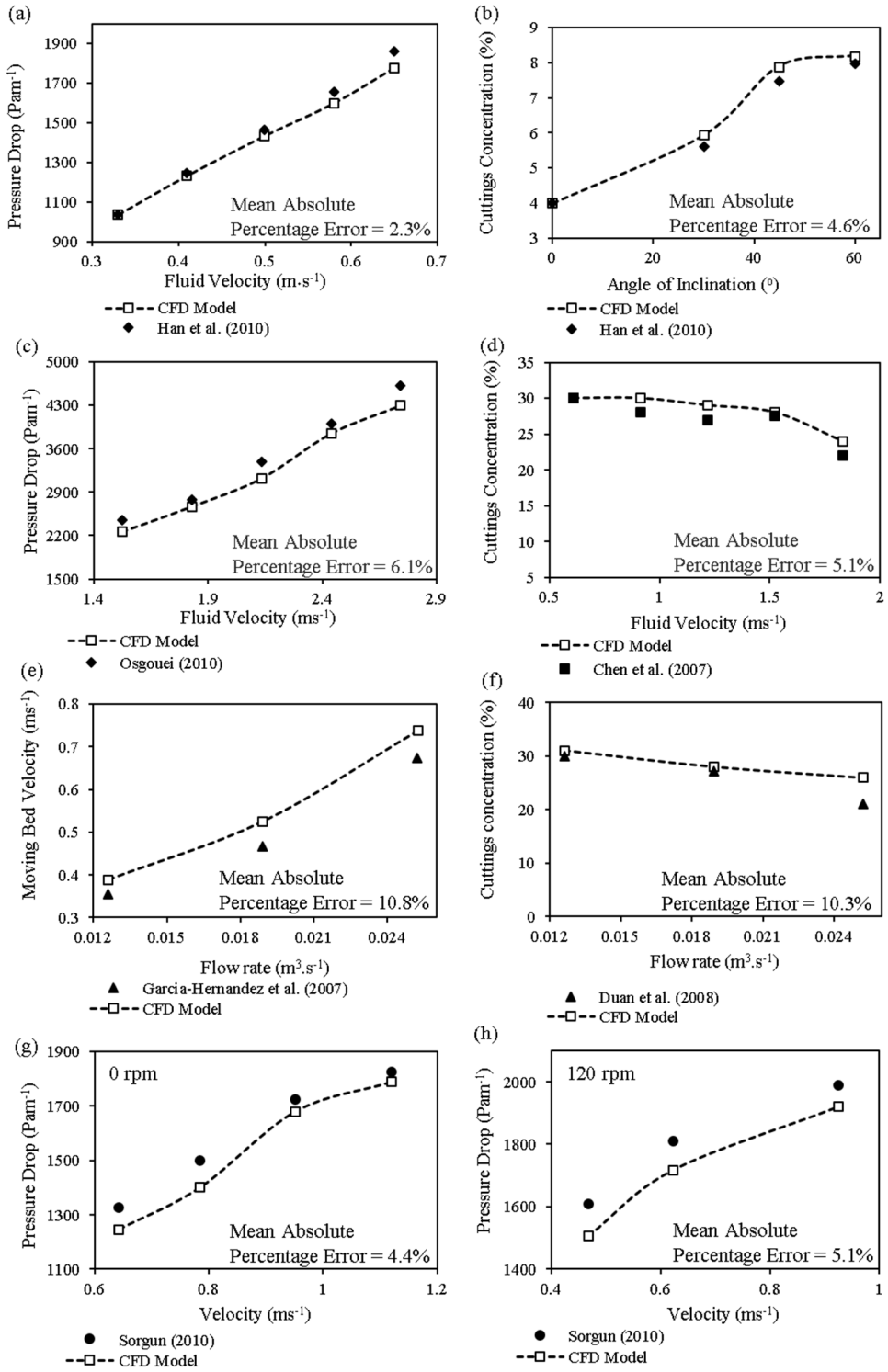

Figure 3.5. Validation of CFD model against experimental data.

Table 3.3. Experimental data summary used for model validation.

	Osgouei (2010)	**Han et al. (2010)**	**Chen et al. (2007)**	**Garcia-Hernandez et al. (2007)**	**Duan et al. (2006)**	**Sorgun (2010)**
Flow Geometry						
Drill pipe diameter (m)	0.0470	0.030	0.0889	0.1143	0.1143	0.0457
Hole diameter (m)	0.0739	0.044	0.1463	0.2032	0.2032	0.0739
Computational Length (m)	6.40	1.80	22.25	30.48	30.48	3.66
Particle Properties						
Cuttings density ($kg.m^{-3}$)	2761.4	2550	2610	2610	2610	2610
Cuttings diameter (m)	0.00201	0.001	0.003	0.004	0.0014	0.003
Cuttings bed porosity (%)	-	-	38	-	-	-
Fluid Properties						
Fluid type	Water	0.4% CMC sol	80% quality foam	Water	Water	Water
Density ($kg.m^{-3}$)	998.5	998.5	285	998.5	998.5	998.5
Consistency index, K ($Pa.s^n$)	0.001	0.048	3.385 (Rooki et al., 2015)	0.001	0.001	0.001
Flow behaviour index (n)	1.0	0.75	0.439 (Rooki et al., 2015)	1.0	1.0	1.0
Drilling variables						
ROP ($ft.hr^{-1}$)	80	62	50	30	30	30
Fluid circulation velocity ($m.s^{-1}$)	1.524 – 2.743	0.32 – 0.66	0.3 – 1.83	1.1 – 1.5	1.1 – 1.5	0.64 – 1.20
Flow regime	Steady-state turbulent	Steady-state laminar	Steady-state laminar & turbulent	Steady-state laminar	Steady-state laminar	Steady-state laminar
Drill pipe rotation (rpm)	0	0	0	0	0	0, 120
Hole eccentricities (e)	0.623	0	0	0.8	0.8	1
Hole inclination from vertical (^{o})	90	0 - 60	90	90	90	90
Cuttings injection rate ($kg.s^{-1}$)	0.0803	0.0204	0.115	0.358	0.215	0.0284
Temperature (K)	298	298	299.8	-	298	-
Operating Pressure (psig)	0	0	100	-	0	-

Table 3.4. Comparison between experimental data and model predictions of cuttings concentration and cuttings velocity.

Han et al. (2010)			**Chen et al. (2007)**			**Duan et al. (2006)**			**Garcia-Hernandez (2007)**		
Cuttings concentration			Cuttings concentration			Cuttings concentration			Cuttings velocity		
Exptl. (%)	CFD (%)	RE (%)	Exptl. (%)	CFD (%)	RE (%)	Exptl. (%)	CFD (%)	RE (%)	Exptl. ($m.s^{-1}$)	CFD ($m.s^{-1}$)	RE (%)
4.00	4.01	0.25	30.0	30.02	0.33	29.90	31.00	3.68	0.35	0.39	9.86
5.60	5.94	6.07	28.0	29.85	6.61	27.10	28.00	3.32	0.47	0.53	12.87
7.50	7.90	5.33	27.0	29.10	7.78	21.10	26.00	23.81	0.67	0.74	9.79
8.00	8.20	2.50	27.5	28.00	1.82	-	-	-	-	-	-
-	-	-	22.0	24.00	9.09	-	-	-	-	-	-

The relative errors (RE) between experimental results and CFD predictions are compared and summarised in Tables 3.4 and 3.5. Additionally, the residual plots (Fig. 3.6) illustrate that the cuttings concentration were, in most cases, slightly overpredicted by the Eulerian-Eulerian model. Conversely, the pressure drop predictions were in all cases, lower than the experimental results. Accurate prediction of final cuttings concentration is significantly dependent on the accuracy of the inlet cuttings volume fraction supplied to the simulator.

Table 3.5. Comparison between experimental and predicted pressure drop.

Han et al. (2010) 0 rpm			**Osgouei (2010) 0 rpm**			**Sorgun (2010) 0 rpm**			**Sorgun (2010) 120 rpm**		
Pressure drop			Pressure drop			Pressure drop			Pressure drop		
Exptl. ($Pa.m^{-1}$)	CFD ($Pa.m^{-1}$)	RE (%)	Exptl. ($Pa.m^{-1}$)	CFD ($Pa.m^{-1}$)	RE (%)	Exptl. ($Pa.m^{-1}$)	CFD ($Pa.m^{-1}$)	RE (%)	Exptl. ($Pa.m^{-1}$)	CFD ($Pa.m^{-1}$)	RE (%)
1038.0	1035.0	0.29	2443.0	2262.0	7.41	1326.0	1245.3	6.11	1609.3	1505.2	6.46
1247.1	1233.0	1.12	2782.3	2669.2	4.07	1500.4	1400.1	6.67	1811.0	1717.1	5.19
1464.2	1435.0	1.98	3393.1	3121.6	8.00	1725.0	1680.0	2.61	1989.1	1920.0	3.47
1659.1	1600.0	3.56	4003.8	3845.5	3.95	1826.1	1789.6	2.03	-	-	-
1867.0	1780.2	4.66	4614.5	4614.5	6.86	-	-	-	-	-	-

This parameter (inlet volume fraction) is not often stated in most experimental studies and hence, must be estimated. The uncertainty in the estimation of this variable in relation to the actual experimental inlet conditions is a possible reason for the observed errors in cuttings concentration. Besides inter-particle collision, the frequency of particle collisions with the walls of the drill pipe and casing pipe, which possess some degree of roughness, affects the pressure drop predictions by the CFD model. Accounting for these effects would warrant a more complex four-way coupling of the fluid and solid momentum

equations. While predictive accuracy is not always guaranteed by model complexity, maintaining a computationally acceptable trade-off between accuracy, run time and model simplicity is essential and thus constituted a guiding principle in this study.

Similar pressure drop predictions have been performed by Ofei et al. (2014) using the experiments of Han et al. (2010) and Osgouei (2010). The Eulerian-Eulerian model implemented in their work yielded a mean error of less than 5%. This is not far that obtained in the present study (Figs. 3.5a and c). Furthermore, the predictions of cuttings concentration using experimental data of Chen et al. (2007) are slightly better (Fig. 3.5d) than those of Rooki et al. (2015) in which the mean error was somewhat less than 8%. Although the Eulerian-Eulerian model was also implemented in their work, the very fine meshes adopted for the computations in this work is the apparent reason for the observed model performance.

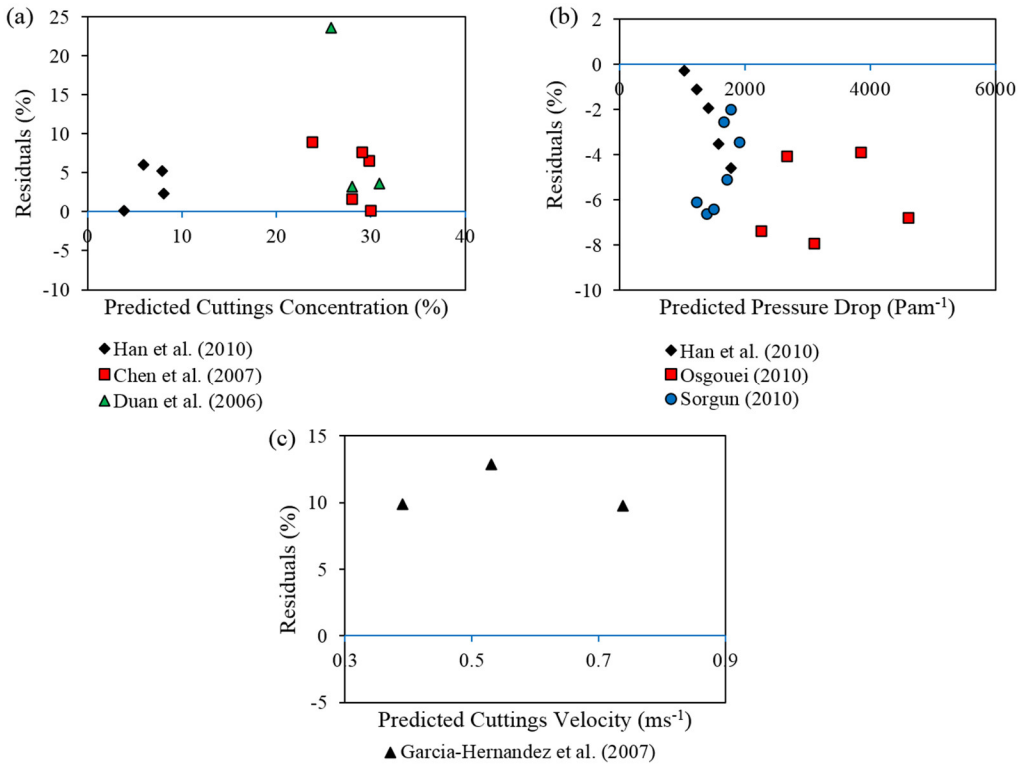

Figure 3.6. Residual plots of cuttings concentration, pressure drop and cuttings velocity predictions.

The broad range in the fluid and solid properties, geometric and drilling parameters, as shown in Table 3.3 is well accounted for by the simulation strategy adopted, hence further demonstrating the robustness of the CFD model. The impact of several drilling

operational parameters on the cuttings removal efficiency was studied as a function of the resultant pressure drop and cuttings concentration. Contour plots of phase velocities and volume fractions are also presented in the results section.

3.5 Sensitivity Analyses

In this section, the impact of drilling fluid parameters on the efficiency of cuttings transport is analysed with more than 30 separate simulations which incorporate these parameters.

3.5.1 Effect of Fluid Circulation Velocity

Two important characteristics of annular solid-liquid flow are the pressure drop versus mixture velocity relationship and the resultant cuttings concentration that ensue as a result of the fluid velocity used for hole cleaning. In this study, fluid circulation velocity is varied under laminar conditions at different drill pipe rotations, eccentricities and inclination angles from the vertical. Figs. 3.7a-b represent the impact of fluid velocity on the pressure drop and cuttings concentration at different pipe rotations in a horizontal eccentric annulus. An increase in pressure drop is observed as the velocity increases for all pipe rotations; however, this increase is more pronounced when the drill pipe is stationary. For example, pressure drop increased from 1886 $Pa.m^{-1}$ at 0.61 $m.s^{-1}$ to 2223 $Pa.m^{-1}$ at 1.524 $m.s^{-1}$ without drill pipe rotation. This is a more significant increase compared to the slight increase from 2163 $Pa.m^{-1}$ to 2239 $Pa.m^{-1}$ observed at 70 rpm within the same velocity range. Drill pipe rotation aids cuttings removal, according to Fig. 3.7b, but this occurs at the expense of a higher pressure drop. Furthermore, the narrowly spaced cuttings concentration trends are indicative of the fact that increasing drill pipe rotation has minimal impact on cuttings concentration.

Despite the application of several technologies that seek to ensure a centralised drill pipe during drilling operations, the impact of gravity and mechanical vibrations often cause the hole configurations to vary significantly from concentric to fully eccentric. Figs. 3.7c-d represent the impact of varying eccentricities on the pressure drop and cuttings concentration. An eccentric hole configuration yields a lower pressure drop compared to a concentric hole, and the magnitude of this reduction increases with a higher eccentricity of 0.8. This reduction in pressure drop can be attributed to the decreased mixture velocity encountered at the narrower part of the annulus. Furthermore, a more eccentric hole

implies a more significant suspended layer area and thus a lower resistance to flow. Unlike the Cuttings Transport Ratio (CTR), cuttings concentration is a better indication of the cuttings transport efficiency especially in deviated wellbores when cuttings buildup or bed formation occurs (Tomren et al., 1986). It is shown in Fig. 3.7d that cuttings concentration is lower when the inner drill pipe is concentric with the outer pipe/wellbore and buildup of cuttings increases as the configuration becomes more eccentric. At a circulation velocity of 0.61 $m.s^{-1}$ the cuttings concentration increases by 51% when the hole configuration changes from 0 to 0.8 eccentricity. Thus, the best carrying capacity of the fluid occurs with reducing eccentricity. The disparity between the cuttings concentration observed for both 0.4 and 0.8 hole eccentricities decreases as the fluid circulation velocity increases. This further explains the dominating impact of increasing fluid velocity on transport efficiency compared to other drilling variables.

Cuttings deposition could also occur at the bottom of the drill pipe in the axial direction when fluid velocity is not sufficient to overcome the axial or radial components of the gravitational force acting in the flow domain due to hole inclination. An important observation shown in Fig. 3.7e is the slightly decreasing pressure drop with increasing fluid velocity at near-vertical annular configurations (0^o and 20^o). Conversely, pressure drop slightly increases with fluid velocity as the inclination from the vertical increases (40^o and 60^o). The relative contributions of gravity and friction to the overall pressure drop at different inclination angles is a possible explanation for the observed pressure drop trends.

As seen in Fig. 3.7f, cuttings concentration increased from 10% to 14% as the hole configuration changed from an inclination of 0^o to 40^o at 1.22 m.s-1. This change in concentration was accompanied by a 15% decrease in pressure drop. The higher pressure drop values obtained at near-vertical configurations represent the enormous power requirements required for good hole cleaning. The implementation of deviated and horizontal well drilling thus implies that a lower fluid pumping requirement is needed but with an increased in-situ cuttings concentration. The results of Figs. 3.7e-f thus explain the fact that a higher circulation fluid velocity is required in deviated wellbores to maintain continuous removal of drill cuttings.

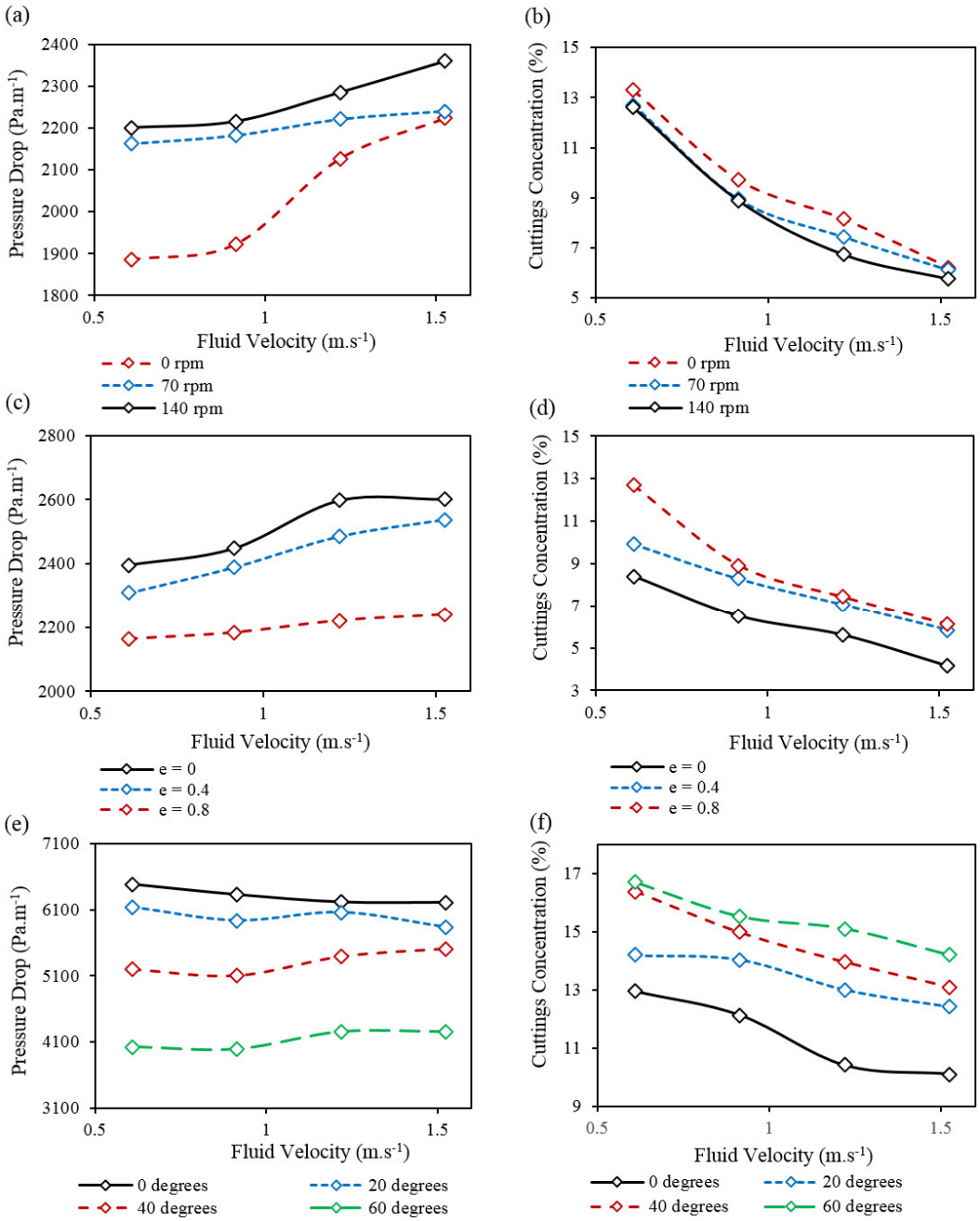

Figure 3.7. Effect of fluid circulation velocity on cuttings concentration and pressure drop at: e = 0.8, 50 ft.hr^{-1}-ROP, 90° – (a,b); 70 rpm, 50 ft.hr^{-1}-ROP, 90° – (c,d); e = 0.8, 70 rpm, 50 ft.hr^{-1}-ROP – (e,f).

3.5.2 Effect of Drill Pipe Rotation

Figs. 3.8a-d show the impact of drill pipe rotation on pressure drop and cuttings concentration at different penetration rates and hole eccentricities (e). A slightly increasing trend in pressure drop is observed with an increase in rotation for both cases when ROP and eccentricity were varied (Figs. 3.8a and d). This behaviour can be explained by the centrifugal forces, shear instabilities and unsteady flow that ensue as a result of a rotating

drill pipe (Demiralp, 2014). Also, increasing friction, velocity fluctuation and collision between particles and walls and particles themselves are major factors that contribute to the pressure drop increase. Fluid-particle flow through the concentric annular configuration experienced a higher pressure drop compared to the other eccentric flow geometries. The predominance of shear-thinning effects over inertial effects during rotation, and the inevitable viscosity reduction especially in the narrow parts of the eccentric annulus (Demiralp, 2014), is a plausible explanation for the reduced pressure drop.

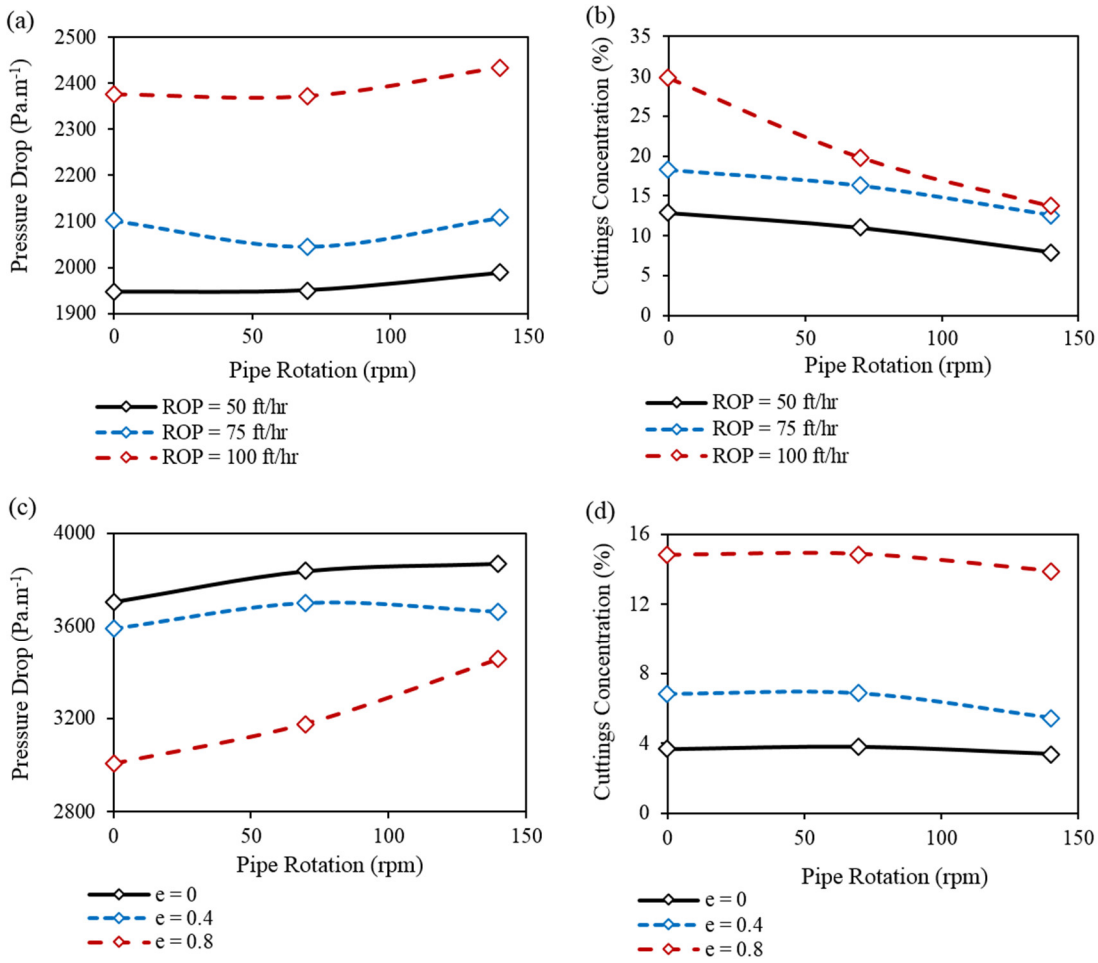

Figure 3.8. Effect of drill pipe rotation on cuttings concentration and pressure drop at: V_{mud} = 1.22 m.s^{-1}, e = 0.8, 90° – (a, b); V_{mud} = 1.22 m.s^{-1}, 50 ft.hr^{-1} ROP, 90° – (c, d).

A remarkably high pressure drop was observed (Fig. 3.8a) when the penetration rate was 100ft.hr^{-1}. This is due to the increased mixture density and bulk viscosity following the corresponding increase in cuttings concentration (Fig. 3.8b). The change in cuttings concentration with pipe rotation was more sensitive to ROP than to eccentricity (Fig.

3.8d). At a constant ROP of 100ft.hr^{-1}, the cuttings concentration decreased from 30% to 15% as drill pipe rotation increased from 0 rpm to 140 rpm; whereas, the decrease in cuttings concentration due to increased rotation (0 rpm to 140 rpm) was only from 14.8% to 13.9 % at an eccentricity of 0.8 (Fig. 3.8d). As explained in section 4.1, a concentric annulus always favours cuttings removal; this effect is seen in the reduced concentration values for the concentric flow configuration in Fig. 3.8d. Furthermore, Fig. 3.8d illustrates that when no pipe rotation was included, cuttings concentration increased from 6.8% to 14.8% as the flow domain changed from moderately eccentric (e = 0.4) to highly eccentric (e = 0.8); this explains the cleaning difficulty that ensues as a result of increased hole eccentricity.

3.5.3 Effect of Rate of Penetration

Figs. 3.9a-d illustrate the effect of increasing ROP on the pressure drop and cuttings concentration at different hole eccentricities and inclinations. It is shown that the calculated pressure drop values are generally higher in deviated and vertical wellbores (Fig, 9c) than in the horizontal cases (Fig. 3.9a). It is also observed in Fig. 3.9c that the difference in pressure drop at all rates of penetration gradually reduces as the flow orientation becomes vertical. Furthermore, the pressure drop increases from 4257 Pa.m^{-1} to 6223 Pa.m^{-1} (at 50 ft.hr^{-1}) when the flow domain changes orientation from 60^{o} inclination to a vertical condition (0^{o}) (Fig. 3.9c).

This is inevitably due to the increased contribution of gravity which the mixture has to overcome to retain upward flow. According to Fig. 3.9b, the concentric flow domain is seen to still favour cuttings removal at the expense of a higher pressure drop compared to the eccentric cases. Similar pressure drop and cuttings concentration are observed for the highly and moderately eccentric flow conditions at 50ft.hr^{-1} (Figs. 3.9a-b). However, at increased penetration rates, a greater disparity is observed between the two eccentric configurations. This explains the fact that, at high penetration rates, drastic reductions in hole cleaning efficiency can be attributed to changing annular eccentricities along the entire wellbore. As shown in Fig. 3.9d, increasing inclination angle and penetration rate forces more cuttings towards the lower part of the annulus, thus reducing the particle lift force generated by the fluid. Also, in Fig. 3.9d, the cuttings concentration is seen to increase from 10% to 14.6% as the ROP increased from 50ft.hr^{-1} to 100 ft.hr^{-1} at 0^{o} inclination from the vertical. With a 20^{o} change in inclination, cuttings concentration

increases from 12.1% to 15.8% between 50ft.hr^{-1} and 100ft.hr^{-1} ROP respectively; this increase is consistent with all other inclination angles. Although a high ROP is an indicator of good drill bit performance, the results show that it has to be carefully controlled/optimised to ensure that the drilling mud can adequately and promptly clean the volume of cuttings generated.

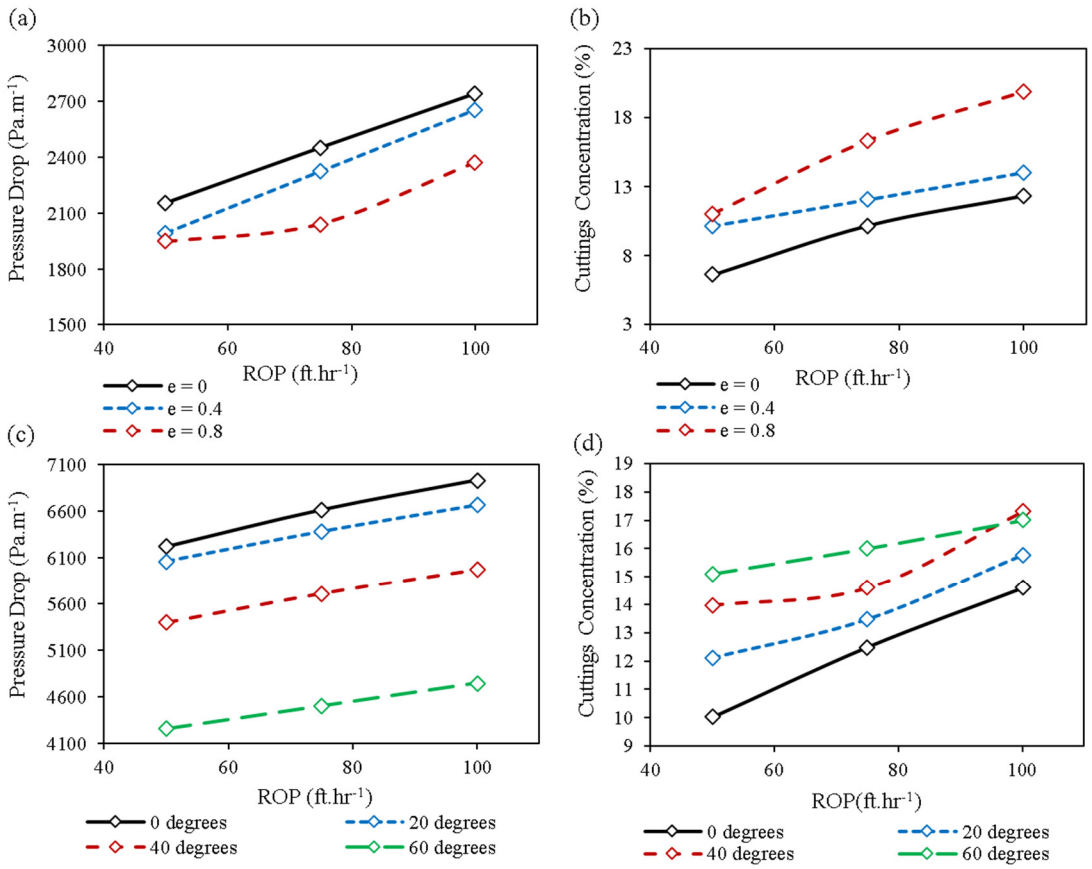

Figure 3.9. Effect of Rate of Penetration on cuttings concentration and pressure drop at: V_{mud} = 1.22 m.s^{-1}, 70 rpm, 90^{o} – (a, b); V_{mud} = 1.22 m.s^{-1}, 70 rpm, e = 0.8 – (c, d).

3.5.4 Effect of Inclination Angle

Figs. 3.10a-d show the effect of inclination angle at different drill pipe rotations and eccentricities. In both cases of changing rotation and eccentricities, the pressure drop is seen to reduce with an increase in the inclination angle; however, the change in pressure drop is more rapid between 40^{o} and 60^{o} compared to other angles. The reverse is the case with cuttings concentration where the change in concentration between 40^{o} and 60^{o} is not as high as that observed for other angles. Experimental observations of Han et al. (2010) and Tomren et al. (1986) also support this behaviour which occurs due to the impact of gravity, thus making the transport of cuttings at these angles more difficult. Another

explanation of the observed behaviour (Figs. 3.10b and 3.10d) presented in the experimental observations of Tomren et al. (1986), is the concept of particle recycling. Particles lifted from a sliding bed are not readily recycled into the high-velocity region at these inclinations angles; hence the fluid's lift force on the particle is overcome by the particles' tendency to settle. Pipe rotation had a slightly more significant impact on cuttings concentration compared to eccentricities at all inclination angles. For example, during vertical flow conditions, as shown in Fig. 3.10b, cuttings concentration decreased from 10% to 5.9% when pipe rotation was increased from 70 rpm to 140 rpm. On the contrary, changing hole eccentricity from 0.8 to 0.4 only changed the cuttings concentration from 10% to 8.7% (Fig. 3.10d).

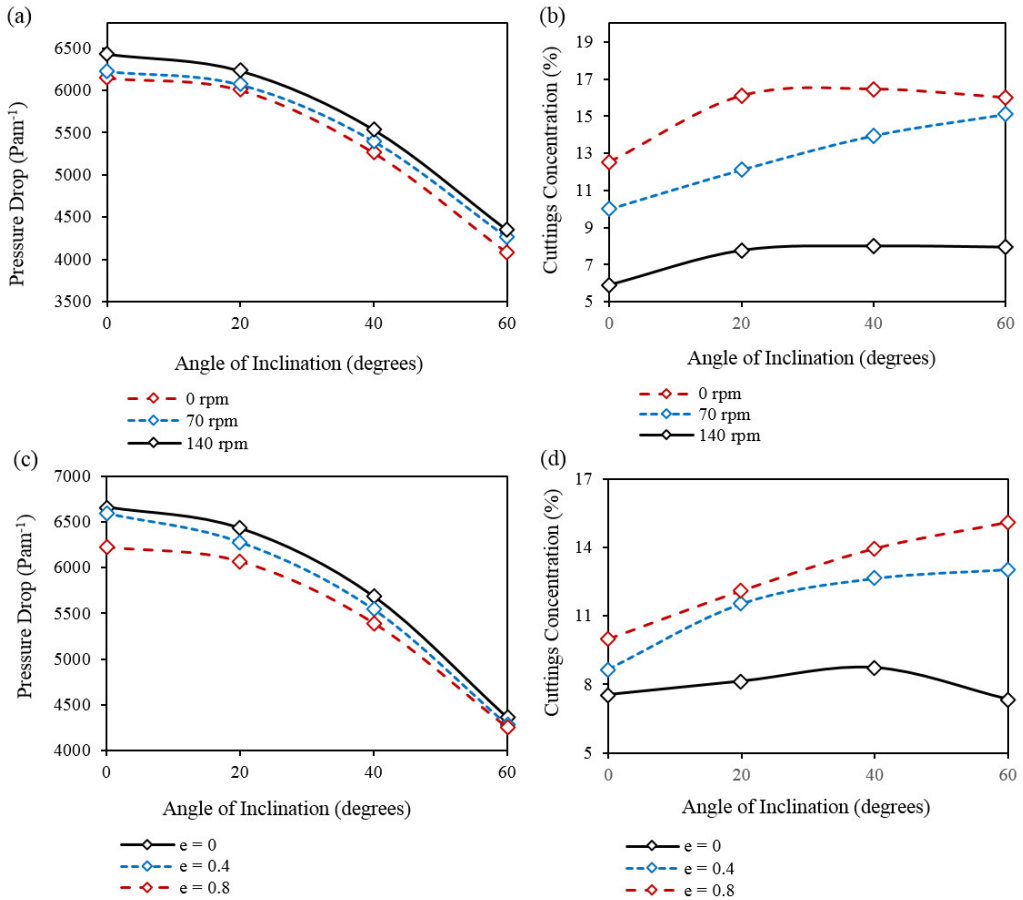

Figure 3.10. Effect of inclination angle on cuttings concentration and pressure drop at: V_{mud} = 1.22 m.s^{-1}, e = 0.8, 50 ft.hr^{-1} ROP – (a, b); V_{mud} = 1.22 m.s^{-1}, 50 ft.hr^{-1} ROP, 70 rpm – (c, d).

The obtained results further explain the fact that cuttings distribution and particle-phase segregation in the annulus are greatly influenced by hole inclination. Besides the impact of gravity, particle inertia effects are more pronounced when the hole is inclined.

Furthermore, the fairly large particles size and shape considered in this study, suggests that they engage in sliding, suspended and rolling motion during transport. The dominating mechanism of particle motion depends on the hole inclination, and this, in turn, affects the pressure drop and cuttings concentration. Since perfectly spherical particles are considered, it implies that particles readily roll over one another as they are transported. However, this tendency is bound to reduce as the inclination from the vertical increases; thus causing an increase in the particle inertia and a corresponding gradual buildup in cuttings concentration. However, the formation of a bed of immobile cuttings is not significant due to the high carrying capacity of the fluid and the relatively low inlet volume fractions of cuttings used in the simulations. Minor particle deposits are observed when water is used as the drilling fluid in a horizontal annulus (Fig. 3.11a).

3.5.5 Effect of Fluid Rheology

By comparing the carrying capacity of water (a Newtonian fluid) with the drilling mud as a function of pressure drop and cuttings concentration, it was possible to evaluate if, at any conditions, the performance of both fluids became similar. No such conditions were observed as shown in Fig. 3.11. The drilling mud clearly outperforms water which results in poor hole cleaning (depicted by the higher cuttings concentration). While a more segregated flow pattern exists for the water transport case (Fig. 3.11a), a more evenly distributed transport system is noticed around the annulus when the drilling mud is used (Fig. 3.11b). Another important observation is the low-pressure drop values associated with the water transport case. The relatively lower water viscosity is inevitably the reason for this observation, hence its low cuttings suspension and carrying capability. It is also illustrated in Figs. 3.11a and b, that the transport performance of the two fluids reduces with increasing eccentricity (illustrated in the maximum cuttings concentration); thus, non-Newtonian fluid properties help overcome problems posed by inherently complicated geometries during hole cleaning.

3.6 Visualisations of Annular Velocity and Cuttings Distribution Profiles

The contours of cuttings volume fraction and solid velocities are shown in Figs. 3.12 and 3.13, respectively. The flowrate of drill cuttings is often higher in the paths of least resistance. However, this effect is lessened (Fig. 3.13) due to the excellent fluid rheological properties, high fluid circulation velocity and high cuttings injection velocity

implemented. The velocity contours for the solid phase shown in Fig. 3.13 obey the no-slip boundary conditions implemented on the walls of the flow domain. Also, the increase in cuttings transport velocity as a result of drill pipe rotation is well illustrated in Fig. 3.13 at all eccentricities; hence, the occurrence of stagnated regions with high cuttings concentration is further mitigated in the annulus. However, the reduction in the cuttings concentration is not very significant, as seen in Fig. 3.12, in which the maximum cuttings concentration reduced from 21.8% to 20.5% in the concentric annulus, with the application of rotation.

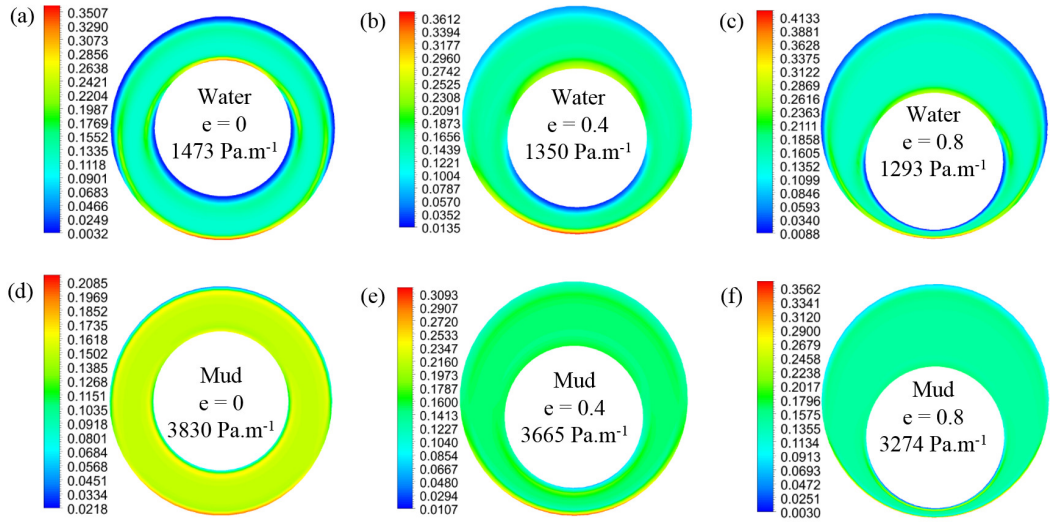

Figure 3.11. Effect of fluid type on cuttings concentration at 70 rpm, V_{mud} = 1.22m.s^{-1} and 50 ft.hr^{-1} ROP in horizontal annuli.

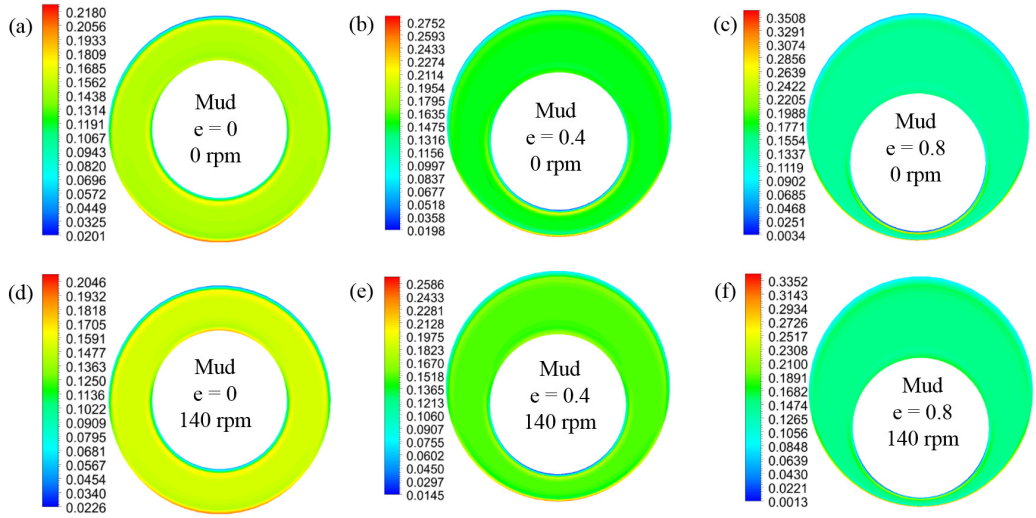

Figure 3.12. Contour plots of cuttings volume fraction at different eccentricities and drill pipe rotation with drilling mud as circulation fluid (1.22 m.s^{-1}) in horizontal annuli.

Water, a less viscous transport fluid, inhibits an organised and stable transport of drill cuttings; this relatively increases the particle inertia; thus, resulting in a less stable particle trajectory compared to cuttings transport using a drilling mud. There is also a loss of kinetic energy and a slight decrease in the cuttings transport velocity, as observed in Fig. 3.14, compared to Fig. 3.13 when the drilling mud is used. Essentially, the slip on the solid phase is reduced by the drilling mud due to the increased lift force it provides on the cuttings. This finding agrees with the results of Garcia-Hernandez et al. (2007), where cuttings lag in horizontal and deviated wells were determined experimentally. It can be observed in Fig. 3.14 that pipe rotation increases the cuttings velocity in all annular configurations considered. The maximum cuttings velocity observed in the concentric annulus when no rotation was included was 0.9144 $m.s^{-1}$; an increase to 0.9468 $m.s^{-1}$ occurs when pipe rotation was 140 rpm. This effect can be further explained by the reduced particle drag and slip velocity, which arises as a result of the uniformity in particle trajectory with pipe rotation (Garcia-Hernandez et al., 2007).

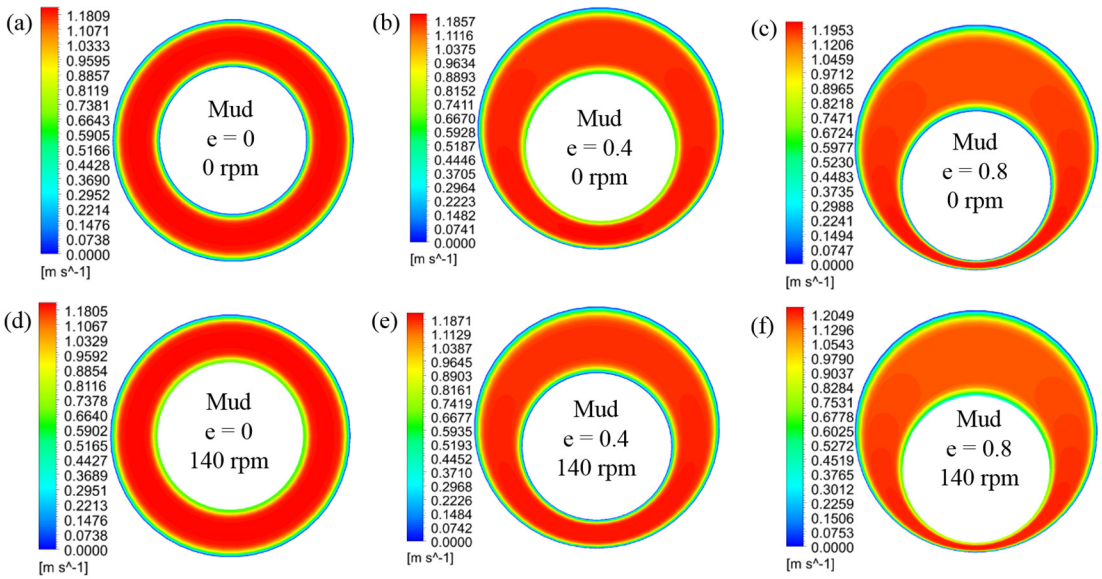

Figure 3.13. Contour plots of cuttings annular velocity at different eccentricities and drill pipe rotation with drilling mud as circulation fluid (1.22 $m.s^{-1}$) in horizontal annuli.

3.7 Chapter Conclusions

An analysis of a two-phase, solid-liquid flow was carried out under laminar, steady-state and isothermal conditions to determine the impact of drill pipe rotation, ROP, angle of inclination, hole eccentricity and fluid circulation velocity on the pressure drop and

cuttings concentration. The following conclusions can be drawn based on the observations made during this study:

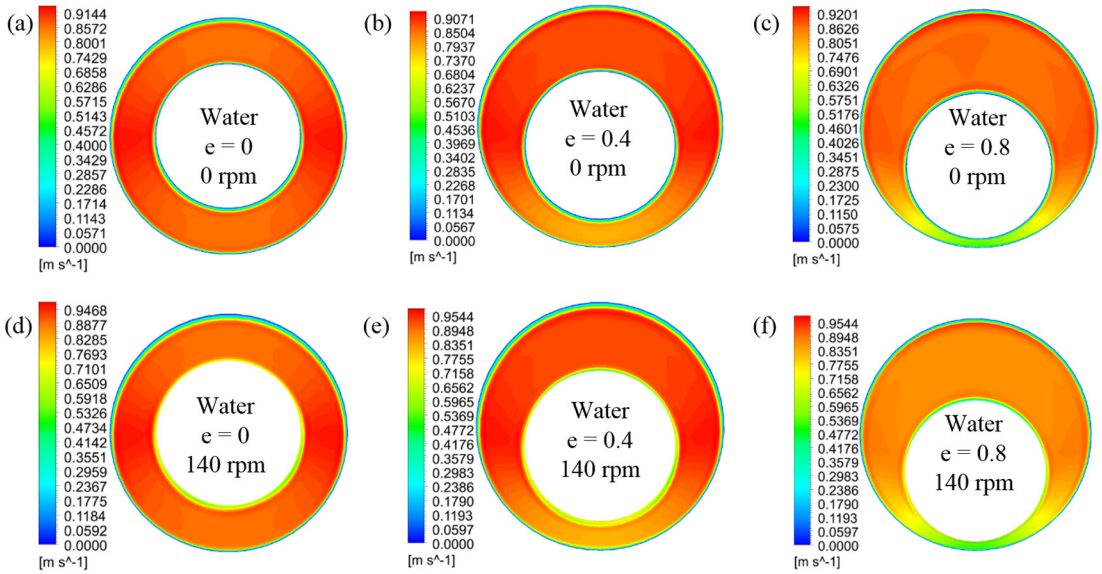

Figure 3.14. Contour plots of cuttings annular velocity at different eccentricities and drill pipe rotation with water as circulation fluid (1.22 $m.s^{-1}$) in horizontal annuli.

- Numerical simulations of pressure drop and cuttings concentration showed good physical agreement with experimental data. Mean percentage error in pressure drop and cuttings concentration predictions were less than 11%. This illustrates the reliability of CFD simulations in describing physical multiphase flow phenomena and consequently, the validity of the model used in this work. However, uncertainties in experimental investigations and the averaging property of the RANS equations compared to DNS simulations pose flow prediction difficulties. From an operational point of view, such an error level is not likely to yield a misleading understanding of the transport phenomena. Thus, adequate planning of well trajectory, proper rheological design of drilling fluids, and surface pumping requirements can be attained with the insights provided in this work.

- Fluid circulation velocity plays a crucial role in ensuring continuous cuttings removal from the annulus. Laminar flow conditions were sufficient to provide good hole cleaning with generally low cuttings concentration observed. A significant increase in annular pressure drop ensues when fluid velocity increases. Increased fluid velocity

and its impact on the particles, coupled with frictional flow effects, are the main contributing factors to the observed phenomena.

- For most flow configurations and conditions, increasing drill pipe rotation slightly aids the cuttings removal process with accompanying slight pressure increase. For all pipe eccentricities considered, the maximum reduction in cuttings concentration with the onset of drill pipe rotation was only 8%. Furthermore, the additional whirling motion that occurs, increases particle-particle and particle-wall collisions and is thus responsible for the pressure drop increase. Drill pipe rotation also plays a significant role in particle distributions around the annulus, which often yields an asymmetric flow pattern at low transport velocities.
- At all conditions of transport, the cuttings concentration is lowest when the drill pipe was concentric with the outer pipe. However, pressure drop reduces with increasing eccentricity and cleaning difficulty increases as the flow domain becomes more eccentric. On the other hand, hole cleaning becomes even more complicated with increasing penetration rates due to the rapid ingress of cuttings into the annulus.
- Fluid pump pressure requirements dramatically increase as the inclination from the vertical reduces. The change in pressure drop is highest between inclination angles of 40^{o} and 60^{o}; hence, cuttings transport within these angles can be energy demanding. Similarly, cuttings concentration in the annulus could increase by 51% when the flow configuration changes from vertical to 60^{o} inclination. To limit the formation of a cuttings bed, the annular mud velocity in directional wells has to be significantly higher than in vertical wells. In cases where a well's orientation must be inclined, the velocity of the drilling fluid employed must be able to counteract the effects of gravity, which aids particle settling. It was also discovered that the effect of increasing inclination angle with increasing cuttings concentration is more significant with the onset of hole eccentricity.
- When water (a Newtonian fluid) was used for hole cleaning, particle buildup in the annulus increased compared to when the power-law fluid was used. Hence, non-Newtonian fluids, (if properly designed) ensure proper hole cleaning even under transport configurations that are inherently difficult to clean.

This work was strictly limited to a steady state solid-liquid system; hence no consideration was given to the third gas phase which could occur when an aerated drilling fluid is applied, or when there is a gas influx from the reservoir due to the application of underbalanced drilling technology. Further work should, therefore, consider the steady and transient behaviours of a system containing all three phases to better describe the cuttings transport phenomena under these complex operational conditions.

Chapter 4 Steady-State and Transient Analysis of Multiphase Annular Turbulent Flows

Increased cuttings transport efficiency in most drilling operations (Fig. 4.1) is mostly characterised by an increase in mud circulation velocity; this creates complex turbulent interactions between the solid and liquid phases. The study of cuttings dispersion, in relation to their axial, tangential, and slip velocity profiles in the annulus is carefully investigated under steady and transient conditions and presented in this chapter. Computational Fluid Dynamics models (Eulerian-Eulerian, Lagrangian-Eulerian/ Discrete Element Method) are utilised for this purpose. The implementation of the Eulerian-Eulerian model provides a macroscopic description of the distribution of fundamental flow properties such as pressure, volume fractions and velocities of each phase. Furthermore, a direct description of the particulate flow, inherent transient motion, interparticle and particle-wall collisions are obtained with the particle tracking functionality of the Lagrangian-Eulerian/DEM technique.

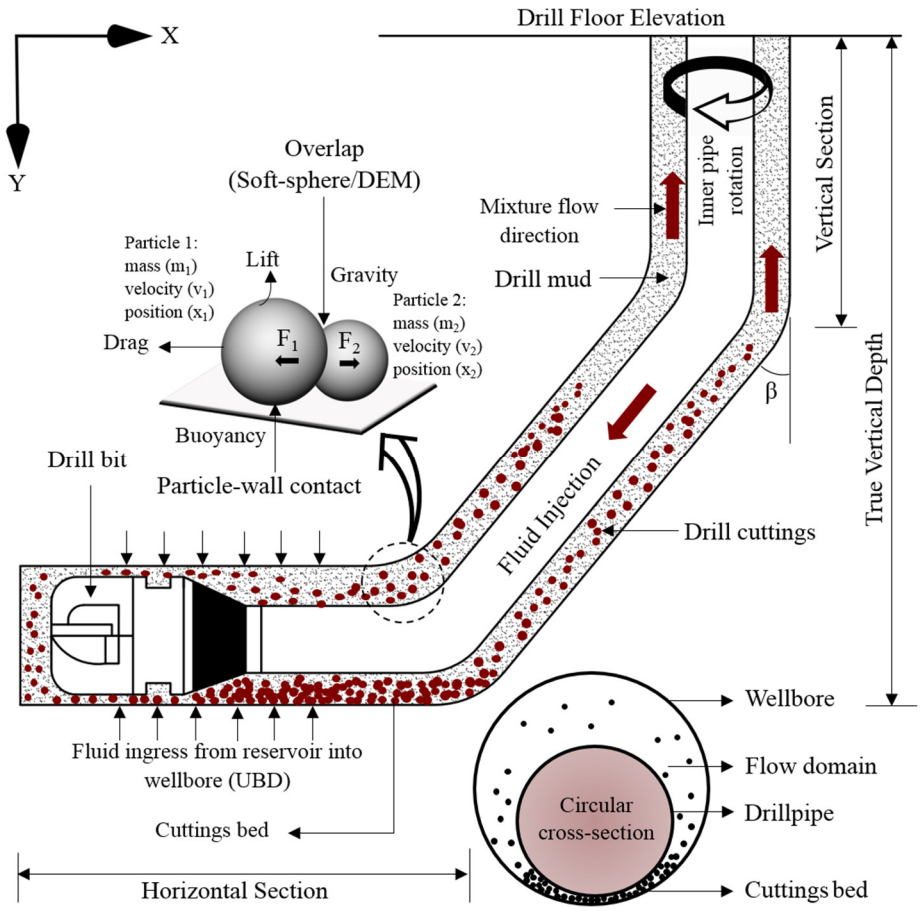

Figure 4.1. Wellbore cleaning schematic, showing fundamental modelling concepts.

4.1 Particle Handling and Flow Turbulence

Both the Eulerian and Lagrangian approaches are adopted for the analysis of cuttings transport phenomena in this study. The Eulerian-Eulerian (EE) model in which particles act like a continuum phase is adopted for steady-state modelling. Phase interactions are thus expressed in a continuous form, and the transport and turbulent properties of each phase determined. Appropriate closure models are implemented to recapture critical particle phenomena lost due to the inherent averaging property of this model (Liu, 2014). Interphase drag, shear, bulk and granular viscosities are the main phenomena which are necessary for complete closure and solvability of the governing flow equations (presented in Chapter 3).

The principal motivation for applying the Lagrangian approach is that the physics of flow emerges in a more natural way (Roco, 1993), thus providing further insight into the transport phenomena of cuttings. In essence, a statistical description of the dispersed phase is coupled with an Eulerian statistical representation of the carrier fluid phase (Subramaniam, 2013). In this approach, an understanding of the time dependency of turbulent diffusion is substituted for the determination of the spatial variation of a diffusion coefficient used in the Eulerian model (Binder and Haratty, 1991). Another element of superiority of the LE model is seen in the way gravitational settling in horizontal flows (which causes asymmetries in particle concentration profiles) is handled. The EE model takes this into account by assuming the settling velocities of the particles to be equal to their terminal values in the constitutive/closure equations. This could be slightly inaccurate because the particles might not have been in the field long enough to attain free fall; the use of an equation (LE) for the particle trajectory in the description of diffusion from a small wall source addresses this limitation (Roco, 1993; Fan and Zhu, 2005).

Discrete Phase Model (DPM) and the Discrete Element Method (DEM) are concurrently implemented in the Lagrangian-Eulerian (LE) approach in ANSYS Fluent. By using both methods, the limitation of the DPM model in handling dilute flows (with particle volume fractions less than 12%) is circumvented (Fluent, 2017). Tracking of particles trajectory using the DEM method allows interparticle and particle-wall collisions that dominate dense flows to be accurately captured (Subramaniam, 2013). At higher particle concentrations, a whole spectrum of complications arises in which the motions of the

dispersed and continuous phase are simultaneously affected; thus, necessitating a 2-way coupling solution (Brennen, 2005).

Furthermore, the complexity of turbulence and particle interactions as it relates to drilling operations has three major aspects: the dispersion of particles due to turbulence of the carrier fluid, particle segregation due to complex unsteady motions (non-uniform particle spatial distribution) and the modulation of the turbulence due to the presence and motion of particles (Hetsroni, 1989). It is possible to visualise (via CFD), that turbulence may be enhanced by the wakes and other structural disturbances that the motion of the particles instigate or dampened by the apparent bulk viscosity that the presence of particles introduces (Brennen, 2005). In order that these concepts are accurately accounted for, appropriate wall treatment is essential. The Standard k-ω model was considered the most suitable due to its superior performance for wall-bounded/boundary layer flows, transitional flow modelling capability and its adaptability to flows involving rotation. Despite the robustness of the k-ε models, the method of handling near-wall flows via wall functions made them less suitable compared to the Standard k-ω model. These wall functions neglect the flow field in the buffer region (Fig. 4.2) and assume an analytical solution in the viscous layer; this is not necessary for the k-ω model because they are valid all the way to the wall provided the mesh used is sufficiently fine (Fluent, 2017).

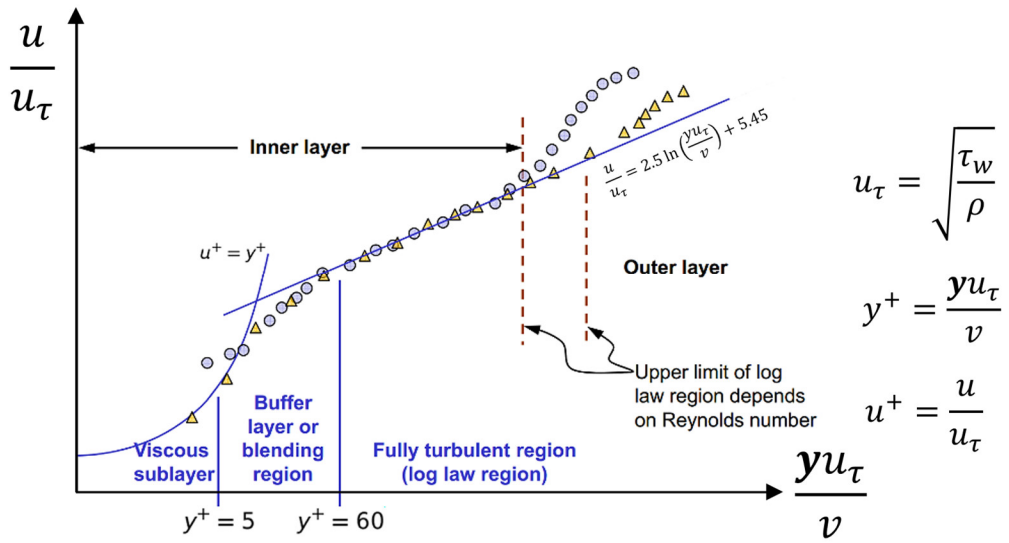

Figure 4.2. The law of the wall (Fluent, 2017).

4.2 Equations of the Lagrangian-Eulerian (LE) Model

ANSYS Fluent predicts particle trajectory of the discrete phase by integrating the force balance on the particle in the Lagrangian reference frame. This force balance can be described as:

$$\frac{d\vec{v}_p}{dt} = F_D\left(\vec{v}_f - \vec{v}_p\right) + \frac{\vec{g}(\rho_p - \rho_f)}{\rho_p} + \vec{F} \tag{4.1}$$

Where $\vec{F}$ is an additional force, consisting of the lift, and other negligible forces (virtual mass and pressure gradient forces, which are not necessary when the density of the fluid is much lower than the density of the particles); $F_D\left(\vec{v}_f - \vec{v}_p\right)$ is the drag force per unit mass, $\vec{u}$ is the fluid velocity, μ_f is the molecular viscosity of the fluid, ρ_f is the fluid density, ρ_p is the density of the particle, and d_p is the particle diameter. Re_{ss} is the relative Reynolds number, defined as:

$$F_D = \frac{18\mu_f}{\rho_p {d^2}_p}\frac{C_D Re_s}{24} \tag{4.2}$$

$$Re_{ss} \equiv \frac{\rho_f d_p \left|\vec{v}_f - \vec{v}_p\right|}{\mu_f} \tag{4.3}$$

$$\vec{F}_{lift} = \frac{2Kv^{0.5}\rho d_{ij}}{\rho_p d_p (d_{lk} d_{kl})^{0.25}}\left(\vec{v}_f - \vec{v}_p\right) \tag{4.4}$$

$\vec{F}_{lift}$ is the Saffman's lift force, v is the kinematic viscosity, $K = 2.594$; d is the deformation tensor. When a moving reference frame is involved, the additional force term incorporates the forces on particles due to drill pipe rotation. For rotation about the z-axis, the forces in Cartesian x and y coordinates can be written as (Eq. 4.5 and 4.6, respectively):

$$\left(1 - \frac{\rho_f}{\rho_p}\right)\Omega^2 x + 2\Omega\left(v_{p,y} - \frac{\rho_f}{\rho_p} v_{f,y}\right) \tag{4.5}$$

Where $v_{p,y}$ and v_y are the particle and fluid velocities in the Cartesian y-direction, Ω is the RPM, and

$$\left(1 - \frac{\rho_f}{\rho_p}\right)\Omega^2 y + 2\Omega\left(v_{p,x} - \frac{\rho_f}{\rho_p} v_{f,x}\right) \tag{4.6}$$

Where $v_{p,x}$ and $v_{f,x}$ are the particle and fluid velocities in the Cartesian x-direction. Turbulent dispersion of particles in the fluid phase can be predicted using the stochastic tracking (random walk) model, which includes the effect of instantaneous turbulent velocity fluctuations on the particle trajectories. Details of this method, the Discrete Element Method (DEM) for interparticle collisions and accompanying equations are presented in the ANSYS Fluent Theory Guide (Fluent 2017). Furthermore, in order to determine the appropriate entry conditions for the cuttings, Eqs. (3.34 – 3.36) were used.

4.3 Simulation Strategy & Computing Requirements

The Reynolds Averaged Navier Stokes (RANS) equations (continuity, momentum and transport equations) are numerically solved in a discretised domain using the finite-volume formulation. In the steady-state turbulent Eulerian-Eulerian approach, pressure-velocity coupling was effected using the phase coupled Semi-Implicit Method for Pressure-Linked Equations (SIMPLE) scheme. The effect of numerical diffusion on the solution accuracy is mitigated by employing second-order accurate solution schemes (Second Order Upwind) for the momentum and turbulent parameters. The volume fraction is spatially discretised using the Quadratic Upstream Interpolation for Convective Kinematics (QUICK) method. Iterative convergence is achieved with at least three orders of magnitude decrease in the normalised residuals for all equations solved. Also, under-relaxation factors were appropriately tuned to avoid unphysical oscillations in the calculations, thus ensuring stable convergence. A velocity inlet boundary condition (Table 4.1) is specified alongside a pressure outlet at atmospheric pressure. The nature of the flow condition being studied (fully-developed internal annular flow), warranted the specification of the turbulent intensity and hydraulic diameter as the turbulent mixture boundary conditions. These were estimated to be 4.5% and 0.07 m respectively. The wall boundaries were treated according to the conventional fluid mechanics no-slip condition. Furthermore, the Lun et al. (1984), Gidaspow, (1994) and Saffman-Mei (Saffman, 1965; Mei and Klausner, 1994) models were the main closure models implemented to account for the viscosity, drag and lift forces of the granular phase respectively. The general procedure with the LE approach is usually to solve the RANS equations of the continuous phase first without particle injections for convergence before introducing the particles. Very similar specifications to the EE model were adopted in the unsteady state turbulent LE approach; however, the transient flow modelling and the treatment of the discrete

phase are extra complications that required additional specifications. Firstly, the mean flow residence time (ratio of characteristic length to mean flow velocity) in the flow domain was determined to be 1 second. The simulation was run for a few mean flow residence times until Statistically Stationary State (SSS) was achieved. The 'Data Sampling for Time Statistics' tool in Fluent was employed for post-processing the mean (time-averaged) values of the velocities and volume fractions. Good convergence at each time step of the transient calculations was attained by implementing the 'Extrapolate Variables' option in Fluent (This enables prediction of the solution variables of the subsequent time step using a Taylor series expansion).

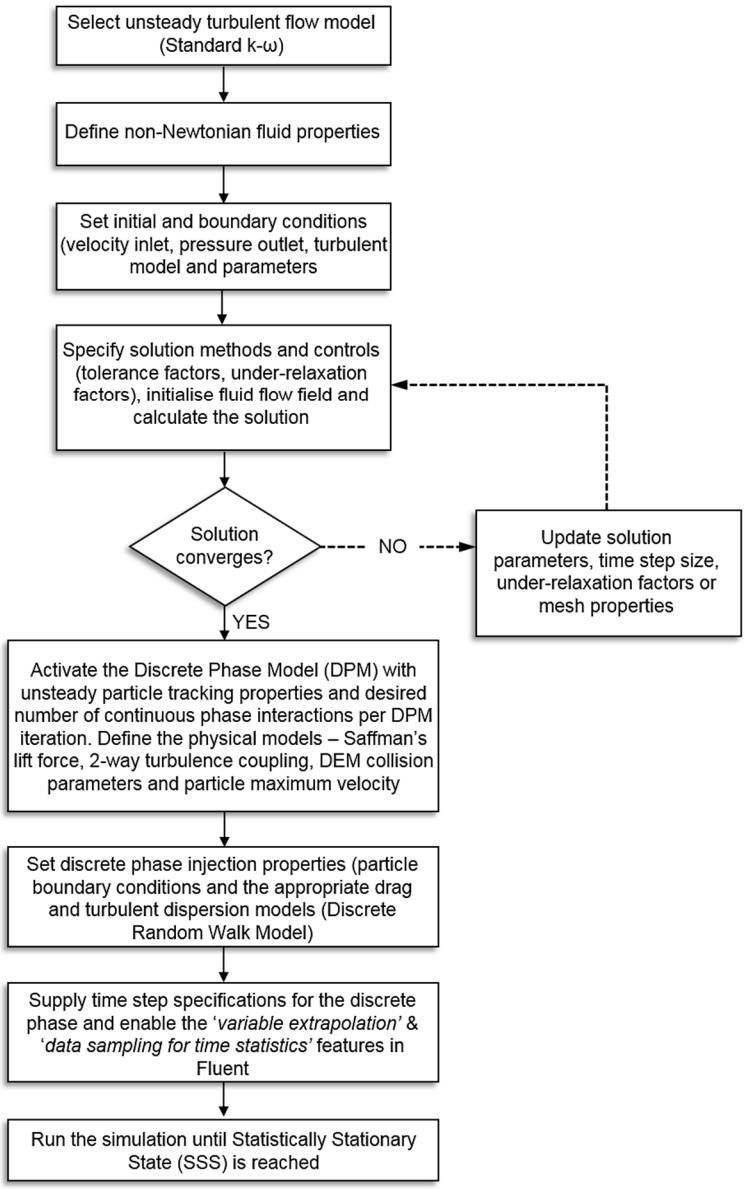

Figure 4.3. Simulation procedure for the Lagrangian-Eulerian model.

Johnson and Jackson (1987) showed that the manner of entry of granular material into an annulus affects the transport phenomena down the annulus. They discovered that the flow behaviour far from the entry position was affected by the inlet conditions at high flow rates as opposed to low flowrates. Turbulent conditions used in this study thus required a careful selection of the boundary conditions. Particles of uniform diameter were injected at an inlet fraction of 20% and a 50 $ft.hr^{-1}$ ROP. The method proposed by Larsen et al. (1997) was used for the determination of the inlet velocity (Eqs. 3.29-3.30). The relatively high (>12%) entry particle volume fraction implies that stochastically tracked particle trajectories would be affected by the interparticle collision, particle-wall collisions and particle–fluid interactions; hence the DEM method (soft sphere approach in which particles slightly overlap) and 2-way turbulence coupling is implemented in Fluent. In order to effect this, the number of discrete phase iterations per continuous iterations was set to a sufficiently large value to allow the continuous phase to absorb the change in momentum through the source terms of the discrete phase. The Discrete Random Walk Model is also included in the simulation setup to incorporate the effect of turbulence on the fluctuations in particle velocities due to eddy formation. Fig. 4.3 summarises the simulation procedures implemented for the steady and transient studies, respectively. The computational time is significantly affected by the chosen turbulent model and the phase interaction mechanisms. Also, accurate evaluation of the dynamic character of the mobile liquid and particle phases in Lagrangian coordinates requires the implementation of stochastic trajectory models, in which thousands of trajectories are determined (Fan and Zhu, 2005). High computing power is thus needed to carry out the numerous iterations necessary to obtain converged solutions for all phases. Conversely, the steady-state Eulerian-Eulerian calculations, are, to a great extent, computationally less intensive than the transient CFD/DEM method. Simulations were run for approximately 30 days on the University's high-performance computing facility (Eddie mark 3 – Scientific Linux 7 Operating System) with 16 cores (2.4GHz Intel®-Xenon® CPU processor) and 64GB of RAM.

4.4 Drilling Fluid Rheology and Annular Flow Geometry

In both steady and transient simulations, the adopted drilling fluid was a 0.5 wt. % aqueous CMC solution with power-law parameters determined from the experimental and numerical investigations of Eesa and Barigou (2009). In order to comparatively

evaluate the performance of the drilling mud of non-Newtonian rheology with a Newtonian carrier fluid, simulations are also carried out using water. Fluid and solid properties used in this study are shown in Table 4.1.

Table 4.1. Simulation parameters.

	Eulerian-Eulerian	**Lagrangian-Eulerian**
Geometry		
Drill pipe diameter (m)	0.10795	0.10795
Wellbore diameter (m)	0.17780	0.17780
Computational length (m)	11	2
Particle properties (spherical)		
Cuttings diameter (mm)	1, 5,10	1, 5, 10
Cuttings density ($kg.m^{-3}$)	2610	2610
Fluid properties		
Density ($kg.m^{-3}$)	1000	1000
Consistency index, K ($Pa.s^n$) = τ/γ^n	0.16	0.16
Flow behaviour index (n)	0.81	0.81
Drilling variables		
ROP ($ft.hr^{-1}$)	50, 100	50, 100
Fluid circulation velocity ($m.s^{-1}$)	1.5	2
Flow regime	Steady-state turbulent	Unsteady state turbulent
Drill pipe rotation (RPM)	100, 400	100, 400
Hole eccentricities (e)	0, 0.6	0.6
Hole inclination from vertical (degrees)	0, 45, 90	0, 45, 90

The flow geometry considered comprises of two walls. The stationary outer wall represents the wellbore while the inner wall was modelled with a rotation effect in order to simulate the rotation of the drill pipe. The magnitudes of this rotary motion were 100 RPM and 400 RPM, respectively. On the other hand, the translational motion of the drill pipe was considered negligible and ignored. Although some researchers have developed empirical correlations for the entrance length prediction of fully developed turbulent flows (Nikuradze, 1933; Lien et al. 2004), test simulations were carried out to monitor the development of the velocity boundary layer before deciding on the length of the flow main. As seen in Table 4.1, the length of 2m was used for the CFD/DEM simulation and

is considerably lower than that adopted for the steady-state simulation. This is obviously due to the high computational burden of transient multiphase flow simulations. Also, concentric and eccentric flow configurations were separately analysed for their flow attributes. Tables 4.2 and 4.3 summarise the geometric properties of both configurations (Fig. 4.4 and 4.5).

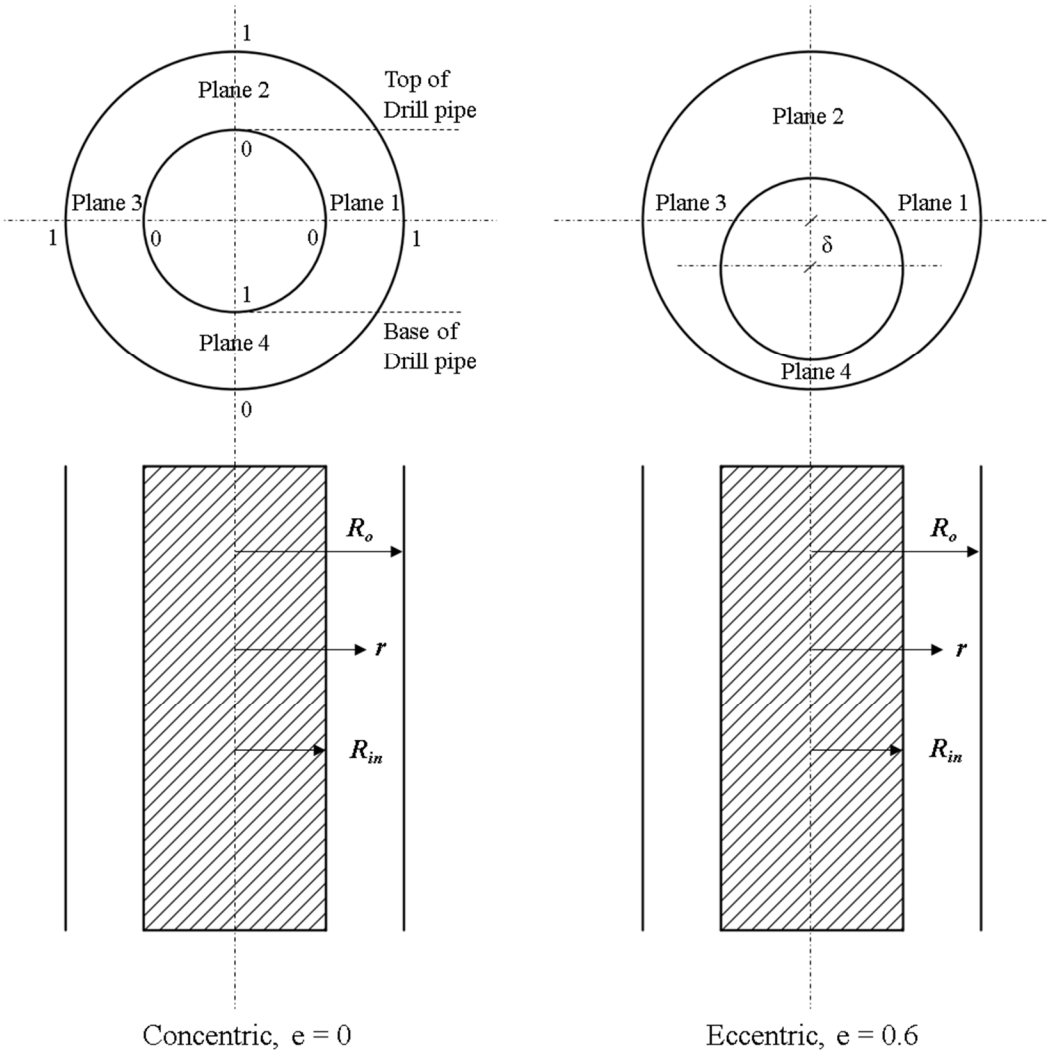

Figure 4.4. Geometric setup with line-planes used for the analysis of cuttings transport phenomena showing the dimensionless annular spaces (from 0 to 1) along all lines.

4.5 Mesh Independence Study

Sufficiently fine hexahedral structural meshes were implemented for the concentric and eccentric configurations comprising of 2.5×10^6 elements (11 m computational length) for the Eulerian-Eulerian model and 3.3×10^5 elements (2 m computational length) for the Lagrangian-Eulerian model. For the concentric flow configuration, 60 edge divisions and

30 radial divisions were adopted whereas 70 edge divisions and 20 radial divisions were implemented in the eccentric case, thus yielding excellent mesh resolution capable of capturing near-wall effects. These corresponded to a uniform first-layer thickness of 1.2 mm in the concentric domain, while 0.5 mm and 1.9 mm were the minimum and maximum values in the eccentric domain. It was thus necessary to estimate the wall-adjacent cell centroid/dimensionless wall distance (y^+) before generating the mesh. This dimensionless quantity majorly ranged between 15 and 17 depending on the wall shear stress, and skin friction coefficients computed for the different flow conditions studied. While the CFD/RANS/DEM community continues to seek wall treatments methods that are insensitive to y^+ values as the mesh is refined, we have exploited the independence of the Standard k-ω model on damping wall functions. Mesh qualities (orthogonality, skewness and aspect ratio) reported in Tables 4.2 and 4.3 further illustrate the credibility of the adopted meshing technique.

Solutions of velocity profiles, volume fractions and pressure drop are presented over a range of significantly different grid resolutions in order to demonstrate grid-independent/gird-convergent results. The mesh independence study was carried out using different total face divisions (number of edge division × number of radial divisions) while retaining the number of axial divisions. The simulation set up consisted of a horizontal annulus with 100 RPM inner pipe rotation, and only profiles along plane 4 (See Fig. 4.6) are shown.

Table 4.2. Computational mesh properties of the concentric flow domain.

Edge ø	Radial ø	y (mm)	Total Face ø	No. of Elements	No. of Nodes	Min. ϭ	Max. ς	Max. AR
50	10	3.49	500	613,000	674,850	0.998	0.040	3.14
50	20	1.75	1000	1,226,000	1,288,350	0.998	0.040	6.34
60	20	1.75	1200	1,765,200	1,854,720	0.999	0.033	5.28
70	20	1.75	1400	2,402,400	2,523,990	0.999	0.029	4.52
60	***30***	***1.16***	***1800***	***2,647,800***	***2,737,920***	***0.999***	***0.033***	***7.95***
70	30	1.16	2100	3,603,600	3,725,890	0.999	0.029	6.81

ø – Number of divisions/segments; ϭ – Orthogonality; ς – Skewness; AR – Aspect Ratio

Table 4.3. Computational mesh properties of the eccentric flow domain.

Edge ø	Radial ø	Min. y (mm)	Max. y (mm)	Total Face ø	No. of Elements	No. of Nodes	Min. ϭ	Max. ς	Max. AR
50	10	5.59	1.40	500	637,500	2,742,882	0.779	0.438	6.62
50	20	2.79	0.70	1000	1,275,000	5,294,412	0.751	0.438	13.31
60	20	2.79	0.70	1200	1,750,800	7,269,540	0.963	0.176	11.6
70	***20***	***2.79***	***0.70***	***1400***	***2,453,760***	***10,187,506***	***0.830***	***0.364***	***10.07***
60	30	1.86	0.47	1800	2,626,200	10,772,940	0.960	0.176	17.43
70	30	1.86	0.47	2100	3,680,640	15,097,156	0.805	0.364	15.12

ø – Number of divisions/segments; ϭ – Orthogonality; ς – Skewness; AR – Aspect Ratio

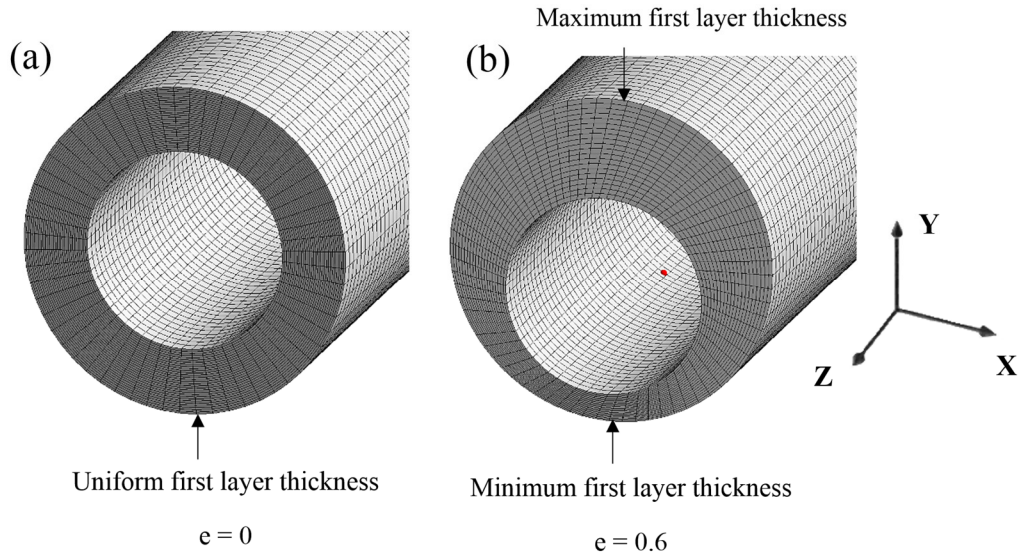

Figure 4.5. Computation mesh for the concentric and eccentric flow configurations.

4.6 Model Validation

As pointed out earlier, comprehensive measurements of the particle velocity profiles in solid-liquid flows are very scarce due to the inherent difficulty of performing such measurements with the available techniques. However, Eesa and Barigou (2009) have carried out extensive experiments using the PEPT technique to determine the trajectories and velocity profiles of coarse solid particles flowing in non-Newtonian CMC carrier fluids. These unique experimental results are used to assess the accuracy of the numerical CFD simulations. Furthermore, the work of Garcia-Hernandez et al. (2007) provides some experimental measurements of cuttings lag velocity in an annulus, which is also used for validation purposes.

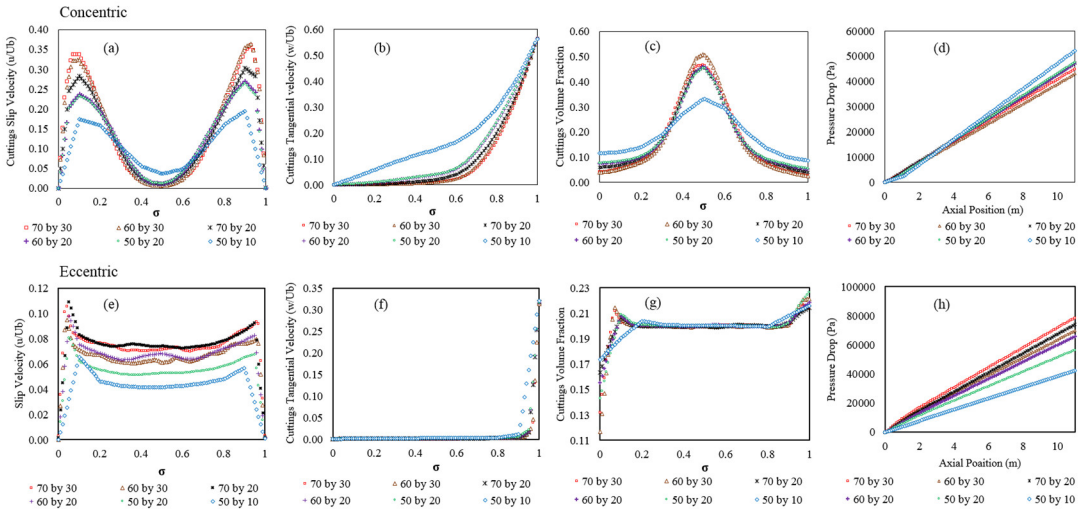

Figure 4.6. Mesh independence study for concentric and eccentric flow domains.

It is important to bear in mind that the data provided in these studies do not consider the tangential velocities of the phases that ensue as a result of the inner pipe rotation (Table 4.4). Hence, experimental results of (Nouri and Whitelaw, 1997; Escudier et al. 2002) whose studies take this into account, although with the turbulent flow of the carrier fluid alone, are useful for the validation process.

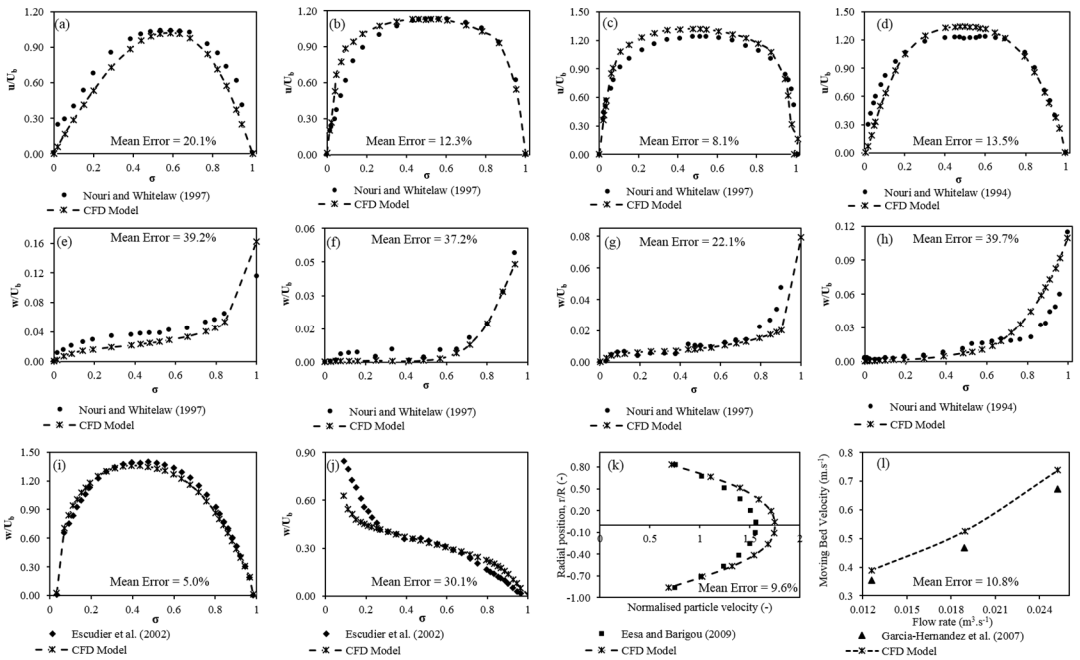

Figure 4.7. CFD model validation against experimental data.

Fig. 4.7 shows good CFD predictions of the axial and tangential velocities of both phases using the Eulerian-Eulerian model with mean absolute errors less than 11%; thus

illustrating the capability of our CFD model to reasonably predict flow phenomena encountered during drilling.

Table 4.4. Experimental data summary used for model validation.

	Nouri & Whitelaw (1994)	**Nouri & Whitelaw (1997)**	**Escudier et al. (2002)**	**Garcia Hernandez et al. (2007)**	**Eesa & Barigou (2009)**
Flow Geometry					
Drill pipe diameter (m)	0.0200	0.0200	0.0508	0.1143	-
Hole diameter (m)	0.0403	0.0403	0.1004`	0.2032	0.045
Computational Length (m)	2.32	2.32	5.775	30.48	0.6
Particle Properties					
Cuttings density ($kg.m^{-3}$)	-	-	-	2610	1,020
Cuttings diameter (m)	-	-	-	0.004	0.007
Fluid Properties					
Fluid type	0.2% CMC	0.2% CMC	0.1% (XG+CMC)	Water	0.5% CMC
Density ($kg.m^{-3}$)	1,000	1,000	1,100	998.5	1,000
Consistency index, K ($Pa.s^n$)	0.044	0.044	1.305 (Cross)	0.001	0.16
Flow behaviour index (n)	0.75	0.75	0.509 (Cross)	1.0	0.81
Drilling variables					
ROP ($ft.hr^{-1}$)	-	-	-	30	-
Fluid circulation velocity ($m.s^{-1}$)	2.78	2.72	0.203	1.1 – 1.5	0.125
Flow regime	Steady-state turbulent	Steady-state turbulent	Steady-state laminar	Steady-state laminar	Steady-state laminar
Drill pipe rotation (RPM)	300	300	50	0	-
Hole eccentricities (e)	0	0.5	0	0.8	-
Hole inclination from vertical (^{o})	0	0	90	90	90

4.7 Analysis of Cuttings Velocity and Volume Fraction Profiles in a Concentric Annulus using the EE model

The impact of drill pipe rotation, inclination angle, particle diameter and fluid rheology on the velocity profiles (axial, slip and tangential), volume fraction and pressure drop are presented and carefully examined in a concentric annulus. The presented profiles which

give some insight into the flow phenomena were generated from regions of fully developed flow in the annulus. All velocities are normalised by the bulk velocity (U_b), and the spatial variation of flow properties is determined as a function of the dimensionless annular space (σ).

4.7.1 Effect of Drill Pipe Rotation

Fig. 4.8 shows a uniform magnitude in cuttings axial velocity across all planes with the highest values at the central annular regions. As observed in Fig. 4.8a-d, there is a slight degree of asymmetry in the axial velocity profiles with an increase in drill pipe rotation; this is more noticeable on planes 2 and 3. The profiles of axial velocity mostly overlap in the other planes (1 and 4) and are relatively insensitive to the rotation effect. The slip velocity profiles (Fig. 4.8e-h) exhibit a spike at the near-wall regions and a minimum at the centre of the annulus in all plane sections considered, thus explaining the spatial variation in flow resistance demonstrated by the solid phase relative to the fluid. At planes 2 and 4, the effect of pipe rotation is more pronounced.

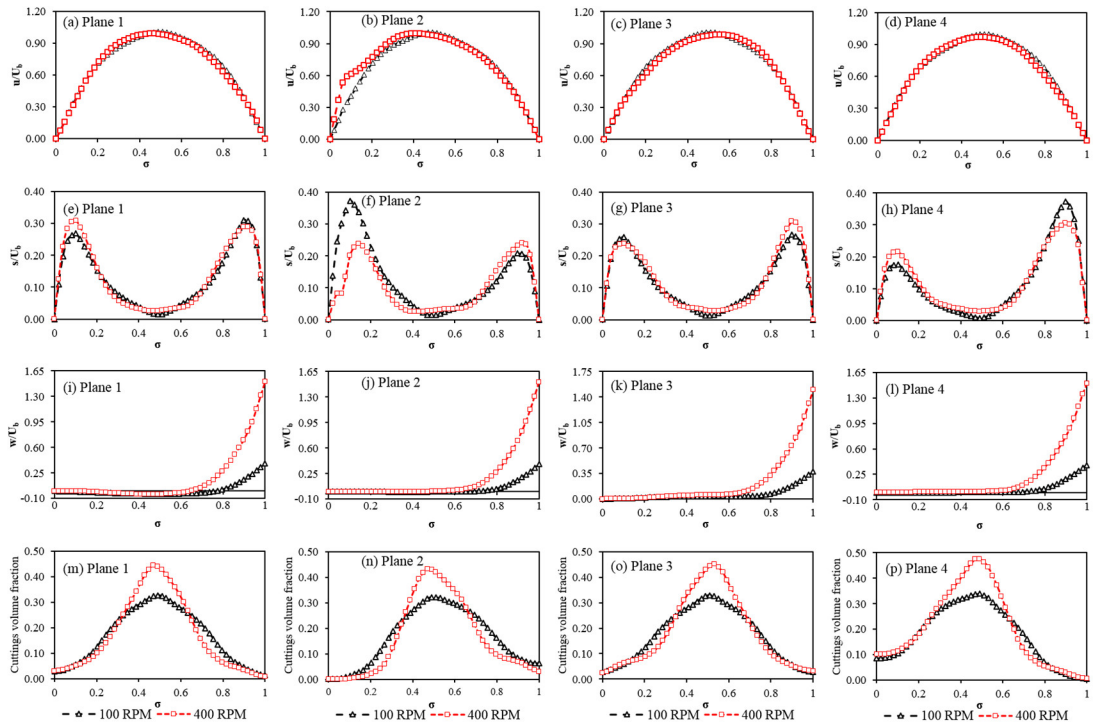

Figure 4.8. Effect of drill pipe rotation on cuttings velocity profiles and volume fraction in a concentric annulus with the drilling mud as the carrier fluid, wellbore inclination of 45°, ROP of 50 ft.hr^{-1} and 5 mm cuttings diameter.

The impact of gravity in the inclined annulus is bound to increase the slip of the solid phase; however, an increased rotation effect tends to reduce the slip velocity (and eventual phase segregation), thus improving the efficiency of the transport process. The tangential velocity profile (Fig. 4.8i-l) shows a sharp increase with the particles' position in the annulus approaching the rotating drill pipe. Obviously, this effect is higher with a rotation of 400 RPM compared to 100 RPM. It is possible to visualise the lifting effect rotation has on the particles, which is better explained by observing the volume fraction profiles (Fig. 4.8m-p). Compared to the slight spreading of particles observed at 100 RPM, the volume fraction is seen to have a slender peak at the centre position of the annulus at 400 RPM. This illustrates that more particles tend to travel in the centre region of the annulus with increased rotation (due to particle lifting). The volume fraction profiles illustrated in planes 2 and 4 reveal that pipe rotation effects are more potent along the longitudinal section of the annulus, as observed in the asymmetric profiles. Furthermore, the inclined configuration of the annulus implies the top part of the annulus and the lower part of the drill pipe are almost void of cuttings; this is shown in planes 2 and 4 (Fig. 4.8n and p).

4.7.2 Effect of Wellbore Inclination

Frictional resistance to flow or irreversible energy losses in the upward flow direction is much less in the liquid phase than in the solid phase; thus, the presence of slippage is unavoidable at any inclination for heterogeneous flows. Unlike the cuttings axial velocity profiles, slip velocities reveal more intricate flow features, with the change in hole inclination (Fig. 4.9e-h). It is observed that the horizontal configuration (90^{o}), although with a considerable portion of flow exposed to gravitational resistance, shows the lowest slip in all planes. Conversely, the vertical flow configuration generally shows higher slip velocities. However, in planes 2 and 4 with the strongest impact of pipe rotation as stated previously, we observe the inclined configuration (45^{o}) dominating in the magnitudes of slip velocities on different halves of the plane. Furthermore, tangential velocity profiles on these planes show very similar profiles; hence we resort to planes 1 and 3 for a better understanding of the impact of hole inclination on tangential velocity. Fig. 4.9i and k show that the resultant absolute tangential velocity of particles increases with the increase in inclination angle from the vertical. A plausible explanation for the negative tangential velocities observed could be that the effect of pipe rotation induces velocity fluctuations (but with a general cuttings displacement pattern that maintains the streamline

momentum). Turbulent granular flows are characterised by incoherent and rapid shearing motions of the particles. Consequently, the boundaries of the flow domain generate energy at a rate equal to the product of the slip velocity and shear stress at the wall. Similarly, inter-particle interactions and particle interactions with the boundaries dissipate fluctuation energy via inelastic collisions. These energies can be transferred from one point to the other (granular conduction) in the annulus. The direction of granular conduction is determined by the wellbore inclination, which in turn determines the solids fraction distribution in the flow (Ahn, 1989). The volume fraction profiles in Fig. 4.9m-p illustrate that fluctuation energy is being conducted from the base of the annulus (where energy is generated) to the bulk of the flow (where energy is mostly dissipated, due to the high particle concentration and increased interactions). Hence, the solid fraction is low at the base, reaches a maximum towards the centre and then decreases near the drill pipe. Unless the energy generated supersedes the energy dissipated, there can be no sustained transport of the cuttings for a particular inclination, and cuttings build-up becomes inevitable. The skewness in volume fraction, as previously indicated in Fig. (4.8n and 4.8p) is seen to be replicated in Fig (4.9n and p).

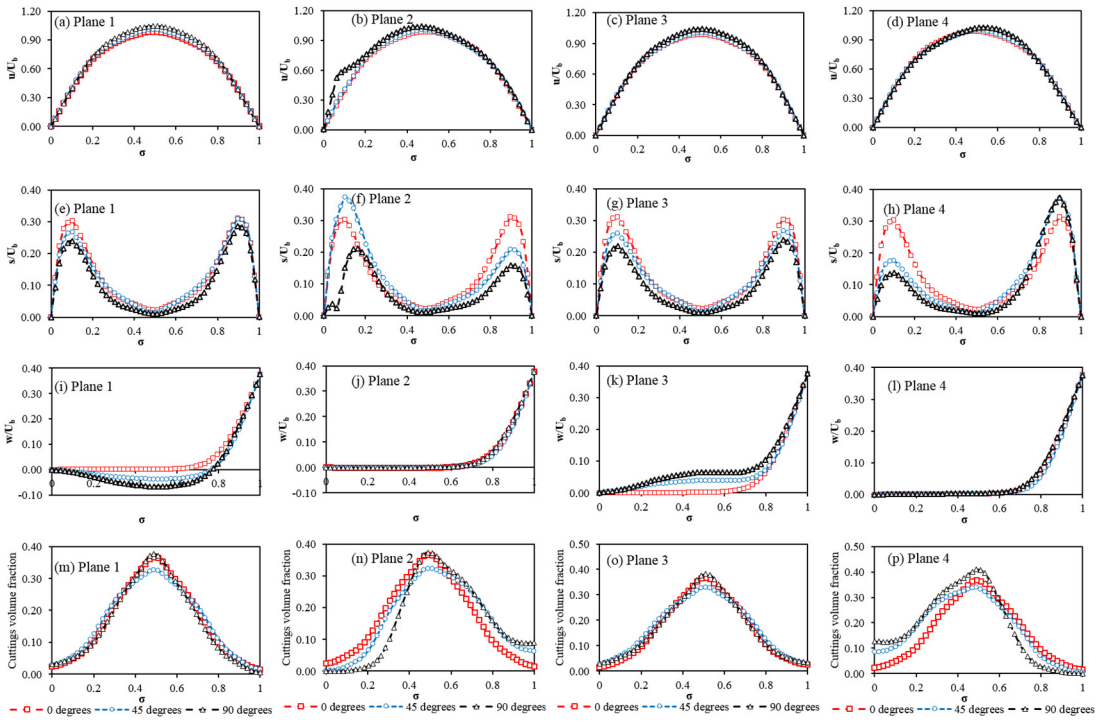

Figure 4.9. Effect of wellbore inclination on cuttings velocity profiles and volume fraction in a concentric annulus with the drilling mud as the carrier fluid, drill pipe rotation of 100 RPM, ROP of 50 ft.hr^{-1} and 5 mm cuttings diameter.

4.7.3 Effect of Particle Diameter

At this point, it is vital to consider the impact of the particles on the developed turbulent flow. When the response times of particles are short compared to typical times associated with the fluid motion, it is possible to have an apparent alteration in the fluid's effective properties (effective density and viscosity). This is the case with the smallest (1 mm) particles which tend to follow the fluid's turbulent motion closely. The results shown in Figs. 4.10a-d indicate that the cuttings axial velocity is to a large extent affected by the particle diameter. A greater dampening of the fluid's velocity is the case with very large particles (10 mm) as compared to smaller-sized particles (1 mm).

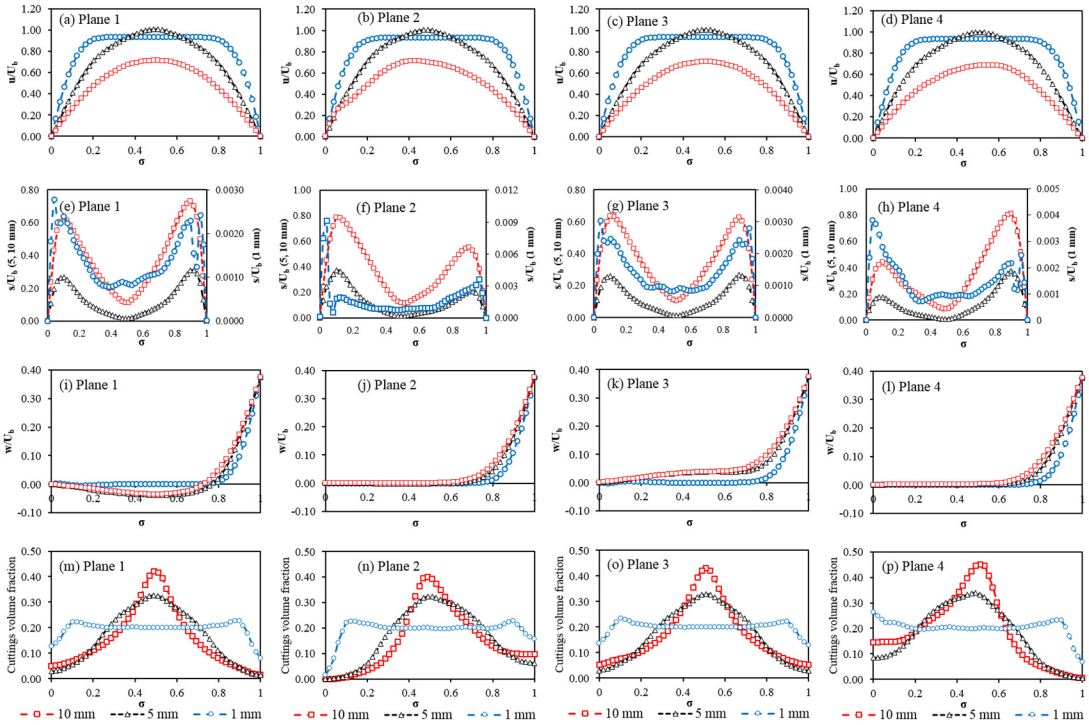

Figure 4.10. Effect of particle diameter on cuttings velocity profiles and volume fraction in a concentric annulus with the drilling mud as the carrier fluid, wellbore inclination of 45o, ROP of 50 ft.hr^{-1} and drill pipe rotation of 100 RPM.

Smaller-sized particles exhibit a flatter velocity profile with high velocities (the typical fluid turbulence behaviour). The slip velocities further elucidate this in Figs. 4.10e-h, where the slip velocities of the smallest particles are approximately two orders of magnitude lower than the slip velocities the 5 mm and 10 mm particles. The slip velocities observed with the 10 mm particles are higher than the slip velocities experienced by the 5 mm particles. This could be explained by the mechanism of turbulence suppression, which is attributable to the increase in velocity gradients in the flow (additional energy dissipation).

However, a well-rounded indication of the particles' impact on flow turbulence should not only be thought of as a function of the velocity modulation they pose to the fluid; careful consideration of the disorderliness and chaotic structures they create in the flow as they interact with the continuous phase ought to be similarly made. The use of the Lagrangian-Eulerian approach presented subsequently, pays more attention to the latter. The profiles of tangential velocities show that the larger particles possess higher tendencies to travel along the rotating path of the drill pipe compared to the smaller particles (10 mm particles have the highest tangential velocities). Given that the 1 mm sized particles are impacted more significantly by the fluid's motion, the drill pipe has a lower effect on their motion compared to the larger particles.

Thus, the conduction of the fluctuation energy (granular temperature) not only varies over the depth of the flow domain but also with the radial and azimuthal positions along the annulus. The movement of particles to regions originally devoid of particles (spreading) is observed with the 1 mm diameter particles, thus further demonstrating its tendency to behave in a continuous manner as the carrier fluid (Fig. 4.10m-p). The profiles of the 1 mm particle volume fraction show two mild off-centre peaks at regions close to the walls, which signify the spreading limit of the small cuttings in the annulus.

4.7.4 Effect of Fluid Rheology

Water, a less viscous fluid compared to the drilling mud, lacks the suspension ability to maintain the continuous transport of cuttings in the annulus. Hence, the cuttings travel at a lower velocity compared to the drilling mud along the main flow axis Figs. 4.11a-d. The slip velocities noticed with water also indicate that water hardly overcomes the large cuttings density during transport, thus yielding increased particle inertia against the direction of bulk fluid flow. This is further reflected in the high volume fractions exhibited by the cuttings Fig. 4.11m-p. This effect is more evident in plane 4 (the base of the 45^{o} inclined annulus) which is more susceptible to the impact of gravitational resistance. On the other hand, the tangential velocity profiles of the cuttings with water are generally higher than that of the mud. This is also illustrated in the fluid velocity streamlines shown in Fig. 4.15f with the DEM model (Fig. 15f). While the use of water induces an increased circular motion in the annulus due to its relatively lower viscosity, the drilling mud has its annular velocity channelled significantly in the axial direction. There is thus a clear outperformance of water by the drilling mud.

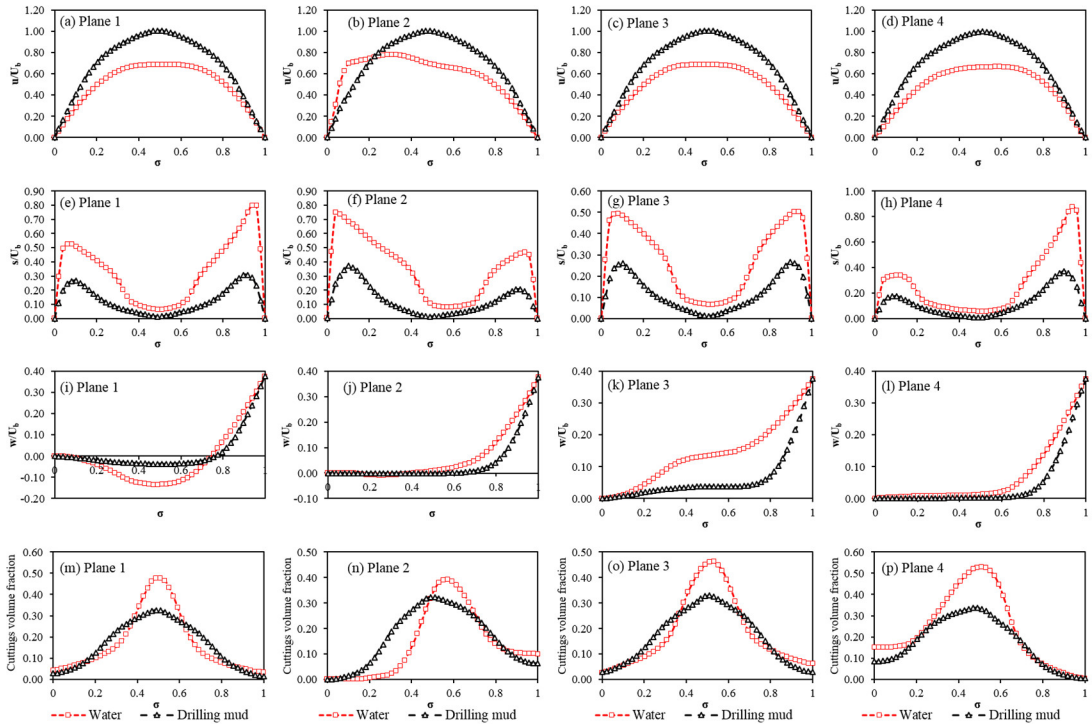

Figure 4.11. Effect of fluid rheology on cuttings velocity profiles and volume fraction in a concentric annulus at a wellbore inclination of 45°, ROP of 50 ft.hr^{-1}, drill pipe rotation of 100 RPM and 5 mm cuttings.

4.8 Analysis of Cuttings Velocity and Volume Fraction Profiles in an Eccentric Annulus using the EE model

As in the concentric case, same parametric variation is carried out in the eccentric annulus. Although most of the already observed and discussed phenomena are replicated here, there are subtle differences in the velocity and volume fraction profiles, and they carefully examined next.

4.8.1 Effect of Drill Pipe Rotation

As expected, increased frictional resistance is responsible for the lower velocities experienced by cuttings in the lower part of the eccentric annulus (Fig. 4.12d). Also shown in Fig. 4.12d is the more substantial impact of drill pipe rotation in the lower part of the eccentric annulus (Plane 4) compared to other regions. Tangential velocity is seen to increase with inner pipe rotation; thus, low-velocity cuttings close to the inner pipe and at the base of the annulus are swung into the bulk flow region. Besides the clearly illustrated trends (Figs. 4.12e-h), which explain that increased rotation causes a reduction in slip velocity, it can also be observed that the slip velocity profiles of the eccentric

annulus display a sustained central flattened region compared to the concentric annulus (except in plane 4). It could, therefore, be argued that the effect of drill pipe rotation is stronger in the eccentric annulus than the concentric annulus. This is because the shear-thinning behaviour of the non-Newtonian fluid makes it experience viscosity variations around the eccentric annulus with varying shear rates.

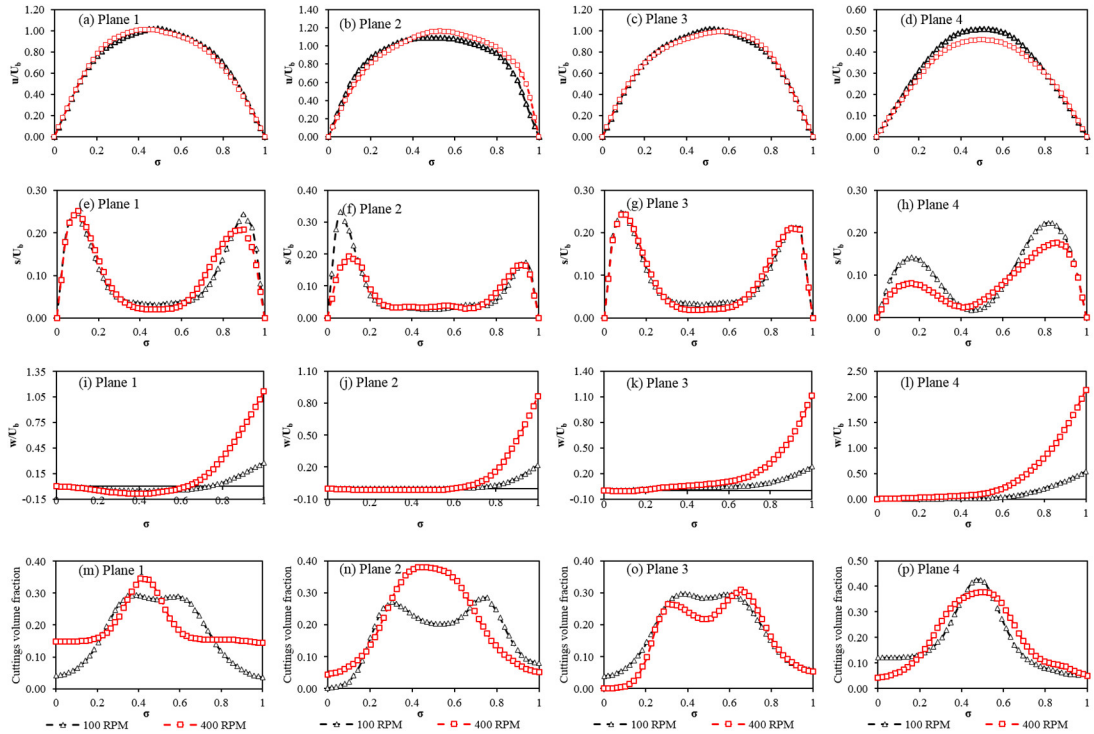

Figure 4.12. Effect of drill pipe rotation on cuttings velocity profiles and volume fraction in an eccentric annulus with the drilling mud as the carrier fluid, wellbore inclination of 45°, ROP of 50 $ft.hr^{-1}$ and 5 mm cuttings diameter.

In the broader part of the annulus (low-shear region), the viscosity of the fluid is relatively higher, thus leading to an increase in its carrying capacity. Conversely, at the narrow annular section (high-shear region), the viscosity is lower, and a reduction in the fluid-carrying capacity ensues. The concentric annulus, however, experiences a pseudo-uniform shear rate with similar fluid performance irrespective of cuttings location. This increased shear thinning effect with increased pipe rotation is also the most probable reason for the slightly reduced cuttings velocity (at 400 RPM – Fig. 4.12d). Furthermore, while the extended flattened central regions are relatively similar for both rotations in the eccentric annulus; this is not the case in the concentric annulus slip velocity profiles (Fig. 4.8e-h). At 400 RPM, the central part is more flattened compared to the slip velocities at 100 RPM (Fig. 4.8e-h). Thus the impact of drill pipe rotation could be advantageous because slip

velocities are reduced, but can be unfavourable (specifically at the lower parts of the annulus) due to increased shear thinning in eccentric configurations. The coupled manifestation of both phenomena is a possible reason why various researchers (Ofei et al. 2014; Han et al. 2010; Duan et al. 2008) have discovered only slight improvements in cuttings transport efficiency when drill pipe rotation is increased. The volume fraction/distribution of solids are distinct in each plane with off-centre peaks appearing in both drill pipe rotation profiles. Additionally, the solid-phase volume fractions close to the drill pipe and wellbore are less than other regions; this allows faster fluid movements relative to the solid, hence the two peaks experienced in the slip velocity profiles. It is however noticed that the dual peaks in volume fraction profiles (Fig. 4.12m-o) which are most likely attributable to the eccentric flow configuration are absent in Plane 4 – the base of the annulus. Inevitably, this occurs due to the build-up of cuttings (reflected in the higher volume fractions – Fig. 4.12p).

4.8.2 Effect of Wellbore Inclination

The cuttings axial velocity profiles illustrate that the horizontal flow configuration slightly favours the transport of cuttings (Fig. 4.13a-c); however, slip velocities show more pronounced effects with changes in the hole inclination. As observed, the slip velocities are lowest in the horizontal annulus. This is because the impact of gravitational flow resistance (due to the density difference between both phases) is not as high as when the wellbore is inclined or vertical. Additionally, the impact of pipe rotation reflected in the tangential velocities (Fig. 4.13i-l) is higher in the horizontal and inclined configurations compared to the vertical configuration. A possible reason for this is that the improvement in cuttings transport phenomena is very noticeable for a system characterised by relatively large velocity gradients (some particles moving with bulk fluid and others gliding over a bed or stationary, such as the case in horizontal or inclined annuli). On the other hand, a flow system in which these gradients are relatively lower does not seem to experience to the same degree, the impact of drill pipe rotation (which is to sweep cuttings from the narrower region to the wider region in the annulus). For the same previously explained reasons, the narrower section shows higher tangential velocities. Except for plane 4 with the highest volume fraction, the dual off-centre peaks in volume fraction are exhibited by all inclination angles in planes 1, 2 and 3 (Fig. 4.13m-p).

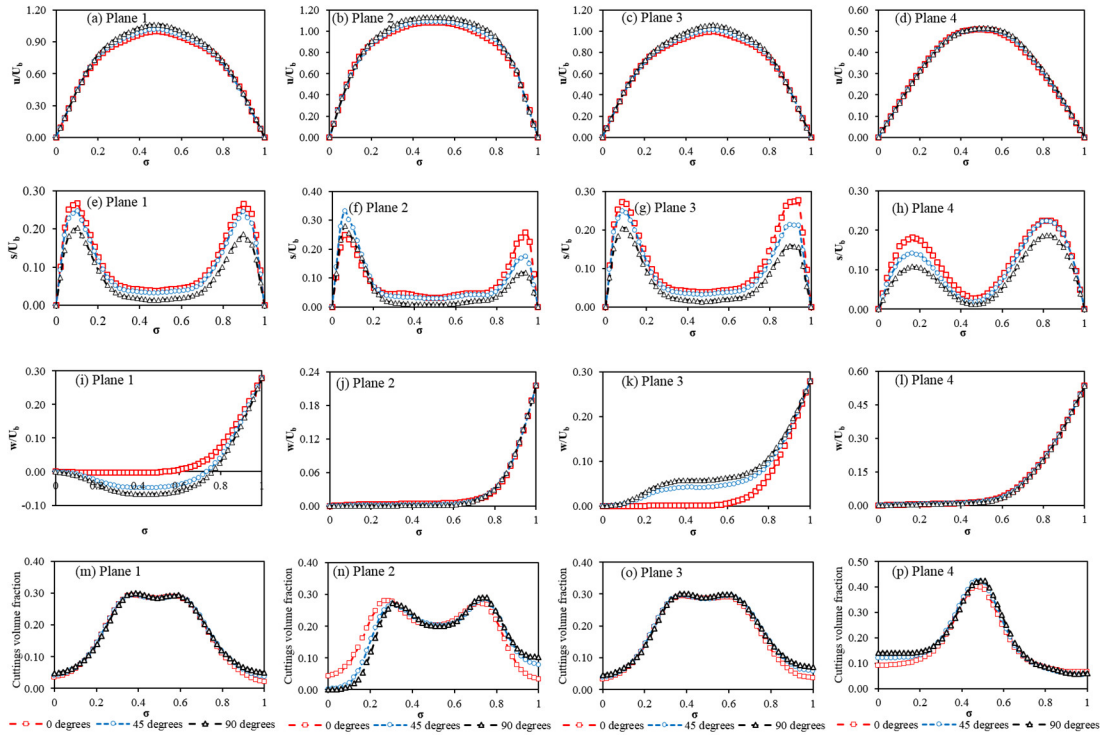

Figure 4.13. Effect of wellbore inclination on cuttings velocity profiles and volume fraction in an eccentric annulus with the drilling mud as the carrier fluid, drill pipe rotation of 100 RPM, ROP of 50 ft.hr^{-1} and 5 mm cuttings diameter.

4.8.3 Effect of Particle Diameter

Particle spread around the annulus is higher with the 1mm particles than other particle sizes. Consequently, at the base of the annulus, smaller particles travel fastest (Fig. 4.14d). Not only do the 5mm particles exhibit lower slip velocities, they also have a more flattened profile at the central part of the annulus compared to the 10mm particles; hence demonstrating their relative ease of transport. The 1mm particles, on the other hand, have very low slip velocities (about two orders of magnitude less than the other particles). Similar to the concentric case, larger particles show a greater tendency to rotate along the circular path of the drill pipe compared to the 5mm and 1mm particles. Also, the cuttings distribution along all planes illustrate the spreading tendencies of the individual particle sizes. 10 mm particles have their peak concentrations in the middle of the annulus with a steep-sided drop until the boundaries are reached; whereas, 1mm particles show a reasonably constant concentration throughout, but drop abruptly close to the walls. Smaller particles will tend to respond faster to the fluid flow and would faithfully follow the fluid path lines compared to larger particles. Larger particles, due to increased inertia

effects will take a relatively long time to respond to the fluid flow and hence would most likely continue in near rectilinear trajectories or independent random trajectories that could impose more turbulence to the flow. The explained phenomena are observed in the trajectories of particles shown in Fig. 4.18b, which further describes the spreading phenomena.

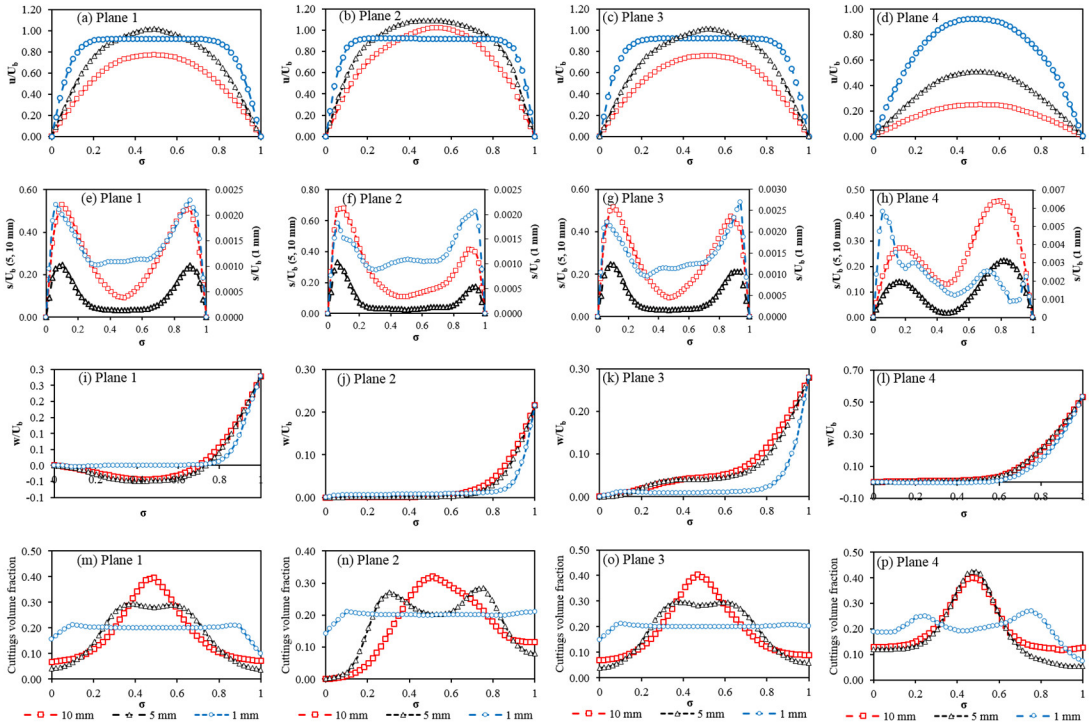

Figure 4.14. Effect of particle diameter on cuttings velocity profiles and volume fraction in an eccentric annulus with the drilling mud as the carrier fluid, wellbore inclination of 45°, ROP of 50 ft.hr^{-1} and drill pipe rotation of 100 RPM.

4.8.4 Effect of Fluid Rheology

Besides the occurrence of dual off-centred peaks in the volume fraction profiles of the eccentric annulus (Fig. 4.15m-p), all other profiles and explanations are similar to the concentric annulus. For the range of varied parameters, no volume fraction profile in the concentric annulus portrayed the dual-peak phenomenon; hence, its occurrence is most likely due to the peculiarities of the shearing mechanism and granular conduction in the eccentric configuration.

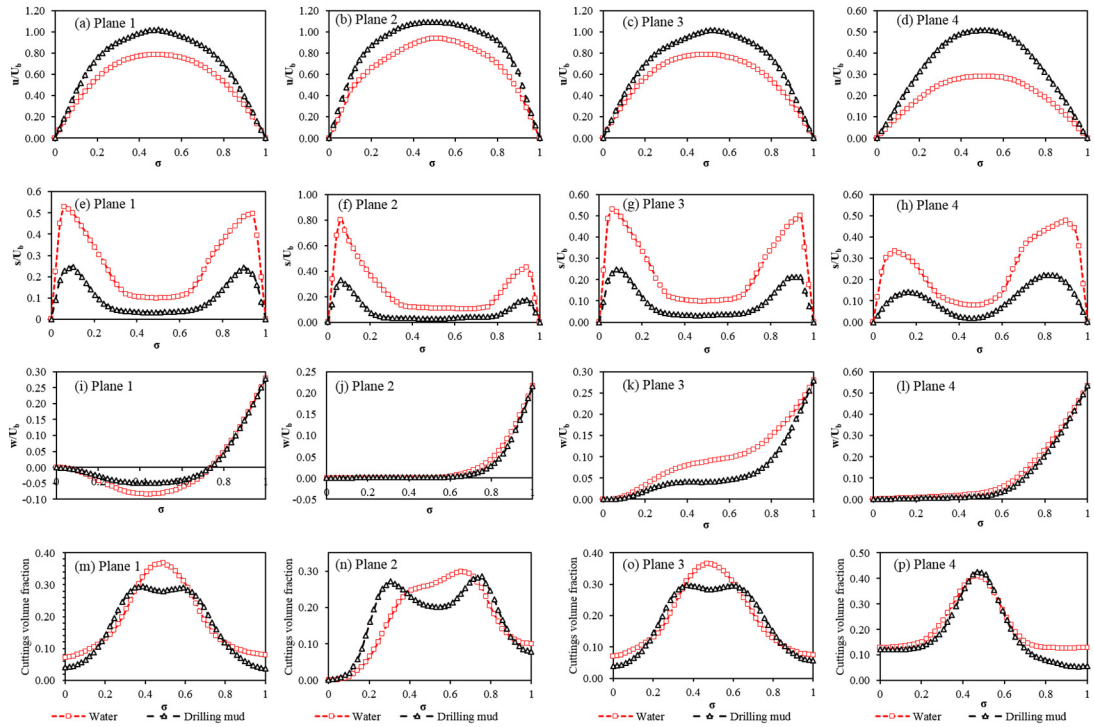

Figure 4.15. Effect of fluid rheology on cuttings velocity profiles and volume fraction in an eccentric annulus at a wellbore inclination of 45°, ROP of 50 ft.hr^{-1}, drill pipe rotation of 100 RPM and 5 mm cuttings.

4.9 Analysis of Pressure Drop Profiles in Concentric and Eccentric Annuli

Fig. 4.16 shows the pressure drop profiles for the different flow configurations. With an increase in pipe rotation, only a slight increase in pressure drop is observed in the concentric annulus. The eccentric annulus, however, shows no difference. The slight increase is attributable to the shear instabilities that ensue as a result of the rotary motion of the drill pipe. The impact of gravity in both annuli is the inevitable reason for the higher pressure drop values noticed with the vertical configuration. Pressure drop is seen to reduce as the annulus becomes horizontal. Furthermore, increased particle inertia with increased particle size and collision frequency indicate a higher pressure drop is necessary for their transport. Thus, 10mm particles have the highest pressure drop in both concentric and eccentric annuli. Compared to the eccentric wellbore, the 10mm particles in the concentric configuration induce a pressure drop which is considerably higher than those observed with the smaller-sized particles - 1mm and 5mm (Figs. 4.16c and g). Viscosity differences between the drilling mud and water and the accompanying shear

forces majorly constitute the reasons for the increased pressure drop associated with the mud. Better hole cleaning is achievable with the use of the mud compared to water as the carrier fluid.

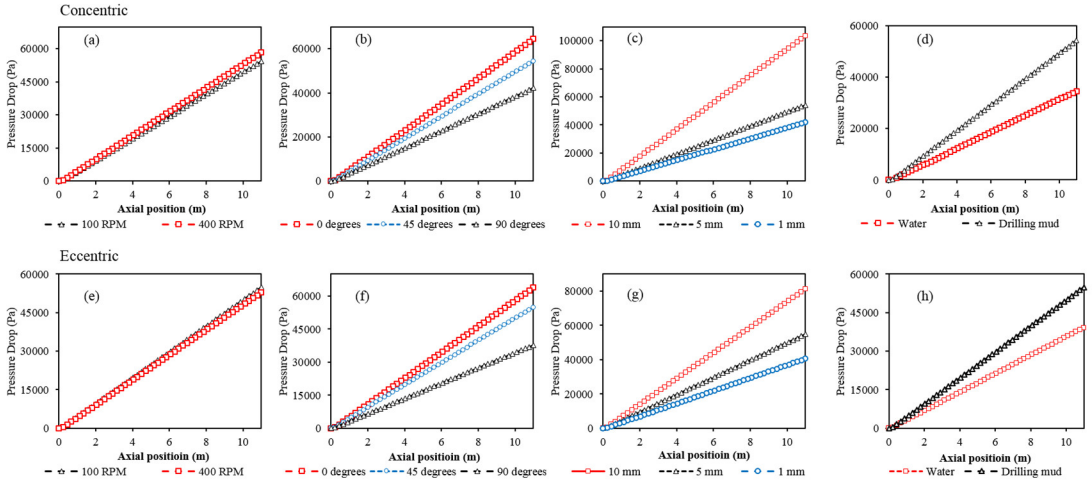

Figure 4.16. Pressure drop profiles.

4.10 Analysis of Fluid Streamlines and Particle Trajectories using the Lagrangian-Eulerian Model

Although, the Eulerian-Eulerian approach earlier seen requires transport quantities of all phases to be continuous throughout the computational domain, in reality, these phases could be time-dependent and as well, be discretely distributed. In this section, we address flow conditions in which the direct inter-particle and particle-wall interactions play the most important role in determining the flow mechanics. Through the consideration of time dependency and the use of appropriate boundary conditions, it is possible to gain better insight into the transport phenomena; one of which is the combined effects of turbulence and gravity on particle settling. Only the eccentric configuration is considered in this case due to its greater prevalence in drilling operations and the computational expense involved. Except where specified, particle diameter = 5mm; drill pipe rotation = 100 RPM, ROP = 100 $ft.hr^{-1}$; wellbore inclination = 90^{o} (horizontal wellbore); and the carrier fluid is drilling mud.

4.10.1 Fluid Streamlines

Fig. 4.17 shows the streamlines of the fluid velocities at different flow conditions after a simulation time of 3.5 seconds (sufficient for the attainment of SSS). The wider annular sections generally display high fluid velocities due to the lower flow resistance

encountered. In the case where 1mm particles are used, a relatively large region of lower fluid velocities is noticed. This is because the particles assume a more continuous flow mechanism, thus, altering the effective fluid viscosity. With wellbore inclination (0° and 45° from the vertical), the fluid velocity is hindered by gravitational resistance. At a drill pipe rotation of 400 RPM, the swirling frequency of the fluid increases, as shown in the slightly more concentrated streamlines of (Fig. 4.17d), compared to Fig. 4.17c at 100 rpm. Furthermore, when water is used as the carrier fluid, a highly circumferential transport mechanism is noticed compared to other flow conditions (Fig. 4.17f). This further substantiates the observations of tangential velocity profiles seen in Fig. 4.11i-l and 4.15i-l. A higher Rate of Penetration (ROP) implies more cuttings ingress, which causes an increase in the shear rate, particularly at the base of the annulus where the particles tend to settle. This is depicted as the high-velocity region at the lower section of the annulus (Fig. 4.17e) compared to other regions.

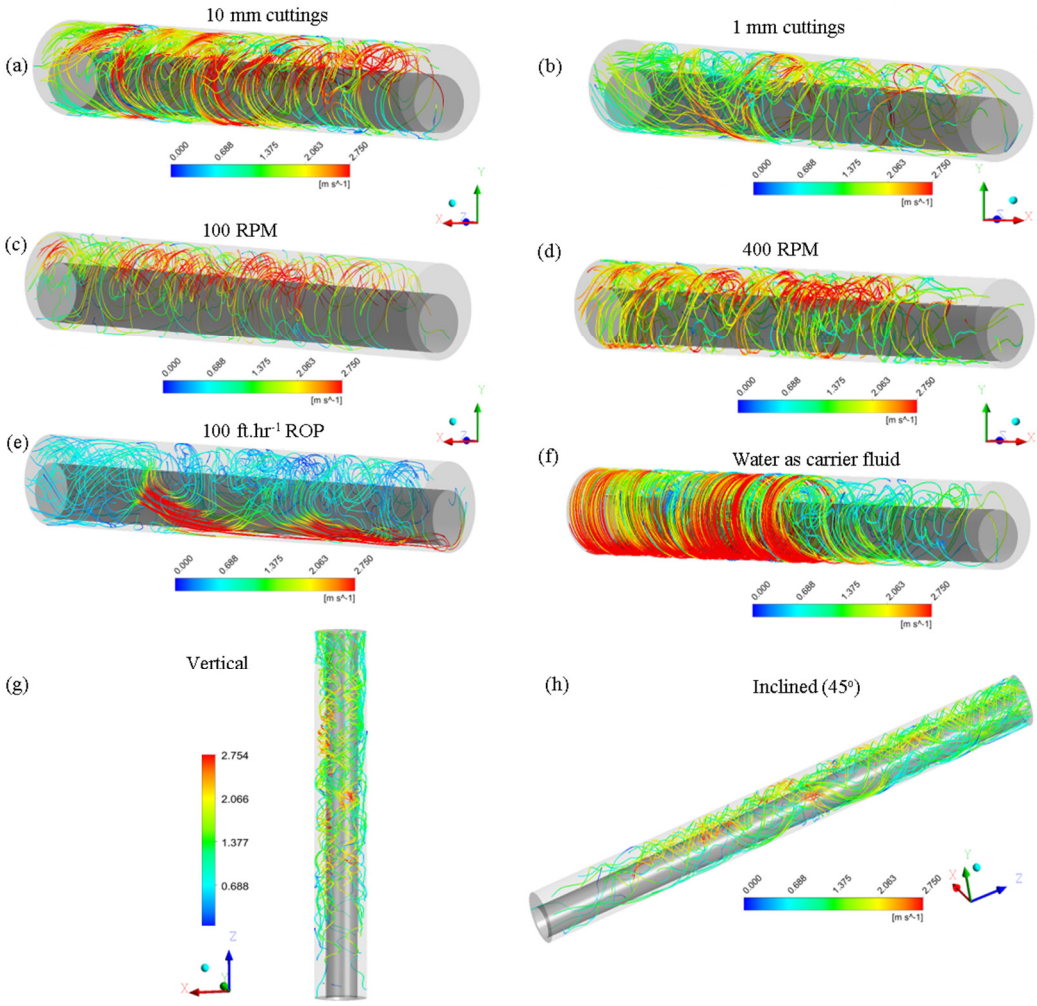

Figure 4.17. Fluid streamlines at different flow conditions.

4.10.2 Particle Trajectories

Compared to the rather continuous fluid streamlines, the particles' trajectories are highly discontinuous (Fig. 4.19a-h), thus explaining the haphazard motion of the particles associated with the turbulent motion of the fluid. Particles generally displayed oscillatory movements due to pipe rotation from the animations of particle tracks developed. Also, the inclined, vertical and 100 $ft.hr^{-1}$ (ROP) flow conditions revealed pronounced reverse flows in particle motion. The reasons are, of course, related to the impact of gravity and increased particle ingress into the annulus. The impact of rotation on the 10 mm particles appears to be the strongest (Fig. 4.19a). The trajectories (Fig. 4.19a) show that the particles traverse the circular path (around the drill pipe) to a greater extent compared to the 1mm and 5 mm particles. Again this was demonstrated in the tangential velocity profiles using the Eulerian-Eulerian model (Fig. 4.10i-l and 4.14i-l). A high interpenetration of particle lines at the sides of the annulus is observed with the 1mm particles (Fig. 4.19b); the degree of this particle dispersion can be scaled with the Stokes number (Roco, 1993). Fig. 4.18 shows the calculated Stokes numbers and turbulent eddy frequencies for the different particle diameters. Chein and Chun, (1987) observed that a Stokes number close to unity indicates the tendency of particles to attain maximum spread in the flow domain; which corresponds with results obtained so far with the EE model. However, Tang et al. (1992) discovered a rather dramatic phenomenon in which large scale turbulent structures could lead to an organised concentration pattern of small-sized particles in localised regions of the flow; thus demonstrating that the existence of turbulence does not always guarantee the production of a homogeneous mixture. This is a reasonable explanation for the observed structures along the sides of the annulus for the 1mm cuttings (Fig. 4.19b). The turbulent eddy frequency was used as an index of the particles' impact on fluid turbulence. As clearly illustrated in Fig. 4.18, larger particles exhibit the highest frequency; thus, implying a greater tendency to induce turbulence. The 5 mm particles follow next in magnitude, while the smallest particles exhibit the lowest frequencies. With the results obtained from the Eulerian-Eulerian model and the Lagrangian-Eulerian model, we infer that modulation/dissipation of fluid turbulence and the generation of turbulence to the flow are intricately dependent on the particle size.

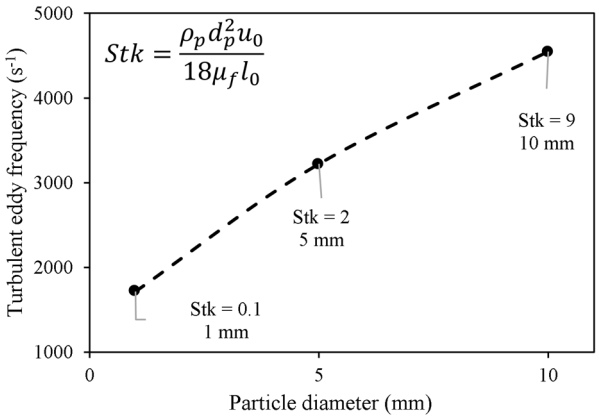

Figure 4.18. Contribution of particles to the turbulence of flow.

Although the impact of hole eccentricity in the vertical flow configuration is relatively less significant, Fig. 4.19g shows that particles tend to travel along the sides of the annulus.

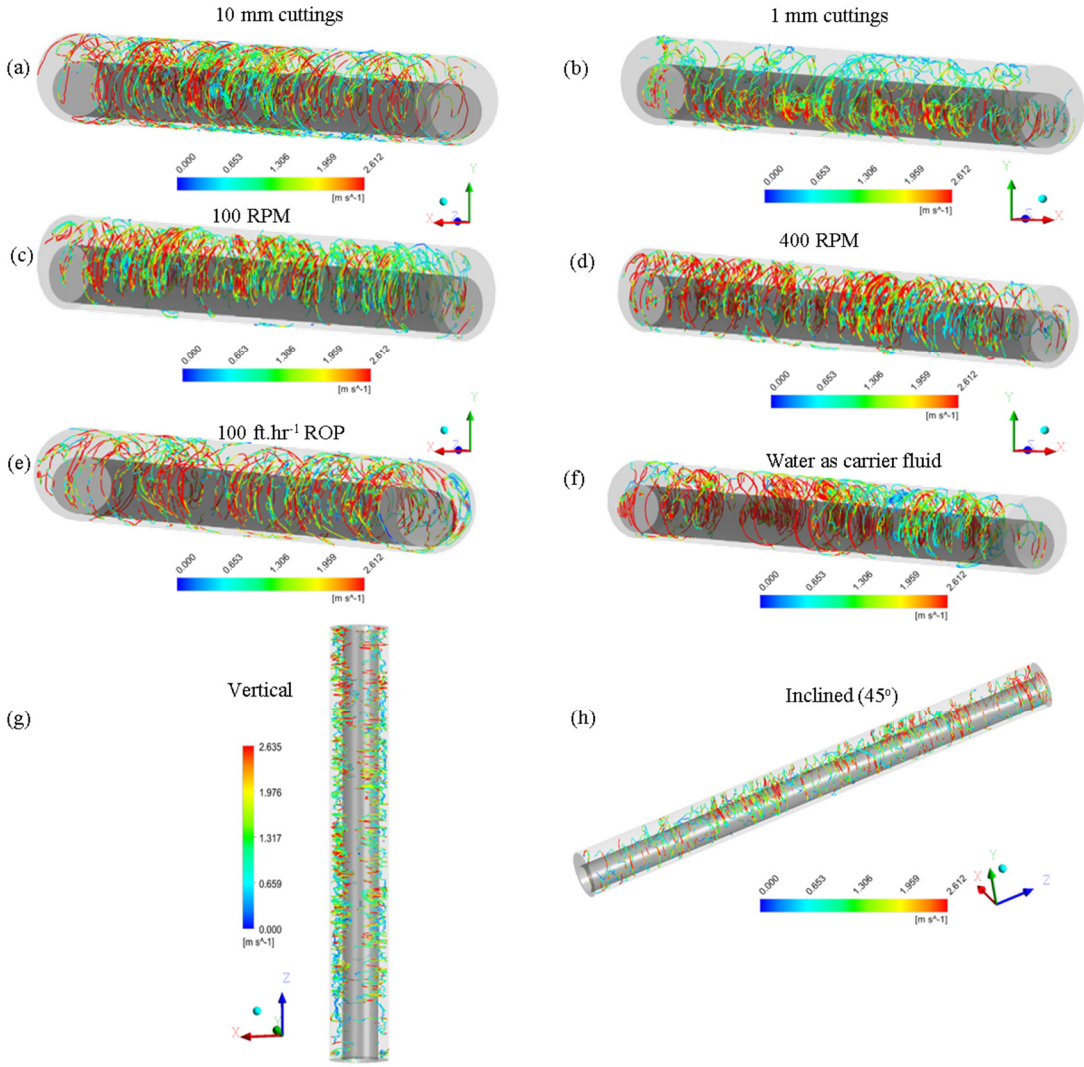

Figure 4.19. Cuttings trajectories at different flow conditions.

The broader region of the annular space leaves a large section of the flow open to gravitational resistance compared to sides, thus explaining the most likely reason for the observed transport mechanism. Observed cuttings velocity in the vertical and inclined annuli are generally lower than those observed in the horizontal flow conditions.

4.10.3 Fluid Velocity Vectors

Besides affecting the unsteady nature of the shear layer, the occurrence of particles can also affect the growth and vorticity profiles in the developing layer, thus giving rise to some organised structures in the fluid (Crowe et al., 1985; Roco, 1993; Crowe et al., 2011). Analysing the velocity vectors of the fluid in both normal and tangential directions along the longitudinal YZ Plane (Fig. 4.20) could provide deeper insight into the underlying phenomena. Kline et al. (1967), Hetsroni, (1989) and Roco (1993) pointed out the formation of coherent structures at the wall (organised streak-like fluid structures moving at different velocities due to shearing forces) visually observed in two-phase solid-liquid flows; it was also discovered that turbulence energy production is a consequence of this phenomena.

These streak-like structures observed in Fig. 4.20, originate from the wall and generally lift particles into the bulk flow region. After these ejected particles travel a certain distance from the wall, they experience a loss in their upward momentum and return towards the wall. This occurs continuously throughout the flow and is termed 'particle recycling' (Tomren et al. 1986; Crowe et al. 1985). The frequency of these ejections from the boundaries significantly depends on the particle properties.

As flow progresses, eddies developed by the particle-fluid interaction in the bulk flow are transformed into higher frequencies turbulent motion depending on the magnitude of the slip velocity; thus larger particles may cause increased formation of these coherent structures.

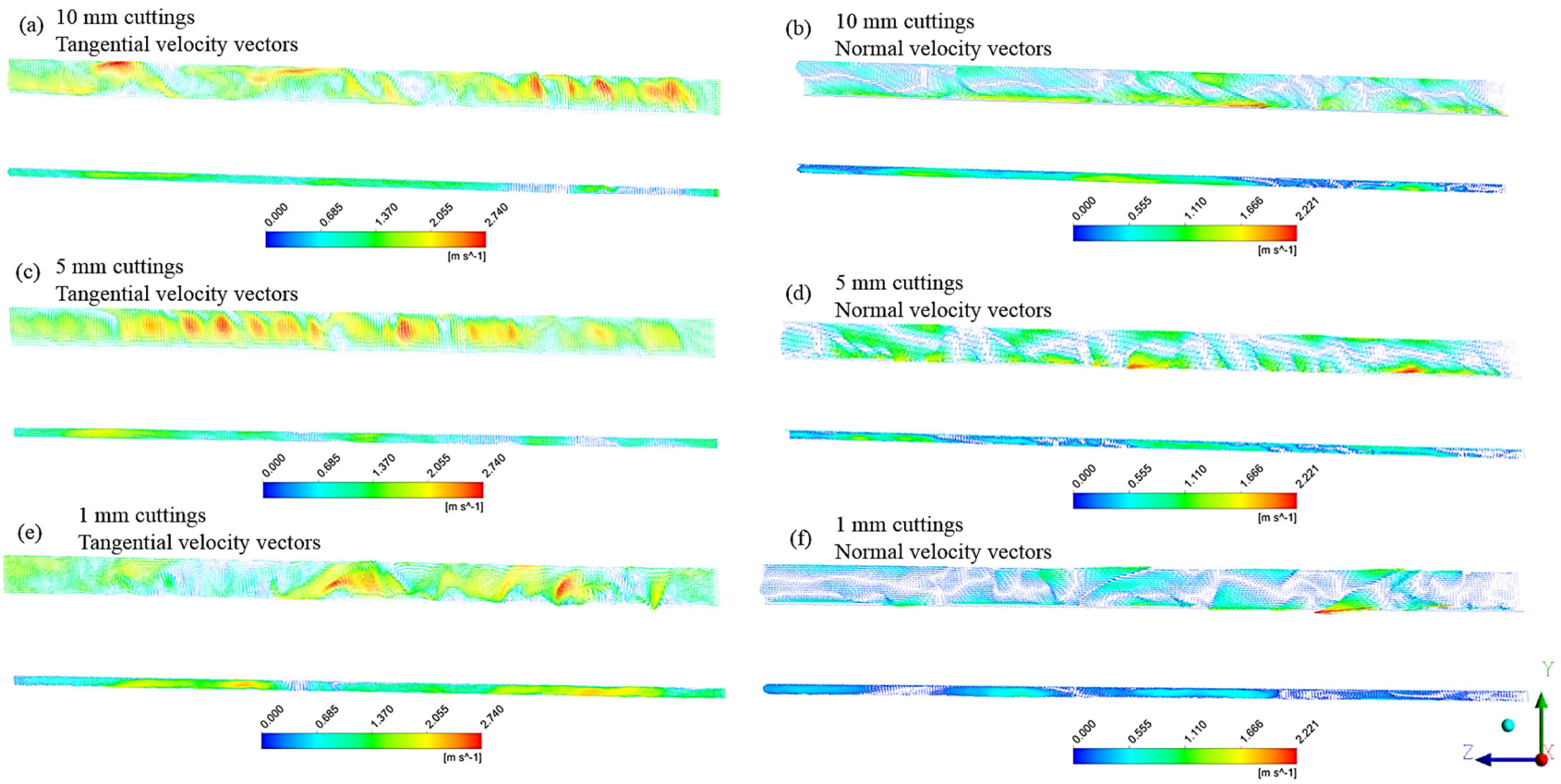

Figure 4.20. Fluid velocity vector plots showing ejections from the walls.

4.10.4 Cuttings Volume Fraction

Time-averaged volume fractions over a simulation time of 3.5 s are displayed in Fig. 4.21. The particle volume fraction is seen to increase at the narrower annular section in virtually all flow configurations besides the vertical (in which particles concentrate around the sides). The use of water as the carrier fluid results in higher particle concentrations; this increases further when the drilling mud is used but at a higher penetration rate of 100 $ft.hr^{-1}$.

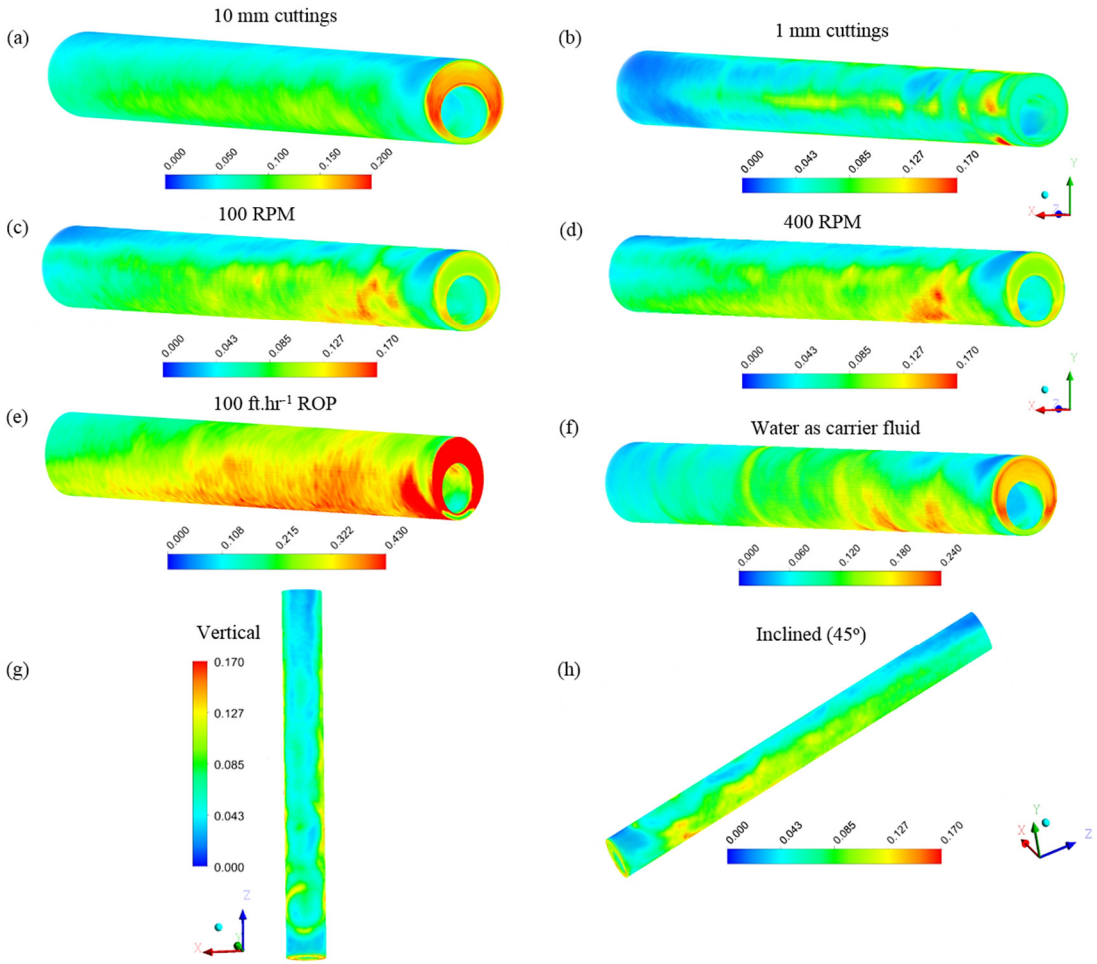

Figure 4.21. Cuttings volume fraction at different flow conditions.

High rates of penetration induce increased fluctuations in particle velocity, which prevent free particle movements from one annular location to another, thus increasing the velocity gradients and eventual deposition tendencies. Flow animations produced from the simulation of the cuttings transport phenomena at high ROP reveal considerable reverse flow in particle motion which was more pronounced at the entry up until mid-way the annulus. A further explanation of the impact of high ROPs is that the friction at particle-

particle and particle-wall contacts increases and this correspondingly increases the cuttings velocity lag, relative to the fluid axial motion. This, in turn, exposes the cuttings to higher tangential motion impacted by the rotating drill pipe. As previously explained, a local concentration of the 1mm particles occurs along the lateral annular section. In all cases of Figs. 4.21a-h, the impact of drill pipe rotation is generally observed to affect the particle distribution, particularly at regions close to the entrance of the annulus. Accurate determination of hole cleaning performance significantly depends on the predictability of cuttings annular distribution under different drilling conditions, and this has so far been demonstrated.

4.10.5 Contour Plots and Flow Visualisations

Fig. 4.22a shows increased concentration on the sides of the annulus; however, the concentric case (Fig. 4.22b) has an even distribution of cuttings in the central region.

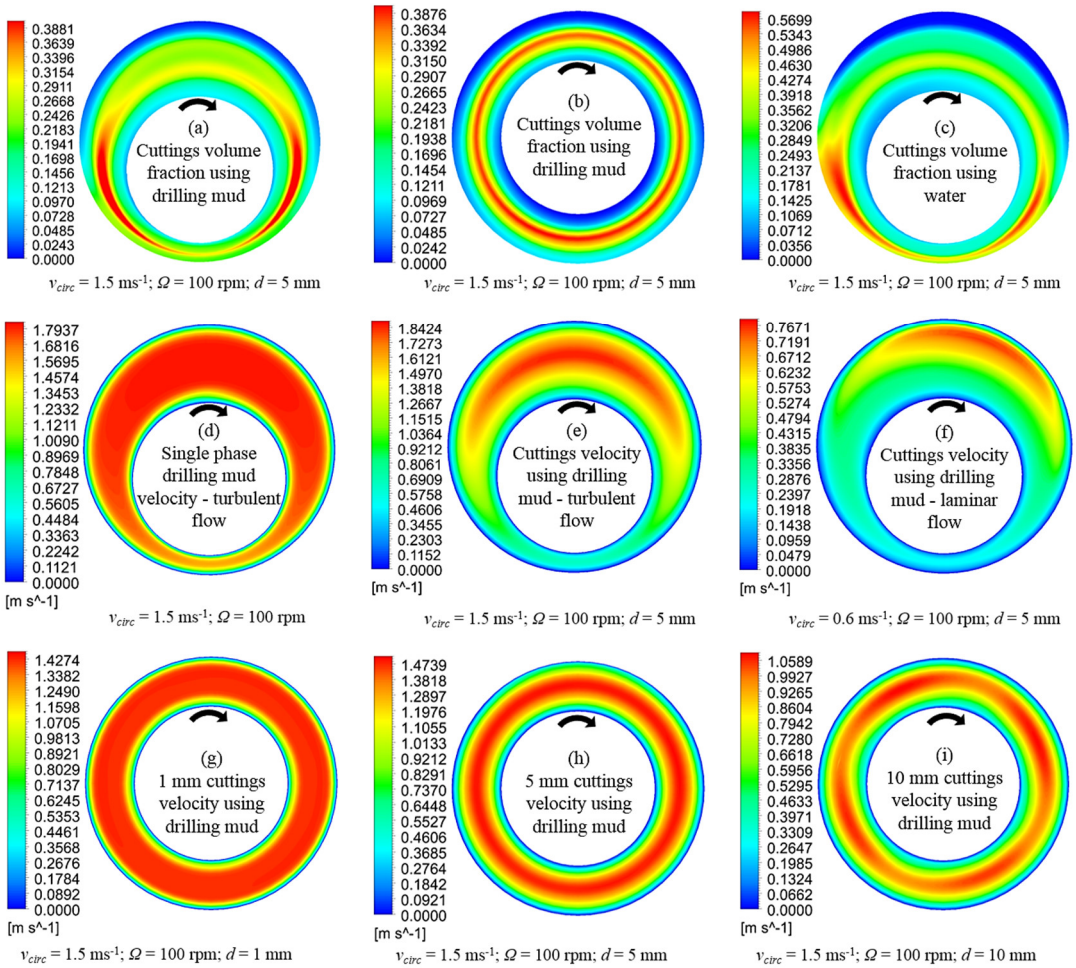

Figure 4.22. Contour plots of volume fraction and velocities of the drill cuttings and carrier fluid at different flow conditions.

An increased deposition is noticed with water as the carrier fluid (c). Previous work with a drilling mud of higher quality (Epelle and Gerogiorgis, 2017) showed even cuttings velocity profiles; however, the cuttings distribution observed here exhibit a strong spatial variation around the annulus. Fig. 4.22(d) shows the high fluid velocity obtainable in single-phase flow; this is dampened by the introduction of cuttings (Figs. 4.22e and f). The impact of drill pipe rotation on the asymmetric velocity distribution is more substantial under laminar conditions; this is not noticed in Fig. 4.21e. The region of high cuttings velocity around the annulus (an indication of particle dispersion) decrease with the increase in cuttings diameter as seen in Figs. 4.22g, h and i, respectively.

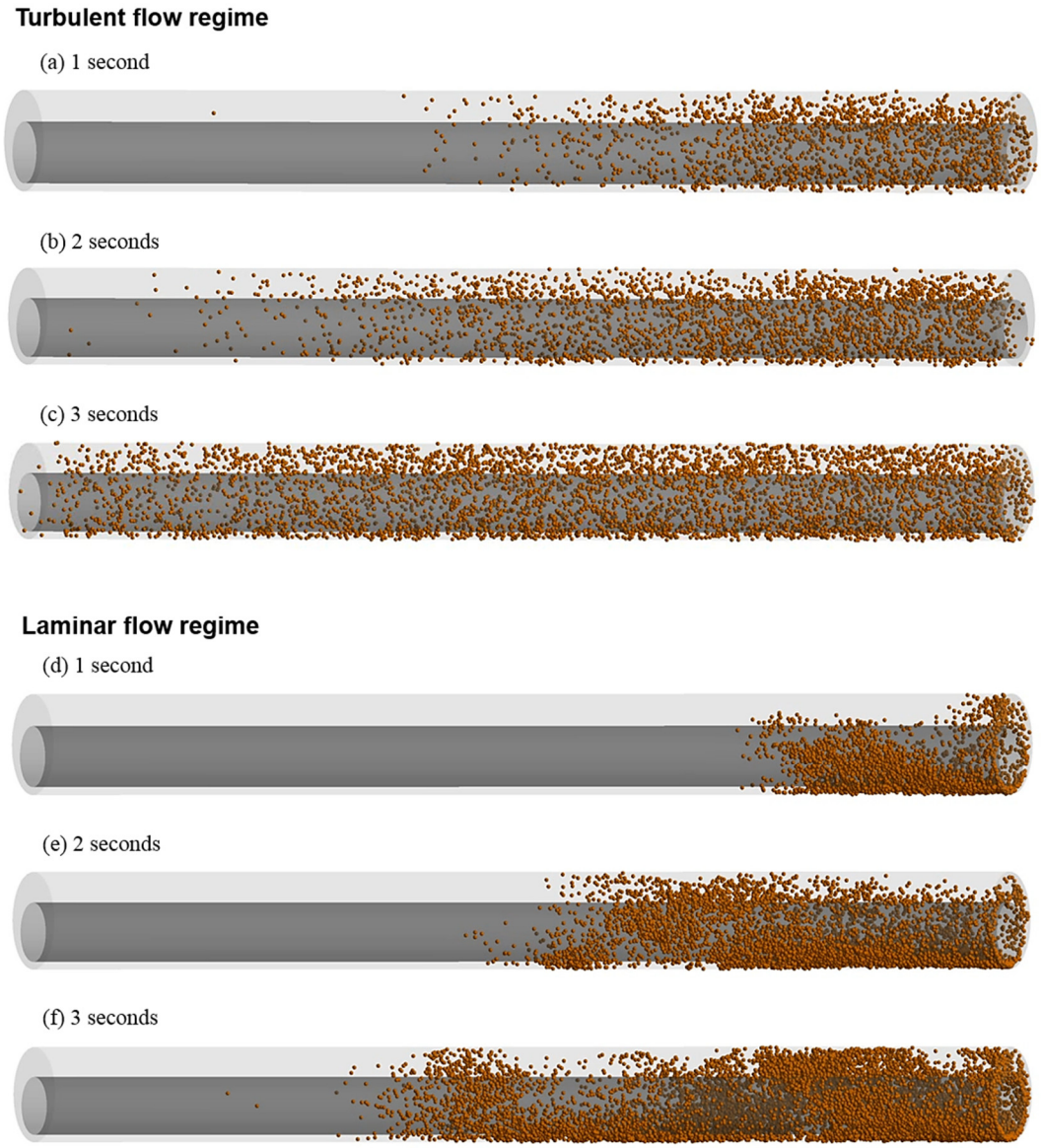

Figure 4.23. Snapshots of particle (5 mm) flow behaviour in turbulent (a-c) and laminar (d-f) flow regimes.

In order to qualitatively understand the impact of turbulence (v_{circ} = 2 ms^{-1}) on cuttings transport, laminar flow conditions (v_{circ} = 0.6 ms^{-1}) were also simulated (Fig. 4.23). With increased flow time, particles gradually fill up the annulus in a uniform manner under turbulent conditions. In the laminar flow regime, inter-particle spacing is low, thus yielding slight cuttings deposition. Drill pipe rotation (100 RPM) is seen to lift and sway particles as the flow progresses, and this aids the transport process. In order to attain a statistically steady-state (in which particles fully traverse the annular length) at laminar conditions, the simulation has to be run for longer periods.

4.11 Chapter Conclusions

This study presents the steady and unsteady state analysis of drill cuttings transport phenomena under turbulent conditions using the Eulerian-Eulerian and Lagrangian-Eulerian multiphase modelling methods. It was discovered that the complex boundary phenomena that evolve in multiphase flows containing solid particles could not be understood independently of the flow field and thus an evaluation of the velocity and volume fraction profiles at different flow conditions was carried out. Further observations made during this study lead to the following conclusions:

- Slip velocity profiles generally displayed a convex signature in the central regions of all annular planes considered. Increased pipe rotation (400 RPM) in the concentric annulus is seen to yield more flattened central profiles compared to lower rotation velocities of 100 RPM. Drill pipe rotation thus aids homogeneity in cuttings removal.
- The tangential velocity experienced by particles is higher when the flow configuration is horizontal. Also, large (10 mm) particles tend to closely follow the rotational motion of the drill pipe compared to cuttings of smaller sizes (1mm and 5mm).
- We infer that there is some slight modification of the effective fluid properties (increased viscosity and density) by the cuttings of 1 mm diameter (low Stokes number). Hence the lower fluid velocities observed compared to other particle diameters.

- The profiles of volume fraction using the Eulerian-Eulerian model show that 1mm particles are more readily dispersed around the annulus compared to larger particles. While the 10 mm particles tend to dampen the flow turbulence as demonstrated in the cuttings axial velocity profiles, they may also enhance turbulence by increasing the occurrence of large and small scale eddies. Turbulent eddy frequencies were observed to be larger with particles of 10mm diameter compared to the frequencies produced by the 1 mm and 5 mm particles respectively.

- The occurrence of coherent structures (streak-like fluid ejections emanating from the wall) is observed using the Lagrangian-Eulerian model. These structures are mainly responsible for the lifting of particles into the bulk flow region. It is also possible that these structures are enhanced by the rotary motion of the drill pipe.

- Particle trajectories and 3D volume fraction profiles in the vertical flow configuration reveal that particles tend to travel along the sides of the annulus compared to other annular regions.

While experimental measurements of cuttings velocity during high-speed turbulent flows with high Stokes numbers could be difficult to obtain because of the increasing gravitational effects for large particles, CFD/DEM models implemented in this work show remarkable potential for predicting and understanding such flow conditions in a cost-effective way. Although significant progress has been made, a lot remains to be done; particularly investigating new phenomena surrounding flows with non-uniform particle size distribution and the occurrence 3 phases (solid, liquid and gas) during underbalanced drilling operations. Consequently, more experimental data on cuttings velocity profiles would be necessary for further validation of these CFD models, especially in the context of major technological developments, such as nanoparticle-based drilling fluids and their complex rheology (Kelessidis et al., 2006; Reilly et al., 2016; Vryzas and Kelessidis, 2017).

Chapter 5 Cuttings Transport in Annular Bends: Effects of Particle Sphericity

The current status of understanding of the motion of non-spherical particles (Fig. 5.1) during drilling operations has some limitations; one of which is related to the apparent simplicity, that perfectly spherical particles provide particularly in modelling. Particles encountered during drilling are hardly spherical; hence, extra parameters are necessary for increased accuracy as far as their flow description and prediction are concerned. Exact mathematical quantification of the geometry of complex irregular solid particles is challenging; however, the concepts of particle equivalent diameter and shape factors of different types (Corey shape factor, roundness and sphericity) are usually employed in several process engineering applications. Despite the existence of these descriptors of particle irregularity such as Wadell roundness, Dobkins and Folk roundness, Power's roundness, Wadell sphericity, Krumberin sphericity, Sneed and folk sphericity and Riley sphericity, the Wadell sphericity is the most widely implemented single measure of particle shape characterisation. This is undoubtedly attributable to its ease of implementation with existing drag models for spherical particles.

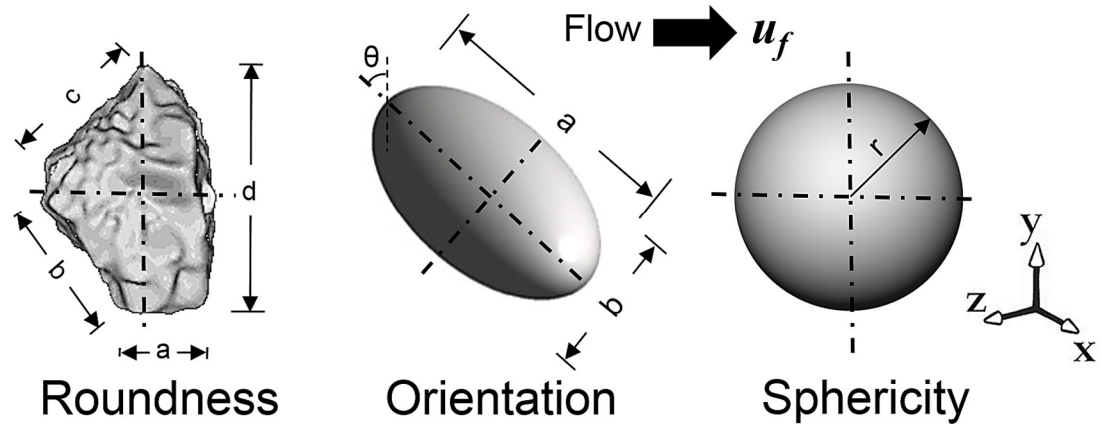

Figure 5.1. Particle shape descriptors.

The previous chapter considered turbulence modulation by particles of different sizes on the transport fluid during drilling operations but neglected flow complexities that arise due to the shape of the particles. It is expected that the particle shape will have substantial effects on the turbulent modulation and dispersion characteristics as well as the particle-fluid interactions. Considering this limitation, and the scarceness of published literature which addresses this challenge, we aim to incorporate the effect of particle shape into the

modelling equations by a slight modification on the exchange coefficient in the Syamlal-O'Brien (SO) model. Furthermore, we analyse solid-liquid flow in a fairly different geometry compared to what has been previously applied using two types of drilling mud. Such geometry (Fig. 5.4) considered here is often realisable in extended-reach and deviated well drilling. We aim not only to provide some insight into the dynamics of the transport process but also to present a modification strategy which could be extended for capturing more advanced phenomena such as turbulence.

5.1 CFD Model Description

The Eulerian-Eulerian (EE) multiphase flow model describes the behaviour of multiple, separate and yet interacting phases (Fluent, 2017). Unlike the computationally expensive Lagrangian-Eulerian (LE) model in which statistically computed particle trajectories are evaluated for a large number of particles, the EE model evaluates the particle concentration across the entire flow field while considering the particle fluxes with a significantly reduced computational cost. The occurrence of particles with non-uniform size and shape distribution (which is accounted for in the LE model) is almost inevitable in most industrial applications, and this could be a limiting factor of the EE model, except additional transport equations (continuity and momentum balance equations) are incorporated and solved for each size and shape. The interaction between phases is handled by pressure and interphase mass and momentum exchange coefficients; these coefficients are key parameters of the EE model and determine the peculiarities of the flow (Sobieski, 2010). Furthermore, their description and formulation principles depend on the type of phases present (solid, liquid or gas), and the resulting momentum exchange coefficients, i.e. fluid-fluid, solid-solid or fluid-solid exchange coefficients.

5.2 Particle Drag and Sphericity

It has been proven that the shape of a particle strongly influences the drag force experienced by the particle and its terminal velocity during flow; thus, improved flow prediction can be attained by an enhanced shape description of the particles (Chhabra et al., 1999). Accounting for the particle sphericity is usually done in two ways: first, is the modification of the drag coefficient according to experimental findings, i.e. for a specific shape, the drag coefficient can be found as a function of the Reynolds number in a similar way to the expressions for perfectly spherical particles. This is, however, cumbersome,

considering the broad range of possible shapes particles could take in practical operations. Second, is the use of size and shape factors to describe an equivalent spherical particle (Mandø et al., 2007). In a bid to implement the second method, we have modified the Syamlal-Obrien model by re-defining the exchange coefficient. Several published works (Chhabra et al., 1999; Sobieski et al., 2010; Hua et al., 2015) reveal comparable performance between the Gidaspow model and the Syamlal and Obrien (1987) model (SO); however, the relative ease of implementation of this slight modification (Eq. 5.1) in the exchange coefficient compared to that of Gidaspow influenced our choice of the SO drag model. Essentially, the need for a switch/blending function to ensure a smooth transition between conditions of high and low particle concentration is not necessary when using the SO model. This absence of the switch function in the SO model makes the application of the shape modification factor relatively straightforward (Section 2.2).

5.3 Fluid-Solid Momentum Exchange Coefficient

In the SO model, the fluid-solid exchange coefficient is defined as:

$$K_{sl} = \frac{3\alpha_s\alpha_l\rho_l}{4v_{r,s}^2 d_s} C_D\left(\frac{Re_s}{v_{r,s}}\right)|\vec{v}_s - \vec{v}_l| \tag{5.1}$$

Several other models exist for determining the fluid-solid interphase exchange coefficient: they include the Gidaspow, Di-Felice, Gibilaro, Wen-Yu, Ergun, Ma-Ahmadi, and others. However, the extent of application of these models depends majorly on the velocity of flow and the degree of granular phase packing they can accommodate (Sobieski, 2009). Both flow conditions (dilute and dense granular flows) can be captured by the SO model. The drag function (C_D) in Eq. 5.1 has a form derived by Dalla Valle (1943), Re_s is the particle Reynolds number, $v_{r,s}$ is the terminal velocity correlation for the solid phase and μ_l the viscosity of the liquid phase.

$$C_D = \left(0.63 + \frac{4.8}{\sqrt{\frac{Re_s}{v_{r,s}}}}\right)^2 \tag{5.2}$$

$$Re_s = \frac{\rho_l d_s|\vec{v}_s - \vec{v}_l|}{\mu_l} \tag{5.3}$$

$$v_{r,s} = 0.5\left(A - 0.06Re_s + \sqrt{(0.06Re_s)^2 + 0.12Re_s(2B - A) + A^2}\right) \tag{5.4}$$

where:

$$A = \alpha_l{}^{4.14} \tag{5.5}$$

and

$$B = 0.8\alpha_l{}^{1.28}\ for\ \alpha_l \leq 0.85\ and\ B = 0.8\alpha_l{}^{2.65}\ for\ \alpha_l > 0.85 \tag{5.6}$$

α_l is the liquid phase volume fraction.

Although the particle diameter also appears in the definition of the Reynolds Number, in the SO model (Eqs. 5.1-5.6), the sphericity coefficient is implemented only in the equation describing the interphase momentum exchange coefficient. A similar modification strategy was adopted for the Gidaspow model in the work of Sobieski (2010). It is worth mentioning that the drag coefficient is only found in the Wen-Yu formula of the Gidaspow (1994) model; the effect of the drag coefficient in the Gidaspow model is restricted to dilute granular flow only (i.e. at low particle concentration, so that there is free movement in the liquid phase). It further implies that incorporating the sphericity coefficient into the drag coefficient of the Gidaspow model would not adequately describe dense granular flow conditions. This is because the drag coefficient does not exist in the Ergun equation of the Gidaspow formulation, which captures particle flow behaviour at high concentrations. Although the SO formulation handles this complexity of dilute and dense granular flow differently, it is possible to infer that a better modification strategy for the SO model, especially due to the prevalence of dense granular flow in our application, is to introduce the sphericity directly into the exchange coefficient rather than the drag coefficient. Additionally, several experimental measurements of drag coefficient for a wide range of particle shapes exist, but a functional relationship of this coefficient in terms of the Reynolds number, particle orientation and geometry is very scarce. This further substantiates our approach of incorporating the shape descriptor into the interphase exchange coefficients (Eqs. 5.7-5.10).

$$K_{sl}' = \eta K_{sl} \tag{5.7}$$

Where

$$K_{sl}' = \frac{3\alpha_S \alpha_l \rho_l}{4 v_{r,s}^2 \psi d_s} C_D \left(\frac{Re_s}{v_{r,s}}\right) |\vec{v}_s - \vec{v}_l| \tag{5.8}$$

$$\eta = \frac{1}{\psi} \tag{5.9}$$

$$\psi = \frac{A_s}{A_c} \tag{5.10}$$

Where η is the drag modification factor, ψ is the particle sphericity (the ratio between the surface area of a sphere with the same volume as the particle - A_s, and the surface area of the actual particle - A_c), d_s is the volume equivalent diameter (diameter of a sphere having the same volume as the non-spherical particle). It is worth emphasising that the sphericity coefficients are model constants selected during computations, and no experiments have been performed to determine the values for rock cuttings. Experimental determination of cuttings transport phenomena which measure the sphericity of the rock cuttings are rare; this scarcity of data can be partly attributed to the difficulties of surface area measurement of irregular particles. It has been argued that the application of the sphericity coefficient is more suitable for particles whose sphericity coefficient approach unity (Chhabra et al., 1999) and that the accuracy of sphericity-based correlations reduces when complex shapes with high aspect ratios and very low sphericities are modelled (Clift et al., 2005). However, recently improved applications of the DEM-CFD coupled technique have shown remarkable predictions of pressure drop in fluidised beds (Vollmari et al., 2016). This recommendation and the continuous phase assumption of the discrete phase in the Eulerian-Eulerian (EE) model constitute the rationale for choosing particle sphericities shown in Table 5.1. The application of this model provides some fundamental insight into the modifications non-spherical particles add to the flow, as explained subsequently in the result section.

5.4 Assumptions, Initial Conditions and Boundary Conditions

The following assumptions are made in the CFD model used to describe the effect of particle shape on cuttings transport phenomena in an annulus.

- Particles and the conveying medium (non-Newtonian fluid) are regarded as continuous.

- No-slip condition, between continuous phases and the walls (drill pipe and wellbore).
- Particles are represented by mono-sized non-spherical and spherical geometries; the shape factor is not included in the lift coefficient, and non-spherical particle orientation is not considered.
- There is no change in shape or mass due to particle-particle interactions.
- Restitution coefficients determine the friction between particles and the wellbore/drill pipe walls (a value of 0.9 is adopted).
- Annular walls are assumed to be smooth (no roughness factor is incorporated).
- A fluid velocity inlet (shown in Table 5.1) and atmospheric pressure outlet are the adopted boundary conditions.
- Particle inlet velocity of 0.5 $m.s^{-1}$ is adopted.

5.5 Model Validation and Simulation Strategy

Although experimental data on flow through the geometry considered here with particle shape considerations are very scarce, we apply similar principles of the CFD model development adopted (Chapters 3 & 4) here for validation purposes using spherical particles. We observe a reasonably accurate performance of our model with the data, as shown in Fig. 5.2.

In order to determine how strongly the simulation model changes with a change in the interphase momentum exchange coefficient (a function of particle sphericity), RANS equations were numerically solved using the finite volume formulation. The Semi-Implicit Method for Pressure Linked Equations (SIMPLE) was adopted as the pressure-velocity coupling scheme. Spatial discretisation of all equations was carried out using the Quadratic Upstream Interpolation for Convective Kinematics (QUICK) method. In order to avoid divergence of the numerical solution and non-physical flow patterns, the convergence of the unsteady particle-fluid calculations is confirmed by negligible values (10^{-4}) at each time step of the global mass and momentum imbalances in the computational domain. A time step of $5{\cdot}10^{-4}$ was used for the transient simulations (second-order implicit) which were run for a total period of 5 seconds in each test case. Convergence was attained in less than 10 iterations of each time step. The difference between the averaged flow properties at this time and successive time steps was negligible (statistically steady-state condition). Computations were carried out on the University's high-performance computing facility

(Eddie Mark 3 – Scientific Linux 7 Operating System) with 32 cores (2.4GHz Intel®-Xenon® CPU processor) and 64GB of RAM.

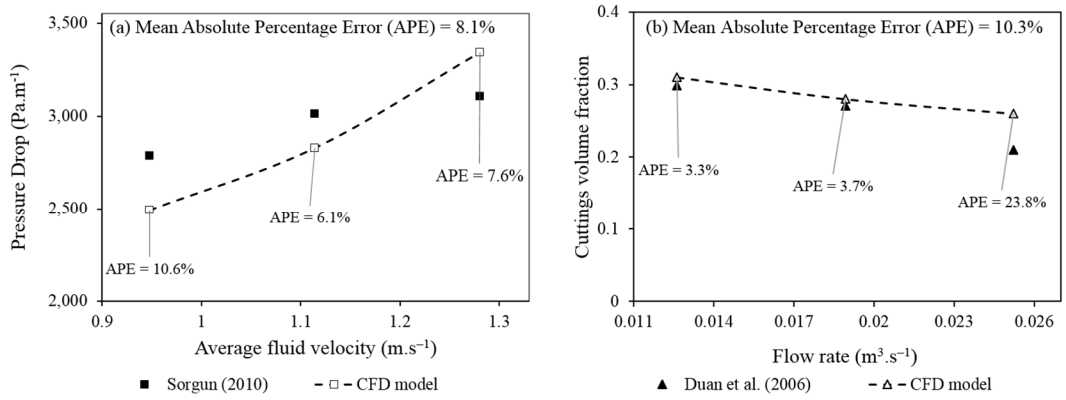

Figure 5.2. Validation of CFD model against experimental data.

5.6 Fluid Rheology, Flow Geometry and Meshing

The properties of the drilling fluids (1 and 2) used in this study were adapted from the work of Abu-Jdayil and Ghannam (2014); their performances (transport efficiencies) were comparatively analysed using the power law (0.5% Carboxymethyl cellulose – CMC) and Herschel-Bulkley models (0.5% CMC + 4% Bentonite) for their rheological description. More simulation parameters are given in Table 5.1.

Table 5.1. Mesh resolution and properties.

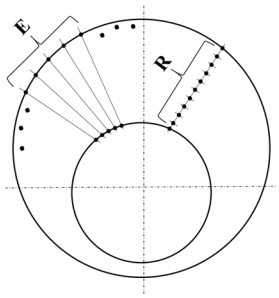

Mesh ø	Total Faces (E×R)	No. of Nodes	No. of Elements	Min. ϭ	Max. ς
50by10	500	143,550	130,000	0.36	0.79
60by20	1200	393,120	373,200	0.71	0.50
70by20	1400	536,550	509,600	0.47	0.70
80by20	**1600**	**700,560**	**665,600**	**0.72**	**0.49**
70by30	2100	792,050	764,400	0.42	0.70
Mesh ø	Total Faces (E×R)	Max. AR	Min. Face Size (m)	Max. Face Size (m)	AWT (hr)
50by10	500	9.01	0.0003	0.03	1.41
60by20	1200	15.31	0.0003	0.03	3.60
70by20	1400	13.03	0.0003	0.03	4.52
80by20	**1600**	**11.42**	**0.0003**	**0.03**	**8.17**
70by30	2100	19.61	0.0003	0.03	10.66

AWT – Average Wall clock Time for two simulations (0.002 m and 0.008 m in the grid independence study), ϭ – Orthogonality; ς – Skewness; AR – Aspect Ratio; E – Edge divisions; R – Radial Divisions

A description of the flow geometry and the meshing style and associated properties is shown in Fig. 5.4. A mesh independence study revealed that 665,600 elements were sufficient to obtain accurate results. Table 5.2 shows the properties of the significantly different mesh resolutions tested. In the description of mesh divisions 'E × R', 'E' represents the number of edge divisions around the circular outer and inner sections of the annulus, and 'R' represents the radial face divisions of the circular section.

Table 5.2. Simulation input parameters.

	Drilling Mud 1	**Drilling Mud 2**
Geometry		
Drill pipe diameter, d_{pipe} (m)	0.113	0.113
Wellbore diameter, d_{wb} (m)	0.180	0.180
Computational length, L (m)	2.340	2.340
Particle properties		
Cuttings diameter, d_s (m)	0.002, 0.003, 0.004, 0.005 and 0.008	0.002, 0.003, 0.004, 0.005 and 0.008
Cuttings density, ρ_s (kg.m^{-3})	2800	2800
Sphericity, ψ	0.50, 0.75, 1.00	0.50, 0.75, 1.00
Fluid properties		
Composition	0.5% CMC Solution	0.5% CMC + 4% Bentonite
Density, ρ_l (kg.m^{-3})	1000	1030
Yield stress, τ_0 (Pa)	0	46.5
Consistency index, K (Pa.s^n)	0.5239	0.6482
Flow behaviour index, n	0.60	0.7
Drilling variables		
Fluid circulation velocity, v_l (m.s^{-1})	0.8	0.8
Cuttings inlet velocity, v_s (m.s^{-1})	0.5	0.5
Drill pipe rotation, Ω (rpm)	100	100
Hole eccentricity, e	0.6	0.6

Our choice of mesh used in this study was strongly influenced by the quality (Table 5.2) and the nature of results obtained, as shown in Fig. 5.3. We observe that upon successive refinements, the results produced by the finest resolution mesh ('70by30') differ insignificantly from the results of the '80by20' mesh, which we deem the most appropriate. It can also be observed in Table 5.2 that the average wall clock time for running a single simulation varies considerably with the mesh resolutions. By changing the resolution from '70by20' to '80by20', the run time is almost doubled; however, the higher skewness factor and lower orthogonality make this mesh ('70by20') less preferred.

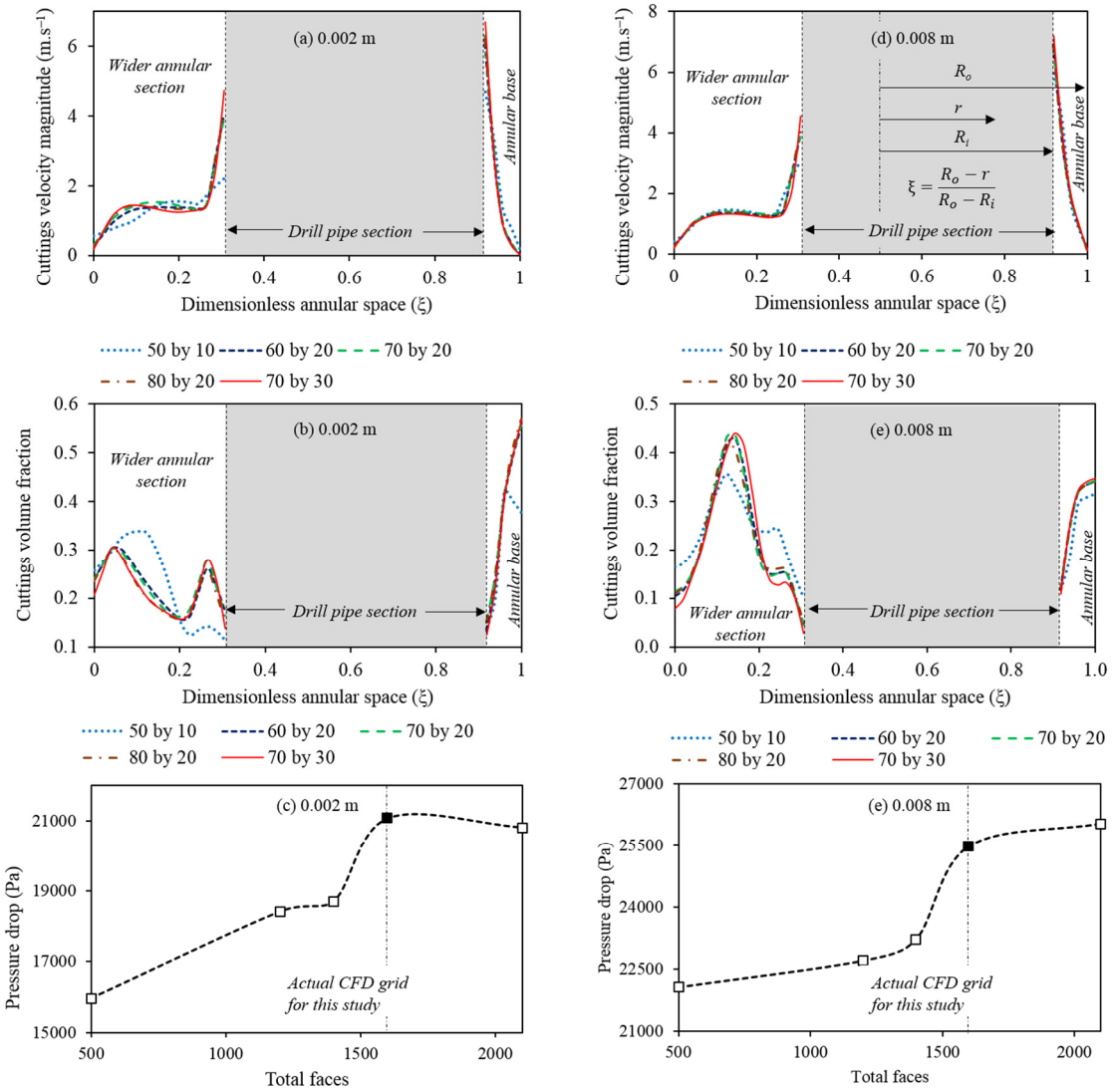

Figure 5.3. Grid independence study. Velocity and volume fraction profiles are obtained from the horizontal-to-inclined bend of the annulus at t = 5 seconds.

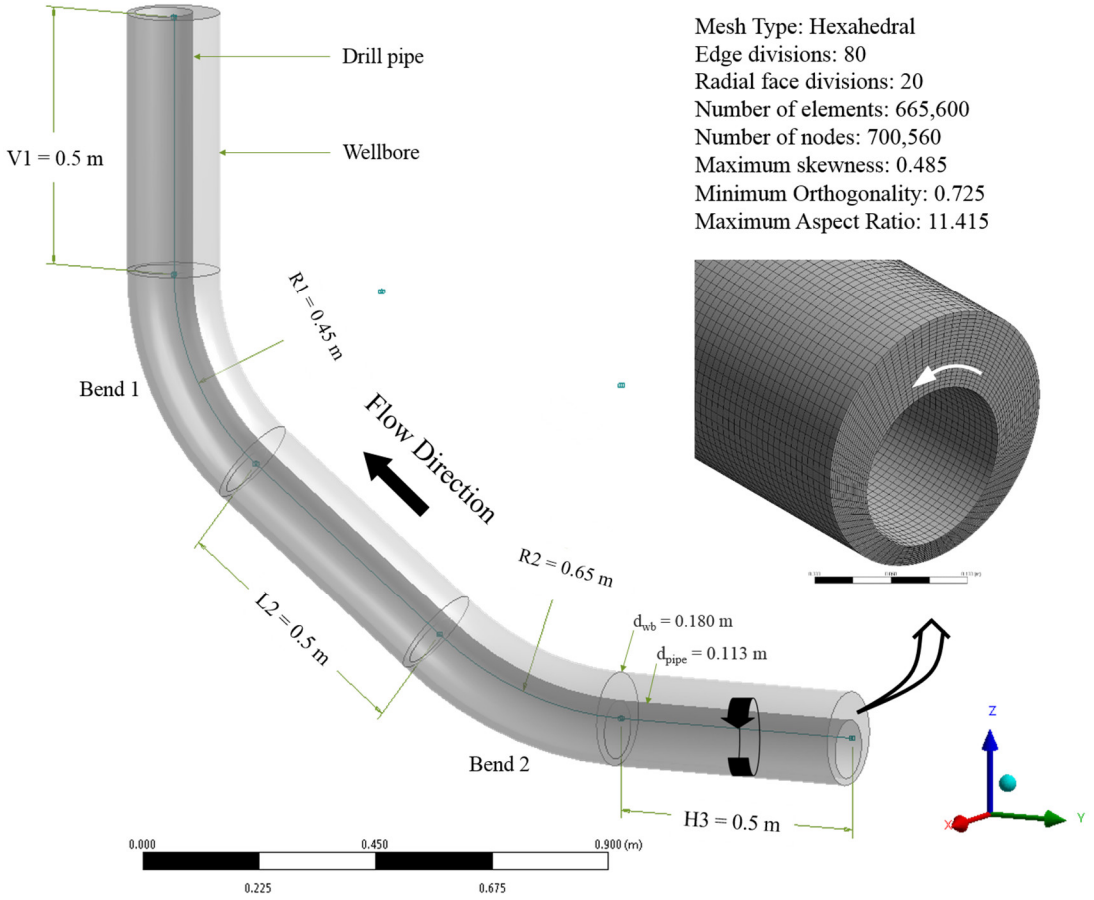

Figure 5.4. Annular flow geometry.

5.7 Cuttings Velocity and Concentration Profiles

The computed time and volume averages of the particle velocities, volume fraction and overall pressure drop in the entire flow domain for a 5-second run-time are presented and discussed. Results obtained using the two drilling fluids reveal considerable differences in rheological performance for the transport of cuttings of all sizes considered. Before presenting the main results, it is important to demonstrate the concept of skewness in deposition patterns which is a vital finding of this work. As seen in Fig. 5.5, cuttings deposition on either side of the rotating drill pipe differ significantly. This depends on the drill pipe rotation and other factors which are subsequently explained. This phenomenon was also observed by Akhshik et al. (2015) using the Discrete Element Method (DEM) coupled with CFD.

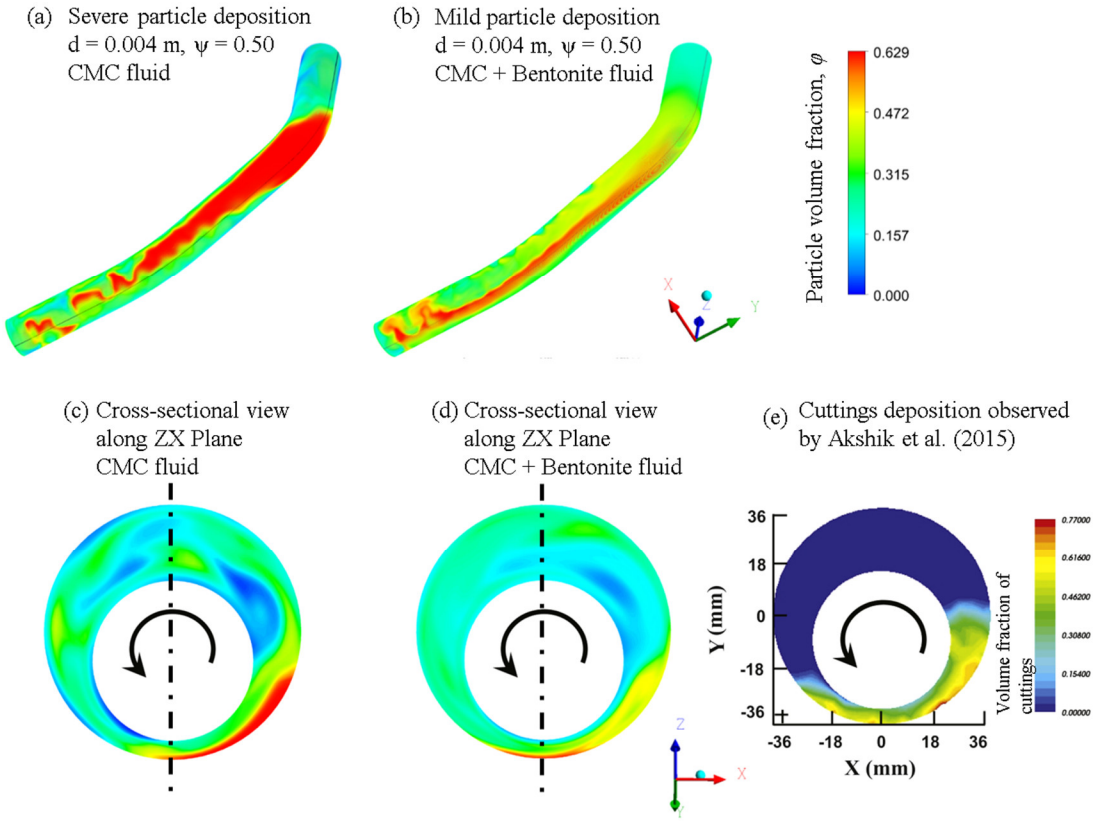

Figure 5.5. Skewed particle deposition in the annulus with a rotating drill pipe at 100 rpm for two different drilling fluids and comparison with Akhshik et al. (2015) A reduction in skewness is observed by using the second drilling fluid with superior rheological properties (b and d).

5.7.1 Flow Profiles using Drilling Mud – 1

Fig. 5.6 illustrates the behaviours of particles of different sphericities when transported with the 0.5 wt. % CMC drilling fluid. It is observed that non-spherical particles (of all diameters considered) remain longer in the bulk flow and travel faster than perfectly spherical particles before settling at the base of the annulus (Figs. 5.6a and d). This finding agrees with experimental observations of Byron (2015) and numerical investigations of Yilmaz (2012). The secondary motion (oscillatory and tumbling) exhibited by non-spherical particles when transported by a fluid tends to reduce the settling velocity compared to spherical particles (Mandø et al., 2007). This increased settling velocity of perfectly spherical particles in the partially inclined geometry considered here is the most probable reason for the increased deposition, as shown in Fig. 5.6d. The studies of Losenno (2004) and Njobuenwu and Fairweather (2014) further pointed out that non-spherical particles experience a higher dispersion effect compared to spherical particles

due to the action of lift forces; this dispersion effect usually aids the transport process. Irregular particles generally have a higher drag coefficient than regular particles; Yow et al. (2005) reported that this increased drag coefficient decreases the response time in the fluid, thus enabling better response to velocity fluctuations as shown in Fig. 5.6a. Thus, spherical particles whose primary motion is to roll towards or against the principal axial flow direction in a cuttings bed could in combination with their settling behaviour, pose greater resistance to flow compared to the frictional resistance of irregular particles (due to increased interparticle and particle-wall contact area).

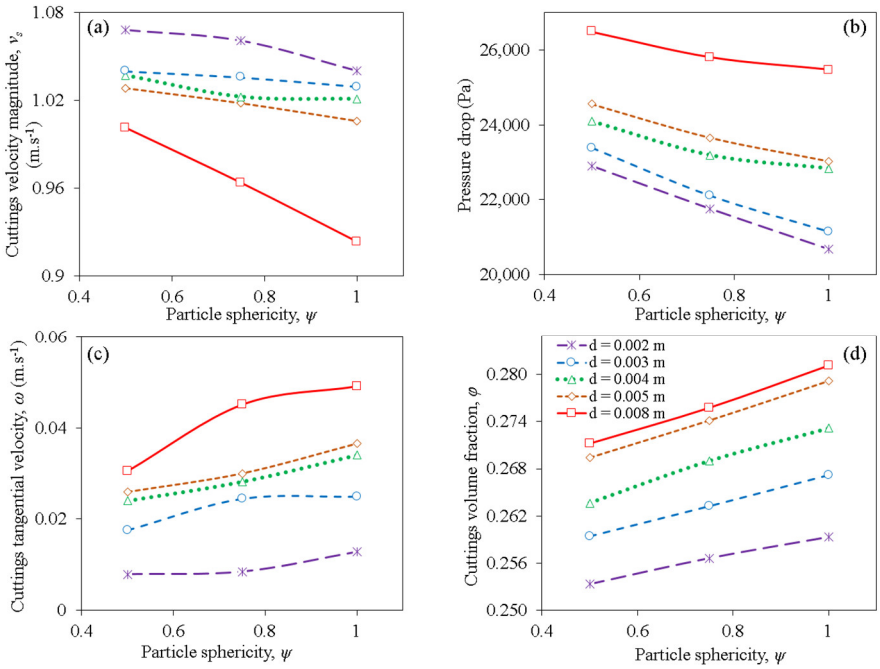

Figure 5.6. Profiles of cuttings velocity magnitude, tangential velocity, pressure drop and volume fraction for sphericities of 0.5, 0.75 and 1.0 respectively using drilling mud 1.

It is also observed in Fig. 5.6a that drill cuttings with 0.002 m diameter travel faster in the annulus than the larger cuttings (> 0.002 m) with higher inertia. However, a stronger tangential motion is noticed with the larger particles (Fig. 5.6c). The behaviours of the different particle shapes with respect to their tangential velocities are also depicted in Fig. 5.6c. It is observed that spherical particles will more readily respond to the tangential motion of the rotating drill pipe compared to non-spherical particles which exhibit a more chaotic flow behaviour. Particles with a sphericity of 0.5 yield the lowest tangential velocity. It is important to differentiate the inherent oscillatory motion of non-spherical particles from their tangential motion due to drill pipe rotation. While this oscillatory motion is usually about the particles' axis, it may be independent of the principal axis of

the rotating drill pipe. We infer that the combined effects of oscillatory and tangential motion yield the increased dispersion of the non-spherical particles in the flow domain earlier pointed out.

Anisotropic stress distribution produced by non-spherical particles, increased velocity due to secondary motion, higher particle-fluid interactions coupled with the increased drag and frictional forces are the most probable reasons for the increased pressure drop observed with the non-spherical particles compared to those of perfect sphericity (Fig. 5.6b). As observed, these effects increase in magnitude with an increase in particle diameter and reduced sphericity. Furthermore, the impact of particle shape appears to be more significant on the transport velocity of the largest particles (0.008 m) relative to the smaller particles (Fig. 5.6a). We further observe that for particles of $\psi = 0.5$, the assumption of absolute sphericity ($\psi = 1$) could yield a decrease of 11%, 10%, 6%, 7% and 4% in pressure drop for the 0.002 m, 0.003 m, 0.004 m, 0.005 m and 0.008 m particles respectively (Fig. 5.6b). Similarly, approximately 5% decrease in cuttings volume fraction ensues between perfectly spherical particles and particles of 0.5 sphericity for all particle diameters (Fig. 5.6d). These numerical differences provide some insight into the disparities that could arise when the results of CFD simulations with the perfect sphericity assumption are applied to the design of practical drilling operations, which usually involve cuttings of varying sphericities and non-uniform size distribution.

Increased particle deposition is generally observed at the inclined-to-vertical (upper bend) of the annulus compared to other regions (Fig. 5.7). This deposition is also observed in the inclined section of the annulus with the 0.002 m particles displaying a more even deposition pattern (Figs. 5.7a-c). The skewed deposition patterns of the larger particles (> 0.002 m) further explain the stronger impact of drill pipe rotation on the larger particles as seen in Figs. 5.7d-o. This skewness is particularly noticed in the inclined, and horizontal sections of the annulus and its effect increases with the particle diameter). The rotary drill pipe motion has been shown to sway particles in the direction of rotation (Epelle and Gerogiorgis, 2018b); thus yielding the skewed deposition observed with the larger particles (Figs. 5.7d-o). This phenomenon is further reflected in the relatively uniform particle concentrations (Figs. 5.7j-o) in the horizontal and inclined sections compared to the varying particle distribution (yellow patches) observed with the smaller particles (< 0.005 m) (Figs. 5.7a-i). However, the impact of gravity, as noticed in the vertical section

(Figs. 5.7j-o), is stronger because of the relatively heavier particles involved (this region is low in particle concentration). Conversely, the vertical section (Figs. 5.7a-i) is observed to be more uniform in particle distribution (and more densely concentrated), since lighter particles experience an apparent reduction in gravitational resistance in the carrier fluid.

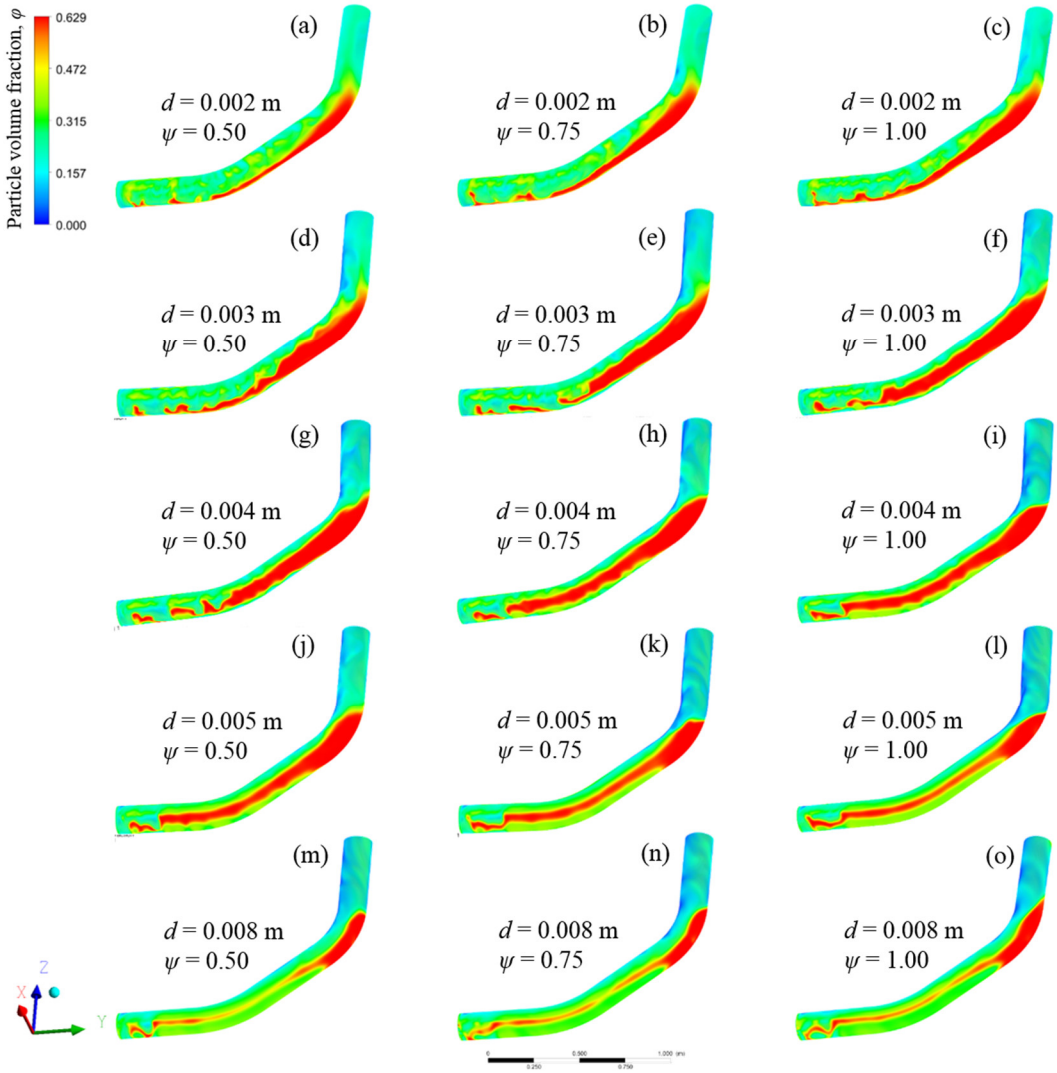

Figure 5.7. Contour plots (at 5 seconds) showing the impact of particle diameter and sphericity on the volume fraction in the annulus using drilling mud 1.

5.7.2 Flow Profiles using Drilling Mud – 2

Very similar flow property trends were observed with the first case (drill mud 1). However, it can be seen that cuttings travel at a slightly higher velocity with the rheological improvement of the drilling mud (Figs 5.6a and 5.8a). This viscosity improvement, coupled with the increased transport velocity, yield a corresponding higher pressure drop

for all particle diameters (Figs. 5.6b and 5.8b). Additionally, Fig. 5.8c shows slightly reduced cuttings tangential velocities compared to Fig. 5.6c (using the lower quality drilling mud). This implies that the improved drilling mud basically reduces the cuttings tangential motion by enhancing the transport of cuttings in the principal bulk flow direction. A major difference between the performances of both fluids is reflected in the cuttings volume fraction (particle concentration) profiles, as shown in Fig. 5.8d. Unlike the first drilling mud which showed a higher volume-averaged particle concentration for the 0.008 m particles compared the cuttings of smaller diameters, drilling mud 2 reveals a rather different phenomenon. It is essential to mention that the volume-averaged cuttings concentration (Fig. 5.8d) considers both the suspended and deposited cuttings in the averaging procedure throughout the flow domain; thus, a more descriptive indication of transport phenomena may be obtained from the contour plots (Fig. 5.9). Additionally, the actual mean volume fraction and its change with sphericity observed here are much lower than that observed with the first drilling mud. Compared to the 5% reduction earlier noticed with all particle diameters (Fig. 5.6d), the change in volume fraction here is less than 0.7% for all particle diameters (Fig. 5.8d).

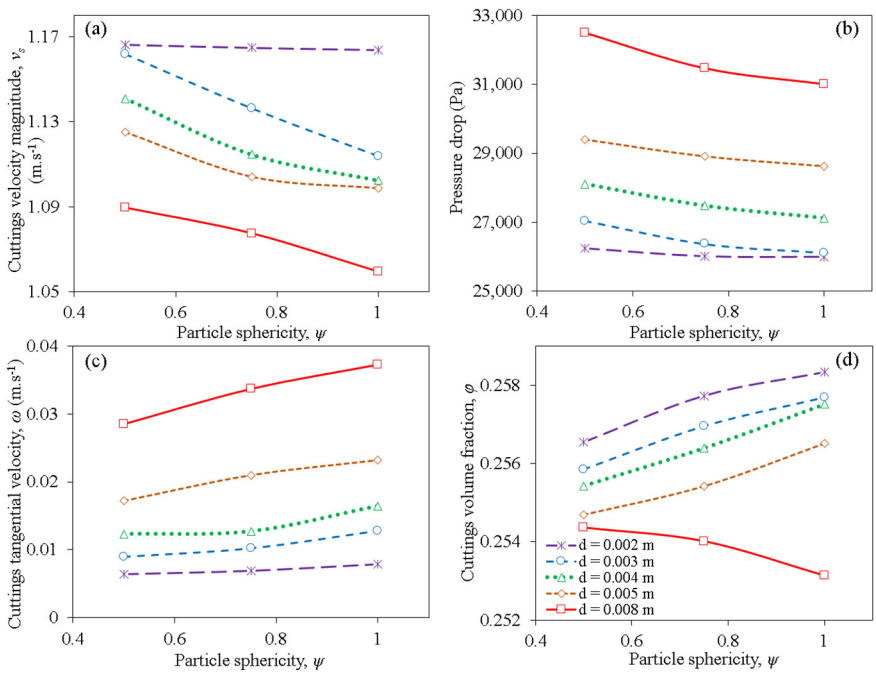

Figure 5.8. Profiles of cuttings velocity magnitude, tangential velocity, pressure drop and volume fraction for sphericities of 0.5, 0.75 and 1.0 respectively using drilling mud 2.

The reverse volume fraction profile observed with the 0.008 m particles (Fig. 5.8d) indicates that frictional resistance of non-spherical particles plays a dominating role in the

transport process compared to the (usually higher) settling velocities of spherical particles. However, the bulk velocity profile (Fig. 5.8a) is retained for the 0.008 m particles. This phenomenon is attributed to the reduced cross-sectional area (due to increased deposition of the non-spherical particles), which yields an increased averaged velocity (Akhshik et al., 2016). The slip velocity profile observed for the 0.008 m particles also further reflects the non-conformity observed in Fig. 5.8d; this, we attribute to the varying dominance of frictional and drag forces during transport. Considering the significant impact of cuttings diameter on the flow phenomena, it is worthwhile to investigate (in future work), the nature of particle deposition that ensues when a non-uniform size distribution of cuttings is applied.

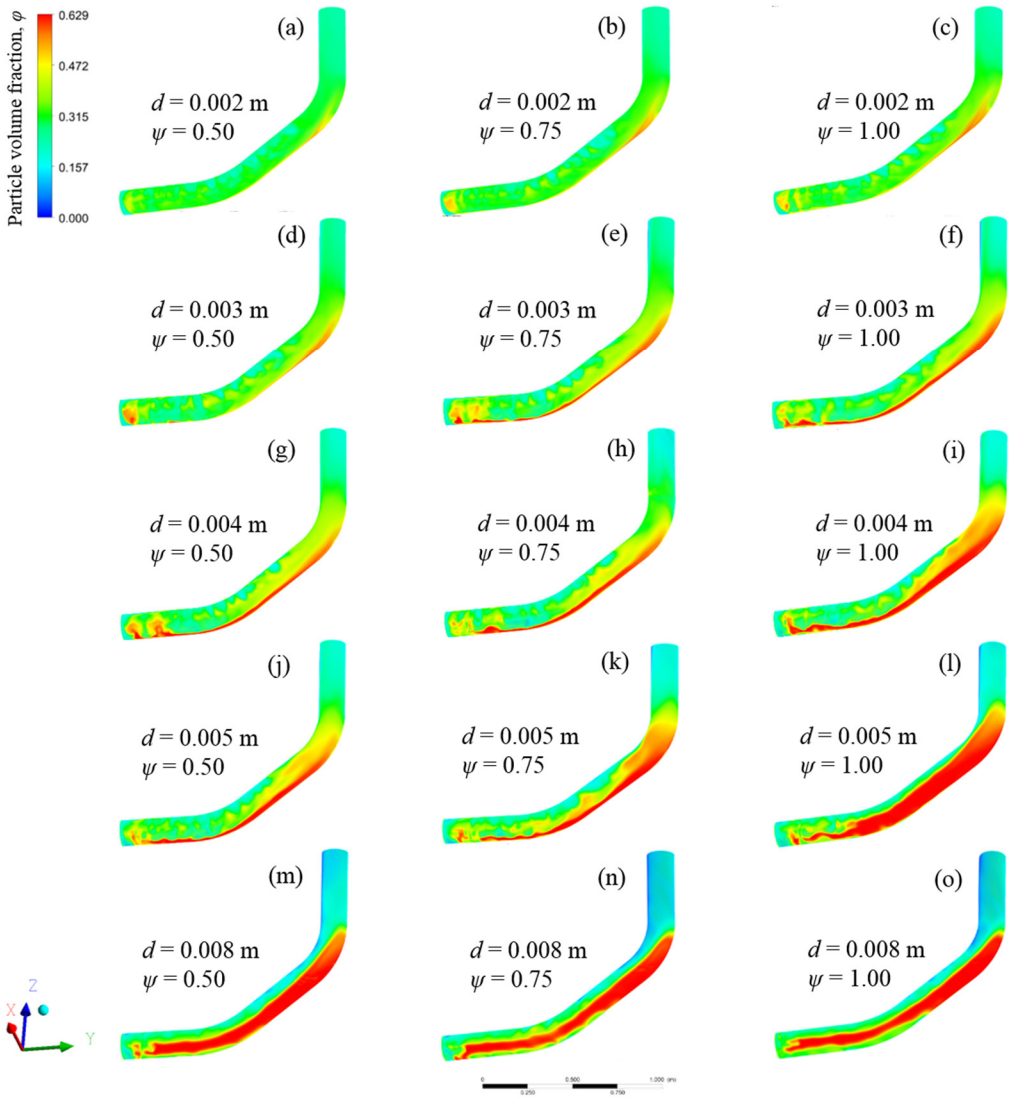

Figure 5.9. Contour plots (at 5 seconds) showing the impact of particle diameter and sphericity on the volume fraction in the annulus using drilling mud 2.

Figs. 5.9a-c show a uniform distribution of the cuttings (0.002 m) around the annulus with only slight deposition at the base of the flow domain; improved transport (particularly with $\psi = 0.5$ and $\psi = 0.75$ – Figs. 5.9j-k vs. Figs. 5.7j-k) is also noticed for the 0.005 m cuttings. This is due to the increased carrying capacity of the superior drilling mud. However, with 0.008 m particles, increased particle deposition occurs (Figs. 5.9d-f). This deposition appears to be more significant compared to results obtained with the first drilling mud (Figs. 5.7d-f); thus indicating that an increase in the mud viscosity does not always guarantee improved transport of drill cuttings. Cuttings deposition close to the drill bit is particularly increased (Figs. 5.9m-o) compared to the first case (Figs. 5.7m-o). An explanation of the observed phenomena could be derived from the increased resistance the highly viscous fluid poses to the rotary drill pipe motion; which induces a reduction in penetration rate (ROP) in industrial applications; CFD studies are hence paramount to the delicate rheological design of drilling muds in any practical operation. We also observe that for particles of $\psi = 0.5$, the assumption of absolute sphericity ($\psi = 1$) yields a decrease of 1%, 3.5%, 3.5%, 4.4% and 5% in pressure drop for the 0.002 m, 0.003 m, 0.004 m, 0.005 m and 0.008 m particles respectively (Fig. 5.8b).These are generally lower than the reductions observed with the first drilling mud; thus implying that the operational difficulties introduced by particle shape complexity can be mitigated by high-quality drilling muds. The minor differences in volume fraction (Fig. 5.8d) earlier explained also substantiate this deduction. Compared to Fig. 5.7, we observe that the skewness in cuttings deposition is significantly decreased by using a superior drilling mud. These deposition patterns generally observed are not only determined by drill pipe rotation and gravitational forces, but also the eccentric geometry of the annulus. This narrower lower area of the annulus causes severe flow restrictions for the cuttings and hence accumulation along the base and sides of the annulus. This severe restriction in the lower annular regions is also the reason for the increased asymmetry in deposition patterns observed with increasing particle diameter in Figs. 5.7, and 5.9.

It is also generally observed in Figs. 5.7 and 5.9 that, three separate regions exist in the annulus considered: the region of intense cuttings deposition (red), regions of mild cuttings concentration (yellow), and regions with a low cuttings concentration (light green/blue). We liken these regions to the stationary bed, moving bed and heterogeneous suspension experimentally observed in the work of Doron and Barnea (1993).

5.8 Particle Trajectory and Slip Velocity

The time and volume-averaged slip velocities of the small and large particles of different sphericities are shown in Fig. 5.10. It is illustrated that larger particles have higher slip velocities compared to the smaller particles. Epelle and Gerogiorgis (2018a; b) attributed this effect to the higher spreading tendencies of smaller particles and the ability of smaller-sized particles to readily follow/respond to the motion of the fluid. The relatively smooth and spherical particles would have less contact time with the fluid than non-spherical particles during flow interactions; thus yielding higher slip velocities. Conversely, the secondary motion exhibited by non-spherical particles enables increased particle-fluid interaction; hence the lower slip velocities encountered (Figs. 5.10a and b). With the second drilling mud (of higher viscosity), the slip velocities of the larger particles observed are much lower (by an order of magnitude) compared to the lower viscosity mud; thus demonstrating its superior carrying capacity.

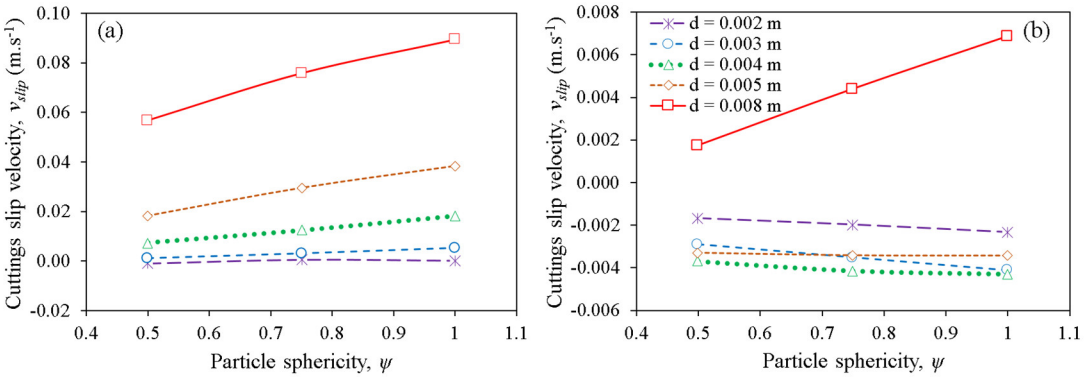

Figure 5.10. Cuttings slip velocities at different sphericities using drilling mud 1 (a) and drilling mud 2 (b).

The particle trajectories shown in Fig. 5.11a-j, indicate that the impact of drill pipe rotation on particle motion in the vertical section of the annulus is much lower compared to the inclined and horizontal sections, respectively. This effect was noticed for all particle sphericities considered. Furthermore, this reduced impact of drill pipe rotation due to the transition in the annular geometry coupled with the eccentric configuration of flow, are the major reasons for increased particle deposition noticed around the upper bend (inclined-to-vertical) compared to other areas in the annulus. It is also observed (Fig. 5.11) that the rotary motion of cuttings induced by the drill pipe is slightly more substantial in the CMC fluid (Figs. 5.11a-e) compared to the tracks of cuttings velocity when the

superior drilling mud is used (Figs. 5.11f-j). This further demonstrates the increased axial bulk transport of cuttings the superior drilling mud provides.

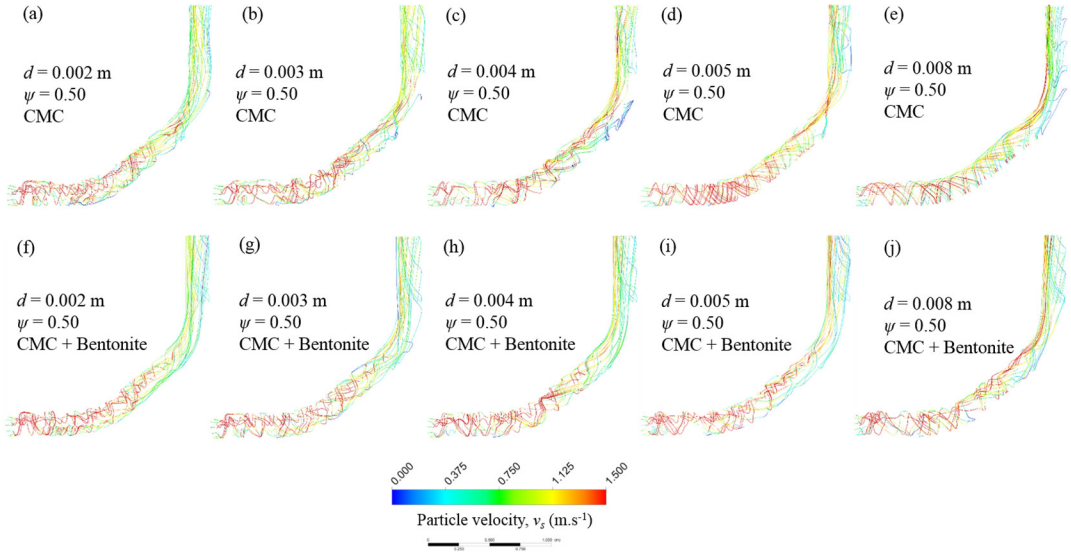

Figure 5.11. Particle trajectories (at 5 seconds) for all diameters and sphericity of 0.5 using drilling mud 1 and 2.

5.9 Chapter Conclusions

It is evident from this study that flow characteristics present in practical applications are different but share some similarities with a single-particle flow in a fluid. The presence of other interacting particles and bounding walls (stationary and rotating) in the flow domain are the primary sources of increased complexity. By implementing the Eulerian-Eulerian model, we have been able to determine the flow peculiarities non-spherical cuttings add to the transport phenomena in an annular flow geometry. This was specifically achieved by incorporating the particle sphericity into the interphase exchange coefficient of the Syamlal-O'Brien drag model. The following conclusions can be drawn from the observations made in this study:

- Compared to other regions in the flow domain, the inclined-to-vertical (upper) bend is the most susceptible location to particle deposition. The combined effects of annular eccentricity, reduced particle lifting effects, and gravitational resistance are the main reasons for this observation.
- Non-spherical particles generally experience increased dispersion and travel faster than perfectly spherical particles in the annulus. We attribute this observation to the secondary motion usually experienced by non-spherical particles.

- As far as the cuttings transport velocity is concerned, the impact of particle sphericity is more significant with the larger (0.008 m) particles compared to the smaller-sized particles (0.002 m - 0.005 m).
- Drill pipe rotation has a more pronounced impact on larger particles, especially in the horizontal and inclined regions of the annulus. An increased asymmetry in the deposition pattern occurs with larger particles compared to those of a smaller size.
- Drill cuttings experience translational motion in the vertical annular sections compared to the predominantly swirling motion observed in other sections of the annulus.
- With the application of drilling mud 1, the assumption of a perfectly spherical particle geometry (ψ = 1.0 in place of ψ = 0.5) could lead to a decrease of 11%, 10%, 6%, 7% and 4% in the actual pressure drop for 0.002 m, 0.003 m, 0.004 m, 0.005 m and 0.008 m particles respectively. These differences are much lower when using the second drilling fluid of superior rheology. Reliable predictions of cuttings deposition, re-suspension, dispersion and carrier fluid pumping requirements thus depend on the particle shape, especially when the project's economics constrain the choice of drilling mud.
- Viscosity improvement (by the addition of 4 wt. % Bentonite) to the basic drilling mud (0.5 wt. % CMC) increases the cuttings transport efficiency, particularly with smaller-sized particles. This increase is not always guaranteed when larger particles are transported due to increased particle deposition (higher than that the respective one noticed with a less viscous mud). Thus, the application of optimisation techniques for CFD/fluid rheological design, particularly considering the complex particle deposition tendencies is an area that deserves more attention.

Experimental investigations of drill cuttings transport phenomena that consider the effect of particle shape are extremely scarce; this influenced our relatively straightforward implementation of the sphericity coefficient. Incorporating the effects of the particle aspect ratio, incidence angle and orientation in the drag and lift forces is a more sophisticated modification of the Eulerian-Eulerian multiphase flow model and constitutes an area for which future investigations are needed; such efforts would be

motivated by the availability of experimental data for validation purposes. It will also be worthwhile to evaluate the improvement in experimental data prediction by including these extra parameters (asides the sphericity and volume equivalent diameter used in this work). Due to the model limitations discussed, we aim to explore adaptive mesh procedures which refine cell sizes based on the local instantaneous solid volume fraction in the entire computational domain. With this technique, a limit can be enforced on the spatial grid sizes, towards ensuring the validity of the Eulerian continuum assumptions on the solid phase. The application of the sphericity coefficient in the Eulerian multiphase model in this study has successfully shown that flow dynamics of perfectly spherical particles differ considerably from those of non-spherical particles with an equivalent volume diameter and density; the quantification of this disparity is of definite industrial importance.

Chapter 6 Cuttings Transport Phenomena: A Multiphase Flow Analysis of Positional Variability

A major attribute of previous studies that model annular cuttings transport is that several flow conditions are tested over a constant wellbore geometry or at best, with a variation in the angle of inclination of the entire wellbore. In these CFD studies (Section 2.1), the variability in transport properties has only been accounted for along the wellbore's axial length and the radial direction in either wholly vertical, inclined or horizontal annuli. However, the impact of the annular geometry on the cuttings transport phenomena has been limited to scenarios in which the eccentricity (Epelle and Gerogiorgis, 2017a; 2018a; Heydari et al., 2017), wellbore-drill pipe diameter ratio (Ofei et al., 2014) and whirling drill pipe motion (Demiralp, 2014) are varied.

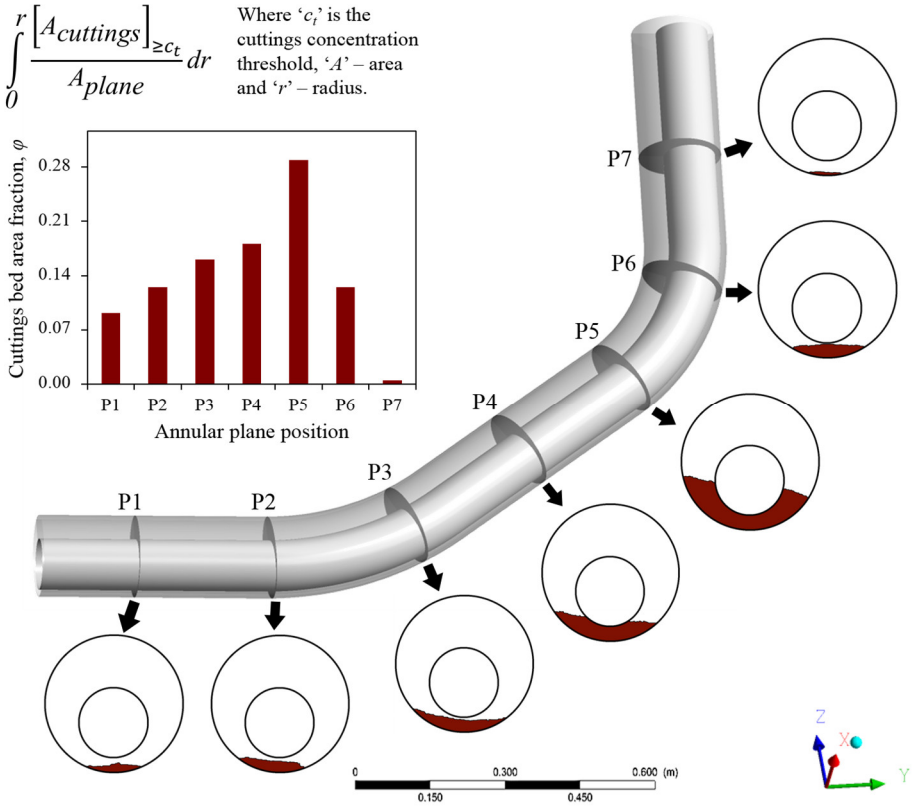

Figure 6.1. Sectional analysis along circular planes in the annular domain.

These studies accounting for the annular geometrical complexities have shown its tremendous impact on the overall cuttings transport behaviour. The impact of geometrical changes (especially with some degree of deviation at different wellbore

sections) on the transport phenomena has not been adequately studied. In this chapter, a physics-based multidimensional CFD approach is applied for the elucidation of annular geometrical intricacies (Figs. 6.1 and 6.2) on the transport phenomena of drill cuttings. The work herein stems from the results of the previous analysis (Chapter 5) that considers the effect of particle sphericity on cuttings transport (Epelle and Gerogiorgis, 2018b). The obtained results have been post-processed in a different way (by extracting flow information from strategically positioned lines and planes in the annular domain, as well as considering concentration threshold values) for better understanding of the cuttings transport phenomena. By adopting the positional variability analysis herein, we can numerically quantify in much greater detail (compared to the previous chapter), the disparity between transport velocity and volume fraction between different particle shapes, but also offer a detailed visualisation in flow space. No previous study has evaluated the impact of particle shape on the degree of deposition asymmetry (on either side of a deviated annulus) at a microscopic level in different annular regions. This has been one of the foci of this study, which offers novel detailed results. Furthermore, our postprocessing method using cuttings concentration thresholds is new and has not been carried out in any previous study on cuttings transport, to the best of our knowledge. We expect this to hopefully establish a new trend for other researchers towards understanding their CFD results in depth.

In this study, the two-fluid Eulerian-Eulerian approach is adopted for the simulation of the cuttings transport phenomena. Both phases (cuttings and drill mud) are separate but assumed as interpenetrating continua (Fluent, 2017). The governing equations include mass (Eq. 3.4), and momentum (Eq. 3.5) balances ensemble averaging for the respective phases. Phase interactions are incorporated into the EE model via the interphase momentum exchange coefficient (Syamlal and O'Brien, 1987; Eq. 5.1). Furthermore, particle sphericity (distinguishing spherical and non-spherical particles) is captured by the Wadell sphericity coefficient (ψ) and the related fluid-solid momentum exchange coefficient (K_{sl}, both in Eq. 3.5), using the Dalla-Valle drag coefficient (C_D) correlation (Eq. 5.2). The Wadell sphericity coefficient is the ratio of the surface area of an equivalent-volume sphere to the surface area of the actual non-spherical particle (Sobieski, 2009).

Compared to the present CFD approach, earlier industrially adopted correlations, e.g. those by Hopkins (1967) and Larsen et al. (1997) allow for quick determination of cuttings

slip velocity and Critical Transport Fluid Velocity, *CTFV* (Eqs. 6.1-6.5); where *CTV* is the cuttings transport velocity, *ESV* is the estimated slip velocity, μ_a is the apparent viscosity, and μ_{pl} is the plastic viscosity. However, with increasingly difficult-to-drill environments and highly complex multiphase flow scenarios, such empirical methods break down because of their limited extent of applicability. Therefore, numerical-based CFD methods (described here) gain overwhelming acceptance in the industry compared to these empirical correlations and simplistic single-phase analytical models (such as the Hagen-Poiseuille equation – Eq. 6.6, which can only capture incompressible Newtonian laminar flow and thus cannot credibly handle real-world drilling systems).

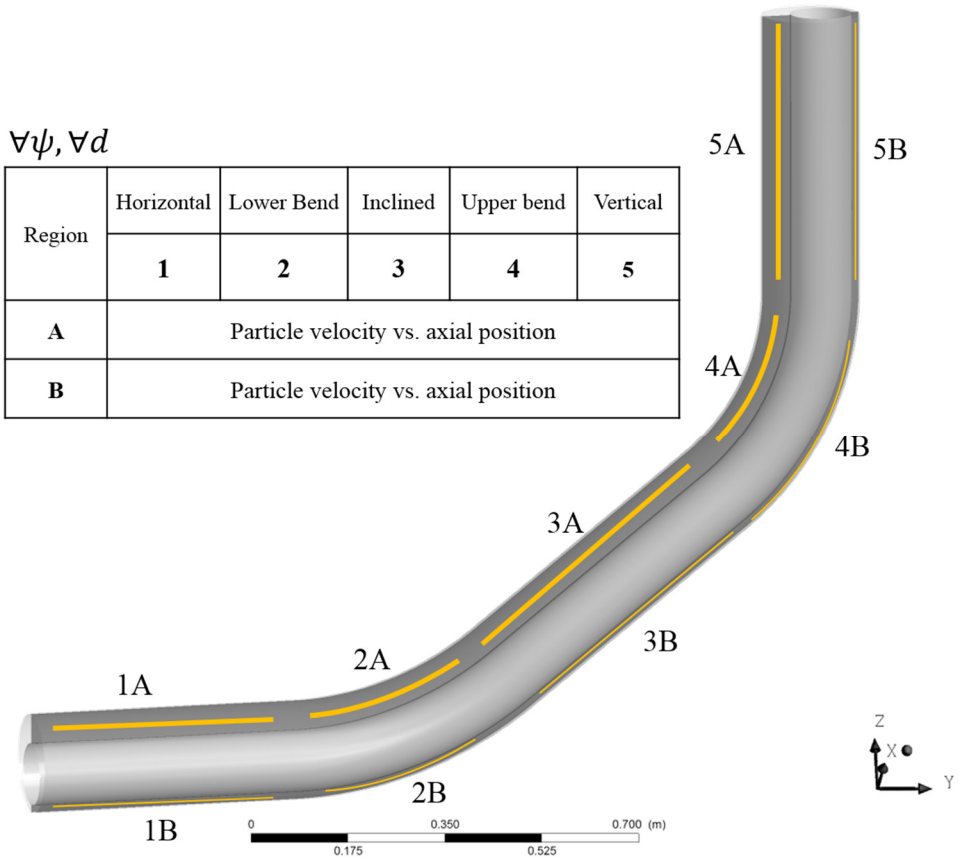

Figure 6.2. Sectional analysis along line segments in the annular domain.

$$CTFV = CTV + ESV \tag{6.1}$$

$$CTV = \frac{1}{\left[1 - \left(\frac{D_{pipe}}{D_{wb}}\right)^2\right]\left(0.64 + \frac{18.16}{ROP}\right)} \tag{6.2}$$

$$ESV = 0.00516\mu_a + 3.006 \; for \; \mu_a < 53cP \tag{6.3}$$

$$ESV = 0.02554(\mu_a - 53) + 3.28 \; for \; \mu_a > 53cP \tag{6.4}$$

$$\mu_a = \mu_{pl} + \frac{5Y_p(D_{hole} - D_{pipe})}{CFTV} \tag{6.5}$$

$$Q = -\frac{dP}{dx}\frac{\pi}{\mu}\left[R_2^4 - R_1^4 - \frac{(R_2^2 - R_1^2)^2}{\ln\left(\frac{R_2}{R_1}\right)}\right] \tag{6.6}$$

6.1 Line Segment Analysis of Cuttings Velocity using Drilling Mud - 1

It can be observed that all particles within the sphericity range considered demonstrated significant velocity fluctuations at the entrance (Regions 1A and 1B) of the flow domain (Figs. 6.3 and 6.4). As the particles move further into the annulus, the frequency of the velocity fluctuations reduces and the velocity profiles depicted become more tractable. The profiles in Region 1A thus represent turbulence-induced fluctuations; this effect reduces as the particles travel further into the annulus due to the inevitable drop in pressure. It is generally noticed that an abrupt drop in velocity ensues as the particles enter the inclined sections (Region 3, Figs. 6.3 and 6.4) of the annulus, which is 40° from the horizontal. This observation is similar to that of Pang et al. 2018a in which they discovered that well inclination around 35° – 65° were the most difficult cuttings transport conditions. The occurrence of this abrupt velocity reduction is particularly intensified at the narrower annular sections (Region B), as shown in Fig. 6.4. Also observed is the lower cuttings velocities in the lower Region B compared to the upper Region A. The eccentric configuration of the domain favours the flow of cuttings in the wider region where spatial flow resistance (due to the boundaries) is least.

As the particles travel up the annulus, it is noticed that the highest flow velocities are dependent on the particle size and sphericity. In Region A – Fig. 6.3a & b, (for d = 0.002 m and d = 0.003 m), it is difficult to tell which of the particles (highly non-spherical, ψ = 0.50, moderately non-spherical, ψ = 0.75, or the perfectly spherical particles, ψ = 1.00), consistently has the highest velocity. This alternating dominance in travel velocity displayed by these smaller particles is highly location-dependent (1A, 2A, 3A, 4A and 5A). However, with the increase in particle size (d = 0.004 m, 0.005 m, & 0.008 m), it becomes

clearer that the highly non-spherical particles tend to dominate the velocities of the other particles (ψ = 0.75, 1.00). Furthermore, as the particles get larger, the difference in the velocity profiles of the considered sphericities gets larger, particularly for the 0.005 m and 0.008 m particles (Figs. 6.3d and e). This finding compares favourably with experiential findings, which reveal that non-spherical particles interact more with the fluid by engaging in secondary motion about the particles' axis (Yow et al., 2005; Mandø et al. 2007; Byron et al. 2015). This, in turn, yields a better response of non-spherical particles to the fluid motion compared to spherical particles, which do not engage in this kind of motion and hence tend to fall through the fluid more easily.

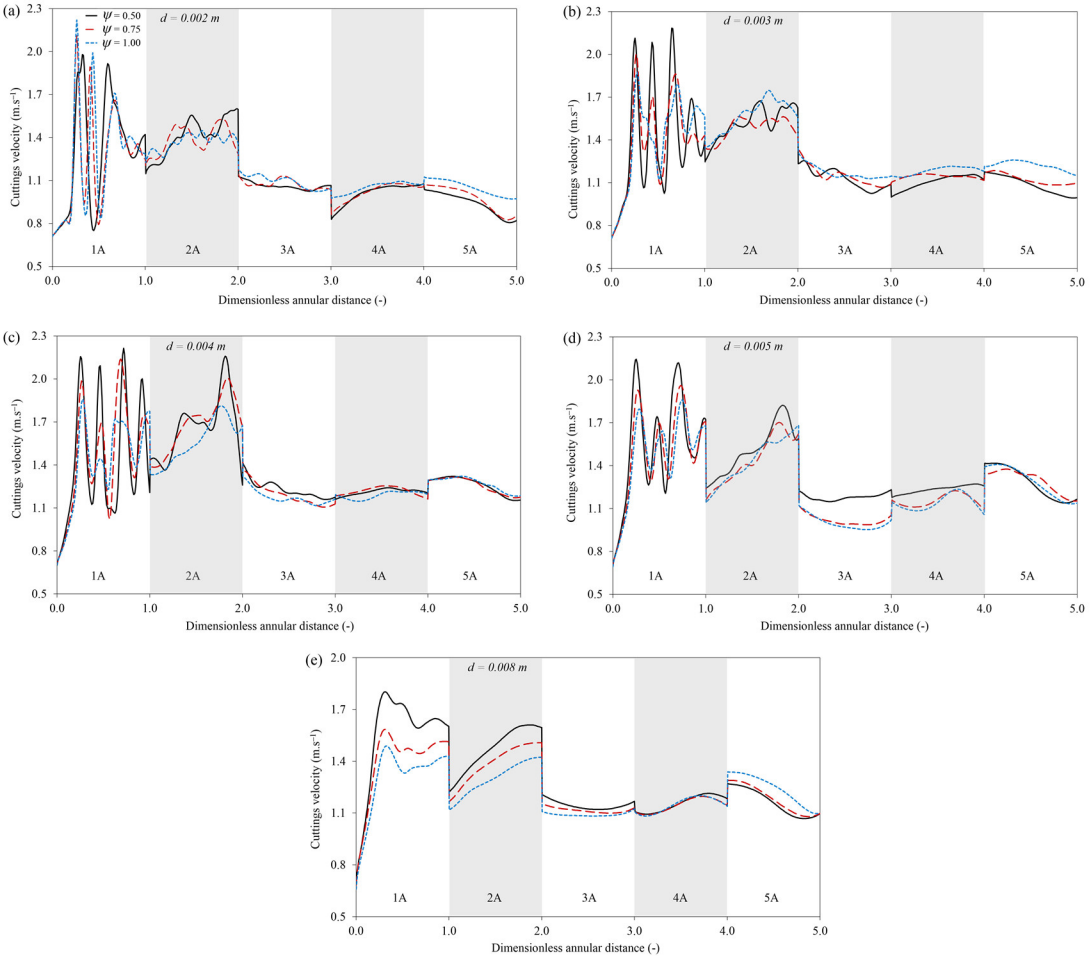

Figure 6.3. Cuttings velocity profiles in the line segments of the wider annular region "A" using drilling mud 1.

It is also observed (Figs. 6.4a-d) that the perfectly spherical particles tend to have the highest velocities at most line segments in the lower/narrower annular region (Region B).

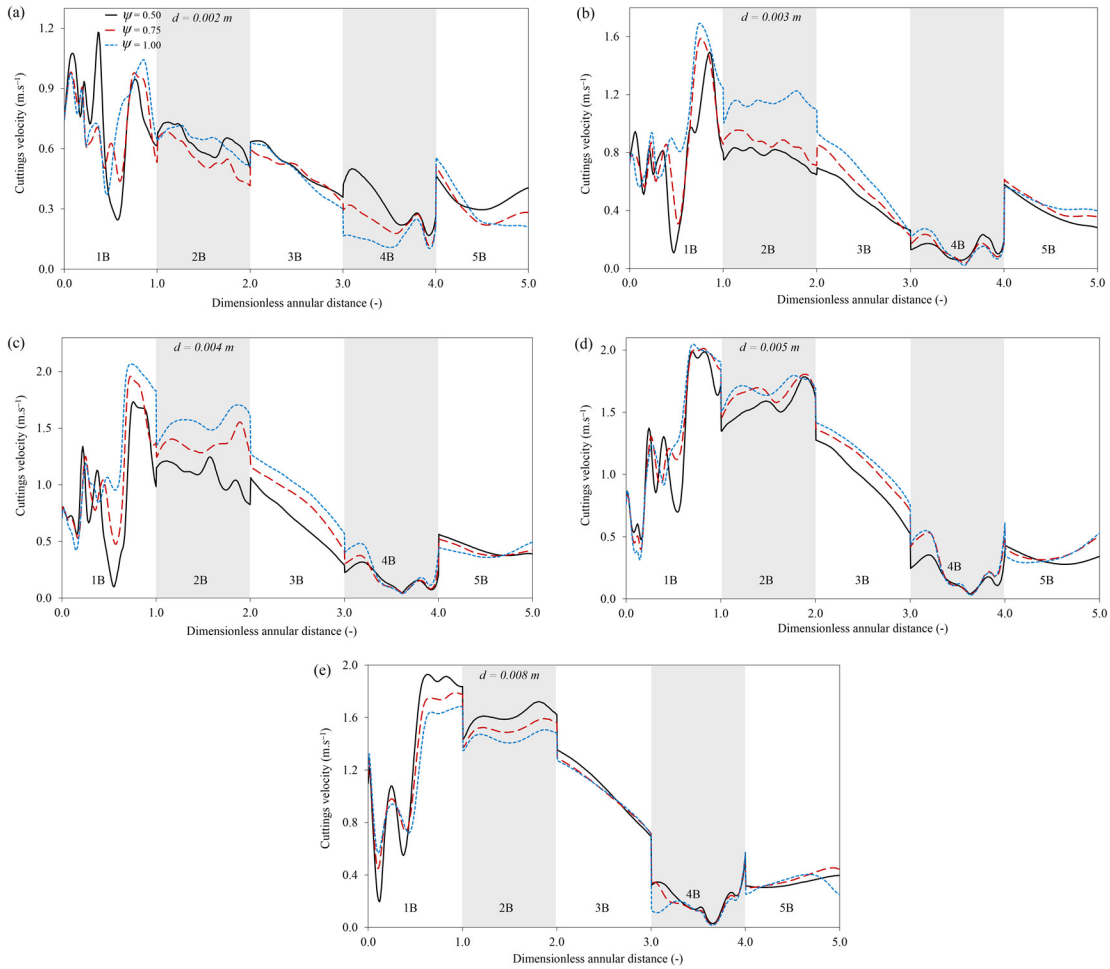

Figure 6.4. Cuttings velocity profiles in the line segments of the narrower annular region "B" using drilling mud 1.

This effect is significant in the inclined regions (Region 3B, Fig. 6.4). This occurrence demonstrates the strong disparity between dilute granular flow in the wider section (lower particle concentration relative to the fluid – Region A) and dense granular flow (high particle concentration relative to the fluid – Region B). We attribute this effect to the lower drag of spherical particles and their tendency to engage in rolling motion (compared to non-spherical particles); this kind of motion is hardly possible for non-spherical particles, which naturally engage in sliding motion under a densely concentrated/packed flow scenario. Furthermore, the packing behaviour of spherical particles allows extra fluid interaction with these particles due to larger void spaces created, compared to a tighter packing (reduced void spaces) that is attainable with non-spherical particles. These factors are responsible for the higher velocities experienced by the spherical particles in the dense flow regions.

However, in Fig. 6.4e, for the largest particles (d = 0.008 m), it is noticed that the highly non-spherical particles dominate the group velocity profile. This is contrary to what is observed in Figs. 6.4a-d. We attribute this phenomenon to the highly skewed (shifted to one side of the YZ Plane) deposition pattern of the largest particles (0.008 m) compared to other smaller particles (0.002 – 0.003 m); so that the line segments (Regions 1B – 3B) pass through annular locations exposed to dilute granular flow conditions as in Region A. Hence non-spherical particles still possess the highest travel velocities in Fig. 6.4e. This shifted deposition pattern will be further discussed in the analysis of the cuttings deposition patterns across the sectional planes. Although the EE model adopted here is unable to fully resolve/directly capture the kinematics of particle rolling (spherical) and sliding (non-spherical) motion, it is observed that pertinent geometry-related flow attributes of these particles illustrated in the simulation results, conform to their actual physical behaviour.

6.2 Line Segment Analysis of Cuttings Velocity using Drilling Mud - 2

Very similar observations to those of drilling mud-1 are made in the case of drilling mud 2. However, some subtle differences exist which are discussed. Compared to the first drilling mud, for each particle size (Fig. 6.3), there is a minimal disparity between the velocity profiles for the particles of different sphericities (Fig. 6.5) when the second drilling mud is used. The viscosity enhancement of drilling mud-2 thus reduces the velocity disparities initially noticed with the CMC fluid for the different particle shapes. The difference in the velocity profiles, however, only gets clearer with the largest particle size (Fig. 6.5e). Again, we notice the highly non-spherical particle having the highest velocity.

In the lower annular sections (Region B, Fig. 6.6), it is particularly observed that for all particle sizes, the different particle shapes experience very similar transport velocities as they enter the upper bend and vertical regions respectively (Regions 4B and 5B). This implies that the complexities of particle shape significantly affect the transport process in the horizontal and inclined regions respectively compared to the vertical regions.

For all cases considered (including drilling mud 1), the particles experience the lowest transport velocities in Region 4B; this is the region that is most susceptible to particle deposition and will be further discussed in Sections 6.3 and 6.4 respectively.

It is well established that non-spherical particles generally travel faster when transported in an annulus (as demonstrated in the volume-averaged analysis of Epelle and Gerogiorgis, 2019a; b and experiments of Byron, 2015). The results presented herein (based on a regional postprocessing analysis) reveal that this is not necessarily the case in all annular regions. Our positional variability analysis shows this variable dominance of non-spherical and spherical particle velocities significantly depends on the nature of the flow and the annular region considered (i.e. dense granular flow or dilute annular flow in the upper and lower sections respectively).

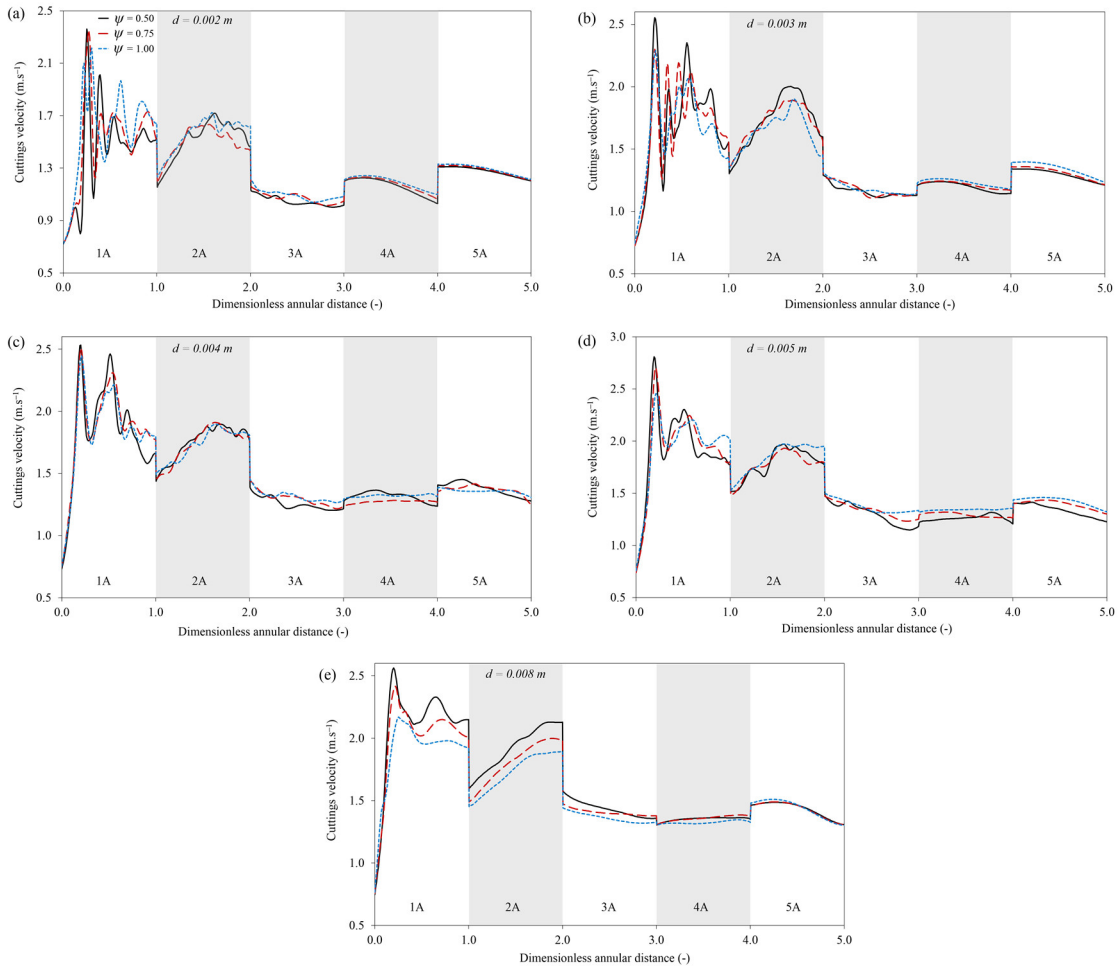

Figure 6.5. Cuttings velocity profiles in the line segments of the wider annular region "A" using drilling mud 2.

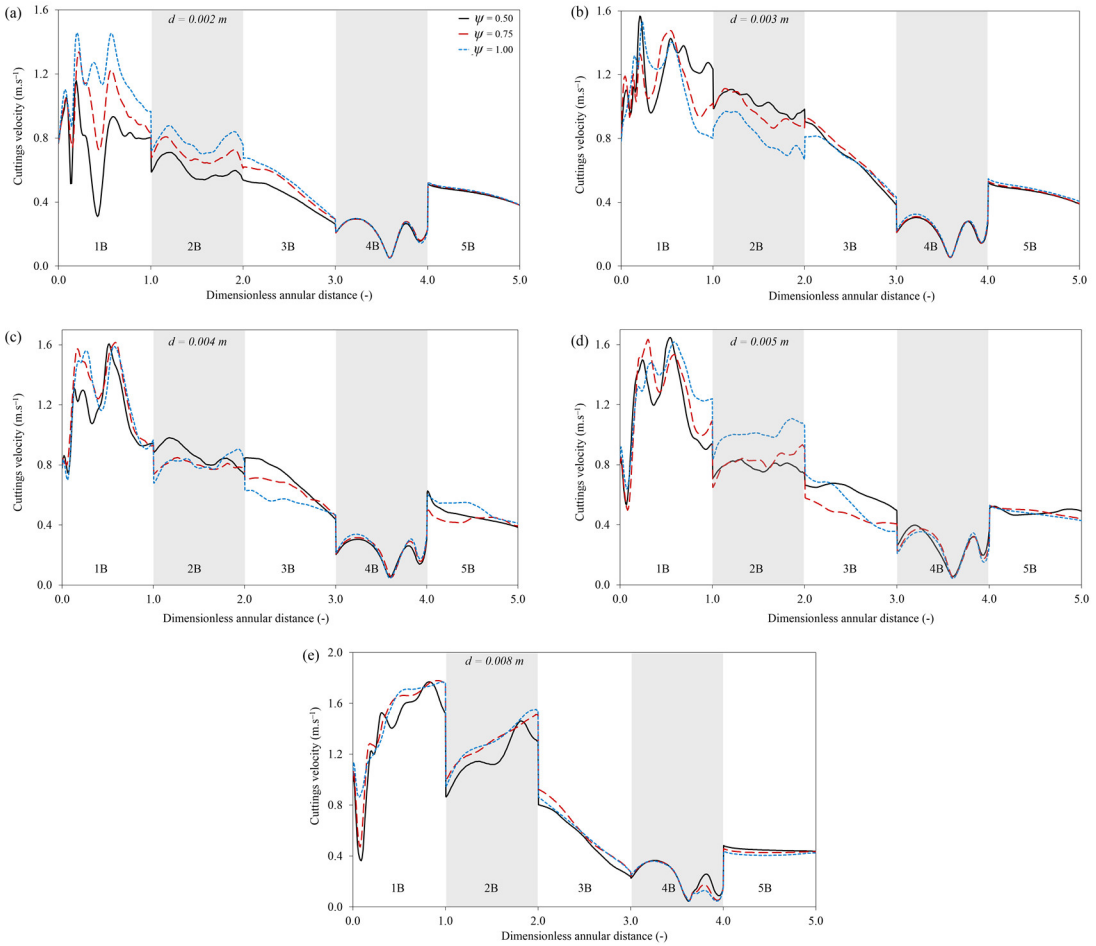

Figure 6.6. Cuttings velocity profiles in the line segments of the narrower annular region "B" using drilling mud 2.

Furthermore, the rather mild impact of cuttings sphericity on the travel velocity reflected in the volume-averaged results (in Chapter 5) is seen to only manifest in certain regions of the annulus in this chapter. This study shows this disparity is more significant in other regions (especially 1 and 2), demonstrating the inherent transport differences of all particle shapes considered. These observations are similar but different to those obtained in our cuttings concentration analyses in the previous chapter.

6.3 Sectional Analysis of Cuttings Deposition using Drilling Mud - 1

As demonstrated in Fig. 6.7a, seven equidistant perpendicular cross-sections of the annular geometry are used to gain further insight into the cuttings transport phenomena. The area fraction of the cuttings bed across the different planes is found using the expression in Fig 6.7a.

Thresholds of cuttings concentration (c_t = 0.4 and 0.5) are respectively applied over the averaged volume fraction in the flow domain, before evaluating the expression. A similar procedure is adopted to analyse cuttings deposition along the symmetric YZ plane (Fig. 6.2 and 6.11), which divides the annular flow domain into two main halves (front and back). The results are systematically grouped to analyse the impacts of particle sphericity and diameter coherently. Figs. 6.7 – 6.10 illustrate the cuttings concentration profiles under different transport conditions.

As expected, there is a general reduction in the cuttings deposition area as the cuttings concentration threshold increases. A consistent peak in cuttings concentration is also noticed in plane 5 (Fig. 6.7). This is in accordance with the earlier explained intense deposition at the upper annular bend (Region 4B; Figs. 6.3-6.6). More importantly, increased variability of the cuttings concentration with respect to sphericity is noticed in all cases compared to the volume-averaged analysis in (Epelle and Gerogiorgis, 2018b). For a threshold of 0.4 and a particle diameter of 0.008 m (Fig. 6.7i), we observe two peaks in the concentration profile, which correspond to the upper and lower bend, respectively. The plots shown with respect to the particle diameters (Figs. 6.7b-d) reveal that the 0.008 m particles often peak in concentration at the sixth plane compared to other diameters with peaks at plane 5 (Figs. 6.7b-d; Figs. 6.8b-d).

As will be subsequently shown, this increased deposition of bigger particles observed in Fig. 6.7i still poses a challenge to the wellbore cleaning process despite the rheological enhancement of the drilling mud. The proposed CFD modelling methodology is thus capable of providing critical insight into the dynamics of cuttings transport, and the resulting computational observations are consistent with relevant experimental investigations. This positional variability analysis has shown that the variable dominance of non-spherical and spherical particles' concentration significantly depends on the fluid rheology particle size and particle sphericity.

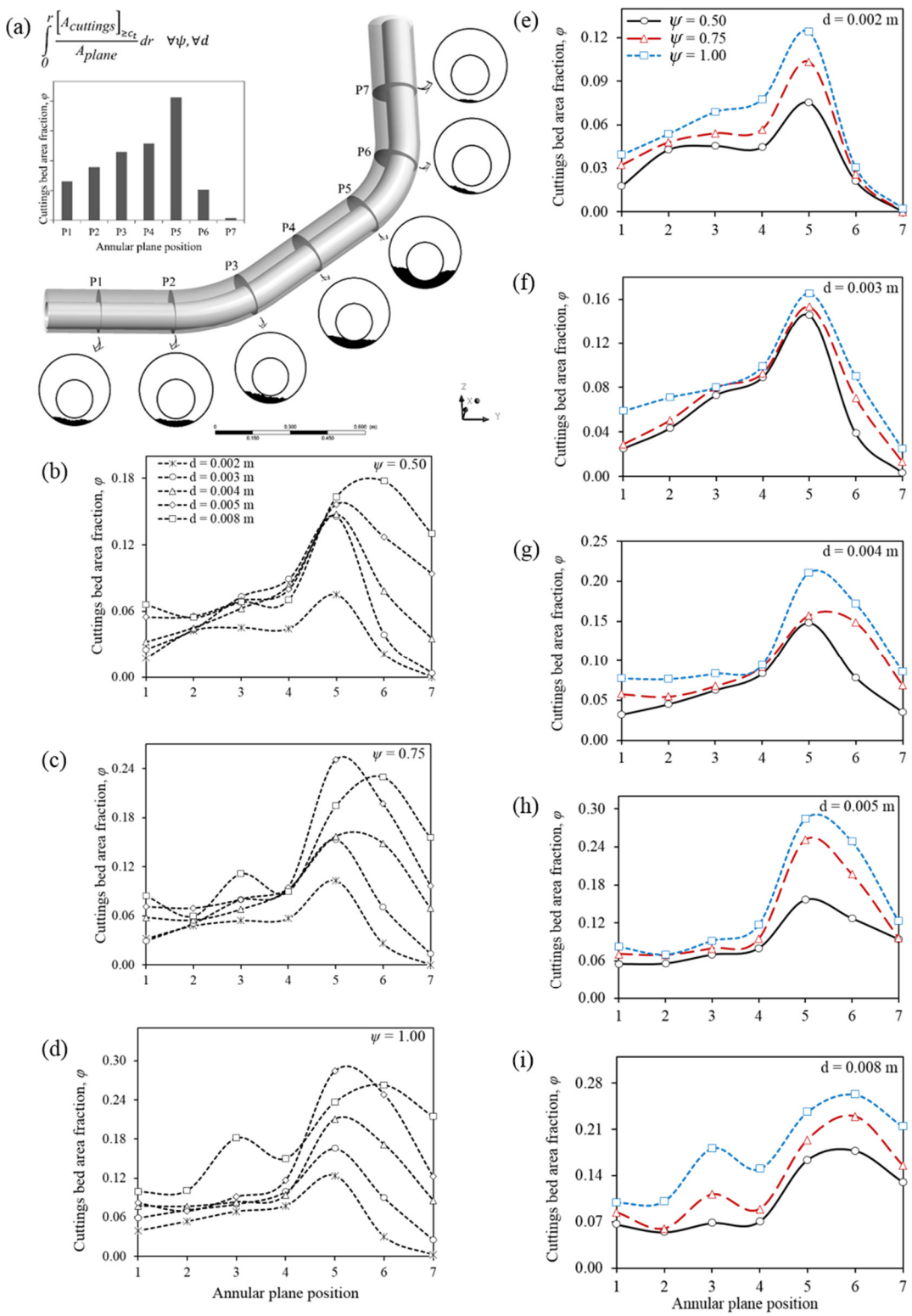

Figure 6.7. Analysis of particle concentration along the annulus, using a cuttings concentration threshold of c_t = 0.4 and the CMC drilling mud 1.

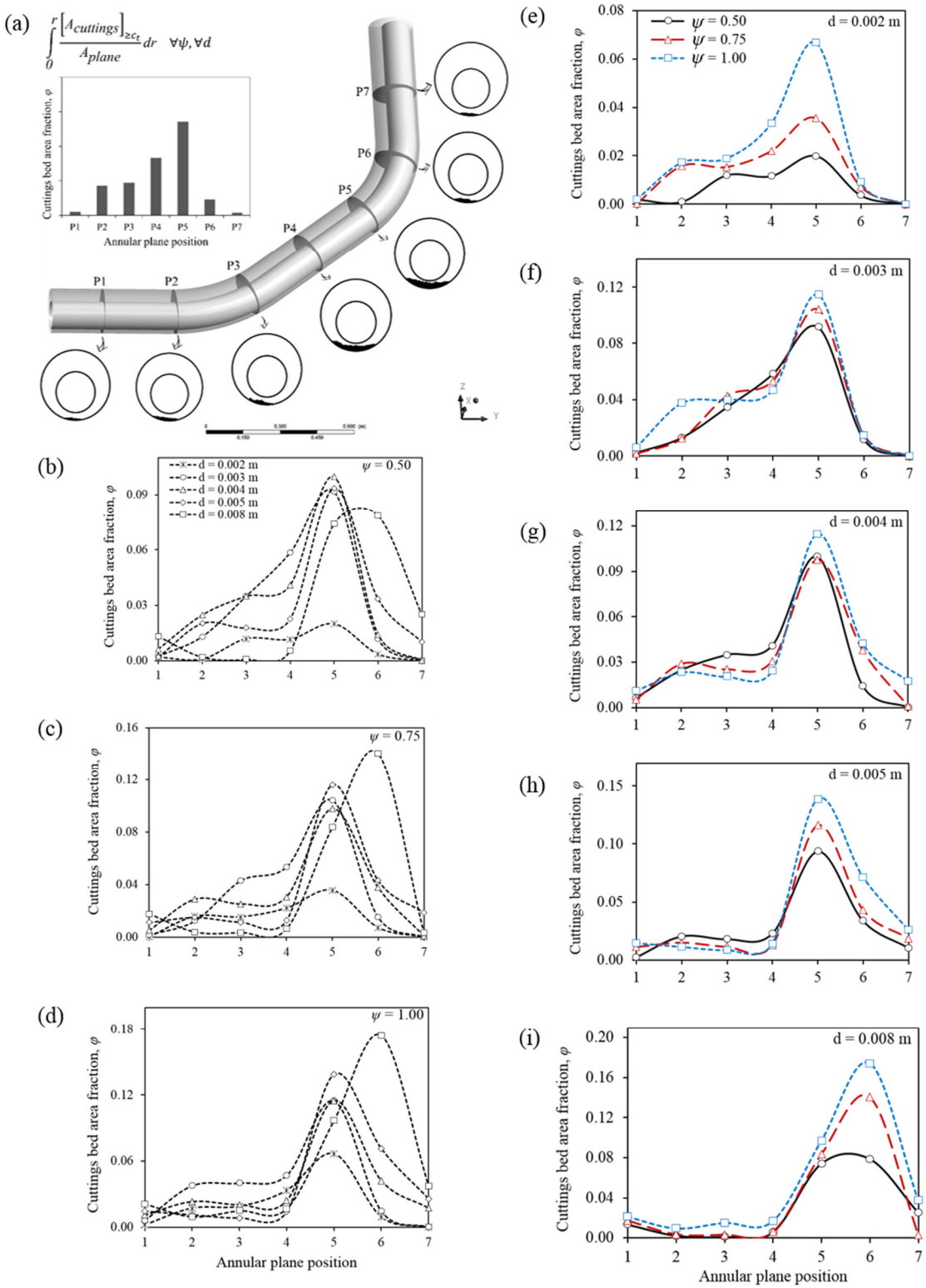

Figure 6.8. Analysis of particle concentration along the annulus, using a cuttings concentration threshold of c_t = 0.5 and the CMC drilling mud 1.

6.4 Sectional Analysis of Cuttings Deposition using Drilling Mud - 2

A similar analysis to that applied using mud-1 is also utilised here. Figs. 6.9 and 6.10

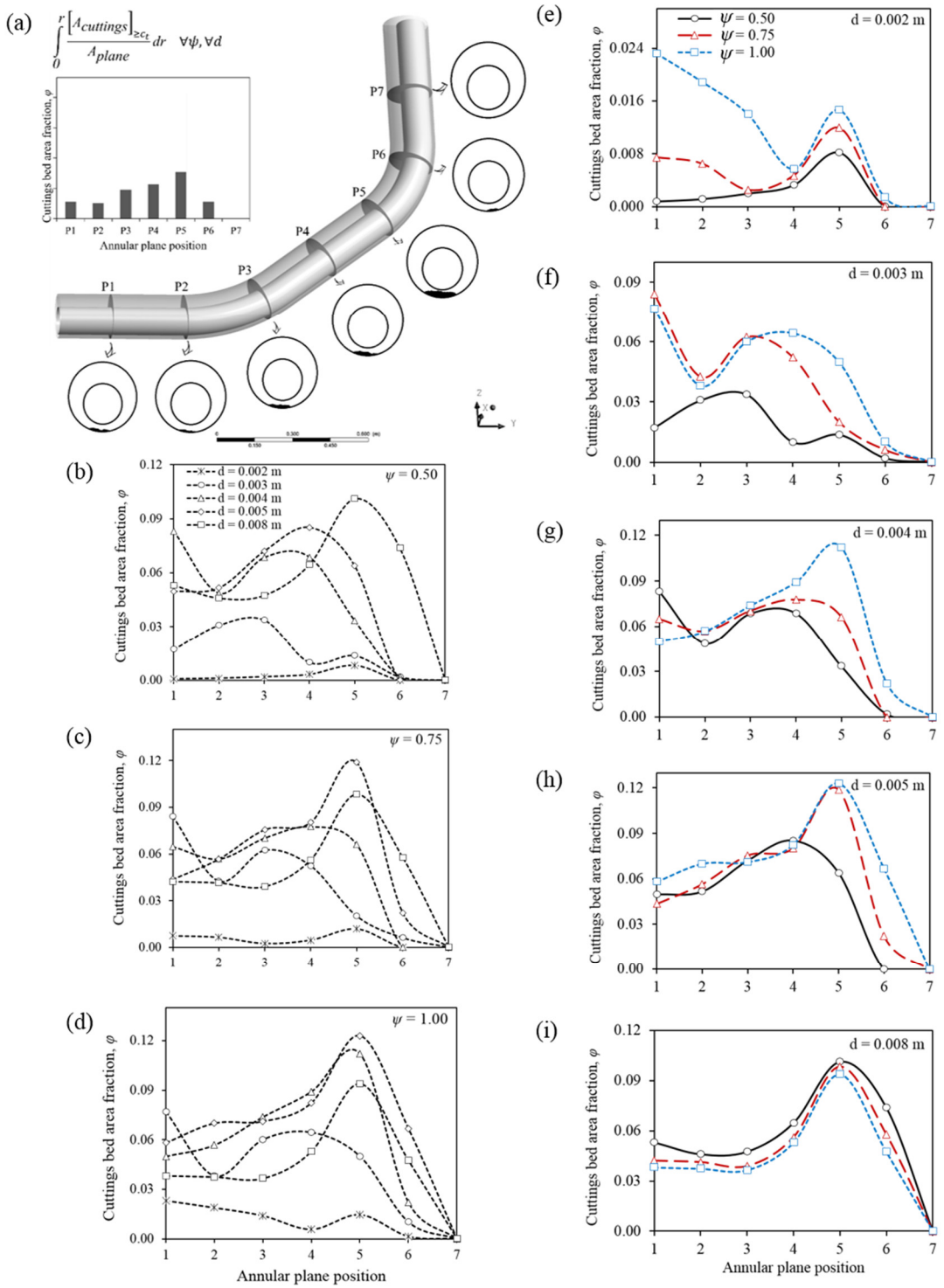

Figure 6.9. Analysis of particle concentration along the annulus, using a cuttings concentration threshold of c_t = 0.4 and the CMC + Bentonite drilling mud 2.

illustrate the peculiarities of the cuttings deposition pattern observed as a function of particle sphericity and diameter using the superior drilling fluid 2.

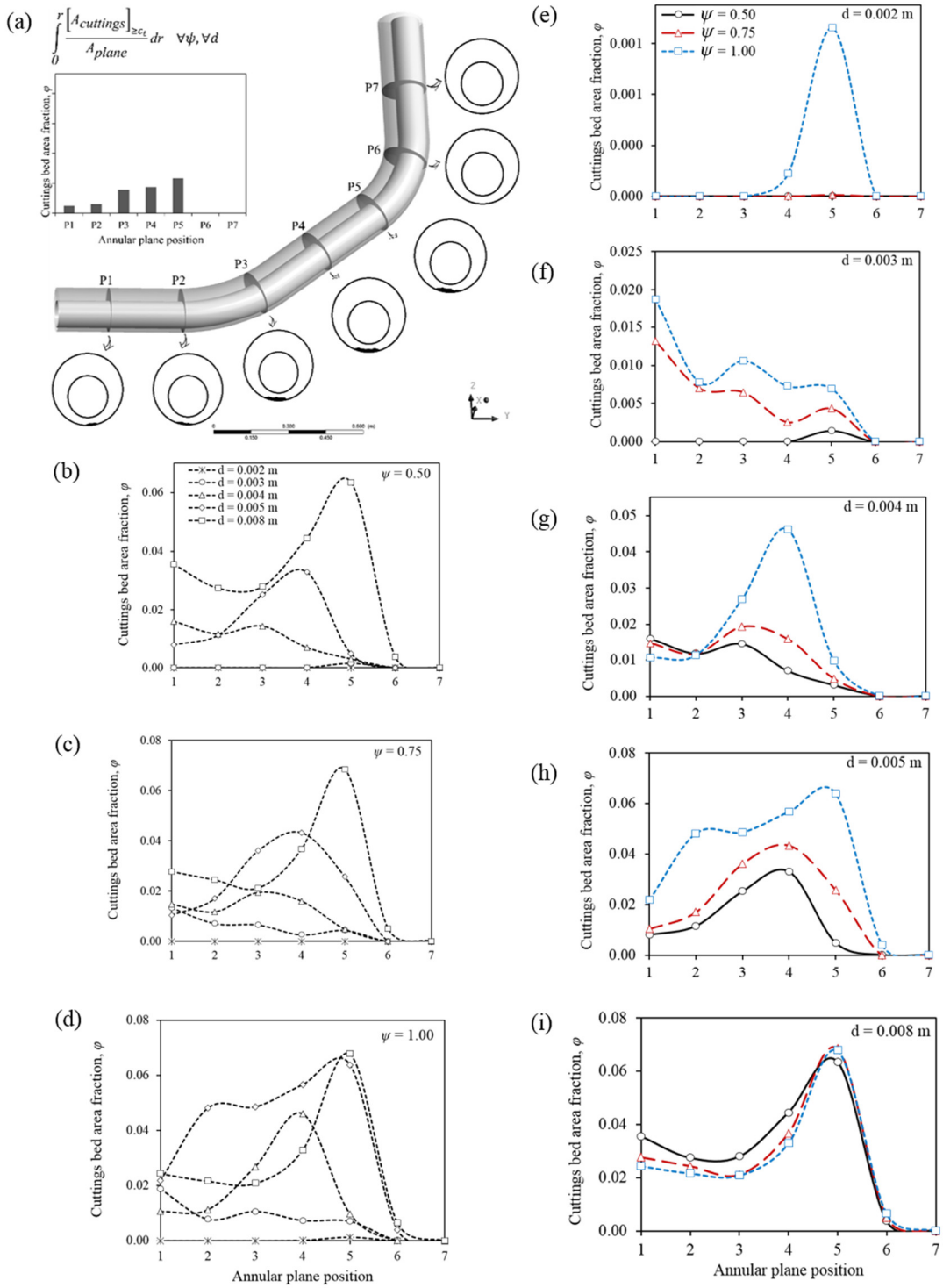

Figure 6.10. Analysis of particle concentration along the annulus, using a cuttings concentration threshold of c_t = 0.5 and the CMC + Bentonite drilling mud-2.

It is generally observed that stronger deposition in the horizontal section (planes 1 and 2; Figs. 6.9e-f) occurs over time with the second drilling mud compared to the deposition pattern observed with the first drilling mud (Figs. 6.9g-i). In addition, there is a reversal in deposition intensity by the 0.008 m cuttings, in the sectional analysis performed herein. This phenomenon may be attributed to the reduced cross-sectional area (due to increased deposition of the non-spherical particles), which translates to an increased averaged velocity, especially in the dilute flow regions (Region A). The second drilling mud (Figs. 6.9 and 6.10) reveals no deposition in planes 6 and 7 due to the near-vertical alignment of the geometry and the superior mud performance.

Since the YZ plane in Fig. 6.2 divides the annulus into two halves along the flow direction; it is possible to evaluate the impact of particle sphericity and diameter on the symmetry of the deposition pattern. When the first drilling mud is used, it is observed that the cuttings concentration decreases as the diameter increases for a threshold of 0.4 and 0.5, respectively (Fig. 6.11). This explains the increased asymmetry (shifted deposition to one side of the annulus – non-centralised along the YZ plane) caused by larger particles as discussed in detail by Epelle and Gerogiorgis (2018b; 2019c). This shifted deposition pattern can be attributed to the effect of drill pipe rotational/swaying motion on the particles and also because the increase in particle size makes it difficult for the particles to fit in a compacted manner in the narrower annular region (B). Thus, the intense and centralised particle deposition that can be captured by the YZ plane (Fig. 6.2) for the smaller-sized particles is often not shown by the same plane for the larger sized particles. This phenomenon is reflected in the velocity profiles in Fig. 6.4e and discussed in section 6.2.

The second drilling mud is able to maintain uniform positional displacement of drill cuttings as a result of its superior viscosity characteristics shows a different profile. While the smaller particles (0.002 m) are readily carried with little or no deposition (Figs. 6.11c and d), larger particles yield an increased deposition along the YZ plane until a slight reduction ensues from a diameter of 0.005 m. This observed pattern compared to Figs. 6.11a and b; is indicative of the somewhat centralised deposition pattern, which the cuttings of various sizes experience with the second drilling mud. Thus, the strongly shifted deposition pattern observed with drilling mud 1 is not the case with drilling mud 2. While the 0.4 and 0.5 thresholds are generally representative of the holistic transport

behaviour of the densely concentrated regions, the profiles of the 0.6 cuttings concentration threshold (not shown herein) were severely affected by the inherent stochasticity of the transient transport process. Furthermore, the simulation settings of CFD solver (Fluent 17.1) ensures that the solids packing density is limited to a value of 0.63. This allows for some void space (occupied by the liquid) between the particles so that there is minimal momentum transfer from the drilling mud to the particles. As the applied cuttings concentration threshold approaches this value (0.63), it is likely that the uncertainty in the transient statistical averaging of the cuttings concentration becomes more significant. Accounting for this uncertainty is a subject of future investigations.

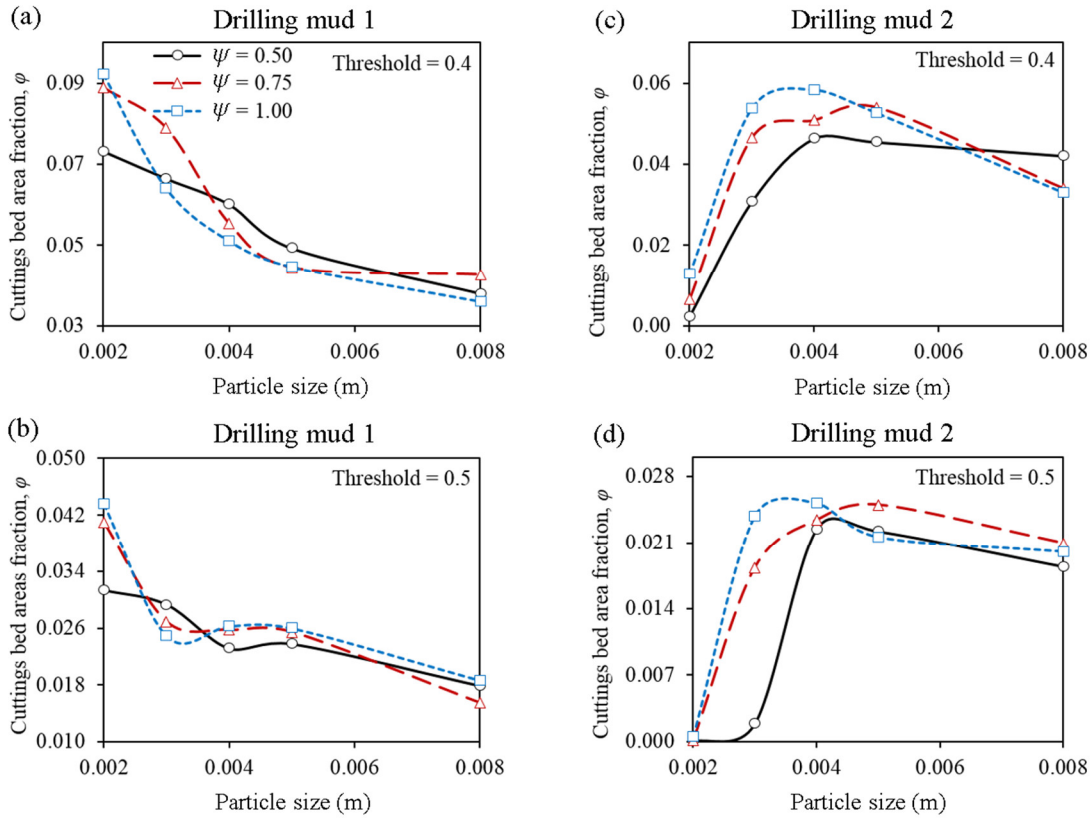

Figure 6.11. Analysis of particle concentration along the YZ symmetrical plane in the annulus, using a cuttings concentration threshold of c_t = 0.4 and c_t = 0.5 for both drilling muds.

6.5 Chapter Conclusions

This study presents a transient analysis of drill cuttings transport behaviour in a deviated annulus using the Eulerian-Eulerian model in Ansys Fluent. Principally demonstrated in this work is the application of several line segments and cutting planes for the elucidation

of the position-dependent cuttings transport behaviour in the annulus. We draw the following conclusions from the observations made.

- Despite the fact that CFD simulations carried out here only consider a mono-dispersed particle distribution (both in terms of size and shape), the presented profiles indicate that flow complexity will further increase due to polydispersity and its multiple momentum transfer mechanisms (particle-fluid and particle-particle interactions). CFD studies accounting for polydispersed cuttings distribution are scarce (if any), implying great opportunities for future research.
- Although the velocity analyses here are carried out along lines, a holistic picture of the transport velocities' dependence on particle shape is attainable via a volume-averaged analysis over the entire multifaceted domain. Just as the overall macroscopic phenomena over the entire flow domain is often desired, analysis via enhanced spatial resolution that yields the cuttings transport behaviour at a more refined level cannot be neglected.
- Sectional analysis of cuttings deposition along several planes in the annulus provided better variability in cuttings concentration as a function of particle sphericity compared to the volume-averaged analysis.
- The sectional analysis of the deposition profiles has shown that the narrower region of the upper annular bend is most likely to retain the highest amount of drill cuttings.
- Neglecting particle shape effects could result in severe underestimation of the required velocity and thus the pressure drop necessary for a deposition-free transport scenario.
- Spatial velocity variation in the annulus shows that the wider annular sections more readily experience a dilute flow of cuttings (due to high velocity of travel) compared to the lower annular regions where dense granular flow is prominent.
- The particle shape with the dominant velocity depends on the annular location and the nature of the flow (dilute or dense). Non-spherical particles tend to dominate the group velocity profiles in the dilute granular flow region (A), whereas spherical particles have the highest velocities in the dense granular regions (B).

- The results presented herein (based on a regional postprocessing analysis) reveal that the velocity of non-spherical particles is not necessarily higher than those of spherical particles in all annular regions. Our positional variability analysis has shown that the variable dominance of non-spherical and spherical particles' velocities significantly depends on the nature of the flow (i.e. dense granular flow or dilute annular flow in the upper and lower sections respectively).

PART III: MATHEMATICAL OPTIMISATION OF OIL & GAS PRODUCTION SYSTEMS

Chapter 7 Multiperiod Optimisation for Rate Allocation of Oil & Gas Production and Injection Wells

An oil and gas field requires careful operational planning and management via production optimisation for increased recovery and long-term project profitability. It is estimated that oil companies produce up to three barrels of water for each barrel of oil from depleting reservoirs and this costs approximately $40 billion annually to handle (Bailey et al., 2000). Field engineers in the oil and gas industry are constantly faced with the challenge of maintaining profitability amidst several operational constraints, such as the optimal water injection strategy for mature fields undergoing secondary production.

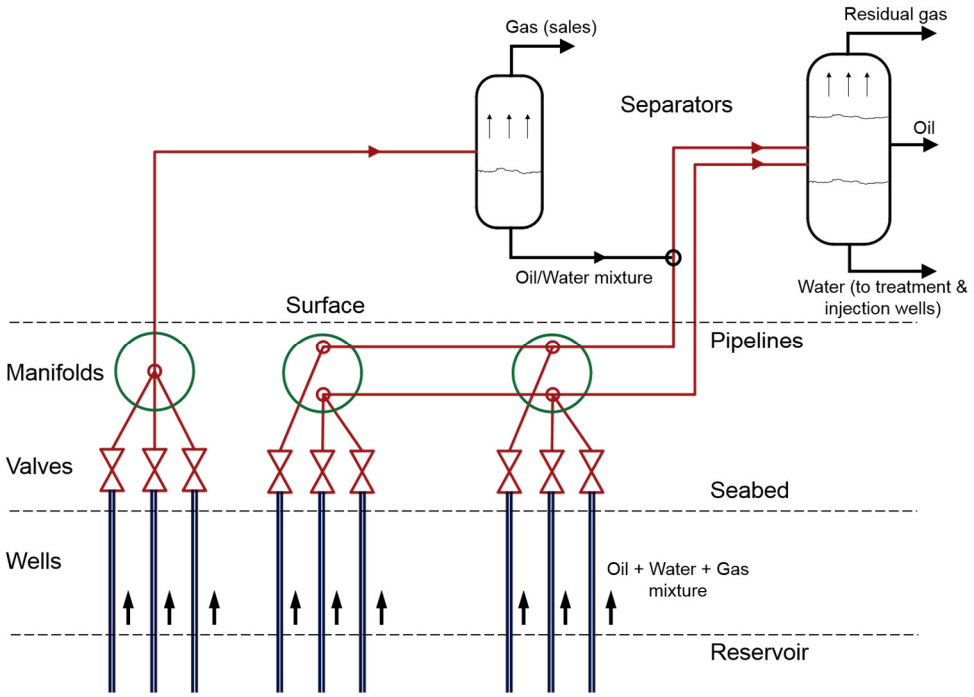

Figure 7.1. Typical Layout of a production system.

However, the study presented herein is premised on industrial findings that controlling injected water rates and hence volumes of produced water is one of the fastest and least expensive ways to reduce field operating costs and increase hydrocarbon recovery simultaneously (Bailey et al., 2000). This ultimately depends on the production and injection rates of the wells, rock and fluid properties, the method of water handling amongst many other factors. Hence, exploiting a process systems engineering description of the problem aids operational decisions by providing an optimal production and water

injection strategy for the considered case studies. By applying sound mathematical-oriented optimisation methods, the dependence on heuristic-based diagnostic methods for production and water injection control can be reduced and thus, used as a complementary tool.

This chapter addresses the challenge of production optimisation in a field undergoing secondary recovery by water flooding. The field operates with limited processing capacity at the surface separators, pipeline pressure constraints and water injection constraints; an economic indicator (Net Present Value – NPV) is used as the objective function. The formulated optimisation framework adequately integrates slow-paced subsurface dynamics using reservoir simulation and the fast-paced surface dynamics using sophisticated multiphase flow simulation in the upstream facilities. Optimisation of this holistic long–term model is made possible by developing accurate second-order polynomial proxy models at each time step. The resulting formulation is solved as a Nonlinear Program (NLP) using commercially available solvers. By implementing two synthetic case studies, the presented mathematical programming approach determines the optimal production and injection rates of all wells. This method further demonstrates considerable improvement to the NPV obtained by simultaneously applying the tools of reservoir, streamline, and surface facility simulation for well rate allocation.

7.1 Production System Modelling

Fig. 7.1, illustrates a typical production system involving the flow of hydrocarbons over a sufficient pressure gradient from the reservoir to the separators operating at a known constant pressure. To model this complex system, pressure and flow rates can be analysed by decomposing the system into two main rigorously modelled sections. First, is the reservoir to wellbore flow section as described mathematically by the well's Productivity Index (PI), Vertical Flow Performance and Inflow Performance Relationship (IPR), respectively (Fig. 7.2). In addition, Eqs. 7.1-7.3 are the PI calculation methods for an oil well, a gas well and an oil well operating below its bubble point (Vogel's IPR).

Just as the Productivity Index (PI) characterises the performance of a production well, the Injectivity Index (II) is a performance indicator of water injection wells (Eq. 7.4); we assume an incompressible water phase and the injection pressure is below the formation's

fracture pressure. The injector efficiency (via streamline simulation) is another performance metric for injection wells considered here.

In Eq. 7.1-7.11, Q_o represents the oil production rate from a well, which could be vertical, Q_{ov} or horizontal, Q_{oh}. P_r is the average reservoir pressure, P_{wf}, the bottomhole flowing pressure, r_e, the radius of drainage, r_{eh}, the effective drainage radius of a horizontal well, and r_w, the wellbore radius. The oil and gas viscosities are denoted as μ_g and μ_o, respectively. The net thickness of the formation is represented as h, k_h is the horizontal permeability, k_v is the vertical permeability, and k is the geometric average permeability; s is the total skin, Z is the gas deviation factor determined at an average temperature, T; B_o and B_g are the oil and gas formation volume factors, respectively. For horizontal wells, L is the horizontal well length, and a is half the distance of the major axis of the drainage ellipse (Joshi, 1991).

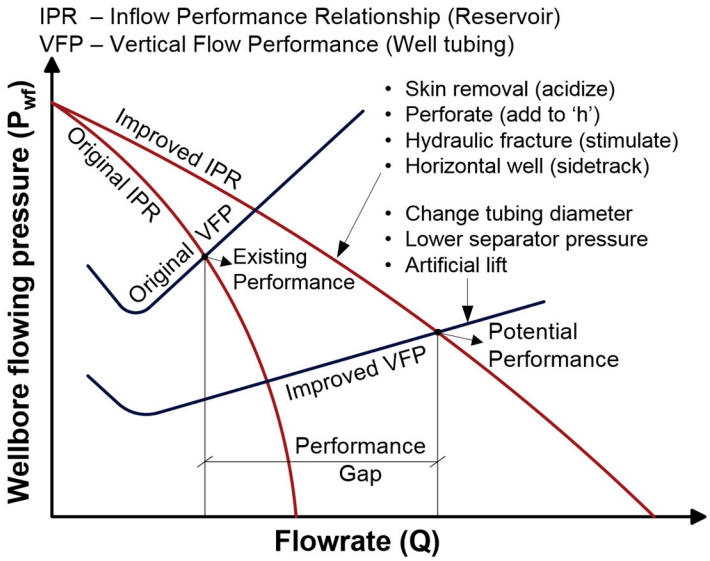

Figure 7.2. Inflow Performance Relationship (IPR) and Vertical Flow Performance (VFP) curves.

The flowrates of the respective fluids from the reservoir are dependent on the reservoir properties, as shown in Eq. (7.5–7.8), and are based on Darcy's law. For horizontal wells, a more complex relationship exists between the productive length of a well and its productivity index (Eq. 7.7 and 7.8).

The second aspect, is the multiphase flow description of the produced fluids in the pipelines (from the wellhead to pipelines and separators) under varying inclinations and flow regimes using robust multiphase correlations (Eq. 7.12). The pressure drop per unit

length is represented as dP/dL. Optimisation of a coupled system of equations representing both sections is a highly challenging task, for which several solution approaches have been proposed. The increasing number of contributions can be attributed to the advances in the development of specialised algorithms, accompanying computational power and most importantly proxy modelling techniques (polynomials, spline kriging, Artificial Neural Networks). A detailed description of the system components, modelling and simulation strategy follows.

$$PI_L = \frac{Q_o}{(P_r - P_{wf})} \tag{7.1}$$

$$PI_G = \frac{Q_g}{({P_R}^2 - {P_{wf}}^2)} \tag{7.2}$$

$$Q_o = Q_b + \left(\frac{PI \times P_b}{1.8}\right)\left[1 - 0.2\frac{P_{wf}}{P_b} - 0.8\left(\frac{P_{wf}}{P_b}\right)^2\right] \tag{7.3}$$

$$Q_w = II_W \times (P_{wf} - P_r) \tag{7.4}$$

$$Q_{ov} = \frac{7.08 \times 10^{-3} k_h h(P_r - P_{wf})}{\mu_o B_o \left[ln\left(\frac{r_e}{r_w}\right) - 0.75 + \boldsymbol{S}\right]} \tag{7.5}$$

$$Q_{gv} = \frac{7.03 \times 10^{-4} k_h h(P_r^2 - P_{wf}^2)}{\mu_g ZT \left[ln\left(\frac{r_e}{r_w}\right) - 0.75 + \boldsymbol{S}\right]} \tag{7.6}$$

$$Q_{oh} = \frac{7.08 \times 10^{-3} k_h h(P_r - P_{wf})}{\mu_o B_o \left\{ln\left[\frac{a + \sqrt{a^2 - \left(\frac{L}{2}\right)^2}}{\left(\frac{L}{2}\right)}\right] + \frac{\beta h}{L} ln\left(\frac{\beta h}{(\beta + 1) r_w}\right)\right\}} \tag{7.7}$$

$$Q_{gh} = \frac{7.06 \times 10^{-4} k_h h(P_r^2 - P_{wf}^2)}{\mu_g ZT \left\{ln\left[\frac{a + \sqrt{a^2 - \left(\frac{L}{2}\right)^2}}{\left(\frac{L}{2}\right)}\right] + \frac{\beta h}{L} ln\left(\frac{\beta h}{(\beta + 1) r_w}\right)\right\}} \tag{7.8}$$

$$a = \frac{L_h}{2}\left[0.5 + \sqrt{0.25 + \left(\frac{2r_{eh}}{L_h}\right)^4}\right]^{0.5} \tag{7.9}$$

$$\beta = \sqrt{\frac{k_h}{k_v}} \tag{7.10}$$

$$k = \sqrt{(k_h k_v)} \tag{7.11}$$

$$\left(\frac{dP}{\mathrm{dL}}\right)_{total} = \left(\frac{dP}{\mathrm{dL}}\right)_{friction} + \left(\frac{dP}{\mathrm{dL}}\right)_{gravity} + \left(\frac{dP}{\mathrm{dL}}\right)_{acceleration} \tag{7.12}$$

7.2 Reservoir Simulation

Before applying mathematical optimisation, we adopt reservoir engineering tools (PETREL™, ECLIPSE™ 100, and FRONTSIM™) for modelling fluid flow in porous media (Schlumberger, 2019a; b; c; d; e). Firstly, we construct and discretise the reservoir (using PETREL™) and run a test forecast simulation (using ECLIPSE™ 100) to determine the performance of each well and the increment in oil production due to water flooding – 'x' (Fig. 7.3a). This increment is obtained at each time step (Δt). In running this test case for the determination of initial guesses, we first adopt a constant injection rate over the entire time horizon (Figs. 7.3c-i) and then apply injection rates derived from the injection efficiency calculations (Section 3.2).

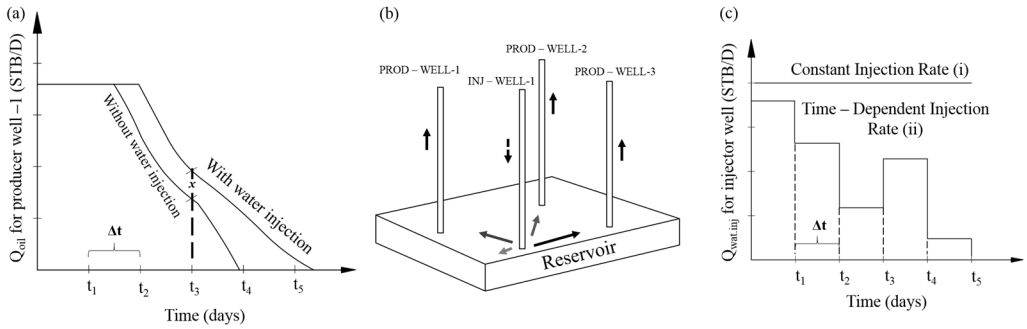

Figure 7.3. Oil production and water injection profiles in the reservoir; Δt is taken to be 365 days.

In order to perform porous media flow simulations of the water flooding process, the following set of nonlinear material balance equations, in each cell (Figs. 7.9 and 7.12) are solved for each phase.

$$\sum_{l\in\psi_n} T_{o_{f,n}}^{n+1}\left[(p_{o_f}^{n+1} - p_{o_n}^{n+1}) - \gamma_{o_{l,n}}^{n}(Z_f - Z_n)\right] + \sum_{f\in\xi_n} q_{osc_{f,n}}^{n+1} + q_{osc_n}^{n+1} = \frac{V_{b_n}}{\alpha_c \Delta t}\left\{\left[\frac{\varphi(1-S_w-S_g)}{B_o}\right]_n^{n+1} - \left[\frac{\varphi(1-S_w-S_g)}{B_o}\right]_n^{n}\right\} \tag{7.13}$$

$$\sum_{f\in\psi_n} T_{w_{f,n}}^{n+1}\left[(p_{o_f}^{n+1} - p_{o_n}^{n+1}) - \left(P_{cow_f}^{n+1} - P_{cow_n}^{n+1}\right) - \gamma_{w_{f,n}}^{n}(Z_f - Z_n)\right] + \sum_{f\in\xi_n} q_{wsc_{f,n}}^{n+1} + q_{wsc_n}^{n+1} = \frac{V_{b_n}}{\alpha_c \Delta t}\left\{\left[\frac{\varphi(S_w)}{B_w}\right]_n^{n+1} - \left[\frac{\varphi(S_w)}{B_w}\right]_n^{n}\right\} \tag{7.14}$$

$$\sum_{f\in\psi_n} T^{n+1}_{g_{f,n}}\left[(p^{n+1}_{o_f}-p^{n+1}_{o_n})+\left(P^{n+1}_{cgo_f}-P^{n+1}_{cgo_n}\right)-\gamma^{n}_{g_{f,n}}(Z_f-Z_n)\right] \tag{7.15}$$
$$+(T_oR_s)^{n+1}_{f,n}\left[(p^{n+1}_{o_f}-p^{n+1}_{o_n})-\gamma^{n}_{o_{f,n}}(Z_f-Z_n)\right]$$
$$+\sum_{l\in\xi_n}[q^{n+1}_{fgsc_{f,n}}+R^{n+1}_{s_n}q^{n+1}_{osc_{f,n}}]+[q^{n+1}_{fgsc_{f,n}}+R^{n+1}_{s_n}q^{n+1}_{osc_{f,n}}]$$
$$=\frac{V_{b_n}}{\alpha_c\Delta t}\left\{\left[\frac{\varphi(S_g)}{B_g}\right]^n_n-\left[\frac{\varphi\left(S_g\right)}{B_g}\right]^n_n+\left[\frac{\varphi R_s(1-S_w-S_g)}{B_o}\right]^{n+1}_n\right.$$
$$\left.-\left[\frac{\varphi R_s(1-S_w-S_g)}{B_o}\right]^n_n\right\}$$

Table 7.1. Fluid and reservoir properties.

Fluid properties at reservoir conditions	Value
Gas density (kg.m^{-3})	0.8117
Oil density (kg.m^{-3})	801
Water density (kg.m^{-3})	1,020
Gas viscosity (cP)	0.0214
Oil viscosity (cP)	0.4610
Water viscosity (cP)	0.3989
Gas formation volume factor (RB/STB)	0.854
Oil formation volume factor (RB/STB)	1.191
Water formation volume factor (RB/STB)	1.013
Gas compressibility (1/psi)	0.000251
Oil compressibility (1/psi)	0.000012
Water compressibility (1/psi)	0.00000273
Water salinity (ppm)	30,000
Initial reservoir pressure (psia)	3,300
Reservoir dimensions (100 × 50 × 10)	Value
DX (m)	20,000
DY (m)	10,000
DZ (m)	1,000

7.2.1 Reservoir Modelling Assumptions

- Reservoir rock and fluid (light oil/gas) properties (Table 7.1) are available (3D dimensions, absolute and relative permeability data, porosity, fluid density, viscosity, compressibility, oil/gas formation volume factors, initial reservoir pressure, residual water and gas saturations).

- The reservoir is considered infinite acting with no near-by boundaries such as faults present.
- Number and locations of producers and injectors are known; all wells are drilled at the same time and commence operation (production and injection) simultaneously.
- The statistical distributions of porosity and permeability are considered known, as shown in (Fig. 7.4).
- Production time horizon is known (T = 6 years).
- Capillary pressure effects are insignificant in the reservoir.
- Economic parameters such as the unit volumetric costs for oil and gas sales and water production costs are available.

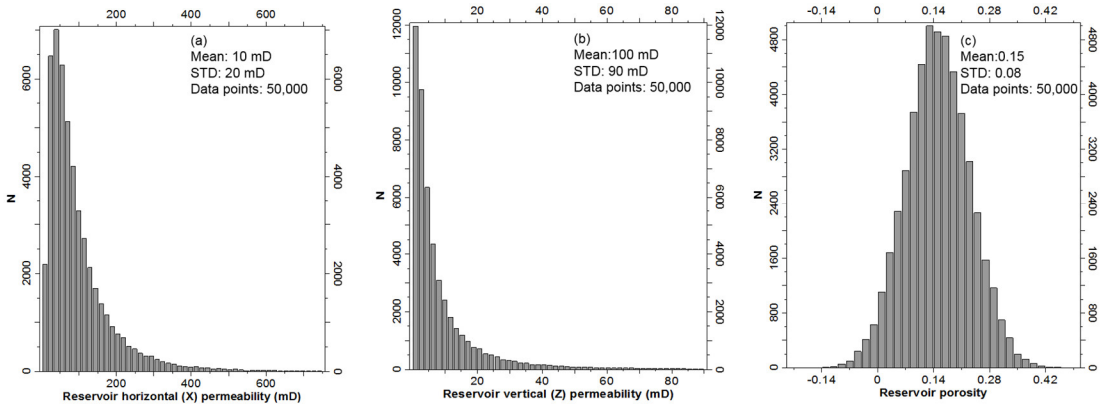

Figure 7.4. Statistical distributions of horizontal permeability (a), vertical permeability (b) and porosity (c).

7.3 Streamline Simulation

Streamlines describe the tangential velocity vectors in a field at any point in time by solving a 1D transport problem along each line (Thiele and Batycky, 2006). Thus, multiphase flow effects and the resultant fluid distribution can be captured while accounting for the uneven well production rates and the underlying permeability distribution. Time-dependent Well Allocation Factors (WAFs) between injection and production wells can be derived from the results of the streamline simulation and used for the calculation of the injection efficiency (IE). The method of calculating IE proposed in the work of Thiele and Batycky (2006) was applied here. Through the use of this performance indicator, it is possible to determine how much additional oil can be produced per unit volume of water injected by an offset injector.

$$IE_{i,t} = \frac{offset\ oil\ production}{water\ injection} \tag{7.16}$$

$$IE_{i,t} = \frac{\sum_{k=1}^{K}(WAF_{k,i,t} \times q_{o,k,t})}{q_{w,i,t}} \tag{7.17}$$

$$WAF_{k,i,t} = \frac{Number\ of\ streamlines\ connecting\ producer, k\ \ and\ injector, i\ (N_{k,i,t})}{Number\ of\ streamlines\ for\ producer, k\ (N_{P,t})} \tag{7.18}$$

Although we aim to optimise the production-injection-surface facility network using a classical optimisation algorithm, the number of variables involved implies that their initial guesses significantly affect the quality of the solution obtained. Hence, streamline simulation (using FRONTSIM™), a vital tool, is implemented for the generation of more reliable initial guesses for speedy computation by the optimisation algorithm. Similarly, well rates from the reservoir simulator (ECLIPSE™ 100) serve as good starting points for the optimiser. Improved oil recovery is thus possible by employing the tool of mathematical optimisation without neglecting fundamental reservoir engineering judgement. With the calculated injector efficiencies at each timestep, and the total daily available water capacity, a reliable estimate of the injection rates at each time step can be determined (Fig. 7.3c-ii). These new and more accurate injection rates are used to re-run a forecast of the field's oil production. By doing this, we obtain the Productivity Index (PI) of the production wells, the field's Gas Oil Ratio (GOR) and Water Cut (WC) as functions of time. Thus, the GOR and WC signatures over the production horizon (embedded in the optimisation model) inherently capture the impact of the injection wells on the oil production rate of the production wells (injector-to-producer flow behaviour in the reservoir); so that, the optimal injection rates can be determined by the optimisation model using these dynamic properties (GOR and WC) and the surface wellhead injection pressures. The final injection rates determined by the optimisation model significantly depend on the initial guesses of the injection rates derived from the calculation of the injection efficiencies. It is necessary to emphasise that IE is not directly used in the optimisation model but affects the GOR and WC, which in turn affect the oil, water production rates and pressure responses at the surface. The following points are also worthy of note:

- The injection well efficiency (IE) exists for each injector well (i) at every time step (t).
- $WAF_{k,i,t}$, $q_{o,k,t}$, $q_{w,i,t}$ are obtained from streamline simulation using a tool called FRONTSIM™. IE at each timestep is calculated from Eq. 7.17 and used to

heuristically determine the water allocation ratios to the respective wells. These ratios are then used to run a reservoir simulation using ECLIPSE™.

- The reservoir simulation with ECLIPSE™ outputs GOR and WC at each time step.
- We use GOR and WC at each time step to determine the pressure-rate responses using the tool, PIPESIM™ (that accounts for pressure drop).
- These pressure-rate responses from PIPESIM™ are used to develop the proxy models in the optimisation formulation.

However, an alternative approach is to redefine the injection rates as a function of the production rates (of each phase) for each well pair, based on the WAFs and IEs at each timestep. This would require proxy models to be developed that relate $q_{p,k,t}$ to $q_{p,i,t}$ (in Eqs. 7.26 and 7.27); hence, enabling a direct manipulation of the injection rates for determining the optimal injection strategy. Furthermore, direct calls to the ECLIPSE reservoir simulator (a more challenging approach, due to the difficulty posed by access to the simulator's source code) or the application of the adjoint-gradient functionality of ECLIPSE E300 as demonstrated by Hørsholt et al. (2018) may be pursued for increased accuracy. Nevertheless, the method presented in this chapter, which depends on the reservoir-engineering supplied initial guesses of the injection rates is sufficient to yield operationally-relevant results of reasonable accuracy. In Chapter 10, an approach that utilises adjoint equations in an open-source reservoir simulator (with access to gradient information) for algorithmic manipulations of the injection rates is presented; thus yielding a better evaluation of the optimal injection strategy.

7.4 Incorporating Wellbore Hydraulics

Subsequent to obtaining the above-listed parameters at each time step (Δt) is the use of a multiphase flow simulator (PIPESIM™) to estimate pressure drops in the wellbores and pipelines, respectively. The PI, II, GOR, WC at each timestep are required inputs in PISESIM for pressure drop calculations (Fig. 7.5). The well trajectory and well completion details (casing size, tubing size and perforation intervals), are also imported from PETREL™ and used in the pressure drop calculations in PIPESIM™. A sensitivity analysis is run on the wells and pipelines to obtain high-resolution data tables at each time step, as shown in Table 7.2.

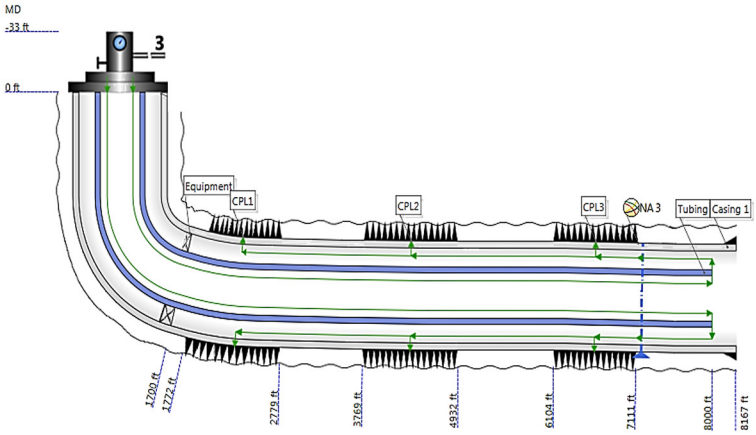

Figure 7.5. Well schematic showing completion details for pressure drop estimation.

Table 7.2 shows the data construction strategy for the wells. Data sets obtained are imported into MATLAB, and multivariate nonlinear regression is employed to generate polynomial proxy models. Here, we assume that all wells are connected to one principal pipeline without a need for routing constraints.

Table 7.2. Structure of data obtained for each well and pipeline from PIPESIM™ at each timestep.

P_{wh} (psia)	$Q_{well,oil}$ (STB/day)	$Q_{well,gas}$ (MSCF/day)	$Q_{well,water}$ (STB/day)
t_1 = 365 days			
50	✓	✓	✓
….	✓	✓	✓
2500	✓	✓	✓
t_2 = 730 days			
50	✓	✓	✓
….	✓	✓	✓
2500	✓	✓	✓
:	:	:	:
t_n = 2190 days	✓	✓	✓

This table is generated for all producer wells and injector wells in the field. Note that the injector wells contain only a single fluid – water. A similar strategy is used for the pipelines in which the wellhead pressure column in the table is replaced with the pipeline pressure drop.

7.5 Proxy Modelling and the Optimisation Framework

Proxy modelling is increasingly becoming applicable to highly complex processes such as a petroleum production system with many variables per system component. However, the requirements of a proxy model are usually high since it is desired that they capture highly nonlinear system behaviour embedded in a relatively low number of representative samples/original simulation runs (Zangl et al., 2006). The entire optimisation problem

can be divided into four elements: (a) subsurface flow dynamics, (b) wellbore flow dynamics, (c) surface flow pressure drops (d) economic considerations. Besides the economic considerations reflected in the objective function of the problem, numerous reservoir and multiphase flow simulations are required to capture the reservoir, well and surface dynamic behaviour. Running these complex and rigorous simulations within an optimisation routine is computationally expensive. This disadvantage can be overcome by developing robust proxy models (simplified response surface representations) of similar accuracy with the simulators. To circumvent the unnecessary complexity of coupling the interface of all simulators used in this work, it was necessary to generate high-resolution data tables for the proxy modelling phase before calling the optimisation algorithm. Up to 30 different wellhead pressures/surface injection pressures (for the producers and injectors, respectively) and 50 different liquid production rates (within practical and acceptable ranges) were used for the development of the proxy models, thus yielding a total of 3060 simulations for the different phases, at the respective time intervals.

The work of Yeten et al., (2005) showed comparable performance of quadratic polynomials (especially with cross terms) to other complex response surfaces (Kriging, splines and ANN) when space-filling design methodology is applied. They attributed this performance of quadratic polynomials to the fact that they are not data exact and are not severely affected by instantaneous local changes in erratic data compared to kriging and splines which tend to satisfy the local dramatic changes in the data. This motivated our choice of quadratic polynomials for the proxy model generation aspect of this work. In order to improve the accuracy of the parameter estimation procedure for the pipeline proxy models, a sub-optimisation problem is formulated using Genetic Algorithm for the error minimisation between simulator data and proxy model data using the regression results as initial guesses. The error function is given by Eq. 7.19, where APD represents the average percentage deviation, SD, the simulation data, and PD, the proxy model data. The structure of the proxy models used for the wells and pipelines are shown in Eqs. 7.26, 7.27 and 7.28, respectively: A summarised coupling methodology and the adopted simulation-based optimisation approach are shown in Figs. 7.6 - 7.7.

$$APD = \frac{|SD - PD|}{SD} \times 100 \tag{7.19}$$

7.5.1 Objective Function

$$\max(NPV) = \sum_{t=1}^{N_t} \left[\frac{TOP^t + TGP^t - (TWP^t + TWI^t)}{(1+b)^{\frac{t}{t_{ref}}}} \times \Delta t \right] \tag{7.20}$$

$$TOP^t = r_{op} \times \sum_{k=1}^{Nprod} q_{op,k,t} \tag{7.21}$$

$$TGP^t = r_{gp} \times \sum_{k=1}^{Nprod} q_{gp,k,t} \tag{7.22}$$

$$TWP^t = r_{wp} \times \sum_{k=1}^{Nprod} q_{wp,k,t} \tag{7.23}$$

$$TWI^t = r_{win} \times \sum_{i=1}^{Ninj} q_{win,i,t} \tag{7.24}$$

7.5.2 Optimisation Constraints

$$\sum_{k=1}^{Nprod} q_{gp} \leq C_{g,sep} \tag{7.25}$$

$$q_{p,k,t} = a_1 + a_2 P_{k,t}^w + a_3 (P_{k,t}^w)^2 \tag{7.26}$$

$$q_{p,i,t} = b_1 + b_2 P_{i,t}^w + b_3 (P_{i,t}^w)^2 \tag{7.27}$$

$$\begin{aligned} \Delta P_{l,t} = {} & c_1 + c_2 q_{lg,t} + c_3 q_{lo,t} + c_4 q_{lw,t} + c_5 (q_{lg,t})^2 + c_6 (q_{lo,t})^2 + c_7 (q_{lw,t})^2 \\ & + c_8 q_{lg,t} q_{lw,t} + c_9 q_{lg,t} q_{lo,t} + c_{10} q_{lo,t} q_{lw,t} \end{aligned} \tag{7.28}$$

$$P^s = P^m - P_{l,t} \tag{7.29}$$

$$P^m < P_k^w \tag{7.30}$$

$$P_{inj} < P_{frac} \tag{7.31}$$

$$\sum_{k=1}^{Nprod} q_{p,k,t} = q_{p,l,t} \tag{7.32}$$

$$\sum_{i=1}^{Ninj} q_{winj} \leq Q_{inj,tot} \tag{7.33}$$

We adopt the method proposed by Foss and co-workers (Gunnerud and Foss, 2010; Gunnerud et al., 2013) in which the production network is broken down into several black boxes and formulate explicit relations, rather than treating the entire network as a single black box. They argue that although proxy models are required for each section of the entire production network, configuring the optimiser to search using smaller simulators yields faster computations compared to searching over the entire production network.

The surrogate modelling approach adopted here also presents an excellent platform for the implementation of a gradient-based optimisation solver. The control variables include choke valve settings at the wellhead which ensure there is no material back flow, gas and water handling capacity constraints and pressure bounds on the pipelines. The algorithm aims to determine the optimum injection profile that maximises the oil production and the field revenue in terms of the NPV. Eqs. (7.26-7.27) represent the well flow rates for each phase as a function of the wellhead pressures. This was obtained by running a nodal analysis in PIPESIM™ at different wellhead pressures and subsequently developing a quadratic proxy model by regressing the data. Similarly, the nonlinear relationship between the pipeline pressure drop and the flow rates of the respective phases is obtained by running a sensitivity analysis in PIPESIM™ (P/T profile or system analysis) at different pipeline liquid flow rates. Eq. 7.32 is a mass balance constraint that ensures the well flows of the respective phases are routed to the pipeline between the manifold and the separator. It is also necessary to constrain the manifold pressure (Eq. 7.30), ensuring forward flow of all phases for the wells. The available water for injection in the field is limited to 10,000 STB/day (Eq. 7.33).

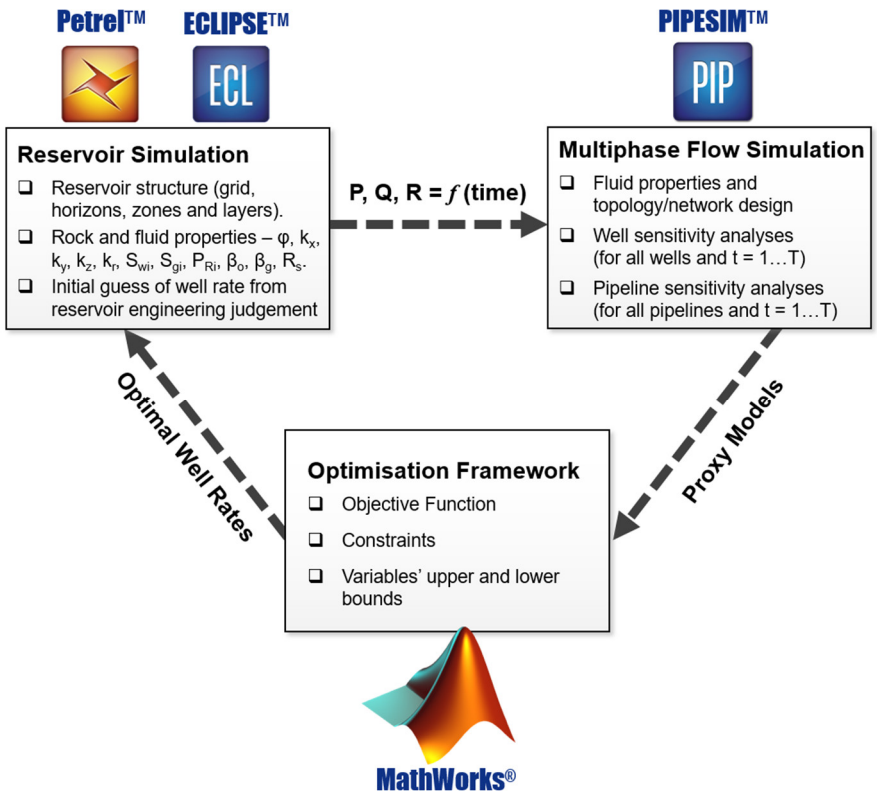

Figure 7.6. Coupling procedure. *P*, reservoir pressure, *Q*, flowrates and *R*, ratios (WC & GOR).

The results of the optimisation problem (NLP) are the optimal production and injection rates that satisfy all constraints and maximise the objective function. Based on the number of variables and the nonlinearities involved, and preliminary analysis carried out, it was discovered that the obtained results are dependent on the initial guesses. With the reasonable initial guesses obtained by applying reservoir simulation, we propose bounds to the decision variables, assume a uniform distribution between the upper and lower bounds of the respective variables and perturb the initial guesses 1000 times between the bounds; thus facilitating convergence to a global solution. We also compare the performance of the 'IPOPT' solver and MATLAB's '*fmincon*' for their robustness (number of iterations required and solution times). The optimisation procedure was carried out using the OPTI toolbox platform in MATLAB that interfaces with many high-quality optimisation codes. Through this toolbox, the Interior Point Optimiser (IPOPT solver) was called to solve the optimisation problem written in MATLAB. The default *fmincon* solver (with the interior point algorithm) in MATLAB was also implemented for comparison purposes.

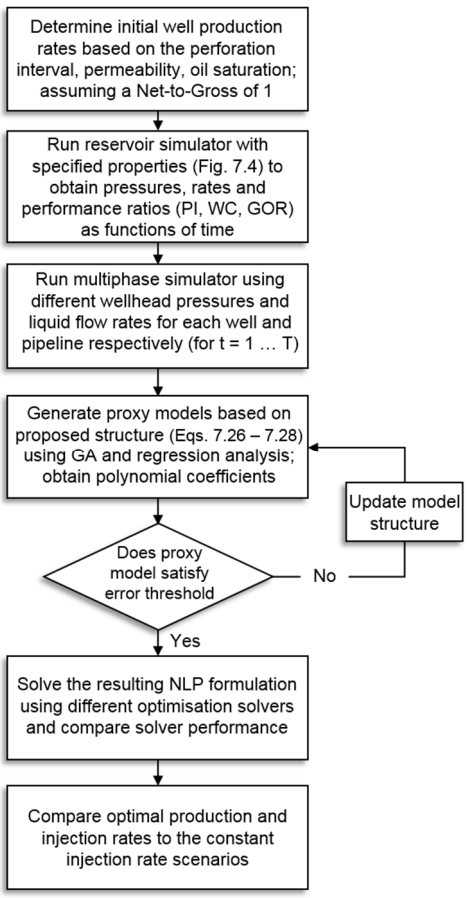

Figure 7.7. Summary of simulation and optimisation methodology.

The implementation of the interior point algorithm in MATLAB involves a solution of a sequence of approximate optimisation problems (equality-constrained problems) which are easier to solve than the original inequality-constrained problem. To solve the approximate problem, the algorithm attempts to take a direct step (Newton step) first, which if unsuccessful results in the application of a conjugate gradient step using a trust region. The IPOPT solver, on the other hand, implements an interior point line-search filter method; the interested reader is referred to the mathematical formulation of the algorithm documented in several publications (Watcher and Biegler, 2005; Watcher and Biegler, 2006, Nocedal et al., 2009). The solver implements a 2-phase algorithm which comprises of a main phase and a feasibility restoration phase. In the main phase, the classical infeasibility start method is used to simultaneously search for optimality and feasibility; whereas, the feasibility restoration phase seeks to minimise primal infeasibility.

This phase is only called when the main phase fails. The main drawback of the algorithm is the difficulty of detecting infeasibility; it often fails when the feasibility restoration phase is called too close to the optimal solution (Hinder & Ye, 2018). Although several modifications (Nocedal et al., 2014) to the algorithm have been made, such as the one-phase interior point method for non-convex optimisation (Hinder & Ye, 2018), the 2-phase algorithm was sufficient to solve the presented case studies to convergence within a reasonable time.

7.6 General Problem Description

7.6.1 Case Study 1 (CS1)

The petroleum field considered here (Figs. 7.8-7.10, Tables 7.3-7.4) is one undergoing secondary production with already located 3 producer wells and 1 injector well. The reservoir is primarily sandstone with established properties (absolute and relative permeability, porosity, compressibility, initial pressure and initial phase saturations). The produced fluids (light oil and gas and water) are modelled using a black oil simulator (ECLIPSE™, 2015). In solving this case study, we aim to answer the following questions: can we determine an optimal injection strategy/schedule for the field? Do we maintain a constant flooding/injection rate for the entire production horizon considered (6 years); or is there an optimal way of performing time-dependent water flooding in which injected water rate changes over the time horizon to yield maximum oil production and consequently field profitability?

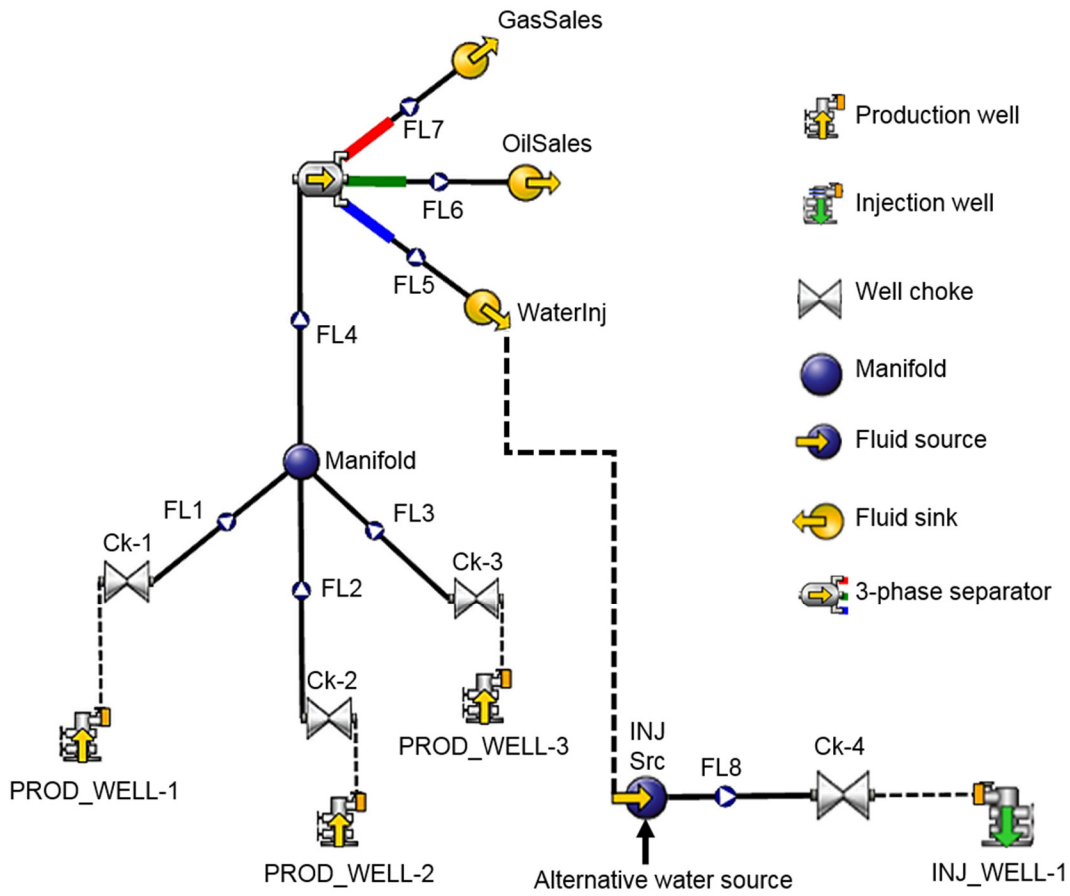

Figure 7.8. PIPESIM™ multiphase flow model for wellbores and pipelines (CS 1).

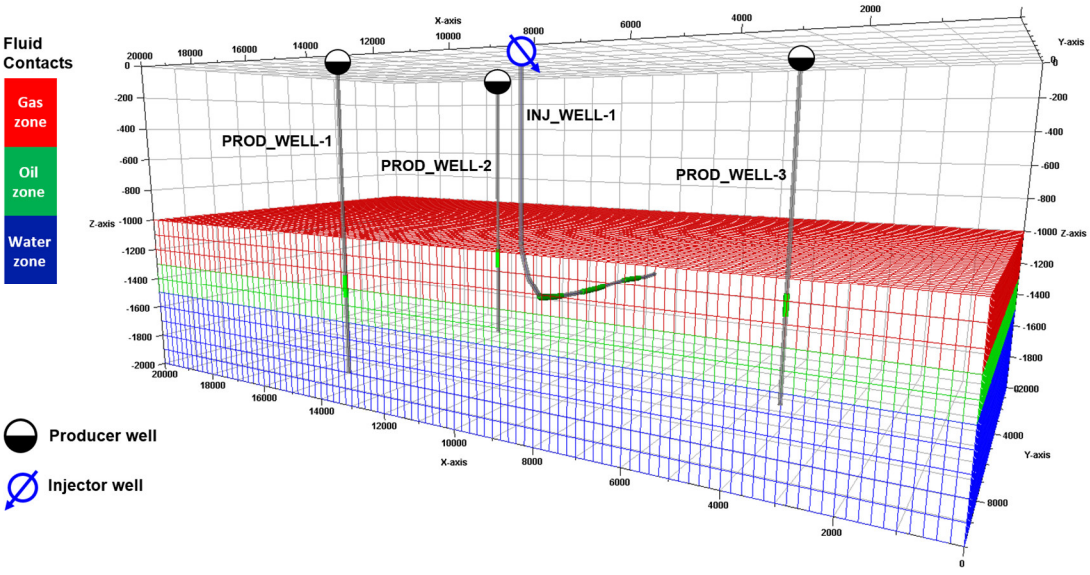

Figure 7.9. Reservoir structure showing the fluid regions, drilled and completed wells (CS 1).

Certainly, this is to be done with pivotal concentration on operational constraints such as the size of the surface facilities (separators), available treated water for injection daily, fracture pressure of the reservoir (formation fracture could occur when surface injection pressure supersedes reservoir pressure), wellbore performance hydraulics and operational running costs.

Table 7.3. Injection and production well properties (CS 1).

Well	Type	Surface position X (ft)	Surface Position Y (ft)	Perforation interval (ft)	
				Top	Bottom
INJ_WELL-1	Horizontal	9,067	8,774	1,772 3,769 6,104	2,779 4,932 7,111
PROD_WELL-1	Vertical	15,000	8,000	1,331	1,483
PROD_WELL-2	Vertical	14,286	1,891	1,322	1,471
PROD_WELL-3	Vertical	4,475	4,497	1,329	1,464

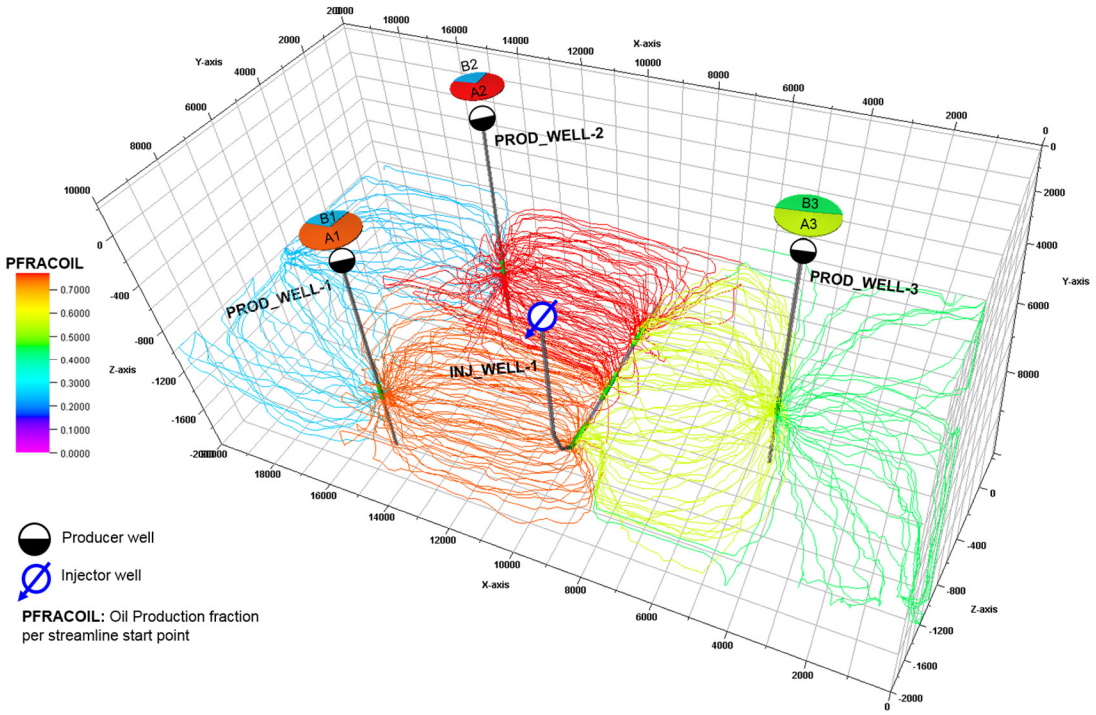

Figure 7.10. Oil production fraction per streamline start point after 365 days (CS 1).

The results of streamline simulation generally show good hydraulic injector-producer connection (Fig. 7.10). This is aided by the relatively simple geometry of the reservoir with no isolating fault blocks or other complicating boundaries. In case study 1, A1, A2 and A3 represent the contribution of the injector to the oil production in the 3 producing wells, respectively. PROD_WELL-2 experiences the highest pressure support and thus increased oil production due to injector action (red sector).

We particularly observe in Fig. 7.10 that, PROD_WELL-3 it is less impacted by the flooding process (illustrated by sector A3 in the pie-chart) compared to the other 2 wells (A1 & A2). B1, B2 and B3 represent production due to other means such as fluid expansion (i.e. as though the injector were absent). This phenomenon is due to the complexity of the underlying permeability distribution.

Table 7.4. Computational Summary (CS 1).

Property	**Value**
Number of producer wells	3
Number of injector wells	1
Number of pipelines	1 major pipeline
Number of objective functions	1
Number of time step discretisation (6-year horizon)	6
Number of constraints (nonlinear, linear, equality, inequality)	159
Total number of variables	114

7.6.2 Case Study 2 (CS2)

This case study (Figs. 7.11-7.13, Tables 7.5-7.6) involves 4 injection wells and 4 producing wells with some of the wells having deviated geometries. Case 2 maintains a similar concept, with the following modifications vs. case 1.

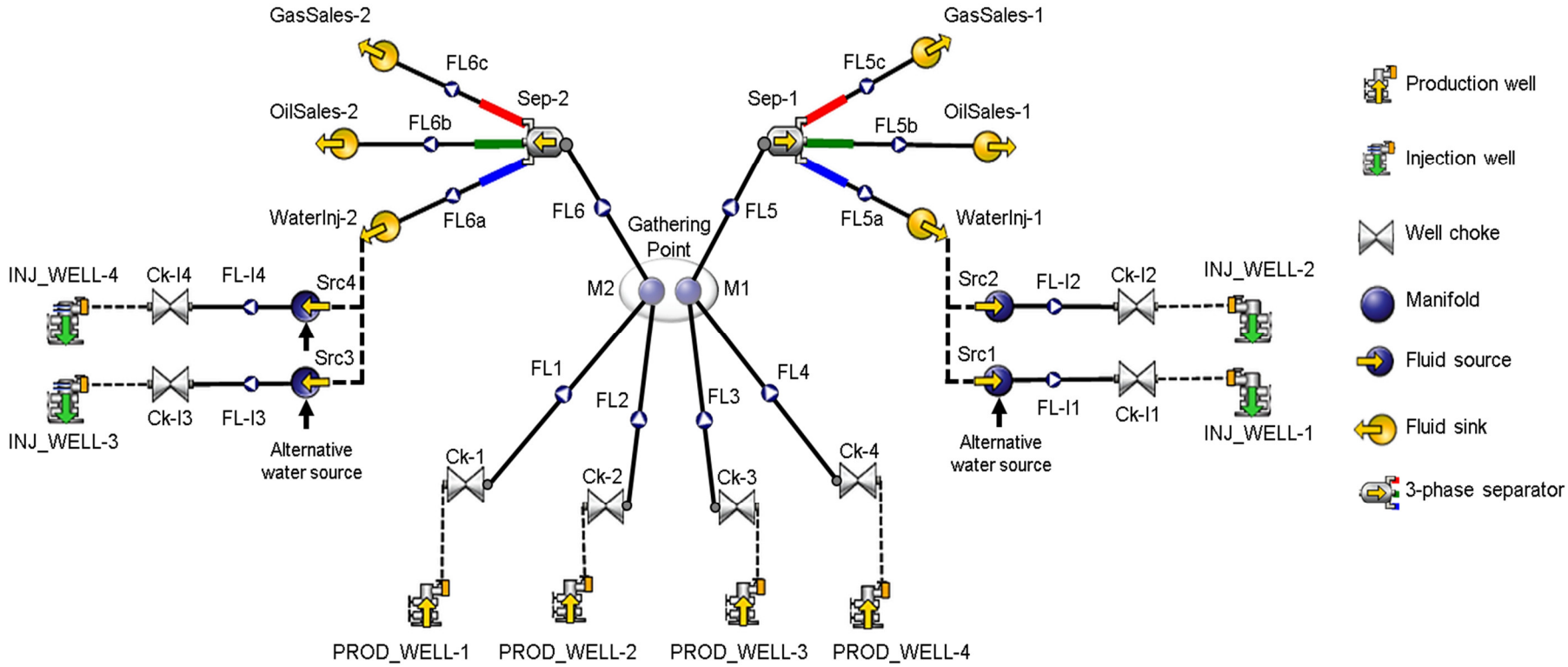

Figure 7.11. PIPESIM™ model for the pressure drop determination in wellbores and pipelines (CS 2). Flow splitting at the manifold is not modelled; the direction of fluid flow from the wellheads to the manifold is fixed in the optimisation formulation.

Besides the time-dependent allocation problem for a single injector well, another level of complexity arises when we want to know the optimal way to split the injection rates between the various injectors so that oil production is maximised based on the total available field water capacity. Streamline simulation and injector efficiency calculations are employed again.

The network here consists of 2 pipelines that route fluid production from the reservoir to the surface facilities (Fig. 7.11). We do not introduce routing constraints at this stage (which would lead to an MINLP) problem; instead, we assume that the 2 horizontal producer wells are connected to the first major pipeline (FL5), and the other 2 vertical wells are connected to the second major pipeline (FL6).

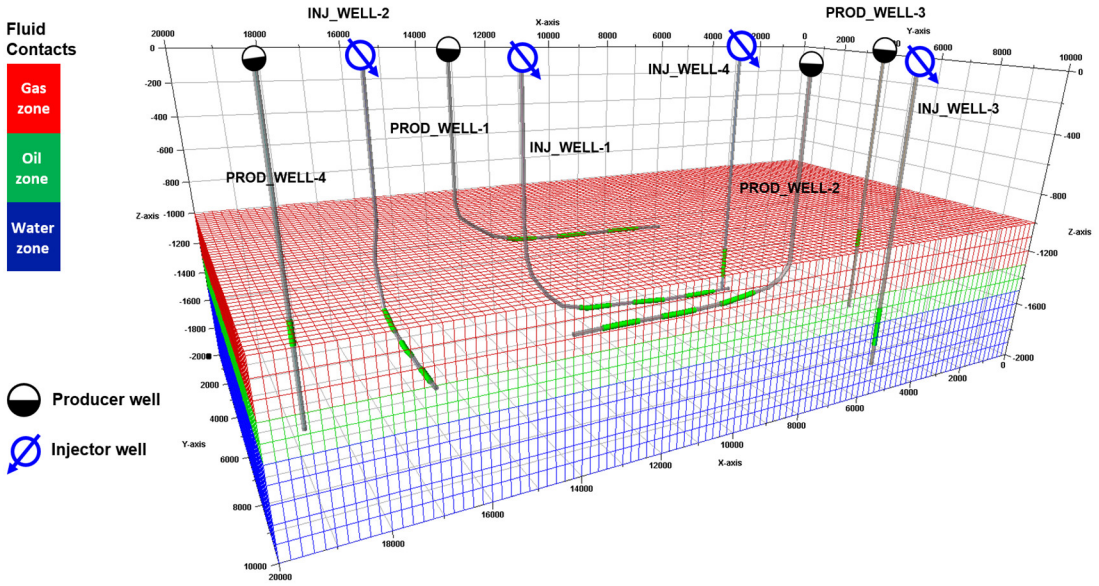

Figure 7.12. Reservoir structure showing fluid regions, drilled/completed wells (CS 2).

Field water injection commences at the start of the 3rd production year. At this time, the steady production period of the respective producer wells has ended, and a decline is already occurring. In case study 2 (b), the colour of the injector well labels corresponds to the colours of the respective sectors, which in turn represent the contribution of an injector to the oil flow rate delivered by a particular producer well. For example, water injection from INJ_WELL-2 contributes to the production rates of PROD_WELL-1 (B1) and PROD_WELL-2 (B2) and PROD_WELL-4, respectively. However, both horizontal producers, receive the greatest injection support from INJ_WELL-2; sectors C1 & C2, respectively.

Table 7.5. Injection and production well properties (CS 2).

Well	Type	Surface Position X (ft)	Surface Position Y (ft)	Perforation interval (ft)	
				Top	Bottom
INJ_WELL-1	Horizontal	12,957	4,788	2,813 4,494 6,287	3,766 5,520 7,303
INJ_WELL-2	Horizontal	16,090	2,681	1,884 3,354 4,940	2,774 4,168 5,591
INJ_WELL-3	Vertical	4,135	8,697	1,576	1,849
INJ_WELL-4	Vertical	4,168	1,678	1,620	1,870
PROD_WELL-1	Horizontal	13,543	1,300	2,620 4,257 6,017	3,529 5,219 7,118
PROD_WELL-2	Horizontal	7,098	8,138	2,328 4,106 5,679	3,345 5,046 6,634
PROD_WELL-3	Vertical	1,301	4,942	1,328	1,465
PROD_WELL-4	Vertical	18,737	5,324	1,323	1,472

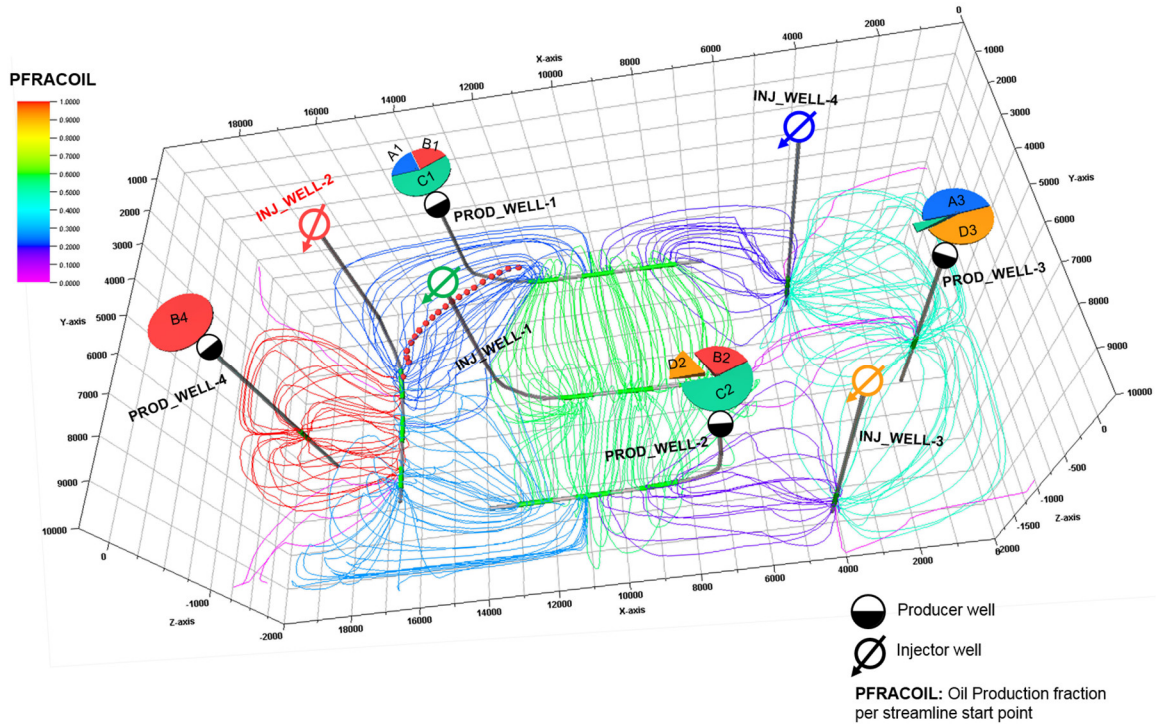

Figure 7.13. Oil production fraction per streamline start point after 365 days (CS 2).

Table 7.6. Computational Summary (CS 2).

Property	Value
Number of producer wells	4
Number of injector wells	4
Number of pipelines	2 major pipelines
Number of objective functions	1
Number of time step discretisation (6-year horizon)	6
Number of constraints (nonlinear, linear, equality, inequality)	252
Total number of variables	198

7.7 Optimisation Results

7.7.1 Optimal Injection Strategy (Case Study 1)

Initial averaged results obtained by running the reservoir simulator with injection rates (derived from streamline simulation) are shown in Figs. 7.14 and 7.15. Field performance ratios (gas-oil ratio and water cut) and the reservoir pressure are shown in Fig. 7.14c. The very high GOR values noticed in Fig. 7.14a is a reliable indicator of how light the oil is and its tendency to form hydrates. As expected, there is a consistent drop in the reservoir pressure with time but to a lesser extent compared to the decline obtainable with heavier oils. This is attributable to the simultaneous gas production and expansion, which provides some pressure support (solution gas drive) in the reservoir. The onset of water injection suppresses the GOR (as seen in its stabilisation, Fig. 7.14a) but conversely increases the field water cut (Fig 7.14b).

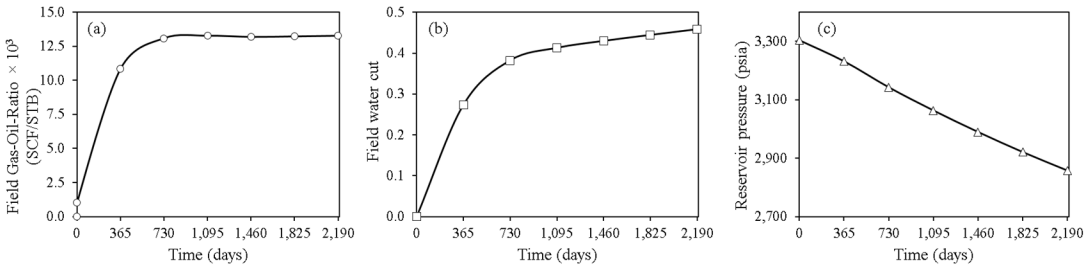

Figure 7.14. Dynamic reservoir pressure profile and performance ratios (water cut and GOR) – CS 1.

It is important to ascertain the time-dependent performance of each well in the field. The productivity index (Eq. 7.1) and injection efficiency are established methods of determining the performance of producer and injector wells, respectively.

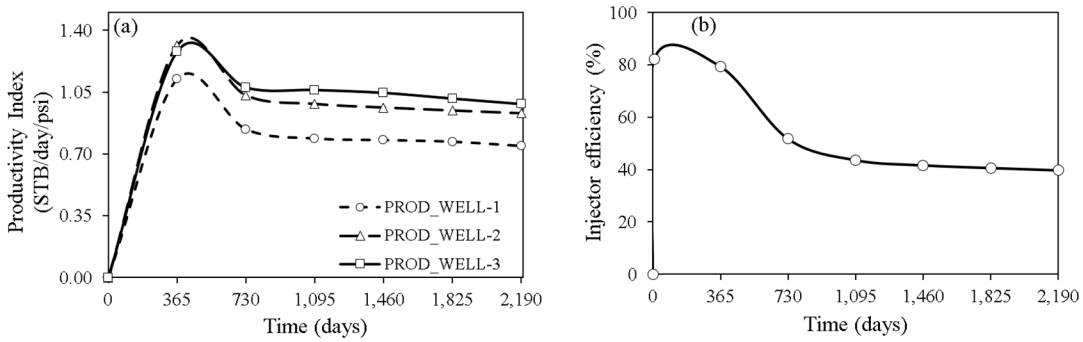

Figure 7.15. Production and injection well performance indicators (CS 1).

The rapid increase in the productivity index at the start of production occurs due to the high initial reservoir pressure and injection support. The drop in injection efficiency and reservoir pressure are also reflected in the productivity decline of the respective wells. PROD_WELL-3 is the best performing well; the porosity and permeability distribution around the well is the main factor influencing its performance compared to the other wells. It can also be observed that the injector efficiency computed from the well allocation factors reduces with time and enters a stabilisation zone from 1,095 days. This implies that there is a possibility to reduce this injection rate and yet obtain good performance. By exploiting the reservoir's properties, it is possible to find the optimal injection strategy that utilises the least amount of injected water, while maintaining/increasing oil production. The oil, water and gas production profiles and the cumulative production for the respective production wells are shown in Fig. 7.16. It can be observed that the algorithm was able to determine the oil and gas production decline with time for all wells, with PROD_WELL-3 performing best as reflected in the PI. The sharp increase in water production noticed in Fig. 7.14b occurs when the injector performance is at its best (Fig. 7.15b); the minimal change in injection efficiency (after 730 days) is captured by the algorithm as reflected in the near-stable water production rates (Fig. 7.16b) after the sharp increase, particularly for PROD_WELL-3 and PROD_WELL-2. We also present a second scenario in which the injection profile is kept constant (at 10,000 STB/day), and the production performance of the wells alone is optimised. It is worth mentioning that beyond this rate, there is only a marginal increase in oil production as determined from reservoir simulation. The production profiles are compared to the scenario in which an optimal injection strategy s sought.

The production profiles are compared to the first case in which an optimal injection strategy is sought. We observe that for PROD_WELL-1 and PROD_WELL-2, the oil

and gas production rates for the constant injection rates are slightly higher than the optimal injection scenario (Fig. 7.17a). However, the optimiser has taken advantage of the productivity of PROD_WELL-3 to enhance the final NPV (Fig. 7.17a). It is important to mention that this occurs at the expense of the water production rate of PROD_WELL-3 (Fig. 7.17b).

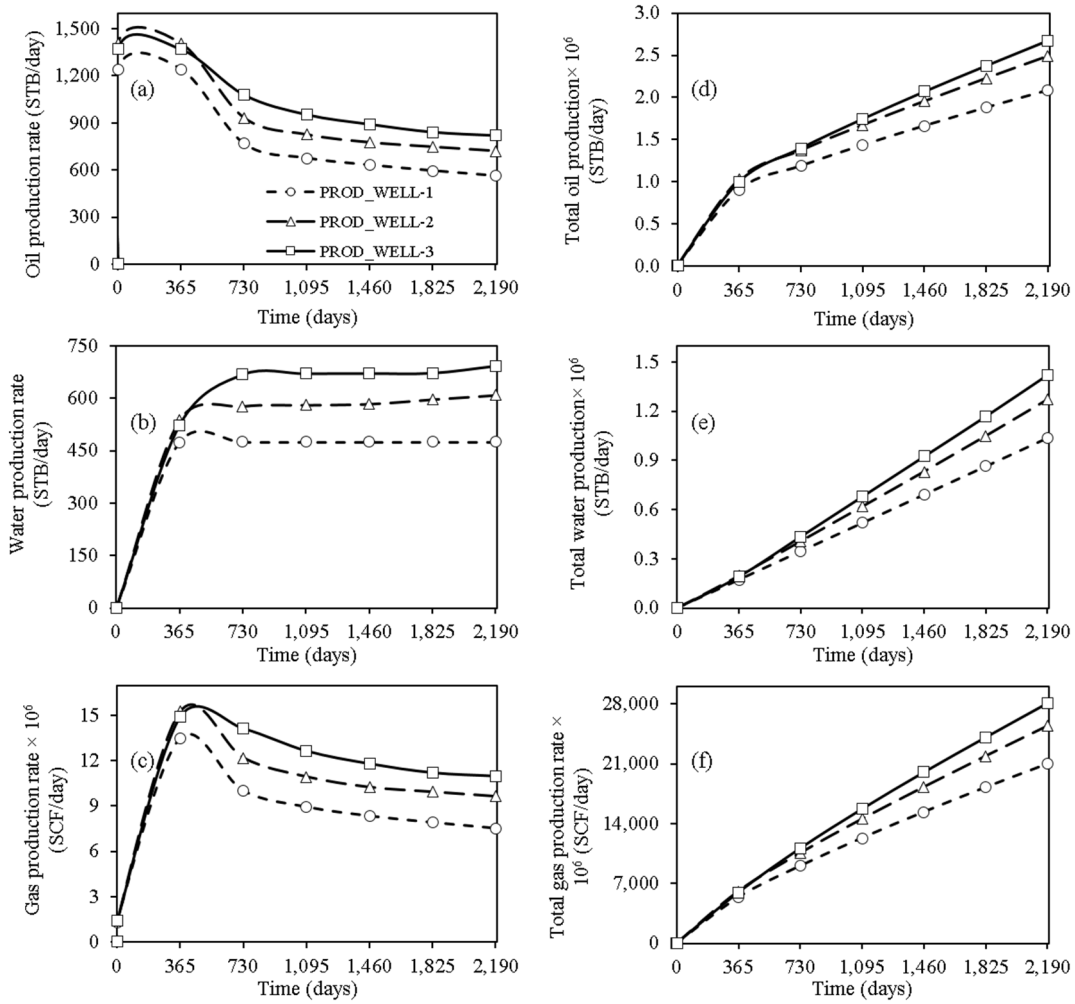

Figure 7.16. Optimal oil, water and gas flowrates from the production wells (CS 1).

There is a considerable difference in the water production rates between the optimal and constant injection cases for PROD_WELL-1, PROD_WELL-2 and PROD_WELL-3, respectively (Fig. 7.17b). We attribute this to the permeability distribution and the distance between the respective production wells and the injection well; these factors greatly influence the water breakthrough time. Fig. 7.18 shows the optimal injection strategy as determined by the implemented optimisation framework. At the beginning of production, it can be observed that the optimal injection strategy shows a continuous increase in the

injection rate and subsequently, a decreased injection rate. It can be deduced that a 30% decrease in the total injected water across the time horizon considered still yields a 1% higher profitability (Fig. 7.19). Calculated voidage replacement ratios (VRR) are between 0.2 and 0.4 for both case scenarios. The VRR is simply the ratio of injected fluid to the reservoir barrels of the produced fluid. It determines whether the reservoir pressure is maintained (VRR=1), increased (VRR>1) or experiences a decline (VRR<1) at a particular point in time.

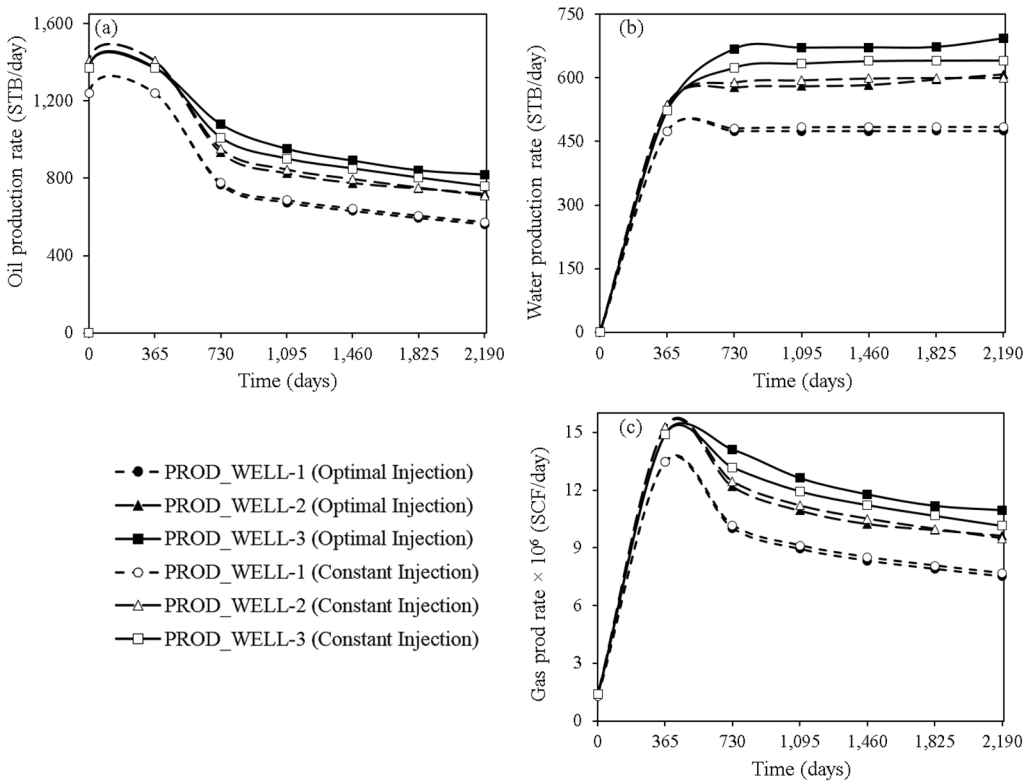

Figure 7.17. Comparison of the rate profiles for the constant and optimised injection scenarios (CS 1).

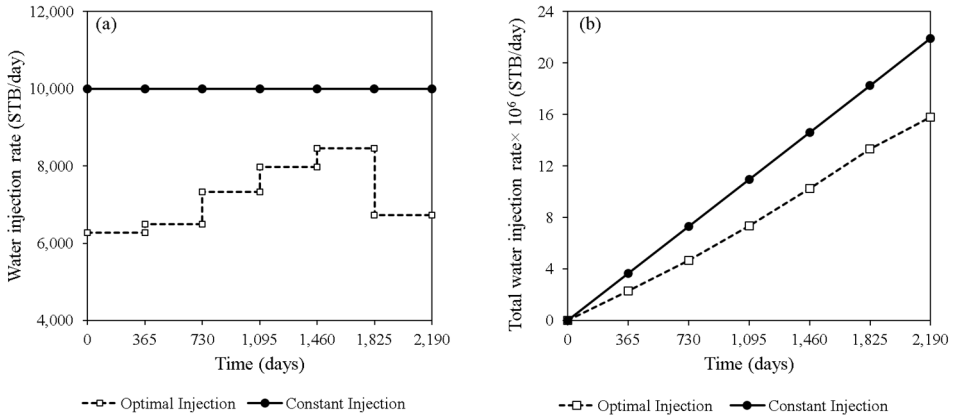

Figure 7.18. Optimal injection strategy and cumulative injection rates (CS 1).

The obtained results thus indicate that the reservoir pressure is declining despite the injection of water to the reservoir; more injection wells need to be drilled in order to maintain the reservoir pressure. It also indicates that the obtained production rates are not only due to the injected water volume but also fluid expansion within the reservoir. Also worth mentioning is the fact that the optimisation framework adopted here does not only seek to improve the water injection strategy but also the production strategy.

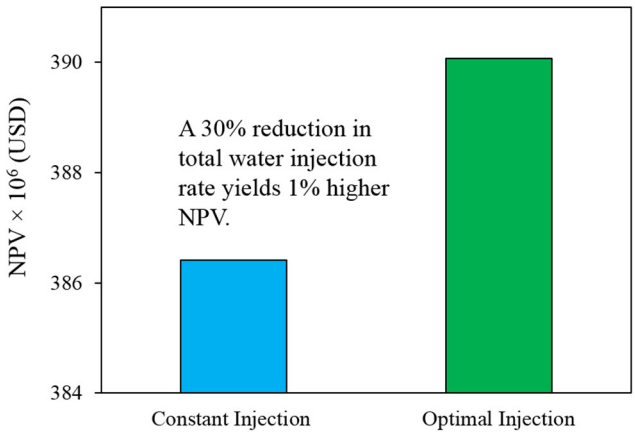

Figure 7.19. NPV analysis for both scenarios (CS 1).

Based on the supplied objective function, the algorithm determines if much attention is given to the injection component of the system or the production component while ensuring all constraints are satisfied and the NPV maximised.

7.7.2 Optimal Injection Strategy (Case Study 2)

Fig. 7.20 shows in more detail (compared to Fig. 7.14) the water cut, GOR and pressure decline for the production wells in the field. The effect of water injection is reflected in the sharp decrease in the GOR, which can be attributed to reduced gas saturation and increased water mobility in the reservoir. The GOR for wells, however, picks up over time except that of PROD_WELL-3, which is the least affected by the water injection process (Fig. 7.20a). This behaviour can be further understood by examining the water cut profile. Besides having the earliest breakthrough time, the relative increment in the water cut at the start of water injection supersedes other wells. PROD_WELL-1 and PROD_WELL-2 have very similar performance ratios. It is also shown in Fig. 7.20b that the water production in these wells does not commence until the 365th day of production. This further indicates that they have been strategically positioned to reduce the adverse effects of possible water coning and early water breakthrough.

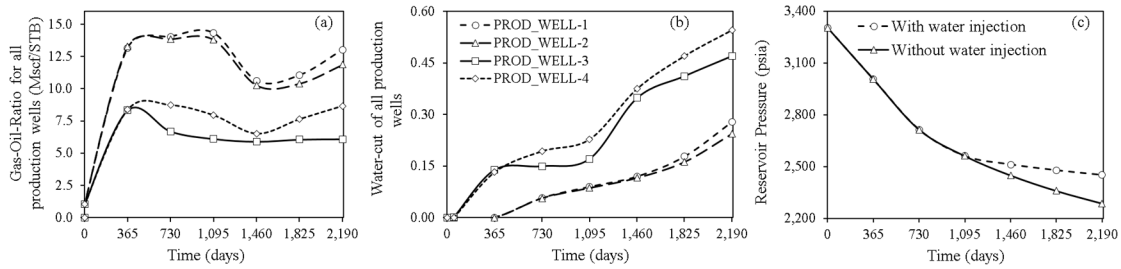

Figure 7.20. Dynamic reservoir pressure profile and performance ratios (water cut and GOR) (CS 2).

In order to demonstrate the extent of pressure support in the field, a plot of the reservoir pressure with and without water injection is shown in Fig. 7.20c. It is clearly demonstrated that the rate of pressure decline is faster when water injection is neglected. Without increased production time, this could reduce further below the bubble point, thus triggering increased gas production.

The productivity indices and injector efficiencies of the production and injection wells are shown in Fig. 7.21b. We observe that PROD_WELL-1 slightly outperforms PROD_WELL-2; their equidistant locations from the INJ_WELL-1 and similarity in the permeability distribution around them implies they experience similar levels of contribution from the injection well (Fig. 7.13). Also observed, is the reduced productivity of the vertical wells (PROD_WELL-3 and PROD_WELL-4) compared to the horizontal wells (PROD_WELL-1 and PROD_WELL-2).

This is inevitably due to the higher drainage area, which the horizontal wells are exposed to in the reservoir (Fig. 7.21a). The considerable disparity observed in the well productivity profiles is not the case with the streamline-derived injection efficiencies (Fig. 7.21b). Despite the favourable well geometry of INJ_WELL-2 (horizontal) compared to INJ_WELL-4 (vertical), they both exhibit similar efficiencies. The interaction of INJ_WELL-1 with the horizontal producers is the main factor contributing to its relatively higher efficiencies, as indicated by the well allocation factors obtained from streamline simulation (Fig. 7.21b). With the daily available field water injection rate of 75,000 STB/day, it was possible to propose initial injection rates to the optimisation algorithm.

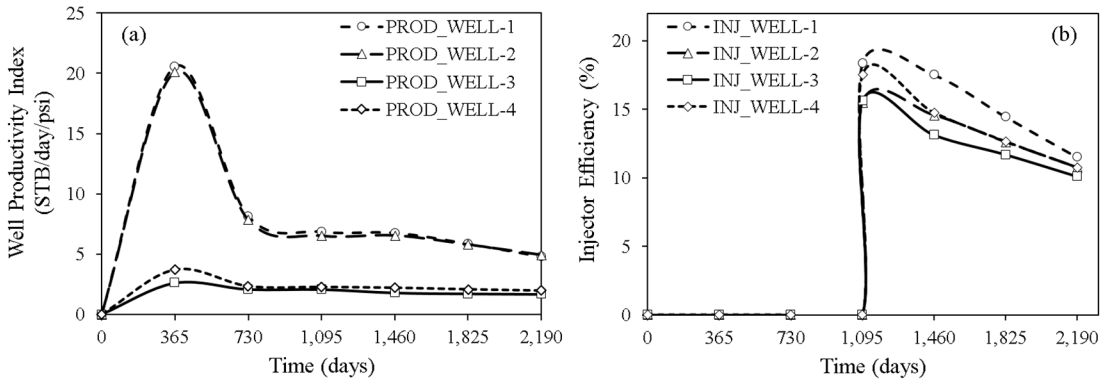

Figure 7.21. Production and injection well performance indicators (CS 2).

The production rate profiles for the oil, gas and water phase of the respective production wells are presented in Fig. 7.22. Based on the production data supplied and the proxy modelling techniques adopted, the algorithm captures the increment in oil production at the start of injection and the reduction in the decline rate (Fig. 7.22a). The water production rates observed are well representative of the water cut profiles obtained from the reservoir simulator in Fig. 7.20b, with the 2 horizontal producers, yielding lower water production rates compared to the vertical producers. Just like the oil production rate profile, the gas production rates of the respective wells also shows an increment in production due to water injection, and this is more significant for the horizontal wells.

In the second scenario, in which the injection rate is maintained at the maximum allowable rate for each injection well, we observe that the superior performance of the horizontal wells has been exploited by the optimisation algorithm for the improvement in the total production (Fig. 7.23b). This was similarly observed in case study 1, in which PROD_WELL-3 had the highest contribution to the difference in NPV noticed for the 2 scenarios. For the other vertical producers, there is no difference between the observed production rates for the optimal and constant injection scenarios. The optimal injection strategy and the corresponding cumulative injection rate for each well are shown in Fig. 7.24. It is illustrated that a stepwise increase in the injection rate for INJ_WELL-1 and a constant injection rate for the rest of the wells is guaranteed is increase the NPV of the field by 6% (Fig. 7.25) and also reduce the total water consumption by 11%.

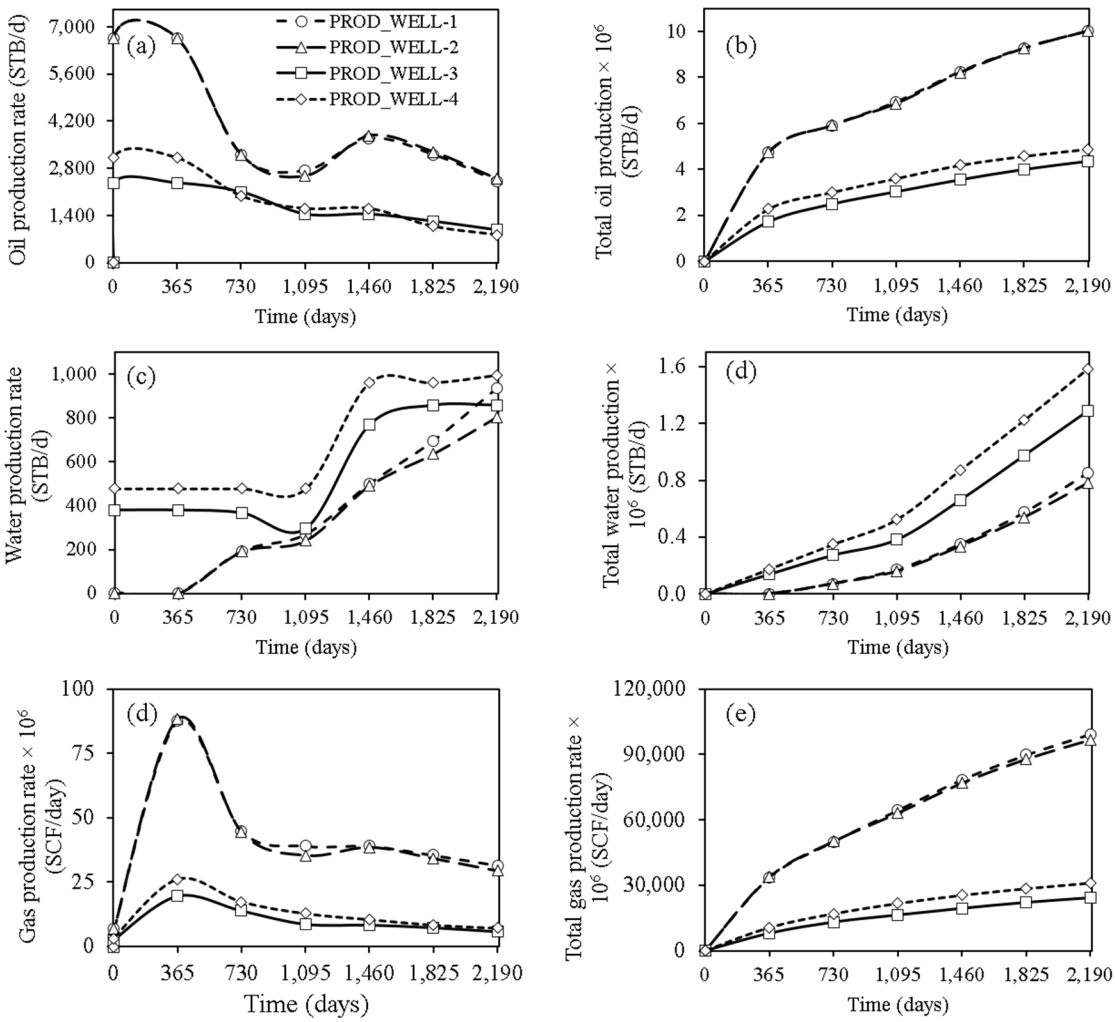

Figure 7.22. Optimal oil, water and gas flowrates from the production wells (CS 2).

The drilling of 1 new producer well and 3 more injector wells in case study 2, resulted in the increase of the VRR to a range of 0.25 – 0.50 for the optimal and constant injection scenarios. As explained in case study 1, more recovery mechanisms are activated when VRR<1 compared to a VRR of 1. Complementing the water injection process with some other production enhancement mechanism may lead to increased oil production. Although more water can be injected to increase the VRR considerably, the field engineer must ensure that this is not at the expense of the field water cut, which if too high could create a new set of operational problems.

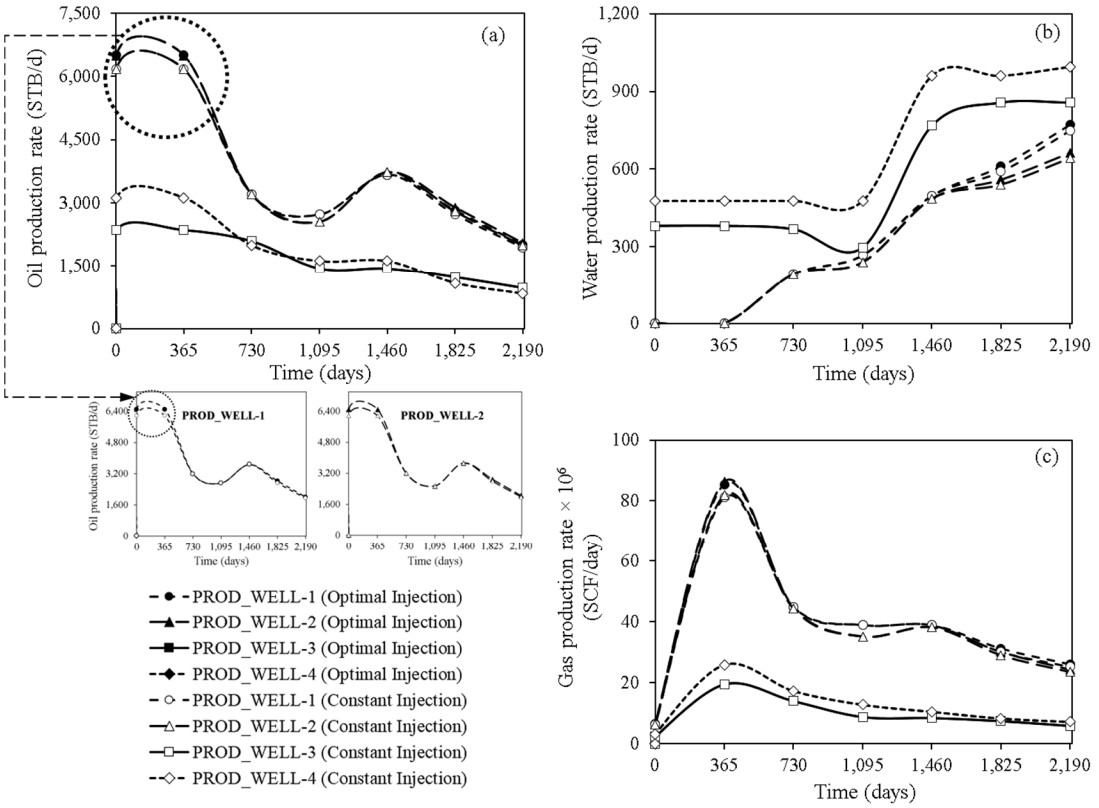

Figure 7.23. Comparison of rate profiles for the constant and optimised injection scenarios (CS 2).

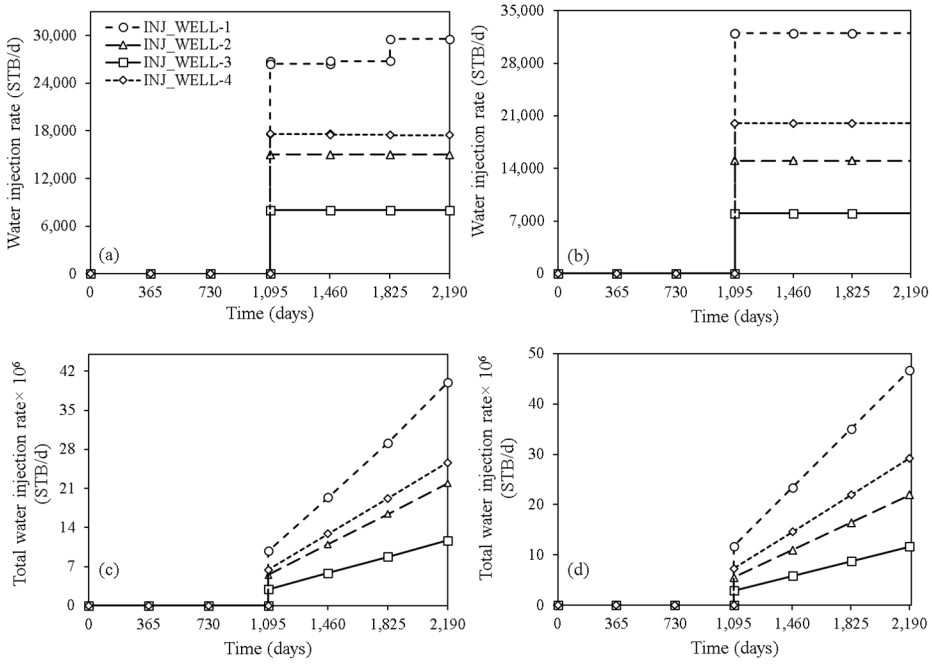

Figure 7.24. Injection rates for optimal (a and c) and constant injection scenarios (b and d) – (CS 2).

7.8 Solver Performance and Scaling

Different types of algorithms have been implemented on a wide variety of production optimisation problems, and this is dependent on the characteristics of the objective function and constraints. Local searching methods equipped with quadratic proxy models and many reasonable initial guesses are able to exploit smooth features of the objective function and converge rapidly to a global optimum. Majority of the computational effort involved in solving problems with discrete variables can be attributed to the piecewise linearisation procedure and the number of breakpoints required to capture nonlinearities in well and pipeline models (Foss and Gunnerud, 2010). The absence of these variable types in our case studies grossly reduces the computational effort as reflected in Table 7.7 compared to the MILP/MINLP studies. Although the proposed optimisation formulation is not guaranteed to find a globally optimal solution, a useful, feasible solution is found within a very short duration; this demonstrates its applicability as a viable tool during oilfield planning and operation.

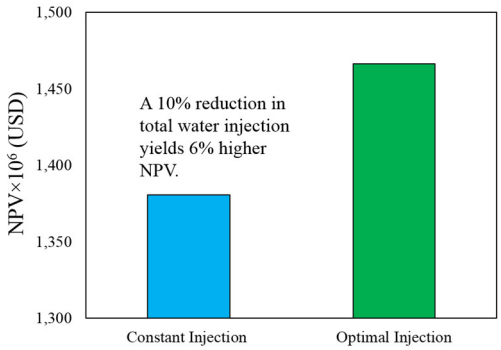

Figure 7.25. NPV analysis for both scenarios (CS 2).

Short solution times observed (Table 7.7) can be attributed to a reduced simulator search time in the respective component simulators. This is obtained without the parallelisation of the different component simulators or the optimisation algorithm adopted. This facilitates the real-time application of the proposed method for supporting operational decisions. The parallelisation adopted here was to assign the computations of the optimisation algorithm for the 1000 initial guesses to the different processing cores of the computer used. With the implemented parallel computing procedure and the convergence speed for each set of initial guesses, running the algorithm several times proved fruitful. The average variation across all initial starting points was 5%; although some occasional convergence difficulties were observed for some sets of initial guesses applied; these were

discarded. Thus, this demonstrates the robustness of the formulation. It is also possible to attribute this value to the efforts put in place via sophisticated reservoir simulation to ensure that the perturbation of the initial guesses was between operationally feasible bounds. It should be noted that with an increase in problem size (production system components), comes a rapid increase in the number of variables and thus an increase in the solution times. The structural breakdown of the network also implies, more proxy model evaluations at the different periods would be necessary. Generally, considerable presolving effort is required for the multiperiod proxy model generation; the time for data generation and coefficient determination based on the proxy model structure is not reflected in Table 7.7.

Furthermore, an essential aspect of the multiperiod proxy modelling technique adopted here is the fact that abrupt changes in multiphase flow behaviour can be easily incorporated. However, we avoid these sudden changes in pipeline conditions by ensuring that the operating pressure and temperature in the pipeline are outside the hydrate formation region. If such conditions exist, it is possible to have discontinuities in the pressure-rate response of the pipeline. This, in turn, affects the accuracy of the relatively straight forward quadratic polynomial proxy model and also the accuracy and applicability of the optimisation results. In cases where such abrupt flow regime changes cannot be avoided, cubic spline interpolation may serve as a more sophisticated tool for capturing the nonlinearities.

Although we have assumed a 1-year interval update in our case studies, this is specific to the nature of the dynamic reservoir behaviour. It is expected that a more frequent update of the reservoir properties in the optimisation formulation yields more accurate results; however, we have chosen this time frame in such a way that the overall reservoir properties' dynamic trend is still observed and taken into consideration (via time averaging analysis for the PI, WC and GOR respectively). This was possible because of the relatively simple geometry of the reservoir and the permeability distribution. It is thus worth noting that a satisfactory trade-off has to be made between the model formulation time (by applying smaller time discretisation) and its quality/accuracy. Although the application of GA yielded only a marginal improvement in proxy model accuracy attained via least squares regression, mean errors obtained by comparing simulator data and proxy model data were less than 2%. Ensuring that simulation results are history-matched to real field

data is an important step but can only be done if data is available. Although no field data were used in this case study, synthetic data adopted are well representative of practical conditions obtainable during field operations.

The disparity in the magnitude of the different variables has to be reduced by adopting systematic scaling methods to ensure excellent performance of the optimisation solvers. This is because convergence tolerances and other stopping criteria in an unscaled NLP problem may cause convergence difficulties. Thus, we mainly ensured that each constraint (especially constraints involving the gas flow rates) is well-conditioned with respect to perturbations of other variables.

Table 7.7. Solver performance analysis.

	Case Study 1		**Case Study 2**	
Solver	**Average solution time (sec)**	**Average number of iterations**	**Average solution time (sec)**	**Average number of iterations**
IPOPT	21	600	133	2600
MATLAB fmincon	>50	>1000	772	> 4000

Reported data is for a single set of initial guesses for both the optimised and constant injection rates.

A comparison of the solvers' performance is shown in Table 7.7 and Fig. 7.26. In case study 1, it is observed that the IPOPT solver converges to a higher NPV than the MATLAB's *fmincon* solver. Although similar production profiles were obtained using the MATLAB *fmincon* solver, they are not presented here because *fmincon* failed to satisfy all constraints within the acceptable tolerance.

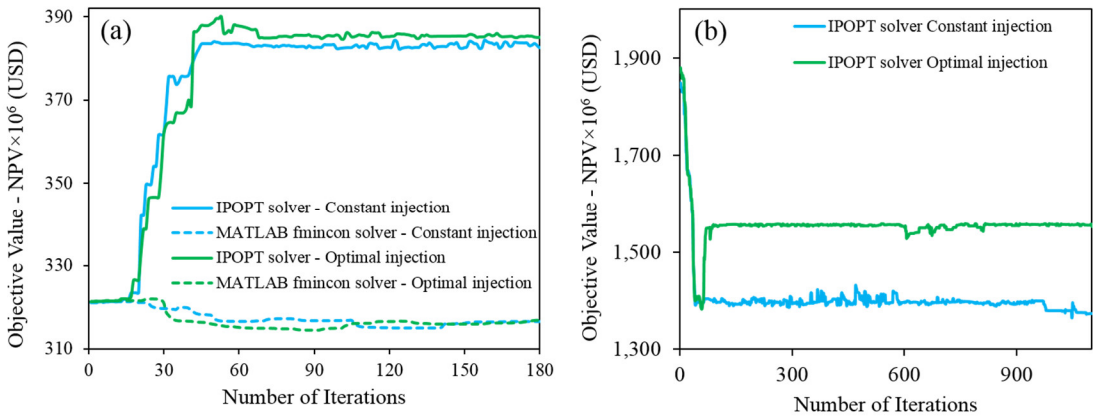

Figure 7.26. Solver performance for constant and optimised injection scenarios (CS 1: a, CS 2: b).

Furthermore, in case study 2, the MATLAB fmincon solver was unable to yield satisfactory results that met the convergence criteria; hence its function evaluation history is also not presented. It is also worth mentioning that the highest NPV from the 1,000 initial guesses supplied and the corresponding parameters for that NPV value were chosen as the optimal parameter set.

7.9 Chapter Conclusions

In this work, we have simultaneously addressed a production and injection optimisation problem with an economic objective function in terms of the Net Present Value (NPV) subject to practical constraints that ensure operational feasibility. Also demonstrated in this chapter is the multifaceted nature of a petroleum production system that allows its components to be treated independently; however, with an objective function that integratedly captures individual component characteristics. Based on the computations performed, we derive the following conclusions:

- The application of streamline-based well allocation factors and injector efficiency is a reliable method of obtaining good initial guesses for the time-dependent injection rates. Furthermore, the sensitivity of the optimiser to the supplied initial guesses can be reduced by perturbing sound initial guesses within reasonable bounds; thus yielding a near-global solution.
- High-resolution data tables obtained via numerous simulation runs and quadratic proxy modelling are very useful tools for approximating nonlinear system behaviour, providing an excellent platform for the application of gradient-based optimisation methods.
- Although it is usually expected that an increased water injection rate yields a higher oil sweep efficiency, the underlying permeability distribution and other reservoir properties could complicate this expectation. The developed optimisation framework has shown that a systematic variation of the injection rates, wellhead pressures and production rates yields increased field profitability. In our considered case study -1, a slightly improved NPV (1%) is achievable with an optimal injection strategy which decreases field water consumption by 30%. Implementing a similar strategy on the second case study yields 6% improvement in the NPV and a corresponding 11% decrease in the total field water consumption.

- The IPOPT solver showed superior performance to the MATLAB fmincon solver as far as the number of iterations and simulation time are concerned in our case study. The fmincon solver performance worsened with increased problem size and complexity. However, considering the limitations of the two-phase IPOPT algorithm, in which the feasibility restoration phase may fail when called, algorithmic modifications such as the one phase interior point method by Hinder and Ye (2018) can also be pursued in future work. The work herein coincides with software developments, which foster interoperability between proprietary system simulation suites and open-source optimisation solvers, paving the way for new advances

The water flooding optimisation approach (Thiele & Batycky, 2006) is a heuristic reservoir engineering-driven method that does not guarantee optimality. Nevertheless, the simulation-based optimisation approach suggested in this work is an improvement in the state of the art, integrating the concepts reservoir, streamline and surface facility simulation to ensure a more robust and optimal operating strategy. A performance comparison between the method presented in this chapter and this heuristic method constitutes future research efforts.

Chapter 8 Mixed-Integer Nonlinear Programming for Production Optimisation of Naturally Flowing and Artificial Lift Wells with Complex Routing Constraints

Real-time decision making by production engineers in a petroleum field can be very challenging, especially when multiple wells with diverse operating conditions and production behaviours are present (Fig. 8.1). Hence, semi-analytic or heuristic procedures are unlikely to yield an optimal operating strategy. High-fidelity simulators employed in the petroleum industry can be very complex due to size, the type of physical phenomena modelled and accompanying model uncertainty; thus, yielding significant computational time (Epelle and Gerogiorgis, 2018b; c).

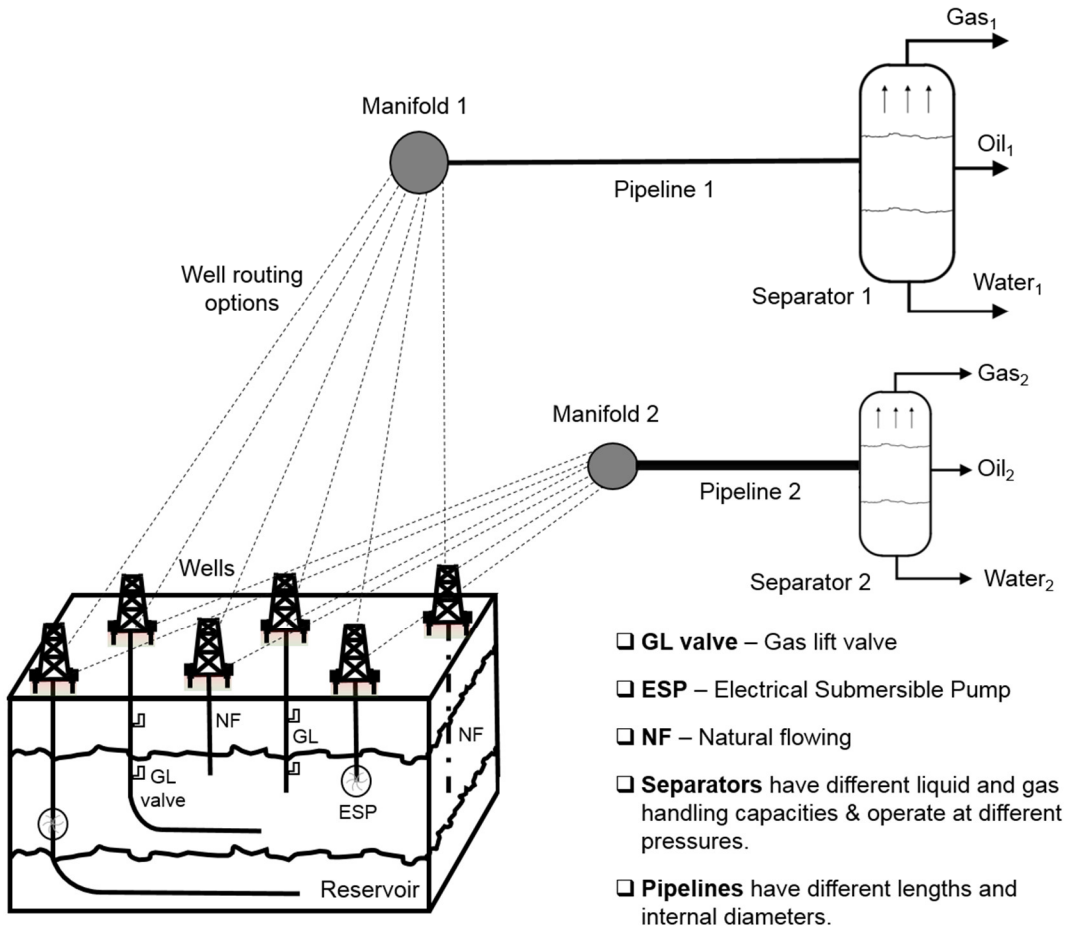

Figure 8.1. Petroleum production network structure and critical elements.

In this chapter, it is demonstrated that an independent application of network simulation of an operating field does not yield the best possible improvement in oil production.

Rather, a methodical application of simulation-based optimisation methods guarantees process enhancement. This is achieved by developing explicit surrogate models (reduced-order models obtained by querying a black box production network simulator multiple times using different inputs) in combination with well-routing constraints which are compatible with the adopted optimisation algorithms; thus resulting in an MINLP formulation. A Real-Time Production Optimisation (RTPO) approach to maximising production from naturally flowing, gas-lifted and Electrical Submersible Pump (ESP)-assisted wells while satisfying multiple operational constraints is presented herein. Also exploited in this work is the inherent decomposable property of the production network, into smaller components (wells, valves pipelines and separators), such that mass balance equations comprise the algebraic constraints of the optimisation framework. The adopted formulation also offers the advantage of flexibility for problem adjustment under different practical operating scenarios which are presented as case studies.

8.1 Methodology: Design and Simulation Considerations

The proposed methodology is presented in two parts. The first part outlines the modelling and design considerations when creating the surface network and its components; the second explains the detailed problem formulation for which mathematical optimisation is applied. A real-time optimisation scenario is considered here; thus, a detailed reservoir model which captures the slow-paced dynamic reservoir behaviour, fluid properties, and production pressures and rates is not necessary.

8.1.1 Naturally Flowing (NF) Wells

Standard design procedures (casing, tubing and perforation design) are adopted in modelling the behaviour of naturally flowing wells in a multiphase flow simulator (PIPESIM™ v2017.2). Robust multiphase flow correlations are employed for the pressure drop determination in the well tubing (Vertical Lift Performance curves–VLP); based on the well geometry and completion properties. Inflow Performance Relationships (IPR) are generated and coupled with the VLPs to obtain the wells' operating points in the multiphase flow simulator. These curves principally relate the multiphase flow rates in the wellbore to the bottomhole pressure and wellhead pressures. In order to obtain the pressure-rate response of a well, a nodal analysis (Fig. 8.2a) is run at different wellhead pressures. The obtained results can be approximated as algebraic functions, which constitutes the constraints of the optimisation formulation. A similar procedure is

adopted for the GL and ESP wells, but with extra nodal parameters such as the injection gas rate and the pump frequency. A detailed description of modelling considerations for the artificially lifted wells is presented next.

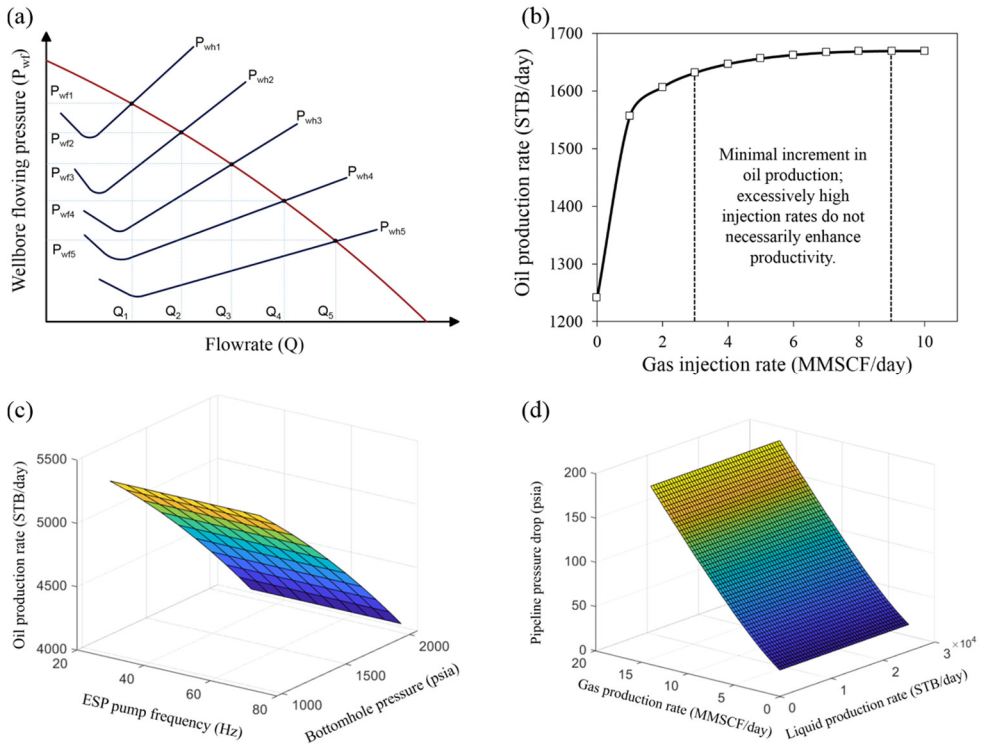

Figure 8.2. Typical nodal analysis (a) and gas lift optimisation curves (b); proxy model plots for an ESP well (c) and a pipeline (d).

8.1.2 Gas Lift (GL) Wells

In continuous gas lift (adopted here), a certain amount of gas at high pressure is introduced to aerate the fluid column (the tubing) so that the fluids readily flow to the surface (due to lower hydrostatic pressure). In order to perform this operation efficiently, it is often desired that injection is done via a single valve at the deepest possible point (this depends on the available surface injection pressure). In designing the gas lift system in the wellbore simulator, it was necessary to ensure that this single point injection scenario (Mukherjee and Economides, 1991; Gerogiorgis et al., 2006; Gerogiorgis and Pistikopoulos, 2008; Guo, 2011; Epelle and Gerogiorgis, 2019a; b). Based on various lift gas availabilities, a production system analysis is necessary to ascertain well operating points using the bottom hole as the principal node of analysis. In performing this analysis, it was important to determine the injection rate that was sufficient to enable liquid production and avoid excessive injection, which prevents liquid flow due to pipe friction

produced by the gas. Furthermore, excessive gas injection can significantly increase the gas capacity-handling requirement with minimal increment in oil production (Fig. 8.2b).

For a field-scale evaluation, the optimisation framework is designed to determine the optimal lift gas allocation to the respective wells based on their productivities and the total available gas for injection. Liquid fall-back during the unloading process of gas lift operations (especially during intermittent gas lift) induces a back pressure effect on the formation (Guo, 2011). This could cause erratic rates and also affect flow rates of other wells close by (well flow interdependence); this could be detrimental to the flowline shared by these wells. The continuous gas lift operation adopted here significantly minimises this effect. Since the wells are connected to downstream separators operating at a specified pressure, any possible pressure fluctuations will be more pronounced in the wellbore than in the pipeline network (Kritsadativud et al., 2015). Furthermore, the short term horizon considered here implies that the reservoir and fluid properties do not vary significantly. Thus, back pressure effects at the surface pipeline can be considered negligible. However, the pressure drop along flowlines (between junctions J-i and manifolds M-i in Fig. 8.4) is assumed negligible and ignored in the optimisation computations.

8.1.3 Electrical Submersible Pump (ESP) Assisted Wells

The application of ESPs is particularly favourable for lifting high liquid volumes from wellbores with high productivity. Based on the desired volumetric flow rate of the well and the wellbore depth, the pump specifications (power, frequency and number of stages) can be calculated using the wellbore simulator. In order to avoid pump cavitation due to excessive free gas produced, high-efficiency downhole separation is employed in the ESP design model. Since pump performance curves are based on water systems, a viscosity correction is also implemented to account for the oil phase. Sand production is another critical factor influencing the ESP performance; thus, it was important to estimate the critical drawdown pressure for limiting the liquid production, based on the nodal analysis plots of the well. With the available pump manufacturer specifications, it was vital to ensure that the tubing size (internal diameter) selected could accommodate the outside diameter of the ESP with enough downhole clearance for the pump's liquid intake. This enabled the accurate determination of the Total Dynamic Head (TDH) of the pump. ESP frequency was chosen as the main influencing parameter on the production capacities of the ESP wells. The power requirement of the pumps can be calculated subsequently from

the optimal frequency and wellhead pressure of an ESP-assisted well. Incorporating constraints on the power requirements of the ESP was not necessary, because careful selection of high-efficiency pumps based on the manufacturer's specifications characterised the ESP design process.

8.1.4 Other Network Components

The internal diameter, thickness, length and elevation difference were the pipeline specifications required for accurate pressure drop calculations. However, considerable effort was necessary for data generation at different operating conditions in the simulator. Based on the gas-oil ratio (GOR), water cut (WC) and liquid rate (LR) ranges for the respective wells; system analysis was performed multiple times to obtain high-resolution data tables which were used for proxy model development and verification. In generating the proxy models, 25 data points are utilised for each well and 60 data points for each pipeline.

The choke flow model is based on PIPESIM's™ mechanistic correlation that calculates the pressure drop across the choke using a weighted average of the liquid and gas phase pressure drops. The liquid and gas-phase pressure drops are based on Bernoulli's equation. The critical pressure ratio is calculated using the Ashford-Pierce (1975) equation; this distinguishes subcritical from supercritical flow. However, the latter (supercritical flow conditions) represents a situation that rarely occurs in reality (PIPESIM, 2017); and does not manifest in our simulations. The choke bean size is a constant value in the simulations performed and is initially assumed 100% open for all wells (including the ESP and GL wells). Binary variables are introduced to route production from wells only. In the case that a well violates the separator capacity or water cut constraints, the algorithm automatically shuts the well. Besides the binary variables present ($x_{k,g,inj}$, $x_{k,liq,ESP}$, $x_{k,p}$), all other variables are continuous.

In generating the well and pipeline proxy models, the Hagedorn and Brown (1965) correlation is adopted for the vertical multiphase flow; whereas the revised Beggs and Brill (1973) correlation is utilised for horizontal multiphase flow calculations. The underlying assumption for the friction model (Moody, 1944) is that the pressure drop during transient flowing conditions is the same as the steady flowing conditions using an average instantaneous transient velocity and the apparent mixture properties.

8.2 Problem Definition and Optimisation Algorithm

8.2.1 Proxy Model Formulation and Validation

Given the network superstructure (Fig. 8.4), comprising of a single reservoir, 6 wells (3 pairs of NF, GL & ESP wells), 2 manifolds, 2 pipelines and 2 separators, the aim is to optimise the Net Present Value (NPV) by determining the optimal well controls, lift gas allocation and routing strategy on a real-time basis. Operational constraints include the wellbore- and pipeline-approximated models, mass balances across the network, upper and lower bounds on all operating pressures and flow rates (for the avoidance of sand production). In the mathematical description, wells are assigned the index *k*, manifolds, *m*, pipelines, *l*, separators, *s*, oil, water, liquid, and gas phases, *o, w, liq,* and *g*, respectively; all phases are collectively represented as *p*.

$$\text{Max}\,(NPV) = ROP + RGP - CWP - CQ_{g,inj} - CQ_{l,ESP} \tag{8.1}$$

The objective function (Eqs. 8.1-8.6) maximises the Net Present Value (NPV) of the production system while ensuring the wellbore pressures (wellhead, *wh* and bottomhole, *wf*) are within acceptable ranges that prevent sand production (Eq. 8.7-8.11). In the objective function (Eq. 1), *ROP* represents the revenue obtained from oil production; *RGP*, the revenue from gas production; *CWP*, the cost of water production; $CQ_{g,inj}$, the cost of gas injection and $CQ_{l,liq,ESP}$, the cost of operating the ESP. The cost indices r_o, r_g, r_w, $r_{g,inj}$, and $r_{l,ESP}$ were \$70/STB, \$2000/MMSCF, \$20/STB, \$10,000/MMSCF, and \$12/STB respectively. The total revenue from the produced gas (Eq. 3) excludes the quantity of injected gas in the GL wells. Well flow behaviour is approximated via the algebraic relationships (Eqs. 8.12, 8.13 and 8.15) for the NF, GL and ESP wells, respectively. Eq. 8.14 ensures that the allocated lift gas to the GL wells is below the field available gas for injection. Binary variables $x_{k,p}$ assigned to each well ensure that the produced fluids from a well are routed to one of the pipelines. Eq. 8.16 represents the well choke settings which ensure that if a well is routed to a particular pipeline, then the manifold pressure must be lower than the wellhead pressure of the well to avoid the backward flow of material. The mass balance constraint between wells and pipelines is represented as Eq. 8.17. In the formulation, it is assumed that the separators operate at a fixed, known pressure, P^s; thus, Eqs. 8.19 and 8.20 ensure that the manifold pressure, P^m, is sufficient to overcome the pressure drop in the pipelines and that the fluids eventually reach the separator at the desired pressure. Liquid and gas capacity constraints of the separators are represented by

Eqs. 8.21 and 8.22, respectively. The proxy model generation (Figs. 8.2a – 8.2d) using the least-squares method and the optimisation formulation (objective and constraint functions) were written in MATLAB and solved using the Basic Open-source Nonlinear Mixed Integer Programming (BONMIN) solver via the Opti toolbox interfacing platform (Currie and Wilson, 2012).

$$ROP = r_o \times \sum_{k=1}^{Nprod} q_o \quad (8.2)$$

$$RGP = r_g \times \sum_{k=1}^{Nprod} q_g \quad (8.3)$$

$$CWP = r_w \times \sum_{k=1}^{Nprod} q_w \quad (8.4)$$

$$CQ_{g,inj} = r_{g,inj} \times \sum_{k=1}^{Ng,inj} [x_{k,g,inj} \times q_{g,inj}] \quad 8.5)$$

$$CQ_{liq,ESP} = r_{liq,ESP} \times \sum_{k=1}^{N_{liq,ESP}} [x_{k,liq,ESP} \times q_{liq,ESP}] \quad (8.6)$$

$$P_k^{wf} = f_{NF}(P_k^{wh}, D_{choke}) \ \forall \ NF\ k \quad (8.7)$$

$$P_k^{wf} = f_{GL}(P_k^{wh}, Q_{g,inj}) \ \forall \ GL\ k \quad (8.8)$$

$$P_k^{wf} = f_{ESP}(P_k^{wh}, f_{ESP}) \ \forall \ ESP\ k \quad (8.9)$$

$$P_{k,min}^{wf} \le P_k^{wf} \le P_{k,max}^{wf} \quad \forall\ w \quad (8.10)$$

$$P_{k,min}^{wh} \le P_k^{wh} \le P_{k,max}^{wh} \quad \forall\ w \quad (8.11)$$

$$q_{p,k,NF} = f_{NF}(P_k^{wh}, D_{choke}) \ \forall\ p, \forall\ k \quad (8.12)$$

$$q_{k,GL} = f_{GL}(P_k^{wh}, Q_{k,ginj}) \ \ \forall\ k \quad (8.13)$$

$$Q_{k,ginj} \le Q_{k,ginj}^{max} \quad (8.14)$$

$$q_{p,k,ESP} = f_{ESP}(P_k^{wh}, f_{p,k,ESP}) \ \forall\ p, \forall\ k \quad (8.15)$$

$$x_{k,l} P^m \le P_k^{wh} \quad \forall\ k, \forall\ l \quad (8.16)$$

$$Q_{p,l} = \sum_k (x_{k,l} \times q_{p,k}) \ \ \forall p, \forall\ l \quad (8.17)$$

$$\sum_p x_{k,p} \le 1 \quad (8.18)$$

$$\Delta P = f(q_{l,o}, q_{l,w}, q_{l,g}) \quad (8.19)$$

$$P^s = P^m - \Delta P \quad (8.20)$$

$$\sum_l q_{g,l} \le CG^s \quad (8.21)$$

$$\sum_l (q_{o,l} + q_{w,l}) \le CL^s \quad (8.22)$$

The functional forms of the proxy models used in this work are shown in Eqs. 8.23-8.26 respectively

$$Q_{o,NF} = \alpha_0 + \alpha_1 P_{wh} + \alpha_2 P_{wh}^2 \quad (8.23)$$

$$Q_{o,GL} = \beta_0 + \beta_1 P_{wh} + \beta_2 Q_{g,inj} + \beta_3 P_{wh}^2 + \beta_4 Q_{g,inj}^2 + \beta_5 P_{wh} Q_{g,inj} \quad (8.24)$$

$$Q_{o,ESP} = \delta_0 + \delta_1 P_{wh} + \delta_2 f_{ESP} + \delta_3 P_{wh}^2 + \delta_4 f_{ESP}^2 + \delta_5 P_{wh} f_{ESP} \quad (8.25)$$

$$P_l = \varepsilon_0 + \varepsilon_1 Q_{l,g} + \varepsilon_2 Q_{l,o} + \varepsilon_3 Q_{l,w} + \varepsilon_4 (Q_{l,g})^2 + \varepsilon_5 (Q_{l,o})^2 + \varepsilon_6 (Q_{l,w})^2 + \varepsilon_7 Q_{l,g} Q_{l,w} + \varepsilon_8 Q_{l,g} Q_{l,o} + \varepsilon_9 Q_{l,o} Q_{l,w} \quad (8.26)$$

Where $Q_{o,NF}$, $Q_{o,GL}$ and $Q_{o,ESP}$ represent the oil flowrates of the NF, GL and ESP wells respectively, P^{wh}, the wellhead pressure, $Q_{g,inj}$ the gas lift injection rate, f_{ESP}, the ESP frequency. Subscripts o, w, g, represent the oil, water and gas phase and l represents the pipeline. Coefficients of the proxy models are α, β, δ, and ε, respectively.

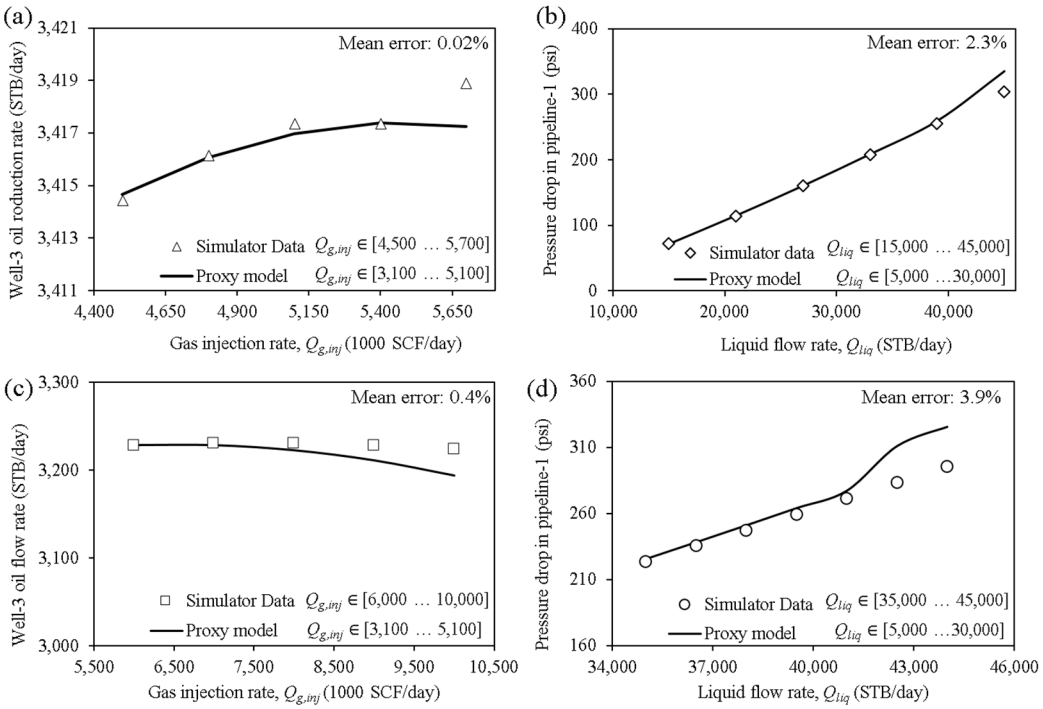

Figure 8.3. Well and pipeline proxy model validation using PIPESIM^{TM} simulation data.

The performance of the implemented proxy models (Eqs. 8.23-8.26) is shown in Fig. 8.3. For brevity, only the proxy models for the gas lift well-3 and pipeline-1 are presented. In performing the validation procedure, a mixture of datasets used in the model development phase and simulation datasets outside this range are applied (Figs. 8.3a-b). In Figs. 8.3c-d, the datasets utilised are entirely outside the data range used for the proxy model development. As expected, the proxy model performance with the mixed data set is better than that with the entirely different data range (as reflected in the absolute mean errors). Furthermore, it can be observed from all the plots, that a critical point is reached when the proxy model performance begins to diverge and become inaccurate. This is why an iterative proxy model updating procedure is essential and implemented.

8.2.2 Optimisation Solvers and Algorithm

The 'B-BB' and 'B-OA' algorithms of BONMIN were utilised in finding good local solutions. The former (B-BB), implements a simple branch and bound algorithm based

on the solution of the continuous NLPs at each node of the search tree and subsequently branching on the integer variables. This is made possible by modifying CBC (a mixed-integer linear programming solver) so that LP solutions at each node of the tree are replaced by NLP solutions (Bonami et al., 2008). NLP solutions at each node are obtained speedily using the IPOPT solver.

This B-BB algorithm of BONMIN is similar to the one implemented in the solver, 'SBB'. The latter (B-OA), is an outer-approximation branch and cut algorithm, similar to that implemented in DICOPT. It iteratively solves and improves the MIP relaxation of the MINLP problem and also solves the NLP subproblems (Gupta and Ravindran, 1985; Fletcher and Leyffer, 1994). In the algorithm, a single tree search is performed, and the resulting NLP solutions are used to progressively tighten the MILP relaxation. The motivation of this approach was to avoid the sequential solution of several relaxed MILPs; thus increasing the computational speed (Bonami et al., 2008).

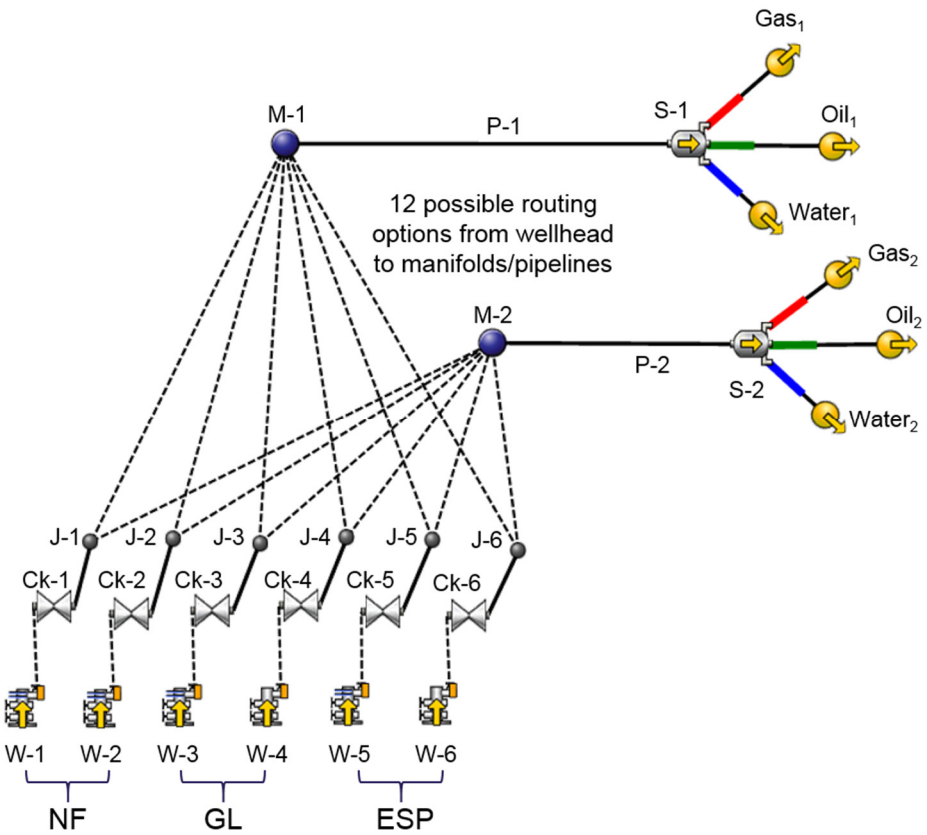

Figure 8.4. Superstructure of network connections for the petroleum production system.

Successful implementation of the described formulation (Eqs. 8.1-8.22) requires that proxy models are developed within a specific range of wellhead and bottomhole pressures

in which these models accurately approximate the simulator outputs; it is preferable that this range is not very far from the initial guesses. From preliminary tests performed, the optimisation algorithm fails after a certain number of iterations when the input range (search space involved) is very large, or the upper and lower bounds of the independent decision variables are very loose. Thus, it is imperative that reasonably tight bounds are set and that the parameters of the proxy model are updated via rerunning the black box simulators; especially when operating conditions change significantly (e.g. a change in flow regime or well productivity). Gunnerud et al. (2013) provide recommendations/ algorithmic modification strategies for updating the proxy models and their corresponding trust regions.

Table 8.1. Separator capacities and operating pressures for all cases explored.

Case study	Separator	Operating pressure (psia)	Liquid capacity (STB/day)	Gas Capacity (MMSCF/day)
Base Case (BC)	S–1	80	15,000	9
	S–2	50	10,000	6
Case Study 1 (CS1)	S–1	80	15,000	9
	S–2	50	15,000	9
Case Study 2 (CS2)	S–1	80	15,000	9
	S–2	50	10,000	6
Case Study 3 (CS3)	S–1	80	15,000	9
	S–2	50	10,000	12
Case Study 4 (CS4)	S–1	80	15,000	10
	S–2	50	15,000	10

8.3 Optimisation Results

The superstructure of the production network with all possible connections is shown in Fig. 8.4; 12 possible routing options exist for which the optimisation algorithm is expected to find the best well-manifold connections that guarantee an optimal NPV.

Furthermore, four case scenarios are compared to a base case in which all wells have good performance with high productivity indexes (>1 STB/day.psi), relatively low average water cut (30%), an average GOR of 800 SCF/STB and limited water and gas handling capacities (Table 8.1).

Table 8.2. Reservoir, well and pipeline parameters.

Parameter	W–1	W–2	W–3	W–4	W–5	W–6	P–1	P–2
Reservoir pressure (psia)	3,800	3,800	3,800	3,800	3,800	3,800	–	–
Well type	Deviated	Vertical	Deviated	Vertical	Deviated	Vertical	–	–
GOR (SCF/STB)	800	780	810	785	800	800	–	–
WC (%)	30	30	25	30	30	28	–	–
True Vertical Depth – TVD (ft)	9,000	10,000	9,500	10,000	9,500	10,000	–	–
BHP constraint to avoid sand production (psi)	700	700	700	700	700	700	–	–
Productivity Index (STB/day.psi)	2.5	1	2.3	1.5	2.8	2	–	–
TVD of gas lift valve (ft)	–	–	5,800	7,500	–	–	–	–
Assumed temperature along wellbore (^oF)	200	200	200	200	200	200	200	200
Tubing diameter (in)	3.5	3.5	3.5	3.5	3.5	3.5	–	–
Pipeline length (ft)	–	–	–	–	–	–	6,000	4,000
Pipeline internal diameter (in)	–	–	–	–	–	–	10	12
Pipeline internal roughness (in)	–	–	–	–	–	–	0.001	0.001

By considering these case studies, the flexibility of the optimisation formulation is demonstrated.

- Base Case (BC): Limited separator handling capacities.
- Case Study 1 (CS1): Increased liquid and gas handling capacities of S-2.
- Case Study 2 (CS2): Decreased well productivity and increased water cut for the NF well (W-1).
- Case Study 3 (CS3): Well intervention on the W-5 and W-6 due to ESP damage.
- Case Study 4 (CS4): Switching W-3 to ESP mode with increased separator handling capacities.

The separator, well, and pipeline characteristics are given in Tables 8.1 and 8.2, respectively. S-1 is connected to M-1 (Figs. 8.1 and 8.4) by a longer pipeline (but with a smaller internal diameter) compared to S-2. The well characteristics are very similar, as shown in Table 8.2; however, their perforation intervals and permeabilities around the well are different, thus resulting in the varying production responses observed in Fig. 8.5.

The parameters in Table 8.3 represent the input data to the surface network simulator for accurate fluid description through the wells, chokes, flowlines, manifolds, pipelines and separators, respectively.

Table 8.3. Parameters used in the surface network model.

PVT model	Black oil model
Gas-oil ratio (SCF/STB)	720-800
Water cut (%)	20-45
Oil specific gravity (API)	45
Gas density (lbm/ft^3)	0.0507
Bubble point pressure (psi)	1500
Pipeline temperature (^{o}F)	100

Fig. 8.5 illustrates the production rates obtained via simulation with the multiphase simulator at a wellhead pressure of 380 psia before the proposed optimisation formulation is applied. Based on the optimal wellhead pressures and flowrates, the optimal routing configurations are determined for the 5 different case scenarios and presented next.

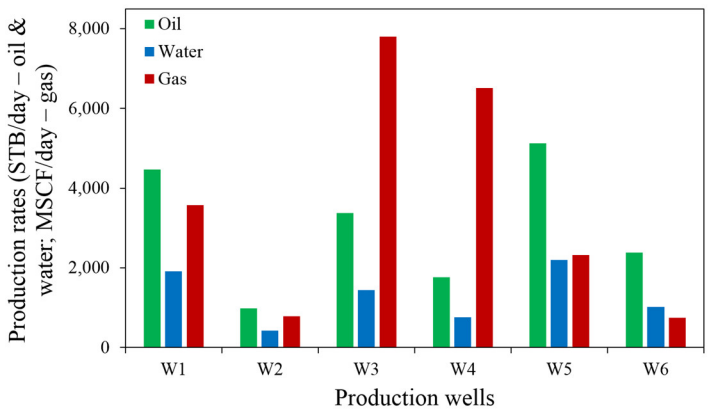

Figure 8.5. Simulated well production performance.

8.3.1 Base Case

It is illustrated in Fig. 8.6 that the optimal routing strategy involves connecting the GL well (W-4) and the ESP wells (W-5 and W-6) to M-1, and routing the NF wells to M2; whereas, W-3 is shut. A physical explanation for this routing strategy is that the gas handling capacity of the separators is relatively lower than the combined gas production rates from W-3 and W-4. These high gas production rates can be attributed to the originally injected gas during the gas lift operation. For W-3 to be shut in place of W-4 (Fig. 8.6), it implies that the revenue due to additional oil production does not outweigh the cost of gas injection in this well (W-3), ass depicted in Fig. 8.5.

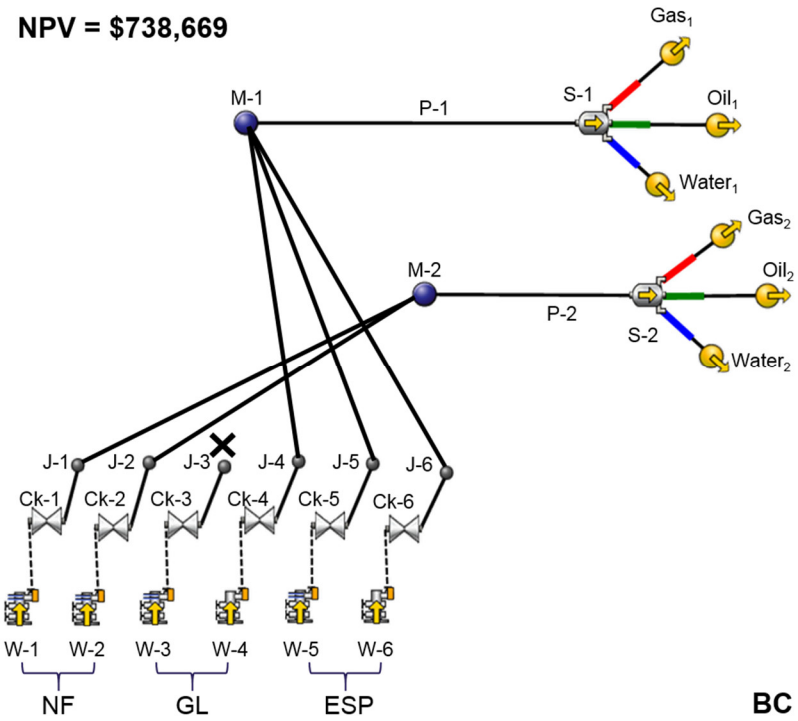

Figure 8.6. Optimal routing structure for the Base Case.

Conversely, W-4 remains open, despite its lower oil production rate, compared to W-3 (Fig. 8.5). It is also worth noting the higher water production rate of W-3 in comparison to W-4 (Fig. 8.5) has made it a less preferred candidate for improving the NPV. Typical heuristic approaches which might involve opening high oil-producing wells, without a full-scope consideration of the gas and liquid capacities of the separating units would not guarantee a significant improvement in field profitability. Enhancing the performance of W-3 and W-4 could involve more strategic positioning of well perforations that would

prevent gas and water coning, thus reducing the wells' GOR and WC. Furthermore, ESPs could be used in place of GL in these wells for GOR reduction.

8.3.2 Case Study 1 (Increased Liquid and Gas Handling Capacities)

Increasing the liquid and gas handling capacities of S-2 to 15,000 STB/day and 9 MMSCF/day (same as the capacities of S-1, Table 8.1), changes the routing structure. As observed in Fig. 8.7, there is an increase of 1.8% in the NPV (compared to the base case) due to the capacity enlargement of S-2.

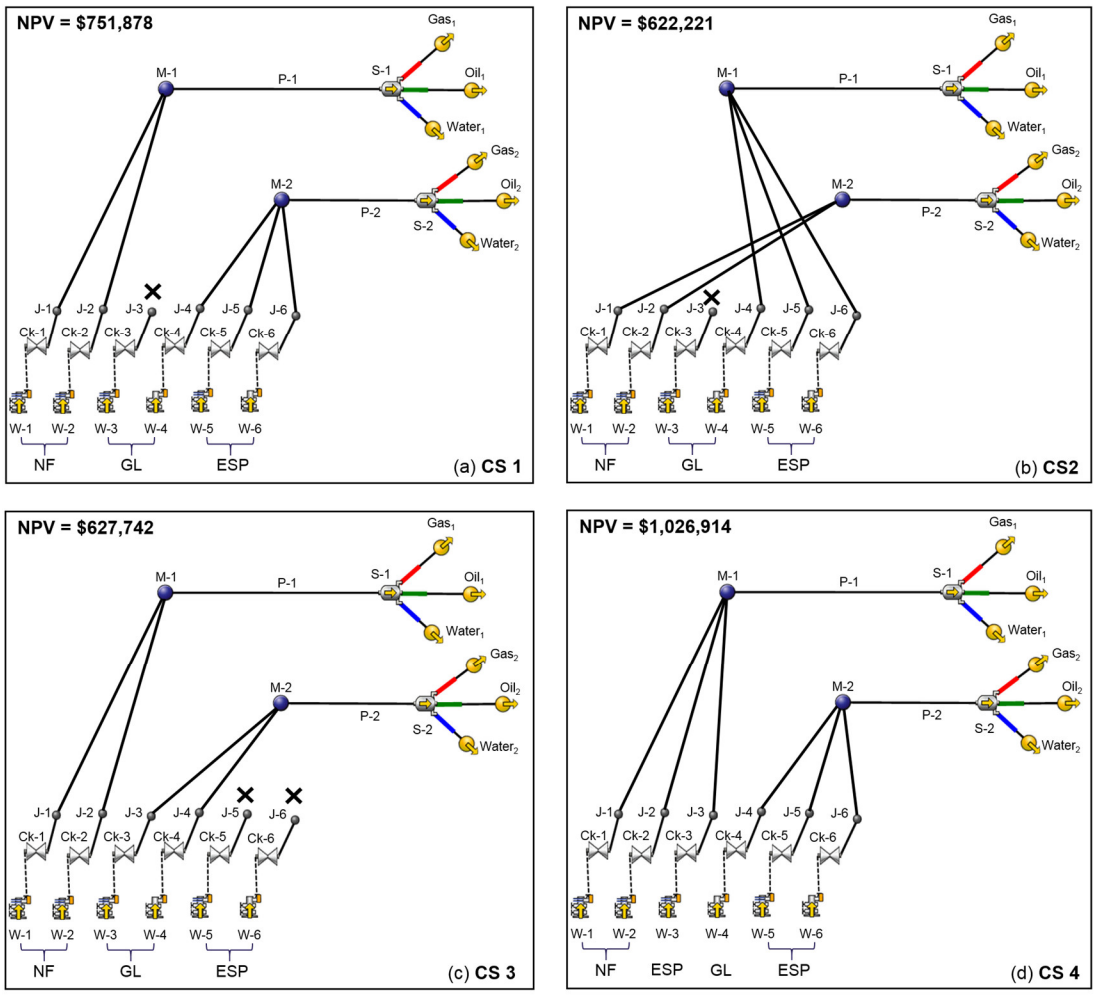

Figure 8.7. Optimal routing structures for all case studies (CS1, CS2, CS3 and CS4) explored.

Although the cost of this enlargement is not included in the optimisation formulation, this 1.8% improvement would cumulatively surpass the expansion costs over a long production horizon. It is observed in Fig. 8.7 that the shorter pipeline (P-2) connected to a low-pressure separator (S-2) is the preferred routing option for W-4, W-5 and W-6,

respectively. Besides the increased separator capacity, another factor influencing this optimal routing option is the size and length of the pipeline (P-2); its shorter length and larger diameter imply that the pressure drop through the pipeline (P-2) is lower than P-1. Furthermore, the lower operating pressure of the separator (S-2) implies that a lower manifold pressure and in turn, a reduced wellhead pressure would guarantee forward flow of the fluids from the wells. This reduced wellhead pressure translates to a higher production rate response from these wells. Due to capacity constraints, W-3 is still shut, and W-1 and W-2 are routed to S-1 via P-1.

8.3.3 Case Study 2 (Decreased Well Productivity and Increased Water Cut)

In this case study, the reservoir permeability of the Joshi steady-state IPR model (for the deviated well W-1) is reduced from 100 mD to 80 mD, and the water cut of the well is increased from 30% to 45%. The operating gas and liquid handling capacities are the same as that of the base case. Although there is an inevitable reduction in the NPV by 16% compared to the base case, the routing structure is maintained (same as the base case). Besides the capacity limitations earlier explained in Section 4.1, this structure remains the optimal, because by closing W-3, the pressure drop in either of the pipelines (that would have ensued if W-3 were connected to M-1 or M-2) is significantly reduced, and the production rate from other wells is consequently increased. Considering the intricacy and the number of parameters to consider simultaneously, heuristic methods cannot guarantee the optimality of the routing structure of this production network. Additionally, it becomes impossible to apply such methods when the network becomes very large as there would be several routing possibilities.

8.3.4 Case Study 3 (Well Intervention due to ESP Damage)

In this illustrative example, a well intervention is carried out on the ESP assisted wells in order to perform maintenance activities and subsequently reinstall the ESPs. Hence W-5 and W-6 cannot produce and are considered closed wells by the optimisation solver. Furthermore, the liquid and gas handling capacities of S-1 are retained at the same values as the base case; similarly, the liquid handling capacity of S-2 is maintained at the base case value. However, only the gas handling capacity of S-2 has been increased from 6 MMSCF/day to 12 MMSCF/day. The resulting routing configurations based on these

modifications are shown in Fig. 8.7. It is observed that the high gas producing wells (W-3 and W-4) are preferably routed to the separator with the highest gas handling capacity (S-2); whereas the NF wells are preferably routed to S-1 with the lower gas handling capacity. Despite shutting the 2 ESP wells, the NPV of CS3 $627,742 is comparable to that of CS2 (in which only 1 well is shut) with a $622,221 NPV. On analysing the field production rates of all phases in Table 8.4, an explanation for this similarity can be derived. Although CS2 yields a 23% higher oil production rate, its water production rate and thus its production cost is significantly higher (50%) than that of CS3 (Table 8.3). Furthermore, the gas production rate of CS3 is 29% higher than CS2. The cumulative effect of these differences is a slight enhancement (0.9%) in the profitability of CS3 over CS2, as reflected in the NPV.

8.3.5 Case Study 4 (Switched Well Operation Mode)

Given the previously identified problems with W-3, its performance is enhanced by switching the artificial lift operation from gas lift to an ESP in this case study. This translates to an increase in the oil production rate of this well compared to the increment in oil production that was obtainable via gas lift operation. It is illustrated in Fig. 8.7 that the optimal status of the network is now to open W-3 and route it to M-1.

The increased separator capacities compared to the base case also resulted in the opening of all wells; thus resulting in a 39% increase in the NPV compared to the base case. Despite the pressure drop differences in the pipeline, the similarity of separator capacities has allowed a correspondingly equal split in the produced fluids from the 6 wells (3 wells each). It can thus be inferred that the handling capacities of the produced fluids and the wells' mode of operation significantly influence the optimal routing strategy.

Table 8.4 also illustrates the proper utilisation of the liquid and gas storage capacities by the optimisation algorithm for all case studies. However, CS 4 ranks highest with 91% capacity usage for the liquid phase, whereas the base case ranks highest with 85% usage of the total gas capacity. It is worth mentioning that the separator capacities mentioned here do not necessarily imply the capacity of a single separating vessel but rather multi-stage separation/separators equipped with extra storage is also possible. Although the detailed design of the separating vessels and capacities is not within the scope of this

study, the optimisation methodology applied here could aid production engineers in the choice of appropriate vessel capacities in order to avoid redundancy.

Table 8.4. Optimal field production and injection rates, ESP power requirements and routing strategy.

Field parameter			**BC**	**CS1**	**CS2**	**CS3**	**CS4**
Oil production rate (STB/day)			14,930	15,209	13,476	10,924	19,064
Water production rate (STB/day)			6,399	6,518	7,016	4,682	8,171
Liquid production rate (STB/day)			21,328	21,726	20,492	15,605	27,235
Available liquid capacity (STB/day)			***25,000***	***30,000***	***25,000***	***25,000***	***30,000***
Liquid capacity utilized (%)			*85.3*	*72.4*	*82.0*	*62.4*	*90.8*
Gas production rate (MMSCF/day)			12.81	12.91	11.64	16.34	16.00
Available gas capacity (MMSCF/day)			***15.00***	***18.00***	***15.00***	***21.00***	***20.00***
Gas capacity utilized (%)			*85.4*	*71.7*	*77.6*	*77.8*	*80.0*
Total gas injection rate (MMSCF/day)			3.8	3.8	3.8	7.6	3.8
Total ESP power requirement (hp)			520.3	574.8	522.1	–	702.5
Optimal routing strategy of the surface production network for all case studies considered							
$x_{1,1}$	W-1	PIPELINE 1	0	1	0	1	1
$x_{2,1}$	W-2		0	1	0	1	1
$x_{3,1}$	W-3		0	0	0	0	1
$x_{4,1}$	W-4		1	0	1	0	0
$x_{5,1}$	W-5		1	0	1	0	0
$x_{6,1}$	W-6		1	0	1	0	0
$x_{1,2}$	W-1	PIPELINE 2	1	0	1	0	0
$x_{2,2}$	W-2		1	0	1	0	0
$x_{3,2}$	W-3		0	0	0	1	0
$x_{4,2}$	W-4		0	1	0	1	1
$x_{5,2}$	W-5		0	1	0	0	1
$x_{6,2}$	W-6		0	1	0	0	1

8.4 Solver Performance

It can be shown in Table 8.5 that optimal results are obtained in a relatively short time; although this is mostly due to the problem size, decomposition techniques that enhance solution speed (such as the Dantzig-Wolfe and Lagrange decomposition within a reformulated MILP) can readily be applied to larger problems (Gunnerud and Foss, 2010).

The run time required for the applied method in this study demonstrates its applicability to real-time decision making in practical operations. A major influencing factor on the solution time required is the number of discrete variables present. It is observed in CS3 that, where the number of routing variables becomes 8 (compared to the base case in which 12 routing variables are present), the solution runtime reduces by two orders of magnitude (Table 8.5).

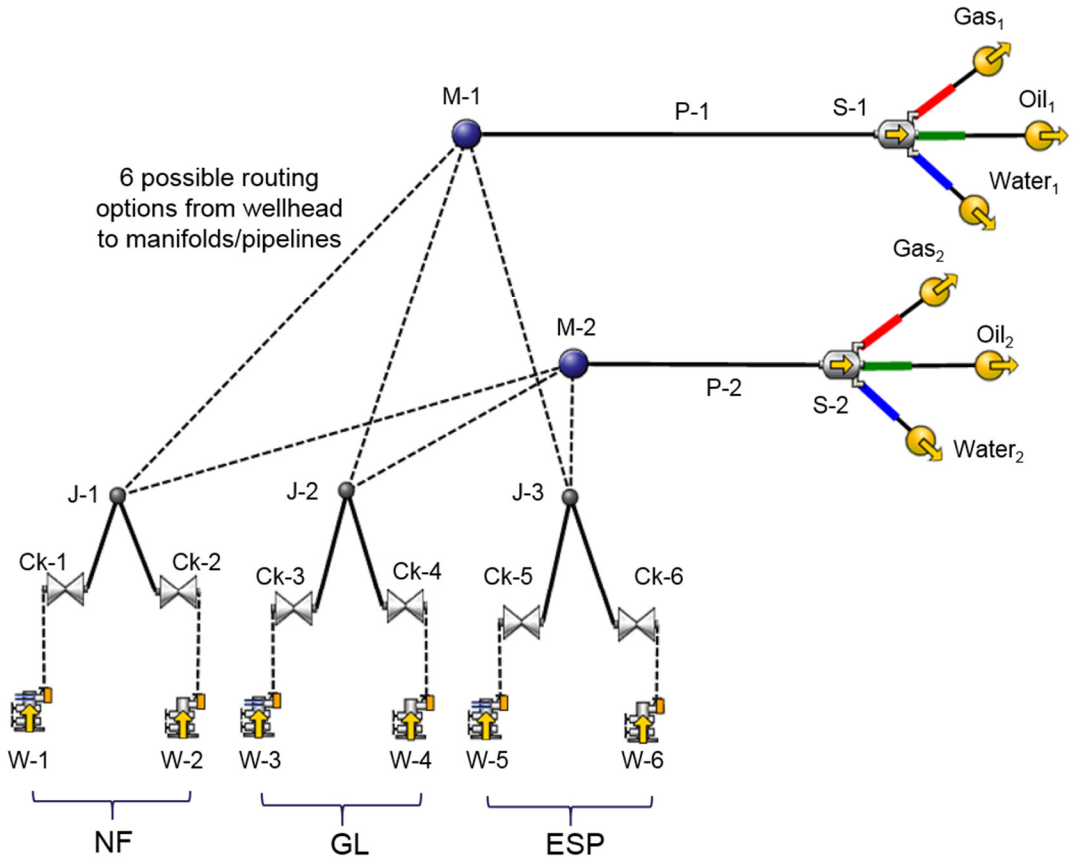

Figure 8.8. Network superstructure with reduced routing options.

In addition, the optimality gap and number of iterations are significantly reduced, thus indicating the relatively lower computational effort required for a good-quality solution. Hence, for very complex networks in which the number of wells becomes very large, a possible strategy for run time reduction is to group the production wells into clusters, as shown in Fig. 8.8 so that the number of routing variables is reduced. Although this is usually done in practical operations (gathering wells at different clusters or junctions, J-1, J-2 and J-3 – Fig. 8.8), this approach further constrains the optimisation algorithm (and may yield suboptimal results) compared to a scenario in which the algorithm's exploration space for better possible routing options is more extensive. However, it is vital to maintain

a balance between solvability of the optimisation problem and the desired accuracy at all times. Moreover, in a situation where the well positions/gathering network already exists/are fixed (which is the case in this study), the existing structure has to be maintained, and the well routing options alone optimised. Infrastructural planning problems, which involve well placement decisions, can incorporate these different routing decisions (Figs. 8.4 and 8.8) as additional constraints.

Although the B-OA algorithm of BONMIN was able to provide good solutions in much faster time (<10 sec) compared to the B-BB algorithm in a few cases, it was desirable to progressively monitor the change in the objective value at each iteration which was only outputted by the B-BB algorithm. This provided some insight into troubleshooting an unsuccessful optimisation run (changing variable bounds, or initial guesses). Furthermore, in the preliminary test cases run, the B-BB algorithm proved more stable, with higher NPVs obtained compared to the B-OA algorithm for the problem described herein. Considering the problem's non-convexity, and the fact that no specific heuristic method for treating non-convex problems is implemented within the OA framework (Bonami and Lee, 2007), the B-BB algorithm was adopted for all optimisation runs in this study.

Table 8.5. Solver performance analysis (BONMIN B-BB algorithm).

Case Study	Run time (sec)	Number of nodes	Number of iterations	Optimality Gap	NPV ($) MINLP solution	NPV ($) NLP solution	Absolute percentage difference (%)
BC	96	4	423	0.131	738,669	738,659	0.001
CS1	74	40	1346	0.197	751,878	751,878	0.00
CS2	81	6	709	0.232	622,221	633,910	1.90
CS3	0.9	2	23	0.003	627,742	627,742	0.00
CS4	102	8	4612	0.006	1,026,914	1,026,918	0.00

Several factors are responsible for the solver performance shown in Table 8.4. One of the steps taken to ensure the stability of the solver and repeatability of optimal solutions upon several runs was to reduce the relative disparity in the magnitude of the different variables, particularly during the proxy model generation. Furthermore, obtaining accurate proxy models that represent the simulator output within the supplied input range is vital for excellent solver performance. Generated well proxy models had an average error of 0.5% whereas that for both pipelines was 0.9%. In both cases, the maximum error was less than

4%, thus demonstrating the structure/formulation quality of the proxy models. In order to investigate possible improvements in solution quality in terms of the NPV, the discrete variables obtained by solving the MINLP problem using BONMIN (shown in Table 3) are fixed, and the resulting NLP problem is solved using IPOPT. This idea stems from the work of Gupta and Grossman (2012), in which they sought improvements (increased NPV) to their local MINLP solutions after fixing the optimal discrete solutions obtained. Following a similar approach, we have checked for the possibility of obtaining improvements in the NPV and discovered that this technique worked fine with a 1.9% discrepancy in NPV for CS2 as detailed in Table 8.5. We attribute both occurrences to the use of a local, not a global NLP solver (IPOPT) in our study (the solver may have been trapped at a local solution with the MINLP solution, particularly in CS2). However, the percentage differences between the NPVs of the MINLP and the NLP formulations of the base case, CS3 and CS4 are negligible.

8.5 A Comparison of Heuristic and Optimisation Methodologies

Thus far, we have presented, formulated and analysed a unified MINLP-based computational approach which combines polynomial-based surrogate models and operational constraints that simultaneously account for chokes, pipelines and wellbore physics (of different types – NF, GL, ESP) in the same oil field for various cases.

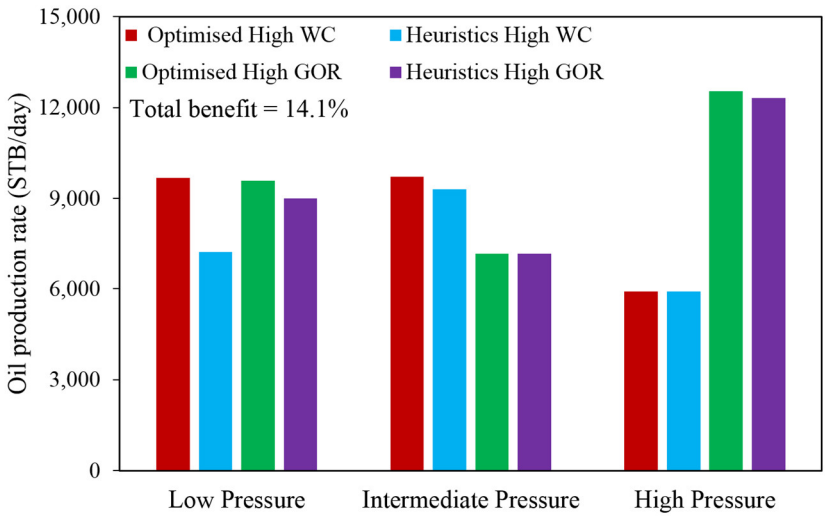

Figure 8.9. A quantitative comparison of heuristic and optimisation methods for oil production optimisation.

Although a direct comparison of heuristic and deterministic methodologies escapes the scope of this study, a summary of the computational evaluation of both methodologies (Kosmidis et al., 2005) is given in Fig. 8.9. They realise a 14.1% improvement in oil production compared to the heuristic method that is based on choke diameter reduction and the incremental GOR concept. Thus, demonstrating the economic benefits of mathematical optimisation, when applied to oil-producing fields. The current work builds upon that of Kosmidis et al. (2005) by incorporating novel elements presented in this chapter.

8.6 Chapter Conclusions

In this chapter, an optimisation framework that simultaneously considers the production behaviours of naturally flowing, gas-lifted and ESP-assisted wells is proposed. Simulation and computational analyses based on algebraic proxy models were carried out considering a synthetic but practical production network. Compared to previous optimisation formulations, this work has implemented a more realistic objective function in determining the optimal operating conditions and routing configurations. Specifically, the optimal field power requirements for the respective ESPs and the optimal gas injection rates are determined.

- Separator handling capacities of the respective gas and liquid phases is a highly influential factor that affects the optimal routing strategy. Considering the combination of several other contributing factors, such as the pipeline pressure drop and separator operating pressure, heuristic-based routing methodologies may not guarantee an optimal operating configuration.
- Rapid computations of the resulting MINLP problem using robust MINLP algorithms ensure that solutions of the optimal routing strategy in a production network can be obtained in real-time. Expansion of the applied formulation to larger fields with more wells will likely yield solutions within short periods, provided a systematic model parameter update loop in embedded in the formulation. Although the time required for proxy model data generation is not included in the analysis, automated data generation capabilities are emerging attributes of high-fidelity simulators that can be exploited for further computational time reduction.

- The proposed optimisation formulation demonstrates proper utilisation of separator capacity for routing produced fluids. It is thus useful for production network design purposes when decisions relating to the size of separation facilities are to be made. Furthermore, its robustness is also illustrated by the similar NPV results obtained between the MINLP and NLP formulations (based on discrete solutions of the MINLP formulation).
- The adaptability of the proposed formulation to changing operational conditions is also demonstrated via 5 different case studies. It was discovered that changing the artificial lift mechanism could result in a 39% improvement in the NPV.

Future investigations could consider the option of routing well fluids to more than one pipeline at a time. Furthermore, incorporating piping costs in the NPV objective function is an essential extension of the current work that is worth investigating.

Chapter 9 Oil Production Optimisation using Piecewise Linear Approximations (MILP): A Computational Performance Comparison vs. MINLP Formulation

As described in previous chapters, an aggregate production system model consists of several models corresponding to the production system components (reservoir model, well model and surface facility models for the pipelines and separators). These models must be maintained by frequent calibration using acquired data of the system (Fig. 9.1). With this information, production optimisation can be performed to obtain the system's optimal operating conditions. Mixed-Integer Nonlinear Programming (MINLP) which combines the modelling capabilities of integer and nonlinear programming into a flexible and multifaceted framework, could result in formulations which are difficult to solve.

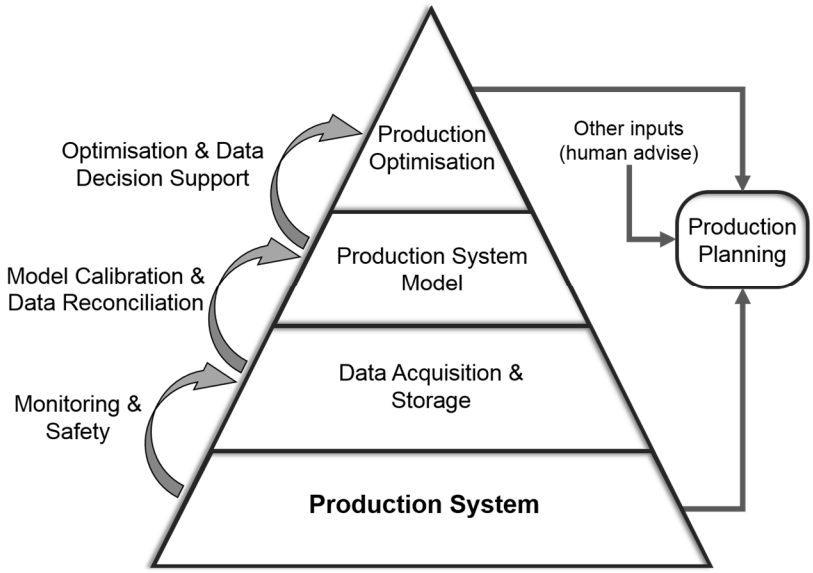

Figure 9.1. Technology pyramid of production optimisation (Grimstad, 2015).

Typical sources of nonlinearity in the production system include the production wells' pressure-rate responses, the pipeline and valve pressure drops and multiphase flow rate relationships (Epelle and Gerogiorgis, 2019b). These complex relationships are usually not explicitly known and are dependent on several operational parameters estimated via high fidelity simulators. Piecewise linear models have the advantage of establishing linear relationships directly from the simulator sample points; a property that may reduce problem complexity. A frequently adopted simplification approach is to convert the MINLP to a Mixed Integer Linear Program (MILP) via piecewise linear approximations

(Gerogiorgis et al., 2006; Silva and Camponogara, 2014; Kronqvist et al., 2019). A computational performance comparison of the trade-offs to be made when deciding the structure of the optimisation formulation is scarce in the literature. This work provides some insights via a detailed analysis of the computational performance of both formulations.

The objective of this chapter is to develop a surrogate model-based production optimisation formulation which when solved, is capable of providing optimal operational settings that maximise a field's Net Present Value (NPV) while satisfying imposed operational constraints. To achieve this, this study incorporates the benefits of MILP on a synthetic but realistic case study. The obtained solutions of the MILP and that of the original MINLP are compared and an evaluation of the impact of the number of linearisation breakpoints on the solution time, accuracy, modelling effort and ease of automation is performed. It is ensured that high accuracy is maintained in the nonlinear models and piecewise approximations in comparison to the simulation data while carrying out optimisation calculations. The novel analysis presented herein enables quality assessment of the relative performances of the respective MILP formulations and their impact on the overall oil production. Another novel element of this study is the combination of operationally distinct well behaviours with complex flow physics within an optimisation formulation. Flow routings at 2 levels (well-to-manifolds and pipelines to separators) are also modelled, as shown in Fig. 9.4. Comparisons with PIPESIM's™ network optimiser are made to demonstrate the robustness of the proposed formulation. This study also incorporates well coning behaviour, which has hardly been accounted for in production optimisation literature (Hasan et al., 2013).

9.1 Methodology

The surface network model is first constructed in a steady-state multiphase flow simulator (PIPESIM™ v 2019.3). As shown in Fig. 9.4, the model consists of the wells, chokes, flowlines, manifolds, pipelines and separators, which are all connected. Robust multiphase flow correlations are adopted to capture complex flow physics in the respective network components. Some of these phenomena include water coning behaviour, non-vertical/deviated well trajectories and downhole pressure assistance to maintain production by utilising Progressive Cavity Pumps (PCPs) and Electrical Submersible Pumps (ESPs).

9.1.1 Steady-State Model Development

Water coning is a common problem in the oil and gas industry; it involves the upward movement of water into the perforations of a producing well due to drawdown pressure fluctuations and changes in the oil-water contact (to a bell-shaped form) in the reservoir (Fig. 9.2a). Although water coning is a transient process, the steady-state simulator (PIPESIM™) is capable of modelling this process using data tables (implemented herein) that describe oil production rate as a function of the water cut. This could cause changes to the Vertical Flow Performance (VFP) curves of a well and eventually reduce the oil production rate (Figs. 9.2b and c). In addition, several design considerations are also made during the selection of the PCPs and ESPs for optimal oil delivery from the wells. Some of the considered factors include: the depth at which the pumps should be placed in the well, the main influencing parameter on pump performance (to be used in the optimisation formulation), viscosity correction factors (due to oil-water emulsions in the well) and the downhole clearance for the pump's liquid intake.

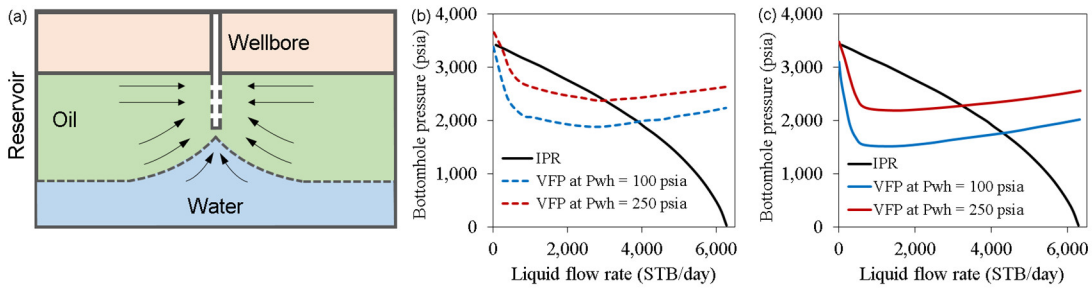

Figure 9.2. Water coning in a vertical production well (a) VFP curves of a well with water coning (b) VFPs of a well without water coning; IPR represents the Inflow Performance Relationship curve.

To model the flow behaviour in the wells and pipelines, the Hagedorn and Brown (1965) correlation is adopted (for the vertical multiphase flow), whereas the revised Beggs and Brill (1973) correlation is utilised for horizontal multiphase flow calculations in PIPESIM™. The vertical wells' performances are modelled in the simulator by supplying a productivity index value, while, the Joshi inflow performance relationship (IPR) is employed for the horizontal wells.

9.1.2 Optimisation Formulation

The surface network design procedure was followed by the generation of large data tables. This involved performing several simulations at different well and pipeline conditions,

which correspond to different wellhead pressures and liquid production rates. Using these data, algebraic (polynomial) proxy models are developed for each network component. These proxy models are then utilised together with an objective function (Eq. 9.5) to optimise the Net Present Value (NPV) of the surface network. The performance of these proxy models is dependent on the data range used in their development. Once the network's operating conditions significantly change, the model parameters are recalibrated. This methodology takes advantage of the decomposable nature of the production network, in that separate equations can be written for each component, and these constitute the optimisation constraints. The complexity of the optimisation problem herein stems from the presence of discrete routing variables at different levels: the well-to-manifold level and the pipeline-to-separator level. The nonlinear pressure-rate responses of the wells and pipelines coupled with these routing decisions inevitably result in an MINLP, (Bussieck and Pruessner, 2003; Wächter and Biegler, 2005; Gunnerud and Foss, 2010) as described in Table 9.1.

Piecewise linear formulations split the domain of a nonlinear function into a set of polytopes $\boldsymbol{P} \in \wp$; where each polytope has a set of vertices $V(\boldsymbol{P})$, and for each vertex $\boldsymbol{v} \in V(\boldsymbol{P})$ of a polytope, there exists a corresponding continuous variable, $\lambda_{\boldsymbol{P},\boldsymbol{v}}$ (Silva and Camponogara, 2014) as shown in Fig. 9.3. According to Vielma (2010), if $D \subseteq \mathbb{R}^n$ is a compact set, a continuous function $\boldsymbol{f}: D \subset \mathbb{R}^n \rightarrow \mathbb{R}$ is piecewise linear if and only if there exists $\{m_P\}_{P\in\wp} \subseteq \mathbb{R}^n, \{c_P\}_{P\in\wp} \subseteq \mathbb{R}$, and a finite family of polytopes $\wp$ such that $D = \bigcup_{P\in\wp} \boldsymbol{P}$ and $\boldsymbol{f}(x) = \{m_P x + c_P, \quad x \in \boldsymbol{P} \; \forall \, \boldsymbol{P} \in \wp\}$. If $x \in \boldsymbol{P_1} \cap \boldsymbol{P_2}$, for 2 polytopes $\boldsymbol{P_1}, \boldsymbol{P_2} \in \wp$, the above definition infers that $m_{\boldsymbol{P_1}} x + c_{P_1} = m_{\boldsymbol{P_2}} x + c_{\boldsymbol{P_2}}$; this ensures the continuity of $\boldsymbol{f}$ on D. Thus, a convex combination of the vertices of each polytope represents a point (on a graph) of the function. A disaggregated convex combination of polytopes is given by (Eqs. 9.1-9.4):

$$\sum_{\boldsymbol{P}\in\wp} \sum_{\boldsymbol{v}\in V(\boldsymbol{P})} \lambda_{P,v} \boldsymbol{v} = x, \quad \sum_{\boldsymbol{P}\in\wp} \sum_{\boldsymbol{v}\in V(\boldsymbol{P})} \lambda_{\boldsymbol{P},\boldsymbol{v}} (m_{\boldsymbol{P}} x + c_{\boldsymbol{P}}) \leq f(x) \tag{9.1}$$

$$\lambda_{\boldsymbol{P},\boldsymbol{v}} \geq 0 \quad \forall \boldsymbol{P} \in \wp, \;\; v \in V(\boldsymbol{P}) \tag{9.2}$$

$$\sum_{v\in V(P)} \lambda_{\boldsymbol{P},\boldsymbol{v}} = y_{\boldsymbol{P}} \;\; \forall \boldsymbol{P} \in \wp \tag{9.3}$$

$$\sum_{\boldsymbol{P}\in\wp} y_{\boldsymbol{P}} = 1 \quad y_{\boldsymbol{P}} \in \{0,1\} \;\; \forall \boldsymbol{P} \in \wp \tag{9.4}$$

Table 9.1. Optimisation formulations (MINLP and MILP).

Objective function

$$\text{Max}\,(NPV) = ROP - CWP \quad (9.5)$$

$$ROP = r_o \times \sum_{k=1}^{Nprod} q_o \quad (9.6)$$

$$CWP = r_{wt} \times \sum_{k=1}^{Nprod} q_w \quad (9.7)$$

Constraints of the MINLP formulation

$$P_{k,min}^{wh} \le P_k^{wh} \le P_{k,max}^{wh} \quad \forall\, k \quad (9.8)$$

$$q_{p,k,NF} = f\left(P_k^{wh}\right) \;\forall\, p, \forall\, k \quad (9.9)$$

$$q_{p,k,ESP} = f\left(P_k^{wh}, f_{p,k,ESP}\right) \quad \forall\, p, \forall\, k \quad (9.10)$$

$$q_{p,k,PCP} = f\left(P_k^{wh}, \Omega_{p,k,PCP}\right) \;\forall\, p, \forall\, k \quad (9.11)$$

$$\Delta P_l = f\left(q_{l,o}, q_{l,w}\right) \quad \forall\, l \quad (9.12)$$

$$y_{k,l} P^m \le P_k^{wh} \quad \forall\, k, \forall\, l \quad (9.13)$$

$$z_{l,s} P^s \le P^m \quad \forall\, l, \forall\, s \quad (9.14)$$

$$Q_{p,l} = \sum_k (y_{k,l} \times q_{p,k}) \;\; \forall\, p, \forall\, l \quad (9.15)$$

$$LC^s = \sum_l (z_{l,s} \times Q_{p,l}) \;\; \forall\, p, \forall\, s \quad (9.16)$$

$$\sum_l y_{k,l} = 1 \quad (9.17)$$

$$\sum_s z_{l,s} = 1 \quad (9.18)$$

$$P^s = P^m - \Delta P \quad (9.19)$$

$$\sum_l q_l \le LC^s \quad (9.20)$$

Piecewise linearisation in 2 dimensions

$$P_k^{wh} = \sum_{\boldsymbol{j^n} \in J} \sum_{\boldsymbol{k^n} \in K} \lambda_{\boldsymbol{j^n},\boldsymbol{k^n}} P_{(k)\boldsymbol{j^n}}^{wh} \quad (9.21)$$

$$f_{w,ESP} = \sum_{\boldsymbol{j^n} \in J} \sum_{\boldsymbol{k^n} \in K} \lambda_{\boldsymbol{j^n},\boldsymbol{k^n}} f_{(k,ESP)\boldsymbol{k^n}} \quad (9.22)$$

$$q_{w,ESP} = \sum_{\boldsymbol{j^n} \in J} \sum_{\boldsymbol{k^n} \in K} \lambda_{\boldsymbol{j^n},\boldsymbol{k^n}} q_{(k,ESP)\boldsymbol{j^n},\boldsymbol{k^n}} \quad (9.23)$$

$$\sum_{\boldsymbol{j^n} \in J} \sum_{\boldsymbol{k^n} \in K} \lambda_{\boldsymbol{j^n},\boldsymbol{k^n}} = 1 \quad (9.24)$$

$$\delta_{\boldsymbol{j^n}} = \sum_{\boldsymbol{k^n} \in K} \lambda_{\boldsymbol{j^n},\boldsymbol{k^n}} \quad \forall\, \boldsymbol{j^n} \quad (9.25)$$

$$\delta_{\boldsymbol{k^n}} = \sum_{\boldsymbol{j^n} \in J} \lambda_{\boldsymbol{j^n},\boldsymbol{k^n}} \quad \forall\, \boldsymbol{k^n} \quad (9.26)$$

$$\lambda_{\boldsymbol{j^n},\boldsymbol{k^n}}, \delta_{\boldsymbol{j^n}}, \delta_{\boldsymbol{k^n}} \ge 0 \quad (9.27)$$

$$\delta_{\boldsymbol{j^n}} \; and \; \delta_{\boldsymbol{k^n}} \; are \; SOS2 \quad (9.28)$$

Piecewise linearisation in 1 dimension

$$P_k^{wh} = \sum_{\boldsymbol{j^n} \in J} \lambda_{\boldsymbol{j^n}} P_{(k)\boldsymbol{j^n}}^{wh} \quad (9.29)$$

$$q_w = \sum_{\boldsymbol{j^n} \in J} \lambda_{\boldsymbol{j^n}} q_{(k)\boldsymbol{j^n}} \quad (9.30)$$

$$\sum_{\boldsymbol{j^n} \in J} \lambda_{\boldsymbol{j^n}} = 1 \quad (9.31)$$

$$\lambda_{\boldsymbol{j^n}} \; is \; SOS2 \quad (9.32)$$

Linearising bilinear terms of type ($C_1 \cdot C_2$ and $B \cdot C$)

$$C_1 \cdot C_2 = \xi_1^2 - \xi_2^2 \quad (9.33)$$

$$\boldsymbol{L}_1 \le C_1 \le \boldsymbol{U}_1; \quad \boldsymbol{L}_2 \le C_2 \le \boldsymbol{U}_2 \quad (9.34)$$

$$\xi_1 = 0.5(C_1 + C_2); \quad 0.5(\boldsymbol{L}_1 + \boldsymbol{L}_2) \le \xi_1 \le 0.5(\boldsymbol{U}_1 + \boldsymbol{U}_2) \quad (9.35)$$

$$\xi_2 = 0.5(C_1 - C_2); \quad 0.5(\boldsymbol{L}_1 - \boldsymbol{U}_2) \le \xi_2 \le 0.5(\boldsymbol{U}_1 - \boldsymbol{L}_2) \quad (9.36)$$

$$\tau = B \cdot C; \;\; 0 \le C \le \boldsymbol{U} \quad (9.37)$$

$$\tau \le \boldsymbol{U} \cdot B \quad (9.38)$$

$$\tau \ge \mathrm{C} - \boldsymbol{U}(1 - B) \quad (9.39)$$

$$\tau \ge 0; \quad \tau \le \mathrm{C} \quad (9.40)$$

Proxy model structure $$q_{o,ESP} = \alpha_0 + \alpha_1 P_{wh} + \alpha_2 f_{ESP} + \alpha_3 P_{wh}^2 + \alpha_4 f_{ESP}^2 + \alpha_5 P_{wh} f_{ESP} \quad (9.41)$$

A better representation of piecewise linear functions was proposed by Beale and Tomlin (1970) based on the convex combination of $\boldsymbol{\lambda_{P,v}}$. They proposed that only 2 consecutive weighting variables can be non-zero in the branch and bound (BB) algorithm. These sets are named Special Ordered Sets of Type II (SOS2) and are implemented in this study. The MINLP formulation is linearised in 3 ways to generate MILPs; the computational performance of these 4 formulations (including the MINLP) are compared. The first MILP formulation (MILP-3) applies standard algebraic transformation and SOS2 constraints to linearise nonlinear terms (quadratic and bilinear terms – products of 2 continuous variables and products of a continuous and binary variable) in the MINLP formulation using 3 breakpoints.

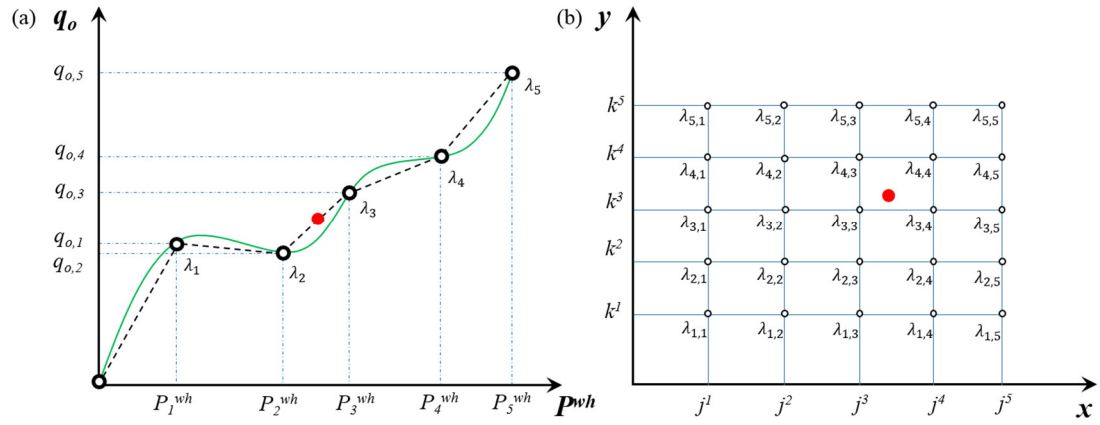

Figure 9.3. Piecewise linearization in 1 (a) and 2 (b) dimensions.

The second MILP formulation (MILP-5) uses 5 breakpoints instead; the third (MILP-LKT) directly utilises the look-up data tables for linear interpolation in 1 and 2 dimensions. Table 9.1 presents the detailed formulations for the MINLP and MILP, respectively. The aim is to maximise the objective function (in terms of the Net Present Value – *NPV*, Eq. 9.5); where the Revenue from Oil Production (ROP) and Cost of Water Production (CWP) are given by Eqs. 9.6 and 9.7, respectively; r_o is the oil price (USD/STB), r_{wt} denotes the water production unit cost (USD/STB), and N_{prod} is the number of wells. Eq. 9.8 ensures that the wellhead pressure (P^{wh}) is tightly bounded. The proxy models for the Naturally Flowing (NF) well, ESP well, PCP well and pipelines are given by Eqs. 9.8–9.11 respectively; q represents the flowrate, f_{ESP} the ESP frequency, Ω, the PCP impeller rotation speed and ΔP_p, the pipeline pressure drop.

The indices o, w, p, k, l, wh, m, s represent the oil phase, water phase, all phases, wells, pipelines, wellheads, manifolds, and separators respectively. Whereas, P^m and P^s denote the manifold and separator pressure. Binary variables $y_{k,p}$ assigned to each well ensure that the produced fluids from a well are routed by the choke (Eq. 9.13) to one of the pipelines. Similarly, $z_{l,s}$ in Eq. 9.14 ensures that the fluids in the pipelines are routed to the separator. The mass balance constraint between wells and pipelines is represented by Eq. 9.15; whereas, Eq. 9.16 ensures material balance between the pipelines and the separators (which operate at a fixed pressure).

The selection of only 1 binary variable is enforced using Eqs. 9.17–9.18. The constraint defined by Eq. 9.19 ensures the target separator pressure is met, while the liquid capacity constraints of the separators are represented by Eqs. 9.20. The procedure for linearising functions in 2D and 1D are shown in Eqs. 9.21–9.32, respectively; where $\boldsymbol{j}^n$ and $\boldsymbol{K}^n$ represent the breakpoints associated with the different variables. Bilinear terms which occur in the MINLP formulation as shown in the typical proxy model structure (Eq. 9.41) are linearised using Eqs. 9.33–9.40. In these equations, C represents, a continuous variable, and B a binary variable; $\boldsymbol{L}$ and $\boldsymbol{U}$ denote the lower and upper bounds of a continuous variable. ξ and τ are additional variables introduced in the linearisation procedure. BONMIN (v.1.8.6), CBC (v.2.9.8), SCIP (v.3.2.1 & v.5.0.1) and CPLEX (v.12.8.0.0) are adopted for solving the MINLP and MILP formulations respectively. We present 3 case studies, which are all solved using the formulation described in Table 9.1.

9.2 Case Study Description

9.2.1 Case Study 1 (CS 1)

In this case study (Fig. 9.4), a production network consisting of 4 production wells, 4 choke valves, 2 manifolds, 2 pipelines and 3 separators is optimised. Flow routing constraints at 2 levels (from wells to manifolds and from pipelines to separators) are applied to the MINLP and MILP formulations respectively. A wellhead pressure range of 300 – 380 psia is employed for all wells in the proxy model development phase. Further details of the production network, which were the input parameters for the modelling phase of the procedure are given in Table 9.2.

Table 9.2. Reservoir, well and pipeline parameters for CS1 & CS2.

Parameter	W–1	W–2	W–3	W–4	P–1	P–2
Reservoir pressure (psia)	3,800	3,800	3,800	3,800	–	–
Well type	Vertical	Deviated	Vertical	Deviated	–	–
Well PI (STB/day/psi)	1.7	3.7	2.5	3.3	–	–
GOR (SCF/STB)	500	500	500	500	–	–
WC (%)	20-32	20-32	20-32	20-32	–	–
TVD (ft)	10,000	10,000	10,000	10,000	–	–
Tubing diameter (in)	3.5	3.5	4.5	4.5	–	–
Pipeline length (ft)	–	–	–	–	6,000	4,000
P-ID (in)	–	–	–	–	10	11
P-IR (in)	–	–	–	–	0.001	0.001

RP: Reservoir Pressure; P-ID: Pipeline Internal Diameter; P-IR: Pipeline Internal Roughness; PI: Productivity Index

9.2.2 Case Study 2 (CS 2)

This case study is similar to CS1 in terms of size and the parameters shown in Table 9.2. However, we increase the optimisation search space in this case study by widening the wellhead pressure range (50 – 500 psia). We then examine the performance of this case study in comparison to CS1, for differences in the optimal routing structures, NPV and computation time.

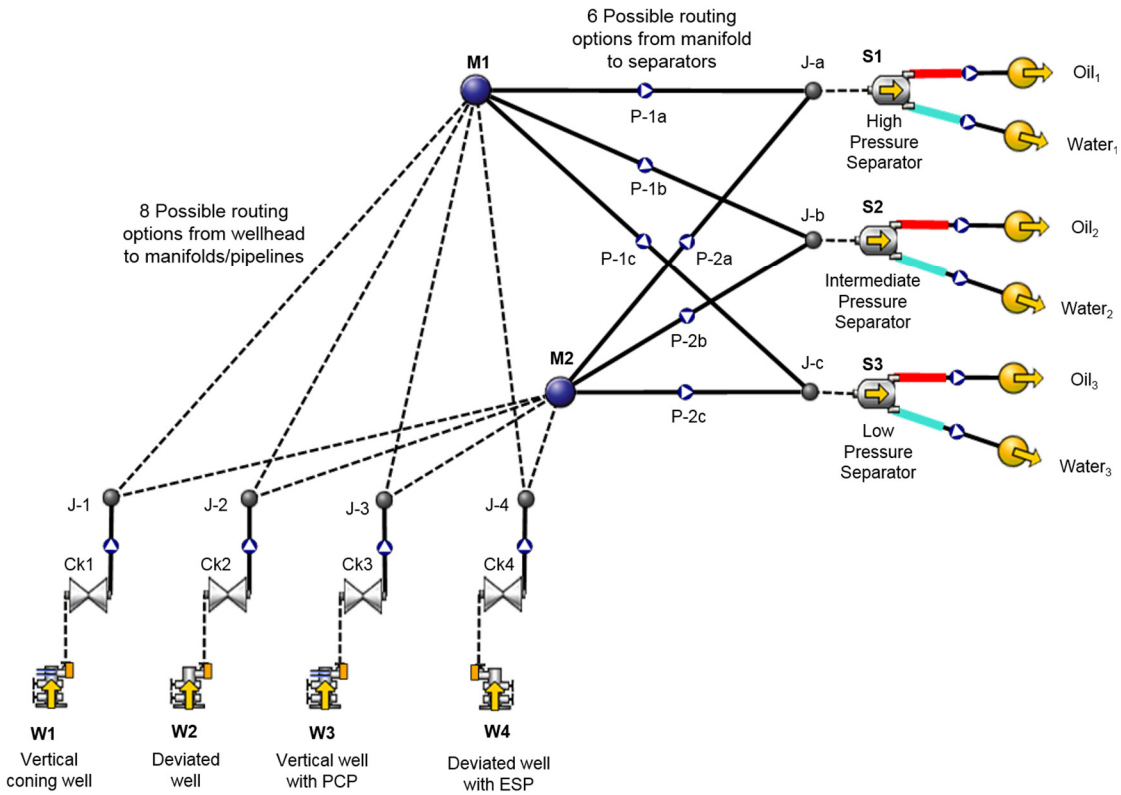

Figure 9.4. Surface production network and routing superstructure for CS1 and CS2.

9.2.3 Case Study 3 (CS 3)

In this case study (Fig. 9.5), a larger production network consisting of 12 production wells with varying operating modes is solved. CS3 demonstrates the scalability and adaptability of the proposed formulation to bigger production systems. The wider wellhead pressure range is adopted here, and the parameters for each well are shown in Table 9.3.

Table 9.3. Reservoir, well and pipeline parameters for CS3.

Parameter	**W–1**	**W–2**	**W–3**	**W–4**	**W–5**	**W–6**	**P–1**
Reservoir pressure (psia)	3,800	3,800	3,800	3,800	3,800	–	–
Well type	Vertical	Deviated	Vertical	Vertical	Deviated	Deviated	–
Well PI (STB/day/psi)	1.5	3.7	2	2.5	2.5	2.5	–
GOR (SCF/STB)	500	500	500	500	500	500	–
WC (%)	20-32	20-32	20-32	20-32	20-32	20-32	–
TVD (ft)	10,000	10,000	10,000	10,000	10,000	10,000	–
Tubing diameter (in)	3.5	3.5	4.5	4.5	4.5	4.5	–
Pipeline length (ft)	–	–	–	–	–	–	6,000
PID (in)	–	–	–	–	–	–	10
PIR (in)	–	–	–	–	–	–	0.001
Parameter	**W–7**	**W–8**	**W–9**	**W–10**	**W–11**	**W–12**	**P–2**
Reservoir pressure (psia)	3800	3800	3800	3800	3800	–	–
Well type	Vertical	Deviated	Vertical	Deviated	Vertical	Deviated	–
Well PI (STB/day/psi)	1	3.1	1.2	4.5	1.8	1.9	–
GOR (SCF/STB)	500	500	500	500	500	500	–
WC (%)	20-32	20-32	20-32	20-32	20-32	20-32	–
TVD (ft)	10,000	10,000	10,000	10,000	10,000	10,000	–
Tubing diameter (in)	3.5	3.5	3.5	3.5	3.5	3.5	–
Pipeline length (ft)	–	–	–	–	–	–	4,000
PID (in)	–	–	–	–	–	–	11
PIR (in)	–	–	–	–	–	–	0.001

Other input data applied in the surface network simulator for data generation include the oil specific gravity (45 API) and the pipeline temperature (100°F). The separators liquid handling capacities and operating pressures are also shown in Table 9.4.

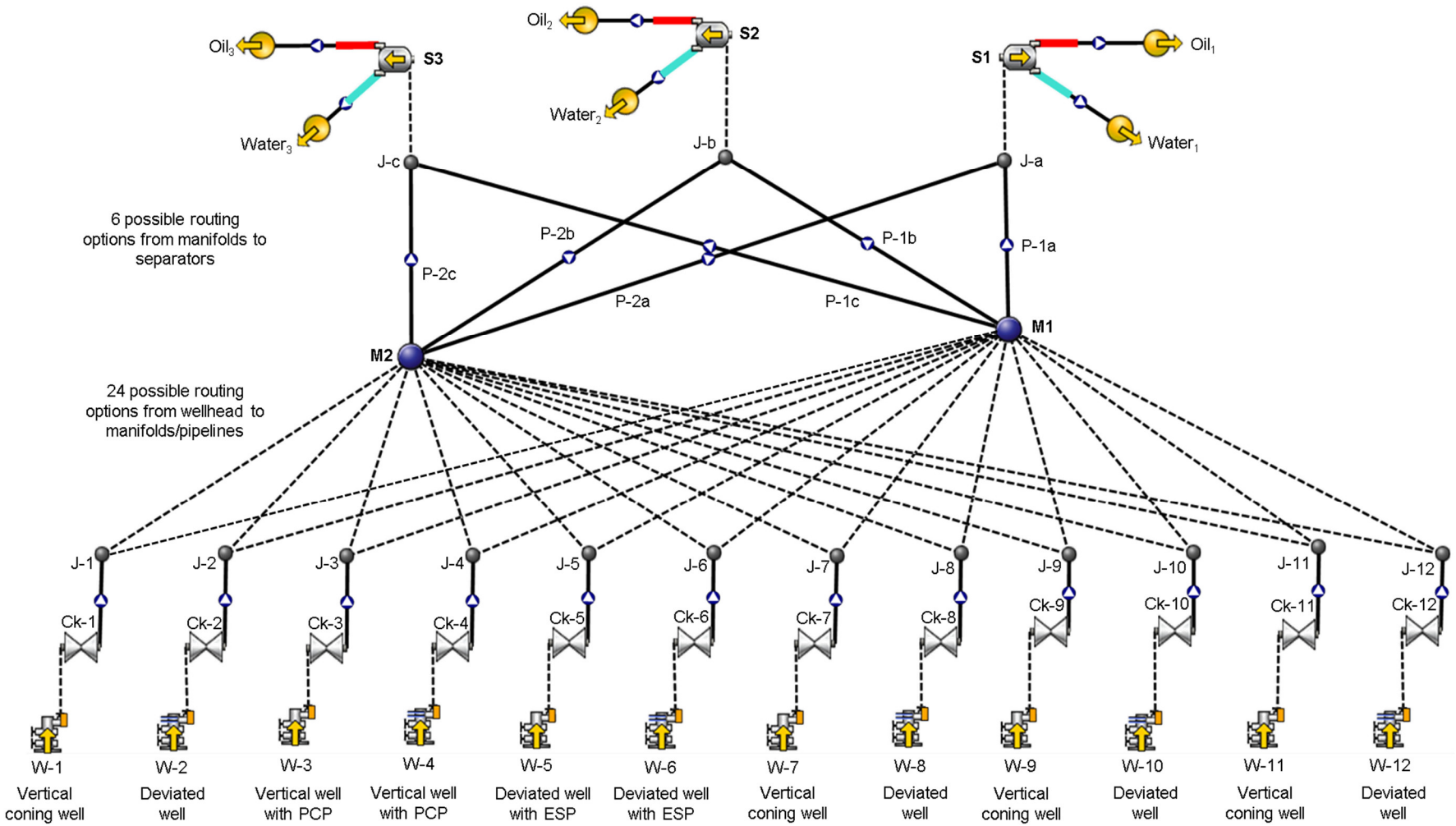

Figure 9.5. Surface production network and routing superstructure for CS3.

Table 9.4. Separator capacities and operating pressures for all cases studies.

Case study	Separator	Operating pressure (psia)	Liquid capacity (STB/day)
Case Study 1 (CS1)	Sep – 1	45	8,000
	Sep – 2	35	10,000
	Sep – 3	25	12,000
Case Study 2 (CS2)	Sep – 1	35	12,000
	Sep – 2	25	10,000
	Sep – 3	20	8,000
Case Study 3 (CS3)	Sep – 1	35	25,000
	Sep – 2	25	18,000
	Sep – 3	20	15,000

9.3 Optimisation Results

The proposed formulations were programmed in MATLAB® R2016a, using OptiToolbox v2.28 (Currie and Wilson, 2012) and solved on an Intel Core i7-6700 processor at 3.40 GHz running on a 64 bit Windows workstation with 16GB of RAM. By implementing the proposed formulations, repeated calls to the simulator are avoided, thus enabling faster computations. The three separate MILP formulations and the MINLP problem are solved to optimise the production networks of CS1, CS2 and CS3 respectively.

9.3.1 Case Study 1

The MILP-LKT formulation consisted of 25 polytopes (squares) for the well performance function (5 breakpoints for the ESP frequency/rotational speed and 5 breakpoints for the wellhead pressure). For the pipelines, 144 polytopes (squares) were adopted (12 breakpoints for the oil and water phases respectively). This resulted in a total of 8,702 variables; this is significantly larger than the number of variables required in the other formulations (as shown in Table 9.5). Despite this number of variables, the MILP-LKT formulation is solved in a shorter time compared to the MINLP formulation with only 36 variables. This increase in problem size (number of constraints and variables) that ensues with an increasing number of data points makes the implementation of the SOS formulation laborious; this is a significant drawback of this formulation; hence, it is only suitable for low dimensional problems. With the MINLP, the increase in the number of data points would hardly affect the approximations of the simulator output. In this regard, the MINLP formulation can be considered more scalable compared to the MILP. The

convergence of the proposed formulations to different optimal routing configurations (Table 9.5) is an indication of the non-convexity of the optimisation problem. However, good quality solutions were obtained from all formulations, as demonstrated in the relative gap obtained (Table 9.5). The MINLP formulation gave the best solution in terms of the NPV.

Table 9.5. Computational performance of optimisation formulations for CS1.

Optimisation formulation	MINLP	MILP-3 (SOS2)	MILP-5 (SOS2)	MILP-LKT (SOS2)
Solver used	BONMIN	CPLEX	CPLEX	CPLEX
Number of constraints	34	184	184	340
Number of variables	36	134	170	8702
Relative gap (%)	0.00	0.00	0.00	0.00
Solution time (s)	0.536	0.111	0.152	0.287
Number of nodes	0	229	253	292
NPV (USD)	989,228	979,934	986,832	979,261
Total oil production rate (STB/day)	15,219	15,076	15,182	15,066
Total water production rate (STB/day)	3,803	3,767	3,794	3,766

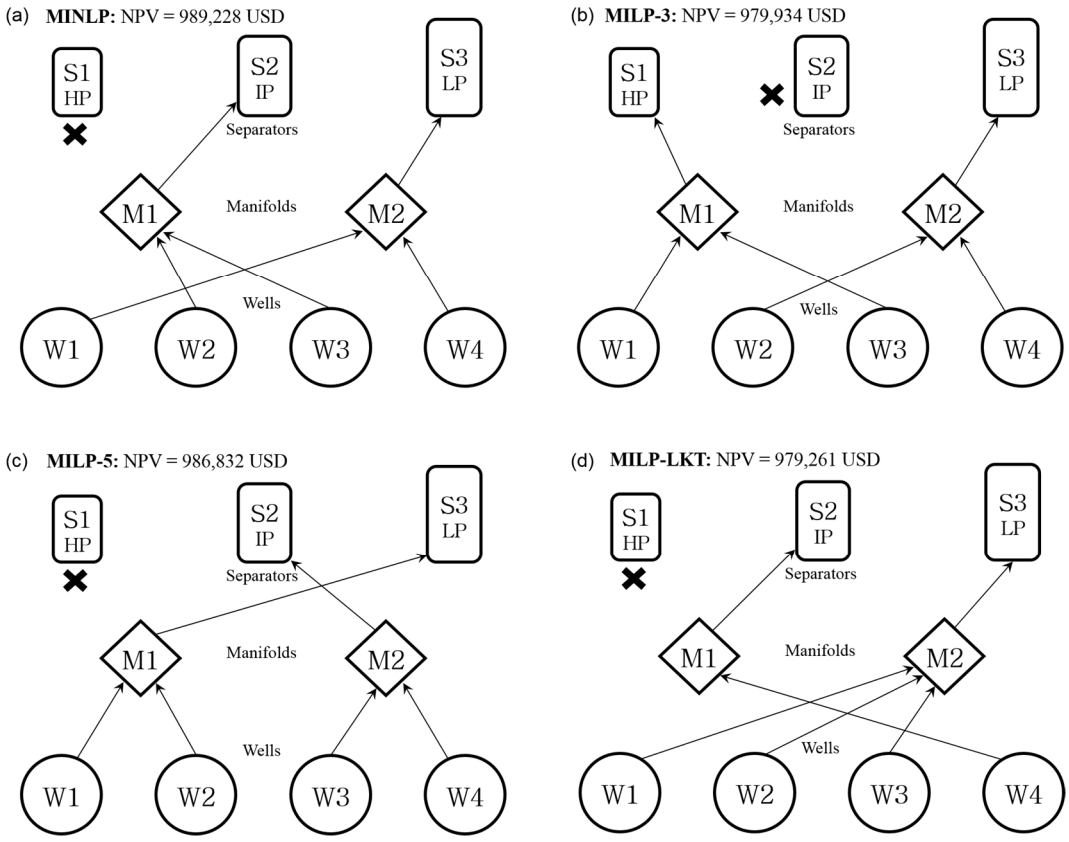

Figure 9.6. Optimal discrete routing structure for all formulations of CS1.

Our computational analysis has also shown that the improvement in resolution quality affects the solution quality of the MILP-5 and MILP-3 formulations. With 5 breakpoints (MILP-5), the NPV obtained is closer to that of the MINLP compared to the lower resolution formulation, consisting of 3 breakpoints (MILP-3). The MILP-LKT formulation gave the lowest NPV (1% lower than the MINLP). This may be attributed to the table resolution implemented. Although water coning behaviour is a known source of nonlinearity in the wellbore model, the quadratic proxy model is able to accurately capture this smooth nonlinear behaviour, and so do the MINLP, MILP-3 and MILP-5 formulations, compared the MILP-LKT formulation. The complex multiphase flows between each network component and the narrower search space (in terms of the wellhead pressure) is another possible explanation. However, as will be presented in CS2 and CS3 (with a wider optimisation search space), the MILPs show improved results.

It can also be observed that the high-pressure separator with lower capacity (S1) is the least preferred option for routing fluids from the manifolds (Fig. 9.6). The pipeline diameter and length, and the high-pressure drop that ensues, make it difficult for fluids to be delivered to S1, which operates at 45 psia compared to S2 and S3 at 35 psia and 25 psia respectively. The algorithm has shown proper utilisation of separator capacities for routing the fluids. As shown in Table 9.5, the MILP formulations converge faster than the MINLP.

Furthermore, the time required for proxy model development if incorporated, will further make the MINLP slower compared to the MILP (which directly use the table data points). It can also be observed that the oil and water production rates of the respective formulations are similar, despite the different optimal routing structures obtained. This indicates that the algorithmic treatment of discrete variables can be complicated, especially when they exist at different levels. However, the number of nodes utilised for finding the optimal solution in all formulations reflects the efficiency of the CPLEX solver (which uses the Branch and Bound algorithm). However, on applying the CBC solver (based on the Branch and Cut algorithm) to our problem, the number of nodes reduces by an order of magnitude, although with a higher relative gap and a longer computational time. A detailed comparison of solver performances is presented in Section 9.4.

9.3.2 Case Study 2

Fig. 9.7 shows the optimal routing structure for CS2. Although different optimal routing strategies are obtained between the formulations, the MILP-5 and MINLP formulations yield exactly the same optimal configuration.

Table 9.6. Computational performance of optimisation formulations for CS2.

Optimisation formulation	MINLP	MILP-3 (SOS2)	MILP-5 (SOS2)	MILP-LKT (SOS2)
Solver used	BONMIN	CPLEX	CPLEX	CPLEX
Number of constraints	34	184	184	340
Number of variables	36	134	170	8702
Relative gap (%)	0.0057	0.00	0.00	0.00
Solution time (s)	23.4	0.182	0.188	0.460
Number of nodes	46	316	388	514
NPV (USD)	1,013,938	979,934	986,832	979,261
Total oil production rate (STB/day)	16,083	16,202	16,207	15,787
Total water production rate (STB/day)	5,593	5,635	5,637	5,494

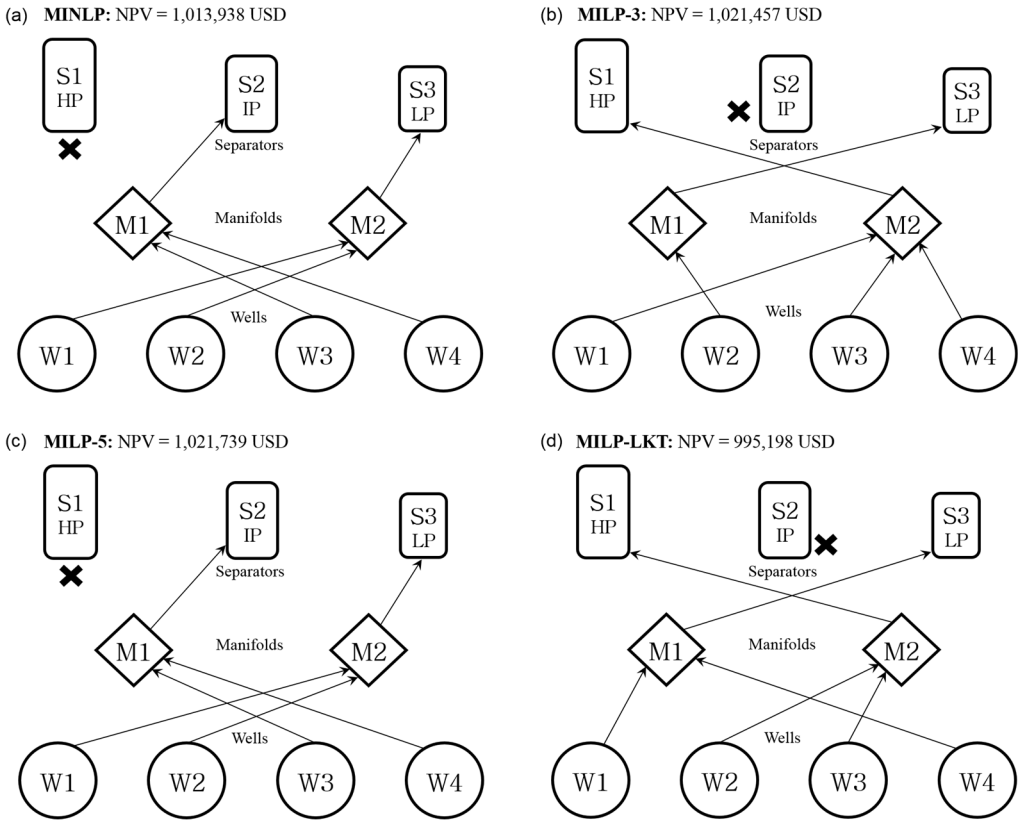

Figure 9.7. Optimal discrete routing structure for all formulations of CS2.

Furthermore, the MILP-3 and MILP-5 formulations yield improved oil production rates (Table 9.6) and correspondingly increased NPVs compared to the MINLP formulation. Thus, it can be stated that widening the optimisation search space causes the local trapping of the MINLP formulation at suboptimal solutions; whereas, MILP-3 and MILP-5 are able to further explore the optimisation search space for improved results. However, the MILP-LKT formulation does not yield improved results compared to the MINLP. Again, this may be attributed to the adopted table resolution, which will affect the accuracy since the obtained solutions lie on linear segments generated by the SOS2 formulation.

The MILP-LKT formulation is also unable to extrapolate beyond the sampled region in which the quadratic approximation of the MINLP was fitted. Thus, the MINLP, MILP-3 and MILP-5 formulations can check for the existence of better-operating conditions. It is also observed that improving the resolution quality (i.e. when the number of sampled breakpoints is increased from MILP-3 to MILP-5) positively impacts the performance of the MILP formulation. The MILP-5 formulation reached a better solution, yielding a slight increase in the NPV. Compared to the MILP formulations which are solved in less than a second, the MINLP solution to CS2 was obtained in 23.4 s (without exploring the possibility of parallel computing).

These rapid computational times are due to the decomposable nature of the entire production network with proxy models developed for each component. Hence the simulator search space is considerably reduced (fewer dimensions) compared to the scenario in which an optimisation search occurs over the entire network. Furthermore, as shown in Fig. 9.7, S3 is the most preferred separator; since fluids are routed to this vessel after solving all formulations. This is attributable to its lower operating pressure, which in turn accommodates a lower operating wellhead pressure and thus, increased production. This was also observed in CS1.

9.3.3 Case Study 3

In this case study, we increased the number of production wells in the network (from 4 to 12) and evaluated the performance of the MINLP, MILP-3 and MILP-5 formulations. As a result of the number of variables involved in the MILP-LKT formulation and the lower NPV's obtained compared to the other formulations in CS1 and CS2, the MILP-

LKT formulation was not applied in CS3. As previously observed, improved solutions (in terms of the total oil production and NPV) are obtained for the MILPs in comparison to the MINLP (Table 9.7). It is thus illustrated via CS2 and CS3 that, increasing the optimisation search space favours the MILPs over the MINLPs.

Table 9.7. Computational performance of optimisation formulations for CS3.

Optimisation formulation	MINLP	MILP-3 (SOS2)	MILP-5 (SOS2)
Solver used	BONMIN	CPLEX	CPLEX
Number of constraints	80	396	396
Number of variables	78	270	334
Relative gap (%)	0.0327	0.00	0.00
Solution time (s)	607.26	0.498	0.438
Number of nodes	758	25,644	22,514
NPV (USD)	2,597,821	2,609,320	2,612,370
Total oil production rate (STB/day)	41,342	41,520	41,571
Total water production rate (STB/day)	14,805	14,854	14,880

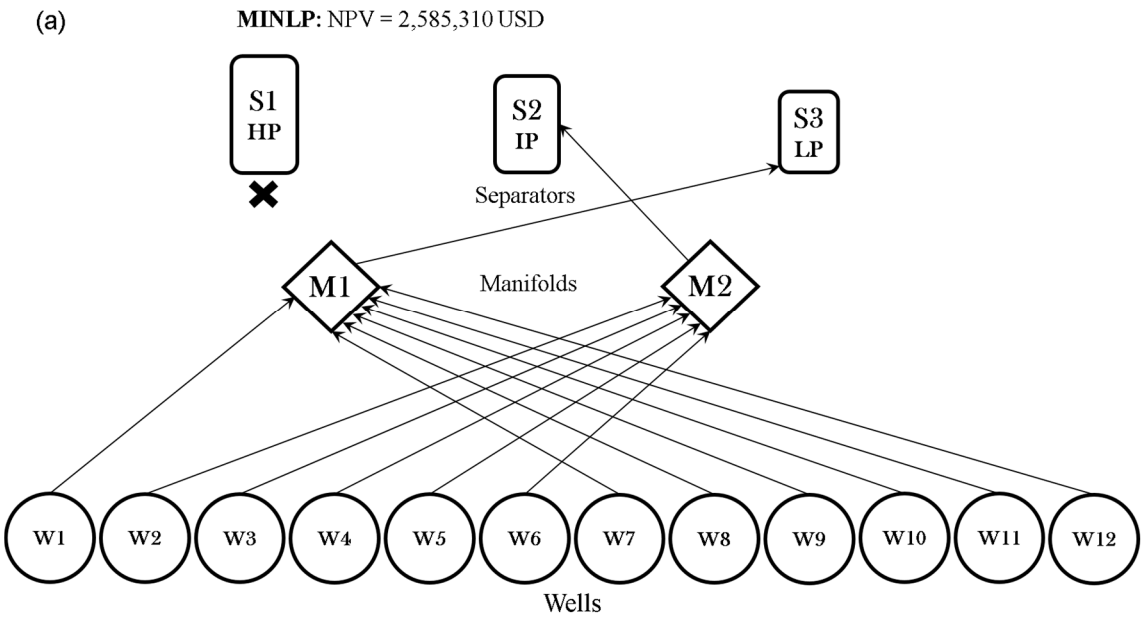

Figure 9.8a. Optimal discrete routing structure for all formulations of CS3.

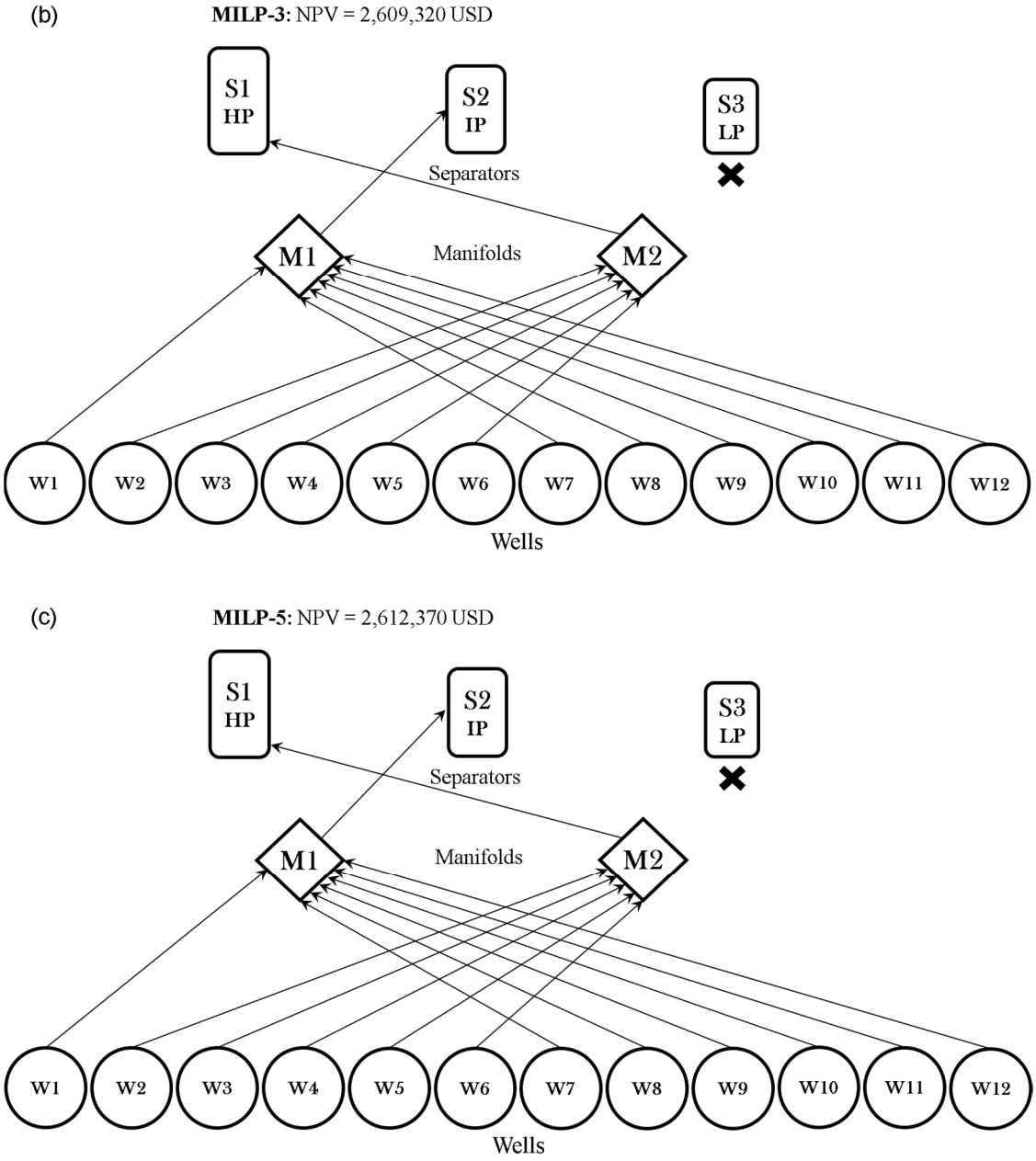

Figure 9.8 b,c. Optimal discrete routing structure for all formulations of CS3.

While the MILPs are solved in less than a second (using CPLEX) for this case study, the MINLP takes approximately 10 mins to solve with a higher relative gap compared to the MILP solutions; thus demonstrating the increased computational efficiency of the proposed MILPs (Table 9.7). Compared to CS1 and CS2, the optimal routing configurations obtained in this case study (CS3) are somewhat similar. Fig. 9.8 shows the same routing structure from wells to manifolds for all formulations. However, the manifold-to-separator routings are different for the MILPs and MINLPs. In this case study, S2 is the most utilised, as seen in Fig. 9.8.

9.4 Solver Performance and Comparison with PIPESIM's™ Network Optimiser

Table 9.8 summarises the computational performance in terms of the number of nodes, relative gap and the solution times for the different optimisation solvers (CBC, CPLEX, SCIP and BONMIN) applied to the respective formulations. Table 9.8 shows that the fewest number of nodes are utilised by the CBC solver, although with the highest relative optimality gap compared to the other solvers. However, the overall solution quality obtained from all solvers is reasonable, as illustrated by the obtained optimality gaps. As expected, longer simulation times are observed with the larger case study (CS3); nonetheless, CPLEX still solves this problem in less than a second; thus making it the best performing solver for our presented case studies compared to CBC and SCIP. In this section, the performance of the global optimisation solver (SCIP) in solving the MINLPs for the three case studies is also reported in comparison to the local MINLP solver BONMIN. It is observed that SCIP slightly outperforms BONMIN in terms of the optimality gap and the NPVs obtained, but is still inferior to the MILP solutions. However, the computational time required by the SCIP solver is significantly higher than the other solvers (Tables 9.8).

One of the case studies presented in a recent study of Gupta and Grossmann (2012) discusses a similar observation of inferior performance of a global MINLP solver (in their case, BARON) compared to solutions obtained from an equivalent MILP formulation (solved by CPLEX). Computational experiments performed and published by Gondzio and Yildirim (2015) echo and corroborate this observation. This phenomenon may be attributed to several factors: model complexity, non-convexities, model sensitivity to perturbed inputs, optimisation search space and, most importantly, the reformulation strategy applied. By reformulating the problem as an MILP, we address the non-convexity challenges of MINLPs and the difficulties they pose to global MINLP solvers (provided all functions are separable); thus, better performance can be achieved. This is why all 3 solvers applied to the MILP problem (SCIP, CPLEX, CBC) produce the same NPV, except CS3 (SCIP fails to converge, Table 9.9). Besides applying the standard Branch-and-Bound or Branch-and-Cut or decomposition algorithms, solvers may also include the implementation of special presolving/preprocessing procedures to which the disparities in performance can be attributed. A more detailed investigation exceeds our scope but

seems in order, considering the two cited precedents which feature similar performance observations. We also compare the performance of PIPESIM's™ (v. 2019.3) new optimisation toolbox with our optimisation methodology. In comparison to this toolbox, we generally observe faster solution times for all solvers with the presented formulations (except in CS3, MINLP-BONMIN); thus demonstrating the superior performance of our implemented formulation (Fig. 9.9). Although the computational time required is expected to increase with larger production networks, the fast solution times obtained herein are more attributable to the nature of our optimisation formulation than the size of the production network. The network size (CS3) considered herein is comparable to those utilised previous comparative studies such as Silva and Camponogara (2014). Furthermore, by using the SCIP solver for the MINLP problem, a long solution time of up to 36 mins is obtained as reported in Table 9.8; thus demonstrating that the run times achieved are also dependent on the type of optimisation solver implemented. The implemented optimisation methods see decreased speed when the network components increase. Moreover, the SOS2 formulations are significantly affected because of the drastic increase in the number of data points and variables with bigger-sized production systems (more wells, manifolds, pipelines, and separators). However, this will hardly be a problem for the MINLP (when evaluating the proxy models). Hence, there is always a trade-off between the quality of obtained solutions, the solution time and the model development time. Thus, the increased difficulty of handling SOS2-based formulations is reflected in the number of variable involved, which require significant effort for their implementation/development compared to the MINLP with considerably fewer variables.

It is particularly observed in Table 9.8 that the time taken by the CBC solver to find a solution for MILP3 is higher than that for MILP5. A possible explanation to this is that stronger/more rigorous branching and interpolation are required for the optimisation problem with just 3 breakpoints (MILP3) compared to the problem with 5 (MILP5), as reported in the iteration history of the CBC solver (for a good solution to be found). It may be argued that the time required for this strong branching supersedes the extra computational effort resulting from an increased number of variables in the MILP5 formulation. However, this is not the case with other solvers.

Table 9.8. Summary of the computation performances of different solvers.

Solution Property	Optimisation Formulation	CS1 (4 Wells)			CS2 (4 Wells)			CS3 (12 Wells)		
		CBC	CPLEX	SCIP	CBC	CPLEX	SCIP	CBC	CPLEX	SCIP
Number of Nodes	MILP3	2	229	87	6	316	28	8,563	25,644	6,517
	MILP5	24	253	347	7	388	222	1,734	22,514	10,000
	MILP-LKT	150	292	7	117	514	114	–	–	–
	MINLP (BONMIN)	0			46			758		
	MINLP (SCIP)	39			85			4,222,889		
Relative Gap	MILP3	0.029	0.000	0.000	0.032	0.000	0.000	0.018	0.000	0.000
	MILP5	0.022	0.000	0.000	0.032	0.000	0.000	0.016	0.000	0.021†
	MILP-LKT	0.016	0.000	0.000	0.077	0.000	0.000	–	–	–
	MINLP (BONMIN)	0.000			0.006			0.033		
	MINLP (SCIP)	0.000			0.000			0.000		
Solution Time (sec)	MILP3	0.05	0.11	0.17	0.06	0.18	0.16	35.04	0.50	14.46
	MILP5	0.08	0.15	0.46	0.09	0.19	0.38	9.12	0.44	35.50
	MILP-LKT	5.42	0.29	1.14	2.65	0.40	4.13	–	–	–
	MINLP (BONMIN)	0.54			23.41			607.26		
	MINLP (SCIP)	0.73			1.27			2134.10		
	PIPESIM™	**28.21**			**31.11**			**178.12**		

†: *SCIP terminated after reaching the maximum number of nodes.*

Table 9.9. NPV summary for all formulations and optimisation solvers used.

Solution Property	Optimisation Formulation	CS1 (4 Wells)			CS2 (4 Wells)			CS3 (12 Wells)		
		CBC	CPLEX	SCIP	CBC	CPLEX	SCIP	CBC	CPLEX	SCIP
NPV (USD)	MILP3	979,934	979,934	979,934	1,021,457	1,021,457	1,021,457	2,609,320	2,609,320	2,609,320
	MILP5	986,832	986,832	986,832	1,021,739	**1,021,739**	1,021,739	2,612,370	**2,612,370**	2,596,330†
	MILP-LKT	979,261	979,261	979,261	995,198	995,198	995,198	–	–	–
	MINLP (BONMIN)	**989,228**			1,013,938			2,597,821		
	MINLP (SCIP)	**989,230**			1,013,944			2,585,350		
	PIPESIM™	***912,000***			***912,000***			***2,437,896***		
NPV Increment (%)		8.47			12.03			7.16		

†: *SCIP terminated after reaching the maximum number of nodes.*

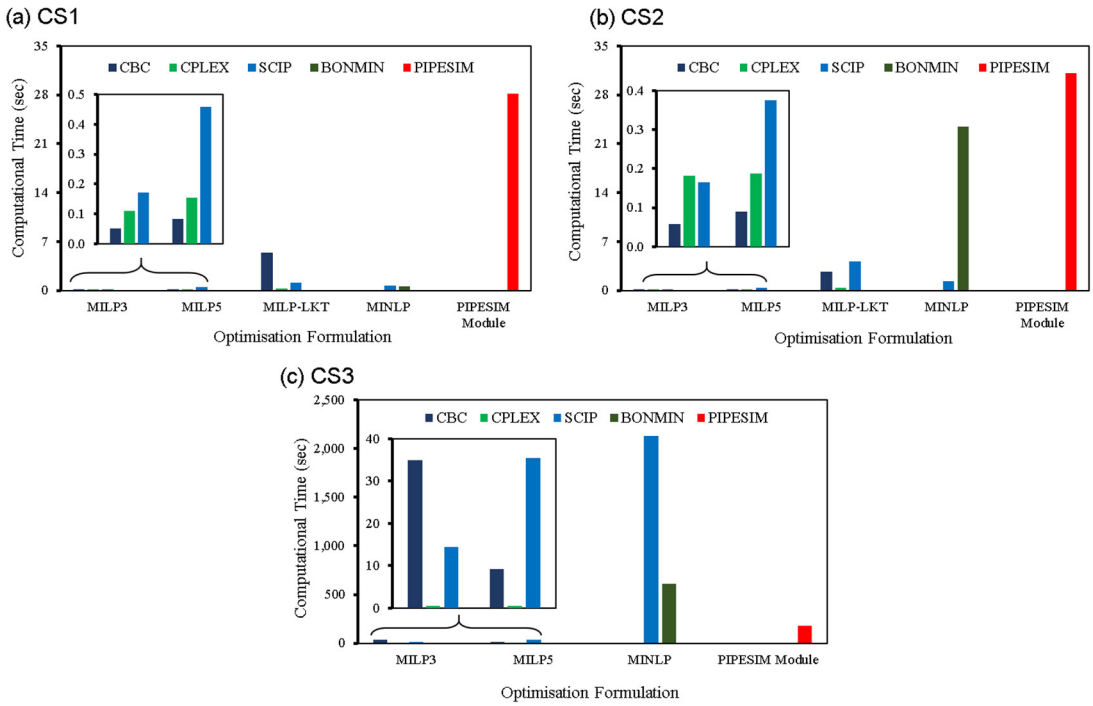

Figure 9.9. Comparison of computational times for the different optimisation solvers and case studies.

Table 9.9 and Fig. 9.10 summarise the obtained NPVs using all solvers for the different formulations in comparison to those obtained from PIPESIM's™ network optimisation module. It is worth mentioning that the NPVs in PIPESIM™ were calculated by optimising the oil production rate while constraining the water production rate according to the objective function) presented in Eq. 9.5. For all formulations, the obtained NPVs for CS1 and CS2 are the same. However, when the SCIP solver was applied to the MILP-5 formulation of CS3, a lower NPV was obtained compared to CBC and CPLEX. The reason for this observation is that the SCIP solver timed out when the maximum number of nodes was reached for the MILP5 problem of CS3. Regardless of the initial settings for the optimisation run, the solver did not converge to the global solution. This effect is also clearly observed in Table 9.8, where the relative optimality gaps are reported. However, CBC fully converged within the default setting of the relative optimality gap.

Compared to CS1, the NPVs obtained in CS2 are generally higher. By widening the optimisation search space (in terms of the operating wellhead pressures), increased oil production can thus be attained. However, depending on the field's operation, this range is often bound by constraints that prevent sand production due to excessively high drawdown pressures and inadequate fluid lifting capacity in the well tubing as a result of

liquid loading. Furthermore, it is observed that the NPVs obtained by applying PIPESIM's™ optimisation toolbox are 8%, 12% and 7% lower than our best-case scenario (in bold) for CS1, CS2 and CS3 respectively (Table 9.9). This also demonstrates the computational efficiency of the proposed formulation.

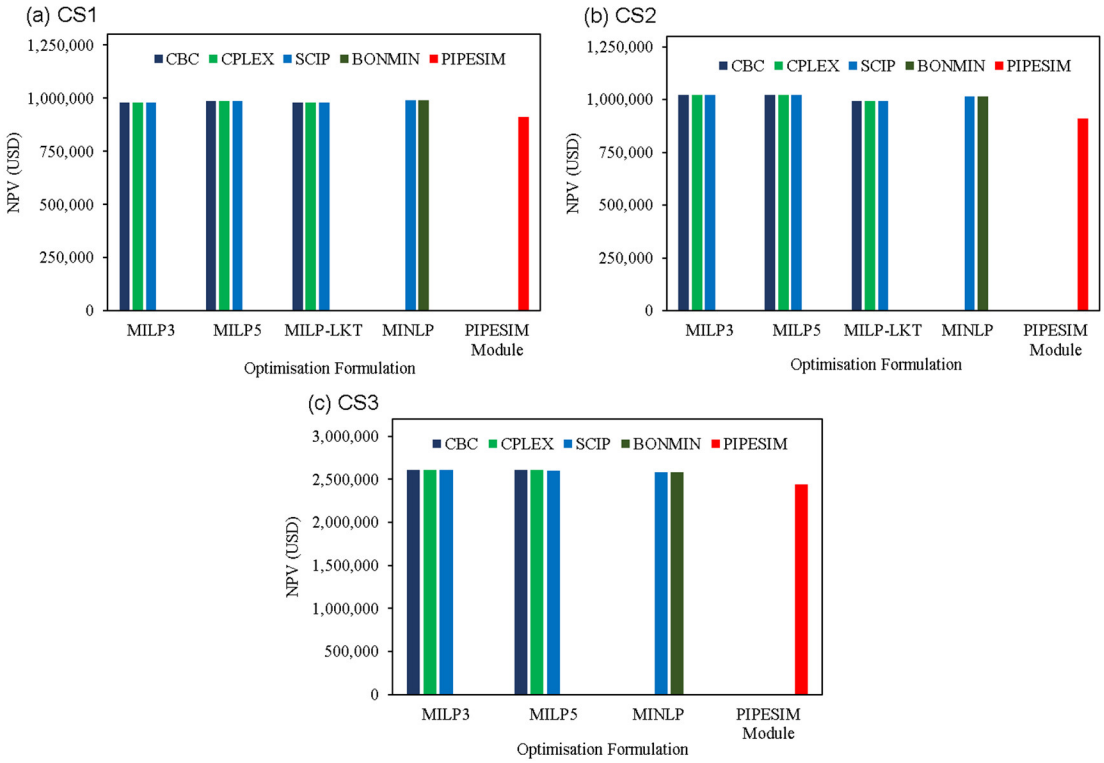

Figure 9.10. Comparison of the NPVs obtained for the different optimisation solvers and case studies.

The presented approach is thus useful for real-time decision support in the oil and gas industry considering its competing performance with an industry applied simulator and optimiser. However, it is important for further implementations of this method to incorporate network changes that extend the boundaries of its applicability. For example, the change in the physical properties of the system, reservoir dynamics, network expansion (addition of new wells and pipelines) and flow regime changes are possible occurrences that may significantly change the production data; thus, necessitating proxy model reconstruction and updates of the respective optimisation formulations (Ursin-Holm et al., 2014). The presented formulations are easily adaptable to these changes, with considerable effort required.

9.5 Chapter Conclusions

This study has proposed MINLP and MILP formulations for optimising production from a synthetic oil field consisting of 3 separators, 2 manifolds and 4-12 wells with complex downhole/multiphase flow physics. The nonlinear models were developed using regression analysis that resulted in algebraic polynomial models; whereas piecewise linear models were developed from production points sampled from the look-up table and via linearisation of the MINLP formulation. The following conclusions can be derived from the computational analyses performed herein.

- The resulting number of variables and the model development time for the MILP are significantly higher than that of the MINLP.
- Increased resolution of the MILP formulations from 3 to 5 breakpoints resulted in an improved NPV.
- CPLEX was the best performing solver with rapid computational speeds and low optimality gaps obtained for all MILP formulations.
- A computational analysis performed on the 4 formulations of CS1 showed superior performance of the MINLP formulation in terms of the NPV compared to the MILPs. However, for this case study (CS1), all formulations were solved in less than a second. Despite the similarities in the oil and water production rates of CS1, different optimal routing strategies are obtained for all formulations.
- Increasing the optimisation search space (in terms of the wellhead pressure) as demonstrated in CS2 and CS3 favours the MILP-3 and MILP5 formulations. Higher NPVs are obtained in comparison to the MINLP because of the reformulation, even vs. a global MINLP solver.
- Compared to PIPESIM's™ optimisation module, our optimisation formulation solves faster and yields higher NPVs.

Future research could analyse in greater detail how the obtained solution times scale up with increased problem size (e.g. for fields containing hundreds of wells, manifolds and separators). This will further verify the adaptability of these formulations for real-time decision support. Incorporating the effect of temperature on the pressure drop functions, as well as other downhole phenomena like sand production is also worth investigating.

Chapter 10 Infrastructural Planning & Well Placement Optimisation under Geological Uncertainty

So far, the optimisation of production system operations and scheduling over short- and long-term horizons has been presented. In this chapter, a more complex infrastructural optimisation problem is tackled – that of well placement under geological uncertainty. It is worth re-emphasising that incorporating specific geological knowledge about the reservoir into the optimisation problem is a vital step for the determination of feasible well locations that may be explored by the algorithm; thus enabling practical solutions. Although these optimisation methodologies may be prone to multiplicity of solutions after several runs for varying problem configurations, candidate solutions may be evaluated by the engineering and geology teams for the most practical and cost-effective implementation. Our focus in this study is thus an integration of vital geological considerations when carrying out well placement optimisation studies with robust algorithms.

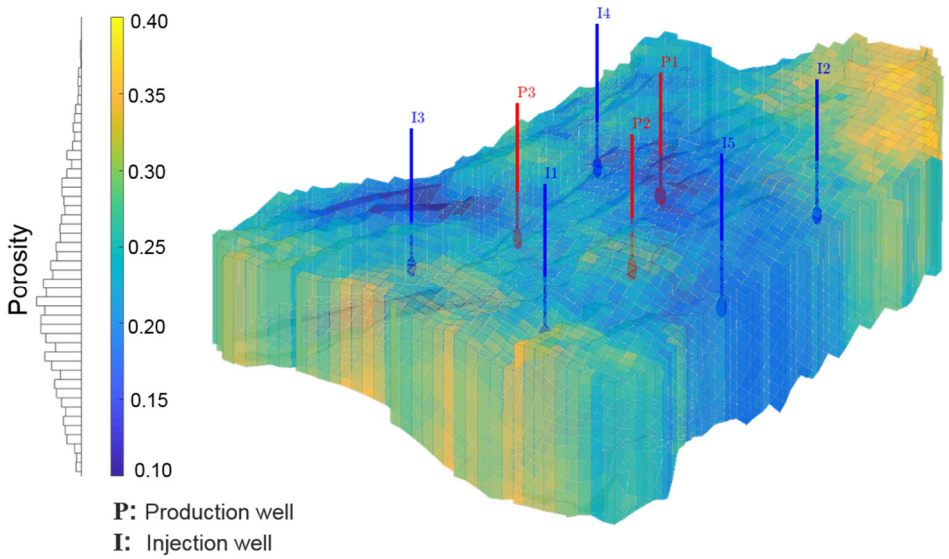

Figure 10.1. Reservoir model showing the spatial variability of the porosity and the initial well locations.

To capture the uncertainties in the subsurface geological/reservoir model in this work, geostatistical realisations of the model are obtained using available information (permeabilities and porosities). We also apply specialised algorithms within the MATLAB Reservoir Simulation Toolbox – MRST (interfaced with PETREL™) to optimally vary

the well locations and production rates, thus maximising the field's oil recovery. A new modification of an existing pseudowell-based injection well placement algorithm is presented herein with the application of adjoint-computed gradients of an auxiliary objective function (the Lorenz coefficient). The difficulty of this problem is characterised by the presence of discrete variables, a nonlinear and nonconvex objective function and complex constraints. The developed workflow is applied to a realistic case study, for which robust optimality is demonstrated using the worst-case realisation for the determination of optimal well locations and controls. A comparative investigation of optimising injection well location vs. simultaneous optimisation of injection and production well placement is also presented. In our presented case study, we further discover that increasing the optimisation search space does not necessarily guarantee improved results.

10.1 Static Reservoir Modelling

The general procedure begins by constructing a static reservoir model, generating several realisations of the reservoir model and applying the optimisation algorithms to our case study. Before providing details of each procedure, the assumptions made in this work are stated.

- Reservoir rock and fluid properties are fully available (3D dimensions, permeability, porosity and fluid density).
- The reservoir is considered infinite acting with many permeable fault boundaries.
- Economic parameters such as the unit volumetric costs for oil and gas sales and water treatment costs are available.
- Reservoir fluids are oil and water.
- Number of production and injection wells are known
- Production time horizon is known (T = 1 – 5 years).
- Injection and production wells are vertical.

The first step in this stage involves mapping the horizons and faults from the available seismic data in PETREL™ (Figs. 10.2a and b). This is followed by the creation of surface maps that mark the reservoir's boundary (Fig. 10.2c). Well log interpretations are carried

out next to identify the productive geological zones based on the reservoir's lithology, porosity and fluid resistivity (Fig. 10.2d). This is the zone that is perforated for fluid flow into the wellbore. The result of this interpretation is the final static model, as shown in Fig. 10.2e, which is upscaled for dynamic simulation purposes (Fig. 10.2f). The field contains 5 injection wells and 3 production wells in operation. Since the focus of the study is an integration of geological considerations/modelling and optimisation, the model construction procedure included in this work gives non-experts in the field an idea of the procedures required to attain optimal well placements from both geological and mathematical optimisation perspectives. Furthermore, we intend to stimulate the interests of geologists regarding how reservoir model development affects subsequent dynamic simulation and optimisation tasks by engineers.

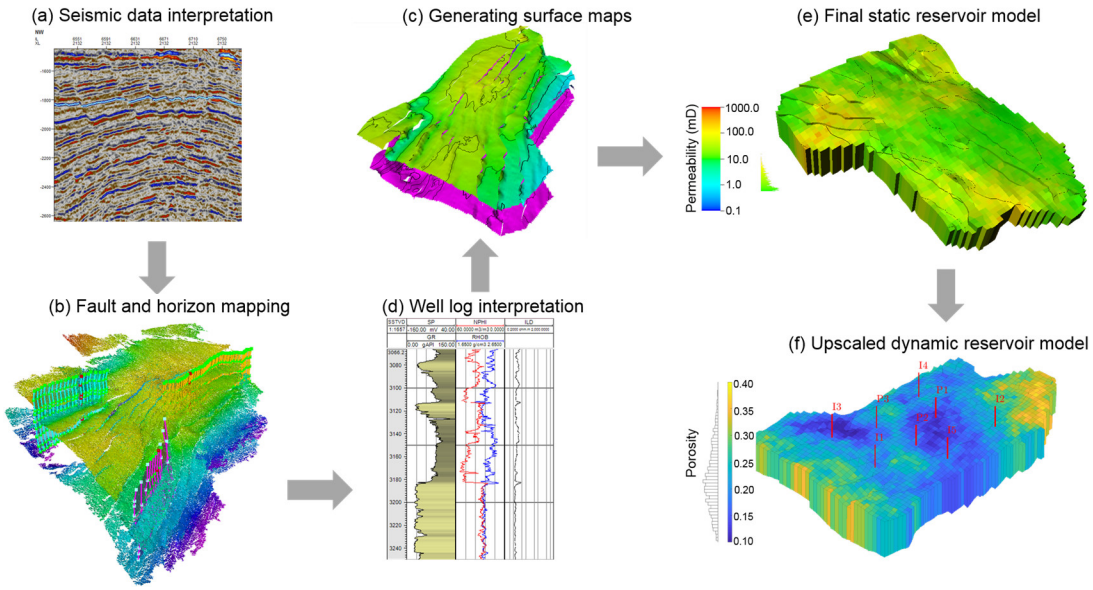

Figure 10.2. Static & dynamic model development (from data interpretation in PETREL™ to optimisation in MATLAB).

10.2 Incorporating Geological Uncertainty

Geological uncertainty exists because it is difficult to know the exact properties of every section of the realistic reservoir (Rahim and Li, 2015). Using the Sequential Gaussian Simulation (SGS) functionality of PETREL™, 50 realisations of the reservoir's permeability (horizontal and vertical) are generated (Fig. 10.3). The grid structure and the fluid and rock properties of each realisation are imported into MATLAB (where optimisation tasks are performed using the MRST toolbox). In ranking these realisations, the pressure distribution, flow capacity, storage capacity and the Lorenz coefficient (Fig.

10.4c) of the reservoir are computed for each scenario to assess the uncertainty of the water flooding operation while assuming all realisations are equiprobable. Further details of the ranking procedure can be found in Shook et al. (2009), Møyner et al. (2015) and Lie (2019). Since a rigorous treatment of geological uncertainty via stochastic optimisation (Wang et al., 2012; Li et al., 2013; Rahim and Li, 2015) is beyond the scope of this study, it was necessary to obtain operationally feasible realisations without numerical artefacts in the simulated field. SGS (a popular method) was chosen to stochastically populate a grid with a Gaussian random field (such as permeability). The method involves visiting each node of the computational grid sequentially and evaluating the probability distribution based on previous values using kriging (Nussbaumer et al., 2018). The order in which the nodes are visited and simulated (simulation path) may influence the accuracy of simulations; however, studies that examine and quantify the influence of the simulation path on the existence and magnitude of possible statistical bias are scarce. PETREL's implementation of the SGS algorithm used herein is an industrially accepted and widely applied method in the oil and gas industry. The robustness of this implementation guarantees successful application to even more complex reservoirs with challenging geological features (such as high/low permeability channels and reservoir compartmentalisation). We have also applied SGS to the Norne field, as shown in Fig. 10.16.

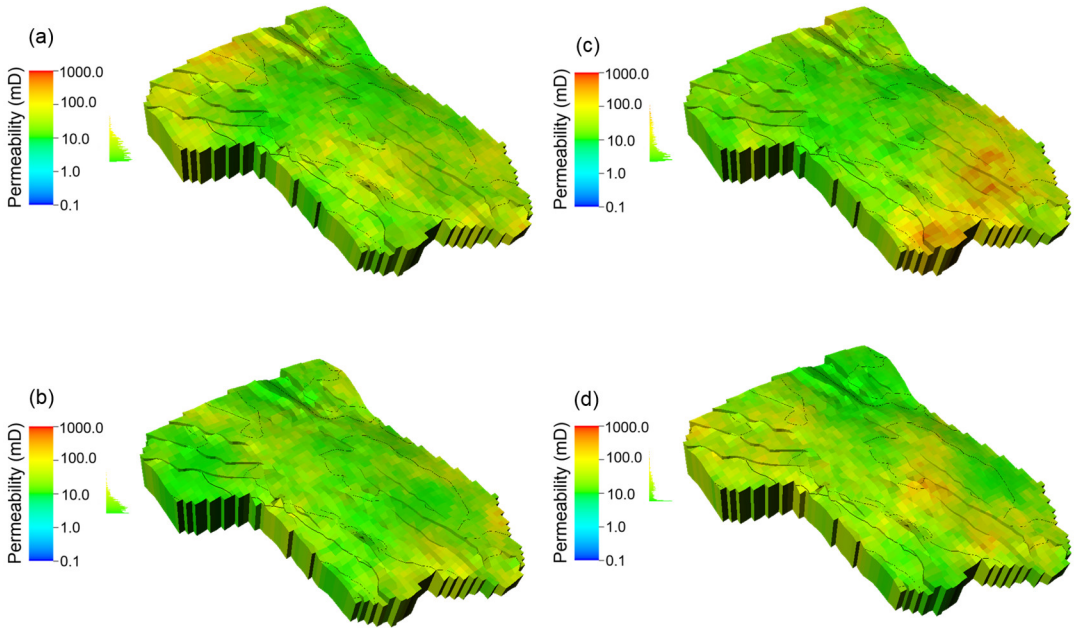

Figure 10.3. Geological realisations implemented (4 out of 50, a–d).

10.3 Dynamic Modelling and Optimisation Formulation

Optimisation tasks are carried out over the worst-case scenario after ranking the geological realisations; thus ensuring robust feasibility of the obtained solution (worst-case optimisation) (Krishnamoorthy, 2016). Although this is a very conservative approach, it is justifiable when limited production data is available for history matching purposes (Jansen et al., 2009), especially at the early stages of field operation. Optimising the expected value of the objective (a less conservative approach) can be pursued with good knowledge of the field's production history. The mathematical formulation of the reservoir model, objective function, operational constraints and adopted solution strategy are shown in Table 10.1.

The dynamic reservoir model (Eqs. 10.1–10.3) describes the flow field in the reservoir and the time-of-flight (TOF, the time required for a fluid particle to travel along a streamline from its starting point to the current position). The pressure is denoted as p, the TOF, τ, the Darcy velocity, $\vec{v}$, the reservoir's storage capacity, ϕ (Fig. 10.4c), the permeability tensor **K**, and the fluid mobility, λ_f. Flow in the reservoir can be driven by wells, n_{bh}, which are controlled by the bottomhole pressure (BHP) and wells, n_r, which are controlled by the flow rate. Both well types, n_w, have perforations, n_{pf}, through which fluid flows from the reservoir into the wellbore. All wells are modelled using the Peaceman well model (Eq. 10.4) in which the well perforation fluxes are denoted by q_{pf}. The index of the well to which perforation number j belongs is denoted as $N_w(j)$; k is the well index and W^j_{pf} is the Peaceman well index. Furthermore, a set of controls (in the form of closure relations) for each well type is specified (Eqs. 10.5 and 10.6); where **u** is the control vector. Besides the well placement optimisation, rate control optimisation is subsequently performed on the optimally located wells. The first objective function (Eq. 10.7) is applied to the well placement optimisation task; the objective function is based on the Lorenz coefficient (Eq. 10.7), which is written in terms of the flow capacity, F, and the storage capacity, ϕ (Fig. 10.4c). This coefficient measures how the oil displacement efficiency for a given well pattern differs from that of an ideal (piston-like) displacement pattern in the reservoir (Shook et al. 2009). Thus, this coefficient is a measure of the optimality of the water flooding operation and hence the oil recovery in the reservoir.

Table 10.1. Modelling and optimisation framework.

Reservoir Model

$$\mathcal{P}(q,\vec{v}) = \nabla \times \vec{v} - q = 0 \tag{10.1}$$

$$\mathcal{V}(p,\vec{v}) = \vec{v} + \mathbf{K}\lambda\nabla p = 0 \tag{10.2}$$

$$\mathcal{T}(\tau,\vec{v}) = \vec{v} \times \nabla\tau - \phi = 0 \tag{10.3}$$

$$\mathcal{Q}^{j}\left(q_{pf}, q_{pf}, p\right) = q_{pf}^{j} - W_{pf}^{j}\lambda\left[p_{bh}^{N_w(j)} - p\right] = 0;\ \ \boldsymbol{j} = 1, \dots, n_{pf} \tag{10.4}$$

$$\mathcal{C}_{bh} = u_{bh}^{k} - p_{bh}^{k} = 0; k = 1, \dots, n_{bh} \tag{10.5}$$

$$\mathcal{C}_{r} = u_{r}^{k} \ - \sum_{\boldsymbol{j}\in N_{pf}(k)} q_{pf}^{j} = 0; k = 1, \dots, n_{r} \tag{10.6}$$

Objective Function & Constraints

$$L_{c,o} = 2\int_{0}^{1}\left[F(\phi) - \phi\right] S_o d\phi \tag{10.7}$$

$$NPV(T) = \int_{t=0}^{T}\sum_{p=o,w}\left(r_p q_p + r_{pi} q_{pi}\right)(1+b)^{-1} dt \tag{10.8}$$

$$u \leftarrow u - P\left(\alpha\frac{dG_\lambda}{d\boldsymbol{u}}\right)^{T} \tag{10.9}$$

$$q_{c,min} \le q_c \le q_{c,max} \tag{10.10}$$

$$\sum q_i \equiv \sum q_p \tag{10.11}$$

Solution Strategy

$$\begin{bmatrix} 0 & \partial_v\mathcal{P} & \partial_q\mathcal{P} & 0 & 0 \\ \partial_p\mathcal{V} & \partial_v\mathcal{V} & 0 & 0 & 0 \\ \partial_p\mathcal{Q} & 0 & \partial_q\mathcal{Q} & \partial_{p_{bh}}\mathcal{Q} & 0 \\ 0 & 0 & \partial_q\mathcal{C} & \partial_{p_{bh}}\mathcal{C} & 0 \\ 0 & \partial_v\mathcal{T} & 0 & 0 & \partial_\tau\mathcal{T} \end{bmatrix}\begin{bmatrix} \delta\mathbf{p} \\ \delta\mathbf{v} \\ \delta\mathbf{q} \\ \delta\mathbf{p_{bh}} \\ \delta\tau \end{bmatrix} = -\begin{bmatrix} \mathcal{P}(\mathbf{q},\mathbf{v}) \\ \mathcal{V}\,(\mathbf{p},\mathbf{v}) \\ \mathcal{Q}(\mathbf{p},\mathbf{v},\mathbf{p_{bh}}) \\ \mathcal{C}(\mathbf{q},\mathbf{p_{bh}}) \\ \mathcal{T}(\mathbf{v},\tau) \end{bmatrix} \tag{10.12}$$

Adjoint Formulation

$$G_\lambda = G[\boldsymbol{x}(\boldsymbol{u}),\boldsymbol{u}] + \boldsymbol{\lambda}^T g[\boldsymbol{x}(\boldsymbol{u}),\boldsymbol{u}] \tag{10.13}$$

$$\frac{dG_{\boldsymbol{\lambda}}}{d\boldsymbol{u}} = \frac{\partial G}{\partial \boldsymbol{u}} + \left(\frac{\partial G}{\partial \boldsymbol{x}} + \boldsymbol{\lambda}^T\frac{\partial g}{\partial \boldsymbol{x}}\right)\frac{\partial x}{\partial \boldsymbol{u}} + \boldsymbol{\lambda}^T\frac{\partial g}{\partial \boldsymbol{u}} + \boldsymbol{g}^T\frac{\partial \boldsymbol{\lambda}}{\partial \boldsymbol{u}} \tag{10.14}$$

$$\left(\frac{\partial g}{\partial \boldsymbol{x}}\right)^T\boldsymbol{\lambda} = J^T\boldsymbol{\lambda} = -\left(\frac{\partial G}{\partial \boldsymbol{x}}\right)^T \tag{10.15}$$

$$\frac{dG_{\boldsymbol{\lambda}}}{d\boldsymbol{u}} = \frac{\partial G}{\partial \boldsymbol{u}} + \boldsymbol{\lambda}^T\frac{\partial g}{\partial \boldsymbol{u}} \tag{10.16}$$

A simplified NPV expression (without well installation costs) is utilised as the objective function of the rate control procedure (Eq. 10.8). T represents the length of the time horizon, q_c and q_{ci} are the field production and injection rates of components p (oil and water) respectively. The revenues and costs of production and injection of components p are denoted as r_p and r_{pi} respectively, and b is the discount rate. $\boldsymbol{Q}, \boldsymbol{C}, \boldsymbol{P}, \boldsymbol{V}$, and $\boldsymbol{T}$ represent the discretised system of equations in terms of variables, q_{pf}, p_{bh}, p, v, τ. The production and injection rates are constrained according to Eq. 10.10 and we ensure voidage replacement by enforcing Eq. 10.11. To perform optimisation computations, the primary variables (pressure, rates and TOF) in Eqs. 10.1–10.3 are solved for, and the objective function gradients are computed for a set of controls. The solution strategy (two-point flux approximation for spatial discretisation – Eq. 10.12) minimises computational workload and makes it adaptable to different linear algebraic solvers. The adjoint equations comprise the Lagrange function for the problem (Eq. 10.13), its derivatives (Eq. 10.14) and simplifications (Eqs. 10.15 and 10.16) that yield an objective function which depends on the state variables, **x** and not on the control variables **u**. Eq. 10.14 can be simplified to Eq. 10.16 by applying the adjoint equation (Eq. 10.15) and taking $\mathbf{g}[\mathbf{x}(\mathbf{u}), \mathbf{u}] = 0$, for a feasible state x. $\mathbf{x}^T$ is a vector of the solution quantities $\mathbf{p}^T$, $\mathbf{v}^T$, τ^T, $\mathbf{q}^T$ and $\mathbf{p}_{bh}{}^T$. $G[\mathbf{x}(\mathbf{u})]$ represents the objective function and $\mathbf{g}[\mathbf{x}(\mathbf{u}),\mathbf{u}] = 0$ represents a set of constraints; λ is the Lagrange multiplier, **J**, the Jacobian, and superscript T, the matrix transpose.

10.4 Well Placement Algorithm

As depicted in Fig. 10.4, the algorithm begins by adding pseudowells with a zero-rate in the region around each injector and computes the gradients of the added wells (based on the Lorenz coefficient – the objective function). The original well is then shifted to the position of the pseudowell with the largest gradient. This process is repeated until all wells are stationary. Since vertical wells that penetrate the entire depth of the reservoir are assumed in this work, the optimisation variables also consist of the wells' area locations (x, y) – integer variables. Thus, the number of variables is bound to increase with increasing number of wells in the field. In a field with many wells (in hundreds for example), it becomes essential to impose an inter-well minimum distance constraint to avoid well interference effects during production. The multiplicity of infeasible solutions and the presence of integer variables complicates the computations, especially when the number of wells is an unknown variable. All optimisation tasks are performed using the

MATLAB Reservoir Simulation Toolbox (MRST) (Møyner et al. 2015; Lie, 2019). MRST is an open-source simulator that also allows the inclusion of custom modelling, optimisation and computational methods for specific problems. We apply the two-phase fluid model of MRST which implements the simplified Corey model with relative permeabilities for the oil and water phases calculated as $k_{rw} = (S_w)^2$ and $k_{ro} = (1 - S_w)^2$.

10.5 Optimal Well Controls

A steepest-descent algorithm is implemented for finding optimal controls (Eq. 10.9). This utilises the *NPV* objective function (Eq. 10.8), the well rates bounds (maximum and minimum) (Eq. 10.10) and voidage replacement constraints (Eq. 10.11) which are supplied in the code; a represents the step size, and P is a projection to the constraints. While evaluating the objective, the value of a is adjusted, and the algorithm stops when the improvement in the objective function between 2 successive iterations is within a specified tolerance (5×10^{-4}).

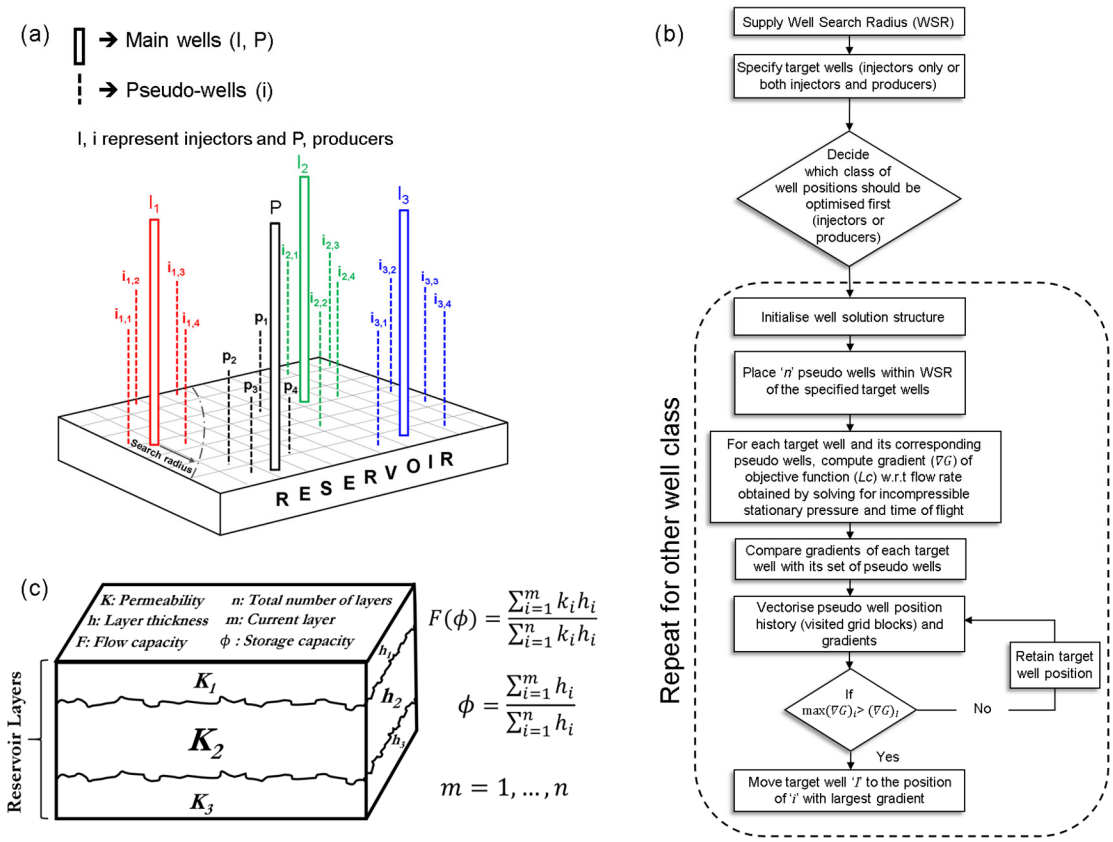

Figure 10.4. Well placement algorithm showing pseudowells and search radius; a radius of 10 grid cells around each well was implemented in CS1 and CS2 respectively (a, b). The definitions of the flow capacity (F) and storage capacity (ϕ) used in the calculation of the Lorenz coefficient are shown in (c).

Compared to the rate control optimisation procedure in which the NPV is the objective function (conventionally defined by Eq. 10.8), we have decided to apply a more representative parameter of the reservoir's geology for the well placement optimisation procedure (the Lorenz coefficient). By establishing the well placement optimisation problem as a direct function of the reservoir parameters, we obtain improved oil displacement (compared to the use of the NPV as the objective function, which depends mostly on the production and injection rates from the wells – Fig. 10.15b).

Another motivation for this sequential multi-objective optimisation method implemented herein is that geologists and reservoir engineers often rely on quantities like porosity and permeability when deciding well positions in a field. For process systems engineering tools to gain increased penetration and application in industrial oilfield operations, the techniques and methods involved should directly utilise these geological parameters within algorithmic manipulation routines. The application of the Lorenz coefficient is an essential step towards enhancing the application of the proposed methodology for real field applications (beyond academic research alone). This strategy also constitutes an element of novelty in this work and may be applied in similar future studies. An optimised Lorenz coefficient yields an equilibrated length of all flow paths in the reservoir; this translates to an improved displacement of oil per unit volume of water injected; thus maximising oil sale revenue and minimising the water injection and production costs; which are components of the NPV objective function. The NPV and Lorenz coefficient are thus connected. However, if primary production were the case (without water flooding), the NPV objective function would have been best-suited (compared to the Lorenz coefficient).

Table 10.2. Reservoir simulation parameters used in this study.

Parameter	Value
Grid-cell dimensions	19,063 m × 15,503 m × 1,469 m
Grid size	47 × 58 × 1
Fluid densities, ϱ_o and ϱ_w	859 and 1,014 kg.m^{-3}
Fluid viscosities, μ_o and μ_w	2 and 0.5 cP
Initial reservoir pressure, P_0	500 bar
Well BHP range, P_{bh}	150 – 700 bar
Control interval, t	50 days
Maximum water injection rates, Q_i	500 m^3.day^{-1}
Maximum oil production rates, Q_p	500 m^3.day^{-1}

10.5.1 Optimal Injection Well Placement (Case Study 1 – CS1)

In carrying out the optimisation procedure, it is assumed that the production wells have been drilled, whereas the injection wells are yet to be drilled. Thus, the aim of the optimisation task to determine the optimal injection well positions that yield the best possible displacement of the residual oil in the reservoir. Details of the fluid properties and reservoir geometry are given in Table 10.2.

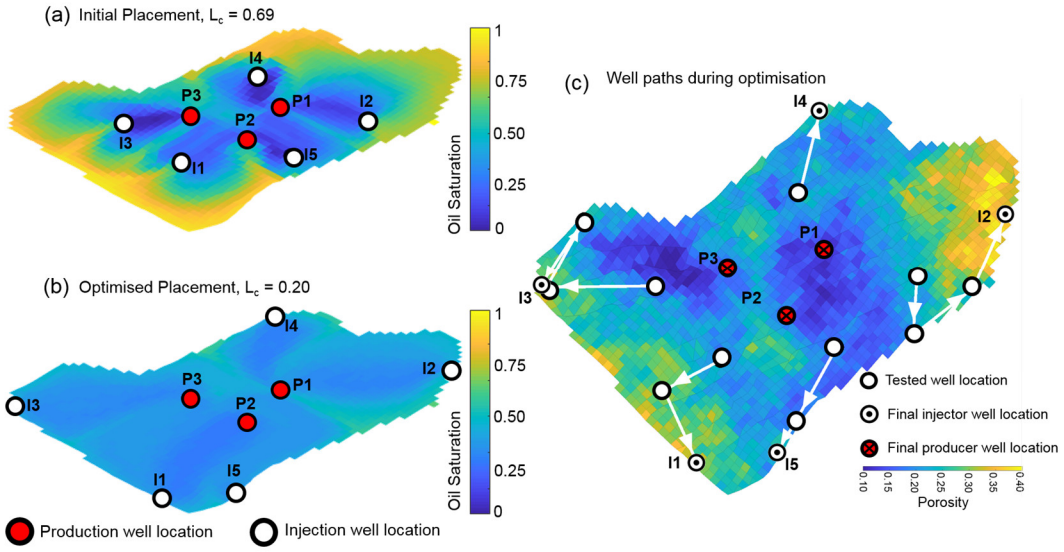

Figure 10.5. Oil saturation distribution with the initial well placements (a), optimal (b) well placements and well paths taken during optimisation computations (c). *PX* represents the production wells and *IX* the injection wells; where *X* is the well number (CS1).

The initial injector placement was set in such a manner as to maintain good hydraulic connectivity between the injection and production wells, given the faulted nature of the reservoir – this is based on reservoir engineering judgement (Fig. 10.5a). However, on applying the well placement algorithm, optimal injector locations that guarantee improved oil sweep are obtained. This can be observed in the oil saturation plots for both placement patterns (unexplored regions of the reservoir - the yellow patches in Fig 10.5a are absent in Fig. 10.5b). The saturation plots are obtained by running a simulation (production forecast) for a 5-year production horizon. Furthermore, the well paths taken by the algorithm during the search for optimal injector well position are shown in Fig. 10.5c. The Lorenz coefficient (a measure of reservoir heterogeneity and the efficiency of oil displacement) is also shown for the two placement scenarios. This coefficient is a function of the flow and storage capacities (F and ϕ). It was highlighted as the most robust measure of reservoir heterogeneity and the best metric for ranking earth models in the work of

Shook et al. (2009). A smaller value of this parameter represents a better displacement scenario; this is the case with the optimised well positions, as shown in Fig. 10.5b compared to Fig. 10.5a.

F/ϕ denotes the ratio of flow capacity of the reservoir to its storage capacity (Fig. 10.6a). For a perfect/idealised displacement of oil in the reservoir, the F/ϕ ratio = 1 (this is never the case in real field operations). It is observed that the optimised well placement yields an F/ϕ curve closer to an idealised displacement scenario compared to initial well positions. In order to further validate the optimality of the new well configurations determined by the algorithm, we run multiphase flow simulations for a production timeframe of five years and obtain the oil recovery over this period.

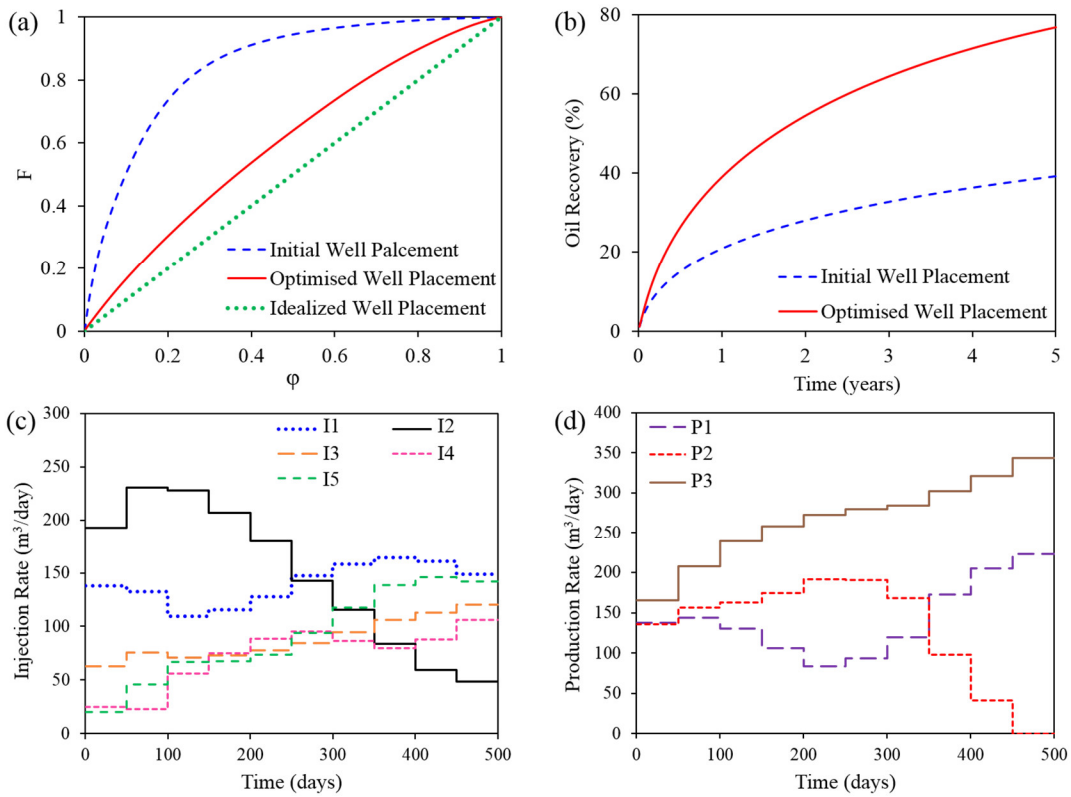

Figure 10.6. Oil displacement efficiency – F-ϕ diagram (a), percentage oil recovery and optimal controls for the injection (c) and production wells in the field (CS1).

It is shown in Fig. 10.6b that the oil recovery of the optimised well placement far supersedes that of the initial well placement (twice the recovery of the initial placement at the end of the production forecast – Fig. 10.6b). This is indicative of the fact that intuitive-based well placements will hardly yield similar performance and oil recovery (field profitability) to that obtained by sound mathematical-based techniques. The well

placement algorithm has thus capitalised on the underlying permeability distribution for the optimal determination of injection well locations.

In determining the optimal well controls, a production horizon of 500 days is considered with a time step of 50 days. This facilitates a better understanding of the rates to apply over a shorter duration since well controls in practice are typically carried out frequently. Re-optimising after this 500-day time horizon can always be done when significant changes in reservoir dynamics (such as the onset of water or gas coning and variations in pressure responses due to a previously undetected sealing fault) occur. These changes could also affect well flow dynamics and cause multiphase flow problems such as slugging.

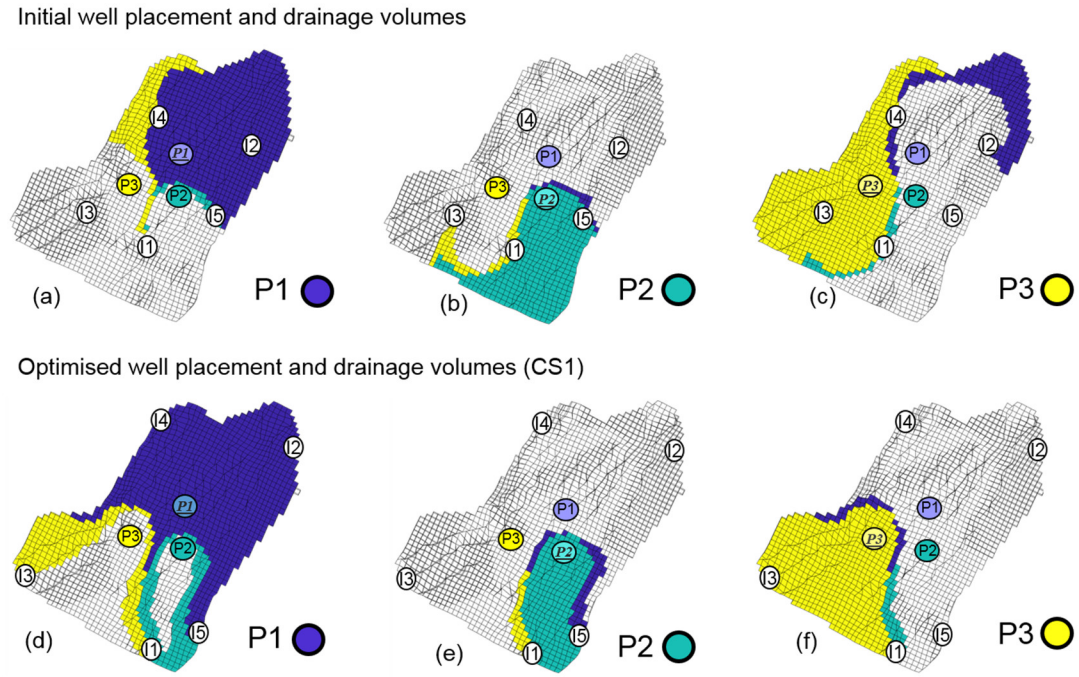

Figure 10.7. Drainage volumes for the initial and optimised well placements (CS1).

The optimal control configurations of the injection and production wells based on the new well placements are shown Figs. 10.6c and d, respectively. The application of the rate optimisation algorithm, which is based on the NPV indicates that injection well I2 with a steady decreasing injection rate at each timestep should be allocated the highest injection rate at the start of production. Next in magnitude is I1 with a relatively lower injection rate. I4 has the lowest injection rate compared to other injection wells and may be considered the least effective. However, to fully ascertain the efficiencies of these wells, further evaluation using well allocation factors is necessary (Fig. 10.8). Since operators have control over the injection rates at the surface, it can be said that the rate optimisation

algorithm also inherently solves a rate allocation problem over a practical time step of 50 days (this is reasonable since reservoir dynamics is slow-paced). The production rate responses from the different wells indicate that P3 is the most productive well and significantly contributes to the overall field NPV.

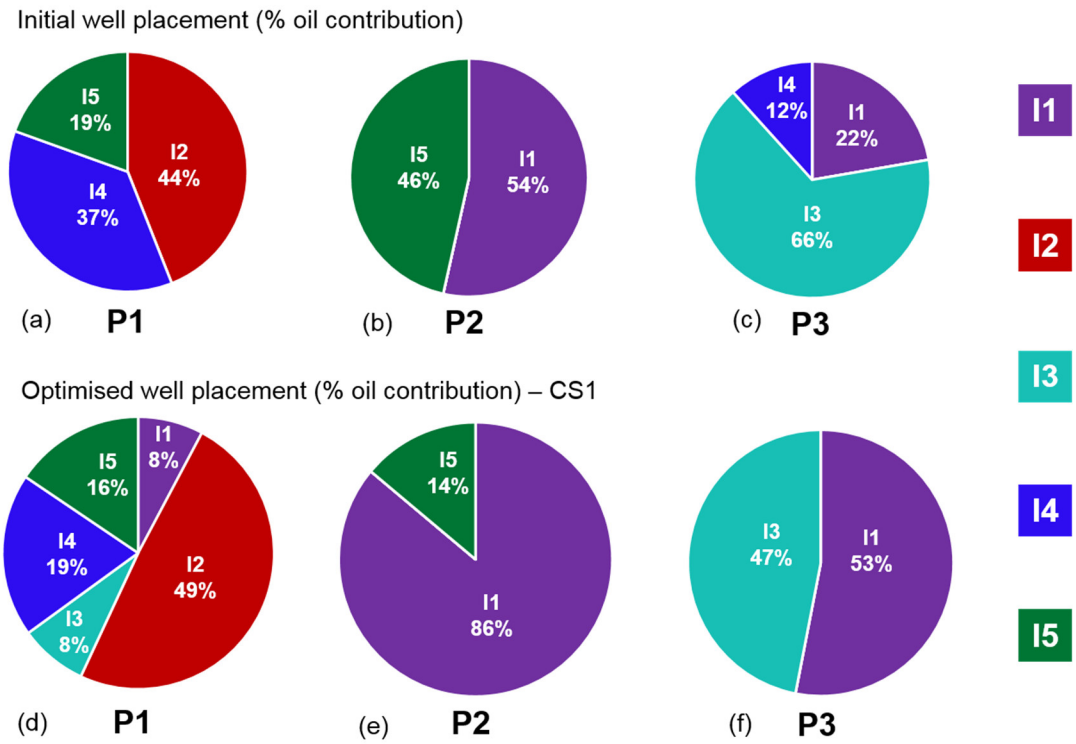

Figure 10.8. Well allocation factors for the initial and optimised well placements (CS1).

To further evaluate the performance of the water flooding operations, we examine drainage volumes of the respective wells before and after the well placement optimisation (Fig. 10.7). The intersecting drainage volumes imply that injection and production wells have good connectivity. Although the drainage volume of P1 is increased on applying our optimisation algorithm, it is observed that P2 and P3 have lower drainage volumes in the optimal scenario. This can be likened to a compensating action (by the algorithm) to ensure drainage of the remaining reservoir regions. The algorithm has incorporated the local permeability distribution around the wells and their new positions to determine which well should drain a wider region of the reservoir to ensure increased profitability (in this case, P1). Fig. 10.8 shows the well allocation factors (the fraction of a producer's inflow that can be attributed to a particular injection well); it quantifies the influences that well pairs have on each other. As shown in Fig. 10.8a, the production rate of P1 was initially only influenced by 3 injection wells (I2, I4, I5); however, the optimised scenario

shows that better performance can be obtained when all injection wells contribute to its production. However, this is not always the case. For well P2, we observe an increased contribution of I1 compared to the somewhat similar contributions from I1 and I5, respectively in the initial scenario. Despite the relatively low injection rate of I5 at the early production period (Fig. 10.6), its contribution to the oil production is still somewhat significant. It is vital to bear in mind that the oil production reflected in Fig. 10.8 relates to that obtainable via water injection, whereas, in Fig 10.6d, the rate response observed is due to both the effects of the reservoir's primary energy and the injection support. The applied methodology has quantified the performance of these wells; thus enabling decision support.

10.5.2 Optimisation of Injection and Production Well Placement (Case Study 2 – CS2)

The results presented thus far have only considered injector well placement while retaining the positions of the production wells. In this section, we simultaneously account for both well types by performing algorithmic adjustments of their positions in a similar way to the previous case study. However, we implement a looped optimisation algorithm in 2 ways. In the first scenario, the production well positions are optimised first in the loop, after which the injection wells positions are optimised. This scenario is denoted as CS2-PI. The second scenario is the reverse of the first and is denoted as CS2-IP. In addition to the well paths taken during the optimisation procedure and the Lorentz coefficient, the recovery at the halfway point (T = 2.5 years) is plotted and compared with CS1.

Table 10.3. Performance evaluation of CS1 and CS2.

Case Study	L_c of optimised placement (-)	Oil recovery at T = 2.5 years (%)	Oil recovery at T = 5 years (%)	Computational Time (mins)
CS1	0.20	60	77	2.38
CS2-PI	0.20	58	74	3.14
CS2-IP	0.14	62	80	2.42

It is observed that the Lorentz coefficients for both CS1 and CS2-PI are the same; however, there is a difference of 2% in the final oil recovery, as shown in Table 10.3. While it is expected that a combined optimisation of injector and producer well placement

would yield significantly better oil recovery compared to the optimisation of injection well placements alone, this study has shown that this is not always the case.

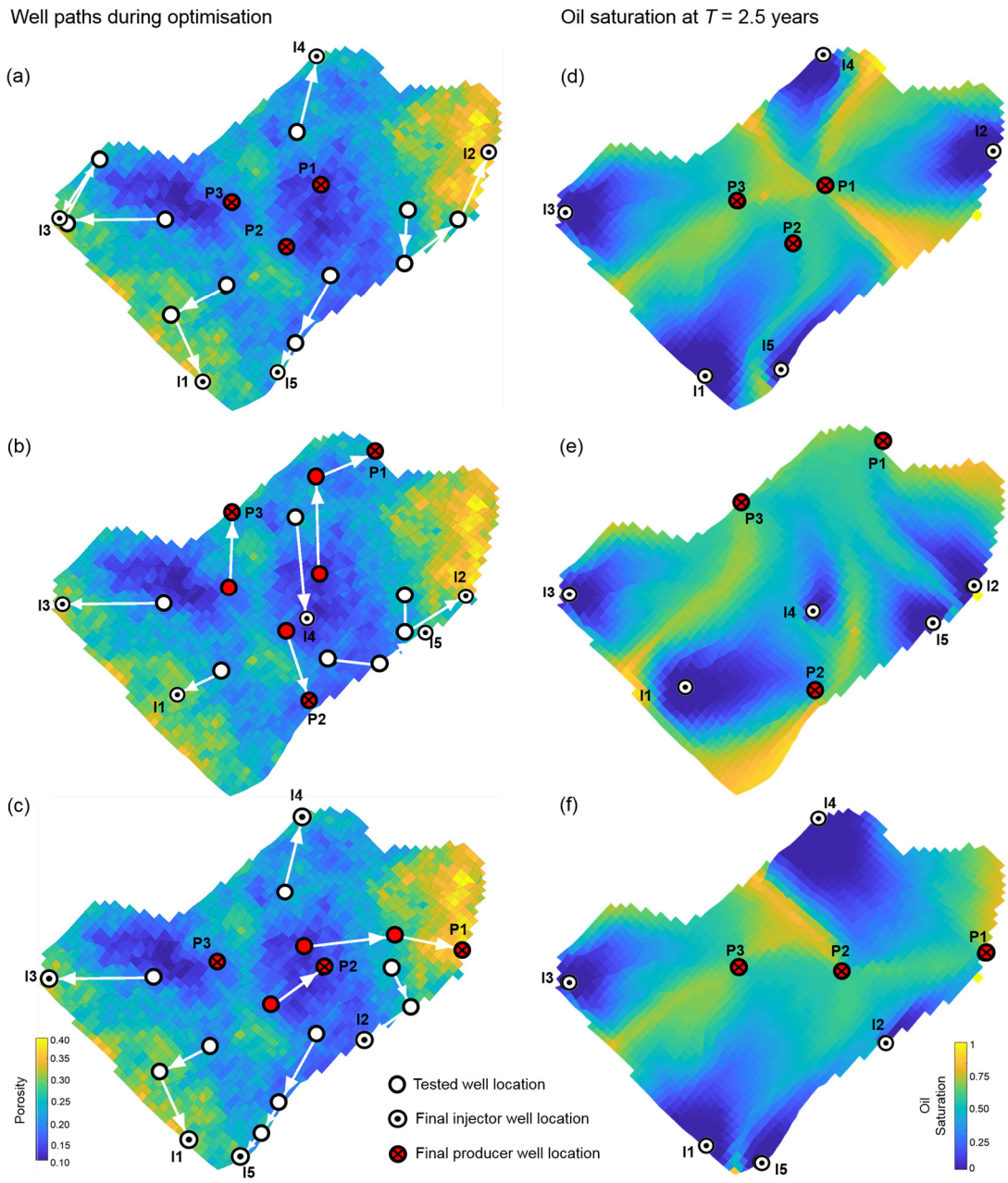

Figure 10.9. Paths taken by the well placement algorithm and the oil saturation for CS1 (a, d) CS2-PI (b, e) and CS2-IP (c, f) respectively.

Based on this observation, it can be concluded that the performance of the algorithm shows some sensitivity to the well type used in the outer loop. CS2-IP showed the best performance with a 30% decrease in the Lorentz coefficient and a corresponding 3% increase in recovery at the end of the production horizon compared to CS1. With an

increased time horizon, this difference in the recovery is expected to rise further. For the production field considered in this work, it can be stated that the position of the injectors is more influential on the oil recovery obtained than the producers' placements.

As observed in Fig. 10.9, the well paths taken during the optimisation and the resulting reservoir fluid distributions differ significantly in all case studies. For each well position, it is observed that the best position is found in less than 4 iterative steps; thus demonstrating the computational efficiency of the pseudo-well algorithm implemented herein. An exhaustive search approach (implemented in most evolutionary algorithms) may not achieve similar performance. In CS2-IP, the algorithm has retained the position of P3 as the optimal; the production wells are also somewhat aligned (Fig. 10.9f) along a straight line, thus creating a staggered injector-producer arrangement. We can also visualise the potential for water breakthrough at the respective production wells from the oil saturation plots (Figs. 10.10d, e, and f). In CS1, the production wells maintain a fixed centralised pattern and may experience water breakthrough at the same time. Although the location of P1 in CS2-PI is farthest from the injection wells, the fluid flow pattern/direction in the reservoir is generally towards this well. This may induce faster water breakthrough despite a high oil production rate. Furthermore, compared to CS2-PI in which the injector I2 is situated in the high porosity region (Fig. 10.9e), well P1 has been moved to this position in CS2-IP (Fig. 10.9f). It is thus shown that the production well can take better advantage of this high porosity region for enhancing oil recovery, as shown in Table 10.3. Although these computations are based on the initial well positions in Fig. 10.1, preliminary tests were performed by changing the initial well locations and convergence to similar well configurations in Fig. 10.10 were obtained; this is an inherent advantage of the well placement algorithm as also demonstrated by Zandvliet et al. (2008).

Based on the superior performance of CS2-IP over CS2-PI, CS2-IP is the preferred case study for carrying out further rate control optimisation computations and flow diagnostics (in terms of drainage volumes and well allocation factors), which we present next. It is observed in Fig. 10.10a that the *F*- ϕ curve obtained for CS2-IP is closer to the idealised scenario than CS1. This improvement by increasing the degrees of freedom of well positions is also shown in the oil recovery plots (Fig. 10.10b) – final recoveries are also shown in Table 10.3. On analysing the water injection controls for the respective wells (Fig. 10.10c), it is observed that I1 and I4 are rate-dominant wells. However, I2 can be

shut until the 450th day, compared to CS1 in which the water injection rate at the start of the production horizon was the highest.

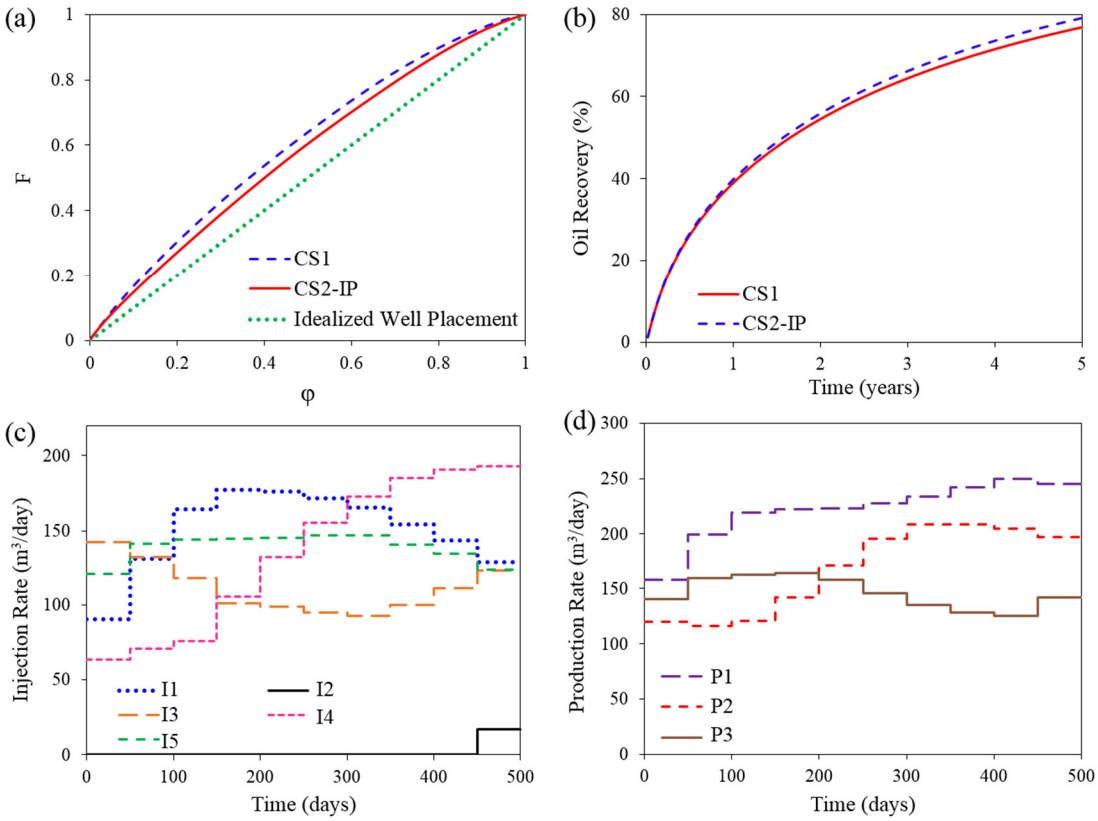

Figure 10.10. Oil displacement efficiency – *F*-ϕ diagram (a), percentage oil recovery and optimal controls for the injection (c) and production wells in the field (CS2-IP).

The new position of P1 in CS2-IP has now made it the best performing production well, as shown in Fig. 10.10d, whereas P2 dominates P3 from the 200th day of production.

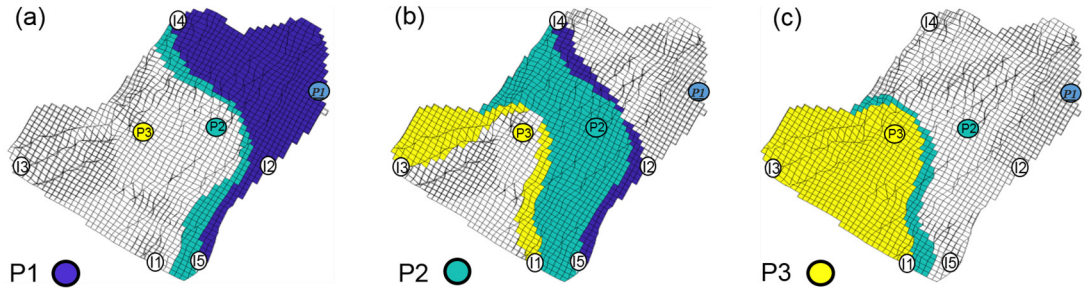

Figure 10.11. Drainage volumes for the optimised well placements (CS2-IP).

Despite the retainment of P3 at its initial location (Fig. 10.9c), the optimal rate controls have changed (Fig. 10.10d) in comparison to CS1 (Fig. 10.6d). The difference in the reservoir fluid distribution and resulting mobility changes around each well are the most

likely reasons for this observation. The drained volumes for the production wells in CS2-IP are shown in Fig. 10.11. Compared to CS1, in which P2 drained a considerably smaller portion of the reservoir (Fig. 10.7e), the drained volume here (Fig. 10.11b) is larger. In addition, the drained volume of P1 has been reduced in this case study compared to CS1. It is also observed that a somewhat similar split in the drained volumes of each production well of CS2-IP exists compared to a scenario in which the production well locations are not optimised (CS1). Thus, the result of our positional optimisation of both well types is to equilibrate the drainage volumes between all production wells. The results also show that a production well's performance may be significantly hindered by the local reservoir permeability distribution, which is, in turn, a function of its location in the reservoir.

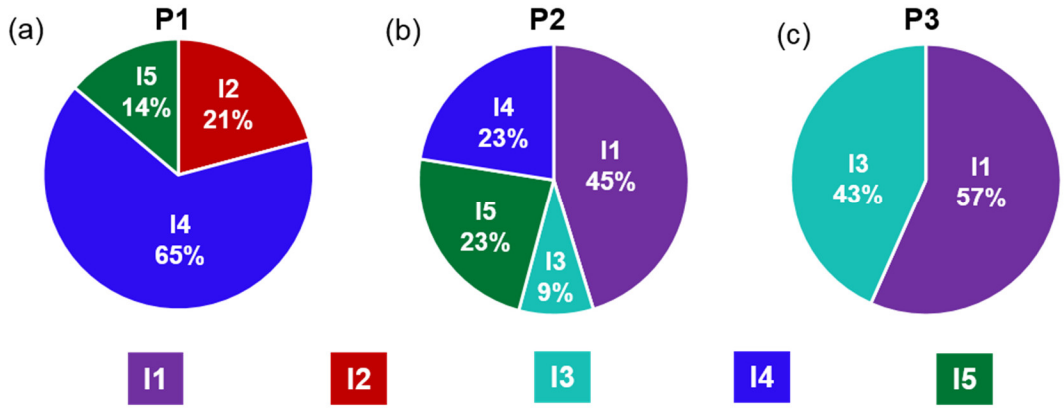

Figure 10.12. Well allocation factors for the optimised well placements (CS2-IP).

The well allocation factors of CS2-IP show that injection well I2, does not contribute to the oil production of any other well except P1 (Fig. 10.12a). This may also be observed in Fig. 10.9f in which the magnitude of the waterfront from I2 is relatively low and only in the direction of P1. Injectors I1 and I4 have significant contributions to the respective production wells. The high injection rates, as displayed in Fig. 10.10c is the reason for this observation; hence, they may be termed the high-efficiency injectors. Furthermore, injection wells I1 and I3 maintain good hydraulic connectivity with P3 and are the main contributors to its performance (Fig. 10.12c). Since P2 and P3 are aligned (Fig. 10.9f) along the flow path from I3 (with P3 being the first encountered well by the pressure wave), P2 thus receives a relatively lower contribution from injector I3 (Fig. 10.12b). P1, which is further up the reservoir, receives no support from this injection well I3 (Fig. 10.12a).

10.5.3 Field Pressure Distribution in the Reservoir (CS1 & CS2)

The reservoir pressure distributions before and after the well placement optimisation are shown in Fig. 10.13. It is observed that the optimal placement of the wells has resulted in a slower decline in the reservoir pressure over the production time horizon of 5 years. Improved pressure support by changing the well locations has thus been demonstrated (similar results are obtained for CS1 and CS2-IP respectively). Nonetheless, compared to a primary production scenario, the pressure decline in the initial case will be slower, due to the action of injectors; thus favouring improved oil recovery. The regions of lowest pressure are mostly around the production well positions (due to their draining action); however, the lower region of the field (orange coloured) represent areas for which new production wells may be drilled after an in-depth analysis of the water breakthrough times for the respective production wells.

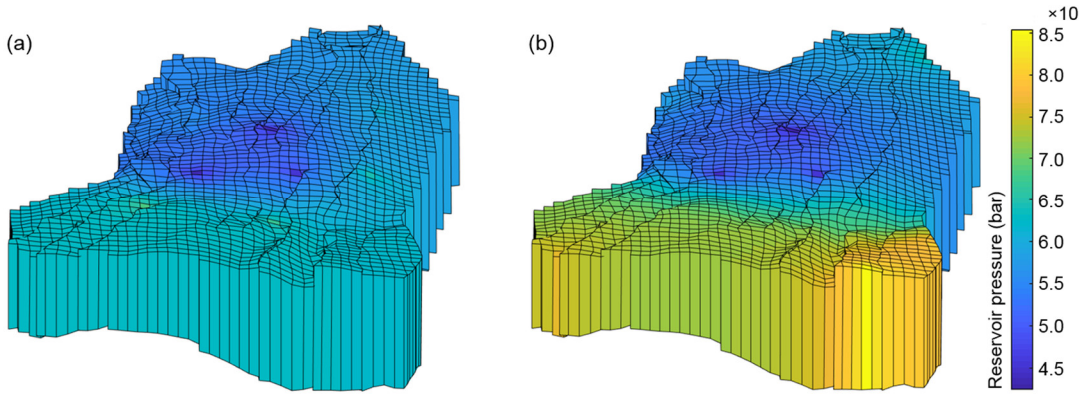

Figure 10.13. Reservoir pressure distribution for the initial (a) and optimised (b) well placements.

10.5.4 Computational Performance of CS1 and CS2

Well placement optimisation and rate control optimisation are the two main computations performed in this work. Both steps were completed in less than 15 mins of computational time (Table 10.3 and Fig. 10.14). The application of the Lorentz coefficient as the ranking metric and the objective function of the well placement problem ensures that only a few timesteps of a given streamline model computation are required to achieve an optimal solution (Shook et al., 2009). Thus, the reservoir heterogeneity (irrespective of the number of cells) is easily and quickly accessible. In addition to the computational time required for the rate control optimisation step, we present the time required for the entire

workflow (Fig. 10.14). It is observed that the bulk of the time is spent on the static model development and preliminary dynamic simulations to ascertain its performance.

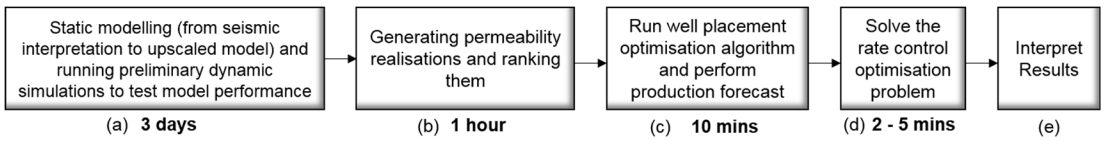

Figure 10.14. Time requirement for each step of the workflow for CS1 and CS2.

The evolution of the NPV objective function for the rate control optimisation is shown in Fig. 10.15a. As expected, the NPV of the optimised scenario (CS1) is significantly higher (47%) than that obtained for the initial scenario. Moreover, the NPV of CS2-IP is higher (by 5%) than CS1. It is observed that within the first 5 iterations, the algorithm is able to find a near-optimal solution; the solution of CS2-IP is obtained with fewer iterations. Compared to a methodology that requires numerous direct calls to a high-fidelity simulator or an approximation of the simulator's output (as shown in Epelle and Gerogiorgis, 2019c; d; e; 2020a; b; c), the herein implemented algorithm attains optimality in fewer iterations. All computations were performed on an Intel Core i7-6700 CPU @ 3.40GHz machine with 8 processing cores.

Although the presented case study is somewhat small (in terms of the number of wells), such rapid computational performance is also expected when the problem size increases (Møyner et al., 2015). It is also worth mentioning that the computational performance observed herein is a consequence of the sequential optimisation of placement and controls performed. Our rationale for choosing the sequential approach (as opposed to a joint approach) in this work is based on the findings of Humphries and Haynes (2015). They demonstrated via some cases studies, superior performance of a decoupled/sequential approach compared to a joint optimisation method. A possible reason for this is that the initially fixed control scheme is one that is favourable for finding good solutions of well placements. As such, the solution/search space of the problem is significantly reduced, thus yielding a more thorough exploration by the algorithm. Although the solution space of the joint approach contains all solutions the decoupled approach can possibly find, it becomes harder to find these solutions when the search space is larger (Humphries and Haynes, 2015). This concept of limiting the search space for optimal well placements has also been demonstrated by Onwunalu and Durlofsky (2010).

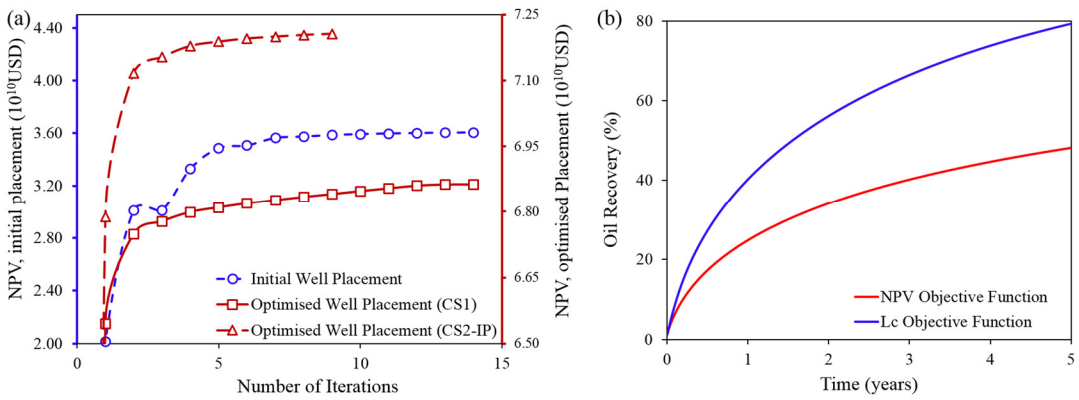

Figure 10.15. Objective function evolution for rate control optimisation for CS1 and CS2 (a); oil recovery obtained when *NPV* and *Lc* are used as the objective function for well placement optimisation.

It may also be useful to optimise the well controls at specific time intervals after optimising the well placements. This utilises the current pressure distribution, fluid saturation profile and other fluid and rock properties in the reservoir, which may have changed significantly. Streamline simulation could also be performed to examine the dynamic injection efficiency so that if there is a drastic change in this efficiency, the re-optimisation of the well controls is justifiable. Although this will inevitably increase the number of functional evaluations, it is expected that the computational cost will be reasonable, given the robust gradient formulation implemented. Fig. 10.15b shows that well placement optimisation based on *Lc* yields a higher recovery compared to the application of the *NPV* as the objective function; thus justifying our multi-objective optimisation strategy.

10.5.5 Case Study 3 (Analysis of the Optimisation Search Space for each Well)

In this case study, we demonstrate the applicability of the presented approach to a more challenging and bigger scenario. We mainly investigate the sensitivity of the optimal oil recovery to the supplied search radius in the well placement algorithm (when optimising both injector and producer placements). In doing so, the strategy presented in CS2-IP is implemented. A more complex geological model of the Norne Field is applied, consisting of 20 production wells and 10 injection wells. The Norne Field (NTNU, 2019) is compartmentalised (2 parts which are in communication through the drilled wells – Fig. 10.16). All drilled wells since 2006 have been included with their original locations retained, but with horizontal well configurations changed to vertical. Furthermore, the

reservoir fluid considered is the same as that used in CS1 and CS2, respectively. The robustness of the SGS algorithm is again demonstrated with the successful generation of permeability distributions, as seen in Fig. 10.16 (a-d).

The resultant effect of 30 wells present in this case study is that the well search radius (WSR) is limited to avoid severe well interference problems and its negative impact on production. Compared to CS1 and CS2 in which the search radius was defied as 10 grid blocks, detailed analysis on this case study utilises a maximum of 5 grid blocks. The well paths taken during the optimisation procedure are shown in Figs. 10.17-10.19. It is observed that the number of well positions explored by the optimisation algorithm increases as the search radius increases. However, the result of this increased search area is not necessarily and increase in the corresponding oil recovery (Table 10.4).

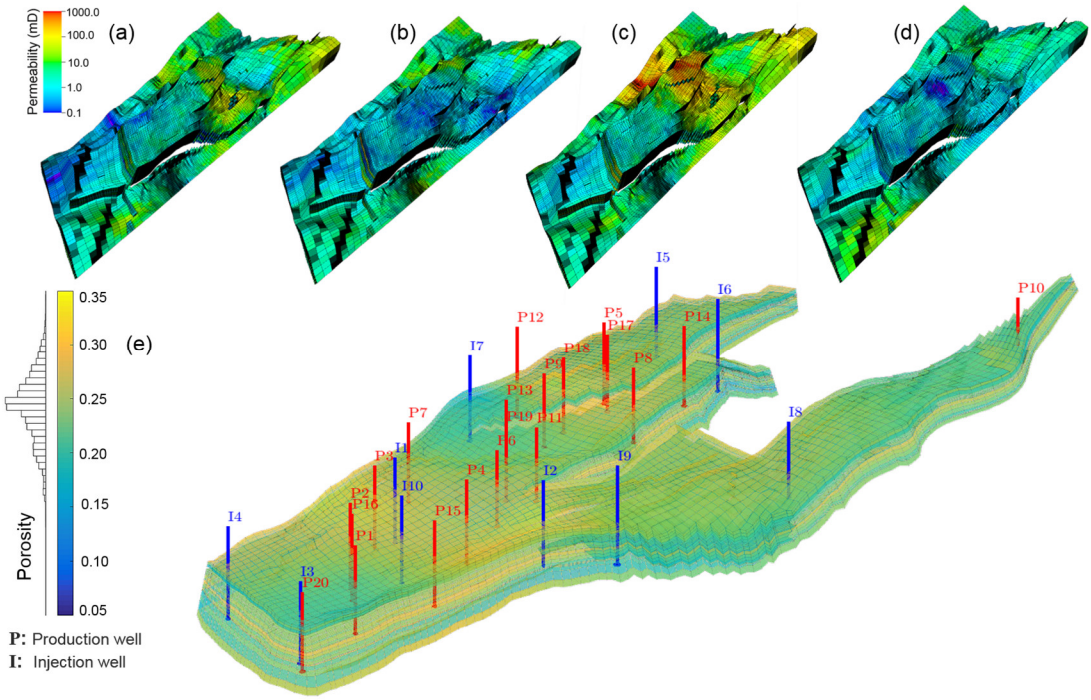

Figure 10.16. The Norne Field showing different realisations of the permeability distribution (4 out of 50 geological realisations, a–d, with active and inactive cells), the field porosity distribution and the initial locations of the wells.

On performing a two-phase flow simulation for 5 years on the optimised well positions, it is observed in Table 10.4 that the oil recovery (at 2.5 years) increases from 66% to 70% when WSR increases from 3 to 4 but reduces to 67% when WSR increases to 5. A similar trend is observed for the recovery at 5 years and the *Lc* respectively. On applying a WSR of 10, the resultant effect was operationally infeasible well clusters with a significantly

reduced recovery of 30%. Thus, careful selection of the well search radius when using the well placement algorithm is essential, especially in fields with several candidate wells. The inclusion of minimum inter-well distance constraints is a possible remedy for improving the algorithms' performance; however, this is subject to further investigation and is beyond the scope of this study.

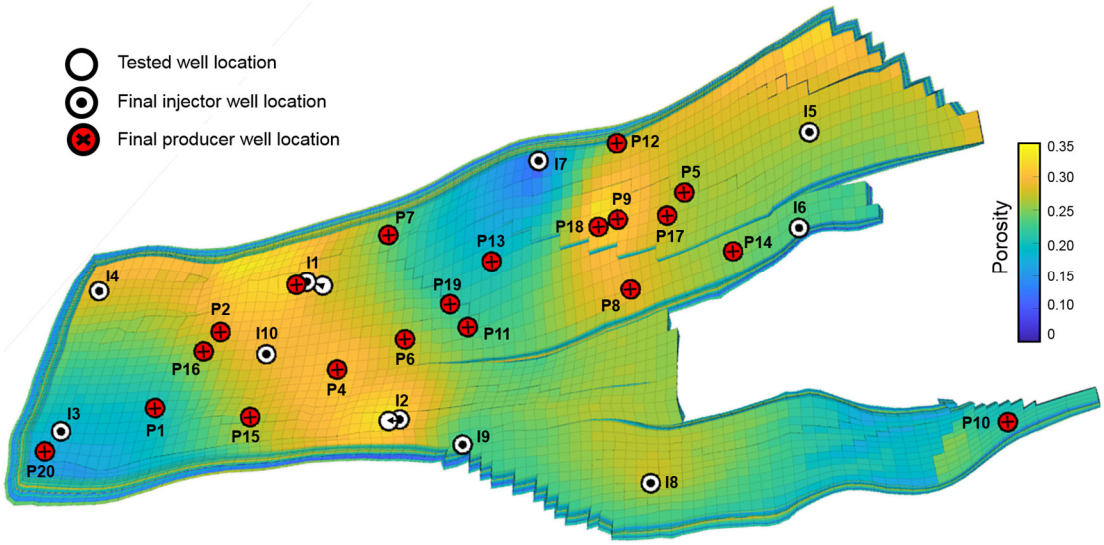

Figure 10.17. Well paths taken during the optimisation procedure for WSR = 3.

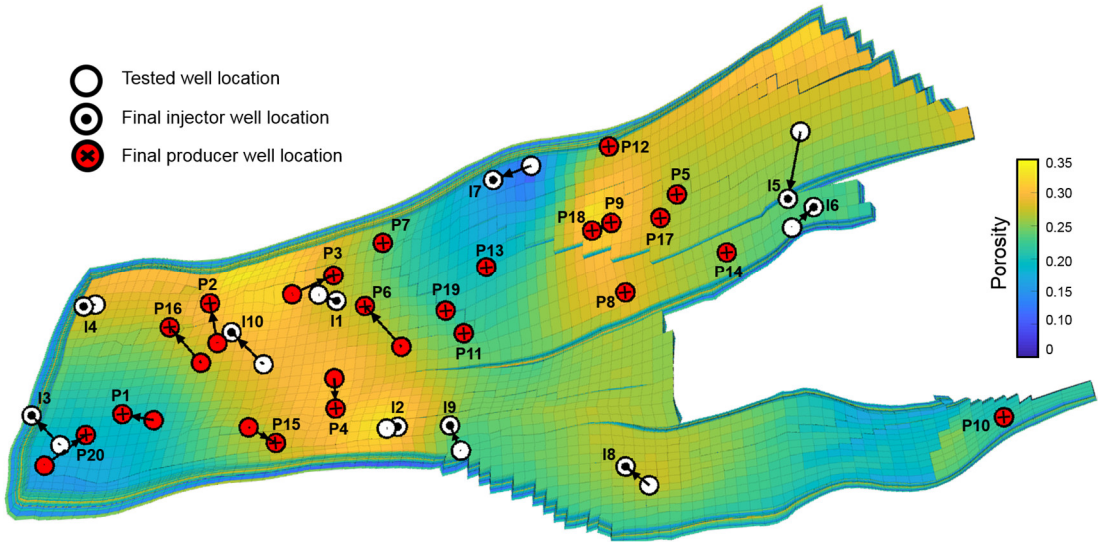

Figure 10.18. Well paths taken during the optimisation procedure for WSR = 4.

It is also observed that the computational time required, as seen from Table 10.4, significantly increases as WSR increases. The time requirements for CS3 are also higher than those of CS1 and CS2, which contain only 8 wells. However, compared to studies

such as Tavallali et al. (2013) with a smaller problem size than CS3 (with computational times reaching 27 hours), the run times achieved in this work are significantly shorter.

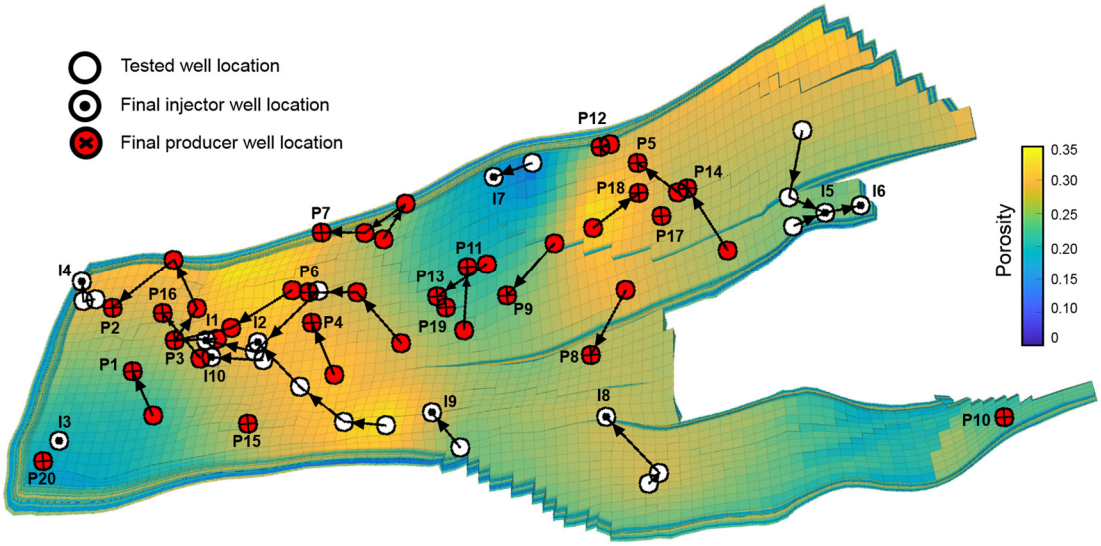

Figure 10.19. Well paths taken during the optimisation procedure for WSR = 5.

Table 10.4. Performance evaluation of CS3.

Case Study	L_c	Oil recovery at T = 2.5 years (%)	Oil recovery at T = 5 years (%)	Computational Time (mins)
Initial well positions	0.56	64	76	-
CS3 (WSR =3)	0.53	66	79	47.4
CS3 (WSR =4)	0.50	70	84	71.4
CS3 (WSR =5)	0.52	67	80	205.2

Fig. 10.20 shows the oil saturation in the field after a production timeframe of 2.5 years for the base case and the different optimal configurations for WSR of 3, 4 and 5, respectively. As can be observed, a WSR of 4 yields the best recovery with a significant portion of the field drained using the same number of wells compared to the other scenarios. Based on the optimal well positions obtained from WSR of 4, the rate control optimisation procedure can be performed to study individual well performance. It is observed that P15 is the best performing well with the highest flow rate (Fig. 10.21b); whereas, injection well I4 can be allocated the highest water injection rate (Fig. 10.21c), as seen in the scaled optimal well controls (Fig. 10.21). The optimal well configurations are obtained in 13 iterations and within 15 mins of computational time (Fig. 10.21d).

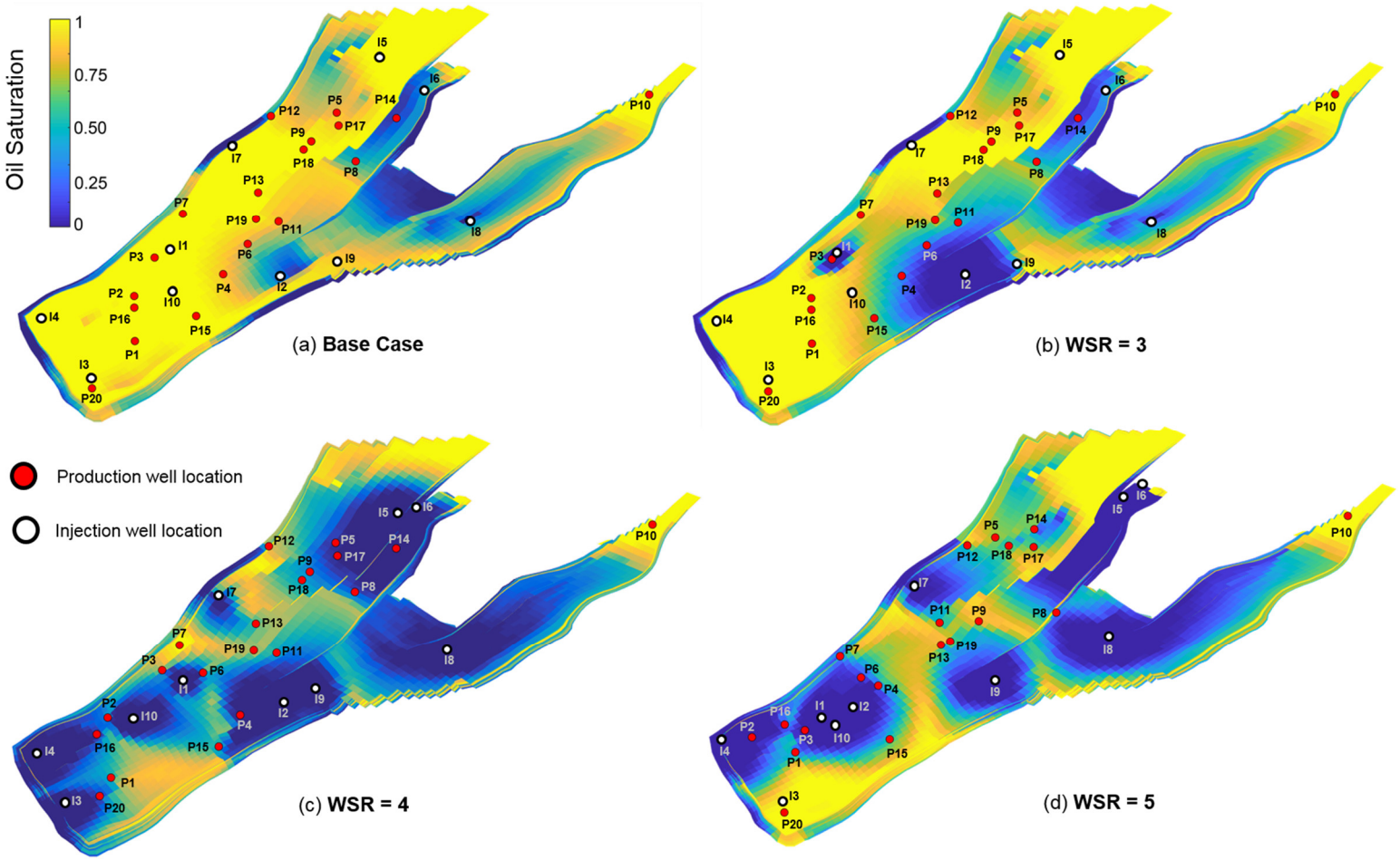

Figure 10.20. Oil saturation at T = 2.5 years for CS3.

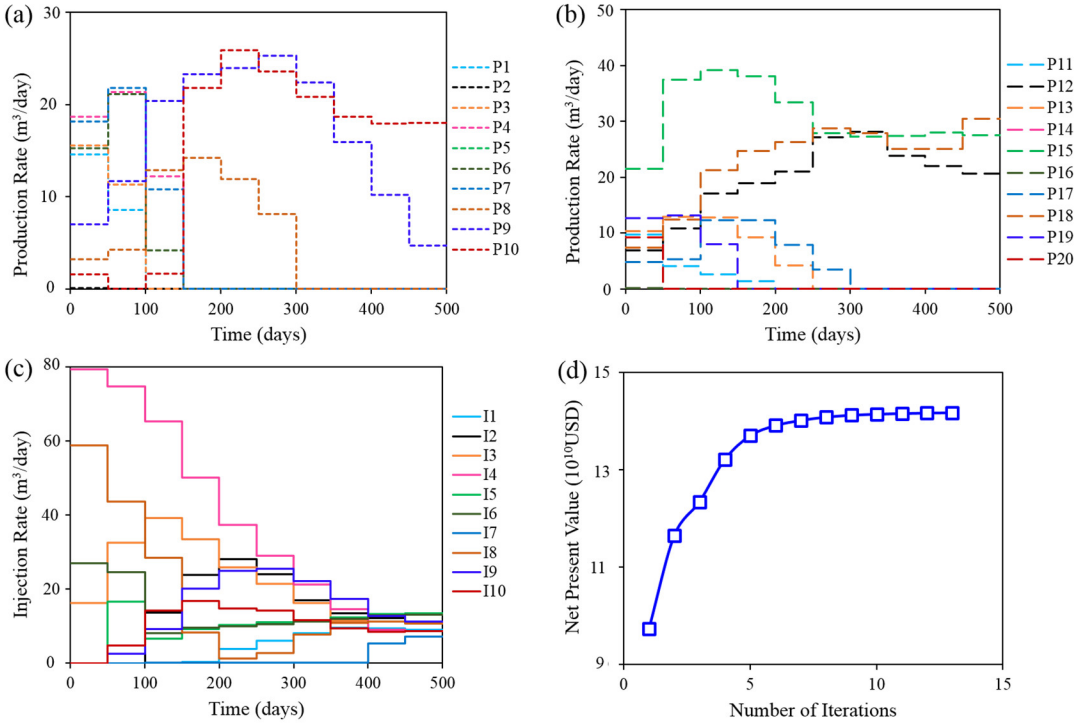

Figure 10.21. Optimal controls for the injection and production wells of CS3.

10.6 Chapter Conclusions

In this work, we have addressed an injection and production well placement and rate control optimisation problem of a realistic field under geological uncertainty. We have incorporated geological uncertainty by using the worst-case scenario of 50 ranked permeability realisations and derived the following conclusions.

- The application of a well placement optimisation algorithm yields a boost in the field's oil recovery – twice the value obtained using intuition-based methods alone.
- Optimal controls for each injection well were determined; thus allowing for a stepwise adjustment of surface injection rates and water allocation in real operations.
- The implemented robust computational approach that utilises an adjoint formulation enables rapid optimisation performed in a matter of minutes.
- Optimising both producer and injection well placement resulted in a 30% reduction in the Lorentz coefficient; this translates to 3% increment in recovery. In our case study, the injector well placement significantly affected final oil recovery compared to producer placements.

- The well placement algorithm is sensitive to the type of wells implemented in the outer optimisation loop (whose location is optimised first). The algorithm performs better when injection wells are first optimised in the optimisation loop compared to production wells.
- There is an equilibration of the respective drainage volumes of the production wells by simultaneously optimising the placements of production and injection wells in the field considered in this work.
- It was shown in this study that an increased search space (in terms of the WSR) for the optimisation algorithm does not necessarily guarantee improved oil recovery. The WSR is also a parameter that may be optimally determined for truly optimal well positions to be attained.

Proper calibration of the reservoir model using industrial field data would constitute the next steps of this work. This is expected to increase the reliability of forecasts and the optimal injection strategy obtained herein. Stochastic optimisation (with the probabilities of the respective geological realisations incorporated) of this history-matched model can then be performed to reduce the conservativeness of the optimal solution (obtained from the worst-case scenario) and hence increase the field's NPV. The drilling sequence/scheduling problem is also worth considering, since all wells are not drilled simultaneously in practical operations. By introducing horizontal/deviated wells, the complexity of the well placement optimisation procedure increases; this requires further investigation. Simultaneous optimisation of well placement and controls using gradient-based methods is still an open research question that requires further investigations. Finally, the adopted objective functions are nonconvex; hence an efficient subdivision of the parameter space to avoid trapping at local optima is a modification that could enhance the performance of the rate optimisation algorithm.

Chapter 11 Future Opportunities for Integrating CFD and Optimisation Methodologies for Enhanced Drilling and Production Operations

The multiphase flow description of fluid and particle transport in an annular wellbore during wellbore drilling has thus far been provided using robust CFD methods. However, the transport of cuttings has received little or no contribution from the PSE community via the application of mathematical optimisation. As highlighted by Epelle and Gerogiorgis (2019e), this may be due to the prevalence of rigorous fluid-particle transient models necessary for studying the transport phenomena of cuttings; such simulations are not readily adaptable to an optimisation routine due to the computational cost required at each iteration; furthermore, coupling the CFD solver with an optimisation solver is also not an easy task (Fig. 11.1). Besides this, not many optimisation solvers are capable of handling optimisation problems constrained by partial differential equations (PDEs), which are typical in CFD-related models. However, several robust empirical cuttings transport models (which are simple nonlinear algebraic equations) developed by Ozbayoglu and co-workers (Ozbayoglu et al., 2005; Ozbayoglu et al. 2010) expand the opportunity for nonlinear optimisation studies in this regard.

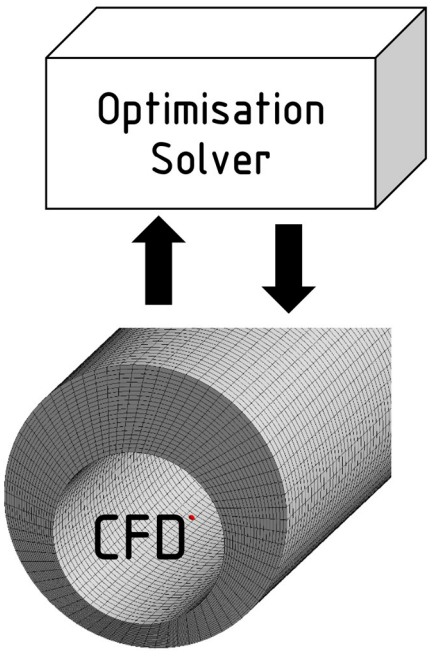

Figure 11.1. Interfacing a CFD model with an optimisation routine.

The potential for maximising the application of lower-fidelity cheaper models within iterative procedures with (occasional and systematic) recourse to the higher-fidelity (and more expensive) models has been demonstrated by Alexandrov et al. (2001) for solving aerodynamic wing design problems. Their procedure can be readily extended to drilling systems. There is also a potential for embedding Artificial Neural Networks (ANN) for model complexity reduction (proxy models) based on numerous reasonably-timed and validated CFD simulations within a stochastic optimisation framework such as genetic algorithm (GA). Despite the scarcity of optimisation studies that consider cuttings transport in drilling operations, it is important to emphasise that other aspects of the drilling operations have received attention from the optimisation community. These include managed pressure drilling for maintaining downhole wellbore stability and preventing blowouts, monitoring drill string mechanics, geo-steering and wellbore trajectory, and drilling scheduling (Tavallali et al., 2016a,b; 2017). Model Predictive Control (MPC) and multiparametric optimisation have been readily applied to enhance these aspects of the drilling operations as demonstrated in the studies of Aarsnes et al. (2016a; b; c) and Eaton et al. (2017) with similar concepts applied in comparison to those presented in Alexandrov et al. (2001). Section 11.2 of this chapter provides a comprehensive overview of PSE-based contributions from a drilling perspective. Further details of these contributions are also summarised in Table C.4.

Although optimisation methodologies have thus far been applied to production systems as seen in Chapters 7, 8, 9 and 10, it is also worth analysing the prevalence of CFD-based contributions for understanding production-related problems. Compared to the scarce application of mathematical optimisation to drilling-related problems, the application of CFD for studying production-related phenomena in wellbores, pipelines, valves and separating vessels abound. Complex multiphase flow phenomena such as slugging in risers and pipelines, phase separation of oil-water-gas mixtures, sand production and its impact on pipe erosion, and other flow assurance related phenomena (such as flow through constricted regions due to intense wax and hydrate formation under different flow regimes) have received significant attention from the fluid dynamics community (Taha and Cui, 2006; Shao et al., 2008; Abdulkadir, 2011; Hossain et al., 2019). Thus, the prospects for a coupled utilisation of both CFD and optimisation methodologies pave the way for more complex operations such as Underbalanced Drilling (UBD) to be adequately

modelled and optimised. In UBD campaigns, the downhole hydrostatic pressure in the wellbore is deliberately maintained at some pressure below that of the reservoir formation. This is achieved by the injection of non-condensable gas within the downhole circulation system, thus enabling wellbore stability, reduced invasive formation damage and enhanced ability for well test procedures to be carried out while drilling (Bennion et al., 1996). However, this procedure creates a pressure gradient that enables fluid entry into the wellbore from the reservoir, thus resulting in a complex mixture of reservoir fluids (oil, water and gas), rock cuttings and the non-condensable gas utilised for pressure control. This is a very rare scenario in which drilling and production occur simultaneously, for which the tools of CFD and production optimisation can be simultaneously applied. However, studies that demonstrate a combined application of these tools for UBD operations are very scarce if at all any exists. However, Akhshik and Rajabi (2018) have presented some new insights on cuttings transport phenomena under such complex conditions, although predominantly using CFD-DEM methods.

A possible reason for the scarcity of these integrated studies is the distinct divide in competence between CFD modelling and optimisation in the academia and industry. A successful application of these tools requires a detailed understanding of flow dynamics, CFD software packages, optimisation methods and algorithms implemented in different open-source and commercial solvers. This cross-disciplinary competence which is needed for such tasks is also hardly found among engineers in the industry (Grimstad, 2015). Consequently, an increase in the number of contributions in this regard will most likely result from collaborations between physicists, chemical engineers and mathematicians. However, this project has demonstrated a strong potential for such integration via detailed considerations of both CFD and optimisation methodologies for enhanced drilling and production operations. Given the well-established and numerous applications of CFD methods for production systems, the subsequent sections of this chapter focus on the few contributions from the PSE community on drilling modelling, control and optimisation; subsequently, we discuss future research opportunities towards the integration of both tools (CFD and optimisation) for drilling systems engineering.

11.1 A Process Systems Engineering Perspective on Drilling Operations

The discussion herein is categorised into four subsections on control and automation of managed pressure drilling, real-time monitoring (using high fidelity and lower order models), drilling optimisation and artificial intelligence techniques for solving drilling-related problems.

11.1.1 Real-Time Monitoring using High-Fidelity and Reduced-Order Models

Nygaard and Naevdal (2006) highlighted that pressure control during pipe connections is often challenged by temporal unavailability of downhole data from a mud pulse telemetry system or via a wired drill pipe.

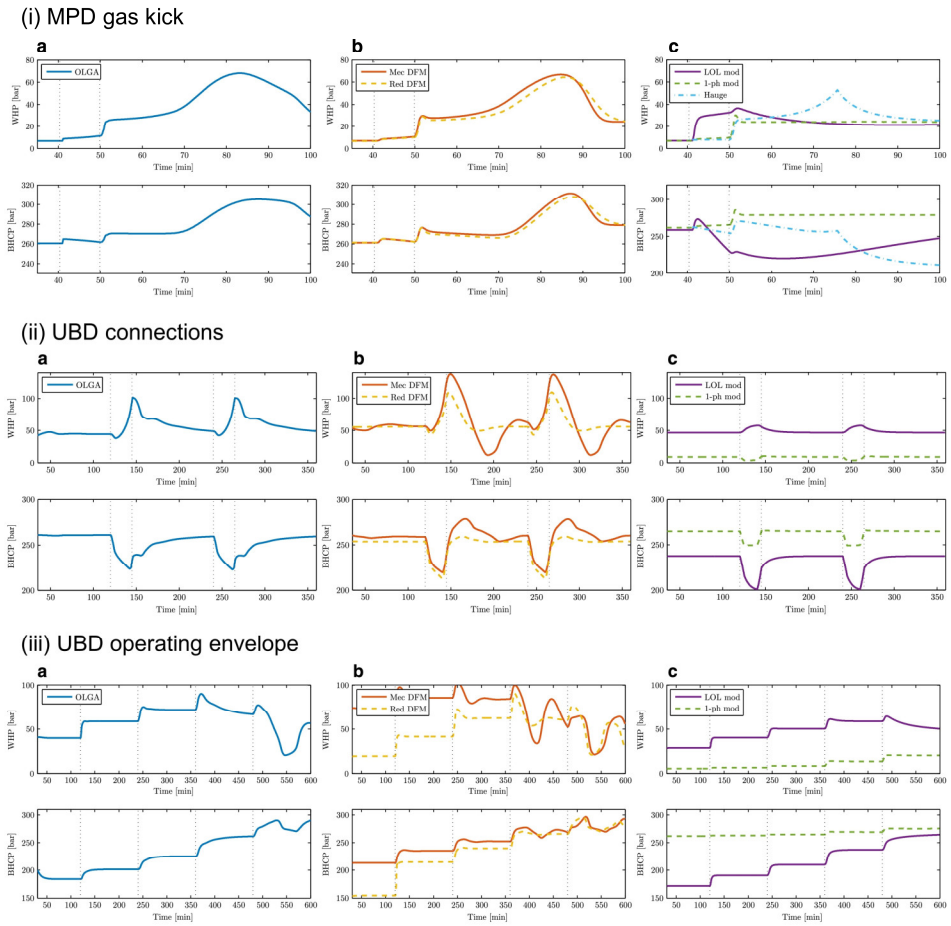

Figure 11.2. Bottomhole pressure and wellhead pressure trends for three operational scenarios and the evaluation of lower-order models (mechanistic and reduced Drift Flux Models, 1-phase model, Hauge et al. (2013) model and the low order lumped model) in comparison with a high fidelity multiphase flow simulator OLGA (Aarsnes et al., 2016a; b).

This is because signal transmission is dependent on the mud circulation, which is stopped during pipe connections. Furthermore, signal cables must be disconnected during connection procedures. Recently, it has been shown that electromagnetic transmission systems may be utilised for data transmission from the rock formation to the surface; however, the attenuation of electromagnetic signals and reduced data quality in very deep wells (> 2500 m) is an encumbrance (Nygaard and Nævdal, 2006; Pixton et al., 2014). These challenges imply that pressure control systems must rely on sufficiently accurate dynamic well hydraulic models. The scarcity of downhole data is another (if not the primary) motivation for the use of robust and calibrated models in most MPD operations (Carlsen et al., 2013; Nikoofard et al., 2013). Models may be used for simulation purposes (during which control parameters may be tuned, tested, and verified); furthermore, these models may be used for estimating the states of the process, especially when noisy measurements occur. Future process behaviour may also be predicted by the model and future setpoints selected (Stamnes et al., 2008; Davoudi et al., 2011; Godhavn et al., 2011; Park et al., 2017).

Model-based control techniques applied in oil and gas drilling systems often impose limitations on the structure of reduced-order models that may be applied for system control. Aarsnes et al. (2016a) classified reduced-order models based on complexity and physical interpretations of the simplifications adopted. Their classification categorises these models into Reduced Drift Flux Models, Lumped Order Lower Models, 1-phase models and Lagrangian models. The performances of these reduced-order models, when compared to an industrially implemented high fidelity simulator (OLGA), are shown in Fig. 11.2. In evaluating the models' performance, three practical scenarios are adopted (MPD gas kick, pipe connections during UBD, different drawdowns from a UBD gas well - UBD envelope). Compared to the other models, the lower order lumped model showed the poorest performance. A lower-order drill string dynamics model developed by Ke and Song (2018) has been utilised for control purposes. The model incorporates axial motion and torsional vibration of the drill string and the bit-rock interactions. This model shows good performance when validated with a high-fidelity drilling dynamics model. The application of local model order reduction techniques for nonlinear PDE systems such as Proper Orthogonal Decomposition (POD), Dynamic Model Decomposition (DMD) and Ensemble Kalman Filters (EnKF) have been applied to

several other oil and gas systems, but have received little attention in drilling systems. These methods often rely on analysing information obtained from a series of observational data of high-dimensional systems to identify coherent patterns embedded in such systems (Narasingam and Kwon, 2017; Narasingam et al., 2017; 2018). The computational cost required for the development of these reduced-order models and their need for frequent calibration may constitute reasons for their limited application in drilling systems. Notwithstanding, quantitative exploration of these reduced model types is required for drilling systems to verify their potential in comparison to the reduced-order models detailed in Aarsnes et al. (2016a).

During mud circulation, a very complex multiphase flow scenario exists; the liquid mud phase interacts with possible fluid influx (gas, oil & water) in the presence of solid rock cuttings that evolve. This occurrence creates an avenue for the application of fluid dynamics concepts in process control (Fig. 11.2). In addition to multiphase flow and wellbore hydraulics, rigorous descriptions of drill string dynamics (Sugiura et al., 2015), rate of penetration and dynamic response of topside equipment are also essential for a full description of the entire process (first principles models). Apart from being complicated and time-consuming to develop, the combination of these rigorous models is computationally demanding when embedded in a control scheme (due to extreme nonlinearity). However, since the emphasis here is placed on pressure control, simplifying assumptions (such as a uniform fluid distribution in the well) are usually made to reduce the complexity from a PDE based model (used in classical fluid dynamics) to a system of ordinary differential equations (lower-order models which focus on fluid flow and the impact on wellbore pressure). However, Nygaard and Naedval (2006) have reported that un-modelled effects due to severe approximations may cause errors in the prediction of the downhole pressures; thus resulting in severe and costly deviations from its nominal value. Although detailed first principles multiphase flow models have been used for simulation and control purposes in (Pantelides and Renfro, 2013; Eaton et al., 2017), the scarcity of some model parameters (which are not easily measured in real drilling operations) places a demand on empiricism for model adjustment purposes. Furthermore, closed-loop empirical model identification can be costly and disruptive to MPD operations; thus causing instabilities.

With the occurrence of sensor failure and loss of feedback signals (common in MPD operations), maintaining control via high fidelity simulators working in parallel with lower-order empirical models becomes very important. Hence, operating and controlling drilling programs with both classes of models has delivered huge benefits while achieving acceptable sustainability, as demonstrated by Eaton et al. (2017). The need for fast computations and increased accuracy has inspired the development of several low order control models in the drilling industry. Some of the prevalently used models include the SINTEF's model (Petersen et al., 2008) and Stammes et al. (2008) hydraulic model.

A subset of these empirical models that describe specific drilling properties such as rate of penetration, frictional pressure drop, rotational dynamics and weight on bit is also under continuous development (Asgharzadeh Shishavan et al., 2016). Besides the literature developed models, several proprietary simulation models (embedded in commercial simulators) have been developed by different oil companies. However, the numerous developments of advanced modelling tools produced by the academia in the last decade have not fully gained industrial acceptance and implementation. The perspective of industrial operators on the use these models as reported by Sugiura et al. (2015) showed that model validation and benchmarking must be carried out; with limitations and assumptions explicitly stated if industrial applicability is desired. The capability of these models to quantify an envelope of safe operating conditions (based on the continuous calculation of the system's boundaries) using the current state of the well and topside machine limitations is also an important attribute of these models affecting their industrial acceptability (Breyholtz et al., 2011; Breyholtz and Nikolaou, 2012).

Real-time measurement techniques used in the drilling industry include wired coiled tubing telemetry (WCTT), Mud Pulse Telemetry (MPT), Wired Drill pipe Telemetry (WDPT), Acoustic Telemetry (AT), and Wireless Electromagnetic Telemetry (WET). The performances of these technologies are summarised in Table 11.1. By using data (manipulated, controlled and inputs) from these telemetric systems, a calibrated annular flow model may be written and controllers designed to achieve a stable annular pressure as described by an objective function (Asgharzadeh Shishavan et al., 2016).

Table 11.1. A comparative performance of LWD telemetry technologies (Mwachaka et al., 2019).

Features	LWD telemetry technology			
	Electromagnetic	Acoustics	Mud pulses	Wired Drill pipe
Maximum transmission data range (bps)	10	20	20	57,600
Maximum depth (m)	5,500	3,700	12,200	Unlimited
Data quantity	Medium	Low	High	Very high
Signal attenuation	High	High	Medium	N/A
Signal interference	High	Medium	medium	low
Installation and other costs	Medium	Medium	Low	High

11.1.2 Control and Automation of Managed Pressure Drilling

Although drilling operations possess some elements of a mechanical system with important associating concerns (vibration control, equipment performance monitoring and maintenance), process control is similarly essential. In the latter, issues like mudflow, surface and downhole pressure management become important for operational efficiency and safety (Breyholtz et al., 2010b). Managed Pressure Drilling (MPD) is an emerging technology formed out of this necessity of precise wellbore pressure control within tight bounds. The use of a closed annulus, valves and additional pumps together with the main fluid circulation pump makes MPD different in contrast to a conventional drilling process (Nikoofard et al., 2013; Breyholtz et al., 2010a; b). In conventional drilling, drill mud is returned to the surface through an open line at atmospheric pressure. The closed circulation nature of MPD operations provides better flexibility than conventional drilling in which pressure control is usually achieved by pump rate and mud weight adjustments alone. According to the SPE/IADC, *MPD is an adaptive drilling process used precisely control the annular pressure profile throughout the wellbore. The objectives are to ascertain the downhole pressure environment limits and to manage the annular hydraulic profile accordingly*. The intricate nature of such a system requires the application of multivariate control strategies, for which model predictive control (MPC) is often preferred; IMC and PI control schemes have also been frequently adopted (Bjorkevoll et al., 2010; Ma et al., 2016; Asgharzadeh Shishavan et al., 2015; 2016). Furthermore, the multiplicity of operational scenarios and the simultaneous considerations needed for the highly interdependent variables (weight on bit, penetration rate, surface flowrates and pressures) characterising the MPD system imply that manual procedures and workflows cannot guarantee the continuous satisfaction of strict pressure

constraints. Control schemes like MPC provide coordinated operability of the process via the automation of lower-level decisions, thus allowing humans to attend to higher-level decisions (Zhou and Nygaard, 2010; Landet et al., 2012; Pixton et al., 2014).

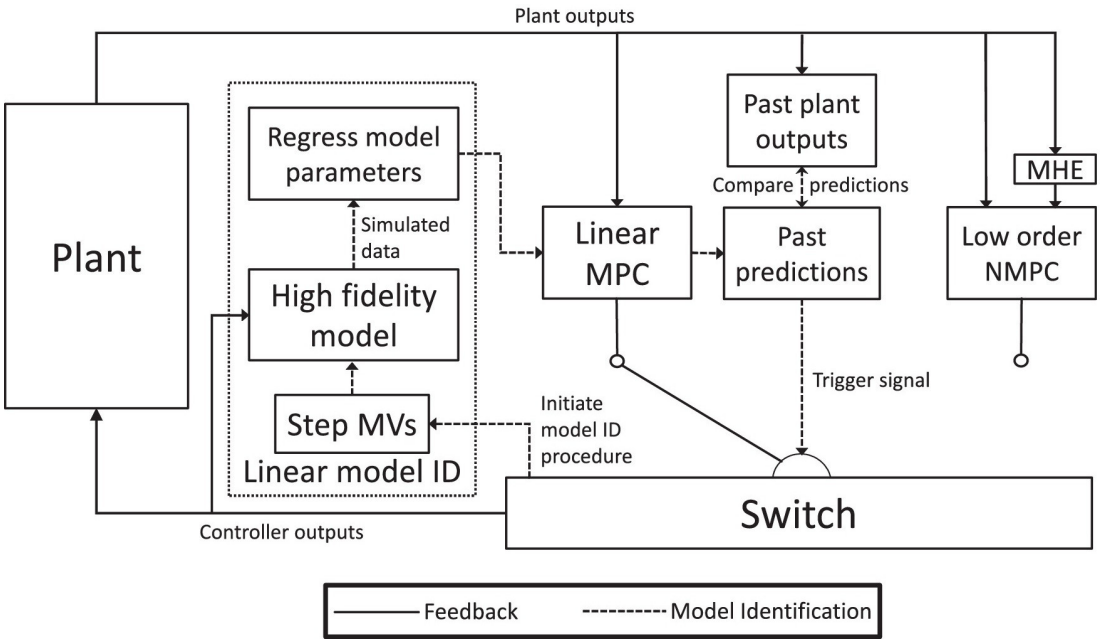

Figure 11.3. Diagram of a switched control system (Eaton et al., 2017).

In exploring the shallow gas Nagar prospect in the southern coast of Myanmar, PETRONAS had to apply MPD technology for quick kick detection and accurate pressure control to maintain economic viability of the project (Fredericks et al., 2008). It was estimated that within 3 minutes, the installed system would have to detect and shut in a gas influx and circulate the gas out the wellbore while controlling the BHP within safe limits of ± 15 psi during active drilling and ± 45 psi during drill pipe connection procedures. This is a classic example that demonstrates the complicated nature of the well control problem. Tackling this challenge with the help of three other service providers made PETRONAS the first to develop and implement an automated real-time pressure control system while drilling. Further details on the implementation of their dynamic annular pressure control (DAPC) system and the lessons learned during the application of this technology can be found in Fredericks et al. (2008) The probability of such successful implementation can be increased if high-quality downhole data becomes available through wired drill pipes (or competitive technology).

High-speed telemetry systems have been applied in the studies of Park et al. (2017), Pixton et al. (2014) and Asgharzadeh Shishvan et al. (2015) for the regulation and control of ROP, BHP and WOB during MPD operations. A nonlinear multivariate MPC framework that directly utilises downhole and surface data is utilised in these studies. Asgharzadeh Shishvan et al. (2016) also applied a similar control strategy with further adjustments of other conditions such as the drill pipe rotation, bottomhole pressure and hook position for dual gradient drilling operations. Their proposed algorithm showed good performance in a high-fidelity simulation environment. With the obvious inability to use high-fidelity models for real-time control purposes (due to computational cost), Eaton et al. (2017) developed a switched control scheme (Fig. 11.3) that implements a linear empirical control model of satisfactory accuracy in comparison to high fidelity models. A lower-order NMPC controller is also utilised for maintaining control over the process during empirical model identification tasks (using simulated data from a high fidelity model); thus reducing the computational cost.

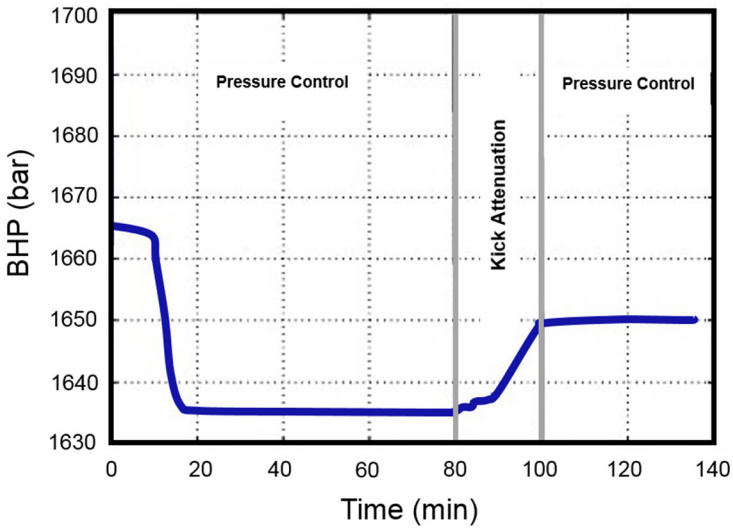

Figure 11.4. Bottomhole pressure control during a kick at 80 mins (Zhou and Nygaard, 2011).

This strategy allows for the inclusion of the slow but very accurate high-fidelity model without interrupting the process. The frequency of gas kicks in most drilling operations has warranted the development of a novel model-based control scheme for kick detection and attenuation by means of real-time pore pressure estimation (Zhou et al., 2009; 2010; Hauge et al., 2013). The proposed method also lends itself to fluid loss mitigation purposes in naturally fractured formations. Robust controller design using linear matrix

inequalities has been formulated for kick handling purposes by Aarsnes et al., (2016a). Handling gas influx during MPD operations depends on the size of the kick (Fig. 11.4); while small kicks may be circulated out by increasing surface backpressure, larger kicks may be handled using standard well control procedures (such as shutting in the well). This is because a planned limit for the influx indicator is usually defined before the MPD operation (Nikoofard et al., 2013). If this limit is exceeded, the conventional well control is usually implemented with considerations on the operational limits of the choke valve and pressure margins that could fracture the formation (Breyholtz and Nikolaou, 2012). These considerations are not only dependent on the prevailing conditions of the downhole conditions, but also on the field and the equipment capabilities.

The application a dynamic programming (DP) approach for the downhole control and optimisation of a drilling system was presented by Ke and Song (2018). They constructed a novel drilling dynamics model and a customised DP algorithm for improved computation efficiency and controller robustness as validated by a higher-order dynamic model. Tian and Song (2018) designed a two-chain observer strategy to estimate real-time states of the drilling system dynamics and the prevalent downhole conditions. Their design showed good performance in addressing measurement/signal delays of mud pulse telemetry systems. Other modelling advancements in this regard include (Narasingam and Kwon, 2017; Narasingam et al., 2017; 2018; Siddhamshetty et al., 2018a; 2018b). Autonomous directional drilling using a mud motor and rotary steerable systems is also an area that has received attention from the process systems and control community using MPC technology (Demirer et al., 2019; Zhao et al., 2019). These systems are often formulated and solved as Mixed-Integer Quadratic Programs due to the presence of binary and continuous quantities. Satisfactory trajectory control of the drill string while satisfying operational constraints has been achieved as detailed in Zhao et al. (2019).

Although downhole uncertainty continues to drive automation-related research endeavours (with increasing contributions in the last decade), the industrial implementation of these automated control methods has remained at a low level (Breyholtz and Nikolaou, 2012; Pournazari et al., 2015). A further complication that limits the holistic automation of drilling systems is that several independent software solutions exist that address the different aspects of the drilling operation in isolation (Busch et al., 2018; Pastusek et al., 2019). Integrating all solutions within a single control framework is

not a trivial task. In order to address this challenge, a control hierarchy design for production optimisation by Saputelli et al. (2003) was adapted to drilling automation operations in the work of Breyholtz and Nikolaou (2012). The multilevel control approach comprises a feedback control level, a supervisory control level and an optimisation level. Despite these advancements, Breyholtz and Nikolaou (2012) highlighted that it is impossible for the automation design to foresee all possibilities in such a complex and uncertain operation as drilling; hence the driller must be able to manually take over the operation at highly critical moments. Furthermore, more recent advancements in sensor design (Pournazari et al., 2015; Chhantyal et al., 2017) also emphasise the need for occasional manual intervention due to sensor drift (from calibration). It is thus evident that the applications of the process control techniques discussed herein show good potential for increased drilling efficiency, safety and reduced cost if they are well integrated into existing manual drilling procedures in industry.

11.1.3 Drilling Optimisation

Depending on the intended application within the multifaceted nature of a drilling program, mathematical optimisation techniques have shown great potential for operational improvement. Downhole pressure control using NMPC schemes is one of the most explored aspects as far as optimisation is concerned (Nikoofard et al., 2013; Aarsnes et al., 2016a; Ma et al., 2016). However, the rate of penetration is a parameter drilling engineers aim to always optimise. Eren and Ozbayoglu (2010) applied multiple linear regression for parameter estimation of an ROP equation (in terms of the WOB, formation depth and rotary speed) based on real-time data. The authors sought to arrive at an optimisation methodology that utilises past drilling data while predicting the drilling trend for optimum drilling parameter selection and cost savings; this was achieved. Based on a similar concept, Rommetveit et al. (2004) similarly, introduced a bit load optimisation module that modulates the rotary speed and WOB for an optimal ROP. With the application of their solution algorithms in the module, they reported that ROP increased by 15-30%. The application of ROP optimisation software developed by Chapman et al. (2012) and Detournay et al. (2008) has shown the possibility of attaining reduced equipment vibration and equipment failure. The software employs a formulation that relates the ROP (depth of cut per revolution) to the WOB and bit torque.

The concept of mechanical specific energy (MSE), introduced by Dupriest & Koederitz (2005) evaluates the efficiency of drill bits in real-time; this approach has been readily applied by drilling operators as an optimisation tool in combination with drilling logs for decision support (Nikolaou et al., 2005). Koederitz and Johnson (2011), achieved semi-autonomous steering optimisation during drilling using the MSE concept. A simulated annealing optimisation algorithm coupled with an abductive neural network was applied by Lee et al. (1998) for the prediction of drilling performance (torque, tool life, metal removal rate, and thrust force) with drill diameter, cuttings speed and feed rate as the input parameters. Several drilling experimental tests performed confirmed the effectiveness of this approach. Enhanced visualisation and interpretation techniques in state-of-the-art drilling simulators provide an optimised 3D tracking of the well trajectory as drilling progresses (Sugiura et al., 2015). It was highlighted that drilling optimisation here is not static because drilling parameters vary as the depth increases. Instead, it is a dynamic function of depth. Hence continuously varying constraints (e.g. due to formation heterogeneities and strengths) and varying optimised parameters cannot be avoided if drilling cost must be minimised. Several other simulation packages for optimising drill string torque and drag, wellbore propagation, well trajectory (inclination and azimuth) and downhole steering have been developed as detailed in Siguira et al. (2015). It is evident from these contributions that classical optimisation in the industry is usually a semi-heuristic based approach that relies on several simulation studies; the use of standard mathematical optimisation concepts has rarely been adopted in the industry.

Drilling rigs are not only used in drilling new wells, but also in servicing existing ones (workover). However, the number of new target well sites and existing wells usually exceeds the number of available drilling rigs; thus increasing the complexity of the operation (Tavallali et al., 2015). This necessitates the determination of optimal rig-to-well allocation, rig routing and scheduling (collectively described as workover rig scheduling – WRS). Although geared towards production optimisation, this aspect of drilling has received considerable attention from Tavallali et al. (2016a; b) and Gupta and Grossmann (2012). Rigorous mixed-integer nonlinear/linear optimisation formulations (with thousands of binary variables) have been formulated with adaptive algorithms for efficient solutions, thus aiding field development decisions. Such depth of work has hardly been adapted to other drilling aspects.

11.1.4 Application of Artificial Intelligence Techniques

With increasing industrial demand for intelligent drilling automation and optimisation, artificial intelligence holds a promising potential for bridging the gap between the two tasks, improving current drilling practices and real-time decision making. The most widely used techniques include artificial neural networks, fuzzy logic, genetic algorithms, support vector machines and hybrid techniques (Bello et al., 2015). Such computational intelligent methods can be used to analyse data from sensors, survey data, geology data and the well plan in order to make real-time closed-loop predictions for fast reaction (prompt flags of potential anomalies) and resolution of drilling dysfunctions (Nunoo et al., 2018). Big data analytics is also an emerging trend in the oil and gas industry that aids the application of AI techniques (Mohammadpoor and Torabi, 2018). After generating a dataset of specific offshore drilling information using fuzzy logic, Mendes et al. (2003) implemented a genetic algorithm for the prediction of feasible trajectories for the wells and directional drilling parameters using retrieved datasets of similar drilling scenarios. Popa et al. (2008) applied case-based reasoning (an AI technique) for the selection of the optimum hole cleaning procedure in unconsolidated sands by collating datasets from nearly 5000 wells; an accuracy of 80% between AI proposed methods and those actually implemented was observed. Wang et al. (2011) applied an artificial neural network model developed by British Petroleum (BP) for the optimal selection of deep-water floating platforms (a decision dependent on many interconnected variables). In solving this model, the Levenberg-Marquardt algorithm was applied. This resulted in 70% accuracy for 10 datasets with limited errors, thus validating this quantitative approach (which would have been otherwise carried using engineering judgement alone).

The capability of ANN for accurate real-time prediction of frictional drag and drill string contact force as a function of the radial clearance, slack-off load, bending stiffness and other drilling parameters was demonstrated by Sadiq and Gharbi (1998) This prediction has tremendous importance when time consumption due to expensive downhole trips (for BHA replacement) are to be avoided. Rooki et al. (2014a; b) applied an experimentally validated back propagation neural network coupled with multiple linear regression for the prediction of cuttings concentration in an annular wellbore during foam drilling. They compared the performance of their ANN model with the results of a mechanistic cuttings transport model and realised an absolute average deviation of less than 6%. A similar

approach by Al-Azani et al. (2019) was adopted for hole cleaning; this was, however, based on 116 experimental data records. Chamkalani et al. (2017) developed a pattern recognition neural network (Fig. 11.5) for the drilling optimisation in shaly formations. An extensive discussion on the application of AI for well integrity problems, operational troubleshooting, real-time drilling optimisation and well planning can be found in Bello et al. (2015) In addition, the application of AI techniques in drilling fluid engineering has been comprehensively reviewed by Agwu et al. (2018a; 2018b). The highlighted applications include rheological parameter determination of various drilling fluids (Rooki et al., 2012; Rooki et al., 2014a), prediction of loss circulation (Toreifi and Rostami, 2014), differential pipe sticking (Murillo et al., 2009), fluid flow patterns (Oladunni and Trafalis, 2011), downhole fluid properties (Gu and Oliver, 2007), mud velocity/flowrates and pressure drop (Kamyab and Rasouli, 2016). It should be pointed out that AI techniques should be applied with care; the necessity of maintaining sensible physical interpretations of predictions cannot be overemphasised, despite high values of statistical correlation indicators (RSME, R^2), which may be misleading. A comparative analysis(Agwu et al., 2018b) based on different AI techniques applied in the drilling industry showed that ANN, SVM, fuzzy logic and GA are robust against noise (in data); whereas, fuzzy logic ranks highest in terms of convergence speed. Nevertheless, the susceptibility to overfitting, limitations of data volume, generalisation and self-organising ability are other criteria that may be assessed when choosing these AI methods.

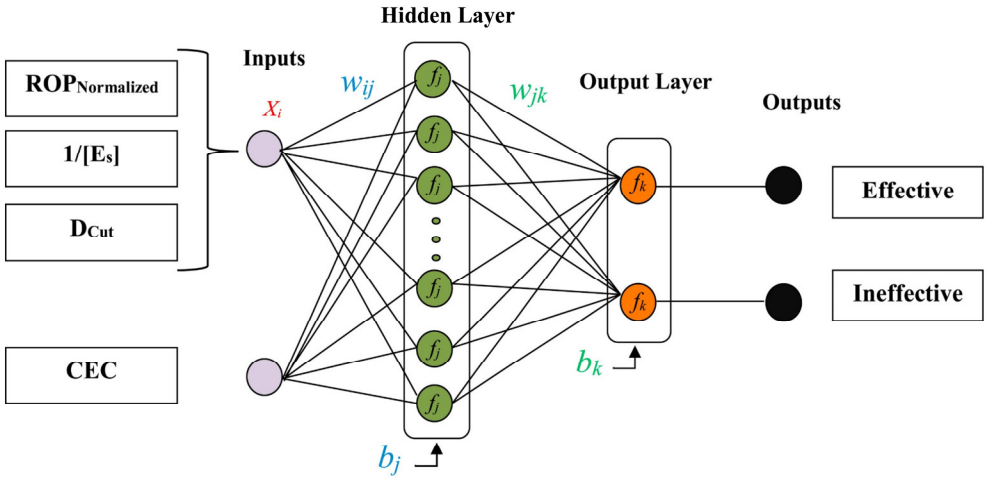

Figure 11.5. Schematic structure of a pattern recognition network (Chamkalani et al., 2017).

11.2 Integrated Application of Process Control (PSE-based) and Fluid-Dynamics (CFD-based) Perspectives for Sustainable Drilling Operations

Process control and optimisation studies have largely simplified or ignored vital phenomena such as the effects of cuttings/particle modulation on the fluid flow profile and wellbore pressure; whereas, cuttings transport studies have neglected the need for real-time monitoring, automation and control of drilling parameters such as downhole pressure. Although some of the developed mechanistic models described thus far, account for downhole pressure variation as a function the mud flowrate and other key parameters, the fast-paced dynamics of drilling operations require frequent calibration using field data for their industrial applicability. Hence, an integrated approach (PSE + CFD) will be desirable for drilling operations. Despite the pronounced difficulty such an attempt may require, Cayeux and co-workers (Cayeux and Daireaux, 2009; Cayeux et al., 2012; 2014) have attempted such integration for real-time applications.

A cuttings transport model was developed by Cayeaux et al. (2014) to monitor two separate drilling operations (conventional and MPD) in the North Sea. Unknown parameters such as the cuttings size were calibrated to yield a good match with topside measurements, such as the slurry flow rate (Cayeux et al., 2014). This enabled precise identification of cuttings bed locations along the wells, and the adjustment of drilling parameters with operational recommendations for bed removal. A real-time operation support tool developed by Cayeux and Daireaux (2009), enabled automatic friction monitoring with the capability of triggering alarms when severe downhole deterioration was detected. The system's online interpretation of large amounts of drilling data aided this early recognition of downhole problems; this was also demonstrated in a similar work of theirs in a North Sea well (Cayeux et al., 2012). Warnings that indicated poor hole cleaning were obtained; thus guiding the operator's decisions on cleaning the wellbore (after stopping the drilling operation) or continuing the drilling process. A similar contribution by Frangos (2017) involved the development of a statistical-based approach (using ensemble Kalman filtering) for the prediction and monitoring of the location and extent of cuttings build-up along a wellbore. Their model can capture the dominant characteristics of the cuttings transport process while incorporating process disturbances and uncertainties in real-time field measurements. Salminen et al. (2017) developed a real-

time method for predicting impending stuck pipe with sufficient warning for its prevention. Their method implements a hydraulic model, real-time and historical data and some data processing techniques for predicting the risk of a stuck pipe. They demonstrated early prediction of stuck pipe incidents; thus allowing preventive measures to be taken. No false alarms were observed using their proposed approach.

It is worth emphasising that similar drilling problems in field operations do not necessarily present themselves with the same pattern of symptoms. Hence, the detection of abnormal drilling conditions depends on rigorous analysis of multiple signals (e.g. abnormal rise in friction factor) if safety must be maintained (Cayeux et al., 2017). These analyses, in turn, require the application of specialised tools, which must be used in an integrated manner. As research in both fields continues to advance, better integration methodologies for sustainable operations should be sought after.

PART IV: RESEARCH CONTRIBUTIONS & THESIS CONCLUSIONS

Chapter 12 Research Contributions and Thesis Conclusions

12.1 Research Contributions

This thesis has bridged the gap between the application of CFD and mathematical optimisation for enhanced drilling and production (Fig. 12.1) operations by producing several novel research contributions detailed herein.

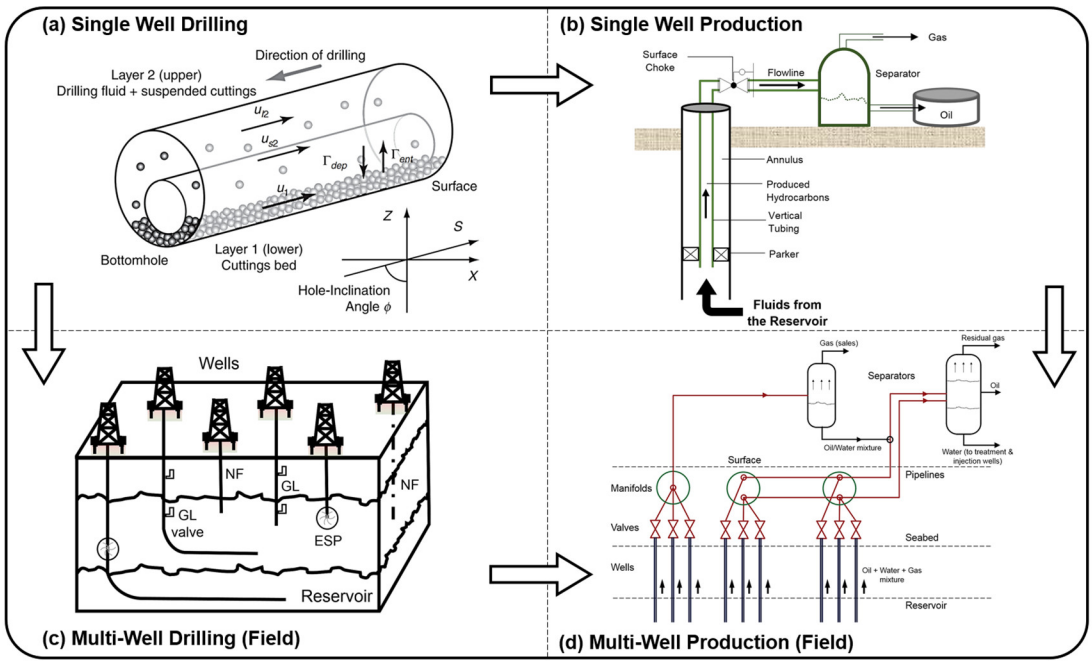

Figure 12.1. Drilling and Production case studies in this thesis (Naganawa et al., 2017; Epelle and Gerogiorgis; 2019a; b; c; d).

12.1.1 Drilling Parameters and Cuttings Transport

For the first time, a CFD-based procedure that simultaneously considers the influence of operational parameters, rock and fluid properties and geometrical parameters on cuttings transport efficiency is presented (Chapter 3). Specifically, no previous study had systematically evaluated the interdependencies between varying drill pipe eccentricities, fluid rheology, pressure drop and cuttings concentration through experimentally validated simulations in a horizontal annulus. Drilling engineers in the oil and gas industry can thus adequately plan wellbore cleaning operations, with well-informed decisions made concerning the surface pumping requirements, based on the insights provided herein. Detailed quantitative analysis on the spatial velocity and concentration variation in an

annulus under turbulent transport conditions has also been performed to elucidate the cuttings transport behaviour. The novel analysis presented in Chapter 4 quantifies the influence of the fluid bulk motion and the drill pipe rotary motion on the axial, tangential and slip velocities of the particles. Striking differences between the velocity profiles of concentric and eccentric annular configurations, turbulence modulation effects due to particle size differences and a replication of some experimentally observed flow behaviours (such as streak-like fluid ejections responsible for particle lift in the bulk flow region in the annulus and particle dispersion effects) are observed in the simulations carried out in this project. These have hardly been reported in previous publications; thus providing new insights on particle transport for sustainable drilling operations. While experimental measurements of cuttings velocity during high-speed turbulent flows with high Stokes numbers are difficult to obtain because of the increasing gravitational effects for large particles and set-up cost, CFD/DEM models implemented in Chapter 4 show remarkable potential for predicting and understanding such flow conditions in a more cost-effective way. In addition to the novel flow physics observed, a new workflow for carrying out mesh quality and independence studies and result post-processing of has been presented in Chapters 4 and 5. This has been readily adopted by more recent publications in the field of particle transport modelling with due reference made to the contributions in this thesis.

12.1.2 Particle Sphericity and its Influence on Cuttings Transport Velocity in Complex Annular Geometries

A limitation of previous CFD-related contributions that study cuttings transport in drilling operations is the simplifying assumption of perfectly spherical cuttings, which is hardly the case in real field operations. The relative ease in mathematical description (when shaped-induced flow complexities are neglected) coupled with rapid computations obtainable are the main reasons for the prevalence of this assumption in most CFD studies. Considering the scarceness of published literature which address this challenge, the effect of particle shape is incorporated into the equations of the Eulerian-Eulerian model by a modification of the Syamlal-O'Brien exchange coefficient as shown in Chapters 5 and 6 respectively. Furthermore, an analysis of cuttings transport in a fairly different geometry compared to what has been previously applied using two types of drilling muds is presented. Such geometry (Fig. 6.1) considered here is often realisable in extended-reach and deviated well drilling. Besides the insights provided on the dynamics

of the transport process, a modification strategy which could be extended for capturing more advanced phenomena (particularly when particle contact models are used within the Lagrangian-Eulerian framework) is also provided. We particularly observe that non-spherical particles tend to travel faster in the annulus when transported by a non-Newtonian fluid compared to spherical particles. However, the dominance of non-spherical particle velocities depends on the nature of granular flow (dense or dilute) as discussed extensively in Chapter 6. The assumption of perfect particle sphericity may lead to a significant decrease in the pressure drop in an eccentric flow domain. These observations have also been experimentally validated by several published studies, as described in Chapters 5 and 6.

12.1.3 The Impact of Fluid Rheology on Particle Deposition Pattern

Field reports of drilling companies have revealed that stuck pipe problems constitute approximately 70% of operational time loss during drilling. This problem is largely attributable to inefficient hole cleaning. Increasingly challenging drilling conditions (such as extended-reach drilling in the arctic) imply the continued prevalence of this problem. However, it has been demonstrated in this thesis, that proper rheological design of drilling muds coupled with an understanding of deposition-prone locations (via physics-based simulations) could significantly facilitate effective hole cleaning operations. For the first time in published literature, it was discovered that the inclined-to-vertical section of a deviated annulus is the most susceptible to cuttings deposition. In conjunction with this observation, a shifted (asymmetric) deposition pattern was also identified and determined to be strongly influenced by the particle size and the drilling fluid's rheological properties. On applying a more suitable fluid with enhanced viscosity characteristics, a more centralised transport behaviour of the drill cuttings was observed; this aids cuttings transport

12.1.4 Development of a Problem Complexity Reduction Strategy for Efficient Production Optimisation

Operational planning and management of an oil and gas field require an integrated application of several models that describe the respective components of a production system (the reservoir, wells, valves, flowlines, pipelines, and separators – Figs. 12.1 and 12.2). However, the operating time scales of these components vary significantly; thus hindering their coupled implementation in an optimisation framework. Previous

contributions in this regard have neglected the dynamic behaviour of certain field components; thus optimising them in a compartmentalised manner (slow subsurface flow dynamics decoupled from the fast flow dynamics of wells, pipelines and other surface facilities). The work described in Chapter 7 addresses this problem by proposing an integrated multiperiod optimisation formulation that couples the dynamic behaviour of all production system components to enhance water allocation among injection wells in a field undergoing secondary production. The coupling of high-fidelity simulators for the respective components is achieved via an effective proxy modelling procedure (Fig. 12.2) described in Chapter 7. Streamline simulation, a sophisticated approach for visualising the reservoir's fluid distribution, is utilised to propose good initial guesses to the NLP formulation. This streamline-based optimisation methodology has hardly been performed in previous contributions. The result of the implementation of this approach is an optimal injection strategy with reduced field water consumption and thus increased NPV; this is attributable to a corresponding reduction in water operating costs. It is estimated that oil companies produce up to three barrels of water for each barrel of oil from depleting reservoirs, and this costs approximately $40 billion annually to handle. Field engineers in the oil and gas industry who are constantly faced with this challenge amidst other operational constraints can benefit from the proposed methodology for enhanced operations. The integration strategy proposed also enables the oil industry to make the most of the simulation tools at its disposal.

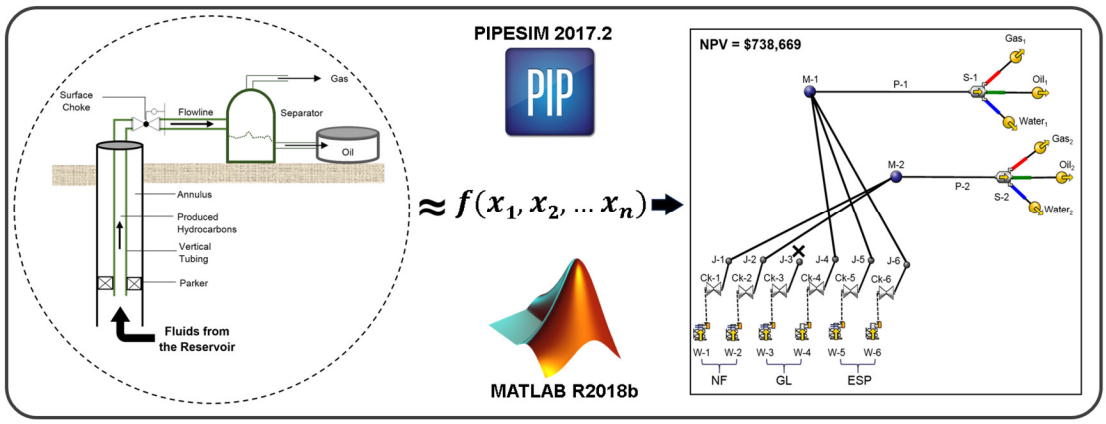

Figure 12.2. Model complexity reduction for efficient production optimisation.

12.1.5 Simultaneous Production Optimisation of Operationally Distinct Well Behaviours

Production wells in oil and gas fields differ in their mode of operation; however, previous production optimisation studies have focused on optimising operating scenarios with similar well types. This is addressed in Chapter 8 by formulating an MINLP optimisation problem consisting of naturally flowing wells, gas lift wells and ESP-assisted wells. This well combination creates complex pressure responses at the manifold and pipeline level, which are accounted for via routing constraints and a complex objective function in terms of the NPV. Furthermore, key attention is paid to the critical drawdown pressure of the respective wells, which in turn affect the wellhead pressure. This is done to avoid sand production which could be detrimental to the overall system's performance as demonstrated in the studies of Tiffin et al. (2003), Wong et al. (2005) and Epelle and Gerogiorgis (2019b). The adaptability and flexibility of the proposed formulation to various operating scenarios and practical operational difficulties is also demonstrated. Specifically, well intervention problems, a switched well operation mode and changes in the water cut, gas-oil ratio and fluid handling capacities of the plant are incorporated via different case studies in the optimisation formulation. In addition, the complexities of varying wellbore geometries with distinct multiphase flow properties are accounted for in the network model development phase. These detailed considerations constitute the novel elements of the presented study (Chapter 8) in comparison to previous work. Another concept of immense significance illustrated herein is the potential for increased petroleum production via optimally determined well routings. Without the implementation of more expensive procedures like well stimulation, secondary production, and installation/expansion changes to production infrastructure, improved fluid recovery can be attained by only changing the well-to-manifold connections systematically. Thus, this represents a cost-effective approach which field engineers can apply to increase production rates and consequently field profitability.

12.1.6 Global Optimisation of Production Systems via Problem Reformulation

MINLPs combine the modelling capabilities and corresponding challenges of integer and nonlinear programming into a flexible and multifaceted framework; thus resulting in formulations which may be very difficult to solve. Additionally, the problem size, complexity and nonconvexity of a production optimisation problem imply that MINLP

solvers are prone to getting trapped at locally optimal solutions in the optimisation search space. To circumvent this problem and obtain improved solutions, various problem reformulation strategies have been proposed in Chapter 9 via piecewise linear approximations using SOS2 constraints. The benefits and demerits of both formulations are systematically studied in terms of their robustness, ease of automation, and computational performance on problems of different sizes. This novel comparative analysis presented in Chapter 9 enables quality assessment on the relative performances of the respective formulations and their impact on the overall oil production. Compared to the MINLP formulation in Chapter 8, the problem in Chapter 9 is of higher complexity with fluid routings occurring at 2 levels (well to manifold and pipeline to separator). Moreover, water coning physics is embedded in the models; this has hardly been studied in production optimisation problems in literature. Most importantly, the performance of the proposed formulations yields increased efficiency (in terms of solution time) and higher NPVs compared to PIPESIM's® network optimiser (a widely used wellbore and surface facility simulator in the oil and gas industry).

12.1.7 Fast Production Optimisation using Adjoint Formulations for Well Placements

In this thesis, the production optimisation-related contributions were not limited to field operations alone but were also extended to infrastructural planning and design (specifically well placement optimisation). To achieve this, the study in Chapter 10 implements a modification of an existing pseudowell-based injection well placement algorithm (Zandvliet et al., 2007) with the application of an auxiliary objective function (the Lorenz coefficient), for the improvement of oil displacement efficiency. We also modify the well placement algorithm in MRST to include both injection and production wells. Furthermore, we computationally compare the different methods of optimising the well positions (injectors only, producers first and injectors next and injectors first and producers next) and examine their efficiencies in terms of the final recoveries and the Lorentz coefficient. Flow diagnostics via enhanced visualisation tools are applied to gain insights into the fluid distributions in the reservoir under geological uncertainty. This study implements an efficient adjoint formulation in MRST for rapid computation of gradients used in the optimisation formulation (for both well placement and control); thus resulting in a reduced number of iterations and computational times compared to previous studies that apply evolutionary and gradient-based algorithms (Tavallali et al.,

2013; Isebor et al., 2014; Onwunalu and Durlofsky, 2010). An investigation on the influence of the solution search space for each well on the final oil recovery, final oil saturation and computational cost is also performed using a rather complicated geological model of the Norne Field consisting of 30 production wells. These points constitute the novel elements of Chapter 10.

12.2 Thesis Conclusions

This PhD thesis has simultaneously addressed key challenges of two important aspects of oil field operations (drilling and production) necessary for sustainable profitability. High-performance CFD modelling methods have been applied to gain novel insights for drilling systems design and operation by employing flow simulations and enhanced flow field visualisations. Moreover, mathematical optimisation procedures have been implemented for improving petroleum recovery of production systems and enabling better infrastructural planning; thus making this thesis, the first to proffer viable solutions to both aspects of oilfield operations within a single framework.

The CFD-based aspect of this PhD thesis implements both Eulerian-Eulerian and Lagrangian-Eulerian modelling methods for the description of cuttings transport phenomena and establishes the interdependencies between several drilling parameters. Through detailed sensitivity analysis, the impacts of drill pipe eccentricity, wellbore inclination, drill pipe rotation, bit penetration rate, fluid rheology, and particle properties on the cuttings concentration, pressure drop profiles and flow velocities of the respective fluid, and solid phases have been quantified for different drilling scenarios, configurations and flow regimes. Enhanced post-processing functionalities of different CFD tools have been applied to evaluate the regions of the annular domain that are prone to deposition in comparison to others. With experimentally validated simulations on cuttings transport, the new understanding gained (detailed in conclusions of Chapters 3, 4, 5 and 6) would facilitate industrial wellbore cleaning operations if methodically applied.

Trailing the development of CFD-models for solving wellbore cleaning problems during drilling, was the development of a mathematical framework for surrogate model-based production optimisation. Motivated by the over-simplifications of the production process in previous studies, this aspect of this thesis focused on a detailed computational optimisation of integrated component models, which describe the entire production field

(from the reservoir to the surface facilities). NLPs MINLPs and MILPs were formulated for this purpose and solved using commercial and open-source optimisation solvers. In comparison to previous work on this subject, complex flow physics and downhole phenomena are incorporated with rapid computational times obtained; this enables real-time decision support.

For both CFD- and optimisation-based procedures, it is discovered that a trade-off must be made between computational time and model complexity. Small models with fewer physics components incorporated are usually solved and optimised faster compared to larger models, which in turn are more complicated. The solution time range obtained varies between, as low as a second to as high as 3 days. However, the optimisation of CFD-based models is still an open research question, as highlighted in Chapter 11. In addition to the specific future research directions proposed in the Chapters 3-10 of this PhD thesis, a summary is presented next with new research directions identified.

12.3 Recommendations for Further Research

The following topics represent some unaddressed challenges that pave the way for potential research opportunities.

12.3.1 A Production Perspective

- The desire to replace super challenging models with calibrated simpler models will increase the need for machine learning (AI techniques). These techniques will also be very suitable for proxy model development from numerous simulations of expensive commercial software, which contain high fidelity models. Hence, the run time may be significantly reduced for future prediction and optimisation studies.

- More studies that analytically combine all aspects of a production system are needed. Although, simplified analytical models of pressure drop and porous media flow will be inevitable, such investigations will open a new area for further research in production optimisation. Furthermore, a comparison of compartmentalised and holistic methods of performing production optimisation tasks are needed.

- Studies that perform production optimisation on fields containing complex well types such as multilaterals are scarce. Handling multiple completions and describing the

productivity index of this kind of wells are the main hindrances towards their implementation in production optimisation frameworks.

- Besides water injection, production optimisation involving other Enhanced Oil Recovery (EOR) methods such as gas-injection and polymer flooding are scare in literature and deserve more attention.

- A comparative analysis of stochastic and gradient-based optimisation methodologies for well placement is also worth investigating in future research. Performance analysis of software packages capable of performing such optimisation tasks such as Stanford GPRS and ECLIPSE will be very useful.

- A recent article by Kronqvist et al. (2019) describes in great detail, the computational performance of solvers and algorithms for MINLPs. Review articles of this kind for NLP and MILP formulations are very needed within a production optimisation context.

12.3.2 A Drilling Perspective

- Advanced drilling optimisation methodologies are required to determine the optimal ROP while ensuring adequate hole cleaning. Although a high ROP is often desired and indicates good drill bit performance, the accompanying increase in cuttings influx rate into the wellbore must be compensated for while drilling. Optimisation studies will also help clarify ambiguities concerning the use of low-viscosity mud (for promoting turbulence and increased transport efficiency) or the use of medium viscosity muds, which promote better suspension.

- Turbulence modelling is still a challenging topic in the field of fluid dynamics. Although several advancements have been made in describing turbulence in single-phase flows, more work is still required for multiphase flows (especially those involving particles). In this age of big data, the combination of machine learning and turbulence modelling (using physics-based and statistical methods) holds great potential for understanding turbulence-induced particle motion. This may also be useful for increasing the accuracy and reducing the uncertainty of RANS models implemented in commercial CFD codes used in cuttings transport studies.

- More research is needed on the coupling of CFD and DEM methods for understanding the effect of particle collision on the dynamics of cuttings transport. However, the accuracy of simulations is dependent on the contact models (Spring-dashpot and Hertzian) and several input parameters of the rock particles (friction coefficients, elasticity properties, Young's modulus, Poisson ratio), which are only obtainable from material calibration studies. Unfortunately, these studies are scarce. The potential for FEM-DEM coupling (Celigueta et al., 2016) in describing cuttings transport needs to be further explored. Further advancements in GPU architecture are required for these time-consuming calculations (Govender et al., 2016).

- UBD operations with numerous phases: gas/oil/water influx, drilling mud, solid cuttings, has hardly been modelled via CFD methods (Akhshik et al., 2016; Akhshik and Rajabi, 2018). A detailed evaluation of the impacts of fluid influx on cuttings transport efficiency is indeed worth investigating.

- Comparative benchmarking studies (via experimental validation) on the use of different CFD software is necessary for ascertaining their limitations in modelling several aspects (turbulence, particle deposition, particle tracking and fluid-particle coupling) of cuttings transport phenomena. Furthermore, studies that compare the accuracy of Eulerian-Eulerian and Lagrangian-Eulerian methods for modelling cuttings transport at different particle concentrations are needed.

- Most CFD studies pertaining to cuttings transport have hardly analysed flow behaviour around bends or with a tortuous wellbore. The effect of particle shape has also hardly been considered experimentally and numerically. An essential factor to consider here will be the particle size to mesh size ratio, especially with highly non-spherical particles. The consideration of the smallest cell size (in a mesh) being large enough to contain each particle in LE or EE frameworks still needs clarification; given the fact that cuttings encountered during drilling may be as large as 10 mm and that the modelling accuracy of the fluid motion must be maintained by a reasonably fine mesh. Some authors (Celmiņš, 1988; Gómez and Miloli, 2005) have reported that there is a minimum mesh control volume over which the volume-averaged Eulerian continuum equations for the solid phase are valid; thus, the main question is how fine/coarse should the mesh be to guarantee accurate modelling of large particles? What are the

limitations of the statistical point approximation process, and the Enskog equations for particle representation in comparison to methods that redefine the control volume (via node averaging) in 1-way, 2-way and 4-way coupling (so that this volume is large enough to contain the largest particle in the domain)? Besides the need for more studies that address these questions, the development of novel multi-mesh modelling strategies that satisfy the mesh resolution accuracies needed for both fluid and solid phases may be beneficial.

- Polydispersed particle systems with the aid of a size distribution model have not been widely considered. Furthermore, industrial sand is the most applied type of solid in experimental campaigns. However, various rock types are encountered during drilling.

- Mechanistic and semi-empirical models hardly consider the effects of turbulence fluctuating velocity on the efficiency of cuttings bed removal (Bizhani and Kuru, 2018). Hence, this prevalent assumption of ignoring the effect of flow turbulence on bed erosion needs to be addressed. Furthermore, the effect of fluid rheology on the drag and lift forces if incorporated is also expected to improve the accuracy of these models. More advanced multi-particle velocity measurement techniques (e.g. particle image velocimetry) in highly turbulent flows are needed for extensive validation of these models.

- Future modelling efforts need to incorporate the effects of downhole uncertainty. Increased economic potential from model-based drilling decisions requires the consideration of complicated, uncertain downhole events.

- The development of additional robust closure relations from experiments or direct numerical simulations will hugely aid two-fluid Eulerian-Eulerian models. The application of stochastic particle collision models based on the Enskog Simulation Monte Carlo approach will be useful for dense particulate flow modelling using the LE approach (Subramaniam, 2013).

- Although the effect of drill pipe rotation on cuttings transport has been widely considered, the impact of drill pipe reciprocating motion requires more experimentation and modelling research contributions. A combination of rotary and reciprocating motion is expected to represent the drill pipe motion better.

- 1D and 2D mechanistic models require improvements in correlations for the friction factor, drag coefficient, shear stress between different interfaces, particle deposition and entrainment rates; thus enhancing the reliability of particle deposition predictions along the entire wellbore profile. Highly accurate models are also required for the determination of the wiper trip speed, especially during coiled tubing cleaning operations.

- The development of benchmarking case studies to assess the performance of open source and commercial codes/software is essential (Pastusek et al., 2019). This would be further facilitated by the availability of open-source (sharable and expandable) data sets for model performance evaluation.

PART V: AUXILIARY CHAPTERS

Appendix A

Nomenclature and Acronyms

A.1 Acronyms

AE	Algebraic Equation
AI	Artificial Intelligence
ANN	Artificial Neural Network
APD	Average Percentage Deviation
APE	Average Percentage Error
AR	Aspect Ratio
AT	Acoustic Telemetry
AWT	Average Wall clock Time
AV	Apparent Viscosity (cP)
BB	Branch and Bound
BC	Boundary Condition
B·C	Product of a Binary and a Continuous variable
BHA	Bottomhole Assembly
BHP	Bottomhole Pressure
BOP	Blowout Preventer
BONMIN	Basic Open-source Nonlinear Mixed Integer Optimiser
BM	Bulk Modulus
BP	Bingham Plastic (Rheology)
BP	British Petroleum (Company)
CBC	Coin-or Branch and Cut
C·C	Product of 2 Continuous variables
CDV	Critical Deposition Velocity ($m.s^{-1}$)
CFD	Computational Fluid Dynamics
CFR	Critical Flow Rate ($m^2.s^{-1}$)
CMC sol	Carboxymethyl Cellulose solution
CSA	Cross-Sectional Area (m^2)
CTE	Cuttings Transport Efficiency (%)
CTR	Cuttings Transport Ratio (-)

CTV	Cuttings Transport Velocity ($m.s^{-1}$)
CTFV	Critical Fluid Transport Velocity ($m.s^{-1}$)
DFM	Drift Flux Model
DAPC	Dynamic Annular Pressure Control
DDPM	Dense Discrete Phase Model
DEM	Discrete Element Method
DMD	Dynamic Model Decomposition
DMDc	Dynamic Mode Decomposition with control
DNS	Direct Numerical Simulations (-)
DP	Dynamic Programming
DVR	Data Validation and Reconciliation
ECD	Equivalent Circulating Density
EE	Eulerian-Eulerian
EnKF	Ensemble Kalman Filters
ESP	Electrical Submersible Pump
ESV	Estimated Slip Velocity
FD	Finite Difference
FEM	Finite Element Method
FPSO	Floating Production Storage and Offloading
FVM	Finite Volume Method
FT	Fluid Type
GA	Genetic Algorithm
GOR	Gas Oil Ratio
GL	Gas Lift
GLR	Gas Liquid Ratio
HB	Herschel Bulkley
HP	High Pressure Separator
HX	Hexahedral
IE	Injection Efficiency
II	Injectivity Index
IP	Intermediate Pressure Separator
IPR	Inflow Performance Relationship
IX	Injection Well 'X'

KOP	Kick-Off Point
KTGF	Kinetic Theory of Granular Flow
LE	Lagrangian-Eulerian
LDPE	Low-Density Polyethylene
LES	Large Eddy Simulation
LKT	Lookup Table
LMI	Linear Matrix Inequality
LOL	Lumped Order Lower Models
LP	Low Pressure Separator
LWD	Logging Dhile Drilling
MPD	Managed Pressure Drilling
MD	Measured Depth
MID or GID	Mesh/Grid Independence Study
MILP	Mixed Integer Linear Program
MINLP	Mixed Integer Nonlinear Program
ModVal	Model Validation Performed?
MPC	Model Predictive Control
MPT	Mud Pulse Telemetry
MPWLP	Multicapacitated Platforms and Wells Location Problem
MSE	Mechanical Specific Energy
MSCF	Mega Standard Cubic Feet
MTV	Minimum Transport Velocity ($m.s^{-1}$)
NF	Naturally Flowing
NMPC	Nonlinear Model Predictive Control
NP	Nanoparticle
NPV	Net Present Value
OBD	Overbalanced Drilling
OBM	Oil Based Mud
ODE	Ordinary Differential Equation
OLGA	Oil and Gas Simulator
OS	Operating System
PCP	Progressive Cavity Pump
PD	Proxy Model Data

PDE	Partial Differential Equations
PI	Productivity Index
PL	Power Law
PLSDA	Partial Least Squares Discriminant Analysis
PLC	Programmable Logic Controllers
POD	Proper Orthogonal Decomposition
PSE	Process Systems Engineering
PSO	Particle Swarm Optimisation
PV	Plastic Viscosity (cP)
PX	Production Well 'X'
QDMC	Quadratic-Dynamic Matrix Controller
QUICK	Quadratic Upstream Interpolation for Convective Kinematics
RANS	Reynolds Averaged Navier Stokes
RPM	Revolution Per Minute
RS	Robertson Stiff (rheological model)
RSME	Root Mean Square Error
ROP	Rate of Penetration
RTPO	Real Time Production Optimisation
SCCO2	Supercritical Carbon Dioxide
SCIP	Solving Constraint Integer Programs
SD	Simulation Data
SETS	Stability Enhancing Two-Step
SIMPLE	Semi-Implicit Method for Pressure-Linked Equations
SOS2	Special Ordered Sets of Type 2
SPE/IADC	Society of Petroleum Engineers/International Association of Drilling Contractors
SPSA	Simultaneous perturbation stochastic approximation algorithm
SS	Steady State
SSS	Statistically Stationary State
STB	Stock Tank Barrel
SVM	Support Vector Machines
TOF	Time of Flight
TOP	Total Revenue from Oil Production

TGP	Total Revenue from Gas Production
TH	Tetrahedral
TS	Transient State
TVD	True Vertical Depth
TWP	Total Water Production Costs
TWP	Total Water Injection Costs
UBD	Underbalanced Drilling
VFP	Vertical Flow Performance
VP	Is Viscosity Data Provided?
WAF	Well Allocation Factor
WBM	Water Based Mud
WC	Water Cut
WCTT	Wired Coiled Tubing Telemetry
WDPT	Wired Drill pipe Telemetry
WET	Wireless Electromagnetic Telemetry
WOB	Weight on Bit
WSR	Well Search Radius
XG	Xanthan Gum
YP	Yield Point

A.2 Variables and Parameters

Latin Letters and Symbols

a	Half the distance of the major axis of the drainage ellipse (ft)
$A_{annulus}$	Annulus cross-sectional area (m^2)
A,B,c,d	Coefficients of the Syamlal-O'Brien drag model (-)
A_{bit}	Cross-sectional area of drill bit (m^2)
A_c	Particle surface area (m^2)
A_{hole}	Hole cross-sectional area (m^2)
A_{pipe}	Drill pipe cross-sectional area (m^2)
A_s	Surface area of volume equivalent sphere (m^2)
APD	Average Percentage Deviation (%)
a_n	Polynomial coefficients – producer well proxy model (-)
b	Discount rate for a certain reference time (-)

b_n	Polynomial coefficients – injector well proxy model (-)
Bo	Oil formation volume factor (RB/STB)
Bg	Gas formation volume factor (RB/STB)
Bw	Water formation volume factor (RB/STB)
c_n	Polynomial coefficients – pipeline proxy model (-)
C_l	Lift coefficient (-)
C_D	Drag coefficient (-)
c_p	Cuttings concentration (%)
c_t	Cuttings concentration threshold (-)
Cg,sep	Separator gas capacity (MSCF/day)
CG^s	Gas handling capacity of a separator (MSCF/day)
CL^s	Separator liquid capacity (STB/day)
$CQ_{g,inj}$	Cost of gas lift operation ($)
$CQ_{l,ESP}$	Cost of ESP operation ($)
$c_{\boldsymbol{P}}$	Intercept (-)
D	Compact set (-)
D_{pipe}	Drill pipe diameter (m)
D_{hole}	Hole diameter (m)
D_{wb}	Wellbore diameter (m)
D	Diameter (m)
D_h	Hydraulic diameter (m)
d_p , d_s	Diameter of solids or volume equivalent solids/particle diameter if nonspherical (m)
dP/dx or dP/dL	Pressure drop per unit length ($Pa.m^{-1}$)
DX	Reservoir dimension along the x axis (-)
DY	Reservoir dimension along the y axis (-)
DZ	Reservoir dimension along the z axis (-)
e, ε	Eccentricity (-)
e_{ss}	Coefficient of restitution (-)
E	Circumfrential mesh divisions (-)
$\boldsymbol{f}$	Continuous function (-)
f_{ESP}	ESP operating frequency (Hz)
$\vec{F}$	Additional force term (N)

F_D	Drag force (N)
F_r,$\boldsymbol{n}$,$\boldsymbol{p}$	Constants in the frictional pressure equation
$\vec{F}_{lift,q}$	Lift force (N)
$\vec{F}_q$, $\vec{F}_s$	External body force (N)
$\vec{F}_{wl,q}$	Wall lubrication force (N)
$\vec{F}_{d,q}$	Turbulent dispersion force (N)
$\vec{F}_{vm,q}$	Virtual mass force (N)
$\boldsymbol{F}$	Flow capacity
$\boldsymbol{g}$	Constraints
G	Objective function
$\vec{g}$	Gravitational acceleration (m.s^{-2})
$g_{0,ss}$	Compressibility transition function (-)
GOR	Gas Oil Ratio (SCF/STB)
h	Net thickness of the formation (ft)
$H3$	Horizontal length (m)
i_{best}	Pseudo well with the highest gradient
I_{2D}	Second variant of the deviatoric stress (-)
$\bar{\bar{I}}$	Unit tensor (-)
IE	Injector efficiency (%)
II_W	Water injectivity index of an injection well (STB/day.psi)
J	Jacobian
K	Permeability tensor (mD)
K, k	Average reservoir permeability (mD)
k_h	Horizontal permeability (mD)
k_v	Vertical permeability (mD)
k_x	Horizontal 'X' permeability (mD)
k_y	Horizontal 'Y' permeability (mD)
k_z	Vertical 'Z' permeability (mD)
$\vec{K}_{pq}$, K_{sl}	Interphase momentum exchange coefficient (-)
$\acute{K}_{sl}$	Modified interphase exchange coefficient (-)
K	Consistency index (Pa.s^n)

L	Computational Length (m)
$L2$	Inclined length (m)
$\boldsymbol{L}$	Lower Bound (-)
$L_{c,o}$	Lorenz coefficient
L_e	Entrance length (m)
L_h	Horizontal well length (ft)
$\dot{m}$	Mass flow rate (kg.s^{-1})
$\dot{m}_{pq}$	Mass transfer from phase p to phase q (kg.s^{-1})
$\dot{m}_{qp}$	Mass transfer from phase q to phase p (kg.s^{-1})
$\dot{m}_{sl}$	Mass transfer from phase s to phase l (kg.s^{-1})
$\dot{m}_{ls}$	Mass transfer from phase l to phase s (kg.s^{-1})
$m_{\boldsymbol{P}}$	Slope (-)
n	Flow behaviour index (-)
N	Number of counts/observations (-)
NPV	Net Present Value ($)
N_{prod}	Number of production wells (-)
N_{inj}	Number of injection wells (-)
$N_{g,inj}$	Number of gas lift wells (-)
$N_{l,ESP}$	Number of ESP-assisted wells (-)
N_t	Total number of timesteps (-)
n_w	Total number of wells (-)
n_{bh}	Number of BHP controlled wells (-)
n_r	Number of rate controlled wells (-)
$N_{pf}(k)$	Perforation belonging to well k (-)
$N_w(j)$	Index of well with perforation j (-)
p,s *(subscripts)*	Secondary/particle/cuttings/solids phase (-)
p_s	Solids pressure (Pa)
$P_{friction}$	Friction pressure (Pa)
p_o	Oil pressure (psia)
P_0	Initial pressure (bar)
P_{ch}, P_{bit}	Choke pressure and Drill bit pressure (psia)
P_{cow}	Oil/water capillary pressure (psi)

P_{cgo}	Gas/oil capillary pressure (psi)
PI_L	Liquid productivity index of a production well (STB/day.psi)
PI_G	Gas productivity index of a production well (MSCF/day.psi)
P_r	Reservoir pressure (psia)
P_{wf}	Bottomhole flowing pressure (psia)
P_j^w	Wellhead pressure of a production well (psia)
P_i^w	Surface injection pressure (psia)
ΔP	Pressure drop (psi)
ΔP^l	Pipeline pressure drop (psia)
P^m	Manifold pressure (psia)
P^s	Separator pressure (psia)
P_{inj}	Injection pressure (psia)
P_{frac}	Formation fracture pressure (psia)
P_{Ri}	Initial reservoir pressure (psia)
P	Pressure (psia)
$\boldsymbol{P}$	Polytope (-)
$\wp$	Set of polytopes (-)
P^{wh}	Wellhead pressure (psia)
$\mathcal{P},\mathcal{V},\mathcal{T},\mathcal{Q},\mathcal{C}$	Discretised system of equations in terms of p, v, τ, q_{pf}, p_{bh}
q	Primary phase – CFD (-)
Q,q	Production optimisation flowrate (m^3/s, STB/day, MMSCF/day)
Q_{ov}	Oil production rate from a vertical well (STB/day)
Q_{gv}	Gas production rate from a vertical well (MSCF/day)
Q_{oh}	Oil production rate from a horizontal well (STB/day)
Q_{gh}	Gas production rate from a horizontal well (MMSCF/day)
$Q_{g,inj}$	GL well gas injection rate (MMSCF/day)
$Q_{l,ESP}$	ESP well liquid production rate (STB/day)
q_{op}	Well oil production rate (STB/d)
q_{gp}	Well gas production rate (MSCF/d)
q_{wp}	Well water production rate (STB/d)
q_{winj}	Injection well water rate (STB/d)
q_{lo}	Pipeline oil flowrate (STB/d)
q_{lg}	Pipeline gas flowrate (MSCF/d)

q_{lw}	Pipeline water flowrate (STB/d)
q_{pf}	Perforation fluxes (STB/d)
q_{sc}	Volumetric flow rate at standard conditions (STB/d)
q_{fg}	Production rate of free gas component at reservoir conditions (RB/d)
q_i	Well injection rate ($m^3.day^{-1}$)
q_p	Well production rate ($m^3.day^{-1}$)
Q_i	Maximum injection rate ($m^3.day^{-1}$)
Q_p	Maximum production rate ($m^3.day^{-1}$)
r	Annular distance
$r_p, r_{p,i}$	Revenue and cost factors for production and injection ($/$m^3$)
r_e	Drainage radius (ft)
r_w	Well radius (ft)
r_{op}	Unit oil price ($/STB)
r_{gp}	Unit gas price ($/MSCF)
r_{wp}	Unit water production cost ($/STB)
r_{winj}	Unit water injection cost ($/STB)
r_{ginj}	Unit gas injection cost ($/MMSCF)
$r_{l,ESP}$	Unit ESP liquid operating cost ($/STB)
R	Radial mesh divisions (-)
Re_t	Tube Reynolds number (-)
R_1	Radius of drill pipe (m)
R_2	Radius of wellbore (m)
$R1$	Upper bend radius (m)
$R2$	Lower bend radius (m)
R_{in}	Drill pipe radius (m)
R_o	Wellbore radius (m)
$\vec{R}_{pq}$	Phase interaction force (N)
Re_p, Re_s	Solid particles Reynolds number (-)
Re_{ss}	Relative Reynolds number (-)
Re_ω	Vorticity Reynolds number (-)
ROP	Revenue from oil production ($)

RGP	Revenue from gas production ($)
Rs	Solution gas ratio (MSCF/STB)
$\mathbb{R}^n$	Real coordinate space of n dimensions (-)
S_q	Source term (-)
s	Slip velocity (m.s^{-1})
$\boldsymbol{S}$	Total skin
S_o	Oil saturation
S_{wi}	Initial water saturation (-)
S_{gi}	Initial gas saturation (-)
S_w	Water saturation (-)
S_g	Gas saturation (-)
Δt	Time interval in a single timestep (days)
t	Timesteps/control time interval (days)
t_{ref}	Reference time (days)
t^{n+1}	Current or new timestep
t^n, n	Previous timestep, where n is superscripted
$T_{o_{f,n}}^{n+1}$	Oil transmissibility between grid blocks f and n at time t^{n+1} (STB/D-psi)
$T_{w_{f,n}}^{n+1}$	Water transmissibility between grid blocks f and n at time t^{n+1} (STB/D-psi)
$T_{g_{f,n}}^{n+1}$	Gas transmissibility between grid blocks f and n at time t^{n+1} (STB/D-psi)
T	Average reservoir temperature (K)
TOP	Total Revenue from Oil Production ($)
TGP	Total Revenue from Gas Production ($)
TWP	Total Water Production Costs ($)
TWP	Total Water Injection Costs ($)
u	Axial velocity (m.s^{-1})
$\boldsymbol{u}$	Control vectors
$\boldsymbol{U}$	Upper Bound (-)
u_r^k	Rate controlled wells
u_{bh}^k	BHP controlled wells

U_b	Bulk velocity (m.s^{-1})
U_τ	Friction velocity at the nearest wall
u_m	Mean flow velocity (m.s^{-1})
v_{cut}	Cuttings velocity (m.s^{-1})
$\boldsymbol{v}$	Vertex (-)
V	Set of vertices (-)
$V1$	Vertical length (m)
v	Local kinematic viscosity (m^2.s^{-1})
v_{circ}	Fluid circulation velocity (m.s^{-1})
$\vec{v}$	Darcy velocity (m/s)
$\vec{v}_{pq}$, $\vec{v}_{sl}$	Interphase velocity (m.s^{-1})
$\vec{v}_f$	Fluid phase velocity (m.s^{-1})
$\vec{v}_{f,x}$	Fluid velocity in the Cartesian x-direction (m.s^{-1})
$\vec{v}_{f,y}$	Fluid velocity in the Cartesian y-direction (m.s^{-1})
$\vec{v}_{p,x}$	Particle velocity in the Cartesian x-direction (m.s^{-1})
$\vec{v}_{p,y}$	Particle velocity in the Cartesian y-direction (m.s^{-1})
$\vec{v}_q$	Primary phase velocity (m.s^{-1})
$\vec{v}_p$	Secondary phase or cuttings/particle velocity (m.s^{-1})
$\vec{v}_s$	Solid-phase velocity (m.s^{-1})
$\vec{v}_l$	Liquid phase velocity (m.s^{-1})
$v_{r,s}$	Terminal velocity (m.s^{-1})
v_{slip}	Cuttings slip velocity (m.s^{-1})
V_a	Volume of annulus (m^3)
V_{b_n}	Bulk volume of block n (ft^3)
V_q	Volume fraction of phase q
w	Tangential velocity (m.s^{-1})
W_{pf}^j	Peaceman well index (-)
$\boldsymbol{x}$	State variables (-)
x_k	Binary routing variable (-)
y	Binary routing variable (-)
$\boldsymbol{y}$	First layer thickness (m)

y^+	Dimensionless wall distance
Y_p	Yield point (Pa)
$\tilde{\chi}$	Binary routing variable (-)
Z	Gas deviation factor
Z_f	Elevation of grid block *f* (ft)
Z_n	Elevation of grid block *n* (ft)

Greek Letters and Symbols – Drilling (CFD)

α_p	Particle volume fraction (-)
α_s	Solid phase volume fraction (-)
α_l	Liquid phase volume fraction (-)
α_f	Fluid phase volume fraction (-)
$\alpha_{s,max}$	Solid volume fraction at maximum packing (-)
$\alpha_{s,min}$	Solid volume fraction after which friction occurs (-)
β	Hole inclination angle (degrees)
γ	Shear rate (s^{-1})
γ_{Θ_S}	Collisional dissipation of energy ($kg.m^{-1}s^{-3}$)
δ	Offset distance (m)
$\tilde{\sigma}$	Orthogonality
ε	Drill pipe eccentricity (-) (Literature Review Tables C1 – C4)
η	Drag modification factor
θ	Wellbore inclination angle (°) (Literature Review Tables C1 – C4)
λ_p	Particle bulk viscosity (Pa.s)
λ_q	Primary phase bulk viscosity (Pa.s)
μ_a	Apparent viscosity (Pa.s)
μ_p	Total particle viscosity (Pa.s)
μ_{pl}	Plastic viscosity (Pa.s)
$\mu_{p,\,col}$	Collisional viscosity (Pa.s)
$\mu_{p,\,kin}$	Kinetic viscosity (Pa.s)
$\mu_{p,\,fr}$	Frictional viscosity (Pa.s)
μ_q	Primary phase viscosity (Pa.s)
μ_l , μ_f	Fluid viscosity (Pa.s)

μ_o	Oil viscosity (cP)
μ_g	Gas viscosity (cP)
ρ_f	Fluid density (kg.m^{-3})
ρ_p	Solid phase density (kg.m^{-3})
ρ_q, ρ_s	Primary phase density (kg.m^{-3})
$\rho_{r,s}$	Phase reference density (kg.m^{-3})
$\hat{\rho}_q$	Effective phase density (kg.m^{-3})
φ	Cuttings bed porosity (%)
σ	Dimensionless annular space (-)
ς	Skewness (-)
τ	Shear stress (N.m^{-2})
τ_0	Yield Stress (N.m^{-2})
τ_w	Wall shear stress
$\bar{\bar{\tau}}_p$	p^{th} Phase stress-strain tensor (-)
ϕ	Angle of internal friction (degrees)
ϕ_{ls}	Energy exchange between fluid and solid phases (kg.m^{-1}s^{-3})
$\varnothing$	Mesh divisions (-)
Θ_p	Granular temperature (K)
ψ	Sphericity (-)
Ω	Angular velocity of rotation (RPM)
ω	Drill pipe rotation (Literature Review Tables, RPM)

Greek Letters and Symbols – Production Optimisation

α_c	Volume conversion factor (-)
a_n, β_n, δ_n, ε_n	Proxy model coefficients (-)
γ_o	Specific gravity of the oil phase at reservoir conditions (psi/ft)
γ_g	Specific gravity of the gas phase at reservoir conditions (psi/ft)
γ_w	Specific gravity of water phase at reservoir conditions (psi/ft)
δ	SOS2 variables – sum of SOS weights (-)
λ	SOS weights (-)
λ_f	Fluid mobility (-)

$\boldsymbol{\lambda}$	Lagrange multiplier (-)
μ_o	Oil viscosity (cP)
μ_w	Water viscosity (cP)
ξ	Linearisation variable (-)
ρ_o	Oil density (kg.m^{-3})
ρ_w	Water density (kg.m^{-3})
τ	Linearisation variable (-)
$\boldsymbol{\tau}$	Time-of-flight – TOF (day)
φ	Reservoir porosity (-)
$\boldsymbol{\phi}$	Storage capacity (-)
ψ	A set containing grid block numbers (-)
Ω_{PCP}	PCP impeller rotation speed (RPM)

Subscripts and superscripts – Production Optimisation

f, n	Grid block indexes (-)
i	Injection well index (-)
$\boldsymbol{j}$	Perforation index for well placement optimisation (-)
$\boldsymbol{f}^n$	Linearisation breakpoints (-)
$\boldsymbol{k}^n$	Linearisation breakpoints (-)
k	Production Well index (-)
l	Pipeline index (-)
liq	Liquid phase index (-)
m	Manifold index (-)
o	Oil phase index (-)
p	Fluid phase index
s	Separator index (-)
T	Matrix transpose (-)
w	Water phase index (-)
wh	Wellhead index (-)

Appendix B

Peer-Reviewed Publications of the Author

The respective studies presented in this PhD thesis (Chapters 1 – 10) have been published in various peer-reviewed publications.

B.1 Published Journal Articles

Epelle, E.I. and Gerogiorgis, D.I., 2020. A computational Performance Comparison of MILP vs. MINLP Formulations for Oil Production Optimisation. *Computers and Chemical Engineering* (in press). https://doi.org/10.1016/j.compchemeng.2020.106903.

Epelle, E.I., Bennett, J., Abbas, H., Schmidt, K.A.G., Vesovic, V., 2020. Correlation of binary interaction coefficients for hydrate inhibition using the Soave-Redlich-Kwong Equation of State and the Huron-Vidal mixing rule. *Journal of Natural Gas Science and Engineering*, ***77***, 103259. https://doi.org/10.1016/j.jngse.2020.103259.

Epelle, E.I. and Gerogiorgis, D.I., 2020. An Adjoint-Based Well Placement Optimisation Approach for Enhanced Oil Recovery under Geological Uncertainty: From Seismic to Production. *Journal of Petroleum Science and Engineering,* ***190***, 107091. DOI: 10.1016/j.petrol. 2020.107091.

Epelle, E.I. and Gerogiorgis, D.I., 2020. A review of technological advances and open challenges for oil and gas drilling systems engineering. *AIChE Journal*, ***65***(6), e16842. DOI: 10.1002/aic.16842

Epelle, E.I. and Gerogiorgis, D.I., 2019. Mixed-Integer Nonlinear Programming (MINLP) for Production Optimisation of Naturally Flowing and Artificial Lift Wells with Routing Constraints. *Chemical Engineering Research and Design*, ***152***, 134–148. DOI: 10.1016/j.cherd.2019.09.042.

Epelle, E.I. and Gerogiorgis, D.I., 2019. Optimal rate allocation for production and injection wells in an oil and gas field for enhanced profitability. *AIChE Journal*, ***65***(6), e16592. DOI: 10.1002/aic.16592.

Epelle, E.I. and Gerogiorgis, D.I., 2019. Drill cuttings transport and deposition in complex annular geometries of deviated oil and gas wells: A multiphase flow analysis of positional variability. *Chemical Engineering Research and Design*, ***151***, 214–230. DOI: 10.1016/j.cherd.2019.09.013.

Epelle, E.I., Gerogiorgis, D.I., 2018. CFD modelling and simulation of drill cuttings transport efficiency in annular bends: Effects of particle sphericity. *Journal of Petroleum Science and Engineering*, ***170***, 992–1004. DOI: 10.1016/j.petrol.2018.06.041.

Epelle, E.I. and Gerogiorgis, D.I., 2018. Transient and Steady-State Analysis of Drill Cuttings Transport Phenomena under Turbulent Conditions. *Chemical Engineering Research and Design*, ***131***, 520–544. DOI: 10.1016/j.cherd.2017.11.023.

Epelle, E.I. and Gerogiorgis, D.I., 2017. A multiparametric CFD analysis of multiphase annular flows for oil and gas drilling applications. *Computers & Chemical Engineering*, ***106***, 645–661. DOI: 10.1016/j.compchemeng.2017.08.011.

B.2 Conference Proceedings

Epelle, E.I. and Gerogiorgis, D.I., 2020. Oil Production Optimisation using Piecewise Linear Approximations (MILP): Computational Performance Comparison vs. MINLP Formulation. *In 30th European Symposium on Computer-Aided Process Engineering; Pierucci, S., Bogle, D., Manenti, F.; Comput.-Aided Chem. Eng.;* Elsevier: in press. https://www.elsevier.com/books/30th-european-symposium-on-computer-aided-chemical-engineering/pierucci/978-0-12-823377-1.

Epelle, E.I. and Gerogiorgis, D.I., 2020. Optimisation of petroleum production well placement under geological uncertainty**.** *In 30th European Symposium on Computer-Aided Process Engineering; Pierucci, S., Bogle, D., Manenti, F.; Comput.-Aided Chem. Eng.;* Elsevier: in press. https://www.elsevier.com/books/30th-european-symposium-on-computer-aided-chemical-engineering/pierucci/978-0-12-823377-1.

Epelle, E.I. and Gerogiorgis, D.I., 2019. A Multiperiod Optimisation Approach to Enhance Oil Field Productivity during Secondary Petroleum Production. In *29th European Symposium on Computer-Aided Process Engineering*; Kiss, A.A., Zondervan, E., Lakerveld, R.,

Özkan, L., Eds.; *Comput.-Aided Chem. Eng.*; Elsevier: ***46***, 1651–1656. DOI: 10.1016/B978-0-12-818634-3.50276-9.

Epelle, E.I., Gerogiorgis, D.I., 2018. A CFD investigation of the effect of particle sphericity on wellbore cleaning efficiency during oil and gas drilling. In *28th European Symposium on Computer-Aided Process Engineering*, Friedl, A., Klemeš, J.J., Radl, S., Varbanov, P.S., Wallek, T., Eds.; *Comput. Aided Chem. Eng.*; Elsevier: ***43***, 127–132. DOI: 10.1016/B978-0-444-64235-6.50024-3.

B.3 Presentations & Symposia

Presenting author in **bold.** Where no author is highlighted in bold, Mr. Samir Diab presented on the authors' behalf

Epelle, E.I.; Gerogiorgis, D.I. Oil production optimisation using piecewise linear approximations (MILP): Computational performance comparison vs. MINLP formulation. Proceedings of the 30th Symposium on Computer-Aided Process Engineering (ESCAPE-30), Milan, Italy, May 24–27, 2020. Accepted for presentation.

Epelle, E.I.; Gerogiorgis, D.I. Optimisation of petroleum production well placement under geological uncertainty. Proceedings of the 30th Symposium on Computer-Aided Process Engineering (ESCAPE-30), Milan, Italy, May 24–27, 2020. Accepted for presentation.

Epelle, E.I.; Gerogiorgis, D.I. Well placement optimisation in a heterogeneous petroleum reservoir with geological uncertainty. Proceedings of the 2019 AIChE Annual Meeting, Orlando (FL), USA, Nov 10–15, 2019.

Epelle, E.I.; Gerogiorgis, D.I. Enhancing petroleum field profitability via optimisation of production and injection operations. Proceedings of the 2019 AIChE Annual Meeting, Orlando (FL), USA, Nov 10–15, 2019.

Epelle, E.I.; Gerogiorgis, D.I. A multiperiod optimisation approach to enhance oil field productivity during secondary petroleum production. Proceedings of the 29th European Symposium on Computer-Aided Process Engineering (ESCAPE-29), Eindhoven, The Netherlands, June 16–19, 2019.

Epelle, E.I.; Gerogiorgis, D.I. Dynamic optimization of water-injection wells operation for enhanced oil production from a mature oil and gas field. Proceedings of the 2018 AIChE Annual Meeting, Pittsburgh (PA), USA, Oct 28–Nov 2, 2018.

Epelle, E.I.; Gerogiorgis, D.I. A CFD investigation of the effect of particle sphericity on wellbore cleaning efficiency during oil and gas drilling. Proceedings of the 28th European Symposium on Computer-Aided Process Engineering (ESCAPE-28), Graz, Austria, June 10–13, 2018.

Epelle, E.I.; Gerogiorgis, D.I. Multiphase flow modelling for enhanced oil & gas drilling and production. Proceedings of the 31st Scottish Fluid Mechanics Meeting, Aberdeen, UK, May 29, 2018.

Epelle, E.I.; Gerogiorgis, D.I. Multiphase flow modelling for enhanced oil & gas drilling and production. The University of Edinburgh, School of Engineering Research Conference, Edinburgh, UK, April 17, 2018.

Epelle, E.I.; **Gerogiorgis, D.I**. A multiparametric CFD analysis of multiphase annular flows for oil and gas drilling applications. Proceedings of the 2017 AIChE Annual Meeting, Minneapolis (MN), USA, Oct 29–Nov 3, 2017.

Research Collaborations

The PhD project has featured two collaborations on interdisciplinary projects: "*The application of Computational Fluid Dynamics (CFD) to three-phase modelling of particle transport phenomena during Underbalanced Drilling (UBD) in the oil and gas industry*" with **Cranfield University** (for which I received the UK Fluids Network, **UKFN** Short Research Visit Funding) and "*The parameterisation of cubic Equations of State for the thermodynamic property prediction of hydrate inhibition systems*" with **Schlumberger** Limited.

Appendix C

Critical Literature Review

CFD CONTRIBUTIONS (DRILLING)

AE-Algebraic Equations; **BC**-Boundary Conditions; **DEM**-Discrete Element Method; **DDPM-**Dense Discrete Phase Model; **DPM-** Discrete Phase Model; **EE**-Eulerian-Eulerian; **FEM-**Finite Element Method; **FVM**-Finite Volume Method; **FT**-Fluid Type; **HX**-Hexahedral; **KTGF**-Kinetic Theory of Granular Flow; **LE**-Lagrangian Eulerian; **MID**-Mesh Independence Study Performed?; **ModVal**-Model Validation Performed?; **ODE**-Ordinary Differential Equations; **OS**-Operating System; **PDE**-Partial Differential Equations; **QUICK**-Quadratic Upstream Interpolation for Convective Kinematics; **ROP**-Rate of Penetration; **SIMPLE**-Semi-Implicit Method for Pressure Linked Equations; **SS**-Steady State; **TH**-Tetrahedral; **TS**-Transient State; **VP**-Is Viscosity Data Provided?; D_{wb} = Wellbore diameter; D_{dp} = Drill pipe diameter; ε = Drill pipe eccentricity; θ = Angle of inclination; L = Computational length; ω = Drill pipe rotation; [?] = Unknown/unreported parameter.

Table C.1. Summary of CFD research contributions for wellbore cleaning operations.

Reference	SS/TS; Particle treatment; ModVal?; Flow regime	Geometry, Fluid Properties & Boundary Conditions				Mesh type, Interpolation/ discretisation scheme, MID?, Max no. elements	Software + computer specifications (run time)	Solution scheme; Interpolation/ coupling scheme; Max. tolerance	Sensitivity Analyses & Results	
		Fluid & Solid Properties	Velocities & Flowrates	Wellbore Geometry	BCs				Analysis	Results
Akhshik and Rajabi (2018)	TS (run time of 40 s with DEM timestep = 0.001 of CFD timestep) LE (CFD-DEM; Volume of Fluid model is applied) Yes Turbulent (standard k-ε) model	*FT* = Water and air *VP* = Yes ϱ_l = 1,000 kg/m^3 d_s = 3.66 mm ϱ_s = 2,400 kg/m^3	q_l = 0.0028-0.017 m^3/s q_g = 5.56× 10^{-5} – 1.4×10^{-4} m^3/s q_s/ROP = 3.67×10^{-5} m^3/s	D_{wb} = 127 mm D_{dp} = 52.4 mm ε = [?] θ = 30, 45, 60, 90^o (from vertical) L = 9 m ω = 0 rpm	Fluid & solid inlet velocity, outlet pressure	[?] [?] Yes 3,124,230 cells for fluid simulation	[?] 32-core 3.4 GHz Intel®-Xeon® CPU processor (Intel Corporation, Santa Clara, CA, USA), 64 GB of RAM; Run time of 90 days	FVM SIMPLEC [?]	The impacts of liquid flow rate, air flow rate, inclination angle, temperature and pressure on the cuttings concentration are analysed.	Increasing the gas injection rate causes a reduction in cuttings concentration. Isolated cuttings dunes are observed at angles <= 45^o. Pressure has a negligible effect on cuttings transport efficiency. Whereas, the cuttings transport efficiency increases and the temperature increases. This effect reduces as the gas injection rate increases.
Akhshik et al. (2015)	TS (run time of 40 s with 0.001 and 0.00001s time step for the CFD and DEM phases) LE (CFD-DEM with the Helmoltz Mindlin model for particle-particle and particle - wall interactions, 4-way coupled) Yes Laminar and turbulent	*FT* = Water and bentonite-based muds *VP* = Yes (PL, HB) d_s = 6.35, 2 mm ϱ_s = 2,619, 2,300 kg/m^3	v_l = 0.58-1.52 m/s q_s/ROP = 0.0051-0.010 m/s	D_{wb} = 127, 73.91 mm D_{dp} = 48.26, 47 mm ε = 0.5, 0.623 θ = 0-90^o (from vertical) L = 12, 7 m ω = 0-120 rpm	Fluid & solid inlet velocity, outlet pressure	[?] [?] Yes [?]	STAR-CCM+® with user subroutines for particle-fluid interactions 32-core 3.4 GHz Intel®-Xeon® CPU processor (Intel Corporation, Santa Clara, CA, USA), 64 GB of RAM; Run time of 30 days	FVM SIMPLEC [?]	The impacts of drill pipe rotation, fluid inlet velocity, ROP, and inclination angle on the cuttings concentration and moving bed velocity are examined.	The developed CFD model accurately predicts observed physical transport phenomena (suspension flow at near-vertical angles, rolling motion at near-horizontal inclinations, and a combination of both phenomena at intermediate angles. A jump behaviour in cuttings concentration is also observed at low fluid velocities and medium inclination angles.
Akhshik et al. (2016)	TS (run time of 60 s with 0.001 and 0.00001s time step for the CFD and DEM phases) LE (CFD-DEM, 4-way coupled) Yes Laminar and turbulent	*FT* = bentonite-based muds *VP* = Yes (PL, HB) ϱ_l = 999-1,013 kg/m^3 d_s = 6.35 mm (Sphericity: 0.79-1) ϱ_s = 2,619 kg/m^3	v_l = 0.305-1.16 m/s q_s/ROP = 0.151 kg/s	D_{wb} = 0.127 m D_{dp} = 0.0483 m ε = 0.5 θ = 0-90^o (from vertical) L = 12.2 m ω = 0, 50 rpm	Fluid & solid inlet velocity, outlet pressure and no slip at walls.	[?] [?] Yes 140,000	STAR-CCM+® with user subroutines for particle-fluid interactions 32-core 3.4 GHz Intel®-Xeon® CPU processor (Intel Corporation, Santa Clara, CA, USA), 64 GB of RAM; Run time of 90 days	FVM SIMPLEC [?]	The impacts of particle shape, fluid circulation velocity, inclination angle, and drill pipe rotation on the cuttings concentration and velocity are examined.	As the particle shape deviated from an ideal sphere, particle concentration increased especially at (40^o, 60^o and 80^o from the vertical). At low inclination angles (0^o, 20^o from vertical), spherical particles exhibit slightly higher concentration compared to non-spherical particles. As particles deviate from perfect spheres, the transport velocity increased at all conditions.

Al-Kayiem et al. (2010)	SS EE No Laminar and turbulent (Standard k-ε model)	*FT* = Xanthan gum solution *VP* = Yes (PL) ϱ_l = 1,042.5 kg/m^3 d_s = 2.54-7 mm (shape factor: 0.85-1) ϱ_s = 2,750 kg/m^3 Limestone rock	q_l = 0.038-0.057 m^3/s q_s/ROP = 0.113 kg/s.	D_{wb} = 0.250 m D_{dp} = 0.127 m ε = 0 θ = 15-25^o (from vertical) L = 0.91 m ω = 0 rpm	Inlet pressure and outlet pressure	[?] [?] [?] [?]	GAMBIT 2.2.30, Fluent 2.2.16 [?]	FVM [?] [?]	The impacts of the annular flow rate, particle diameter, and inclination angle on the cuttings concentration at the well surface are examined.	Smallest particles were the easiest to clean. Higher sphericity resulted in better cleaning efficiency. When the inclination angle becomes 30^o, mud rates higher than 800 gpm are required for effective cleaning.
Amanna and Movaghar (2016)	[?] EE Yes Turbulent (k-ε model)	*FT* = Water *VP* = Yes; ϱ_l = 1,000 kg/m^3 d_s = 2-8 mm ϱ_s = 2,700 kg/m^3	q_l = 0.00252-0.0057 m^3/s q_s/ROP = [?] (cuttings inlet volume fraction: 0.06)	D_{wb} = 0.057 m D_{dp} = 0.105 m ε = 0 θ = 30-90^o (from vertical) L = 4 m ω = 30-80 rpm	Fluid & solid inlet velocity, outlet pressure and no slip condition at the walls.	HX [?] No 250,400	Gambit, Fluent v6.2 [?]	FVM [?] [?]	The impacts of fluid flow rate, inclination angle, drill pipe rotation, and cuttings size on the total cuttings volume concentration are examined.	CFD results showed good comparison with experimental data. Increased turbulent eddy flow associated with increased flow rate causes a decrease in cuttings concentration. Cuttings transport is easier at higher rotation speeds. Buckingham-pi theorem was successfully applied to develop a cuttings transport correlation.
Bilgesu et al. (2002)	SS EE Yes [?]	*FT* = Water & non-Newtonian fluids *VP* = PL model ϱ_l = 999-1,797 kg/m^3 d_s = 2.54-7.0 mm (uniform, spherical) ϱ_s = 2,400 kg/m^3	v_l = 0.0254-1.27 m/s q_s/ROP = [?]	D_{wb} = 0.203, 0.3048 m D_{dp} = 0.102, 0.089 m ε = [?] θ = 0, 90^o (from vertical) L = 100 m ω = 0 rpm	———	[?] Solution adaptive mesh No [?]	Commercial CFD package used but not specified [?]	[?] [?] [?]	The impacts of annular velocity, mud density, cuttings size and inclination angle were examined.	Drilling mud with higher density exhibited better cleaning efficiency at all flowrates. Reported predictions using the CFD model showed good agreement with less than 10% error. Increased model deviation occurred at high velocities (most likely due to the assumption of a uniform size distribution of cuttings). Larger particles require high circulation velocity for their removal compared to smaller particles. Increase in cuttings CTR is more pronounced at low flowrates than at high flowrates.

Bilgesu et al. (2007)	SS EE Yes Turbulent	*FT* = [?] *VP* = No ϱ_l = [?] d_s = 3, 8 mm ϱ_s = [?]	q_l = 0.0076, 0.0095, 0.0114 m^3/s q_s/ROP = 0.00423, 0.0064, 0.0085 m/s	D_{wb} = 0.1524 m D_{dp} = 0.089 m ε = 0 θ = 60, 75, 90° (from vertical) *L* = 13.72 m ω = 30, 60 rpm	Fluid & solid inlet velocity, outlet pressure	[?] [?] [?] [?]	[?] [?]	[?] [?] [?]	The impacts of rotation speed, particle size, penetration rate, fluid circulation rate on the minimum cuttings concentration are examined.	Hole cleaning was easier for larger particles compared to smaller particles. Increased liquid flow rate enhances the transport of smaller particles to a greater extent compared to larger particles. Marginal improvement in cuttings transport is observed by increasing drill pipe rotation. Hole cleaning becomes more difficult as the inclination angle increases.
Celigueta et al. (2016)	TS DEM Yes [?]	*FT* = Water, intermediate and thick mud *VP* = Yes (PL) ϱ_l = 1,030 kg/m^3 d_s = 4.96 mm (sphericity: 0.768) ϱ_s = 2,000 kg/m^3	v_l = 0.025-0.45 m/s q_s/ROP = 1500 m^2/s	D_{wb} = [?] D_{dp} = [?] ε = 0 θ = 45° (from vertical) *L* = [?] ω = 10-100rpm	Dirichlet and Neumann BCs	[?] [?] No [?]	FEM-DEM code (from scratch) [?]	FEM [?] [?]	Flow visualisations of cuttings distribution are presented. A new FEM-DEM coupled method was developed to study cutting s transport.	Accurate prediction of particle velocity is obtained when validated with experimental results. The coupling procedure does not depend on the method used to solve the equations for the fluid. It can thus be applied to other popular CFD methods, such as the Finite Volume Method (FVM).
Demiralp (2014)	TS (run time ≈ 40 sec with a time step size that results in desired parcel diameter) LE (CFD-DEM, 4-way coupled) Yes Laminar & Turbulent (Shear stress SST k-ω)	*FT* = [?] *VP* = Yes (PL) ϱ_l = 1,000 kg/m^3 d_s = 2 mm ϱ_s = 2,762 kg/m^3	v_l = 0.914-2.13 m/s q_s/ROP = 0.009 m/s	D_{wb} = 0.074 m D_{dp} = 0.047 m ε = 0.623 θ = 90° (from vertical) *L* = 2 m ω = 0-120 rpm;	Fluid & solid inlet velocity, outlet pressure	Unstructured HX QUICK Yes 160,000 elements	ANSYS Fluent v15 (with a UDF for particle injection developed in MATLAB) 128 processors using HPC resources; run time of approximately 30 hours	FVM SIMPLE 10^{-4}	The impacts of rotation speed & annular fluid velocities on the cuttings concentration, pressure drop and cuttings velocity are analysed. The impact of drill pipe whirling motion is also studied by dividing the annulus into 8 sectors. Particle trajectories, fluid streamlines and particle annular distribution analyses are also provided.	Drill pipe rotation has a mild effect on cuttings concentration; however, it plays a huge role in asymmetrically distributing the cuttings in the annulus. Increasing whirling rotary speed increases axial cuttings travel velocities. The presence of the plastering effect (smearing of cuttings to the wellbore wall) may be experienced during backward whirling motion, particularly, at the low flow rates.

Duan et al. (2008)	[?] [?] Yes [?]	FT = 0.6-0.9 quality foam VP = Yes (PL) ϱ_l = [?] d_s = [?] ϱ_s = [?]	v_l = 0.37-1.036 m/s q_s/ROP = [?]	D_{wb} = 0.038, 0.15 m D_{dp} = 0.019, 0.089 m ε = 0, 0.8 θ = 0° (from vertical) L = 3.048 m ω = 0-400 rpm	Fluid inlet velocity, outlet pressure; Cuttings bed treated as a fixed boundary	[?] PRESTO [?] [?]	Unspecified commercial simulator [?]	FVM SIMPLE routine [?]	The impact of pipe rotation and flow velocity on the pressure drop and the radial foam velocity distribution in the annulus are analysed. Contour plots of cuttings velocity are also presented.	Compared to incompressible fluids, foam rheology is affected by downhole pressure. Drill pipe rotation increases pressure drop for foam flow in eccentric annuli for a given bed height. At smaller eccentricities (< 0.5), the core of the maximum axial velocity is shifted in the same direction as drill pipe rotation. In fully eccentric annulus with a cuttings bed, this core shifts to the opposite direction of drill pipe rotation.
Dykes (2014)	SS TS EE Yes Turbulent (RSM with standard wall functions)	FT = Water VP = Yes (1× 10^{-6} m^2/s) ϱ_l = 998 kg/m^3 d_s = 6.35 mm ϱ_s = 2,651 kg/m^3	q_l = 0-0.044 m^3/s q_s/ROP = 0.00423 m/s	D_{wb} = 0.127, 0.203, 0.3048 m D_{dp} = 0.0762, 0.048, 0.114 m ε = 0, -0.5, +0.5 θ = 0-90° (from vertical) L = 12.2, 7.62 m ω = 0-140 rpm	Fluid & solid inlet velocity, outlet pressure	Unstructured HX Least squares cell based method & first order upwind No 54,219 & 64,260 cells	ANSYS Fluent 2013a [?]	FVM SIMPLE [?]	The impacts of ROP, inclination angle, particle size, drill pipe rotation, drill pipe eccentricity, annular clearance, and annular flow rate on the cuttings concentration are analysed. Illustrative contour plots of cuttings volume fraction are provided at different conditions.	At a constant flow rate, cuttings concentration is proportional to the square of CSA. If the average annular fluid velocity is sufficiently maintained, the annular clearance rarely affects cuttings accumulation. The effect of drill pipe rotation highly depends on other drilling parameters. Rotation does not always guarantee improved cuttings transport. In the cases of high cuttings accumulation, larger drill pipes stabilize cuttings beds better than smaller drill pipes. Most difficult inclination angle was 60°.
Epelle and Gerogiorgis (2017)	SS EE (KTGF) Yes Laminar / transitional	FT = Water & Xanthan gum VP = Yes (PL) ϱ_l = 998.5-1,036.5 kg/m^3 d_s = 0.003 m; ϱ_s = 2,610 kg/m^3	$\underline{v}_l$ = 0.61-1.52 m/s q_s/ROP = 0.00423-0.00847 m/s	D_{wb} = 0.1463 m D_{dp} = 0.0889 m ε = 0-0.8 θ = 0-60° (vertical) L = 14 m ω = 0-140 rpm	Fluid & solid inlet velocity Outlet pressure, No slip at walls	HX QUICK Yes 2,842,500	ANSYS Fluent (v17.1) (Windows 7, 64-bit OS, 16GB RAM, & QuadCore-i7 processor at 3.40 GHz)	FVM Phase coupled SIMPLE scheme 10^{-3}	The impacts of eccentricity, fluid velocity, inclination angle, drill pipe rotation, ROP, and fluid rheology on the cuttings concentration and pressure drop were analysed.	Cuttings concentration is lower in concentric flow configurations for all transport conditions. Pressure drop reduces with increasing eccentricity. Drill pipe aids particle transport with increased annular pressure drop vs. when rotation is absent.

Epelle and Gerogiorgis (2018a)	SS & TS (>3s with a timestep of 0.0001s) EE (KTGF) & LE (DDPM/DEM) Yes turbulent (k-ω)	*FT* = Xanthan gum *VP* = Yes (PL); ϱ_l = 1,000 kg/m^3; d_s = 0.001m, 0.005 m, 0.010 m; ϱ_s = 2,610 kg/m^3;	v_l = 1.5, 2 m/s q_s/ROP = 0.00423, 0.00847 m/s	D_{wb} = 0.1178 m D_{dp} = 0.1080 m ε = 0, 0.6 θ = 0, 45, 90^o (from vertical) L = 2, 11 m; ω = 100, 400 rpm	Fluid & solid inlet velocity Outlet pressure, No slip at walls	HX QUICK routine Yes 2,626,200 (EE) & 330,000 (LE) elements.	ANSYS Fluent (v16.1 & v17.1) (Windows 7, 64-bit OS, 16GB RAM, & QuadCore-i7 processor at 3.40 GHz); Scientific Linux 7 OS; 16 cores (2.4 GHz Intel®-Xenon® CPU processor) and 64GB of RAM; 30 days total run time	FVM Phase coupled SIMPLE scheme 10^{-4}	Spatial cuttings velocity and concentration distribution and pressure drop in the annulus are studied along different planes by changing the inclination angle, particle diameter, rotation and rheology. Fluid streamlines and particle trajectory analysis are also carried out.	The effect of rotational motion is higher in horizontal flow configuration; drill pipe rotation aids homogeneous transport. Smaller particles are more readily dispersed around the annulus compared to larger particles. Streak-like fluid ejections from the walls of the wellbore aid in particle lifting.
Epelle and Gerogiorgis (2018b)	TS EE (KTGF) Yes transitional	*FT* = CMC/Bentonite solution *VP* = Yes (PL & HB) ϱ_l = 1,000-1,030 kg/m^3 d_s = 0.002-0.008 m (sphericity 0.5, 0.75, 1) ϱ_s = 2,800 kg/m^3	v_l = 0.8 m/s q_s/ROP = 0.5 m/s.	D_{wb} = 0.180 m D_{dp} = 0.113 m ε = 0.6 θ = (combined vertical, inclined 45^o and horizontal sections) $L \approx$ 2.4 m ω = 100 rpm	Fluid & solid inlet velocity Outlet pressure, No-slip at walls	HX QUICK routine Yes 665,600 elements	ANSYS Fluent (v17.1) Scientific Linux 7 OS; 32 cores (2.4 GHz Intel®-Xenon® CPU processor) and 64GB of RAM	FVM Phase coupled SIMPLE scheme 10^{-4}	The impacts of particle sphericity, diameter, and mud rheology on the cuttings deposition pattern and pressure drop are analysed.	The modification of the Syamlal-O'Brien drag model is a reliable way of incorporating the effects of particle sphericity. Non-spherical particle experience increased dispersion and travel faster than spherical particles.
Epelle and Gerogiorgis (2019c)	TS (5s with time step of 0.0001s) EE (KTGF) Yes transitional	*FT* = CMC/Bentonite solution *VP* = Yes (PL & HB) ϱ_l = 1,000-1,030 kg/m^3 d_s = 0.002-0.008 m (sphericity 0.5, 0.75, 1) ϱ_s = 2,800 kg/m^3	v_l = 0.8 m/s q_s/ROP = 0.5 m/s.	D_{wb} = 0.180 m D_{dp} = 0.113 m ε = 0.6 θ = (combined vertical, inclined 45^o and horizontal sections) $L \approx$ 2.4 m ω = 100 rpm	Fluid & solid inlet velocity Outlet pressure, No-slip at walls	HX QUICK routine Yes 665,600 elements	ANSYS Fluent (v17.1) Scientific Linux 7 OS; 32 cores (2.4 GHz Intel®-Xenon® CPU processor) and 64GB of RAM	FVM Phase coupled SIMPLE scheme 10^{-4}	Particle trajectories and distribution in the annulus were analysed as a function of cuttings size and sphericity.	The inclined-to-vertical annular section was the most susceptible to cuttings deposition. The shape of the particle significantly affects larger cuttings transport compared to smaller cuttings.

GhasemiKa-frudi and Hashemaba-si (2016)	SS EE Yes Laminar	FT = [?] VP = Yes (HB) ϱ_l = 1,201-1,450 kg/m^3 d_s = 1-7 mm ϱ_s = 2,550 kg/m^3	v_l = 0.4-1.3 m/s v_s/ROP = [?]	D_{wb} = 0.311 m D_{dp} = 0.127 m ε = 0, 0.8 θ = 0^o (from vertical) L = 6 m ω = 0-9 rads/s	Fluid & solid inlet velocity, atmospheric pressure, no slip at walls	HX QUICK Yes; 270,000	[?] Core i7 processor with 8 GB RAM	FVM SIMPLE [?]	Annular pressure drop, slip velocity, CTR, cuttings axial velocity were analysed as functions of the annular clearance, mud density, mud rheological parameters, and wellbore configuration.	Maximum solid velocity occurred in the middle section of the annulus. The eccentric annulus was more sensitive to the entrance length effect. Drill pipe rotation helps to eliminate stagnation regions. The eccentric configuration caused a reduced pressure drop compared to the concentric case. Fluid flow rate and rheology had the highest impact on the transport process.
Hajidavall-oo et al. (2013)	[?] EE Yes Turbulent	FT = Air VP = Yes ϱ_l = 1,225 kg/m^3 d_s = 0.228-0.911 mm ϱ_s = 2,650 kg/m^3	v_l = 15-20 m/s m_s/ROP = 1.54 kg/s (inlet volume fraction of 4%)	D_{wb} = 0.270 m D_{dp} = 0.089 m ε = 0-0.7 θ = 0^o (from vertical) L = 0.5 m ω = 0-400 rpm	Fluid & solid inlet velocity, outlet pressure	HX [?] [?] 35, 125, and 200 nodes in the radial, azimuthal and axial directions.	Fluent (v6.3.26) [?]	FVM [?] 10^{-5}	Radial distribution profiles of cuttings velocity (axial and tangential), volume fraction are presented. The impact of the eccentricity and drill pipe rotation on the pressure drop are examined with some contour plots of cuttings volume fraction and air velocity presented.	Drill cuttings in a concentric annulus change the air velocity profile significantly by creating two off-centre peaks close to the wall surfaces. Drill pipe rotation produces a quasi-helical flow pattern in the annulus, which improves cuttings transport. This results in increased pressure drop. Increasing eccentricity causes an increase in the pressure drop due to the increased flow restriction and particle contacts at the casing walls.
Heydari et al. (2017)	[?] EE (KTGF) Yes Laminar and turbulent (RSM model)	FT = 80% & 90% quality foam VP = Yes (HB) ϱ_l = 1,078 kg/m^3 d_s = 6.35 mm (spherical) ϱ_s = 2,650 kg/m^3	m_l = 20.4-34 kg/s q_s/ROP = 0.0017 & 0.0042 m/s	D_{wb} = 0.203 m D_{dp} = 0.114 m ε = 0-0.75 θ = 90^o (from vertical) L = 12.2 ω = 0-150 rpm	Fluid & solid inlet velocity, outlet pressure	HX [?] Yes 876,000	ANSYS Fluent [?]	FVM SIMPLEC [?]	The impacts of pipe eccentricity, rotation and fluid flowrate on the cuttings volume fraction and axial velocity are examined.	Drill pipe rotation is more effective when higher ROPs are applied (most severe concentrations of cuttings). However, there is a rotation threshold beyond which there is no improvement in transport efficiency. Eccentric configurations (in which the cuttings bed is in contact with the drill pipe) caused decreased transport efficiency.

Hussain and Sharif (2000)	[?] [?] No Laminar	FT = [?] VP = Yes (Yield PL) ϱ_l = [?] d_s = [?] ϱ_s = [?]	q_l = 0-0.008 m³/s q_s/ROP = [?].	D_{wb} = 0.12 m D_{dp} = 0.06 m ε = 0, 0.5 θ = [?] L = [?] ω = 0, 16.67, 33.34 rad/s	Fluid inlet velocity, outlet pressure	[?] [?] Yes 3600	[?] [?]	FVM SIMPLE routine [?]	The impacts of eccentricity, rotational speed, torque, axial pressure gradient and blockage height on the fluid discharge rate are analysed along with contours of spatial velocity distribution in the annulus.	Axial-flow rate increases with increasing eccentricity and increasing angular velocity of the inner cylinder for the same axial pressure gradient. With increasing eccentricity, the torque required to rotate the drill pipe increases. Secondary flow zone exists in the wider annular area of the eccentric annulus. Blockage in the narrow annular area causes secondary flow to intensify.
Ignatenko et al. (2018)	SS EE Yes Laminar and turbulent (k-ω)	FT = [?] VP = Yes (HB) ϱ_l = 1,414 kg/m³ d_s = 3 mm ϱ_s = 2,650 kg/m³	v_l = 0.957 m/s q_s/ROP = 0.00861 m/s	D_{wb} = 0.254 m D_{dp} = 0.127 m ε = 0-0.7 θ = 90° (from vertical) L = [?] ω = 0-200 rpm	No-slip at boundaries	[?] [?] [?] [?]	[?] [?]	FVM [?] [?]	The impacts of eccentricity, drill pipe rotation, and rheological parameters, on the cuttings bed fraction and pressure drop are analysed. Contour plots of cuttings velocity are also analysed.	Increased fluid viscosity and rotation reduce cuttings concentration. 2 flow regimes were identified: Primary (produced by drill pipe rotation) and secondary flow regime (with dense vortex structures). Primary flow regime has low particle concentration and low pressure drop, whereas the secondary regime is characterised with low rotation rates, high-pressure drop and particle concentration.
Mezherich-er and Levy (2011)	TS LE (CFD-DEM) No Turbulent (Standard k-ε)	FT = Air VP = Yes ϱ_l = kg/m³ d_s = 3 mm ϱ_s = 880 kg/m³	v_l = 12-25 m/s m_s/ROP = 0.093-3.3 kg/s (with inlet volume fraction from 0.014-0.504).	D_{wb} = 0.025 m D_{dp} = [?] ε = [?] θ = 90° (from vertical) L = 1 m ω = [?]	Fluid & solid inlet velocity, outlet pressure	TH PRESTO Second order upwind No 56,384	Gambit 2.4.6, Fluent 12.0.7 [?]	FVM SIMPLE pressure-velocity coupling scheme CFD time step; 100 times smaller than CFD time step	Visualisations of particle dispersion using DEM and DPM models are compared at different air inlet velocities and volume fractions.	The computations performed using the DPM approach give satisfactory results for very dilute particle flow regimes (particle volume fraction < 0.1) compared to DEM. Modifications to Fluent's DPM model is done in order to account to binary particle collision. The nonphysical tendency of the particles to form a “suspended cloud” at the end of the pipe using FLUENT's DPM is significantly reduced when the modified DPM model is used.

Mishra (2007)	SS (70,000 iterations to converge) EE Yes Turbulent (k-ε)	*FT* = Water *VP* = Yes ϱ_l = 1,000 kg/m^3 d_s = 3, 8 mm ϱ_s = 2,610 kg/m^3	q_l = 0.0076-0.0114 m^3/s q_s/ROP = 0.0042-0.0085 m/s (0.1-0.2 m/s cuttings velocity; input volume fraction of 4%).	D_{wb} = 0.152 m D_{dp} = 0.089 m ε = 0 θ = 60-90^o (from vertical) L = 13.72 m ω = 0-60 rpm	Fluid & solid inlet velocity, outlet pressure	HX [?] No 9360 cells	Gambit, Fluent [?]	FVM SIMPLE [?]	The impacts of flow rate, ROP, particle size, inclination angle, and drill pipe rotation on the pressure drop and maximum cuttings concentration are examined.	Increasing the flow rate had a more significant effect on large particles compared to smaller particles. Drill pipe rotation improved cuttings transport only marginally. Hole deviation has the greatest impact on cuttings transport compared to other parameters. Increasing the inclination angle makes cleaning more difficult. The solution of the EE model becomes unstable for the range of flow rates used when the cuttings concentration exceeds 20%.
Mme and Skalle (2012)	[?] LE (DPM) Yes Laminar and turbulent (k-ε model)	*FT* = (CMC+XC) solution *VP* = Yes (PL) ϱ_l = 1,003-1,005 kg/m^3 d_s = 3-7 mm (shape factor: 0.85-1) ϱ_s = [?]	v_l = 0.508-1.778 m/s m_s/ROP = 0.125 kg/s.	D_{wb} = 0.38 m D_{dp} = 0.2 m ε = 0 θ = 5, 10, 15^o (from vertical) L = [?] ω = 300 rpm	———	HX QUICK routine No; 76,457 cells	GAMBIT 2.4.6, ANSYS Fluent [?]	FVM PRESTO & SIMPLEC [?]	The impacts of annular velocity, shape factor, cuttings size and inclination angle on the cuttings concentration at the surface of the well are examined.	The flattened velocity profile provided by turbulent flow is necessary for the production of uniform drag distribution, thus increasing transport efficiency. Fine particles are easier to clean out. High-sphericity particles are better cleaned. Best cleaning conditions are achieved with low viscosity mud in turbulent flow.
Mohammadzadeh et al. (2016)	SS EE Yes Laminar	*FT* = Bentonite-based mud *VP* = Yes (HB) ϱ_l = [?] d_s = 2-8 mm ϱ_s = 2,500-2,800 kg/m^3 (Sphericity: 0.52-1)	v_l = 0.50-1 m/s q_s/ROP = [?] (4% inlet particle volume fraction)	D_{wb} = 0.169 m D_{dp} = 0.076 m ε = 0 θ = 0-90^o (from vertical) L = 6 ω = 0 rpm	Fluid & solid inlet velocity, outlet pressure, no slip at walls.	HX [?] Yes 178,000	[?] Core i7, 2.67 GHz 8 MB cash CPU with 12 GB RAM.	FVM SIMPLE [?]	The impacts of viscosifier content, inclination angle, circulation velocity, particle size and density and fluid and particle density on the particle transport ratio, pressure drop, friction coefficient, slip velocity are analysed.	Spatial variation of the viscosity, slip velocity are also examined. High yield stress fluids are best for cleaning. Increasing viscosifier content increases the mud carrying capacity and increases pressure drop. Fine particles are easiest to clean. Increased cuttings density increases the cuttings volume fraction.

Moraveji et al. (2017)	[?] EE Yes Turbulent (k-ε model)	*FT* = Water, air; *VP* = Yes ρ_l = 1,000, 1,225 kg/m^3 (water and air) d_s = 2 mm ρ_s = 2,761.4 kg/m^3	q_l = 0.0056-0.011 m^3/s v_g = 0.0056-0.011 m^3/s q_s/ROP = 0.0051-0.0102 m/s	D_{wb} = 0.074 m D_{dp} = 0.046 m ε = 0.623 θ = 30-90^o (from vertical) L = 6.4 ω = 0-125 rpm	Fluid inlet velocity, inlet volume fractions and outlet pressure	HX; QUICK scheme Yes 722,000	[?] Core i7, 2.67GHZ with 8 GB RAM	FVM SIMPLE pressure-velocity coupling scheme 10^{-4}	The impacts of air flow rate, water flow rate, rotational speed, cuttings diameter, inclination angle, and the radial distance on the cuttings concentration, pressure drop, and turbulent kinetic energy were analysed, with contour plots also presented.	Pipe rotation has a much greater impact on cutting transport when the inclination (from vertical) is increased. At low inclination and high flow rates of air, increasing the pipe rotation causes a high accumulation of cuttings At high inclination, the cutting concentration in the annulus decreases with increasing pipe rotation, and this is independent of air and water flow rates.
Ofei et al. (2014)	SS (7,200-54,000 sec run time) EE (KTGF) Yes Turbulent (k-ε model)	*FT* = Water and PL fluid *VP* = Yes (PL) ρ_l = 998.5-1,006.3 kg/m^3 d_s = 0.00201 m ρ_s = 2,761.4 kg/m^3	v_l = 1.524-2.743 m/s v_s/ROP = 0.00508 m/s.	D_{wb}/D_{dp}= 0.64-0.90 ε = 0.623 θ = 90^o (from vertical) L = [?] ω = 0, 80, 120 rpm	Mixture inlet mass flow rate, 0-gauge outlet pressure, no-slip at the walls.	TH [?] Yes (0.66-2.15×10^6)	ANSYS CFX 14.0 Windows 7 64-bit operating system, with 4 GB RAM, and Pentium Dual-Core processor at 2.3 GHz	FVM [?] [?]	The impacts of fluid velocity, pipe rotation, mud rheology and diameter ratio on the cuttings concentration and pressure drop are analysed.	Contour plots and streamlines for the visualisation of cuttings velocity and volume fraction are also presented. Accurate model predictions (2.5% mean error) are obtained. Increasing annular velocity increases pressure losses while reducing cuttings concentration. Increasing diameter ratio increases pressure loss significantly with an accompanying decrease in cuttings volume fraction. Increasing drill pipe rotation did not result in a significant contribution to the cuttings transport efficiency. Water and drilling have similar performances at high diameter ratios.
Osgouei et al. (2013)	[?] LE Yes [?]	*FT* = Water *VP* = Yes ρ_l = 998.5 kg/m^3 d_s = 2 mm (gravel) ρ_s = 2,762 kg/m^3	v_l = 0.61-2.74 m/s q_s/ROP = 0.0051-0.0068 m/s	D_{wb} = 0.074 m D_{dp} = 0.047 m ε = 0.623 θ = 90^o (from vertical) L = 0.61 m ω = [?]	Fluid & solid inlet velocity, outlet pressure	[?] [?] [?] 4,107,471	ANSYS CFX [?]	FVM [?] [?]	The impact of water velocity on the pressure drop and cuttings concentration are analysed. Contour plots of the multiphase flow patterns are presented.	Increased annular flow rate decreases cuttings concentration; increased ROP increases the cuttings concentration. Identified flow patterns via CFD include a stationary bed, moving bed, and a dispersed flow region. These correspond with experimental observations.

Pang et al. (2018a)	TS (60 s runtime with time step of 0.00001 s) EE Yes Turbulent (k-ω)	FT = [?] VP = Yes (PL) ϱ_l = 1,437.6 kg/m^3 d_s = 1, 3, 5 mm ϱ_s = 2,550 kg/m^3	v_l = 0.508-2.032 m/s q_s/ROP = [?] (injected volume fraction of 2-8%)	D_{wb} = 0.2032 m D_{dp} = 0.1016 m ε = 0, 0.5 θ = 0, 30, 60, 90^o L = 6.4 m ω = 0-200 rpm	Fluid & solid inlet velocity, atmospheric pressure and no-slip at walls	HX QUICK Yes 640,000 cells	Fluent 14.0 Core i7 processor with 8 cores and 8 GB RAM; 15 days run time	FVM SIMPLE routine, with second-order implicit time integration [?]	Flow visualisations of cuttings annular distribution, velocity are presented. The impacts of well inclination, drill pipe rotation, cuttings diameter, fluid rheology and annular velocity on the pressure drop and cuttings transport ratio are examined.	3 flow regions were observed: (the fixed bed, moving bed and suspension regions). Drill pipe rotation induces cuttings spiral motion and transport enhancement; however, beyond a certain rotational speed, there is no improvement. At high annular velocities, higher apparent viscosity of drilling fluid did not contribute more to the enhancement of cuttings transport but increased the pressure loss. The most difficult of cuttings transport occurs in the well inclinations around 35^o – 65^o.
Pang et al. (2018b)	TS (100 s runtime with time step of 0.00001 s) EE Yes Turbulent (k-ω)	FT = [?] VP = Yes (HB) ϱ_l = 1,437.6 kg/m^3 d_s = 3 mm ϱ_s = 2,550 kg/m^3	v_l = 0.508-2.032 m/s q_s/ROP = [?] (injected volume fraction of 2-8%)	D_{wb} = 0.2032 m D_{dp} = 0.1016 m ε = 0.5 θ = 0, 30, 60, 90^o L = 6.4 m ω = 0-200 rpm	Fluid & solid inlet velocity, atmospheric pressure and no slip at walls	HX QUICK Yes 640,000 cells	Fluent 14.0 Core i7 processor with 8 cores and 8 GB RAM; 15 days run time	FVM SIMPLE routine, with second order implicit time integration [?]	Compared to Pang et al. (2018a), a HB rheological model is applied here. Radial distributions of the cuttings axial and tangential velocity, granular temperature, turbulent kinetic energy and pressure drop are provided for different HB fluids. Contours of volume fraction velocity and the time evolution of cuttings concentration are presented.	Increasing the rheological parameters of the HB fluid increases the apparent viscosity and the fluid's cuttings carrying capacity. Cuttings volume fraction fluctuates over time when the fluids with low 'K_{HB}' and 'n' values are used. This instability is due to the shear-thinning property of the fluid, which is undesirable.

Pereira et al. (2007)	[?] [?] Yes Laminar	FT = [?] VP = Yes (Cross Model) ϱ_l = [?] d_s = [?] ϱ_s = [?]	v_l = 0.203-0.609 m/s q_s/ROP = [?]	D_{wb} = 0.100 m D_{dp} = 0.050 m ε = 0, 0.8 θ = 90° (from vertical) L = 6 m ω = 5.24-5.35 rad/s	Fluid inlet velocity, outlet pressure	HX QUICK & PRESTO No 57,000 (concentric) & 68,400 (eccentric) cells	Gambit, Fluent v6.2.16 [?]	FVM SIMPLE routine [?]	Pressure profiles over the axial annular lengths are examined at different flow rates, shaft rotation speeds and eccentricity.	Velocity contour plots showed uniform velocity distribution in the concentric case; the eccentric case revealed higher velocities in the wider annular region compared to the narrower regions. The fluid flow rate was the operational variable with the highest impact on pressure drop. Increasing the fluid velocity and viscosity increased the pressure drop. Increased drill pipe rotation reduces the pressure loss in a concentric annulus. In an eccentric annulus, increasing drill pipe rotation increases the pressure drop.
Pereira et al. (2010)	[?] LE (DPM) Yes Laminar	FT = Xanthan Gum solution VP = Yes (HB) ϱ_l = [?] d_s = [?] ϱ_s = [?]	q_l = 0.00017-0.00033 m³/s q_s/ROP = [?]	D_{wb} = 0.067 m D_{dp} = 0.032 m ε = 0, 0.75 θ = 90° (from vertical) L = 1.5 m ω = 0-600 rpm	———	HX QUICK routine No 900 cells per face	Fluent (v6.2.16) [?]	FVM PRESTO & SIMPLEC 10^{-4}	Axial pressure drop, axial & tangential profiles of fluid velocity (and the magnitude) along the radial annular space were analysed.	Particle trajectory analyses using the DPM model was also investigated. Pressure drop predictions were in agreement with experiments (< 4% error). In the concentric annulus, particles demonstrated strong helicoidal motion due to drill pipe rotation about its axis; whereas, in the eccentric case, this effect was reduced and core flow was observed.
Qu et al. (2019)	TS (with a time step of 0.001 s & 20 iterations/time step) EE (KTGF) Yes Laminar	FT = 0.4% CMC solution VP = Yes (PL) ϱ_l = 998.5 kg/m³ d_s = 2 mm ϱ_s = 2,550 kg/m³	v_l = 0.49 m/s q_s/ROP = [?] (injected particle volume fraction: 4%).	D_{wb} = 0.044 m D_{dp} = 0.030 m ε = 0 θ = 45° L = 1.8 m ω = 100-400 rpm	Injected particle volume fraction, fluid & solid inlet velocity, outlet pressure	HX QUICK Yes; 688,000	[?] Core i7 processor with 8 cores and a total memory size of 16 GB RAM	FVM SIMPLE 10^{-5}	Particle tangential velocity is radially analysed; contour plots of cuttings volume fraction are also presented.	Swirl number is analysed as a function of the dimensionless axial distance. Swirl number exponentially decays along the flow direction. Cuttings tangential velocity is more significant near the central region and gradually decreases in the direction of the radial wall. The swirl blades attached to the drill pipe significantly reduces the tendency for cuttings deposition.

Rooki et al. (2015)	SS EE Yes Laminar	FT = 0.7-0.9 quality foams VP = Yes (HB, PL) ϱ_l = [?] d_s = 3 mm (38% porosity) ϱ_s = 2,610 kg/m^3	v_l = 0.61-1.52 m/s q_s/ROP = 0.00423 m/s	D_{wb} = 0.146 m D_{dp} = 0.089 m ε = 0, 0.78 θ = 0-90^o (from vertical) L = 22.2 m ω = 0,80,120 rpm	———	HX [?] No [?]	ANSYS Fluent v13 [?]	FVM [?] [?]	The impacts of the rheological model, foam quality, foam velocity, eccentricity, inclination angle on the velocity, cuttings concentration and cuttings transport ratio are analysed.	70% quality foams are best described using the HB model and 80% & 90% foam by the PL model. Model predictions are good with <8% error. The cuttings transport ratio increases with the increase in the foam quality, foam velocity, and drill pipe rotation.
Shen et al. (2011)	SS EE No [?]	FT = Supercritical CO2 VP = Yes (20.1-81.95 × 10^{-6} Pa.s) ϱ_l = 198.5-856.5 kg/m^3 d_s = 0.2 mm (spherical) ϱ_s = 2,650 kg/m^3	v_l = 1.3 m/s v_s/ROP = 0.31m/s	D_{wb} = 0.120 m D_{dp} = 0.060 m ε = 0.6 θ = 90^o (from vertical) L = 10 m ω = 0 rpm;	———	HX [?] No [?]	[?] [?]	FVM [?] [?]	The impact of fluid density on the cuttings volume fraction, and cuttings moving and return velocity are examined.	The cuttings carrying capacity of the drilling fluid increases as the density increases; however, above a certain critical velocity, the improvement is insignificant. When using supercritical CO2 as a drilling fluid, controlling the wellhead backpressure enables the control of the downhole fluid density in order to keep it within the desired range.
Sun et al. (2014)	TS EE No Turbulent (k-ε model)	FT = [?] VP = Yes (30 mPa s) ϱ_l = 1,200 kg/m^3 d_s = 8 mm ϱ_s = 2,500 kg/m^3	q_l = 9.14-15.24 m/s q_s/ROP = [?] (inlet volume fraction of 1%).	D_{wb} = 0.2159 m D_{dp} = 0.127 m ε = 0.5 θ = 45-90^o (from vertical) L = 12 m ω = 80-240 rpm	Fluid & solid inlet velocity, outlet pressure	HX First order upwind scheme No [?]	[?] [?]	FVM [?] [?]	The impacts of drill pipe rotation, annular flow velocity and inclination angle on the cuttings volume and pressure drop are analysed.	Drill pipe rotation is observed to induce an asymmetric distribution of particles along the circumferential direction of the annulus. Increased tangential velocity due to rotation generated a tangential drag force that inhibits bed development. The effect of pipe rotation is more pronounced at low circulation velocities and becomes negligible at high velocities. A user-friendly empirical correlation was developed used Buckingham-pi theorem, least-squares method and the results of CFD simulation.

Sun et al. (2017)	TS (12 sec with Dem time step of 0.000186 sec and CFD timestep of 0.00186 sec-The Rayleigh calculated timestep) LE (CFD-DEM) Yes Turbulent (k-ε model)	*FT* = Water *VP* = Yes ϱ_l = 998 kg/m^3 d_s = 2 mm ϱ_s = 2,381 kg/m^3	v_l = 0.55-1.25 m/s q_s/ROP = [?]	D_{wb} = 0.044 m D_{dp} = 0.030 m ε = 0 θ = 30-90^o (from vertical) L = [?] ω = [?]	Fluid & solid inlet velocity, outlet pressure, Particle feed concentration of 4% and 8%	HX [?] Yes 29,000	ANSYS Fluent (+ a User Defined Function (UDF) interfaced for the DEM algorithm) [?]	FVM [?] [?]	The impact of rotational speed and inclination angle on the cuttings concentration, and Critical Deposition Velocity are examined.	Enhanced visualisations of cuttings deposition profiles are also presented. The CFD-DEM model shows very good comparison with experimental results of Kim et al., (2014). A correlation between the Critical Deposition Velocity (CDV) and the cuttings concentration is established using dimensionless analysis and infinite regression. This correlation is found to accurately predict experimental results (of CDV) of Peden et al. (1990) and Sorgun (2010).
Tersa (2015)	TS (20 s with time step of 0.001 for CFD and 0.00001 for DEM) LE (CFD-DEM, 4-way coupled) Yes Laminar	*FT* = [?] *VP* = Yes (30-75 mPa.s) ϱ_l = 1,000 kg/m^3 d_s = 4-6 mm ϱ_s = 2,500 kg/m^3	v_l = 0.5-0.7 m/s q_s/ROP = Particle insertion frequency of 4 Hz (particle volume fraction: 1-5%)	D_{wb} = 0.250 m D_{dp} = 0.125 m ε = 0-0.8 θ = 0^o (from vertical) L = 1 m ω = 0 rpm	Fluid & solid inlet velocity, outlet pressure, no slip condition at the walls	TH [?] [?] 20,000	Open-source CFDEM v2.6.1, OpenFOAM, LIGGGHTS code [?]	FVM PIMPLE (PISO+SIMPLE) [?]	The effect of eccentricity on particle transport through a vertical annulus was conducted using the CFD-DEM method.	Good experimental predictions were obtained especially at volume fractions <= 2%. At higher particle concentrations, the accuracy of predictions suffers due to the model's limitations in handling frequent inter-particle collisions. Lift forces in upward vertical motion are the main forces of particle migration to faster transport regions. For the first time, constitutive equations are derived for the cuttings transport problem via numerical simulations.
Vieira Neto et al. (2014)	SS [?] Yes Laminar	*FT* = 0.2% XG & 0.2% CMC *VP* = Yes (PL) ϱ_l = [?] d_s = [?] ϱ_s = [?]	v_l = 0.69 m/s q_s/ROP = [?].	D_{wb} = 0.067 m D_{dp} = 0.032 m ε = 0, 0.75 θ = 90^o (from vertical) L = 1.5 m ω = 0-300 rpm	Fluid inlet velocity, outlet pressure	HX QUICK & PRESTO Yes 192,000 cells	Gambit 2.3.16, ANSYS Fluent 12.1 [?]	FVM SIMPLE routine; 10^{-4}	The annular radial distribution of axial and tangential velocity are analysed as functions of fluid rheology and rotational speed along different annular planes.	Reasonably accurate pressure drop predictions are observed with the CFD model when compared with experiments. A decrease in pressure drop is observed with drill pipe rotation in the concentric annulus. The opposite occurred with the eccentric annulus. Simulated axial velocity profiles in the concentric annulus were flat for the XG solution and parabolic for the CMC solution.

Wang et al. (2009)	SS EE Yes, [?]	*FT* = [?] *VP* = Yes (25 mPa.s) ϱ_l = 1,200 kg/m^3 d_s = 0.001 m ϱ_s = [?]	q_l = 0.020-0.100 m^3/s q_s/ROP = [?].	D_{wb} = 0.216 m D_{dp} = [?] ε = 0.5 θ = 90^o (from vertical) *L* = [?] ω = 0-200 rpm	Fluid & solid inlet velocity, outlet pressure	HX [?] Yes 161,280	[?] [?]	FVM [?] [?]	The impacts of rotation speed, pump flow rate, on the cuttings bed height and cuttings velocity are analysed.	Contours of cuttings velocity and particle trajectory are also presented. Drill pipe rotation causes an asymmetric deposition profile an eventually reduces the cuttings concentration. An empirical relationship is derived that relates the cuttings bed thickness to various drilling parameters using multivariate linear regression analysis.
Yilmaz (2012)	TS LE (CFD-DPM, 2-way coupled) Yes Turbulent (SST k-ω)	*FT* = Water, CMC & Tylose solutions *VP* = Yes (Yield PL) ϱ_l = 988-1,318 kg/m^3 d_s = 4-6 mm (non-uniform Rosin-Rammler distribution sphericity: 0.1, 1) ϱ_s = [?]	v_l = 1.04-4.88 m/s (0.019 m^3/s) v_s/ROP = 0-1.8 m/s	D_{wb} = 0.203 m D_{dp} = 0.114 m ε = 0 θ = 70^o (from vertical) *L* = [?] ω = 0-120 rpm	Fluid & solid inlet velocity, outlet pressure	[?] [?] [?] [?]	Fluent 12.1 [?]	FVM [?] [?]	The impacts of flow rate, sphericity, fluid rheology, fluid density, drill pipe rotation and the impact angle on the cuttings velocity, bed height, and number of collisions are analysed.	The capability of DPM to track unsteady particle motion at different flowrates is demonstrated via validation with experimental data. Using the Rosin Rammler size distribution yielded slight differences to a case in which particles of uniform sizes are used. Non-spherical particles are easier to transport as their average transport velocity is found to be higher than spherical particles. Particle suspension considerably increased in fluids with medium effective viscosities compared to water as the carrier fluid.
Zakerian et al. (2018)	SS EE (KTGF) Yes Laminar	*FT* = [?] *VP* = Yes (PL & HB) ϱ_l = 1,198 kg/m^3 d_s = 2.54, 5.08 mm (spherical) ϱ_s = 2,700 kg/m^3	v_l = 0.52 m/s q_s/ROP = 0.00254 m/s	D_{wb} = 0.203 m D_{dp} = 0.102 m ε = 0 θ = 90^o (from vertical) *L* = 3.048 m ω = 50 rpm	Fluid & solid inlet velocity, outlet pressure	TH [?] No [?]	ANSYS Fluent v15 [?]	FVM SIMPLE [?]	The impacts of drilling fluid and cuttings density on the pressure drop, drill string stress and cuttings precipitation are analysed.	Increased cuttings concentration causes increased stress on the drill string. Higher cuttings density leads to a higher precipitation rate and increased pressure drop. As the fluid density approaches the cuttings density, cuttings precipitation increases.

EMPIRICAL AND MECHANISTIC MODELLING CONTRIBUTIONS (DRILLING)

AE-Algebraic Equations; **BC**-Boundary Conditions; **DEM**-Discrete Element Method; **DDPM-**Dense Discrete Phase Model; **DPM-** Discrete Phase Model; **EE**-Eulerian-Eulerian; **FEM-**Finite Element Method; **FVM**-Finite Volume Method; **FT**-Fluid Type; **HX**-Hexahedral; **KTGF**-Kinetic Theory of Granular Flow; **LE**-Lagrangian Eulerian; **MID**-Mesh Independence Study Performed?; **ModVal**-Model Validation Performed?; **ODE**-Ordinary Differential Equations; **OS**-Operating System; **PDE**-Partial Differential Equations; **QUICK**-Quadratic Upstream Interpolation for Convective Kinematics; **ROP**-Rate of Penetration; **SIMPLE**-Semi-Implicit Method for Pressure Linked Equations; **SS**-Steady State; **TH**-Tetrahedral; **TS**-Transient State; **VP**-Is Viscosity Data Provided?; D_{wb} = Wellbore diameter; D_{dp} = Drill pipe diameter; ε = Drill pipe eccentricity; θ = Angle of inclination; L = Computational length; ω = Drill pipe rotation; [?] = Unknown/unreported parameter.

Table C.2. Summary of empirical & mechanistic modelling research contributions for wellbore cleaning operations.

Reference	Model Characteristics + Equations	Limitations / Assumptions	Flow Conditio-ns	System Properties			Sensitivity Analyses		Solution Method	Key Findings
				Fluid & Solid Properties	Velocities & Flowrates	Wellbore Geometry	Dependent Parameter	Independ-ent Parameter		
Avila et al. (2008)	Empirical correlations for the prediction of critical flow rate and cuttings concentration.	Highly empirical	_____	FT = Water+air VP = [?] ϱ_l = [?] d_s = 2.77 mm (27.5% porosity) ϱ_s = 2307 kg/m^3	q_l = 0.0126 - 0.0315 m^3/s q_g = 0.0032-0.0252 m^3/s q_s/ROP = 0.00254 m/s	D_{wb} = 0.203 m D_{dp} = 0.114 m ε = 0-1 θ = 30, 45, 60^o (from vertical) L = 30.48 m ω = 0, 40, 80, 110 rpm	Annular cuttings concentrati-on	Liquid & gas flow rate, inclination angle, drill pipe rotation.	AEs that can be solved using a computer program.	ModVal? Yes (model prediction is better at low inclination angles). For all inclination angles, as the flow rate increases, the cuttings concentration decreases. At 30^o and 45^o, fully suspended cuttings transport is observed. At 60^o, a thin stationary bed is formed which slides downwards against the flow. The combination of centrifugal forces (for a rotated drill pipe) and the radial component of the gravitational forces (in an inclined wellbore) could cause a slight increase in cuttings concentration with drill pipe rotation. At 30^o, centrifugal forces dominate the radial gravitation force; hence, cuttings swirl into the low velocity section (near the wellbore). The reverse is the case at 45^o and 60^o, in which cuttings concentration reduces.
Becker, et al. (1991)	Empirical correlations for the prediction of cuttings annular concentration.	_____	Laminar and Turbulent	FT = Water and bentonite/polymer muds VP = Yes ϱ_l = 995-1,019 kg/m^3 d_s = 6.35 mm ϱ_s = 2,619 kg/m^3	v_l = 0.582-1.164 m/s q_s/ROP = 0.00423 m/s	D_{wb} = 0.127 m D_{dp} = 0.0483 m ε = -0.5, 0 +0.5 θ = 0-90^o (from vertical) L = 12.2 ω = 3-600 rpm	Particle concentrati-on	Fann rotary speed, mud velocity, angle of inclination, eccentricity, fluid rheology.	AEs which can be solved using a computer program.	ModVal? Yes. The best correlating mud parameter with the cuttings concentration was the 6 rpm Fann V-G meter dial reading. Mud shear stress and initial gel strength also showed good correlation with the transport performance. For (0-45^o from vertical) hole angles, transport performance is better in laminar flow; for angles > 60^o, turbulent flow is recommended. In laminar flow, the impact mud rheology on cuttings transport is greater for near-vertical hole angles. In turbulent flow, mud rheology has no noticeable impact on cuttings transport.

Bizanti and Alkafeef (2003)	Simplified model for minimum velocity calculations, rheology factor table, angle factor table, transport index model, minimum flow rate table/chart.	Highly empirical method based on Hopkin's approach for minimum mud velocity calculation.	_____	FT = [?] VP = Yes ϱ_l = 1,114 kg/m^3 d_s = [?] ϱ_s = 2,636 kg/m^3	q_l = calculated q_s/ROP = 0.00021-0.0085 m/s	D_{wb} = 0.216-0.445 m D_{dp} = 0.089-0.114 m ε = [?] θ = 29-71^o (from vertical) ω = 0 rpm	Critical flowrate	Inclination angle and fluid yield point.	AEs solved by hand.	ModVal? Yes. The newly proposed model, along with the Hopkin's method, have been compared with field data and produced reasonably accurate results, especially at inclination angles >45^o. The new method produces lower values of critical flow rate than the Hopkin's method. The new method also compares better with field data than the Hopkin's method.
Cayeux et al. (2014)	Semi-Mechanistic Field-calibrated 1D transient cuttings model; mass, momentum and energy conservation equations, specific heat capacity and thermal conductivity equations, dag, and settling velocity equations, cuttings bed area and drill pipe rotation models.	Common pressure for each phase (in writing the mass conservation equations). Circular Couette flow is assumed due to drill pipe rotation, the separation distance between particles in a layer is isotropic.	Laminar	FT = WBM & OBM VP = Yes (HB & RS) ϱ_l = 1,550-1,740 kg/m^3 d_s = 2-6 mm $\varrho_s \approx$ 2,650 kg/m^3	q_l = 0.032 m^3/s q_s/ROP = 0.0042 m/s	D_{wb} = 0.216-0.311 m D_{dp} = [?] ε = [?] θ = 0^o (from vertical) L = 61-853 m ω = 80 rpm	Fluid velocity, cuttings bed height & concentration, temperature, fluid density, top drive speed, erosion rate and hole cleaning index	Time	PDE's and AEs which can be solved by standard numerical methods using a computer program.	ModVal? Yes-Calibrated against field data (2 wells in the North Sea) by adjusting particle size, cuttings bed erosion factor, with measured cuttings rate at the surface). The model accounts for both fluid-particle transport and drill string mechanics. In a real field case study, it was observed (via the model that the annular velocity was too small in some well regions; hence, increasing the velocity was the recommendation. In another high ROP real scenario, simulations showed that material transport occurred by cuttings bed erosion; hence ROP reduction stabilised the transport process at downhole conditions.
Chen et al. (2007)	Semi-empirical cuttings transport model with foam empirical rheological model; EoS model for foam density; mass and momentum conservation equations, pressure loss model across drill bit. Wellbore has horizontal, inclined and vertical regions.	Steady-state isothermal flow, no inner pipe rotation, fluid rheology is insensitive to temperature, no influx from or lost circulation to the reservoir.	Laminar & Turbulent	FT = 0.255 & 0.5% HEC polymer foam VP = Yes ϱ_l = 1,001 kg/m^3 d_s = 3 mm ϱ_s = 2,600kg/m^3	q_l = 0.0025 m^3/s q_g = 0.57 m^3/s q_s/ROP = [?]	D_{wb} = 0.127 m D_{dp} = 0.216 m ε = 0 θ = 0^o , 40^o, 90^o (from vertical) L = 914.4-3048 m ω = 0 rpm	Fluid velocity, foam quality, foam density, pressure, pressure drop.	Measured depth, fluid composition.	The proposed detailed stepwise algorithm implemented in a visual-basic computer program for iterative calculations (ODEs & AEs).	ModVal? Yes (±20% error band). There is significant variation in the profiles of pressure, foam quality, velocity and foam density when the wellbore changes from vertical to directional to inclined. Foam properties change more rapidly in vertical regions compared to inclined and horizontal sections. Polymer additions to foams increase frictional pressure and hydrostatic pressure gradient. To maintain the BHP at a low value, a lower water injection rate has to be applied. Foam allows the creation of a suitable pressure profile between fluctuating pore pressure and fracture pressure gradients.

Cheng and Wang (2008)	3-layer steady-state model. Mass and momentum balance equations, foam quality model, interfacial shear stress and interlayer friction coefficient model, cuttings concentration model, Bagnold stress model, generalised PL model, modified particle settling velocity model, transitional bed sliding models.	Homogeneous bubble foam flow throughout the annulus, foam compressibility depends only on the gas phase, constant cuttings diameter, sphericity and distribution in each layer, negligible slip between gas and liquid phase, no drill pipe rotation.	Laminar & Turbulent	FT = Water and 90% quality foam VP = modelled ϱ_l = modelled d_s = 12.7 mm ϱ_s = 2,400 kg/m^3	v_l = 0.6-1.2 m/s q_s/ROP = 0.0028 m/s	D_{wb} = 0.2159 m D_{dp} = 0.1143 m ε = 0.8 θ = 0-90^o (from vertical) ω = 0 rpm	Cuttings bed distribution in the annulus	Inclination angle, fluid flowrate and mud rheology.	Propulsion iteration (in each grid of the discretised domain) and trial and error method (for determining cuttings bed thickness).	ModVal? Yes. Experimental predictions carried out yielded errors of less than 15.42%. Annular cuttings concentration reaches its maximum at 55^o. Cuttings bed height increases with a decrease in nominal annular return velocity. Cuttings carrying capacity of foam is 2-5 times better than that of water. Bed height increases rapidly between 30^o and 60^o inclination; remains constant or decreases slightly from 60-90^o.
Clark and Bickham (1994)	1D mechanistic cuttings transport model; Mixture pressure drop model, lift and drag coefficient models, settling velocity correction factors, pressure gradient force model, Kelvin-Helmotz stability model, rolling and lifting bed height equations, equilibrium cuttings bed height model, 5% maximum concentration model.	Steady-state flow, spherical cuttings with the void-free interior; cuttings dynamic forces (drag, lift and pressure gradient) are all assumed to act through the centre of gravity.	Laminar & Turbulent with settling, lifting and rolling motions.	FT = Synthetic-Base; VP = Yes (HB) ϱ_l = 1,498 kg/m^3 d_s = 0.00635 m ϱ_s = 2,300 kg/m^3	q_l = 0.039 m^3/s q_g = [?] q_s/ROP = 0.0042 m/s	D_{wb} = 0.314-0.318 m D_{dp} = 0.127-0.203 m ε = 0 & 1 θ = 0-85^o (from vertical) L = 0-2045 m ω = 0 rpm	Cuttings concentrati-on	Flow rate, cuttings size, wellbore angle.	ODEs and AEs are solved via numerical methods.	ModVal? Yes. Rolling, lifting and settling motions are dominant within a certain range of angles. At high inclination angles, when cuttings bed forms, the transport mechanism is determined by rolling motion. At intermediate angles, where a churning moving bed exists, transport is via lifting. At near-vertical angles, particle settling determines transport. Model predictions are in good agreement with experimental measurements.
Costa et al. (2008)	1D 2-layer transient model, mass and momentum balance equations for solids and liquids in each layer; drag, friction and interfacial shear stress models.	52% solids concentration in bottom layer, isothermal flow, incompressible phases, uniform fluid velocity in the wellbore, non-Newtonian power-law model for the drilling mud.	Laminar & Turbulent	FT = [?] VP = No ϱ_l = 1,198.26 kg/m^3 d_s = 6.35 mm ϱ_s = 2,516 kg/m^3	q_l = 0.0221 m^3/s q_s/ROP = 0.0028 m/s	D_{wb} = 0.221 m D_{dp} = 0.127 m ε = 0.30; θ = 90^o (from vertical) L = 1,200 m ω = 0 rpm	Bed height, annular pressure and ECD	Measured depth	Finite volume method and Newton-Raphson technique for linearization (PDEs and AEs).	ModVal? No. Bed height reduces when the ROP is reduced. In vertical sections, the cuttings concentration is higher. ECD variations resulting from different flow conditions can be predicted with the developed model.

Doan et al. (2003)	1D, 2-layer UBD transient model, consisting of conservation equations (with multi-particle solid-liquid drag forces), power-law rheological model, hydrodynamic shear stress model, interfacial friction coefficient and bed friction model, deposition and entrainment model.	Uniform transport properties of air/water mixture; uniform-sized spherical cuttings, instantaneous and homogeneous mixing of reservoir fluid with drilling mud, with uniform mixture transport properties. Valid empirical relations for describing interphase and interphase momentum transfer.	Laminar & Turbulent	FT = Air+(water, Polyacramide solutions) VP = Yes ρ_l = 1,000-1,190 kg/m^3 d_s = 3.66, 7.32 mm ρ_s = 2,400 kg/m^3	q_l = 0.0017-0.01 m^3/s q_s/ROP = 2.2×10^{-7} – 5×10^{-5} m^3/s	D_{wb} = 0.127 m D_{dp} = 0.026 m ε = 0-1; θ = 0^o-90^o (from vertical) L = 8 m ω = 0 rpm	Cuttings velocity, pressure and cuttings bed height	Flow time, annular distance, cuttings rate.	PDEs and AEs solved using Newton's method with relaxations.	ModVal? Yes. The obtained results demonstrate that slippage is a major determinant of cuttings bed formation. The derived model is useful in estimating the minimum flowrate necessary for cuttings removal in UBD conditions. Calculated cuttings velocity agreed in most cases with the measured values. However, in regions of dilute cuttings injection, the match was poorer; this was attributed to the limitation of the 2-layer model in accurately capturing interfacial phenomena.
Gavignet and Sobey (1989)	2-layer model; momentum balance, interfacial stress models and friction factor equations.	Cuttings bed is assumed to be closely packed with a concentration between 50% and 60%. Steady-state flow is assumed. Saltation/particle dispersion at high flow rates is neglected.	Turbulent flow	FT = Water, Carbopol, high & low viscosity mud VP = Yes (PV, YP) ρ_l = 999-1,012 kg/m^3 d_s = 0.00635 m ρ_s = 2,619 kg/m^3	q_l = 0-0.016 m^3/s q_s/ROP = 0.0042 m/s	D_{wb} = 0.216 m D_{dp} = 0.06-0.127 m ε = 0.5; θ = 0-90^o (from vertical) L = [?] ω = 0 rpm	Bed thickness and critical flow rate.	Pump rate, inclination angle.	System of ODEs and AEs solved by standard numerical methods.	ModVal? Yes. There is often a critical flow rate above which cuttings bed will not form. Highly deviated wells should always be drilled with a large drill pipe as possible. The friction coefficient of the cuttings against the hole wall strongly influences bed formation at high inclination angles. There is reasonable agreement between the proposed model and experiments of Tomren et al., 1986.

Guo et al. (2010)	3-layer (suspension, dispersed and uniform layers) transient cuttings model in extended-reach wells. Continuity and momentum equations for both phases in each layer, drill pipe rotation model. Phase density model, shear stress models (at pipe wall for each layer), drag force and friction coefficient models, cuttings deposition and diffusivity models.	Incompressible solid and liquid phases, physical properties of the drilling fluid are continuous (PL fluid model), cuttings concentration in the suspension layer is low and conforms to diffusion law; cuttings concentration in the uniform layer is 55% and that in the dispersed layer is 0.8 times that in the uniform layer.	Suspensi-on, rolling and sliding cuttings motion.	FT = [?] VP = No (PL assumed); ϱ_l = [?] d_s = [?] ϱ_s = [?]	q_l = 0.05-0.08 m^3/s q_s/ROP = [?]	D_{wb} = [?] D_{dp} = [?] ε = [?] L = (vertical, 800 m, inclined 0-90° and horizontal sections, 1,000-2,000 m) ω = 0, 90 & 180 rpm	Cuttings bed height distribution	Wellbore length, flow time.	SETS numerical solution algorithm for PDE's, and AEs.	ModVal? No. By modifying the fluid velocity in the suspension layer, drill pipe rotation is accounted for. Simulation of dynamic well BHP using a virtual grid tackles the problem of assuming a fixed bit location (used in previous studies). Increasing the flushing rate from 60L/s to 80 L/s results in a drop in cuttings concentration from 18.5% to 11.1%. Drill pipe rotation aids cuttings transport by increasing equivalent mud speed, and by increasing the shear stress between the suspension and cuttings bed layer.
Hopkin (1967)	Empirical correlation for determining particle slip velocity as a function of funnel viscosity. Particle settling velocity mode, Stokes' law for slip velocity, wall connector factor.	Highly empirical	Laminar and Turbulent	FT = Water & polymer based muds VP = Yes ϱ_l = 994-1,054 kg/m^3 d_s = (1.96 mm thickness to 24.2 mm in spheres with sphericity from 0.379-1) ϱ_s = 2,499-2,691 kg/m^3	q_l = 500 gpm (0.19-10.57 m/s) q_s/ROP = 0-0.051 m/s	D_{wb} = 0.203-0.311 m D_{dp} = 0.114-0.140 m ε = 0; θ = 0° (from vertical) L = 2.44 m ω = 35 rpm	Cuttings slip velocity, rate of cuttings removal.	Mud viscosity, drilling rate and hole size.	AEs solved by hand (Charts also provided for easy look-up).	ModVal? Yes. Cuttings slip velocity was found to be a function of the viscosity of the mud. The mud's yield value appears to be the most important component of the viscosity affecting the slip velocity. Slip velocity of drill cuttings can be reduced by increasing mud density. Hole enlargement is an essential factor affecting drill mud performance.

Hyun et al. (2000)	3-layer mechanistic cuttings transport model; continuity and momentum balance equations; friction factor correlation, force balance equations on the moving bed layer/moving bed velocity model, particle settling velocity, cuttings concentration model in the suspension layer, shear stress models. These models are written for the horizontal, inclined and vertical annular configurations, respectively.	2-phase steady-state isothermal incompressible flow, uniform cuttings size and sphericity distribution, cuttings volume fraction in the upper layer is minimal; PL rheological model is adopted, no effect of pipe rotation, no solid-liquid slip.	Laminar and Turbulent	FT = Low viscosity Bentonite VP = Yes (PL) ϱ_l = 1,102 kg/m^3 d_s = 6.35 mm (0.8 sphericity) ϱ_s = 2,620 kg/m^3	v_l = 0.61-1.22 m/s q_s/ROP = 0.15 kg/s	D_{wb} = 0.127 m D_{dp} = 0.048 m ε = -0.5-1 θ = 0-90^o (from vertical) L = [?] ω = 0 rpm	In-situ annular velocity, cuttings area fraction and pressure gradient.	Hole deviation angle, fluid velocity, fluid rheology.	PDE's ODEs and AEs which can be solved by standard numerical methods using a computer program.	ModVal? Yes. Simulation results are in good agreement with experimental data. A balance must be considered between cuttings bed formation, pressure drop and fluid rheology to obtain optimum cleaning conditions in inclined annuli. Single parameter adjustment will not promote cuttings transport. Conventional mudflow velocity range of 0.61-0.91 m/s should be avoided in coiled tubing drilling. A velocity range of 1.1-1.4 m/s is recommended for wells having a long horizontal section. Highly viscous fluids slightly increase the carrying capacity under turbulent flow, as well as the pressure gradient.
Iyoho et al. (1987)	New Material Balance Model for cuttings transport; cuttings transport ration equation, cuttings accumulation rate equation.	The algorithm is unable to hence shale sloughing, gas transport and slug dispersion effects.	Laminar and Turbulent	Geometry and flow conditions are based on Tomren et al. (1986); Hopkin (1967) and O'Brien and Dobson (1985).			Cuttings concentration and slip velocity.	Average nominal fluid velocity, particle diameter, ROP, and hole depth	ODEs solved via the finite difference method using a computer program.	ModVal? Yes (field and experimental data). The proposed model performed better than the Hopkin's method. Larger cuttings are often left back in the annulus, thus leading to degradation, regrinding and a risk of stuck pipe. Increased mud yield values (at a constant pump rate and ROP) improves the transport of larger cuttings by reducing residence time.
Kamp and Rivero (1999)	1D, 2-layer transport model; mass and momentum conservation equations, turbulent suspension model, particle settling velocity model, resuspension model, interfacial and wall shear stress model.	Steady-state flow	Turbulent	FT = [?] VP = No ϱ_l = 1,078 kg/m^3 d_s = 0.0051 m ϱ_s = 2,157 kg/m^3	q_l = 0.0032 m^3/s q_s/ROP = 0.00085-0.0085 m/s	D_{wb} = 0.22 m D_{dp} = 0.114 m ε = 0-1 θ = 90^o (from vertical) ω = 0 rpm	Bed height	ROP, mudflow rate, eccentricity, mud viscosity, cuttings diameter.	ODEs and AEs are written in dimensionless form (for easy matrix inversion) and solved via numerical methods.	ModVal? Yes (with correlation-based model). Bed height increases nearly linearly with ROP. At higher fluid viscosity, a minor decrease in bed height is observed. The authors attribute this to the absence of a turbulence term that flattens out the concentration profile. The absence of this term is also a stated reason for the over-prediction of cuttings transport. The assumption of direct proportionality between the resuspension flux and interfacial friction velocity is another reason for this over prediction. Bed height increases with an increase in cuttings diameter and eccentricity.

Kelessidis and Bandelis (2003)	A 2-layer empirical model for determining bed height using dimensionless analysis.	Turbulent eddies counterbalance the settling of solids due to gravity. 52% cubic packing of the cuttings. Cuttings settling velocity and dispersion coefficient are independent of the vertical distance.	Turbulent	*FT* = CMC water solutions *VP* =Yes ρ_l = 998-1,048 kg/m^3 d_s = 1-4 mm ρ_s = 2,492 kg/m^3	q_l = 0.00035-0.012 m^3/s q_g = [?] q_s/ROP = 0.012 m^3/s (slurry rate)	D_{wb} = 0.070 m D_{dp} = 0.040 m ε = 0 θ = 90^o (from vertical) L = [?] ω = 0 rpm	Cuttings concentrate-on	Annular positions, Peclet number.	ODEs and AEs which can be solved by a simple computer program.	ModVal? Yes. The most influential parameter on the cuttings transport process is the annulus mixture velocity. Eccentricity plays a big role, with significant increase in cuttings bed formation for fully eccentric transport scenario. Maximum flowrates should conform to rates and pressure limitations of the downhole motor for coiled tubing operations.
Larsen et al. (1997)	Empirical cuttings transport model with cuttings transport velocity model, equivalent slip velocity model with correction factors, (inclination angle correction factor, cuttings size correction factor, mud weight correction), critical transport fluid velocity and subcritical fluid flow model.	Steady state flow, open area velocity above the cuttings bed is assumed to be equal to the critical transport fluid velocity.	Laminar & Turbulent	*FT* = Water and mud1-mud5 *VP* = Yes (PV&YP) ρ_l = 1,027 kg/m^3 d_s = 0.0044 m ρ_s = [?]	q_l = 0.0069 m^3/s q_s/ROP = 0.0046 m/s	D_{wb} = 0.127 m D_{dp} = 0.06 m ε = ±0.62 θ = 55-90^o (from vertical) L = 10.67 m ω = 50 rpm	Cuttings velocity and concentrate-on	ROP, mud weight, cuttings size and inclination angle.	The system of AEs can be solved by hand as presented in an example.	ModVal? Yes. Simple empirical calculation that predicts cuttings transport velocity, critical transport fluid velocity, cuttings concentration and subcritical fluid flow conditions were proposed. To reach CTFV, a higher velocity is needed for an increase in ROP. Increased mud weight improves cuttings transport. Low viscosity muds perform better in high angle wells compared to high viscosity muds. Reducing the flowrate from 150 gal/min to 110 gal/min yielded an increase in cuttings concentration by a factor of 1.6.
Li and Kuru (2003)	1D unsteady state mechanistic model with UBD conditions in vertical wells. Continuity and momentum equations which account for formation fluid influx, foam quality, viscosity (power-law) and density models, friction factor correlations; model for foam flow across bit nozzle, and a model for foam flow in drilling pipe.	Model calibration using actual field data not implemented. Foam slugging conditions not accounted for. Homogenous foam mixture assumed.	Laminar	Air + water *VP* = modelled ρ_l = modelled d_s = 0.0127 m ρ_s = 2,700 kg/m^3	q_l = 0.0025 m^3/s q_g = 0.236 m^3/s q_s/ROP = 0.0051 m/s	D_{wb} = 0.2 m D_{dp} = 0.114 m ε = 0 θ = 0^o (vertical) L = 914.4 m ω = 0 rpm	Bottomhole pressure, Cuttings concentrati-on.	Gas flowrate, ROP, well depth, flow time, sphericity, cuttings size.	PDEs, ODEs & AEs using Crowe's modification of SIMPLE method + modifications to facilitate convergence.	ModVal? : Yes Cuttings distribution in well non-uniform even under SS conditions. Water influx from the reservoir decreases foam quality and increases BHP. Gas influx increases foam quality + reduces BHP. Larger cuttings cause increased accumulation. Irregular (non-spherical) cuttings incur decreased accumulation.

Li et al. (2002)	Empirical correlations for the prediction of pressure drop, fluid velocities and cuttings transport.	Each control volume is assumed to have homogeneous properties; empirical-based.	Laminar and Turbulent	*FT* = Xanvis and HEC polymer-based fluids *VP* = No ϱ_l = [?] d_s = [?] ϱ_s = [?]	q_l = 0.0041-0.0049 m³/s q_g = 300 scf/min q_s/ROP = 0.0254-0.0508 m/s	D_{wb} = [?] D_{dp} = 0.025-0.073 m ε = >0 θ = 0-90° (from vertical) L = 2,012-3,048 m ω = 0 rpm	Solids removal rate, wiper trip speed, solids distribution over the wellbore length, critical transport velocity, and cuttings concentrate-on.	Inclination angle, in-situ fluid velocity and time	Well section is divided into 'n' control volumes, and governing equations are solved using the Tornado sand cleanout tool.	ModVal? Yes (The developed simulator was applied to different field cases, and the simulation tool successfully predicted all aspects of the cleanout). The simulator (which is based on comprehensive test data) allows the prediction of the time history of solids volume fraction along the wellbore.
Luo et al. (1992)	Empirical cuttings transport correlation based on dimensionless analysis.	_____	Laminar & Turbulent flow	*FT* = Water, CMC/XC solutions, bentonite muds *VP* = Yes (PL) ϱ_l = 1,000-2,000 kg/m³ d_s = 2 mm ϱ_s = 2,600 kg/m³	q_{mix} = 0.037 m³/s (1.87 m/s) q_s/ROP = 0.0028-0.0083 m/s	D_{wb} = 0.203-0.445 m D_{dp} = 0.127 m ε = 0 θ = 0-90° (from vertical) L = 15 m ω = 0-200 rpm	Minimum ROP, critical flow rate, maximum safe ROP and fluid rheological properties	Hole angle, fluid consistency index and mud flow rate	Simple AEs that can be solved by hand or a computer program.	ModVal? Yes (Model is compared against field data, and good agreement is observed). The model was simplified into a series of easy-to-use charts to facilitate rig-site implementation. The model supports the use of low/high viscosity muds and low-shear enhancers for improving cleaning operations. Critical Flow Rate (CFR) is inversely proportional to the mud density. CFR increases with an increase in ROP. In turbulent flow conditions, reducing the viscosity will reduce the CFR. CFR increases as the hole angle increases and the rate of increase diminishes towards 90°.
Martin et al. (1996)	1D 2 layer model. Momentum balance equation, interfacial stress model, modified friction factor correlation, static force and static friction models, bed height model and a model to handle friction factor uncertainty.	Steady-state flow.	Laminar & Turbulent flow	*FT* = Water, thin, average and thick Xanthan gum muds *VP* = Yes ϱ_l = 1,000-1,300 kg/m³ d_s = 0.081-0.234 in ϱ_s = 2,650 kg/m³ (sandstone)	q_l = [?] q_s/ROP = [?]	D_{wb} = 0.127 m D_{dp} = 0.0508, 0.0635 m ε = 0-1 θ = 90° (from vertical) L = 12 m ω = 0 rpm	Interfacial friction factor	Fluid behaviour index, Reynolds number, particle diameter and hydraulic diameter.	ODEs and AEs which can be solved by a simple computer program.	ModVal? Yes. Newly proposed correlations predicted the interfacial friction factor more accurately than the models in previous literature. More work is required to incorporate the effects of drill pipe rotation on the interfacial friction factor.

Martins and Santana (1992)	2-layer mechanistic dimensionless cuttings transport model. Mass and momentum balance for each phase, shear stress models, static force model (contact between particles in the bed and the well wall), and diffusion model (for particle concentration in the upper layer).	No-slip between solid and liquid phases in each layer, no mass transfer between both phases, gravitational effects are neglected in the momentum transfer equations, constant interface height, incompressible solid-liquid system.	Laminar & Turbulent	FT = [?] VP = Yes (PL) ϱ_l = 1,102 kg/m^3 d_s = 6.3 mm ϱ_s = 2,620 kg/m^3	q_l = 0.022 m^3/s q_s/ROP = 0.0042 m/s.	D_{wb} = 0.216 m D_{dp} = 0.127 m ε = 0.5-1 θ = 40, 60, 80, 90^o (from vertical) ω = 0 rpm	Solids concentration and friction loss	Fluid flow rate, inclination angle and fluid density.	For generating flow maps, a dimensionless rearrangement of the main formulation (ODEs & AEs) is proposed and solved via standard numerical methods.	ModVal? No The use of large diameter pipes, increased fluid density and flowrate increase cuttings transport efficiency. Newly proposed friction loss model is reasonably accurate. Dimensionless diagrams evaluate well cleaning as a function of a modified Lockhart and Martinelli parameter and upper region flow regime.
Martins et al. (1999)	Transient 2-layer model for extended reach drilling. Continuity and momentum balance (for each layer) equations for both phases.	Particles have uniform diameter and sphericity; top layers only contain carrier fluid, no-slip between both phases, solid-liquid system is incompressible, constant height of interface between both layers, and no mass transfer.	Laminar & Turbulent flow	FT = [?] VP = Yes ϱ_l = [?] d_s = [?] ϱ_s = [?]	q_l = [?] q_s/ROP = 0.0056-0.00833 m/s	D_{wb} = 0.31 m D_{dp} = 0.17 m ε = >0 θ = 90^o (from vertical) L = 100-3,000 m ω = 0 rpm	Cuttings bed height	Flow rate, ROP and fluid viscosity, time, annular position.	Finite volume approach (semi implicit).	ModVal? No. The results highlight that steady-state was not attained in some cases even after 5500 sec, thus reinforcing the limitation of the steady-state assumption in some studies. Increasing fluid viscosity, fluid flow rate and reducing the bit ROP enhance cuttings transport in a horizontal eccentric annulus. When there is sufficient hydraulic capacity, low weight muds can be used to clean a wellbore with instability problems.
Mohammad-Salehi and Malekzad-eh (2011)	Larsen's model combined with Moore's correlation for cuttings slip velocity prediction; critical flow rate model, correction factor equations for mud density, angle of inclination and cuttings average size.	Highly empirical method	———	FT = OBM VP = (Yes) ϱ_l = 983.8 kg/m^3 d_s = 3.81 mm ϱ_s = 1,797 kg/m^3	q_l = calculated q_s/ROP = 0.00021 m/s	D_{wb} = 0.217 m D_{dp} = 0.127 m ε = [?] θ = 65.4^o (from vertical) L = (MD, 2,583 m, TVD, 2,465 m) ω = 0 rpm	Rotary torque, cuttings bed height & cuttings returned to the surface.	Mud plastic viscosity, mud flow rate.	Simple AEs that can be solved using a computer program.	ModVal? No. Increasing the mudflow rate increases the amount of returned cuttings at the surface. Proper circulation rate selection results in less drilling torque, increased ROP and better hole cleaning. The torque is a good indication of how readily the drill bit rotates and how easily cuttings are transported. Hole cleaning optimisation can be carried out incorporating the effects of the maximum bit horsepower and jet impact force. By plotting the critical flow rate profile versus PV, YP and AV, one can determine the best rheological fluid properties.

Naganawa and Nomura (2006)	Transient cuttings transport model. Mass and momentum conservation equations, density and solids packing correlations, shear stress for each layer and interfacial shear stress, dry friction force model, cuttings deposition rate model, modified cuttings entrainment rate, simplified model for drill pipe rotation.	Drill pipe rotation is around a fixed axis; cuttings angle of repose was assumed to be 35°. Cuttings entrainment rate from the bed is assumed to be a simple linear function of friction velocity between layers.	Laminar & Turbulent	FT = [?] VP = Yes (PL) ϱ_l = 1,130-1,170 kg/m^3 d_s = 3.175 mm ϱ_s = 2,400 kg/m^3	q_l = 0.031-0.033 m^3/s q_s/ROP = 0.001-0.0015 m/s	D_{wb} = 0.216-0.311 m D_{dp} = 0.127 m ε = 0-1 θ = (vertical, inclined, 55° and vertical) L = (700-1,345 m MD, 0-700 m TVD & 190-246 m section length) ω = 40-70 rpm	Cuttings bed height and pressure drop	Mud flow rate, ROP, measured depth, mud specific gravity, eccentricity, hole size.	Stability-enhancing two-step (SETS) methods, (more stable and less computational time compared to fully implicit finite difference method (PDE's, ODEs, & AEs).	ModVal? Yes. The developed simulator successfully described transient cuttings bed height distribution over the entire well trajectory. The comparison of transient simulation and steady-state model results showed similarity in deposition profiles, but the values of cuttings bed height were slightly different. With a 0-drill pipe eccentricity, cuttings bed height was significantly reduced.
Naganawa et al. (2017)	2-layer transient cuttings transport model with theoretically derived constitutive equations. Mass and momentum balance equations with mass transfer terms between 2 layers shear stress, frictional loss, settling velocity and drag models, critical friction velocity model and drill pipe rotation model.	Spherical cuttings packed in a simple cubic arrangement (52% volume fraction) are assumed; isothermal flow. Angle of repose is assumed to be 35%. At the bottom of the hole, the drill pipe is assumed to be asymmetrically deformed with a maximum eccentricity.	Laminar & Turbulent	FT = [?] VP = Yes (HB) ϱ_l = 1,430-1,470 kg/m^3 d_s = 3.175-6.35 mm ϱ_s = 2,650 kg/m^3	q_l = 0.032, 0.043 m^3/s q_s/ROP = 0.0011, 0.0015 m/s	D_{wb} = 0.216, 0.311 m D_{dp} = 0.127 m ε = 0-1 θ = 0° (from vertical) L = 2,700-4,500 m ω = 80, 120 rpm	ECD, cuttings bed height	Mud flowrate, drill pipe rotation and hole size	Stability enhancing two-step (SETS) method, an extension of the SIMPLE method. Improved computation time via larger timesteps without sacrificing numerical stability are attained.	ModVal? Yes (Validation here is done using field data) in a directional well in which ECD was measured by LWD. Repeated cuttings deposition and erosion were observed in accordance with the actual drilling rate history. ECD in the highly inclined regions generally increases, due to the increase in frictional pressure loss with a small increase in TVD. Further adjustments of friction factors and other model parameters with more detailed drill pipe rotation model are required to enhance the model's performance.

Nguyen and Rahman (1996)	3-layer steady-state model; material balance equation on the entire system, force balance equations of the fluid flow region, force balance equations on the dispersed-layer region, force balance on uniform-concentration layer region; extra equations are also written for 5 identified transport modes which are a combination of the different regions.	Steady-state flow with no-slip between solid and fluid phases.	Turbulent	FT = Low viscosity Bentonite VP = Yes ϱ_l = 134.5 kg/m^3 d_s = 0.00635 m ϱ_s = 2,611 kg/m^3	v_l = 0.213 m/s q_s/ROP = 0.0042 m/s	D_{wb} = 0.127 m D_{dp} = 0.048 m ε = 0, 0.5 θ = 90^o (from vertical) ω = 0 rpm	Cuttings concentration, pressure gradient and uniform layer thickness.	Mean annular velocity, mud rheology, fluid and cuttings density, cuttings bed packing factor, uniform layer velocity and friction coefficient.	System of ODEs and AEs solved by standard numerical methods.	ModVal? Yes. Wellbore eccentricity has an adverse effect on cuttings transport efficiency. Increase in mud weight results in substantial reductions in cuttings concentration compared to the reductions obtained by fluid viscosity enhancement. There is a significant reduction in uniform layer thickness when the cuttings density is reduced. A cuttings bed-packing factor of 62% resulted in a thicker cuttings bed compared to that of 52%.
Okpobiri and Ikoku (1986)	Semi-empirical steady-state model for pressure loss prediction; Mud viscosity correlations, frictional losses/frictional factor correlation, terminal velocity and carrying capacity model, pressure drop across bit nozzles, minimum volumetric gas and liquid requirement model.	Steady-state conditions are prevalent; negligible pressure drop caused by elevation change, flow is isentropic.	Laminar & Turbulent	FT = 65-92% Foam (water+surface active agent+air) VP = modelled (PL) ϱ_l = modelled d_s = 5-25.4 mm ϱ_s = 2,700 kg/m^3	q_g = modelled q_s/ROP = 0.0025-0.0076 m/s	D_{wb} = 0.2-0.23 m D_{dp} = 0.114 m ε = 0; θ = 0^o (from vertical) L = 76.2-3,658 m ω = 0 rpm	Liquid and gas flow rate and the wellhead injection pressures.	Well depth, hole size and annular back pressure.	A computer program was developed (GLVRFD) to solve the system of ODEs and AEs.	ModVal? Yes. Increasing penetrating rate results in only a minor increase in the liquid and gas flow rates. Volumetric requirements must be increased as the size of the particle to be lifted increases. Well cleanout operations can be satisfactorily done with laminar flow conditions of 55%-96% quality foam. Increased hole sizes and depth imply increased rates from cuttings removal. Annular pressure greater than atmospheric pressures are necessary to maintain bottomhole foam quality.

Osunde and Kuru (2006)	1D unsteady state mechanistic model with UBD conditions in inclined wells (2-layer model); Continuity and momentum equations with formation fluid influx, foam quality (via EoS), viscosity/rheology (power-law) and density models, drag and friction factor correlations, a model for the friction force between cuttings and wellbore, re-suspension and deposition velocity model, a model for foam flow across bit nozzle, model for foam flow in drilling pipe and 3-phase pressure drop model.	Homogeneous foam fluid; perfectly spherical cuttings with uniform velocity distribution over the entire cross-sectional area. Influx of reservoir fluid into the wellbore instantaneously reaches mean stream velocity.	Laminar & Turbulent	FT = Air+warter VP = modelled ϱ_l = modelled d_s = 0.0127 m ϱ_s = 2,700 kg/m^3	q_l = 0.0025 m^3/s q_g = 0.0189 m^3/s q_s/ROP = 0.0051 m/s	D_{wb} = 0.216 m D_{dp} = 0.114 m ε = 1 θ = 30^o, 45^o, 60^o (from vertical) L = 121.9 m ω = 0 rpm	Bottomhole pressure, Cuttings concentrate-on.	Gas rate, well inclination, well length, well depth and flow time.	PDEs, ODEs & AEs solved using Crowe's modification of the SIMPLE method, coupled with some modifications by the authors for facilitating numerical convergence.	ModVal? Yes. The developed model under-predicts experimental data within an error range of 4-21%. The effect of the gas injection rate is more pronounced than the liquid injection rate on the cuttings transport process. High gas rates increase the efficiency of cuttings transport. Cuttings transport efficiency decreases with an increase in the angle of inclination. Increasing drilling rate increases the cuttings concentration.
Ozbayoglu et al. (2005)	1D 3-layer steady-state isothermal model; material and momentum balance equations, interfacial shear stress equations, slip velocity model, in-situ concentration model.	Within one cell in the discretised annular system, the velocity, density and other fluid properties are assumed constant. Cuttings are assumed to be perfectly spherical with uniform diameter and density.	Turbulent flow	FT = Water, 70%, 80% & 90% foam (air+water) VP = Yes (PL, BP, HB) ϱ_l = [?] d_s = [?] ϱ_s = [?]	v_l = 0.305-4.88 m/s (foam & water) q_s/ROP = 0-0.0093 m/s	D_{wb} = 0.203 m D_{dp} = 0.114 m ε = 0-1 θ = 70-90^o (from vertical) L = 30.48 m ω = 0 rpm	Ratio of cuttings bed area to annular CSA.	Average annular velocity.	System of ODEs and AEs solved by standard numerical methods.	ModVal? Yes. The model was able to predict experimental measurements of cuttings bed thickness and pressure drop with an error less than 20%. High annular velocities are required when foam is used in order to prevent thick cuttings bed. Increased viscosity of drilling mud causes a thicker cuttings bed compared to less viscous fluids even at lower velocities.
Ozbayoglu et al. (2008)	Empirical cuttings transport correlation based on dimensionless analysis.	_____	_____	FT = Water, Xanthan biopolymer+starch+KCl+soda ash, Xanthan biopolymer+starch+KCL+soda ash+barite VP = Yes (1-12 cP) ϱ_l = 1,000-1,200 kg/m^3 d_s = [?] ϱ_s = [?]	v_l = 0.64-2.2 m/s q_s/ROP = 0.0013-0.0038 m/s	D_{wb} = 0.076 m D_{dp} = 0.038 m ε = 0 θ = 50-90^o (from vertical) L = 3.66 m ω = 0-120 rpm	Cuttings bed area and pressure drop.	Pipe rotation, inclination angle, fluid velocity.	Simple AEs that can be solved by hand.	ModVal? Yes. Pipe rotation improves hole cleaning process, by reducing the cuttings bed area and the critical fluid velocity. For low rotation speeds, the influence of mud viscosity on hole cleaning is significant. As rotation speed increases, this influence decreases. Frictional pressure losses may decrease as pipe rotation increases compared to a no-rotation case in which the reverse happens.

Ozbayoglu et al. (2010)	Empirical cuttings transport correlation based on dimensionless analysis.	Steady state flow.	_____	*FT* = Water *VP* = Yes ϱ_l = 1,000 kg/m^3 d_s = 3 mm ϱ_s = 2,650 kg/m^3	q_l = 0.0025-0.0158 m^3/s q_s/ROP = 0.00085-0.0085 m/s	D_{wb} = 0.102 m D_{dp} = 0.051 m ε = 0 θ = 50-90^o (from vertical) *L* = 4.6 m ω = 0 rpm	Cuttings bed area	Average fluid velocity	Simple AEs that can be solved by hand.	ModVal? Yes. The proposed correlation can estimate the cuttings bed area within an error range of ±15%. 3 reasonably accurate (<= 12.5% error) correlations were proposed for estimating the critical transport velocity. Dimensionless analysis carried out showed that the shear stress acting on the cuttings surface is the main influential parameter of the cuttings bed thickness.
Prasun and Ghalambor (2018)	2-layer steady-state and transient wellbore hydraulics/cuttings transport model; continuity and momentum balance equations for foam and cuttings phase, near-bed velocity model, near-bed wall shear stress model. Wellbore has horizontal, inclined and vertical regions (adapted from Chen, 2007).	Foam is homogeneous compressible stable fluid (no change in rheology), no wall slip, spherical uniform-sized cuttings, diffusion transport due to concentration gradient is neglected, only convective transport considered, no drill pipe rotation, influx water commingles completely with foam and accelerates to new mean foam velocity instantaneously.	Laminar	*FT* = 70-90% foam with HEC solution *VP* = modelled ϱ_l = 995 kg/m^3 d_s = 0.0038 m ϱ_s = 2,277 kg/m^3	q_l = 0.15 kg/s q_g = 6.10-7.62 m/s q_s/ROP = 0.0127 m/s	D_{wb} = 0.230 m D_{dp} = 0.127 m ε = 0-1 θ = 3^o/30.45 m (dog-leg angle) *TVD*= 1,524-3,048 m ω = 0 rpm	Cuttings bed height/cuttings concentration	Measured depth, inclination angle and flow velocity.	Their proposed algorithm divides the wellbore into small segments and solves the governing PDEs, ODEs and AEs in each segment.	ModVal? Yes. A new mechanistic model for predicting the local fluid velocity and near-bed shear stress in an eccentric annular configuration is developed. This model can be used for real-time prediction of cuttings concentration and pressure profile. The Model compares well with experimental data for low-quality foam and low polymer concentrations; discrepancies increase with higher foam quality and polymer concentration. Increased gas & liquid injection, foam quality and lowered backpressure all favour the cuttings transport process. Increased inclination angle yields difficult transport conditions until an angle of repose is reached.
Sample et al. (1978)	Empirical cuttings transport correlation based on friction factor correlations, cuttings slip velocity correlations, (Moore correlation, Chien correlation, Walker and Meyes correlation), cuttings concentration and velocity correlations.	_____	Laminar and Turbulent	*FT* = Water and Biopolymers *VP* = Yes ϱ_l = 1,031-1,797 kg/m^3 d_s = 3.12-10 mm (0.76-1 sphericity; 1.6-3.2 mm thickness) ϱ_s = 2,000-2,500 kg/m^3	v_l = 0-1.27 m/s v_s/ROP = 1.27 m/s	D_{wb} = 0.044-0.3048 m D_{dp} = 0.019-0.102 m ε = [?] θ = 0^o (from vertical) *L* = [?] ω = 0-200 rpm	Cuttings slip velocity.	Annular velocity and mud rheology.	AEs which can be solved by hand or using a computer program.	ModVal? Yes. There exists a linear relationship between cuttings transport ratio and the inverse of annular velocity. At annular velocities < 0.508 m/s, particle slip velocities in both Newtonian and non-Newtonian fluids are independent of annular velocity. The Preston-Moore correlation gave the best estimate of slip velocities compared to other correlations evaluated.

Santana et al. (1998)	2-layer mechanistic cuttings transport model. Mass and momentum balance equations, interfacial shear stress model, static friction force model, cuttings concentration model.	No slip between solid and liquid phases in each layer, pressure drop equalisation in both layers.	Transitional and turbulent flow	FT = [?] VP = Yes (BP, CL, PL, RS, HB) ϱ_l = 1,198 kg/m^3 d_s = [?] ϱ_s = [?]	q_l = 0.0063-0.064 m^3/s q_s/ROP = [?]	D_{wb} = 0.216-0.311 m D_{dp} = 0.127 m ε = >0 θ = 0, 40, 60, 90^o (from vertical) d_s = [?] ω = 0 rpm	Pressure drop and cuttings bed height.	Flowrate, inclination angle, fluid rheological model, hole size.	Numerical solution is done via C++ programming language (ODEs and AEs).	ModVal? No. Major modification to the popular 2-layer model are proposed; these include correlation for interfacial friction factor, implementation of 5 different rheological models and the application of a porous media formulation for fluid flow through cuttings bed. 3 parameter models (HB and RS) showed superior transport performance. The friction factor modification of the new model was highly influential on the cuttings bed height when compared with the Conventional 2-layer model.
Sharma and Chowdhry (1986)	Hydrodynamic 1D isothermal cuttings transport model with air. Mass and momentum conservation equations, frictional pressure drop model, drag model, terminal velocity model, ideal gas equation for air, temperature-dependent viscosity model for air.	Steady state isothermal fully developed flow, no drill pipe rotation, dilute solids concentration (particle-particle or particle-wall interactions), particles reach terminal velocity quickly (no acceleration).	Turbulent	FT = Air VP = standard air viscosity ϱ_l = standard air density d_s = 0.635 mm ϱ_s = 2,650 kg/m^3	q_l = 0.0725-0.115 m^3/s q_s = 0.0436-0.0342 kg/s.	D_{wb} = 0.102 m D_{dp} = 0038 m ε = 0 θ = 0^o (from vertical) L = 4.11 m ω = 0 rpm	Friction factor, pressure drop	Inlet pressure, flow rate.	A step-wise solution of the flow field is carried out using a proposed algorithm in a computer program. (ODEs and AEs).	ModVal? Yes. For reliable and accurate predictions, the model requires accurate input data on inlet temperature, gas mass flow rate and solid mass flow rate. The predictions of pressure distribution for the annular flow of the air-solids mixture was reasonable in comparison with experimental data. The authors attribute discrepancies to the uncertainty and incompleteness of experimental data.
Walton (1995)	Quasi 1D 2-layer mechanistic model. Mass & momentum conservation equations, particle settling velocity and particle diffusivity model, particle suspension model, shear stress models, annular eccentricity and geometric models.	Steady-state flow conditions at a fixed inclination. Cuttings bed is assumed as a non-deformable solid body. Bed depth is assumed uniform, with all variables independent of the axial distance, cuttings concentration at interface equals that of the bed.	Turbulent flow	FT = Water, low-viscosity bentonite Carbopol, High-viscosity bentonite VP = Yes ϱ_l = 998-1,012 kg/m^3 d_s = 6.35 mm ϱ_s = 2,619 kg/m^3	v_l = 0.305-1.16 m/s q_s/ROP = 0.151 kg/s	D_{wb} = 0.127 m D_{dp} = 0.048 m ε = -0.5, 0, +0.5 θ = 0-90^o (from vertical) L = 12.2 m ω = 0, 50, 100 rpm	Cuttings concentration, minimum suspension rate.	Inclination angle.	A standard iterative root-finding scheme is used to solve the system of equations. (ODEs and AEs).	ModVal? Yes. Experimental agreement is good at the lower flow rate and high angles of deviation. At lower angles of deviation, the bed height is overestimated; this could be due to the downward sliding motion of the bed. The generated map shows the type of flow (fully suspended, stationary bed, bed sliding upwards/downward), which are likely to occur and the minimum flowrate for complete suspension as a function of different input parameters. Deep beds tend to be stationary and shallow beds tend to slide upwards or downwards depending on inclination angle. Moderate viscosity fluids are more efficient than low viscosity and high viscosity fluids.

Wang et al. (2009)	2-layer transient mechanistic model for UBD applications; continuity and momentum balance equations, empirical viscosity model, density model (EoS); friction factor and drag coefficient model.	Foam is modelled as a homogeneous non-newtonian Power-law fluid. Uniformly sized perfectly spherical cuttings, with moving cuttings having the same velocity; reservoir flux influx mixes completely with foam and instantaneously accelerates to mainstream velocity; no-slip conditions.	Laminar & Turbulent	FT = 60-90% quality foam (HEC polymer based) VP = modelled ϱ_l = modelled d_s = 0.0127 ϱ_s = 2,400 kg/m^3	q_l = 0.0068 m^3/s q_g = 0.283 m^3/s q_s/ROP = 0.0028 m/s	D_{wb} = 0.2159 m D_{dp} = 0.127 m ε = 1; θ = 90^o (from vertical) L = 450 m ω = 0 rpm	Dimensionless bed height	Foam flow rate, drilling rate, foam quality, eccentricity, cuttings diameter, water and gas influx.	Staggered grid system with SIMPLE algorithm.	ModVal? No. Increasing drill pipe eccentricity, drilling rate and cuttings size increases cuttings bed height; foam quality and flow rate increase, results in decreased cuttings bed height. Gas and water influx from the reservoir positively affect the transport of cuttings.
Wang et al. (2010)	3-layer dynamic cuttings transport model with continuity and momentum equations for all phases in all layers.	Incompressible solid and liquid phases, physical properties of the drilling fluid are continuous (PL fluid model), cuttings concentration in the suspension layer is low and conforms to diffusion law; cuttings concentration in the uniform layer is 55% and that in the dispersed layer is 80% of the uniform layer.	Suspension, rolling and sliding cuttings motion.	FT = [?] VP = Yes (25 mPa.s) ϱ_l = 1,100-1,160 kg/m^3 d_s = 5 mm ϱ_s = 2,600 kg/m^3	q_l = 0.050-0.075 m^3/s q_s/ROP = 0.0028-0.017 m/s	D_{wb} = 0.178-0.34 m D_{dp} = [?] ε = [?] θ = 0-90^o (from vertical) L = 0-8,000 m ω = 0-150 rpm	ECD and cuttings bed height	Fluid flow rate, ROP, and rotation, measured depth.	SETS numerical solution algorithm for PDE's, and AEs.	ModVal? No. Cuttings bed thickness decreases with increasing fluid flowrate and pipe rotation speed; these rates are usually limited to field equipment capabilities and the rock formation conditions.

Xiaofeng et al. (2013a)	Cuttings transport model based on a helical tool used with the drill pipe. Thrust force, frictional force, drag force, centrifugal force, and inertia force equations in vertical and inclined annuli, respectively.	No interaction between particles, spherical cuttings with uniform diameter & without rotation, incompressible steady state flow.	———	FT = [?] VP = [?] ϱ_l = 1,200 kg/m d_s = 0.4 mm ϱ_s = 2,500 kg/m^3	v_l = 1.2-2 m/s v_s/ROP = 1-2 m/s.	D_{wb} = [?] D_{dp} = [?] ε = 0 θ = 60, 70, 80^o (from vertical), helical angle between 20 and 70^o ω = 80-120 rpm	Particle axial and tangential velocity	Helical angle, rotational speed, drilling fluid velocity and inclination angle.	AEs which can be solved using a computer program.	ModVal? No. The use of helical tools enables increased acceleration of the cuttings towards the actual fluid velocity. The helical angle should be put into consideration when designing the drill string. With increased helical angle, cuttings tangential velocity increase but axial velocity decreases. Cuttings are excavated from the bed by the tangential velocity and transported to the surface by the axial velocity. Critical helical angle (45-55^o) should be avoided in the design of helical tools.
Xiaofeng et al. (2013b)	Steady state 2-layer (gas-solid) mechanistic cuttings transport model; mass and momentum balance equations, particle rolling velocity model, geometric descriptors.	52% cuttings concentration in cuttings bed; no drill pipe rotation; no mass transfer; mass and energy balances between wellbore and formation are ignored.	———	FT = Air VP = Yes ϱ_g = 1.2-2 kg/m^3 d_s = >0.965 mm ϱ_s = 2,650 kg/m^3	q_g = 3 kg/m^3 q_s/ROP = 0.002 kg/m^3	D_{wb} = 0.2159 m D_{dp} = 0.127 m ε = 0, 0.5, 1 θ = 60-90^o (from vertical) ω = 0 rpm	Pressure drop and cuttings bed area	Hole inclination, gas viscosity, gas density and eccentricity	A computer program in C# is written to solve the system of ODEs and AEs.	At a constant pipe eccentricity, the cuttings bed area and pressure drop decrease slightly as the inclination angle increases. Cuttings bed area and pressure drop increase with the increase in gas density and gas viscosity.
Zhang et al. (2018)	2-layer steady-state cuttings transport model; mass and momentum conservation equations for vertical, suspension and inclined configurations.	Foam flow is at a stable rate, and no-slip is assumed between gas and liquid phases; Foam is incompressible; uniform particle size and sphericity with even distribution in the flow; no drill pipe rotation is considered.	———	FT = 50-60% quality foam VP = modelled ϱ_l = modelled ω = 0 rpm d_s = 7 mm (0.8 sphericity) ϱ_s = 2,560 kg/m^3	q_{mix} = 0.073 m^3/s q_s/ROP = 0.0021 m/s	D_{wb} = 0.2159 m D_{dp} = 0.127 m ε = 0.6; θ = 0-90^o (from vertical) L = 1,208 m TVD ω = 0 rpm	Dimensionle-ss bed thickness	Well angle, foam quality, flow rate, eccentricity and well depth.	ODEs and AEs which can be solved by standard numerical methods using a computer program.	ModVal? No. With an increase in annular flow velocity, cuttings concentration is first reduced at a fast rate, after which it remains constant. Reduced eccentricity enhances favourable transport. When the critical foam velocity is reached, it is appropriate to reduce foam quality in order to save drilling costs. Cuttings concentration rises rapidly between inclinations of 30 and 60^o.

Zhou (2008)	2 phase hydraulic equations, turbulent boundary layer theory, particle transport mechanistic models (drag, lift buoyancy and gravity) with UBD conditions.	Steady-state isothermal flow in the concentric annulus; gas phase is free of cuttings; uniform-sized spherical particles, no drill pipe rotation and cuttings bed is uniform along the annulus.	Turbulent, slug and bubble flow	FT = Air+water+mud VP = Yes ϱ_l = 600-1,200 kg/m^3 d_s = 0.5-6 mm ϱ_s = 2,000-3,000 kg/m^3	q_l = 0.025 m^3/s GLR = 0-0.85 q_s/ROP = [?]	D_{wb} = 0.146-0.203 m D_{dp} = 0.089-0.114 m ε = 0; θ = 0-90^o (from vertical) ω = 0 rpm	Critical mud velocity	Hole angle, particle size, mud density, cuttings density, GLR, mud rheology and superficial gas velocity.	System of ODEs and AEs solved by standard numerical methods.	ModVal? Yes. Cuttings accumulation in the annulus is very sensitive to the liquid flow rate. Increased GLR enhances cuttings transport. Increased inclination angle (from vertical) results in an increased mud transport velocity. Smaller cuttings are easier to transport compared to larger cuttings, however, sizes <= 0.5 mm impose additional cleaning difficulty. Increased gas injection rate, reduces the minimum liquid transport velocity.

EXPERIMENTAL CONTRIBUTIONS (DRILLING)

AE-Algebraic Equations; **BC**-Boundary Conditions; **DEM**-Discrete Element Method; **DDPM-**Dense Discrete Phase Model; **DPM-** Discrete Phase Model; **EE**-Eulerian-Eulerian; **FEM-**Finite Element Method; **FVM**-Finite Volume Method; **FT**-Fluid Type; **HX**-Hexahedral; **KTGF**-Kinetic Theory of Granular Flow; **LE**-Lagrangian Eulerian; **MID**-Mesh Independence Study Performed?; **ModVal**-Model Validation Performed?; **ODE**-Ordinary Differential Equations; **OS**-Operating System; **PDE**-Partial Differential Equations; **QUICK**-Quadratic Upstream Interpolation for Convective Kinematics; **ROP**-Rate of Penetration; **SIMPLE**-Semi-Implicit Method for Pressure Linked Equations; **SS**-Steady State; **TH**-Tetrahedral; **TS**-Transient State; **VP**-Is Viscosity Data Provided?; D_{wb} = Wellbore diameter; D_{dp} = Drill pipe diameter; ε = Drill pipe eccentricity; θ = Angle of inclination; L = Computational length; ω = Drill pipe rotation; [?] = Unknown/unreported parameter.

Table C.3. Summary of experimental research contributions for wellbore cleaning operations.

Reference	Flow loop components	Flow Conditions	System Properties			Drilling Parameter Variation and Key Findings		
			Fluid & Solid Properties	Velocities & Flowrates	Wellbore Geometry	Efficiency Metric	Varied Parameters	Findings
Adari et al. (2000)	Compressors, mud and air tanks, cuttings hopper, injection auger, shale shaker, drill pipe motor, pumps, valves and other measuring devices.	Laminar and turbulent	*FT* = Polymeric solutions, Poly-Anionic Cellulose (PAC) of different compositions and CMC+XCD based drilling fluid system *VP* = Yes (PL parameters) ρ_f = [?] d_s = 3.2 mm ρ_s = 2,560 kg/m^3	q_f = 0.0095-0.025 m^3/s q_s/ROP = 0.00339 m/s	D_{wb} = 0.203 m D_{dp} = 0.114 m ε = 1 θ = 87-90^o (from vertical) L = 24.4 m ω = 0 rpm	Cuttings bed height	Mud flow rate and circulation time.	It was discovered that cuttings removal was easier with turbulent, than with laminar flow. Increasing the inclination angle results in an increased circulation time for adequate cuttings removal.
Allahvirdizadeh et al. (2016)	Liquid tank, cuttings injection tank, shale shaker, separator, auger, annulus, pump, compressor, camera, and measuring devices/instrumentation	Laminar and Turbulent	*FT* = Water and partially-hydrolysed polyacrylamide (PHPA) polymer solutions *VP* = Yes ρ_f = [?] d_s = 2.75 mm (industrial sand) ρ_s = [?]	q_f = 0.15-0.75 m/s (0.0016-0.0096 m^3/s) q_s/ROP = 0.0047-0.0097 m/s	D_{wb} = 0.074 m D_{dp} = 0.047 m ε = 0 θ = 90^o (from vertical) L = 6.5 m ω = [?]	Pressure drop, cuttings area and drag reduction	ROP, polymer concentration and fluid velocity.	Drag reduction increases with increasing fluid flowrate up until a critical flow rate, after which drag reduction reduces. Optimal polymer concentration was found to be 0.07 wt. % PHPA (38 % reduction in pressure drop), thus indicating that, increasing fluid viscosity does not necessarily guarantee an improvement in cuttings transport at high flowrates.
Altindal et al. (2017)	Horizontal test section, data acquisition, centrifugal pump, valves, hydrocyclone, vertical test section, filter, mixing tank.	Unsteady flow with temperatures from 70-110^{o}F	*FT* = Water based mud, Oil based mud and Synthetic based mud *VP* = Yes ρ_f = 1,007, 1,138, 1,258 kg/m^3 d_s = 4-7 mm; 4-22 mm 3-13 mm ρ_s = 2,600, 2,820, 8,500 kg/m^3	q_f = 0-0.00063 m^3/s q_s/ROP = [?]	D_{wb} = 0.051 m D_{dp} = 0.044 m ε = 0 θ = 90^o (from vertical) L = 3.66 m ω = 0 rpm	Cuttings settling velocity, viscoelastic and time-dependent response of drilling fluid.	Cuttings diameter and flow time	Based on experiments performed, a mathematical model that considers the viscoelastic and time-dependency of drilling fluids was developed to estimate cuttings settling velocity. Good agreement with experimental data was established.
Bizhani et al. (2016)	High-resolution camera, magnetic flow meter, valves, annular test section, differential pressure transducer.	Turbulent flow	*FT* = Water, 0.032, 0.064, and 0.112 wt.% polymer solutions *VP* = Yes ρ_f = [?] d_s = 260-1,240 μm (sub-angular shaped natural Quartz sand) ρ_s = 2,650 kg/m^3	q_f = 0-0.0075 m^3/s q_s/ROP = [?]	D_{wb} = 0.095 m D_{dp} = 0.038 m ε = 0 θ = 90^o (from vertical) L = 9 m ω = 0 rpm	Dimensionless shear velocity, critical velocity, dimensionless shear stress.	Cuttings size and fluid rheology.	It was discovered that water always triggered cuttings movement at lower flowrates compared to the polymer solutions. As fluid viscosity increased, it became more difficult to start cuttings movement. Intermediate sized cuttings were easier to remove than smaller or larger sized cuttings. The impact of cuttings size on critical flow conditions was less than the impact of fluid rheological parameters.

Brown et al. (1989)	Wellbore simulator/annulus, refrigeration system, cuttings circulation pump, mud circulation pump, vibrating screen separator, mud and cuttings tanks and other instrumentation.	Steady flow conditions (laminar and turbulent)	*FT* = Water + 3ppb HEC *VP* = Yes ϱ_l = [?] d_s = 6.4-12.7 mm ϱ_s = 2,680 kg/m^3	q_l = 0.005-0.025 m^3/s (superficial velocity of 1.27 m/s) q_g = [?] q_s/ROP = 0.0315 m^3/s injection rate.	D_{wb} = 0.2032 m D_{dp} = 0.127 m ε = 0-1 θ = 0-90^o (from vertical) L = 15.24 m ω = 0-200 rpm	Minimum transport velocity, cleaning rate	Hole angle	Hole angles in the range of 50-60^o are the most difficult to clean. They demonstrated the applicability of the Gavignet and Sobey model; the model over predicts the cleaning rate when water is used as the cleaning fluid and under predicts the performance of the polymer-based drilling fluid. Hole cleaning is most efficient when water (under turbulent conditions) is used.
Capo et al. (2004)	Cuttings injection tank, annular section, Cuttings collection tank, Surfactant and foam breaker pumps, compressor, mud tank, static mixer and shale shaker.	——	*FT* = 70% quality, 80% quality and volume equalised foams (air + anionic surfactant, Bachman Chemical FF-4,000 @ 1%v/v) *VP* = Yes (PL parameters) ϱ_l = [?] d_s = [?] ϱ_s = [?]	q_l = 0.91-1.52 m/s q_s/ROP = 0.00127-0.00423 m/s.	D_{wb} = 0.203 m D_{dp} = 0.114 m ε = 0 θ = 45^o, 55^o, 65^o (from vertical) L = 27.43 m ω = 140 rpm	In situ cuttings concentration	Foam velocity, inclination angle and foam quality	Foams of low quality perform better in transporting cuttings than higher quality foams. Increasing ROP from 20 to 44 ft/hr resulted in a 7% increase in cuttings concentration under similar conditions. The proposed correlation had an error range of ±17% when compared with experimental measurements.
Chen et al. (2007)	Air compressors, static mixer, separation tower, breaker and metering pumps, mud tanks, cooler and heater, cuttings injection and loading auger, annular section, valves and other measuring devices.	Steady state laminar flow (temperatures from 27^{o}C-77^{o}C; pressures from 0.69- 2.76 MPa)	*FT* = Foam system comprising of 1% v/v surfactant and hydroxylethycellulose polymer (HEC); 70% to 90% quality foam *VP* = [?] ϱ_l = 994.5 kg/m^3 d_s = 3 mm ϱ_s = 2,600 kg/m^3	q_l = 0.61-1.83 m/s q_s/ROP = 0.0042-0.0056 m/s (cuttings injection rate of 0.11-0.15 kg/s).	D_{wb} = 0.146 m D_{dp} = 0.089 m ε = 0 θ = 90^o (from vertical) L = 22.2 m ω = 250 rpm (max)	Cuttings concentration and annular pressure drop	HEC polymer concentration, foam flow velocity, foam quality, temperature and pressure	Increased annular flow velocity decreases cuttings concentration once the critical flow velocity is reached/exceeded. Increasing temperature slightly increases cuttings concentration, whereas increasing pressure slightly reduces cuttings concentration. The addition of viscosifiers (HEC polymer) decreases cuttings concentration and increases frictional pressure loss.
Corredor et al. (2014)	Camera, centrifugal pump, glass annulus, mixing tank, valves, flowmeters, pressure gauge and transducers.	Turbulent; with dunes/saltation, stationary bed, rolling and suspension flow patterns	*FT* = Water, 0.07% & 0.1% PHPA (v/v); rheological properties provided *VP* = Yes ϱ_l = 1,250-1,400 kg/m^3 d_s = 350-1,214 µm ϱ_s = 2,650 kg/m^3	q_l = 0.25-1.3 m/s q_s/ROP = [?]	D_{wb} = 0.095 m D_{dp} = 0.038 m ε = 0 θ = 90^o (from vertical) L = 9 m ω = 30 rpm	Pressure drop, physical flow visualisation	Bulk velocity, particle diameter, fluid rheology	Critical initiation velocities for water were found to be lower with water than that of the drag reducing fluid in all transport modes encountered. As the polymer concentration (and, hence, the viscosity) of the drag reducing fluid increases, a higher critical velocity is required for the initiation of particle movements.
Duan et al. (2006)	Mud tank, cuttings injection and collection tank, shale shaker, annular test section, pumps, valves and control devices.	Steady state flow conditions	*FT* = Water and 0.00071 g/cm^3 Polyanionic Cellulose (PAC) solution *VP* = Yes (PL parameters) ϱ_l = [?] d_s = 0.45-3 mm ϱ_s = [?]	q_l = 0.013, 0.0189, 0.025 m^3/s q_s/ROP = 0.00254 m/s	D_{wb} = 0.203 m D_{dp} = 0.114 m ε = 0.8 θ = 70^o, 90^o (from vertical) L = 30.48 m ω = 0, 80 rpm	Cuttings volume concentration	Circulation flow rate and drill pipe rotation	Compared to larger cuttings, smaller cuttings are more difficult to transport in a horizontal annulus when water is used. The proposed correlation is able to predict experimental results within a 10% error range. Effects of inclination angle are minimal between angles of 70 and 90^o from the vertical.

Duan et al. (2010)	Air compressors, static mixer, separation tower, breaker and metering pumps, mud tanks, cooler and heater, cuttings injection tower, annular section, valves and other measuring devices.	Steady state laminar flow (temperatures from 80°C-160°C; pressures from 100 psig to 400 psig)	*FT* = 60%-90% quality foam (water + air + 1% surfactant concentration) *VP* = Yes ρ_l = [?] d_s = 3 mm ρ_s = [?]	q_l = 0.61-1.52 m/s q_g = [?] q_s/ROP = 0.19-0.26 kg/s cuttings injection rate	D_{wb} = 0.146 m D_{dp} = 0.089 m ε = 0.78 θ = 0°-42° (from horizontal) L = 22.2 m ω = 120 rpm	Cuttings concentration and annular pressure drop	Pipe rotation, circulation velocity, test pressure and temperature and foam quality	In foam drilling, pipe rotation is a major factor that helps decrease the cuttings concentration and frictional pressure loss. At constant foam quality, cuttings concentration slightly decreases with pressure and increases with temperature. Hole cleaning improvement by increasing foam velocity is limited to low to medium quality foams. The developed empirical model predicts experimental results with less than 15% error.
Effiong (2013)	Mud tank, main test section, cuttings feeder, circulation ports and measuring devices	Steady flow conditions	*FT* = HEC + water (HEC concentration from 0-2g) *VP* = Yes ρ_l = [?] ω = 3-600 rpm d_s = 2 mm ρ_s = 2,400 kg/m³	q_l = 0.00022-0.00085 m³/s q_s/ROP = Flow frequencies between 7 & 30 Hz.	D_{wb} = 0.06 m D_{dp} = 0.0545 m; ε = 0 θ = 10° (from horizontal) L = 6 m ω = 3-600 rpm	Bed height	Mud flowrate	It was discovered that the performance of water as a transport fluid could be enhanced by the addition of viscosifiers. Careful consideration of the viscosity effects on pump performance should be made when designing drilling muds.
Ford et al. (1990)	Cuttings transport column, blending tank, centrifugal pumps, flowmeters, valves, video camera and pressure transducers.	Laminar and Turbulent	*FT* = Water + CMC/XC polymers *VP* = Yes (HB parameters) ρ_l = [?] d_s = 1.7-2 mm & 2.8-3.35 mm (Graded silica sand) ρ_s = [?]	q_l = 0.0-2.13 m/s q_s/ROP = [?]	D_{wb} = [?] D_{dp} = 0.0635 m & 0.0762 m ε = 0-0.7 θ = 0-90° (from vertical) L = 6.7 m ω = 0, 60, 120 rpm	Minimum Transport Velocity	Annular inclination angle drill pipe rotary speeds, drilling mud viscosities, and cuttings sizes	The effectiveness of a drilling fluid significantly depends on the flow regime (laminar or turbulent) and not only its rheological characteristics. Pipe rotation has negligible effects on MTV when water is the circulating fluid. Drill pipe rotation has a more pronounced effect when the circulating fluid is more viscous than water.
Garcia-Hernandez et al. (2007)	Cuttings injection tank, mud tank, pumps, moving cameras, annular section, flow measuring devices.	Steady state flow conditions	*FT* = Water and 0.00071 g/cm³ Polyanionic Cellulose (PAC) solution *VP* = Yes (PL parameters) ρ_l = [?] d_s = 0.45-3 mm ρ_s = [?]	q_l = 0.013, 0.0189, 0.025 m³/s q_s/ROP = 0.00254 m/s	D_{wb} = 0.203 m D_{dp} = 0.114 m ε = 0.8 θ = 70°, 90° (from vertical) L = 30.48 m ω = 0 & 40 rpm	Cuttings moving layer velocity and cuttings bed height	Liquid velocity, fluid rheology, drill pipe rotation	It is observed that drill pipe rotation results in a 48% reduction in cuttings concentration and a velocity increase of 18%. In all cases, cuttings slip velocity is > 38%. Rolling, saltation and suspension are main mechanisms of cuttings transport.
Gul et al. (2017)	Gas compressor, air dryer, mud pump, liquid tank, liquid and gas flowmeters, differential pressure gauges and load cells, main test section.	Bubble, elongated bubble, slug and wavy annular	*FT* = Air-water mixture, air-drag reducing polymer fluid mixture (polymer + water), Partially hydrolysed polyacrylamide (PHPA) 0.05-0.10% *VP* = Yes ρ_l = 833 kg/m³ d_s = 2.75 mm (industrial sand, 0.6-4.6 mm) ρ_s = 2,756 kg/m³	q_l = 1.52-2.44 m/s q_s/ROP = 0.0097 m/s.	D_{wb} = 0.074 m D_{dp} = 0.047 m ε = 0 θ = 90° (vertical) L = 6.4 m ω = [?]	Cuttings bed area	Superficial liquid velocity	Wavy annular is the flow most effective for cuttings transport. 0.007% PHPA polymer fluid resulted in reductions of 24% drag + 4% cuttings area

Hakim et al. (2018)	Mud pump, mud tank, shale shaker, polymer separator, main annular test section, flowrate and pressure meters.	———	*FT* = Basic water-based mud (WBM), 15.0 g of bentonite, 85.3 g of barite, 0.25 g of soda ash and 1 g of starch into 350 ml of distilled water (continuous phase). 1-5% of polyethylene and polypropylene beads are added for performance enhancement; *VP* = Yes ϱ_l = [?] d_s = six irregular-shaped sand size distributions (0.5-4 mm) ϱ_s = 2,560 kg/m^3	q_l = 0.69 m/s q_s/ROP = [?]	D_{wb} = 0.051 m D_{dp} = 0.020 m ε = 0 θ = 90^o (vertical) L = 3.96 m ω = [?]	Cuttings transport ratio, cuttings transport efficiency (CTE).	Polymer bead concentration and cuttings sizes.	Increased polymer bead concentration resulted in an increased CTE. Propylene-based drilling mud had better performance compared to polyethylene. Larger cuttings have a lower transport efficiency.
Han et al. (2010)	Annulus, surge tank, heating/cooling tank, pump, flowmeter, pressure tab.	Steady state laminar and turbulent flow	*FT* = 0.4% CMC solution & 5% bentonite solution *VP* = Yes ϱ_l = 998.5-1,041.1 kg/m^3 d_s = 0.001 m ϱ_s = 2,550 kg/m^3	q_l = 0.32-0.66 m/s q_s/ROP = 0.0204 kg/s.	D_{wb} = 0.044 m D_{dp} = 0.03 m ε = 0 θ = 0-60^o (from vertical) L = 1.8 m ω = 0-600rpm	Pressure drop and cuttings volume fraction.	Inclination angle, drill pipe rotation and flow rate.	It was observed that drill pipe rotation generally improves cuttings transport; this improvement is more pronounced at lower circulation velocities and weakened at higher velocities. Pressure drop increases with flow rate, rotation and inclination from the vertical. Axial pressure drop reduces with increase in eccentricity.
Hemphill and Larsen (1996)	Mud tank, cuttings injection auger system, annulus, and instrumentation devices.	Laminar	*FT* = Oil-based mud-OBM and water-based mud-WBM *VP* = Yes ϱ_l = [?] d_s = 6.35-0.127 mm ϱ_s = [?]	q_l = 0.71-1.40 m/s q_s/ROP = 0.0045-0.047 m/s.	D_{wb} = 0.127 m D_{dp} = 0.06 m ε = 0.62 θ = 0-90^o (from vertical) L = 10.67 m ω = 50 rpm	Annular accumulation and critical flowrate.	Average annular velocity and hole angle.	Cuttings bed instability is mostly pronounced at intermediate angles, and this occurs more in OBMs than in WBM. The model of Larsen et al. (1997) is able to predict critical flowrates of OBM with good accuracy.
Kamyab and Rasouli et al. (2016)	Slurry tank, slurry pump, rinse tank, annular test section, pressure transducer, valves, magnetic flow meters and data acquisition system.	Laminar, Transition, Turbulent	*FT* = Water, water + 0.1% w/w polymer, water + 0.1% w/w polymer + 0.1% w/w Xanthan gum *VP* = Yes ϱ_l = [?] d_s = 0.425-4.7 mm ϱ_s = 2,800 kg/m^3	q_{slurry} = 0.07-1.05 m/s q_s/ROP = [?]	D_{wb} = 0.08, 0.07 m D_{dp} = 0.051, 0.038 m ε = 0 θ = 15-90^o (from horizontal) L = 4 m ω = 0 rpm	Minimum Transport Velocity (MTV)	Hole inclination, particle size and fluid rheology	Angles between 30^o and 60^o were deemed the most difficult to clean. Higher viscosity non-Newtonian drilling fluids perform better compared to lower viscosity muds. When water is used as the drilling fluid, the MTV for the different particle sizes are similar.
Kelessidis and Bandelis (2003)	Annulus section, tanks, agitator, pump, data acquisition, and measuring section.	Laminar and turbulent	*FT* = CMC water solutions *VP* = Yes ϱ_l = 998.2-1,048.5 kg/m^3 d_s = 1-4 mm ϱ_s = 2,396 kg/m^3	q_l = 0.305-1.52 m/s q_s/ROP = [?]	D_{wb} = 0.07 m D_{dp} = 0.04 m ε = 0.43 θ = 90^o (from vertical) L = [?] ω = [?]	Visual observation of cuttings deposition pattern.	———	The most significant parameter affecting cuttings transport is the mixture velocity. Eccentricity also plays a significant role. From the modelling review carried out, rheology does not significantly affect cuttings transport; this contradicts previous experimental and field results.

Kim et al. (2014)	Annulus, motor speed controller, tachometer, surge tank, pump, thermometer, electronic scale, sampling tank, valves, pumps, and data acquisition system.	Turbulent flow	FT = Water VP = Yes ρ_f = 1,000 kg/m^3 d_s = 2 mm ρ_s = 2381 kg/m^3	q_f = 23-68 L/min q_s/ROP = 0.0004, 0.00055, 0.00083, 0.00113 m^3/s (at 4, 8, 12 and 16 % sand concentrations).	D_{wb} = 0.044 m D_{dp} = 0.030 m ε = 0 θ = 0-75^o (from vertical) L = 1.7 m ω = 0-400 rpm	Pressure loss, visual observation, particle transport ratio, cuttings volume fraction.	Sand concentration, inclination angle, rotational speed and flow rate.	Correlations developed here were used to predict the cuttings volume fraction, with good accuracy (within 5% of the experimental results). Due to slip phenomenon in the inclined annulus, it is difficult to verify the exact transfer performance only with the particle transport ratio. Pipe rotation obstructed the formation of particle precipitate inside the annulus. With an increasing slope of the annulus, the transport performance of the drilling fluid reduced rapidly.
Larsen et al. (1997)	Mud tank, cuttings injection auger system, annulus, and instrumentation devices.	Steady state flow conditions	FT = Water and 5 other polymer-based muds VP = Yes ρ_f = [?] d_s = 2.2, 4.4, & 7 mm (with bed porosities of 39%, 36% and 41%) ρ_s = [?]	q_f = 0.0069-0.0095 m^3/s q_s/ROP = 0.0023, 0.0046 & 0.0069 m/s.	D_{wb} = 0.127 m D_{dp} = 0.060 m ε = ±0.62 θ = 55-90^o (from vertical) L = 10.67 m ω = 50 rpm	Cuttings velocity and cuttings concentration.	ROP, mud weight, cuttings size and inclination angle.	Based on experiments conducted, empirical correlations that reasonably predict the Critical Transport Fluid Velocity (CTFV) and the cuttings concentration are proposed.
Li and Walker (2001)	Test section, air compressor, disposal tank, separator, pressure transducers, several flow meters, valves and instrumentation systems.	_____	FT = Water, gas-liquid (air-water) mixture with different gas-liquid ratios VP = Yes ρ_f = [?] d_s = 0.762 mm ρ_s = 2,710 kg/m^3	q_f = 0.1-0.8 m^3/min q_s/ROP = 0.0028-0.011 m/s.	D_{wb} = 0.127 m D_{dp} = 0.0603 m ε = ±1 θ = 15-90^o (from vertical) L = 6.1 m ω = 0 rpm	Bed height, hole cleaning time, carrying capacity, in-situ liquid velocity.	Inclination angle, circulation fluid flow rate and gas volume fraction.	It was discovered that the variation of the liquid flowrate rate had a stronger impact on cuttings transport than the gas flowrate when gasified fluids are used. Hole cleaning time decreases nonlinearly with the increase in circulating fluid flowrate. Experimental results obtained aided the development of a computer program for the prediction of bed height; optimisation can thus be carried out.
Li et al. (2002)	Test section, air compressor, disposal tank, separator, pressure transducers, several flow meters, valves and instrumentation systems.	Laminar and Turbulent	FT = Water, HEC and Xanvis polymers VP = Yes ρ_f = [?] d_s = 0.15-7 mm ρ_s = 2,600-2,710 kg/m^3	q_f = 0.127-1.02 m/s q_s/ROP = [?]	D_{wb} = 0.127 m D_{dp} = 0.0603 m ε = 1 θ = 0-110^o (from vertical) L = 6.1 m ω = 0 rpm	Critical velocity, CTR, Effective time, Number of Hole volumes.	In situ liquid velocity and gas volume fractions.	For a fully-horizontal/near-horizontal wellbore, hole cleaning is more efficient if a low-viscosity fluid is pumped in a turbulent flow regime rather than a high viscosity fluid in a laminar regime. Fine particles are the easiest to clean and the 0.76 mm particles are the most difficult to clean. The derivation of a model for predicting cleaning stoppage time is important research area needing more investigation.

Naganawa, et al. (2002)	Cuttings reservoir, cuttings hopper, air compressor, shale shaker, mud pump, 3CCD camera system, annular test section, and measuring devices.	Steady state flow conditions	FT = Water and 0.15 % PHPA VP = Yes (HB parameters) ϱ_l = [?] d_s = 3.636 mm ϱ_s = 2,400 kg/m^3	q_l = 15-70 m^3/hr q_g = 7.5-35 m^3/hr q_s/ROP = 0.0028 m/s (0.000036 m/s injection rate)	D_{wb} = 0.127 m D_{dp} = 0.0524 m ε = 0, 0.8 θ = 30^o, 45^o, 60^o, 75^o, 90^o (from horizontal) L = 9 m ω = [?]	Cuttings volume concentration and Critical Flow Rate (CFR).	Liquid flow rate	Gas-liquid flow pattern (bubbly, slug/churn, stratified-wavy flow) is a major determinant of the cuttings flow behaviour. Stationary cuttings bed occurred at 60^o; this could disappear with high air injection rates. CFR for aerated fluid (water) was lower than that for the base polymer fluid at low-angle and horizontal configurations. The reverse was the case at high inclinations.
Okrajni et al. (1986)	Fluid tank, cuttings hopper, settling chamber, annular test section, support beam, particle collection baskets flow meters and other instrumentation.	Laminar and Turbulent	FT = Water and bentonite/polymer muds VP = Yes ϱ_l = [?] d_s = 6.35 mm ϱ_s = 2,619 kg/m^3	q_l=0.0063-0.013 m^3/s q_s/ROP = 0.152 kg/s	D_{wb} = 0.127 m D_{dp} = 0.048 m ε = -0.5, 0, +0.5 θ = 0-90^o (from vertical) L = 12.2 m ω = 0-150 rpm	Annular cuttings concentration and cleaning rate.	Mud rheology, inclination angle, average fluid velocity, drill pipe rotation and eccentricity.	Under turbulent flow conditions, cuttings transport is not affected by the mud rheological properties. In laminar flow, higher mud yield value provides better transport of cuttings. This effect is negligible at high inclination angles. Worst transport conditions occur at inclination angles between 40-45^o. Increased rotary speed enhances cuttings transport. Regions (0-45^o), (45-55^o) and (55-90^o) are the three separate regions observed during transport. Eccentricity effects are small at low angle wells. Laminar flow predominantly affects cuttings transport at low-angle wells; whereas, turbulent flow is predominant at high angle wells; both flow regimes have similar effects at intermediate angles.
Osgouei (2010)	Drill pipe rotation system, annular test section, cuttings injection system, solid-liquid separation and collection system, high-speed digital cameras, pumps, valves, differential pressure transducers, flow meters.	Laminar and Turbulent	FT = Water and air VP = Yes ϱ_l = 1,000 kg/m^3, 1,225 kg/m^3 d_s = 2 mm ϱ_s = 2,761.4 kg/m^3	q_l = 0.0013-0.0076 m^3/s (0.305-3.05 m/s velocity) q_s/ROP = 0.0051-0.010 m/s	D_{wb} = 0.074 m D_{dp} = 0.046 m ε = 0.623 θ = 0-90^o (from vertical) L = [?] ω = 0-120 rpm	Cuttings bed thickness, pressure drop, and visual/digital observation.	ROP, inclination, fluid circulation velocity. Gas-liquid, Solid-liquid and Gas-liquid-solid flows were studied.	It was discovered that increasing the ROP increases the cuttings concentration and the frictional pressure losses. Increasing the fluid flowrate enhances cuttings travel velocity. The mechanistic model developed aids the calculation of minimum gas superficial velocity for a constant liquid flow rate in order to ensure continuous cuttings removal. The impact of drill pipe rotation on cuttings removal is minimal in 3-phase flows, due to constant gas and liquid flow.
Ozbayoglu et al. (2003)	Annular test section, rotating auger system, tanks and measuring devices.	Laminar and turbulent	FT = Water and 70%-90% foam VP = Yes ϱ_l = [?] d_s = [?] ϱ_s = [?]	q_l = 0.305-5.49 m/s q_s/ROP = 0.00085-0.0076 m/s	D_{wb} = 8 in D_{dp} = 4.5 in ε = 0 θ = 70-90^o (from vertical) L = 30.48 m ω = [?]	Cuttings bed area to wellbore area ratio, pressure gradient.	Mud velocity, ROP, inclination, fluid rheology.	An extensive comparison between the results of their proposed model and experimental measurements was presented. Predictions of cuttings bed thickness and pressure drop are within 15% error when water is used and 25% when foam is used.

Ozbayoglu et al. (2005)	Annular test section, rotating auger system, tanks and measuring devices	Laminar and turbulent	*FT* =Water and 70%-90% foam *VP* = Yes ρ_l = [?] d_s = [?] ρ_s = [?]	q_l = 0.305-4.88 m/s q_s/ROP = 0.00254-0.0093 m/s	D_{wb} = 0.203 m D_{dp} = 0.114 m ε = 0 θ = 70-90° (from vertical) *L* = 30.48 m ω = [?]	Cuttings bed area to wellbore area ratio, pressure gradient	Annular velocity	Experimental results are compared with the developed model predictions of the area ratio and pressure drop. Cuttings bed thickness and pressure gradient for the water and foam systems were predicted with an error of less than 20%. When the viscosity of the drilling fluid is too high, cuttings bed formation could increase compared to when a less viscous fluid is used.
Ozbayoglu et al. (2010)	Drill pipe rotation system, annular test section, cuttings injection system, solid-liquid separation and collection system, pumps, valves differential pressure transducers, flow meters.	———	*FT* = [?] *VP* = No ρ_l = [?] d_s = 3 mm ρ_s = 2,610 kg/m^3	q_l= 0.0025-0.016 m^3/s q_s/ROP = 0.00085-0.0085m/s	D_{wb} = 0.102 m D_{dp} = 0.051 m ε = 0 θ = 50-90° (from vertical) *L* = 4.57 m ω = [?]	Cuttings bed area to wellbore area ratio	Fluid velocity, hole inclination	Based on generated experimental results, empirical correlations (with error range of ±15%) are proposed for estimating the critical fluid velocity (necessary for preventing stationary bed development). Dimensional analyses performed also showed that the shear stress acting on the cuttings bed surface is the most influential parameter on the cuttings bed thickness.
Peden et al. (1990)	Cuttings transport column, blending tank, centrifugal pumps, flowmeters, valves, video camera and pressure transducers.	Laminar and Turbulent	*FT* = Water + CMC/XC polymers *VP* = Yes (HB parameters) ρ_l = [?] d_s = 1.7-2 mm & 2.8-3.35 mm (Graded silica sand) ρ_s = [?]	q_l= [?] q_s/ROP = [?]	D_{wb} = [?] D_{dp} = 0.0635 m & 0.0762 m ε = 0-0.7 θ = 0-90° (from vertical) *L* = 6.7 m ω = 0, 60, 120 rpm	Minimum Transport Velocity (MTV)	Annular inclination angle, drill pipe rotary speeds, pipe eccentricities, annular clearances, drilling mud viscosities, and cuttings sizes.	A model for predicting MTV is proposed and shown to match experiments. The most difficult transport conditions occurred at inclination angles between 40° and 60°. MTV is dependent on critical fluid viscosity and passes through a maximum value with increasing viscosity.
Sanchez et al. (1997)	Mud tank, collection hopper, annular section, shaker, injection hopper, flow meters and other measuring devices.	Steady state flow conditions	*FT* = 2 Bentonite muds and 3 polymer muds *VP* = No ρ_l = [?] d_s = 6.35 mm, 2.5 mm (crushed limestone and river gravel) ρ_s = 2,560 kg/m^3 & 2,640 kg/m^3	q_g = [?] q_s/ROP = cuttings injection rate of 0.00296 m/s.	D_{wb} = 0.2032 m D_{dp} = 0.1143 m ε = 0 θ = 40°, 65°, 80°, 90° (from vertical) *L* = 30.48 m ω = 0-175 rpm	Cuttings weight in the annulus	Rotary speed, flow rate and annular inclination	The authors outlined that smaller cuttings are more difficult to transport; this mitigated by an increase in rotary speed and mud viscosity. In inclined wells, low-viscosity muds clean better than high viscosity muds. The impact of drill pipe rotation is very significant at low flowrates under horizontal transport conditions.
Sayindla et al. (2017)	Annular test section, dry sand feeder, tank-mixer system, flow density meter, pumps and other instrumentation.	———	*FT* = Oil based mud (OBM) and water based mud (WBM) *VP* = Yes (HB parameters) ρ_l = [?] d_s = [?] ρ_s = 2,650 kg/m^3 (sand particles)	q_l= 0.5-1.2 m/s q_s/ROP = 0.0022 m/s (0.043 kg/s sand injection rate).	D_{wb} = 0.1 m D_{dp} = 0.050 m ε = 0 θ = 90° (from vertical) *L* = 10 m ω = 0-150 rpm	Pressure gradient, sand hold up	Liquid velocity and pipe rotation	Higher pressure drop was observed for the WBM compared to the OBM. Pressure drop increases with drill string rotation. In the absence of rotation, OBM performs better than WBM; when the drill string is rotated, the performance of both fluids is similar.

Song et al. (2017)	Fluid tank, solid-liquid separator, cuttings injection tank, annulus, pumps and valves.	Turbulent flow	FT = Water VP = Yes ϱ_l = 1,000 kg/m^3 d_s = 0.003-0.005 m ϱ_s = 2,650 kg/m^3	q_l = 0.00058-0.00078 m^3/s q_s/ROP = 0.00211-0.00636 m/s.	D_{wb} = 0.04-0.08 m D_{dp} = 0.0254 m ε = 0-0.8 θ = 90^o (from vertical) L = 6 m ω = 0 rpm	Cuttings concentration/bed height	Hole eccentricity, cuttings diameter, ROP, and drill pipe/wellbore diameter ratio.	A model for estimating the cuttings volumetric concentration and the cuttings bed height was developed via dimensional analysis. Predictions were good in comparison to experiments. High flow rates, low ROP, low eccentricity, and smaller drill pipe/wellbore ratio induce better cleaning efficiency in microhole horizontal wells.
Sorgun et al. (2011)	Drill pipe rotation system, annular test section, cuttings injection system, solid-liquid separation and collection system, pumps, valves differential pressure transducers, flow meters.	———	FT = Water and 4 different mud types VP = Yes ϱ_l = [?] d_s = [?] ϱ_s = [?]	q_l = 0.0017-0.0076 m^3/s q_s/ROP = 0.0013-0.0038 m/s	D_{wb} = 0.074 m D_{dp} = 0.046 m ε = 1 θ = 90^o (from vertical) L = 3.66 m ω = 0-120 rpm	Cuttings bed thickness and pressure drop.	Fluid rheology, circulation velocity, pipe rotation.	Fluid circulation is the dominant operational parameter influencing cleaning. Pipe rotation enhances cuttings removal significantly especially if the drill pipe is fully eccentric. The presence of drill pipe rotation makes the difference in performance of low and high viscosity fluids insignificant.
Taghipour et al. (2014)	Annular test section, dry sand feeder, tank-mixer system, flow density meter, pumps and other instrumentation.	Transition flow	FT = Water + Xanthan Gum + Laponite VP = Yes ϱ_l = [?] d_s = 10 m ϱ_s = [?]	q_l = 0.55-1.4 m/s q_s/ROP = 0.0022 m/s (0.043 kg/s sand injection rate).	D_{wb} = 0.1 m D_{dp} = 0.050 m ε = 1 θ = 90^o (from vertical) L = [?] ω = 0-150 rpm	Pressure gradient, sand bed height	Average flow velocity	For the first time, an experimental study of cuttings transport was performed in a non-circular wellbore. Critical fluid flowrate is lower in the non-circular geometry than in the circular geometry. The presence of grooves in the non-circular geometry creates swirly fluid motion, which enhances hole cleaning.
Tomren et al. (1986)	Fluid tank, cuttings hopper, settling chamber, annular test section, flow meters and other instrumentation.	Laminar and Turbulent	FT = Water, low-viscosity bentonite Carbopol, High-viscosity bentonite VP = Yes (PL parameters) ϱ_l = 998.7-1,012.5 kg/m^3 d_s = 0.0064 m ϱ_s = 2,619 kg/m^3	q_l = 0.30-1.16 m/s q_s/ROP = 0.15 kg/s	D_{wb} = 0.127 m D_{dp} = 0.048 m ε = -0.5, 0 +0.5 θ = 0^o-90^o (from vertical) L = 12.19 m ω = 0, 50, 100 rpm	Total cuttings concentration, average cuttings transport velocity, fractional bed thickness, theoretical transport ratio.	Inclination angle, average fluid velocity, drill pipe rotation and eccentricity	The use of CTR should be limited to vertical flow as a guide for evaluating drilling fluid performance. Low viscosity drilling mud under turbulent flow possesses similar performance to high viscosity mud in laminar flowing conditions. Inclination angles between 35^o and 55^o are critical due to intense bed formation and bed sliding motion against flow direction. Drill pipe rotation produced slight improvements in transport efficiency.
Wei et al. (2013)	Experimental annulus, air compressor, gas tank, water tank, liquid pump, and flow meter.	Turbulent flow	FT = Compressed air + Water VP = No ϱ_l = [?] d_s = 6 mm ϱ_s = [?]	q_l = 0.00087-0.00325 m^3/s q_g = 0.00087-0.00325 m^3/s q_s/ROP = [?]	D_{wb} = 0.140 m D_{dp} = 0.063 m ε = 0-1 θ = 90^o (from vertical) L = 25 m ω = [?]	Flow visualisations	Injection speeds for the gas, liquid and solid phases	An empirical model is also developed for predicting the critical transport conditions of the fluids. The mechanism of solids transport in horizontal wells is mainly saltation; drill pipe rotation is seen to enhance cuttings transport.

Werner et al. (2017)	Annular test section, dry sand feeder, tank-mixer system, flow density meter, pumps and other instrumentation.	Transition flow with temperatures from 5-50^{o}C	*FT* = OBM and WBM fluids *VP* = Yes ρ_l = 1,190-1,260 kg/m^3 d_s = 0.9-1.6 mm (Quartz) ρ_s = [?]	q_l = 0.5-1.2 m/s q_s/ROP = 0.043 kg/s.	D_{wb} = 0.10 m D_{dp} = 0.050 m ε = 1 θ = 90^{o} (from vertical) L = 10 m ω = 0, 150 rpm	Sand holdup, fluid viscosity, storage and loss modulus.	Average liquid velocity, temperature, shear stress and shear rate.	OBM showed superior transport properties compared to WBM. Emulsion-based fluids have better cuttings suspension capability compared to polymer-based fluids, which could consolidate cuttings beds and make them difficult to remove.
Yeu et al. (2019)	Mud pump, mud tank, motorised feeder, hopper, Low-Density Polyethylene (LDPE) beads separator, ultrasonic flow meters and other measuring devices.	Steady state transition flow	*FT* = Basic water-based mud (WBM) and 1-5% low density polyethylene beads (LDPE) d_s = 1.18-2 mm (sand particles); ρ_s = [?] *VP* = Yes ρ_l = [?] d_s = 1.18-2 mm (sand particles) ρ_s = [?]	q_l = 0.69 m/s q_s/ROP = [?]	D_{wb} = 0.05 m D_{dp} = 0.0126 m ε = 0 θ = 0-90^{o} (from vertical) L = 3.35 m ω = 0 rpm;	Cuttings Transport Ratio, impulsive force.	Polymer bead concentration and hole inclination.	Compared to a horizontal hole, the vertical hole showed the best CTR. The addition of LPDE beads improved the CTR up to a maximum of 15.9%. LPDE beads were observed to collide with cuttings, thus imparting an impulse force and aiding hole cleaning. A higher flow rate resulted in a higher CTR.
Ytrehus et al. (2014)	Annular test section, dry sand feeder, tank-mixer system, flow density meter, pumps and other instrumentation.	Laminar and Turbulent	*FT* = Bentonite-based drilling fluid and KCL-based drilling fluid *VP* = Yes ρ_l = 1,370 kg/m^3 d_s = 0.9-1.6 mm (Quartz) ρ_s = [?]	q_l = 0.3-1 m/s q_s/ROP = 0.0022 m/s (0.043 kg/s sand injection rate).	D_{wb} = 0.102 m D_{dp} = 0.051 m ε = 1 θ = 90^{o} (from vertical) L = 12 m ω = 0, 6, 150 rpm	Pressure gradient, sand holdup.	Circulation fluid velocity and rheological parameters.	For the 2 water-based drilling fluids of similar viscosity profiles, the KCl fluid provided better hole cleaning than the Bentonite fluid at low flowrates. However, the reverse was the case at high flowrates. Accurate rheological modelling is required to reliably predict the hole cleaning capabilities of drilling fluids.
Ytrehus et al. (2018)	Annular test section, dry sand feeder, tank-mixer system, flow density meter, pumps and other instrumentation.	Transition flow	*FT* = OBM *VP* = Yes (HB parameters) ρ_l = 1,410-1,450 kg/m^3 d_s = 0.9-1.6 mm (Quartz) ρ_s = [?]	q_l = 0.5-1.2 m/s q_s/ROP = 0.0022, 0.0044 m/s (0.043, 0.086 kg/s injection rate).	D_{wb} = 0.10 m D_{dp} = 0.05 m ε = 1 θ = 48, 60 & 90^{o} (from vertical) L = [?] ω = 0, 3, 50, 100 rpm	Pressure gradient and relative bed height.	Inlet flow velocity	The main finding from this work is that hole cleaning in the absence of drill pipe rotation is significantly improved if the well angle is less than a critical well deviation angle. This critical angle is less than 60^{o} from the vertical for the experiments performed in this work.
Zhou et al. (2004a)	Storage tanks (for mud and cuttings), heat exchanger, separation tower, compressors, pumps, valves and other instrumentation with a digital information gathering system.	Steady state laminar flow with stratified and slug flow patterns (temperatures from 27^{o}C-79^{o}C; pressures from 0.69- 2.76 MPa)	*FT* = Air-water mixture with volumetric water percentages of 25%, 50% 75% and 100% respectively *VP* = No ρ_l = [?] d_s = 3 mm ρ_s = 2,610 kg/m^3	q_l = 0.0031-0.0158 m^3/s q_g = 0.024-0.071 m^3/s q_s/ROP = 0.125 kg/s.	D_{wb} = 0.152 m D_{dp} = 0.089 m ε = 0; θ = 90^{o} (from vertical) L = 22.25 m ω = 0 rpm	Annular pressure drop; visually observed flow patterns.	Gas Liquid Ratio (GLR) and liquid flow rate.	There is a decrease in frictional pressure loss as temperature is increased. The proposed mechanistic model can predict experimental measurements within an error range of 12.2%. Flow pattern changes from stratified smooth to stratified wavy flow when temperature increases by 60^{o}F.

Zhou et al. (2004b)	Storage tanks (for mud and cuttings), heat exchanger, separation tower, compressors, pumps, valves and other instrumentation with a digital information gathering system.	Steady flow conditions with slug, stratified and annular flows (temperatures from 27°C-80°C; pressures from 1.28-3.45 MPa)	FT = Air + water with a gas liquid ratio (0-0.38) VP = No ϱ_l = [?] d_s = 3 mm (porosity of 38%) ϱ_s = 2,610 kg/m^3	q_l=0.050-0.0094 m^3/s q_s/ROP = 0.11 kg/s	D_{wb} = 0.15 m D_{dp} = 0.09 m ε = 0 θ = 90° (from vertical) L = 22.25 m ω = 0 rpm	Cuttings volume concentration	Gas Liquid Ratio (GLR) and liquid flow rate	There is satisfactory agreement between predicted and measured data when the developed model is applied (maximum average error of approximately 34%). Temperature has a significant effect on transport efficiency of aerated muds; elevated temperatures cause a rise in cuttings concentration. This concentration is also very sensitive to the liquid flowrate.
Zhou et al. (2005)	Storage tanks (for mud and cuttings), heat exchanger, separation tower, compressors, pumps, valves and other instrumentation with a digital information gathering system.	Steady flow conditions with slug, stratified and annular flows (temperatures from 27°C-80°C; pressures from 1.28-3.45 MPa)	FT = Air + water with a gas liquid ratio (0-0.38) VP = No ϱ_l = [?] d_s = 3 mm ϱ_s = 2,610 kg/m^3	q_l= 0.005-0.0095 m^3/s q_s/ROP = 0.125 kg/s.	D_{wb} = 0.152 m D_{dp} = 0.089 m ε = 0; θ = 90° (from vertical) L = 22.3 m ω = 0 rpm	Annular pressure drop; visually observed flow patterns, bed height.	Gas Liquid Ratio (GLR) and liquid flow rate	It was concluded that the pressure loss changes slightly with temperature and pressure. GLR is seen found to have a moderate effect on the pressure drop. The developed hydraulic model is able to predict experimental results with an average error of 19.7%.

PROCESS CONTROL & OPTIMISATION CONTRIBUTIONS (DRILLING)

AE-Algebraic Equations; **BC**-Boundary Conditions; **BM**-Bulk Modulus; **DEM**-Discrete Element Method; **DDPM-**Dense Discrete Phase Model; **DPM-**Discrete Phase Model; **EE**-Eulerian-Eulerian; **FEM-**Finite Element Method; **FVM**-Finite Volume Method; **FT**-Fluid Type; **HX**-Hexahedral; **KTGF**-Kinetic Theory of Granular Flow; **LE**-Lagrangian Eulerian; **MD**-Measured Depth; **MID**-Mesh Independence Study Performed?; **ModVal**-Model Validation Performed?; **ODE**-Ordinary Differential Equations; **OS**-Operating System; **PDE**-Partial Differential Equations; **PI**-Productivity Index; **QUICK**-Quadratic Upstream Interpolation for Convective Kinematics; **ROP**-Rate of Penetration; **SIMPLE**-Semi-Implicit Method for Pressure Linked Equations; **SS**-Steady State; **TH**-Tetrahedral; **TS**-Transient State; **TVD**-True Vertical Depth; **VP**-Is Viscosity Data Provided?; A = Cross-sectional area of annulus; D_{wb} = Wellbore diameter; D_{dp} = Drill pipe diameter; h_r = Reservoir thickness; K_r = Reservoir permeability; L = Computational length; P_{ch} = Choke Pressure; P_{bit} = Drill bit pressure; P_r = Reservoir Pressure; S = Skin factor; m_l = Liquid mass flowrate; q_l = Liquid flowrate; v_l , v_g = Liquid, Gas velocity; V_a = Annulus volume; V_g = Gas kick volume; ε = Drill pipe eccentricity; θ = Angle of inclination; ω = Drill pipe rotation; φ = Reservoir porosity; ϱ_l , ϱ_g = Liquid, Gas density; [?] = Unknown/unreported parameter.

Table C.4. Summary of process control & optimisation research contributions for drilling operations.

Reference	Simulation Model & Components	Controller scheme/solution method	Manipulated (MV), Controlled (CV), Disturbances (D), Optimisation/System Variables (OV/SV)	System Properties		Summary & Key Findings
				Wellbore Geometry & Drilling Parameters	Reservoir Parameters	
Aarsnes et al. (2016a)	Drift Flux Model (DFM) for pressure and flow dynamics in the annular wellbore and drill string, with linear approximations of the boundary conditions of the DFM.	Steady-state analysis and transient simulations of the DFM.	***MV***: injection mass flow rates of liquid and gas, choke opening ***CV***: bottomhole pressure ***D***: severe slugging conditions due to gas and liquid flows.	A = 0.0068 m^2 θ = 90^o (from vertical) MD = 2,530 m; TVD = [?] ϱ_l = 1,000 kg/m^3 v_l = [?] v_g = [?] ROP = [?]	P_r = 27.9 MPa S = [?] K_r [?] φ = [?] h_r = [?] PI_L = 0 kg/s/Pa PI_G = 5×10^{-7} kg/s/Pa	This paper implements the Drift Flux Model with a steady state analysis in order to determine four distinct operating regimes during UBD operations. This enhances the control of bottomhole pressure. It is discovered that the cause of slugging in UBD operations is different from that in production and multiphase transport. An important factor that determines UBD performance is the limit between the intuitive and non-intuitive regimes identified herein.
Aarsnes et al. (2016b)	Reduced-order 2-phase flow pressure dynamics model of the wellbore, with linear approximations.	Static & time-varying controller tuning via LMI optimisation	***MV***: injection mass flow rates of liquid and gas, choke opening ***CV***: bottomhole pressure ***D***: gas kicks into the wellbore	D_{wb} = [?] D_{dp} = [?] θ = [?] MD = [?]; TVD = [?] ϱ_l = [?] v_l = = [?]; v_g = [?] ROP = [?]	P_r = [?] S = [?] K_r [?] φ = [?] h_r = [?] PI = [?]	A controller structure and a first-order model approximation of two-phase flow in an oil and gas well are proposed with particular focus on handling gas kicks. Robust controller design is achieved using Linear Matrix Inequalities - LMI (formulating an LMI optimisation problem). It is shown that acceptable performance can be obtained by using a time-varying controller gain.
Asgharzadeh Shishavan et al. (2015)	Lower order pressure hydraulics model by Stamnes et al. (2008) consisting of flow models through the upstream choke, pump and drill bit, and an empirical ROP correlation. Drill string and WOB dynamic models are also incorporated.	Nonlinear MPCs	***MV***: topside WOB, topside drill pipe rotation, choke opening, pump flowrate ***CV***: downhole pressure, downhole ROP, downhole WOB ***D***: sensor noise, downhole pressure fluctuations.	A = 0.021 m^2 θ = [?] MD = 2,000 m TVD = [?] ϱ_l = 1,200-1,400 kg/m^3 v_l = = [?]; v_g = [?] ROP = 0.01 m/s	P_r = [?] S = [?] K_r [?] BM = 1,400 MPa φ = [?] h_r = [?] PI = [?]	The study combines ROP and BHP into a single comprehensive controller for MPD operations. A combined multivariate controller for ROP and pressure is superior compared to the case where separate controllers are used. High-speed telemetry is critical for this control scheme because it enables high frequency data to both update the underlying models and implement control actions. The developed MPC controller and estimators (extended Kalman filter and moving-horizon estimator) enable an optimised drilling scenario and achieve operational targets.
Asgharzadeh Shishavan et al. (2016)	Industry-validated high-fidelity model and a low order model (WOB dynamics model, rotational dynamics model, empirical ROP correlation, pump and choke models).	Multivariate NMPC	***MV***: rig pump flowrate, choke valve opening, backpressure pump flow, WOB, drill string rotational rate ***CV***: bottomhole pressure, annular pressure, choke valve pressure, ROP ***D***: unexpected gas influx, cuttings build-up, drill string movements	D_{wb} = 3.5 m D_{dp} = 8.625 m A = 0.021 m^2 θ = [?] MD = 2,000 m; TVD = [?] ϱ_l = 1,200-1,400 kg/m^3 v_l = = [?]; v_g = [?] ROP = [?]	P_r = [?] S = [?] K_r [?] φ = [?] h_r = [?] PI = [?]	This research couples drilling hydraulics, rate of penetration and rotational speed control using wired drilled pipe telemetry into a single controller for MPD systems. The designed NMPC controller gives priority to the bottomhole pressure and attenuates unwanted gas influx via switching the control objective from bottomhole to choke pressure. Obtained results show that the multivariate controller decreases drilling costs, reduces operator workload and minimises risks significantly compared to using two independent controllers.

Bjorkevoll et al. (2010)	First-principles tuned hydraulic model by Bjørkevoll et al. (2006) are adopted.	PI control	***MV***: choke opening, backpressure pump ***CV***: bottomhole pressure, ECD, drill pipe rotation ***D***: downhole pressure fluctuations	D_{wb} = [?] D_{dp} = [?] θ = [?] MD = [?]; TVD = [?] ϱ_l = [?] q_l = 0-0.033 m^3/s v_g = [?] ROP = [?] ω = 0-150 rpm	P_r = [?] S = [?] K_r [?] φ = [?] h_r = [?] PI = [?]	An advanced dynamic flow and temperature model was used to optimise and control MPD operations in real-time on the Gulfaks field in the North Sea. The well drilled only had a 7 psia window between pore and fracture pressure. This paper addresses the model-specific challenges and analyses the differences between model predictions and downhole data. It was discovered that the success of the operation depended on the quality of manual input data, real-time signals, the accuracy of the tuning model and good training of personnel with a user-friendly graphical human-machine interface.
Breyholtz et al. (2010b)	Model of Nygaard and Gravdal, 2007.	MPC	***MV***: mud pump flow rate, subsea pump flow rate and drill string velocity ***CV***: bottomhole pressure and hook position ***D***: drillstring movements	D_{wb} = [?] D_{dp} = [?] θ = [?] MD = [?] TVD = [?] ϱ_l = [?] q_l = 0.0167 m^3/s; v_g = [?] ROP = [?]	P_r = [?] S = [?] K_r = [?] φ = [?] h_r = [?] PI = [?]	Computer simulations are used to demonstrate the ability of MPC controllers to control hook position and bottomhole pressure through coordinated manipulation of mud pump flow rate and drill string velocity while satisfying important constraints on the system.
Breyholtz et al. (2010a)	Godhavn (2009) lower-order models	MPC	***MV***: main mud pump flowrate, subsea pump flowrate, drill string velocity ***CV***: BHP, hook position ***D***: pressure fluctuations due to drill string movements	D_{wb} = [?] D_{dp} = [?] θ = [?] MD = [?]; TVD = [?] ϱ_l = [?] q_l = 0.2-3 m^3/s v_g = [?] ROP = [?]	P_r = [?] S = [?] K_r [?] φ = [?] h_r = [?] PI = [?]	A multi-level control approach that consists of three different levels (feedback, supervisory and optimisation) is implemented for MPD operations. The main objective of the formulated strategy is to reduce drilling costs while satisfying safety and performance constraints. The simulations show that even though a linear MPC is used, the algorithm can maintain the BHP at the desired value with only minor deviations during transient periods.
Breyholtz et al. (2011)	High fidelity model of Nygaard and Gravdal (2007)	Linear MPC approach	***MV***: main and backpressure pump/circulation flowrate, reference differential pressure, reference hook position ***CV***: BHP, hook position ***D***: drill string movements and pressure fluctuations	D_{wb} = 0.251 m D_{dp} = 0.127 m θ = [?] MD = 6,040 m; TVD = 4,730 m ϱ_l = 1,580 kg/m^3 v_l = [?]; v_g = [?] ROP = [?]	P_r = [?] S = [?] K_r [?] φ = [?] h_r = [?] PI = [?]	In this paper, the use of MPC is proposed as a multivariate control framework that is capable of co-ordinating multiple drilling variables for better performance, higher reliability and safety compared to current practices. In the dual gradient drilling case study presented, the MPC simultaneously controls BHP and drill string movement by manipulating the main pump flowrate, seabed pump flowrate and drill string velocity. The results show that the proposed formulation results in lower BHP deviations compared to manual control of hook positions alone.
Carlsen et al. (2013)	Lorentzen et al. (2003) multiphase flow model (mass and momentum balance equations with different closure relations for different flow regimes: slug, bubble and transition regimes).	PI, IMC, MPC	***MV***: choke opening of the well control choke ***CV***: bottomhole pressure, Choke pressure ***D***: pump flow rate and pressure fluctuations due to gas influx and fluid expansion in the annulus.	D_{wb} = [?] D_{dp} = [?] θ = [?] MD = 2,300 m TVD = 1,720 m ϱ_l = 1,475 kg/m^3 ω = [?] v_l = [?] v_g = [?] ROP = [?]	P_r = 26.2 MPa S = 0.13 K_r = 100 mD φ = 0.18 h_r = 2 m PI = [?]	Three different control algorithms (proportional-integral, internal model and model predictive control) were proposed to regulate well bottomhole pressure during an unexpected gas influx from a reservoir during managed pressure drilling. It was shown that all control schemes adequately handle disturbances in comparison to manual methods. Further improvement may be attained by updating the wellbore model after the gas influx has occurred.

Cayeux and Daireaux (2009)	Real-time field data available with data filtering technique for noisy and erratic signals. Numerically calibrated mechanical, hydraulic and temperature models are also applied.	Automatic updates (warnings) when significant changes occur in system variables (via friction analysis).	***SV***: Torque, drag, sliding and rotational friction, hook load, temperature, mud density, cuttings buildup	D_{wb} = 0.311 m D_{dp} = 0.089-0.127 m θ = [?] MD = 1,200 - 1,500 m; TVD = [?] ϱ_l = [?] v_l = = [?]; v_g = [?] ROP = [?]	P_r = [?] S = [?] K_r [?] φ = [?] h_r = [?] PI = [?]	This paper presents a computer system used to systematically monitor real-time data in order to analyse downhole conditions based on automatic calibration of numerical drilling models. This automated system is validated using real field data from the North Sea. A data filtering technique is also implemented to eliminate noisy data. The system is capable of triggering alarms and warnings during drilling operations and has shown good performance on several wells.
Cayeux et al. (2012)	Calibrated commercial torque and drag software (Niedermayr, 2010) is adopted.	Comparison of results from calibrated physical model with surface and downhole measurements.	***SV***: Torque, drag, sliding and rotational friction, hook load, temperature, mud density, cuttings proportion, fluid shear stress, free rotating weight deviation, flowrate, rotation, standpipe pressure.	D_{wb} = 0.216 m D_{dp} = 0.127 m θ = [?] MD = [?]; TVD = [?] ϱ_l = [?] v_l = [?]; v_g = [?] ROP = [?]	P_r = [?] S = [?] K_r [?] φ = [?] h_r = [?] PI = [?]	In this paper, a software solution that automatically detects changes in drilling conditions is validated. This is done by comparing results from calibrated physical models of the well with surface and downhole measurements. It is demonstrated that the use of multiple indicators of abnormal drilling conditions is essential because similar problems do not always present themselves in the same pattern. The developed system is shown to provide early warning signs of changing downhole conditions well before an incident.
Davoudi et al. (2011)	2 transient multiphase flow simulators: Das (2007) simulator and a developed simulator with advanced fluid rheological models and friction factor models for accurate pressure drop prediction.	————	***MV***: choke opening, fluid circulation rates ***CV***: bottomhole pressure, choke pressure ***D***: fluid influx/kick, lost circulation	D_{wb} = 0.12-0.23 m D_{dp} = 0.089-0.168 m θ = 0° (from vertical) MD = [?]; TVD = 1,450-4,816 m ϱ_l = [?] v_l = [?]; v_g = [?]; ROP = [?]	P_r = [?] S = [?] K_r [?] φ = [?] h_r = [?] PI = [?]	Simulation-based evaluations of several causes and severities of kicks in different well geometries are carried out for MPD operations. Three responses analysed include casing pressure increase, shutting the well and using an adaptation of the MPD pump shutdown schedule. Although there is no best single response for all situations, the disadvantages and advantages of all three methods were discussed based on the computer simulations carried out.
Eaton et al. (2017)	SINTEF Flow Model (Petersen et al., 2008) comprising of mass & momentum balances for the respective phases and submodels (for estimating fluid density); a low order model is also implemented.	Nonlinear MPC, Linear Empirical MPC and Low order MPC within a switch control scheme	***MV***: valve position and pump flow rate ***CV***: bit/bottomhole pressure ***D***: pressure fluctuations due to gas influx	D_{wb} = [?] D_{dp} = [?] θ = 90° (from vertical) MD = 2,400 m; TVD = 2,400 m P_{cb} = 2.25 MPa; P_{bit} = 37.87 MPa ϱ_l = 1,402 kg/m^3 q_l = 0.0248 m^3/s; V_g = 4.77 m^3 (kick size) ROP = 0.00055 m/s	P_r = [?] S = [?] K_r [?] φ = [?] h_r = [?] PI = [?]	A switched control scheme for MPD operations that uses real time data via a high fidelity model and a linear empirical control model is formulated. It is shown that the proposed scheme allows very accurate predictions of a high fidelity model to be incorporated in real time control without high online computational cost.
Florence and Iversen (2010)	Gravdal (2009) & Gravdal et al. (2010) model (mass and momentum conservation equations, PVT equation of state, fanning friction factor, rheological models, mean cross-sectional velocity equation)	Programmable Logic Controllers (PLC)	***MV***: flowrate, rotation frequency ***CV***: downhole pressure ***D***: downhole pressure fluctuations	D_{wb} = [?] D_{dp} = [?] θ = [?] MD = [?]; TVD = [?] ϱ_l = [?] q_l = 0-0.025 m^3/s v_g = [?] ω = 0-100 rpm ROP = [?]	P_r = [?] S = [?] K_r [?] φ = [?] h_r = [?] PI = [?]	This paper aims to answer questions relating model fidelity in view of automation and control and to elaborate on current activities and challenges relating to drilling automation. This paper provides examples of recent developments within drilling automation, drawing applications of closed-loop control systems in the North Sea. It is discovered that applying real-time models in process control requires extensive model calibration, data quality control and communication reliability. Furthermore, limitations of the hardware and model must be considered when implementing drilling automation systems.

Freij-Ayoub et al. (2007)	Validated finite difference code, FLAC3D for wellbore stability simulations, comprising: Darcy equation, Fourier's heat conduction model, mass and momentum balances, hydrate dissociation model, and constitutive equations.	Fast Lagrangian Analysis of Continua in 3 Dimensions via Finite Differences (FLA3CD).	***SV***: Pore pressure, distance information, porosity, percentage hydrate dissolved, radius of plasticity, reaction front location.	D_{wb} = [?] D_{dp} = [?] θ = [?] MD = [?]; TVD = [?] ϱ_l = [?] v_l = = [?] v_g = [?] ROP = [?]	P_r = 17 MPa S = [?] K_r = 1×15 m^2 BM = 7 GPa φ = [?] h_r = [?] PI = [?]	A model that simulates the stability of a wellbore drilled in a methane-hydrate bearing sedimentary formation is developed. The model couples the thermodynamic stability of hydrates in porous media to fluid transport, thermal transport and mechanical deformation. The model provides an understanding of the effects of drilling a wellbore in hydrate bearing sediments and the impact of drilling fluid temperature and density on changes in formation stresses and pressure
Godhavn et al. (2011)	Stamnes et al. (2008) model, consisting of flow models through the upstream choke, pump and drill bit.	Nonlinear model-based PID controllers with a linear observer.	***MV***: desired flow through choke ***CV***: bottomhole pressure, choke pressure ***D***: downhole pressure fluctuation	D_{wb} = [?] D_{dp} = [?] θ = [?] MD = [?]; TVD = [?] ϱ_l = [?] q_l = 0.0167 m^3/s v_g = [?] ROP = [?]	P_r = [?] S = [?] K_r [?] φ = [?] h_r = [?] PI = [?]	In this paper, nonlinear control methods with experimental methods are applied to improve pressure control during MPD operations. Some control challenges relating to the overall drilling process are also presented and discussed. Problems such a sever wave induced motion in floating drilling rigs, directional drilling (trajectory) control, automatic mud mixing and well pressure control are some identified areas needing more research.
Godhavn (2009)	SINTEF Hydraulic Model (Petersen et al., 2008)	PID controller	***MV***: mud flow rate, choke position ***CV***: downhole annular pressure ***D***: downhole pressure fluctuations, measurement noise.	D_{wb} = [?] D_{dp} = [?] θ = [?] MD = [?]; TVD = [?] ϱ_l = [?] v_l = [?]; v_g = [?]; ROP = [?];	P_r = [?] S = [?] K_r [?] φ = [?] h_r = [?] PI = [?]	This paper explains how StatoilHydro applied automatic MPD operations successfully in the Kvitebjorn field in the North Sea in 2007. The paper presents some key results and discusses automatic control requirements for drilling operations. A simple nonlinear hydraulic model capturing only the main pressure and flow dynamics was developed; this model was applied for controller development and tuning analysis. The application of MPD to the field allowed well drilling in locations that otherwise could not be drilled.
Gravdal et al. (2010)	Wellbore flow model (mass, momentum and energy balance equations), reservoir-to-wellbore influx model.	Standard linear PI controller	***MV***: choke opening ***CV***: annular back pressure, bottomhole pressure ***D***: gas kick	D_{wb} = 0.229 m D_{dp} = 0.114 m θ = [?] MD = 3,383 m; TVD = [?] ϱ_l = 1,250 kg/m^3 v_l = [?]; v_g = [?] ROP = [?]	P_r = [?] S = 0.013 K_r = 20 mD φ = 0.15 h_r = [?] PI = [?]	This work develops a control methodology that utilises improved access to downhole measurements offered by drill pipe telemetry to maintain pressure within desired bounds during kick management. The main objectives are to reduce non-productive time, formation damage and optimise operational limits for the choke and manifold. The proposed pore pressure estimation method showed good performance in reducing kicks and hole-stability problems.
Hague et al. (2013)	Hydraulic model of MPD systems, which consists of a pressure, balance model of the main pump and choke, reservoir-well influx model and the bit flowrate/pressure drop model. OLGA multiphase flow simulator is also applied together with experimental measurements.	A globally exponentially stable adaptive observer with a switched control scheme	***MV***: choke opening and ***CV***: pressure and flow control (no kick), pure flow control (during kick) ***D***: kicks, loss circulation	D_{wb} = 0.2 m D_{dp} = 0.1 m θ = [?] MD = 2,825 m TVD = 1,500 m ϱ_l = 1,007.3 kg/m^3 v_l = [?]; v_g = [?] ROP = [?]	P_r = 19.7 MPa S = [?] K_r [?] φ = [?] h_r = [?] PI = 0.005 m^3/s.MPa	The absence of drilling instrumentation downhole motivated the development of model-based influx and out-flux detection scheme necessary for successful MPD operations. This is based on an adaptive solver (globally exponentially stable) which is also used for the estimation of unknown states and parameters of the system. The developed solver is capable of locating and quantifying fluid influx/outflux from the wellbore when compared with experiments and simulation results.

Hankins et al. (2015)	Drilling data available for 3 wells coupled with an ROP correlation.	Simple algebraic solution of the ROP model	***SV:*** ROP, WOB, bit diameter, rock strength, geometry correction factors, rake angle.	D_{wb} = 0.22 m D_{dp} = [?] θ = [?] MD = [?]; TVD = [?] ϱ_l = 1,019-1,246 kg/m^3 q_l = 0.034-0.038 m^3/s ω = 55-90 rpm v_g = [?] ROP = 0.0045-0.0275 m/s	P_r = [?] S = [?] K_r [?] φ = [?] h_r = [?] PI = [?]	This paper presented a systematic approach to simulate and optimize the operational plan for upcoming wells using offset well data for a field in Northwest Louisiana. A comparative study between simulation results and actual data showed good model performance. The results of the optimized bit, hydraulics, and WOB/RPM show that 62 hours of drilling time can be saved for all 3 wells with a cost reduction of approximately 512,000 USD.
Landet et al. (2012)	New hydraulic model (mass and momentum balance equations, frictional pressure model, Bingham plastic model, turbulent flow model.	_____	SV: mud circulation rate, mud density, flow area, BHP, shear stress, viscosity.	D_{wb} = [?] D_{dp} = [?] θ = [?] MD = [?]; TVD = [?] ϱ_l = [?] v_l = [?]; v_g = [?] ROP = [?]	P_r = [?] S = [?] K_r [?] φ = [?] h_r = [?] PI = [?]	A mathematical well hydraulics model is derived for designing control schemes to actively attenuate fluctuations due to heave motion of floating rigs. The model is also validated using field data of different MPD operations. It is shown by simulations that reduced-order models obtained by applying the method of frequency-weighted-balanced models outperform those obtained by simply reducing the number of control volumes. The contributions of this paper enable the development of control systems for automated MPD operations from floaters.
Landet et al. (2013)	Landet et al. (2012) hydraulic model (mass and momentum balance equations, frictional pressure model, Bingham plastic model, turbulent flow model.	Linear Internal model Controller	***MV***: choke opening ***CV***: BHP ***D***: vertical drill string motion following the heave motion of the rig floating on the waves	D_{wb} = [?] D_{dp} = [?] θ = [?] MD = [?]; TVD = [?] ϱ_l = [?] v_l = [?]; v_g = [?] ROP = [?]	P_r = [?] S = [?] K_r [?] φ = [?] h_r = [?] PI = [?]	In this paper, the authors present two different disturbance (e.g. vertical drill string motion) rejection strategies based on discretized partial differential equations for the well hydraulic system. The performance of the controllers is shown through simulations both under idealized conditions and on a high-fidelity drilling simulator. The field-based calibrated model and the developed controllers demonstrated good attenuation of the heave-induced pressure fluctuations sufficient from a practical point of view.
Lee et al. (1998)	Abductive networks via system decomposition and polynomial function nodes are adopted herein. It involves a training database with respect to drilling parameters.	Simulated annealing optimisation algorithm is used to search for process parameters.	***OV:*** tool life, drilling tool wear, metal removal rate, thrust force, torque	D_{wb} = [?] D_{dp} = 0.009 m, 0.011 m; θ = [?] MD = [?]; TVD = [?] ϱ_l = [?] q_l = 0.08-0.24 mm/rev v_g = [?]; *Cutting speed* = 0.167-0.5 m/s	P_r = [?] S = [?] K_r [?] φ = [?] h_r = [?] PI = [?]	Self-organised abductive networks that model drilling operations are developed. These networks capture the relationship between process parameters and drilling performance A global simulated annealing algorithm is applied to search for the optimal drilling process parameters. The developed model is experimentally validated using the optimised drilling parameters; thus demonstrating the usefulness of the technique.
Misra and Nikolaou (2018)	Available well data is used to build a Partial Least Squares Discriminant Analysis (PLSDA) model, which is applied together with a neural network model.	_____	***SV***: density, viscosity, yield pressure, water/oil composition and gel strength of drilling mud, Surface pump rate.	D_{wb} = [?] D_{dp} = [?] θ = [?] MD = [?]; TVD = [?] ϱ_l = [?] v_l = = [?]; v_g = [?] ROP = [?]	P_r = [?] S = [?] K_r [?] φ = [?] h_r = [?] PI = [?]	In this work, a multivariate statistical neural network model is built from available data of 105 gas wells. The model is designed to predict gas leakage and yields about 75% accuracy based on cross-validation tests performed. The model also ranks decision variables in the order of importance and suggests which variables need more attention. The model can be used to select values of design variables to prevent gas leakage & ensure zonal isolation.

Nikoofard et al. (2013)	Annular fluid dynamic model (IRIS drilling simulator), wave response (due to heave motion) model with corresponding linear approximations.	PID controller, constrained MPC	***MV***: choke opening ***CV***: bottomhole pressure ***D***: heave induced disturbance.	A = 0.0269 m^2 θ = [?] MD = [?]; TVD = [?] ϱ_l = [?] q_l = 369.2 m^3/s v_g = [?] ROP = [?]	P_r = [?] S = [?] K_r [?] φ = [?] h_r = [?] PI = [?]	A constrained MPC scheme for annular pressure regulation in a well during MPD operations form a floating rig subject to heave motion is developed. A dynamic annular pressure model (based on a hydraulic transmission line) is discretised through a finite volume method and applied. The MPC controller shows good disturbance rejection capabilities, with an improved performance compared to the PID controller.
Nygaard and Nævdal (2006)	Lower-order and detailed model (mass and momentum balance of the fluids, pressure balances at the choke and bottom of the drill string), closure relations (frictional pressure loss, productivity index, mixture density, tank pressure).	Manual control, PI control, NMPC	***MV***: mass flowrates of gas and liquid in the drill string and annulus ***CV***: bottomhole pressure, choke opening parameter ***D***: pump inflow rates, drilling rate.	D_{wb} = [?] D_{dp} = [?] θ = [?] MD = 2,000 m TVD = 2,000 m ϱ_l = [?] m_l = 24 kg/s m_g = 2 kg/s ROP = 0.01 m/s;	P_r = 21.5 MPa S = 0.013 K_r = 200 mD φ = 0.18 h_r = 100 m PI = [?]	A control scheme based on a first principles two-phase flow model using spatial discretisation of the complete well is proposed; the model ensures downhole pressure stabilisation during drilling. A comparative analysis of the performances of manual control (used in industry), PI control and MPC control was performed. The nonlinear MPC scheme resulted in the least fluctuations of the bottomhole pressure.
Park et al. (2017)	Physics-based drilling simulator (*Wemod*) is used together with Wired Drill Pipe (WDP) technology.	Hammerstein-Wiener based MPC	***MV***: choke position, pump flowrates ***CV***: bit downhole pressure, mudflow balance ***D***: pressure fluctuations due to drill pipe connections, unwanted kicks.	D_{wb} = 0.229 m D_{dp} = 0.114 m θ = [?] MD = 3,597 m; TVD = [?] ϱ_l = 1,240 kg/m^3 v_l = [?]; v_g = [?] ROP = [?]	P_r = 401×10^5 Pa S = [?] K_r [?] φ = [?] h_r = [?] PI = [?]	In this work, it is shown that improved control can be achieved for MPD operations with the use of high-speed telemetry and physics-based models. A new Hammerstein-Wiener nonlinear MPC for BHP regulation is employed. This new controller is compared to conventional controllers using various scenarios. The new controller developed herein shows superior performance to conventional ones by eliminating uncertainties of predictive BHP estimation.
Pixton et al. (2014)	Stamnes et al. (2008) model, consisting of flow models through the upstream choke, pump and drill bit.	MPC	***MV***: choke valve opening, main pump flow rate, back pressure pump flowrate ***CV***: drill bit pressure, choke valve pressure ***D***: unwanted gas influx.	A = 0.021 m^2 θ = [?] MD = 2,000 m; TVD = [?] ϱ_l = 1,200-1,400 kg/m^3 v_l = [?]; v_g = [?] ROP = 0.01 m/s	P_r = [?] S = [?] K_r [?] φ = [?] h_r = [?] PI = [?]	In this study, specific case studies and lessons learned from using a Wired Drill Pipe in UBD & MPD drilling environments are summarised. Recent enhancements to the WDP system and their impact on operational reliability are also discussed. A nonlinear MPC is used in the automation part of this study. It is discovered that that WDP can add further value to the pressure control process by providing improved responsiveness of the controller and also improved model parameter estimation (friction factor and density).
Song et al. (2016)	Continuity, momentum and heat transfer equations, CO_2 density and isobaric heat capacity models, standard k-ε turbulence model.	Finite volume discretisation of the Eulerian equations	***MV***: temperature, circulation flowrate ***CV***: target bottomhole pressure ***D***: downhole pressure fluctuation and CO2 density variation.	D_{wb} = 0.1143 m D_{dp} = 0.051 m θ = [?] MD = 2,500 m; TVD = [?] ϱ_l = [?] m_l = 4.5 kg/s v_g = [?] T = 253.15K (0.025K/m geothermal gradient) ROP = [?]	P_r = [?] S = [?] K_r [?] φ = [?] h_r = [?] PI = [?]	In this paper, a mathematical model that couples the hydrostatic pressure, temperature and CO_2 properties in a wellbore is established for controlling the BHP during MPD operations. The influences of mass flowrate, well-depth, inlet temperature and surface backpressure were investigated. Surface backpressure decreases with an increase in mass flow rate and increases with the increase in well depth. Inlet temperature has little impact on the annulus pressure profile. Beyond a critical pressure, CO_2 density increases abruptly.

Stamnes et al. (2008)	Pressure dynamics model (based on mass balance), volume flow dynamics model (based on momentum balance) and an observer design model that estimates the downhole bit pressure and adapts to the unknown system parameters.	Nonlinear adaptive observer	***MV***: mud flowrate ***CV***: annular pressure ***D***: downhole pressure fluctuations.	D_{wb} = [?] D_{dp} = [?] θ = [?] MD = 1,825 m; TVD = [?] ϱ_l = 1,210 kg/m^3 v_l = = [?]; v_g = [?]; ROP = [?];	P_r = [?] S = [?] K_r [?] BM = 1400 MPa φ = [?] h_r = [?] PI = [?]	A reduced-order observer (based on a newly developed nonlinear wellbore model) that adapts to unknown friction and density and BHP estimates is presented. Based on a Lyapunov approach, the pressure estimate is shown to converge to the true pressure under reasonable conditions. The application of the observer to real data from a North Sea oil well demonstrates promising behaviour.
Sui et al. (2018)	Mechanistic transport model comprising, density, temperature and pressure drop models. Data Validation and Reconciliation (DVR) techniques are also applied.	DVR Optimisation (error minimisation between measurements and reconciled values of measurements.	Transient measurements of pressure, temperature, from which fluid density, friction factor and heat transfer coefficient are estimated.	D_{wb} = 0.489 m D_{dp} = 0.1282 m θ = [?] MD = 1,980 m; TVD = [?] ϱ_l = 1,100 kg/m^3 v_l = [?]; v_g = [?] ROP = [?]	P_r = [?] S = [?] K_r [?] φ = [?] h_r = [?] PI = [?]	The paper presents an approach for addressing poor data quality during WDP data collection, which enables accurate estimation of unmeasurable parameters that reveal downhole behaviour. The optimisation-based approach is able to distinguish a sensor defect from a kick. The obtained results also show that it is possible to distinguish sensor malfunction from defective calibration. Model parameters are also refined based on continuous additional data available.
Zhou and Nygaard (2010)	Hydraulic model of MPD systems which consists of a pressure balance model of the main pump and choke, reservoir-well influx model and the bit flowrate/pressure drop model (all embedded in Wemod – a drilling simulator)	Nonlinear adaptive observer with a simple PI controller	***MV***: drilling fluid density, main pump fluid flow rate, standby pressure, choke differential pressure, drilling mass rate ***CV***: BHP ***D***: downhole pressure fluctuations.	D_{wb} = 0.22 m D_{dp} = 0.1 m θ = [?] MD = 3,600 m; TVD = [?] ϱ_l = 1,250 kg/m^3 q_l = 0.0167-0.0233 m^3/s v_g = [?] ROP = [?]	P_r = [?] S = [?] K_r [?] φ = [?] h_r = [?] PI = [?]	This paper presents a nonlinear adaptive observer and a simple model-based control scheme that stabilizes the annular pressure profile throughout the wellbore continuously during drilling operations. A simple mechanistic model is presented that captures the dominant phenomena of the drilling system and forms the basis for the model-based observer and control design. The simulation results show that the estimated downhole pressure fits the true variables well, and the controller is able to suppress the changes in downhole pressure with a maximum deviation from the desired pressure of approximately 0.5 MPa.
Zhou and Nygaard (2011)	A high-fidelity simulator that implements a pressure balance model of the main pump and choke, reservoir-well influx model and the bit flowrate/pressure drop model.	Adaptive observer feedback control, attenuation mode control coupled with an automatic switch control algorithm when a kick occurs.	***MV***: pump flowrates, choke opening ***CV***: bottom hole pressure ***D***: gas influx.	D_{wb} = 0.4509 m D_{dp} = 0.1270 m θ = [?] MD = 9,590 m; TVD = 9,587 m ϱ_l = 1,804 kg/m^3 v_l = [?]; v_g = [?] ROP = [?]	P_r = 164 MPa S = [?] K_r [?] φ = [?] h_r = [?] PI = [?]	This paper presents an observer-based control scheme that stabilises the bottomhole pressure with desired bounds; the method also detects and controls kicks for dual-gradient drilling operations. It was discovered the proposed method does not go below the reservoir pressure when attenuating the kick and has good performance in comparison with a high-fidelity drilling simulator.

Zhou et al. (2009)	Hydraulic model of MPD systems which consists of a pressure balance model of the main pump and choke, reservoir pore pressure estimation model, kick detection model, flowrate estimation model, reservoir-well influx model and the bit flowrate model (all embedded in *Wemod* – a drilling simulator).	Nonlinear adaptive observer with a simple PI controller	***MV***: topside choke opening, pump flowrates ***CV***: BHP ***D***: inflow into and outflow from the wellbore.	V_a = 211 m^3 θ = [?] MD = [?]; TVD = [?] ϱ_l = 1,250 kg/m^3 q_l = 0.025 m^3/s BM = 1,305 MPa v_g = [?] ROP = [?]	P_r = [?] S = [?] K_r [?] φ = [?] h_r = [?] PI = [?]	This paper presents a switched control scheme for regulating the annular pressure in a well during drilling. The main feature is automatic kick attenuation while drilling reservoir sections. A simple mathematical model is presented that captures the dominant phenomena of the drilling system and forms the basis for observer and control design. A uniform, global, asymptotic stabilization of the dynamic system is established for pressure regulation and kick attenuation.
Zhou et al. (2010)	Hydraulic model of MPD systems which consists of a pressure balance model of the main pump and choke, reservoir pore pressure estimation model, kick detection model, flowrate estimation model, reservoir-well influx model and the bit flowrate model (all embedded in *Wemod* – a drilling simulator).	Nonlinear adaptive observer with a simple PI controller	***MV***: topside choke opening, pump flowrates ***CV***: BHP ***D***: inflow into and outflow from the wellbore.	V_a = 211 m^3 θ = [?] MD = [?]; TVD = [?] ϱ_l = 1,580 kg/m^3 q_l = 0.025 m^3/s BM = 1,400 MPa v_g = [?] ROP = [?]	P_r = 80-81 MPa S = [?] K_r = 100-400 mD φ = [?] h_r = [?] PI = [?]	In this work, novel adaptive observers for estimating the flow rates through a well are developed for kick and loss detection, and asymptotic convergence properties are established. A switched control algorithm for feedback control of the choke, and the backpressure pump is proposed for pressure control and kick attenuation; asymptotic convergence is achieved. The results show that the proposed observers effectively detect kicks in the early phase and that the automatic control scheme improves kick handling.

MATHEMATICAL OPTIMISATION CONTRIBUTIONS (PRODUCTION)

[?] = Unknown/unreported computer specifications; (-) = Unknown/unreported software used

Table C.5. Summary of production optimisation contributions.

Reference	Type of problem solved	Time horizon	Optimisation formulation	Optimisation algorithm/solver and implementation platform	Well type	Components of production system considered & tools adopted	Production network components	Field production mechanism	Objective function	Computer spec.
Al-Zawawi et al. (2011)	Waterflood management with well placement, and available field injection water constraints.	50 years (long term)	Heuristic reservoir engineering-driven approach.	Streamline simulation for the derivation of injection efficiency.	Vertical and deviated	Reservoir/Streamline (POWERS), wellbore (POWERS)	1 reservoir, 2-4 injectors, more than 1 producer	Secondary production with water injection	Maximize oil production while reducing water production	[?]
Azamipour et al. (2016)	Production allocation during water flooding subject to bottom hole pressure constraints, water cut and available field water for injection.	18,250 days (long term)	Based on coarse/fine grid reservoir models.	Adaptive Simulated Annealing (ASA) coupled with polytope search.	Vertical	Reservoir (-), wellbore (-)	1 reservoir, 33 production wells, 14 injection wells	Secondary production with water injection	Maximization of NPV	[?]
Azamipour et al. (2017)	Production and injection scheduling subject to well capacity and available field injection water constraints.	25,550 days (long term)	Based on coarse/fine grid reservoir models.	Genetic Algorithm	Vertical	Reservoir/Streamline simulation (-), wellbore (-)	1 reservoir, 34 production wells, 14 injection wells	Secondary production with water injection	Maximization of NPV	[?]
Barragan-Hernandez et al. (2005)	One-day gas and oil production planning, subject to technical and topological constraints.	1 day (short term)	NLP	Interior method for nonlinear programming using trust regions (KNITRO); Visual Studio C++ 6.0.	Vertical	Reservoir (-), wellbore (Wellnet), and surface facilities (Wellnet & TState)	1 - 4 producer wells, 4 manifolds, 3 pipelines, 1 separator	Primary production	Minimisation of production costs	Pentium 4, 2.40 GHz
Bellout et al. (2012)	Well placement and rate control optimisation subject to BHP and well location constraints.	2,190 - 2,920 days (long term)	MINLP; adjoint-based formulation in GPRS.	SNOPT, HJDS, GPS, HOSPACK	Vertical	Reservoir (GPRS), wellbore (GPRS)	1 reservoir,1 producer, 4 injectors	Secondary production with water injection	Maximisation of NPV	Distributed computing framework consisting of eight and 20 + 1 computing cores.
Brouwer et al. (2002)	Dynamic optimisation of the water flooding process with smart wells subject to pressure and rate constraints.	950 days (long term)	Adjoint based optimisation	Optimal control theory applied to a discrete-time dynamic system model.	Vertical and deviated	Reservoir (-), wellbore (-)	1 reservoir, 1 injector; 1 producer	Secondary production with water injection	Maximisation of NPV	[?]

Carvalho and Pinto (2005)	Infrastructure planning in offshore fields subject to logical constraints, rate constraints and investments constraints.	10 years (long term)	MILP	Bilevel decomposition algorithm; CPLEX (implemented in GAMS).	Vertical	Reservoir (-), wellbore (-), and surface facilities (-)	3 fields, 14-16, reservoirs, 2-16 well platforms, 30-500 producers	Primary production	Maximisation of NPV	Pentium 4, 2.00 GHz
Codas et al. (2012)	Real-time production optimisation with complex routing and capacity constraints.	Days and weeks (short-term)	Proxy modelling and piecewise linearization to MILP.	AMPL, CPLEX 12.3.0.0	Vertical	Field reservoir data, wellbore (-), and surface facilities (-)	1 reservoir, 7 producers, 4 manifolds, 13 pipelines, 2 separators	Primary production with gas-coning wells	Maximization of oil flowrates	16 GB RAM, 2 processors, each with a six-core AMD Opteron at 2.4 GHz
Codas et al. (2015)	Reservoir-control optimisation with direct multiple shooting method with flowrate and pressure constraints.	3,600 days (long term)	NLP	Sequential quadratic programming algorithm; CPLEX v16.2; (implemented in Matlab R2014a and MRST).	–	Reservoir (ECLIPSE, MRST), wellbore (ECLIPSE, MRST)	1 reservoir, (-)	Primary production	Maximisation of NPV	Intel Xeon E5-1620; 3.60GHz; 32GB RAM
Epelle and Gerogiorgis (2019)	Multiperiod production allocation during water flooding with explicit structural and capacity constraints.	6 years (short-term and long term)	Proxy modelling; NLP	MATLAB *fmincon*, IPOPT (implemented in MATLAB R2016a).	Vertical and deviated	Reservoir/streamline simulation (ECLIPSE/ FRONTSIM), wellbore (ECLIPSE/PIPESIM), surface facilities (PIPESIM)	1 reservoir, 7 producers, 4 injectors, 3 manifolds, 3 pipelines, 3 separators	Secondary production with water injection	Maximisation of NPV	Intel core i7-6700 CPU @ 3.40 GHz; 16GB RAM
Gunnerud and Foss (2010)	Real-time operational production planning with explicit structural and routing constraints.	Days and weeks (short-term)	Proxy modelling; piecewise linearization of MINLP to MILP.	Lagrange Decomposition and Dantzig-Wolfe Decomposition; Xpress-IVE.	Vertical	Reservoir (-), wellbore (-), and surface facilities (-)	1 reservoir, 64 producers, 16 manifolds, 16 pipelines; multi-stage separators	Primary production with gas-coning wells	Maximization of oil flowrates	IBM ThinkPad T60P with a 2.33 GHz processor
Gunnerud et al. (2012)	Real-time operational production planning with explicit structural and routing constraints.	Days and weeks (short-term)	Proxy modelling; piecewise linearization of MINLP to MILP; NLP.	Branch and Price Decomposition; Mosel Xpress-IVE	Vertical	Reservoir (-), wellbore (-), and surface facilities (-)	1 reservoir, 64 producers, 16 manifolds, 16 pipelines; many-stage separators	Primary production with gas-coning wells	Maximization of oil flowrates	Intel E5472, 3.0 GHz, 16 GB RAM
Gunnerud et al. (2013)	Real-time operational production planning with explicit structural and routing constraints.	Days and weeks (short-term)	Proxy modelling; MINLP	NOMAD, BONMIN; (implemented in C++ and MATLAB).	Vertical	Reservoir (-), wellbore (Statoil simulator), and surface facilities (pipeline simulator of Petroleum Experts)	1 reservoir, (3 producers, 1 manifold, 2 pipelines, 1 separator) per cluster	Primary production	Maximization of oil flowrates	[?]

Gupta and Grossmann (2012a)	Multi-Oilfield development planning with complex fiscal rules subject to logical FPSO connection constraints and well flow constraints.	20 years (long term)	Multiperiod MINLP and MILP	Bilevel decomposition, disjunctive branch and bound, & branch and cut CPLEX 12.2 (implemented in GAMS 23.6.3).	–	Reservoir (-), wellbore (-), and surface facilities (-)	3-10 fields, 3FPSO's, >20 producers	Primary production	Maximisation of NPV	Intel Core i7, 4GB RAM
Gupta and Grossmann (2012b)	Strategic planning model for offshore oilfield development with facility allocation, production planning, and scheduling, reservoir performance, surface pressure, and oil rig resource constraints.	21 years (long term)	Proxy modelling (using reservoir simulation data); Multiperiod MINLP and MILP (via piecewise linearization).	Bilevel decomposition, disjunctive branch and bound, branch and cut solution algorithms. DICOPT 2x-C; SBB; BARON; CPLEX 12.2 solver. These models were implemented in GAMS 23.6.3.	–	Reservoir (-), wellbore (-), and surface facilities (-)	3-10 fields, 3FPSO's, >20 producers	Primary production	Maximisation of NPV	Intel Core i7
Humphries and Haynes (2014)	Well placement and rate control optimisation (joint and sequential) subject to location, production and injection constraints on the wells.	3,600 days (long term)	Simulation-based optimisation by interfacing simulator with the optimiser.	Mesh Adaptive Search, Particle Swarm algorithms and hybrid of both (implemented in NOMAD black box software).	Vertical and deviated	Reservoir (IMEX), wellbore (IMEX)	1 reservoir, 2-4 producers, 2 injectors	Secondary production with water injection	Maximisation of NPV	[?]
Iyer and Grossmann (1998)	Planning and scheduling of offshore oil field infrastructure investment and operations subject to surface pressure constraints and drilling rig resource constraints.	6 years (long term)	Multiperiod MILP (via piecewise linear interpolation).	Sequential decomposition algorithm via time aggregation and disaggregation implemented in CPLEX/GAMS.	Vertical and deviated	Reservoir (-), wellbore (-), and surface facilities (-)	3 fields, 16, reservoirs, 2-3 well platforms, 53 producers	Primary production	Maximisation of NPV	HP9000/700
Kosmidis et al. (2004)	Real-time operational production planning with surface capacity and routing constraints.	1 day (short-term)	Proxy modelling; piecewise linearization of MINLP to MILP.	ILOG CPLEX 8.1:	Vertical and deviated	Reservoir (-), wellbore (-), and surface facilities (-)	1 reservoir, 4-25 producer wells, 2-6 manifolds, 2-28 pipelines, 2 separators	Primary production with gas lifted wells	Maximization of profit from oil sales minus gas compression costs	Intel 4 1.8 GHz machine
Kosmidis et al. (2005)	Daily well scheduling with surface capacity and routing constraints.	1 day (short-term)	Proxy modelling; MINLP/MILP	Outer Approximation, CPLEX 8.1	Vertical and deviated	Reservoir (-), wellbore (-), and surface facilities (-)	1 reservoir, 22 wells, 2 manifolds, 22 pipelines, 9 separators	Primary production with gas lifted wells	Maximization of profit from oil sales minus gas compression costs	Intel 4 1.8 GHz machine

Li et al. (2013)	Well placement and production optimisation with uncertainty considerations and well rate constraints.	250 days (long term)	MINLP; Simulation-based optimisation	Simultaneous perturbation stochastic approximation algorithm (SPSA).	Vertical	Reservoir (-), wellbore (-)	1 reservoir, 3 producers, 5 injectors	Secondary production with water injection	Maximisation of NPV	[?]
Mamghaderi et al. (2013)	Water flooding performance optimisation subject to reservoir layer constraints and injection rate constraints.	10-11 years (long term)	NLP	Capacitance-Resistive Model and Genetic Algorithm.	Vertical	Production logging (-)	1 reservoir (multi-layered) 5 injectors; 5 producers	Secondary production with water injection	Error minimisation between real and simulated production rates; oil production minimisation by reallocating the injected water volume	[?]
Silva and Camponogara (2014)	Production optimization of gas-lifted oil wells under facility, routing and pressure constraints.	Days and weeks (short-term)	Proxy modelling; Multidimensional piecewise linearization of MINLP to MILP.	Branch and Bound; AMPL, CPLEX 11.2.	Vertical	Wellbore (-), and surface facilities (-)	16 producer wells, 2 manifolds, >10 pipelines, 2 separators	Primary production with gas lifted wells	Minimisation of a production cost function	Intel Core 2 Quad 2.93 gigahertz processor and 4 gigabytes of RAM
Tavallali et al (2013)	Well placement and production planning with economic, production/injection rate and drilling schedule constraints.	2,190 days (long term)	Proxy modelling (for wellbore pressure drop only); non-convex spatiotemporal MINLP.	Outer-approximation algorithm with equality relaxation and augmented penalty (OA/ER/AP algorithm); GUROBI, CONOPT, CPLEX, IPOPT (implemented in GAMS 23.7.3).	Vertical	Fundamental equations of a black box simulator are written for a 2D model and solved (ECLIPSE simulations are used validation purposes); wellbore (VFPi).	1 reservoir,4 existing injectors; 4 existing producers	Secondary production with water injection	Maximisation of NPV	Intel® Xeon® X5690 CPUs (3.47 GHz and 3.46 GHz) and 192 GB of RAM

Tavallali et al. (2014)	Well Placement, infrastructure design, facility allocation, and production planning in multi-reservoir oil fields with surface facility networks with well location constraints, economic and rate constraints.	1,200 days (long term)	Proxy modelling (for wellbore pressure drop only); non-convex spatiotemporal MINLP.	Outer-approximation algorithm with equality relaxation and augmented penalty (OA/ER/AP algorithm); GUROBI, CONOPT, CPLEX, IPOPT (implemented in GAMS 23.7.3).	Vertical	Fundamental equations of a black box simulator are written for a 2D model and solved (ECLIPSE simulations are used validation purposes); wellbore (VFPi), surface facility - pipelines (VFPi).	4 reservoirs, 5 existing injectors; 4 existing producers	Secondary production with water injection	Maximisation of NPV	Dell Precision T5500 with two Intel Xeon X5650 CPUs (2.67 and 2.66 GHz) and 48 GB of RAM
Tavallali et al. (2015)	Drill rig scheduling subject to constraints on the drilling budget, logical field-wide flow constraints and well selection constraints.	2,190 days (long term)	MINLP	Genetic Algorithm (of MATLAB) coupled with a reservoir simulator.	Vertical	Reservoir (ECLIPSE), wellbore (-), pipelines	1 reservoir, (-)	Secondary production with water injection	Maximisation of NPV	[?]
Tavallali et al. (2016)	Well placement, Planning and production scheduling in a multi-reservoir field subject to economic and pressure drop constraints.	1,201 days (long term)	Proxy modelling (for wellbore pressure drop only); non-convex spatiotemporal MINLP.	Outer-approximation algorithm with equality relaxation and augmented penalty (OA/ER/AP algorithm); GUROBI, CONOPT, CPLEX, IPOPT (implemented in GAMS 23.8.2).	Vertical	Fundamental equations of a black box simulator are written for a 2D model and solved (ECLIPSE simulations are used validation purposes); wellbore (VFPi), surface facility - pipelines (VFPi).	3 reservoirs, 5 existing injectors; 4 existing producers	Secondary production with water injection	Maximisation of NPV	Dell Precision T5500 with two Intel Xeon X5650 CPUs (2.67 and 2.66 GHz) and 48 GB of RAM
Thiele and Batycky (2006)	Waterflood management with geological, and available field injection water constraints.	3,000 days (long term)	Heuristic reservoir engineering-driven approach.	Streamline simulation for the derivation of injection efficiency.	Vertical	Reservoir/Streamline (-), wellbore (-)	1 reservoir, 9 producers, 7 injectors	Secondary production with water injection	Maximize oil production while reducing water production	[?]
van den Heever and Grossmann (2000)	Oilfield infrastructure planning subject to nonlinear reservoir constraints, complex physical and economic constraints.	6 years (long term)	Multiperiod MILP (via piecewise linear interpolation) to MILP.	Logic-based iterative aggregation/disaggregation algorithm (Outer Approximation Algorithm) DICOPT++, CPLEX 6.5, CPNOPT2 (implemented in GAMS).	–	Reservoir (-), wellbore (-), and surface facilities (-)	3 fields, 16, reservoirs, 2-3 well platforms, 4-53 producers	Primary production	Maximisation of NPV	HP9000/C110

van den Heever and Grossmann (2001)	Design and planning of offshore oilfield infrastructure with complex economic constraints, reservoir and surface facility constraints.	3-15 years (long term)	Proxy modelling (using reservoir simulation data); Multiperiod MINLP and MILP.	Logic-based iterative aggregation/disaggregation algorithm DICOPT++, CPLEX 6.6, CPNOPT2 (implemented in GAMS).	–	Reservoir (-), wellbore (-), and surface facilities (-)	>15 well platforms, >1 reservoir, >5 pipelines	Primary production	Maximisation of NPV	HP9000/C110; Pentium III 667 MHz
van den Heever et al. (2000)	Design and planning of offshore oilfield infrastructure solved by disjunctive modelling framework for complex economic constraints, reservoir and surface facility constraints.	Long term	MILP and NLP	Logic-based iterative aggregation/disaggregation algorithm DICOPT++, CPLEX 6.5, CPNOPT2 (implemented in GAMS).	–	Reservoir (-), wellbore (-), and surface facilities (-)	5 platforms, >1 reservoir, >5 pipelines	Primary production	Maximisation of NPV	HP9000/C110
van Essen et al. (2011)	Water injection scheduling and production optimisation with capacity limitations on the wells.	3,600 days (short term and long term)	Simulation-based optimisation using an adjoint formulation.	Hierarchical optimisation via an approximation of the hessian matrix.	Vertical	Reservoir (-), wellbore (-)	1 reservoir, 4 producers, 8 injectors	Secondary production with water injection	Maximization of NPV	[?]
Wang et al. (2012)	Well placement under geological uncertainty constraints.	50 years (long term)	Simulation-based optimisation	Retrospective optimisation (Particle Swarm Algorithm, Simplex linear interpolation-based line search).	Vertical	Reservoir/streamline simulation (ECLIPSE/ 3DSL), wellbore (ECLIPSE)	1 reservoir. 5 producers, 5 injectors	Secondary production with water injection	Maximisation of NPV	2.66 GHz; 1.95 GB RAM

Appendix D

Literature References

Aarsnes, U.J.F., Di Meglio, F., Graham, R. and Aamo, O.M., 2016a. A methodology for classifying operating regimes in underbalanced-drilling operations. *SPE J.*, *21*(02), 423-433.

Aarsnes, U.J.F., Açıkmeşe, B., Ambrus, A. and Aamo, O.M., 2016b. Robust controller design for automated kick handling in managed pressure drilling. *J. Proc. Control*, *47*, 46-57.

Aarsnes, U.J.F., Flåtten, T. and Aamo, O.M., 2016c. Review of two-phase flow models for control and estimation. *Ann. Rev. Control*, *42*, 50-62.

Abdulkadir, M., 2011. Experimental and computational fluid dynamics (CFD) studies of gas-liquid flow in bends. *Doctoral Dissertation, Department of Chemical and Environmental Engineering, University of Nottingham, United Kingdom.*

Abu-Jdayil, B. and Ghannam, M., 2014. The modification of rheological properties of sodium bentonite-water dispersions with low viscosity CMC polymer effect. *Energy Sources, Part A: Recovery, Utilization, and Environ. Effects. 36*(10), 1037-1048.

Adari, R.B., Miska, S., Kuru, E., Bern, P. and Saasen, A., 2000. Selecting drilling fluid properties and flow rates for effective hole cleaning in high-angle and horizontal wells. In *SPE Annual Technical Conference and Exhibition. Dallas, Texas USA.*

Aguiar, M.A.S., Camponogara, E. and Silva, T.L., 2014. A mixed-integer convex formulation for production optimization of gas-lifted oil fields with routing and pressure constraints. *Brazilian J. Chem. Eng.*, *31*(2), 439-455.

Agwu, O.E., Akpabio, J.U., Alabi, S.B. and Dosunmu, A., 2018a. Settling velocity of drill cuttings in drilling fluids: A review of experimental, numerical simulations and artificial intelligence studies. *Powder Technol., 339*, 728-746.

Agwu, O.E., Akpabio, J.U., Alabi, S.B. and Dosunmu, A., 2018. Artificial intelligence techniques and their applications in drilling fluid engineering: A review. *J. Pet. Sci. Eng., 167*, 300-315.

Ahn, H. 1989. Experiments and analytical investigations of granular materials: shear flow and convective heat transfer. *Doctoral Dissertation, California Institute of Technology.*

Akhshik, S. and Rajabi, M., 2018. CFD-DEM modeling of cuttings transport in underbalanced drilling considering aerated mud effects and downhole conditions. *J. Pet. Sci. Eng., 160*, 229-246.

Akhshik, S., Behzad, M. and Rajabi, M., 2015. CFD–DEM approach to investigate the effect of drill pipe rotation on cuttings transport behavior. *J. Pet. Sci. Eng.*, *127*, 229-244.

Akhshik, S., Behzad, M. and Rajabi, M., 2016. CFD-DEM simulation of the hole cleaning process in a deviated well drilling: The effects of particle shape. *Particuology*, *25*, 72-82.

Al-Azani, K., Elkatatny, S., Ali, A., Ramadan, E. and Abdulraheem, A., 2019. Cutting concentration prediction in horizontal and deviated wells using artificial intelligence techniques. *J. Pet. Exploration Prod. Technol.*, 1-11.

Alexandrov, N.M., Lewis, R.M., Gumbert, C.R., Green, L.L. and Newman, P.A., 2001. Approximation and model management in aerodynamic optimization with variable-fidelity models. *J. Aircraft*, *38*(6), 1093-1101.

Al-Kayiem, H.H., Ismail, M.Z.A., Zaki, N.M. and Elfeel, M.E., 2010. Simulation of the cuttings cleaning during the drilling operation. *Am. J. Appl. Sci.*, *7*(6), 800-806.

Allahvirdizadeh, P., Kuru, E. and Parlaktuna, M., 2016. Experimental investigation of solids transport in horizontal concentric annuli using water and drag reducing polymer-based fluids. *J. Nat. Gas Sci. Eng., 35*, 1070-1078.

Altindal, M.C., Ozbayoglu, E., Miska, S., Yu, M., Takach, N. and May, R., 2017. Impact of Viscoelastic Characteristics of Oil Based Muds/Synthetic Based Muds on Cuttings Settling Velocities. In *ASME 2017 36th International Conference on Ocean, Offshore and Arctic Engineering. Trondheim, Norway*.

Al-zawawi, A.S., Hayder, E.M., Baddourah, M., Karim, A., Ghazali, M. and Hidayat, W., 2011. Using streamline and reservoir simulation to improve water flood management. *SPE Middle East Oil and Gas Show and Conference*, *Manama, Bahrain*.

Amanna, B. and Movaghar, M.R.K., 2016. Cuttings transport behavior in directional drilling using computational fluid dynamics (CFD). *J. Nat. Gas Sci. Eng., 34*, 670-679.

Arshad, U., Jain, B., Ramzan, M., Alward, W., Diaz, L., Hasan, I., Aliyev, A. and Riji, C., 2015, Engineered solution to reduce the impact of lost circulation during drilling and cementing in Rumaila Field, Iraq. In *International Petroleum Technology Conference, Doha, Qatar*.

Asgharzadeh Shishavan, R., Hubbell, C., Perez, H., Hedengren, J. and Pixton, D., 2015. Combined rate of penetration and pressure regulation for drilling optimization by use of high-speed telemetry. *SPE Drill. Compl.*, *30*(01), 17-26.

Asgharzadeh Shishavan, R., Hubbell, C., Perez, H.D., Hedengren, J.D., Pixton, D.S. and Pink, A.P., 2016. Multivariate control for managed-pressure-drilling systems by use of high-speed telemetry. *SPE J.*, *21*(02), 459-470.

Ashford, F.E., Pierce, P.E., 1975. Determining multiphase pressure drops and flow capacities in down-hole safety valves. *J. Pet. Technol. 27*(09), 1–145.

Avila, R.J., Pereira, E.J., Miska, S.Z. and Takach, N.E., 2008. Correlations and analysis of cuttings transport with aerated fluids in deviated wells. *SPE Drill. Compl., 23*(02), 132-141.

Awotunde, A.A., 2014. On the joint optimization of well placement and control. In *SPE Saudi Arabia Section Technical Symposium and Exhibition, Al-Khobar, Saudi Arabia*.

Azamipour, V., Assareh, M., Dehghani, M.R. and Mittermeir, G.M., 2017. An efficient workflow for production allocation during water flooding. *J. Energy Resour. Technol.*, *139*(3), 1-10.

Azamipour, V., Assareh, M. and Mittermeir, G.M., 2018. An improved optimization procedure for production and injection scheduling using a hybrid genetic algorithm. *Chem. Eng. Des. Res.*, *131*, 557-570.

Bailey, L., Jones, T., Belaskie, J., Orban, J., Sheppard, M., Houwen, O., Jardine, S. and McCann, D., 1991. Stuck pipe: causes, detection and prevention. *Schlumberger Oilfield Rev.*, *3*, 13-26.

Bailey, B., Crabtree, M., Tyrie, J., Elphick, J., Kuchuk, F., Romano, C. and Roodhart, L., 2000. Water control. *Oilfield Rev.*, *12*(1), 30-51.

Bangerth, W., Klie, H., Wheeler, M.F., Stoffa, P.L. and Sen, M.K., 2006. On optimization algorithms for the reservoir oil well placement problem. *Comput. Geosci.*, *10*(3), 303-319.

Barigou, M. 2004. Particle tracking in opaque mixing systems: an overview of the capabilities of PET and PEPT. *Chem. Eng. Res. Des. 82*(9), 1258-1267.

Barragán-Hernández, V., Vázquez-Román, R., Rosales-Marines, L. and García-Sánchez, F., 2005. A strategy for simulation and optimization of gas and oil production. *Comput. Chem. Eng.*, *30*(2), 215-227.

Becker, T.E., Azar, J.J. and Okrajni, S.S., 1991. Correlations of mud rheological properties with cuttings-transport performance in directional drilling. *SPE Drill. Compl.*, *6*(01), 16-24.

Beggs, D.H., Brill, J.P., 1973. A study of two-phase flow in inclined pipes. *J. Pet. Technol. 25*(05), 607–617

Bello, O., Holzmann, J., Yaqoob, T. and Teodoriu, C., 2015. Application of artificial intelligence methods in drilling system design and operations: a review of the state of the art. *J. Artificial Intelligence Soft Comput. Res.*, *5*(2), 121-139.

Bellout, M.C., Ciaurri, D.E., Durlofsky, L.J., Foss, B. and Kleppe, J., 2012. Joint optimization of oil well placement and controls. *Comput. Geosci.*, *16*(4), 1061-1079.

Belotti, P., Kirches, C., Leyffer, S., Linderoth, J., Luedtke, J. and Mahajan, A., 2013. Mixed-integer nonlinear optimization. *Acta Numerica*, *22*, 1-131.

Bennion, D.B., Thomas, F.B., Bietz, R.F. and Bennion, D.W., 1996. Underbalanced drilling, praises and perils. In *Permian Basin Oil and Gas Recovery Conference*, *Midland, Texas, USA.*

Beykal, B., Boukouvala, F., Floudas, C.A., Sorek, N., Zalavadia, H. and Gildin, E., 2018. Global optimization of grey-box computational systems using surrogate functions and application to highly constrained oil-field operations. *Comput. Chem. Eng.*, *114*, 99-110.

Bilgesu, H. I., Ali, M. W., Aminian, K., & Ameri, S., 2002. Computational Fluid Dynamics (CFD) as a tool to study cutting transport in wellbores. In *SPE Eastern Regional Meeting, Lexington*, *Kentucky, USA.*

Bilgesu, H., Mishra, N., & Ameri, S., 2007. Understanding the effect of drilling parameters on hole cleaning in horizontal and deviated wellbores using computational fluid dynamics. *Eastern Regional Meeting, Lexington, Kentucky, USA.*

Binder, J. L., & Hanratty, T. J., 1991. A diffusion model for droplet deposition in gas/liquid annular flow. *Int. J. Multiph. Flow. 17*(1), 1-11.

Bizanti, M.S. and Alkafeef, S.F., 2003. A simplified hole cleaning solution to deviated and horizontal wells. In *Middle East Oil Show, Bahrain*.

Bizhani, M. and Kuru, E., 2018. Critical review of mechanistic and empirical (semimechanistic) models for particle removal from sandbed deposits in horizontal annuli with water. *SPE J.*, *23*(02), 237-255.

Bizhani, M. and Kuru, E., 2019. Effect of Sand Bed Deposits on the Characteristics of Turbulent Flow of Water in Horizontal Annuli. *J. Fluids Eng.*, *141*(5), 051102.

Bizhani, M., Rodriguez Corredor, F.E. and Kuru, E., 2016. Quantitative evaluation of critical conditions required for effective hole cleaning in coiled-tubing drilling of horizontal wells. *SPE Drill. Compl.*, *31*(03), 188-199.

Bjorkevoll, K.S., Rommetveit, R., Rønneberg, A. and Larsen, B.L., 2006. Successful field use of advanced dynamic models. *In IADC/SPE Drilling Conference, Miami, Florida, USA*.

Bjørkevoll, K.S., Vollen, A.E., Barr Aas, I. and Hovland, S., 2010. Successful use of real time dynamic flow modelling to control a very challenging managed pressure drilling operation in the North Sea. In *SPE/IADC Managed Pressure Drilling and Underbalanced Operations Conference and Exhibition. Kuala Lumpur, Malaysia*.

Bonami, P. and Lee, J., 2007. BONMIN user's manual. *Numer. Math.*, *4*, 1-32.

Bonami, P., Biegler, L.T., Conn, A.R., Cornuéjols, G., Grossmann, I.E., Laird, C.D., Lee, J., Lodi, A., Margot, F., Sawaya, N. and Wächter, A., 2008. An algorithmic framework for convex mixed integer nonlinear programs. *Discrete Optim.*, *5*(2), 186-204.

Bosworth, S., El-Sayed, H.S., Ismail, G., Ohmer, H., Stracke, M., West, C. and Retnanto, A., 1998. Key issues in multilateral technology. *Oilfield Rev.*, *10*(4), 14-28.

Bouzarkouna, Z., 2012. *Well placement optimization. Doctoral Dissertation, Universite Paris-SUD*.

Brennen, C. E. 2005. Fundamentals of multiphase flow. Cambridge university press.

Breyholtz, Ø. and Nikolaou, M., 2012. Drilling automation: Presenting a framework for automated operations. *SPE Drill. Compl.*, *27*(01), 118-126.

Breyholtz, Y., Nygaard, G.H. and Nikolaou, M., 2009. Advanced automatic pressure control for dual-gradient drilling. In *SPE Annual Technical Conference and Exhibition. New Orleans, Louisiana*

Breyholtz, Ø., Nygaard, G. and Nikolaou, M., 2010a. Automatic control of managed pressure drilling. In *IEEE Proceedings of the 2010 American Control Conference. Baltimore, USA*. 442-447.

Breyholtz, Ø., Nygaard, G.H., Siahaan, H. and Nikolaou, M., 2010b. Managed pressure drilling: A multi-level control approach. In *SPE Intelligent Energy Conference and Exhibition. Utrecht, The Netherlands*.

Breyholtz, Ø., Nygaard, G. and Nikolaou, M., 2011. Managed-pressure drilling: Using model predictive control to improve pressure control for during dual-gradient drilling. *SPE Drill. Compl.*, *26*(02), 182-197.

Brouwer, D.R. and Jansen, J.D., 2002. Dynamic optimization of water flooding with smart wells using optimal control theory. In *European Petroleum Conference*, *Aberdeen, United Kingdom.*

Brown, N.P., Bern, P.A. and Weaver, A., 1989. Cleaning deviated holes: New experimental and theoretical studies. In *SPE/IADC Drilling Conference. New Orleans, Louisiana, USA.*

Bussieck, M.R. and Pruessner, A., 2003. Mixed-integer nonlinear programming. *SIAG/OPT Newsletter: Views & News*, *14*(1), 19-22.

Byron, M.L., 2015. The rotation and translation of non-spherical particles in homogeneous isotropic turbulence. *Doctoral Dissertation, University of California, Berkeley, USA.*

Caenn, R., Darley, H.C. and Gray, G.R., 2011. Composition and properties of drilling and completion fluids. Gulf professional publishing.

Calçada, L.A., Neto, O.D., Magalhães, S.C., Scheid, C.M., Borges Filho, M.N. and Waldmann, A.T.A., 2015. Evaluation of suspension flow and particulate materials for control of fluid losses in drilling operation. *J. Pet. Sci. Eng.*, *131*, 1-10.

Camponogara, E., Teixeira, A.F., Hulse, E.O., Silva, T.L., Sunjerga, S. and Miyatake, L.K., 2017. Integrated methodology for production optimization from multiple offshore reservoirs in the Santos Basin. *IEEE Tran. Autom. Sci. Eng.*, *14*(2), 669-680.

Capo, J., Yu, M., Miska, S., & Takach, N., 2004. Cuttings transport with aqueous foam at intermediate inclined wells. *SPE/ICoTA Coiled Tubing Conference and Exhibition, Houston, Texas, USA.*

Carlsen, L.A., Nygaard, G. and Nikolaou, M., 2013. Evaluation of control methods for drilling operations with unexpected gas influx. *J. Proc. Control*, *23*(3), 306-316.

Carvalho, M.C.A. and Pinto, J.M., 2006. An MILP model and solution technique for the planning of infrastructure in offshore oilfields. *J. Pet. Sci. Eng.*, *51*(1-2), 97-110.

Cayeux, E. and Daireaux, B., 2009. Early detection of drilling conditions deterioration using real-time calibration of computer models: field example from North Sea drilling operations. In *SPE/IADC Drilling Conference and Exhibition. Amsterdam, The Netherlands.*

Cayeux, E., Daireaux, B., Dvergsnes, E.W., Saelevik, G. and Zidan, M., 2012. An Early Warning System for Identifying Drilling Problems: An Example from a Problematic Drill-Out Cement Operation in the North Sea. In *SPE/IADC Drilling Conference and Exhibition. San Diego, California, USA.*

Cayeux, E., Mesagan, T., Tanripada, S., Zidan, M. and Fjelde, K.K., 2014. Real-time evaluation of hole-cleaning conditions with a transient cuttings-transport model. *SPE Drill. Compl., 29*(01), 5-21.

Celigueta, M.A., Deshpande, K.M., Latorre, S. and Oñate, E., 2016. A FEM-DEM technique for studying the motion of particles in non-Newtonian fluids. Application to the transport of drill cuttings in wellbores. *Comput. Part. Mech.*, *3*(2), 263-276.

Chamkalani, A., Zendehboudi, S., Amani, M., Chamkalani, R., James, L. and Dusseault, M., 2017. Pattern recognition insight into drilling optimization of shaly formations. *J. Pet. Sci. Eng.*, *156*, 322-339.

Chapman, C.D., Sanchez, J.L., De Leon Perez, R. and Yu, H., 2012. Automated closed-loop drilling with ROP optimization algorithm significantly reduces drilling time and improves downhole tool reliability. In *IADC/SPE Drilling Conference and Exhibition, San Diego, California, USA.*

Chen, Z., Ahmed, R.M., Miska, S.Z., Takach, N.E., Yu, M., Pickell, M.B. and Hallman, J.H., 2007a. Experimental study on cuttings transport with foam under simulated horizontal downhole conditions. *SPE Drill. Compl.*, *22*(04), 304-312.

Chen, Z., Duan, M., Miska, S.Z., Yu, M., Ahmed, R.M. and Hallman, J.H., 2007b. Hydraulic predictions for polymer-thickened foam flow in horizontal and directional wells. In *SPE/IADC Drilling Conference. Amsterdam, The Netherlands.*

Cheng, R.C. and Wang, R.H., 2008. A three-segment hydraulic model for annular cuttings transport with foam in horizontal drilling. *J. Hydrodynamics*, *20*(1), 67-73.

Chhabra, R.P., Agarwal, L. and Sinha, N.K., 1999. Drag on non-spherical particles: an evaluation of available methods. *Powder Technol. 101*(3), 288-295.

Chhantyal, K., Viumdal, H. and Mylvaganam, S., 2017. Soft sensing of non-Newtonian fluid flow in open Venturi channel using an array of ultrasonic level sensors—AI models and their validations. *Sensors*, *17*(11), 2458.

Chein, R., Chung, J.N., 1987. Effects of vortex pairing on particle dispersion in turbulent shear flows. *Int. J. Multiph. Flow 13*(6), 785–802.

Chin, W.C., 2001. Computational Rheology for Pipeline and Annular Flow: Non-Newtonian Flow Modeling for Drilling and Production, and Flow Assurance Methods in Subsea Pipeline Design. Gulf Publishing, Texas, USA.

Ciaurri, D.E., Isebor, O.J. and Durlofsky, L.J., 2010. Application of derivative-free methodologies to generally constrained oil production optimization problems. *Procedia Comput. Sci.*, *1*(1), 1301-1310.

Ciaurri, D.E., Mukerji, T. and Durlofsky, L.J., 2011. Derivative-free optimization for oil field operations. In *Computational Optimization and Applications in Engineering and Industry* (19-55). Springer, Berlin, Heidelberg.

Clark, R.K. and Bickham, K.L., 1994. A mechanistic model for cuttings transport. In *SPE Annual Technical Conference and Exhibition. New Orleans, Louisiana, USA.*

Cleminš, A., 1988. Representation of two-phase flows by volume averaging. *Int. J. Multiph. Flow*, *14*(1), 81-90.

Clift, R., Grace, J.R. and Weber, M.E., 2005. Bubbles, drops, and particles. Courier Corporation. Massachusetts, USA.

Codas, A., Campos, S., Camponogara, E., Gunnerud, V. and Sunjerga, S., 2012. Integrated production optimization of oil fields with pressure and routing constraints: The Urucu field. *Comput. Chem. Eng*, *46*, 178-189.

Codas, A., Foss, B. and Camponogara, E., 2015. Output-constraint handling and parallelization for oil-reservoir control optimization by means of multiple shooting. *SPE J.*, *20*(04), 856-871.

Comer, J.K. and Kleinstreuer, C., 1995. A numerical investigation of laminar flow past nonspherical solids and droplets. *ASME Trans. J. Fluids Eng. 117*, 170-175.

Corredor, F.E.R., Bizhani, M. and Kuru, E., 2014. A Comparative Study of Hole Cleaning Performance—Water Versus Drag Reducing Fluid. In *ASME 2014 33rd International Conference on Ocean, Offshore and Arctic Engineering. San Francisco, California, USA.*

Costa, S.S., Stuckenbruck, S., Fontoura, S.A. and Martins, A.L., 2008. Simulation of transient cuttings transportation and ECD in wellbore drilling. In *Europec/EAGE Conference and Exhibition. Rome, Italy.*

Crowe, C. T., Gore, R. A., & Troutt, T. R. (1985). Particle dispersion by coherent structures in free shear flows. *Part. Sci. Technol. 3*(3-4), 149-158.

Crowe, C. T., Schwarzkopf, J. D., Sommerfeld, M., & Tsuji, Y., 2011. Multiphase flows with droplets and particles. CRC press. Florida, USA.

Currie, J. and Wilson, D.I., 2012. OPTI: lowering the barrier between open source optimizers and the industrial MATLAB user. *Foundations of computer-aided process operations*, *24*, 32-38.

Dalla Valle, J.M., 1943. Micromeritics the Technology of Fine Particles. Pitman Publishing Corporation. New York, USA.

Das, A.K., 2007. Simulation study evaluating alternative initial responses to formation fluid influx during managed pressure drilling. *Master Dissertation, Loiusianna State University, USA.*

Datta-Gupta, A. and King, M.J., 1995. A semi-analytic approach to tracer flow modeling in heterogeneous permeable media. *Advances in Water Resour.*, *18*(1), 9-24.

Davoudi, M., Smith, J.R., Chirinos, J.E. and Patel, B.M., 2011. Evaluation of alternative initial responses to kicks taken during managed-pressure drilling. *SPE Drill. Compl.*, *26*(02), 169-181.

Deen, N.G., Kriebitzsch, S.H., van der Hoef, M.A. and Kuipers, J.A.M., 2012. Direct numerical simulation of flow and heat transfer in dense fluid–particle systems. *Chem. Eng. Sci.*, *81*, 329-344.

Demiralp, Y., 2014. Effects Of Drill-pipe Whirling Motion on Cuttings Transport Performance for Horizontal Drilling. *Master Dissertation, Louisiana State University, USA.*

Demirer, N., Zalluhoglu, U., Marck, J., Darbe, R. and Morari, M., 2019. Autonomous Directional Drilling with Rotary Steerable Systems. In *2019 Am. Control Conf. (ACC)*, 5203-5208.

Detournay, E., Richard, T. and Shepherd, M., 2008. Drilling response of drag bits: theory and experiment. *Int. J. Rock Mech. Mining Sci.*, *45*(8), 1347-1360.

Ding, E.J. and Aidun, C.K., 2000. The dynamics and scaling law for particles suspended in shear flow with inertia. *J. Fluid Mech. 423*, 317-344.

Doan, Q.T., Oguztoreli, M., Masuda, Y., Yonezawa, T., Kobayashi, A., Naganawa, S. and Kamp, A., 2003. Modeling of transient cuttings transport in underbalanced drilling (UBD). *SPE J.*, *8*(02), 160-170.

Doron, P., and Barnea, D. (1993). A three-layer model for solid-liquid flow in horizontal pipes. *Intl. J. Multiph. Flow*, *19*(6), 1029–1043.

Duan, M., Miska, S. Z., Yu, M., Takach, N. E., Ahmed, R. M., & Zettner, C. M., 2006. Transport of small cuttings in extended reach drilling. *International Oil & Gas Conference and Exhibition in China.*

Duan, M., Miska, S. Z., Yu, M., Takach, N. E., Ahmed, R. M., & Hallman, J. H., 2008. The effect of drillpipe rotation on pressure losses and fluid velocity profile in foam drilling. In *SPE Western Regional and Pacific Section AAPG Joint Meeting, California, USA.*

Duan, M., Miska, S., Yu, M., & Takach, N., 2010. Experimental study and modeling of cuttings transport using foam with drill pipe rotation. *SPE Drill. & Compl. 25*(03), 352-362.

Dupriest, F.E. and Koederitz, W.L., 2005. Maximizing drill rates with real-time surveillance of mechanical specific energy. In *SPE/IADC Drilling Conference*, *Amsterdam, The Netherlands.*

Duran, M.A. and Grossmann, I.E., 1986. An outer-approximation algorithm for a class of mixed-integer nonlinear programs. *Math. Prog.*, *36*(3), 307-339.

Dykes Jr, G.B., 2014. Cuttings transport implications for drill string design: A study with computational fluid dynamics. *Master Thesis, College of Earth Resource Sciences and Engineering, Colorado School of Mines, USA.*

Eason, J.P., 2018. A trust region filter algorithm for surrogate-based optimization. *Doctoral Dissertation. Department of Chemical Engineering, University of Tulsa.*

Eaton, A.N., Beal, L.D., Thorpe, S.D., Janis, E.H., Hubbell, C., Hedengren, J.D., Nybø, R., Aghito, M., Bjørkevoll, K., Boubsi, R.E. and Braaksma, J., 2015. Ensemble model predictive control for robust automated managed pressure drilling. In *SPE Annual Technical Conference and Exhibition. Houston, Texas, USA.*

Eaton, A.N., Beal, L.D., Thorpe, S.D., Hubbell, C.B., Hedengren, J.D., Nybø, R. and Aghito, M., 2017. Real time model identification using multi-fidelity models in managed pressure drilling. *Comput. Chem. Eng.*, *97*, 76-84.

Economides, M.J. and Nikolaou, M., 2011. Technologies for oil and gas production: present and future. *AIChE J., 57*(8), 1974-1982.

Eesa, M., Barigou, M., 2008. Horizontal laminar flow of coarse nearly-neutrally buoyant particles in non-Newtonian conveying fluids: CFD and PEPT experiments compared. *Int. J. Multiph. Flow. 34*(11), 997-1007.

Eesa, M., & Barigou, M., 2009. CFD investigation of the pipe transport of coarse solids in laminar power law fluids. *Chem. Eng. Sci. 64*(2), 322-333.

Effiong, F., 2013. Experimental Cuttings Transport in Horizontal Wellbore. *Master Thesis, Department of Petroleum Engineering and Applied Geophysics, Norwegian University of Science and Technology, Norway.*

EIA, US, 2016. Trends in US oil and natural gas upstream costs. *US Energy Information Administration*.

Epelle, E.I. and Gerogiorgis, D.I., 2017. A multiparametric CFD analysis of multiphase annular flows for oil and gas drilling applications. *Comput. Chem. Eng.*, *106*, 645-661.

Epelle, E.I. and Gerogiorgis, D.I., 2018a. Transient and steady state analysis of drill cuttings transport phenomena under turbulent conditions. *Chem. Eng. Res. Des.*, *131*, 520-544.

Epelle, E.I. and Gerogiorgis, D.I., 2018b. CFD modelling and simulation of drill cuttings transport efficiency in annular bends: Effect of particle sphericity. *J. Pet. Sci. Eng.*, *170,* 992-1004.

Epelle, E.I. and Gerogiorgis, D.I., 2018c. A CFD investigation of the effect of particle sphericity on wellbore cleaning efficiency during oil and gas drilling. *Comput. Aid. Chem. Eng.*, *43*, 127-132.

Epelle, E.I. and Gerogiorgis, D.I., 2019a. Optimal Rate Allocation for Production and Injection Wells in an Oil and Gas Field for Enhanced Profitability. *AIChE J.* DOI: 10.1002/aic.16592.

Epelle, E.I. and Gerogiorgis, D.I., 2019b. A Multiperiod Optimisation Approach to Enhance Oil Field Productivity during Secondary Petroleum Production. *Comput.-Aided Chem. Eng.*, *46*, 1651–1656.

Epelle, E.I. and Gerogiorgis, D.I., 2019c. Drill cuttings transport and deposition in complex annular geometries of deviated oil and gas wells: A multiphase flow analysis of positional variability. *Chem. Eng. Res. Des.*, *151*, 214-230.

Epelle, E.I. and Gerogiorgis, D.I., 2019d. Mixed-Integer Nonlinear Programming (MINLP) for Production Optimisation of Naturally Flowing and Artificial Lift Wells with Routing Constraints. *Chem. Eng. Res. Des.*, *152*, 134–148.

Epelle, E.I. and Gerogiorgis, D.I., 2019e. A review of technological advances and open challenges for oil and gas drilling systems engineering. *AIChE J.*, *65*(6). DOI: 10.1002/aic.16842.

Epelle, E.I. and Gerogiorgis, D.I., 2020a. An Adjoint-Based Well Placement Optimisation Approach for Enhanced Oil Recovery under Geological Uncertainty: From Seismic to Production. *J. Pet. Sci. Eng.*, *190*, 107091.

Epelle, E.I. and Gerogiorgis, D.I., 2020. Oil Production Optimisation using Piecewise Linear Approximations (MILP): Computational Performance Comparison vs. MINLP Formulation. *Comput.-Aided Chem. Eng.* (in press).

Epelle, E.I. and Gerogiorgis, D.I., 2020. Optimisation of petroleum production well placement under geological uncertainty**.** *Comput.-Aided Chem. Eng.* (in press).

Eren, T. and Ozbayoglu, M.E., 2010. Real time optimization of drilling parameters during drilling operations. In *SPE Oil and Gas India Conference and Exhibition. Mumbai, India.*

Ergun, S., 1952. Fluid flow through packed columns. *Chem. Eng. Prog.*, *48*, 89-94.

Escudier, M.P.P.J., Oliveira, P.J., Pinho, F. and Smith, S., 2002. Fully developed laminar flow of non-Newtonian liquids through annuli: comparison of numerical calculations with experiments. *Exp. Fluids*, *33*(1), 101-111.

Fan, L. S., & Zhu, C. 2005. Principles of gas-solid flows. Cambridge University Press. UK.

Fan, Z., Cheng, L., Yang, D. and Li, X., 2018. Optimization of Well Pattern Parameters for Waterflooding in an Anisotropic Formation. *Math. Geosci.*, *50*(8), 977-1002.

Fanchi, J.R. and Christiansen, R.L., 2017. Introduction to petroleum engineering. John Wiley. New York, USA.

Fletcher, R. and Leyffer, S., 1994. Solving mixed integer nonlinear programs by outer approximation. *Math. Prog.*, *66*(1-3), 327-349.

Florence, F. and Iversen, F.P., 2010. Real-time models for drilling process automation: Equations and applications. In *SPE/IADC Drilling Conference and Exhibition, New Orleans, Louisiana, USA.*

Fluent, A. 2017. ANSYS Fluent theory guide 17.1. Ansys Inc, USA.

Ford, J.T., Peden, J.M., Oyeneyin, M.B., Gao, E. and Zarrough, R., 1990. Experimental investigation of drilled cuttings transport in inclined boreholes. In *SPE Annual Technical Conference and Exhibition. New Orleans, Louisiana, USA.*

Ford, J., 2017. Drilling Engineering. *Herriot-Watt University, Institute of Petroleum Engineering.*

Frangos, M., 2017. Uncertainty quantification for cuttings transport process monitoring while drilling by ensemble Kalman filtering. *J. Proc. Control*, *53*, 46-56.

Fredericks, P.D., Reitsma, D., Runggai, T., Hudson, J.N., Zaeper, R., Backhaus, O. and Hernandez, M., 2008. Successful implementation of first closed loop, multiservice control system for automated pressure management in a shallow gas well offshore Myanmar. In *SPE/IADC Drilling Conference*, *Orlando Florida, USA.*

Freij-Ayoub, R., Tan, C., Clennell, B., Tohidi, B. and Yang, J., 2007. A wellbore stability model for hydrate bearing sediments. *J. Pet. Sci. Eng., 57*(1-2), 209-220.

Garcia-Hernandez, A.J., Miska, S.Z., Yu, M., Takach, N.E. and Zettner, C.M., 2007. Determination of cuttings lag in horizontal and deviated wells. In *SPE Annual Technical Conference and Exhibition. Anaheim, California, USA.*

Gavignet, A.A. and Sobey, I.J., 1989. Model aids cuttings transport prediction. *J. Pet. Technol.*, *41*(09), 916-921.

Gerogiorgis, D.I. and Pistikopoulos, E.N., 2008. A mixed integer optimization strategy for oil and gas production planning. *Found. Comput. Aid. Process Operations, 1-4.*

Gerogiorgis, D.I., Georgiadis, M., Bowen, G., Pantelides, C.C. and Pistikopoulos, E.N., 2006. Dynamic oil and gas production optimization via explicit reservoir simulation. *Comput. Aid. Chem. Eng.*, *21*(A), 179.

Gerogiorgis, D.I., Kosmidis, V.D. and Pistikopoulos, E.N., 2009. Mixed Integer Optimization in Well Scheduling. *Encyc. Optim.*, 2247-2270.

GhasemiKafrudi, E. and Hashemabadi, S.H., 2016. Numerical study on cuttings transport in vertical wells with eccentric drillpipe. *J. Pet. Sci. Eng.*, *140*, 85-96.

Gidaspow, D., 1994. Multiphase flow and fluidization: continuum and kinetic theory descriptions. Academic press. Boston, Massachusetts, USA.

Gildin, E., Ghasemi, M., Romanovskay, A. and Efendiev, Y., 2013. Nonlinear complexity reduction for fast simulation of flow in heterogeneous porous media. In *SPE Reservoir Simulation Symposium*, Texas, USA.

Godhavn, J.M., 2009. Control requirements for high-end automatic MPD operations. In *SPE/IADC Drilling Conference and Exhibition. Amsterdam, The Netherlands.*

Godhavn, J.M., Pavlov, A., Kaasa, G.O. and Rolland, N.L., 2011. Drilling seeking automatic control solutions. *IFAC Proc. Vol.*, *44*(1), 10842-10850.

Golmohammadi, S.M. and Nakhaee, A., 2015. A cylindrical model for hydrate dissociation near wellbore during drilling operations. *J. Nat. Gas Sci. Eng., 27*, 1641-1648.

Gómez, L.C. and Milioli, F.E., 2005. Numerical simulation of fluid flow in CFB risers: A turbulence analysis approach. *J. Braz. Soc. Mech. Sci. Eng., 27*(2), 141-149.

Gondzio, J. and Yildirim, E.A., 2018. Global Solutions of Nonconvex Standard Quadratic Programs via Mixed Integer Linear Programming Reformulations. *arXiv preprint arXiv:1810.02307*.

Govender, N., Wilke, D.N. and Kok, S., 2016. Blaze-DEMGPU: Modular high performance DEM framework for the GPU architecture. *SoftwareX*, *5*, 62-66.

Gravdal, J.E., 2009, Real-time evaluation of kick during managed pressure drilling based on wired drill pipe telemetry. In *International Petroleum Technology Conference, Doha, Qatar.*

Gravdal, J.E., Nikolaou, M., Breyholtz, Ø. and Carlsen, L.A., 2010. Improved kick management during MPD by real-time pore-pressure estimation. *SPE Drill. Compl.*, *25*(04), 577-584.

Grimstad, B., 2015. Daily Production Optimization for Subsea Production Systems: Methods based on mathematical programming and surrogate modelling. *Doctoral Dissertation, Department of Engineering Cybernetics, Norwegian University of Science and Technology, Norway.*

Gu, Q. and Hoo, K.A., 2014. Evaluating the performance of a fracturing treatment design. *Industrial & Engineering Chemistry Research*, *53*(25), 10491-10503.

Gu, Q. and Hoo, K.A., 2015. Model-based closed-loop control of the hydraulic fracturing process. *Ind. Eng. Chem. Res.*, *54*(5), 1585-1594.

Gu, Y. and Oliver, D.S., 2007. An iterative ensemble Kalman filter for multiphase fluid flow data assimilation. *SPE Journal*, *12*(04), 438-446.

Gul, S., Kuru, E. and Parlaktuna, M., 2017. Experimental Investigation of Cuttings Transport in Horizontal Wells Using Aerated Drilling Fluids. In *Abu Dhabi International Petroleum Exhibition & Conference. Abu Dhabi, UAE.*

Gulas, S., Downton, M., D'Souza, K., Hayden, K. and Walker, T.R., 2017. Declining Arctic Ocean oil and gas developments: Opportunities to improve governance and environmental pollution control. *Marine Policy*, *75*, 53-61.

Gunnerud, V. and Foss, B., 2010. Oil production optimization—A piecewise linear model, solved with two decomposition strategies. *Comput. Chem. Eng.*, *34*(11), 1803-1812.

Gunnerud, V., Foss, B.A., McKinnon, K.I.M. and Nygreen, B., 2012. Oil production optimization solved by piecewise linearization in a Branch & Price framework. *Comput. Operations Res.*, *39*(11), 2469-2477.

Gunnerud, V., Conn, A. and Foss, B., 2013. Embedding structural information in simulation-based optimization. *Comput. Chem. Eng., 53*, 35-43.

Guo, B., 2011. Petroleum production engineering, a computer-assisted approach. Elsevier. USA.

Gupta, V. and Grossmann, I.E., 2012a. An efficient multiperiod MINLP model for optimal planning of offshore oil and gas field infrastructure. *Ind. Eng. Chem. Res.*, *51*(19), 6823-6840.

Gupta, V. and Grossmann, I.E., 2012b. Modelling and computational strategies for optimal development planning of offshore oilfields under complex fiscal rules. *Ind. Eng. Chem. Res.*, *51*(44), 14438-14460.

Gupta, O.K. and Ravindran, A., 1985. Branch and bound experiments in convex nonlinear integer programming. *Manage. Sci.*, *31*(12), 1533-1546.

Gurobi, 2020. https://www.gurobi.com/resource/mip-basics/ (assessed 20 May, 2020).

Guyaguler, B., 2002. Optimization of well placement and assessment of uncertainty. *Doctoral Dissertation, Stanford University*.

Hagedorn, A.R., Brown, K.E., 1965. Experimental study of pressure gradients occurring during continuous two-phase flow in small-diameter vertical conduits. *J. Pet. Technol. 17*(04), 475–484.

Hajidavalloo, E., & Sadeghi-Behbahani-Zadeh, M., 2013. Simulation of gas–solid two-phase flow in the annulus of drilling well. *Chem. Eng. Res. Des. 91*(3), 477-484.

Hakim, H., Katende, A., Sagala, F., Ismail, I. and Nsamba, H., 2018. Performance of polyethylene and polypropylene beads towards drill cuttings transportation in horizontal wellbore. *J. Pet. Sci. Eng.*,, *165*, 962-969.

Han, S., Hwang, Y., Woo, N., & Kim, Y., 2010. Solid–liquid hydrodynamics in a slim hole drilling annulus. *J. Pet. Sci. Eng. 70*(3), 308-319.

Hankins, D., Salehi, S. and Karbalaei Saleh, F., 2015. An integrated approach for drilling optimization using advanced drilling optimizer. *J. Pet. Eng.* DOI: 10.1155/2015/281276

Hasan, A., Foss, B. and Sagatun, S., 2013. Optimization of oil production under gas coning conditions. *J. Pet. Sci. Eng., 105*, 26-33.

Hauge, E., Aamo, O.M., Godhavn, J.M. and Nygaard, G., 2013. A novel model-based scheme for kick and loss mitigation during drilling. *J. Proc. Control*, *23*(4), 463-472.

Hemphill, T. and Larsen, T.I., 1996. Hole-cleaning capabilities of water-and oil-based drilling fluids: a comparative experimental study. *SPE Drill. Compl.*, *11*(04), 201-207.

Hetsroni, G. 1989. Particles-turbulence interaction. *Int. J. Multiph. Flow. 15*(5), 735-746.

Heydari, O., Sahraei, E., & Skalle, P., 2017. Investigating the impact of drillpipe's rotation and eccentricity on cuttings transport phenomenon in various horizontal annuluses using computational fluid dynamics (CFD). *J. Pet. Sci. Eng. 156,* 801-813.

Hinder, O. and Ye, Y., 2018. A one-phase interior point method for nonconvex optimization. *Stanford University*, *arXiv preprint arXiv:1801.03072*.

Hoffmann, A. and Stanko, M.E., 2016. Real-time production optimization of a production network with ESP-boosted wells: A case study. In *SPE Middle East Artificial Lift Conference and Exhibition*, *Manama, Bahrain.*

Hongwei, C., Qihong, F., Xianmin, Z., Sen, W., Wensheng, Z. and Fan, L., 2019. Well Placement Optimization with Cat Swarm Optimization Algorithm under Oilfield Development Constraints. *J. Energy Resour. Technol.*, *141*(1), 012902.

Hopkin, E.A., 1967. Factors affecting cuttings removal during rotary drilling. *J. Pet. Technol.*, *19*(06), 807-814.

Hopkins, C.J. and Leicksenring, R.A., 1995. Reducing the risk of stuck pipe in the Netherlands. In *SPE/IADC Drilling Conference*, *Amsterdam, Netherlands.*

Hørsholt, S., Nick, H. and Jørgensen, J.B., 2018. Oil production optimization of black-oil models by integration of Matlab and Eclipse E300. In *IFAC Workshop Series*, *51*(8), 88-93.

Hossain, M., Chinenye-Kanu, N.M., Droubi, G.M. and Islam, S.Z., 2019. Investigation of slug-churn flow induced transient excitation forces at pipe bend. *J. Fluids Struct.*, *91*, 102733.

Hua, L., Zhao, H., Li, J., Wang, J. and Zhu, Q., 2015. Eulerian–Eulerian simulation of irregular particles in dense gas–solid fluidized beds. *Powder Technol. 284*, 299-311.

Humphries, T.D. and Haynes, R.D., 2015. Joint optimization of well placement and control for nonconventional well types. *J. Pet. Sci. Eng.*, *126*, 242-253.

Hussain, Q.E. and Sharif, M.A.R., 2000. Numerical modeling of helical flow of viscoplastic fluids in eccentric annuli. *AIChE J., 46*(10), 1937-1946.

Hyun, C., Subhash, N.S. and Osisanya, S.O., 2000. A three-segment hydraulic model for cuttings transport in horizontal and deviated wells. In *SPE/CIM International Conference on Horizontal Well Technology. Alberta, Canada.*

Ignatenko, Y., Bocharov, O., Gavrilov, A. and May, R., 2018. Steady-State Cuttings Transport Simulation in Horizontal Borehole Annulus. In *ASME 2018 37th International Conference on Ocean, Offshore and Arctic Engineering. Madrid, Spain.*

Ignatenko, Y., Gavrilov, A., Bocharov, O. and May, R., 2019. Simulation of steady-state cuttings transport through a horizontal annulus channel. In *EPJ Web of Conferences*, 196, 00011.

Isebor, O.J., Echeverría Ciaurri, D. and Durlofsky, L.J., 2014. Generalized field-development optimization with derivative-free procedures. *SPE J.*, *19*(05), 891-908.

Iyer, R.R., Grossmann, I.E., Vasantharajan, S. and Cullick, A.S., 1998. Optimal planning and scheduling of offshore oil field infrastructure investment and operations. *Ind. Eng. Chem. Res.*, *37*(4), 1380-1397.

Iyoho, A.W., Horeth, J.M. and Veenkant, R.L., 1987. A computer model for Hole-Cleaning Analysis. In *SPE Annual Technical Conference and Exhibition. Dallas, Texas, USA*.

Jansen, J.D., Brouwer, R. and Douma, S.G., 2009. Closed loop reservoir management. In *SPE reservoir simulation symposium*. The Woodlands, Texas, USA.

Jesmani, M., Bellout, M.C., Hanea, R. and Foss, B., 2016. Well placement optimization subject to realistic field development constraints. *Comput. Geosci.*, *20*(6), 1185-1209.

Jesmani, M., Jafarpour, B., Bellout, M.C. and Foss, B., 2020. A reduced random sampling strategy for fast robust well placement optimization. *J. Pet. Sci. Eng., 184*, 106414.

Jiang, G., Liu, T., Ning, F., Tu, Y., Zhang, L., Yu, Y. and Kuang, L., 2011. Polyethylene glycol drilling fluid for drilling in marine gas hydrates-bearing sediments: an experimental study. *Energies*, *4*(1), 140-150.

Johnson, P. C., & Jackson, R., 1987. Frictional–collisional constitutive relations for granular materials, with application to plane shearing. *J. Fluid Mech. 176*, 67-93.

Kamp, A.M. and Rivero, M., 1999. Layer modeling for cuttings transport in highly inclined wellbores. In *Latin American and Caribbean Petroleum Engineering Conference. Caracas, Venezuela.*

Kamyab, M. and Rasouli, V., 2016. Experimental and numerical simulation of cuttings transportation in coiled tubing drilling. *J. Nat. Gas Sci. Eng.*, *29*, 284-302.

Karnis, A., Goldsmith, H.L. and Mason, S.G., 1963. Axial migration of particles in Poiseuille flow. *Nature*, *200*(4902), 159-160.

Karnis, A., Goldsmith, H.L. and Mason, S.G., 1966. The flow of suspensions through tubes: V. Inertial effects. *The Can .J. Chem. Eng. 44*(4), 181-193.

Ke, C. and Song, X., 2018. Control of down-hole drilling process using a computationally efficient dynamic programming method. *J. Dyn. Syst. Meas. Control*, *140*(10), 1-10.

Kelessidis, V.C. and Bandelis, G.E., 2003. Flow patterns and minimum suspension velocity for efficient cuttings transport in horizontal and deviated wells in coiled-tubing drilling. In *SPE/ICoTA Coiled Tubing Conference and Exhibition. Houston, Texas, USA.*

Kelessidis, V.C., Maglione, R., Tsamantaki, C. and Aspirtakis, Y., 2006. Optimal determination of rheological parameters for Herschel–Bulkley drilling fluids and impact on pressure drop, velocity profiles and penetration rates during drilling. *J. Pet. Sci. Eng.*, *53*(3-4), 203-224.

Khor, C.S., Elkamel, A. and Shah, N., 2017. Optimization methods for petroleum fields development and production systems: a review. *Optim. Eng.*, *18*(4), 907-941.

Kim, Y.J. and Hwang, Y.K., 2003. Experimental study on the vortex flow in a concentric annulus with a rotating inner cylinder. *KSME Int. J., 17*(4), 562-570.

Kim, Y.J., Woo, N.S., Hwang, Y.K., Kim, J.H. and Han, S.M., 2014. Transport of small cuttings in solid-liquid flow with inclined slim hole annulus. *J. Mech. Sci.Technol.*, *28*(1), 115-126.

Kline, S. J., Reynolds, W. C., Schraub, F. A., & Runstadler, P. W., 1967. The structure of turbulent boundary layers. *J. Fluid Mech. 30*(4), 741-773.

Kocis, G.R. and Grossmann, I.E., 1989. A modelling and decomposition strategy for the MINLP optimization of process flowsheets. *Comput. Chem. Eng.*, *13*(7), 797-819.

Koederitz, W.L. and Johnson, W.E., 2011. Real-time optimization of drilling parameters by autonomous empirical methods. In *SPE/IADC Drilling Conference and Exhibition*, *Amsterdam, The Netherlands.*

Kosmidis, V.D., Perkins, J.D. and Pistikopoulos, E.N., 2004. Optimization of well oil rate allocations in petroleum fields. *Ind. Eng. Chem. Res.*, *43*(14), 3513-3527.

Kosmidis, V.D., Perkins, J.D. and Pistikopoulos, E.N., 2005. A mixed integer optimization formulation for the well scheduling problem on petroleum fields. *Comput. Chem. Eng., 29*(7), 1523-1541.

Kourounis, D., Durlofsky, L.J., Jansen, J.D. and Aziz, K., 2014. Adjoint formulation and constraint handling for gradient-based optimization of compositional reservoir flow. *Comput. Geosci.*, *18*(2), 117-137.

Krishnamoorthy, D., Foss, B. and Skogestad, S., 2016. Real-time optimization under uncertainty applied to a gas lifted well network. *Processes*, *4*(4), 52-69.

Kritsadativud, P., Jafarpour, B. and Ekkawong, P., 2015. Fast production optimization with decline curve analysis under facility constraints: a field case study. In *SPE Western Regional Meeting, Garden Grove, California, USA.*

Kronqvist, J., Bernal, D.E., Lundell, A. and Grossmann, I.E., 2019. A review and comparison of solvers for convex MINLP. *Optim. Eng.*, 1-59.

Landet, I.S., Mahdianfar, H., Pavlov, A. and Aamo, O.M., 2012. Modeling for MPD operations with experimental validation. In *SPE/IADC Drilling Conference and Exhibition. San Diego, California, USA.*

Landet, I.S., Pavlov, A. and Aamo, O.M., 2013. Modeling and control of heave-induced pressure fluctuations in managed pressure drilling. *IEEE Trans. Control Syst. Technol.*, *21*(4), 1340-1351.

Larsen, T.I., Pilehvari, A.A. and Azar, J.J., 1997. Development of a new cuttings-transport model for high-angle wellbores including horizontal wells. *SPE Drill. Compl., 12*(02), 129-136.

Lee, B.Y., Liu, H.S. and Tarng, Y.S., 1998. Modeling and optimization of drilling process. *J. Mater. Proc. Technol.*, *74*(1-3), 149-157.

Li, Y. and Kuru, E., 2003. Numerical modelling of cuttings transport with foam in horizontal wells. *J. Can. Pet. Technol.*, *42*(10), 1-10.

Li, J. and Walker, S., 2001. Sensitivity analysis of hole cleaning parameters in directional wells. *SPE J.*, *6*(04), 356-363.

Li, J., Walker, S. and Aitken, B., 2002. How to efficiently remove sand from deviated wellbores with a solids transport simulator and a coiled tubing cleanout tool. In *SPE Annual Technical Conference and Exhibition, San Antonio, Texas, USA.*

Li, J. and Luft, B., 2014a. Overview solids transport study and application in oil-gas industry-theoretical work. In *International Petroleum Technology Conference. Kuala Lumpur, Malaysia.*

Li, J. and Luft, B., 2014b. Overview solids transport study and application in oil-gas industry-experimental. In *International Petroleum Technology Conference. Moscow, Russia.*

Lie, K.A., 2019. An introduction to reservoir simulation using MATLAB/GNU Octave. Cambridge University Press.UK.

Lien, K., Monty, J. P., Chong, M. S., & Ooi, A., 2004. The entrance length for fully developed turbulent channel flow. In *15th Aust. Fluid Mech. Conf., 15*, 356-363.

Liu, Y., 2014. Two-fluid modeling of gas-solid and gas-liquid flows: solver development and application. *Doctoral Dissertation, Universitätsbibliothek der TU München.*

Lorentzen, R.J., Nævdal, G. and Lage, A.C., 2003. Tuning of parameters in a two-phase flow model using an ensemble Kalman filter. *Int. J. Multiph. Flow*, 29(8), 1283-1309.

Losenno, C.G.R., 2004. An investigation of irregular particles in free-fall. *PhD Thesis, University of Edinburgh.*

Lun, C., Savage, S., & Jeffrey, D., 1984. Kinetic theories for granular flow: inelastic particles in Couette flow and slightly inelastic particles in a general flowfield. *J. Fluid Mech.* 140, 223-256.

Luo, Y., Bern, P.A. and Chambers, B.D., 1992. Flow-rate predictions for cleaning deviated wells. In *SPE/IADC Drilling Conference. New Orleans, Louisiana, USA.*

Ma, T., Chen, P. and Zhao, J., 2016. Overview on vertical and directional drilling technologies for the exploration and exploitation of deep petroleum resources. *Geomech. Geophy. Geo-Energy and Geo-Resour.*, *2*(4), 365-395.

Mamghaderi, A., Bastami, A. and Pourafshary, P., 2013. Optimization of waterflooding performance in a layered reservoir using a combination of capacitance-resistive model and genetic algorithm method. *J. Energy Resour. Technol.*, *135*(1), 1-10.

Mandø, M., Yin, C., Sørensen, H. and Rosendahl, L., 2007. On the modelling of motion of non-spherical particles in two-phase flow. In *6th Int. Conference Multiphase Flow. ICMF*, 9-13.

Martins, A.L. and Santana, C.C., 1992. Evaluation of cuttings transport in horizontal and near horizontal wells-a dimensionless approach. In *SPE Latin America Petroleum Engineering Conference. Caracas, Venezuela.*

Martins, A.L., Sa, C.H.M., Lourenco, A.M.F., Freire, L.G.M. and Campos, W., 1996. Experimental determination of interfacial friction factor in horizontal drilling with a bed of cuttings. In *SPE Latin America/Caribbean Petroleum Engineering Conference. Port-of-Spain, Trinidad.*

Martins, A.L., Santana, M.L., Gonçalves, C.J.C., Gaspari, E., Campos, W. and Perez, J.C.L.V., 1999. Evaluating the transport of solids generated by shale instabilities in ERW drilling-part II: case studies. In *SPE Annual Technical Conference and Exhibition. Houston, Texas, USA.*

Massie, G.W., Castle-Smith, J., Lee, J.W. and Ramsey, M.S., 1995. Amocos training initiative reduces wellsite drilling problems. *Pet. Eng. Int.*, *67*(3), 1-10.

McConnell, D.R., Zhang, Z. and Boswell, R., 2012. Review of progress in evaluating gas hydrate drilling hazards. *Marine Pet. Geology*, *34*(1), 209-223.

Mei, R., & Klausner, J. (1994). Shear lift force on spherical bubbles. *Int. J. Heat Fluid Flow, 15*(1), 62-65.

Mendes, J.R.P., Morooka, C.K. and Guilherme, I.R., 2003. Case-based reasoning in offshore well design. *J. Pet. Sci. Eng., 40*(1-2), 47-60.

Mezhericher, M., Brosh, T. and Levy, A., 2011. Modeling of particle pneumatic conveying using DEM and DPM methods. *Part. Sci. Technol.*, *29*(2), 197-208.

Minton, J.J., 2012. A comparison of common methods for optimal well placement. *University of Auckland, research repository*.

Mishra, N., 2007. Investigation of hole cleaning parameters using computational fluid dynamics in horizontal and deviated wells. *Master Dissertation, West Virginia University, USA.*

Misra, S. and Nikolaou, M., 2018. A data-driven modeling approach to zonal isolation of cemented gas wells. *J. Nat. Gas Sci. Eng.*, *59*, 262-273.

Mme, U. and Skalle, P.A., 2012. CFD calculations of cuttings transport through drilling annuli at various angles. *Int. J. Pet. Sci. Technol.*, *6*(2), 129-141.

Mohammadpoor, M. and Torabi, F., 2018. Big Data analytics in oil and gas industry: An emerging trend. *Petroleum*. DOI: 10.1016/j.petlm.2018.11.001.

Mohammadsalehi, M. and Malekzadeh, N., 2011. Optimization of hole cleaning and cutting removal in vertical, deviated and horizontal wells. In *SPE Asia Pacific Oil and Gas Conference and Exhibition Jakarta, Indonesia.*

Mohammadzadeh, K., Hashemabadi, S.H. and Akbari, S., 2016. CFD simulation of viscosity modifier effect on cutting transport by oil based drilling fluid in wellbore. *J. Nat. Gas Sci. Eng., 29*, 355-364.

Moody, L.F., 1944. Friction factors for pipe flow. *ASME Trans. 66*, 671–684.

Moraga, F., Bonetto, F., & Lahey, R., 1999. Lateral forces on spheres in turbulent uniform shear flow. *Int. J. Multiph. Flow. 25*(6), 1321-1372.

Moraveji, M.K., Sabah, M., Shahryari, A. and Ghaffarkhah, A., 2017. Investigation of drill pipe rotation effect on cutting transport with aerated mud using CFD approach. *Adv. Powder Technol.*, *28*(4), 1141-1153.

Møyner, O., Krogstad, S. and Lie, K.A., 2015. The application of flow diagnostics for reservoir management. *SPE Journal*, *20*(02), 306-323.

Mukherjee, H. and Economides, M.J., 1991. A parametric comparison of horizontal and vertical well performance. *SPE Formation Eval.*, *6*(02), 209-216.

Murillo, A., Neuman, J. and Samuel, R., 2009. Pipe sticking prediction and avoidance using adaptive fuzzy logic modeling. In *SPE Production and Operations Symposium*. Society of Petroleum Engineers, *Oklahoma City, Oklahoma, USA*.

Mwachaka, S.M., Wu, A. and Fu, Q., 2019. A review of mud pulse telemetry signal impairments modeling and suppression methods. *J. Pet. Expl. Prod. Technol.*, *9*(1), 779-792.

Naganawa, S. and Nomura, T., 2006. Simulating transient behavior of cuttings transport over whole trajectory of extended reach well. In *SPE/IADC Asia Pacific Drilling Technology Conference and Exhibition. Bangkok, Thailand.*

Naganawa, S., Sato, R. and Ishikawa, M., 2017. Cuttings-Transport Simulation Combined With Large-Scale-Flow-Loop Experimental Results and Logging-While-Drilling Data for Hole-Cleaning Evaluation in Directional Drilling. *SPE Drill. Compl.*, *32*(03), 194-207.

Naganawa, S., Oikawa, A., Masuda, Y., Tetsuo, Y., Hoshino, M. and Acuna, P., 2002. Cuttings transport in directional and horizontal wells while aerated mud drilling. In *SPE/IADC Asia Pacific Drilling Technology*.

Narasingam, A. and Kwon, J.S.I., 2017. Development of local dynamic mode decomposition with control: Application to model predictive control of hydraulic fracturing. *Comput. Chem. Eng.*, *106*, 501-511.

Narasingam, A., Siddhamshetty, P. and Sang-Il Kwon, J., 2017. Temporal clustering for order reduction of nonlinear parabolic PDE systems with time-dependent spatial domains: Application to a hydraulic fracturing process. *AIChE J., 63*(9), 3818-3831.

Narasingam, A., Siddhamshetty, P. and Kwon, J.S.I., 2018. Handling spatial heterogeneity in reservoir parameters using proper orthogonal decomposition based ensemble Kalman filter for model-based feedback control of hydraulic fracturing. *Ind. Eng. Chem. Res.*, *57*(11), 3977-3989.

Nguyen, D., & Rahman, S., 1996. A three-layer hydraulic program for effective cuttings transport and hole cleaning in highly deviated and horizontal wells. *SPE/IADC Asia Pacific Drilling Technology Kuala Lumpur, Malaysia.*

Niedermayr, M., Pearse, J., Banks, M., Zoellner, P. and Thonhauser, G., 2010. Case Study--Field Implementation of Automated Torque-and-Drag Monitoring for Maari Field Development. *In IADC/SPE Drilling Conference and Exhibition, New Orleans, Louisianna, USA.*

Nikolaou, M., Misra, P., Tam, V.H. and Bailey III, A.D., 2005. Complexity in semiconductor manufacturing, activity of antimicrobial agents, and drilling of hydrocarbon wells: Common themes and case studies. *Comput. Chem. Eng.*, *29*(11-12), 2266-2289.

Nikolaou, M., 2013. Computer-aided process engineering in oil and gas production. *Comput. Chem. Eng.*, *51*, 96-101.

Nikoofard, A., Johansen, T.A., Mahdianfar, H. and Pavlov, A., 2013. Constrained MPC design for heave disturbance attenuation in offshore drilling systems. In *2013 MTS/IEEE OCEANS-Bergen*, Norway. 1-7.

Nikuradze, J. (1933). Regularities of the turbulent flow in smooth pipes (supplement). *Res. Eng.*, *4*(1), 44-44.

Njobuenwu, D.O. and Fairweather, M., 2014. Effect of shape on inertial particle dynamics in a channel flow. *Flow, Turbul. Combust.*, *92*(1-2), 83-101.

Nocedal, J., Wächter, A. and Waltz, R.A., 2009. Adaptive barrier update strategies for nonlinear interior methods. *SIAM J. Optim.*, *19*(4), 1674-1693.

Nocedal, J., Öztoprak, F. and Waltz, R.A., 2014. An interior point method for nonlinear programming with infeasibility detection capabilities. *Optim. Meth. Software*, *29*(4), 837-854.

Nouri, J. M., & Whitelaw, J. H., 1994. Flow of Newtonian and non-Newtonian fluids in a concentric annulus with rotation of the inner cylinder. *Trans.-Am. Soc. Mech. Eng. J. Fluids Eng. 116*, 821-821.

Nouri, J. M., & Whitelaw, J. H., 1997. Flow of Newtonian and non-Newtonian fluids in an eccentric annulus with rotation of the inner cylinder. *Int. J. Heat Fluid Flow. 18*(2), 236-246.

NTNU (Norwegian University of Science and Technology), 2019. *IO Centre – Norne Benchmark Case.* https://www.sintef.no/projectweb/mrst/modules/mrst-core/data-sets/ (assessed 30 January, 2020).

Nunoo, N.A., 2018. Guest Editorial: How Artificial Intelligence Will Benefit Drilling. *J. Pet. Technol.*, *70*(05), 14-15.

Nussbaumer, R., Mariethoz, G., Gloaguen, E. and Holliger, K., 2018. Which path to choose in sequential Gaussian simulation. *Math. Geosci.*, *50*(1), 97-120.

Nygaard, G. and Nævdal, G., 2006. Nonlinear model predictive control scheme for stabilizing annulus pressure during oil well drilling. *J. Proc. Control*, *16*(7), 719-732.

Nygaard, G. and Gravdal, J., 2007. Wemod for matlab user's guide. *International Research Institute of Stavanger AS (IRIS), Bergen, Norway, Tech. Rep.*, *234,* 1-10.

O'Brien, T.B. and Dobson, M., 1985. Hole Cleaning: Some Field Results. In *SPE/IADC Drilling Conference, New Orleans, Louisiana, USA.*

Ofei T.N., Irawan S., Pao W., 2014. CFD method for predicting annular pressure losses and cuttings concentration in eccentric horizontal wells. *J Petrol Eng. 2014*; https://doi.org/10.1155/2014/486423.

Okpobiri, G.A. and Ikoku, C.U., 1986. Volumetric requirements for foam and mist drilling operations. *SPE Drill. Eng.*, *1*(01), 71-88.

Okrajni, S. and Azar, J.J., 1986. The effects of mud rheology on annular hole cleaning in directional wells. *SPE Drill. Eng.*, *1*(04), 297-308.

Oladunni, O.O. and Trafalis, T.B., 2011. Single-phase fluid flow classification via learning models. *Int. J. General Syst.*, *40*(05), 561-576.

Onwunalu, J.E. and Durlofsky, L.J., 2010. Application of a particle swarm optimization algorithm for determining optimum well location and type. *Comput. Geosci.*, *14*(1), 183-198.

Osgouei, R.E., 2010. Determination of cuttings transport properties of gasified drilling fluids. *Doctoral Thesis, Department of Petroleum and Natural gas Engineering, Middle East Technical University, Ankara, Turkey.*

Osgouei, R.E., Ozbayoglu, M.E. and Fu, T.K., 2013. CFD simulation of solids carrying capacity of a Newtonian fluid through horizontal eccentric annulus. In *ASME 2013 Fluids Engineering Division Summer Meeting. Nevada, USA.*

Østergaard, K.K., Tohidi, B., Danesh, A. and Todd, A.C., 2000. Gas hydrates and offshore drilling: predicting the hydrate free zone. *Annals of the New York Academy of Sciences*, *912*(1), 411-419.

Osunde, O. and Kuru, E., 2006. Numerical modelling of cuttings transport with foam in inclined wells. In *Canadian International Petroleum Conference. Calgary, Alberta, Canada.* Petroleum Society of Canada.

Ozbayoglu, E.M., Miska, S.Z., Reed, T. and Takach, N., 2003. Cuttings transport with foam in horizontal & highly-inclined wellbores. In *SPE/IADC Drilling Conference. Amsterdam, Netherlands.*

Ozbayoglu, M.E., Miska, S.Z., Reed, T. and Takach, N., 2005. Using foam in horizontal well drilling: a cuttings transport modeling approach. *J. Pet. Sci. Eng.*, *46*(4), 267-282.

Ozbayoglu, M.E., Saasen, A., Sorgun, M. and Svanes, K., 2008. Effect of pipe rotation on hole cleaning for water-based drilling fluids in horizontal and deviated wells. In *SPE/IADC Asia Pacific Drilling Technology Conference and Exhibition. Jakarta, Indonesia.*

Ozbayoglu, M.E., Sorgun, M., Saasen, A. and Svanes, K., 2010. Hole cleaning performance of light-weight drilling fluids during horizontal underbalanced drilling. *J. Can. Pet. Technol.*, *49*(04), 21-26.

Ozbayoglu, M.E., Saasen, A., Sorgun, M. and Svanes, K., 2010. Critical fluid velocities for removing cuttings bed inside horizontal and deviated wells. *Pet. Sci. Technol.*, *28*(6), 594-602.

Pálsson, B., Hólmgeirsson, S., Guðmundsson, Á., Bóasson, H.Á., Ingason, K., Sverrisson, H. and Thórhallsson, S., 2014. Drilling of the well IDDP-1. *Geothermics*, *49*, 23-30.

Pan, T.W., Joseph, D.D., Bai, R., Glowinski, R. and Sarin, V., 2002. Fluidization of 1204 spheres: simulation and experiment. *J. Fluid Mech.*, *451*, 169-191.

Pang, B., Wang, S., Wang, Q., Yang, K., Lu, H., Hassan, M. and Jiang, X., 2018a. Numerical prediction of cuttings transport behavior in well drilling using kinetic theory of granular flow. *J. Pet. Sci. Eng., 161*, 190-203.

Pang, B., Wang, S., Liu, G., Jiang, X., Lu, H. and Li, Z., 2018b. Numerical prediction of flow behavior of cuttings carried by Herschel-Bulkley fluids in horizontal well using kinetic theory of granular flow. *Powder Technol.*, *329*, 386-398.

Pantelides, C.C. and Renfro, J.G., 2013. The online use of first-principles models in process operations: Review, current status and future needs. *Comput. Chem. Eng.*, *51*, 136-148.

Paris, C.B., Hénaff, M.L., Aman, Z.M., Subramaniam, A., Helgers, J., Wang, D.P., Kourafalou, V.H. and Srinivasan, A., 2012. Evolution of the Macondo well blowout: simulating the effects

of the circulation and synthetic dispersants on the subsea oil transport. *Environ. Sci. Technol.*, *46*(24), 13293-13302.

Park, J., Webber, T., Shishavan, R.A. and Hedengren, J.D., 2017. Improved Bottomhole Pressure Control with Wired Drillpipe and Physics-Based Models. In *SPE/IADC Drilling Conference and Exhibition. The Hague, The Netherlands.*

Pastusek, P., Payette, G., Shor, R., Cayeux, E., Aarsnes, U.J., Hedengren, J., Menand, S., Macpherson, J., Gandikota, R., Behounek, M. and Harmer, R., 2019. Creating Open Source Models, Test Cases, and Data for Oilfield Drilling Challenges. In *SPE/IADC International Drilling Conference and Exhibition. The Hague, The Netherlands.*

Peden, J.M., Ford, J.T. and Oyeneyin, M.B., 1990. Comprehensive experimental investigation of drilled cuttings transport in inclined wells including the effects of rotation and eccentricity. In *European Petroleum Conference. The Hague, Netherlands.*

Pereira, F.A.R., Barrozo, M.A.S. and Ataíde, C.H., 2007. CFD predictions of drilling fluid velocity and pressure profiles in laminar helical flow. *Braz. J. Chem. Eng.*, *24*(4), 587-595.

Pereira, F.A.R., Ataíde, C.H. and Barrozo, M.A.S., 2010. CFD Approach using a discrete phase model for annular flow analysis. *Latin Am. App. Res.*, *40*(1), 53-60.

Petersen, J., Rommetveit, R., Bjorkevoll, K.S. and Froyen, J., 2008. A general dynamic model for single and multi-phase flow operations during drilling, completion, well control and intervention. In *SPE/IADC Asia Pacific Drilling Technology Conference and Exhibition, Jakarta, Indonesia.*

Petex (Petroleum Experts), 2019. https://www.petex.com/products/dof-suite/ifm/ (assessed 05 March, 2020).

Pixton, D.S., Asgharzadeh Shishavan, R., Perez, H.D., Hedengren, J.D. and Craig, A., 2014. Addressing UBO and MPD challenges with wired drill pipe telemetry. In *SPE/IADC Managed Pressure Drilling & Underbalanced Operations Conference & Exhibition. Madrid Spain.*

Popa, A.S., Popa, C.G., Malamma, M. and Hicks, J., 2008. Case-based reasoning approach for well failure diagnostics and planning. In *SPE Western Regional and Pacific Section AAPG Joint Meeting. Bakersfield, California, USA.*

Pouladi, B., Keshavarz, S., Sharifi, M. and Ahmadi, M.A., 2017. A robust proxy for production well placement optimization problems. *Fuel*, *206*, 467-481.

Pournazari, P., Ashok, P., van Oort, E., Unrau, S. and Lai, S., 2015. Enhanced kick detection with low-cost rig sensors through automated pattern recognition and real-time sensor calibration. In *SPE Middle East Intelligent Oil and Gas Conference and Exhibition*, *Abu Dhabi, UAE.*

Prasun, S. and Ghalambor, A., 2018. Transient Cuttings Transport with Foam in Horizontal Wells-A Numerical Simulation Study for Applications in Depleted Reservoirs. In *SPE International Conference and Exhibition on Formation Damage Control. Lafayette, Louisiana, USA.*

Proinov, P.D., 2009. General local convergence theory for a class of iterative processes and its applications to Newton's method. *J. Complexity*, *25*(1), 38-62.

Qi, D. and Luo, L.S., 2003. Rotational and orientational behaviour of three-dimensional spheroidal particles in Couette flows. *J. Fluid Mech.* 477, 201-213.

Qu, J., Yan, T., Sun, X., Li, Z. and Li, W., 2019. Decaying Swirl Flow and Particle Behavior through the Hole Cleaning Device for Horizontal Drilling of Fossil Fuel. *Energies*, *12*(3), 336.

Rahim, S. and Li, Z., 2015. Well placement optimization with geological uncertainty reduction. *IFAC-PapersOnLine*, *48*(8), 57-62.

Reilly, S.I., Vryzas, Z., Kelessidis, V.C. and Gerogiorgis, D.I., 2016. First-principles rheological modelling and parameter estimation for nanoparticle-based smart drilling fluids. In *Comput.-Aid. Chem. Eng.*, *38*, 1039-1044.

Reuge, N., Cadoret, L., Coufort-Saudejaud, C., Pannala, S., Syamlal, M. and Caussat, B., 2008. Multifluid Eulerian modeling of dense gas–solids fluidized bed hydrodynamics: influence of the dissipation parameters. *Chem. Eng. Sci. 63*(22), 5540-5551.

Roco, M. C., 1993. Particulate two-phase flow (Vol. 1002). Butterworth-Heinemann, Boston, MA, USA.

Roco, M. C., & Shook, C. A., 1983. Modeling of slurry flow: the effect of particle size. *Can. J. Chem. Eng. 61*(4), 494–503.

Rodrigues, H.W.L., Prata, B.D.A. and Bonates, T.O., 2016. Integrated optimization model for location and sizing of offshore platforms and location of oil wells. *J. Pet. Sci. Eng.*, *145*, 734-741.

Rommetveit, R., Bjørkevoll, K.S., Halsey, G.W., Larsen, H.F., Merlo, A., Nossaman, L.N., Sweep, M.N., Silseth, K.M. and Ødegaard, S.I., 2004. Drilltronics: an integrated system for real-time optimization of the drilling process. In *IADC/SPE Drilling Conference*, *Dallas, Texas, USA.*

Rooki, R., Ardejani, F.D., Moradzadeh, A. and Norouzi, M., 2014a. Simulation of cuttings transport with foam in deviated wellbores using computational fluid dynamics. *J. Pet. Expl. Prod. Technol.*, *4*(3), 263-273.

Rooki, R., Ardejani, F.D. and Moradzadeh, A., 2014b. Hole cleaning prediction in foam drilling using artificial neural network and multiple linear regression. *Geomaterials*, *4*(01), 47.

Rooki, R., Ardejani, F.D., Moradzadeh, A., Mirzaei, H., Kelessidis, V., Maglione, R. and Norouzi, M., 2012. Optimal determination of rheological parameters for Herschel-Bulkley drilling fluids using Genetic Algorithms (GAs). *Korea-Aust. Rheology J.*, *24*(3), 163-170.

Rooki, R., Ardejani, F.D., Moradzadeh, A. and Norouzi, M., 2015. CFD simulation of rheological model effect on cuttings transport. *J. Disp. Sci. Technol.*, *36*(3), 402-410.

Rooki, R., Ardejani, F.D., Moradzadeh, A. and Norouzi, M., 2015. CFD simulation of rheological model effect on cuttings transport. *J. Disp. Sci. Technol.*, *36*(3), 402-410.

Sadiq, T. and Gharbi, R., 1998. Prediction of frictional drag and transmission of slack-off force in horizontal wells using neural networks. In *SPE Eastern Regional Meeting*, *Pittsburgh, Pennsylvania USA.*

Saffman, P., 1965. The lift on a small sphere in a slow shear flow. *J. Fluid Mech. 22*(02), 385-400.

Salminen K, Cheatham C, Smith M, Valiullin K., 2017. Stuck-pipe prediction by use of automated real-time modeling and data analysis. *SPE Drill. Compl. 32*(03), 184-193.

Sample, K.J. and Bourgoyne Jr, A.T., 1978. Development of improved laboratory and field procedures for determining the carrying capacity of drilling fluids. In *SPE Annual Fall Technical Conference and Exhibition. Houston, Texas, USA.*

Sanchez, R.A., Azar, J.J., Bassal, A.A. and Martins, A.L., 1997. The effect of drillpipe rotation on hole cleaning during directional well drilling. In *SPE/IADC Drilling Conference. Amsterdam, Netherlands.*

Santana, M., Martins, A.L. and Sales Jr, A., 1998. Advances in the Modeling of the Stratified Flow of Drilled Cuttings in High Horizontal Wells. In *SPE International Petroleum Conference and Exhibition, Villahermosa, Mexico.*

Saputelli, L., Economides, M., Nikolaou, M. and Kelessidis, V., 2003. Real-time decision-making for value creation while drilling. In *SPE/IADC Middle East Drilling Technology Conference and Exhibition. Abu Dhabi, United Arab Emirates.*

Sarma, P. and Chen, W.H., 2008. Efficient well placement optimization with gradient-based algorithms and adjoint models. In *Intelligent energy conference and exhibition*, Amsterdam, The Netherlands.

Sayindla, S., Lund, B., Ytrehus, J.D. and Saasen, A., 2017. Hole-cleaning performance comparison of oil-based and water-based drilling fluids. *J. Pet. Sci. Eng.*, *159*, 49-57.

Schaeffer, D., 1987. Instability in the evolution equations describing incompressible granular flow. *J. Diff. Eqns. 66*(1), 19-50.

Schlumberger, 2019a. https://media.corporateir.net/media_files/IROL/97/97513/2016AR/interactive/pore-to-pipeline.html (assessed 05 March, 2020).

Schlumberger, 2019b. PIPESIM™ User Manual. Schlumberger Ltd., Houston, TX, USA.

Schlumberger, 2019c. ECLIPSE™ User Manual. Schlumberger Ltd., Houston, TX, USA.

Schlumberger, 2019d. FRONTSIM™ User Manual. Schlumberger Ltd., Houston, TX, USA.

Schlumberger, 2019e. PETREL™ User Manual. Schlumberger Ltd., Houston, TX, USA.

Shah, M. T., Utikar, R. P., Pareek, V. K., Tade, M. O., & Evans, G. M., 2015. Effect of closure models on Eulerian–Eulerian gas–solid flow predictions in riser. *Powder Technol. 269*, 247-258.

Shao, N., Salman, W., Gavriilidis, A. and Angeli, P., 2008. CFD simulations of the effect of inlet conditions on Taylor flow formation. *Int. J. Heat Fluid Flow*, *29*(6), 1603-1611.

Sharma, M.P. and Chowdhry, D.V., 1986. A computational model for drilled cutting transport in air (or gas) drilling operations. *J. Energy Resour. Technol.*, *108*(1), 8-14.

Shen, Z., Wang, H. and Li, G., 2011. Numerical simulation of the cutting-carrying ability of supercritical carbon dioxide drilling at horizontal section. *Pet. Expl. Dev.*, *38*(2), 233-236.

Shook, C.A. and Roco, M.C., 2015. Slurry flow: principles and practice. Butterworth-Heinemann publishing, USA.

Shook, G.M. and Mitchell, K.M., 2009. A robust measure of heterogeneity for ranking earth models: The F PHI curve and dynamic Lorenz coefficient. In *SPE annual technical conference and exhibition*, *New Orleans Louisiana, USA*.

Siddhamshetty, P., Kwon, J.S.I., Liu, S. and Valkó, P.P., 2018. Feedback control of proppant bank heights during hydraulic fracturing for enhanced productivity in shale formations. *AIChE J.*, *64*(5), 1638-1650.

Siddhamshetty, P., Yang, S. and Kwon, J.S.I., 2018. Modeling of hydraulic fracturing and designing of online pumping schedules to achieve uniform proppant concentration in conventional oil reservoirs. *Comput. Chem. Eng.*, *114*, 306-317.

Silva, T.L. and Camponogara, E., 2014. A computational analysis of multidimensional piecewise-linear models with applications to oil production optimization. *European J. Operation. Res.*, *232*(3), 630-642.

Silva, T.L., Camponogara, E., Teixeira, A.F. and Sunjerga, S., 2015. Modeling of flow splitting for production optimization in offshore gas-lifted oil fields: Simulation validation and applications. *J. Pet. Sci. Eng.*, *128*, 86-97.

Sobieski, W., 2009. Switch function and sphericity coefficient in the Gidaspow drag model for modeling solid-fluid systems. *Drying Technol.* 27(2), 267-280.

Sobieski, W., 2010. Drag Coefficient in Solid–Fluid System Modeling with the Eulerian Multiphase Model. *Drying Technol. 29*(1), 111-125.

Sommerfeld, M., van Wachem, B. and Oliémans, R., 2009. Dispersed turbulent multi-phase flow. *Best practice guidelines, ERCOFTAC.*

Song, X.Z., Li, G.S., Huang, Z.W., Wang, H.Z., Tian, S.C. and Shi, H.Z., 2010. Experimental study on horizontal wellbore cleanout by rotating jets. *J. Pet. Sci. Eng.*, *75*(1-2), 71-76.

Song, W., Wang, R., Ni, H., Huo, H. and Shen, Z., 2015. Multiphase flow mechanism of sand cleanout with supercritical carbon dioxide in a deviated wellbore. *J. Nat. Gas Sci. Eng.*, *25*, 140-147.

Song, W., Ni, H., Wang, R., Shen, Z. and Zhao, M., 2016. Pressure controlling method for managed pressure drilling with supercritical carbon dioxide as the circulation fluid. *Pet. Expl. Dev.*, *43*(5), 857-862.

Song, X., Xu, Z., Wang, M., Li, G., Shah, S.N. and Pang, Z., 2017. Experimental study on the wellbore-cleaning efficiency of microhole-horizontal-well drilling. *SPE J.*, *22*(04), 1-189.

Sorgun, M., Aydin, I. and Ozbayoglu, M.E., 2011. Friction factors for hydraulic calculations considering presence of cuttings and pipe rotation in horizontal/highly-inclined wellbores. *J. Pet. Sci. Eng.*, *78*(2), 407-414.

Sorgun, M., 2010. Modeling of Newtonian Fluids and Cuttings Transport Analysis in High Inclination Wellbores with Pipe Rotation. *Doctoral Thesis, Department, Petroleum and Natural Gas Engineering, Middle East Technical University, Turkey.*

Stamnes, O.N., Zhou, J., Kaasa, G.O. and Aamo, O.M., 2008. Adaptive observer design for the bottomhole pressure of a managed pressure drilling system. In *2008 47th IEEE Conference on Decision and Control. Cancun, Mexico.* 2961-2966.

Subramaniam, S., 2013. Lagrangian–Eulerian methods for multiphase flows. *Progress in Energy and Combust. Sci.*, *39*(2-3), 215-245.

Sugiura, J., Samuel, R., Oppelt, J., Ostermeyer, G.P., Hedengren, J. and Pastusek, P., 2015. Drilling modeling and simulation: Current state and future goals. In *SPE/IADC Drilling Conference and Exhibition. London, England, UK.*

Sui, D., Sukhoboka, O. and Aadnøy, B.S., 2018. Improvement of Wired Drill Pipe Data Quality via Data Validation and Reconciliation. *Int. J. Autom. Comput.*, *15*(5), 625-636.

Sun, B., Xiang, H., Li, H. and Li, X., 2017. Modeling of the Critical Deposition Velocity of Cuttings in an Inclined-Slimhole Annulus. *SPE J.*, *22*(04), 1-213.

Sun, X., Wang, K., Yan, T., Shao, S. and Jiao, J., 2014. Effect of drillpipe rotation on cuttings transport using computational fluid dynamics (CFD) in complex structure wells. *J. Pet. Expl. Prod. Technol.*, *4*(3), 255-261.

Syamlal, M. and O'Brien, T.J., 1987. The derivation of a drag coefficient formula from velocity-voidage correlations. *Technical Note, US Department of Energy, Office of Fossil Energy, NETL, Morgantown, WV*.

Taghipour, A., Lund, B., Ytrehus, J.D., Skalle, P., Saasen, A., Reyes, A. and Abdollahi, J., 2014. Experimental study of hydraulics and cuttings transport in circular and noncircular wellbores. *J. Energy Res. Technol.*, *136*(2), 022904.

Taha, Taha, and Zhanfeng F. Cui., 2006. CFD modelling of slug flow in vertical tubes. *Chem. Eng. Sci. 61*(2), 676-687.

Tang, L., Wen, F., Yang, Y., Crowe, C. T., Chung, J. N., & Troutt, T. R., 1992. Self-organizing particle dispersion mechanism in a plane wake. *Physics of Fluids A: Fluid Dynamics*, *4*(10), 2244-2251.

Tavallali, M.S., Karimi, I.A., Teo, K.M., Baxendale, D. and Ayatollahi, S., 2013. Optimal producer well placement and production planning in an oil reservoir. *Comput. Chem. Eng.*, *55*, 109-125.

Tavallali, M.S., Karimi, I.A., Halim, A., Baxendale, D. and Teo, K.M., 2014. Well placement, infrastructure design, facility allocation, and production planning in multireservoir oil fields with surface facility networks. *Ind. Eng. Chem. Res.*, *53*(27), 11033-11049.

Tavallali, M.S. and Karimi, I.A., 2016a. Integrated oil-field management: from well placement and planning to production scheduling. *Ind. Eng. Chem. Res.*, *55*(4), 978-994.

Tavallali, M.S., Karimi, I.A. and Baxendale, D., 2016b. Process systems engineering perspective on the planning and development of oil fields. *AIChE J.*, *62*(8), 2586-2604.

Tersa, R.A., 2015. Improvements of cuttings transport models through physical experiments and numerical investigations of solid-liquid transport. *Doctoral Thesis, Faculty of*

Mathematics/Computer Science and Mechanical Engineering, University of Clausthal, Clausthal-Zellerfeld, Germany.

Thiele, M.R. and Batycky, R.P., 2006. Using streamline-derived injection efficiencies for improved waterflood management. *SPE Res. Eval. Eng.*, *9*(02), 187-196.

Tian, D. and Song, X., 2018. Observer design for a wellbore drilling system with downhole measurement feedback. *J. Dynamic Syst. Meas. Control*, *140*(7), 1-10.

Tiffin, D.L., Stein, M.H., Wang, X., 2003. Drawdown guidelines for sand control completions. *In: SPE Annual Technical Conference and Exhibition, Denver, Colorado, USA.*

Tomren, P., Iyoho, A., & Azar, J., 1986. Experimental study of cuttings transport in directional wells. *SPE Drill. Eng. 1*(01), 43-56.

Toreifi, H. and Rostami, H., 2014. New method for prediction and solving the problem of drilling fluid loss using modular neural network and particle swarm optimization algorithm. *J. Pet. Expl. Prod. Technol., 4*(4), 371-379.

Ursin-Holm, S., Gunnerud, V., Foss, B. and Sandnes, A., 2014. Note on simulator-based optimization for petroleum production optimization. *NTNU*, 1-30.

van den Heever, S.A. and Grossmann, I.E., 2000. An iterative aggregation/disaggregation approach for the solution of a mixed-integer nonlinear oilfield infrastructure planning model. *Ind. Eng. Chem. Res.*, *39*(6), 1955-1971.

van den Heever, S.A., Grossmann, I.E., Vasantharajan, S. and Edwards, K., 2000. Integrating complex economic objectives with the design and planning of offshore oilfield infrastructures. *Comput. Chem. Eng.*, *24*(2-7), 1049-1055.

van den Heever, S.A., Grossmann, I.E., Vasantharajan, S. and Edwards, K., 2001. A Lagrangean decomposition heuristic for the design and planning of offshore hydrocarbon field infrastructures with complex economic objectives. *Ind. Eng. Chem. Res.*, *40*(13), 2857-2875.

Van Essen, G., Van den Hof, P. and Jansen, J.D., 2011. Hierarchical long-term and short-term production optimization. *SPE J.*, *16*(01), 191-199.

Vieira Neto, J.L., Martins, A.L., Ataíde, C.H. and Barrozo, M.A.S., 2014. The effect of the inner cylinder rotation on the fluid dynamics of non-Newtonian fluids in concentric and eccentric annuli. *Braz. J. Chem. Eng.*, *31*(4), 829-838.

Vielma, J.P., Ahmed, S. and Nemhauser, G., 2010. Mixed-integer models for nonseparable piecewiselinear optimization: Unifying framework and extensions. *Operation. Res.*, *58*(2), 303-315.

Viswanathan, J. and Grossmann, I.E., 1990. A combined penalty function and outer-approximation method for MINLP optimization. *Comput. Chem. Eng.*, *14*(7), 769-782.

Volkov, O. and Bellout, M.C., 2018. Gradient-based constrained well placement optimization. *J. Pet. Sci. Eng.*, *171*, 1052-1066.

Vollmari, K., Jasevičius, R. and Kruggel-Emden, H., 2016. Experimental and numerical study of fluidization and pressure drop of spherical and non-spherical particles in a model scale fluidized bed. *Powder Technol.*, *291*, 506-521.

Vryzas, Z. and Kelessidis, V.C., 2017. Nano-based drilling fluids: A review. *Energies*, *10*(4), 540.

Wächter, A. and Biegler, L.T., 2005. Line search filter methods for nonlinear programming: Motivation and global convergence. *SIAM J. Optim.*, *16*(1), 1-31.

Wächter, A. and Biegler, L.T., 2006. On the implementation of an interior-point filter line-search algorithm for large-scale nonlinear programming. *Math. Prog.*, *106*(1), .25-57.

Waldmann, A.T.A., Martins, A.L., Souza, E.A., Loureiro, S.A., Andrade, A.R., Scheid, C.M., Calçada, L.A., Moreno, R.Z., Dannenhauer, C.E., 2012. R&D efforts to control, monitor and identify drilling fluid invasion into reservoir rocks. In *Proceedings of the 1st International Conference on Upstream Engineering and Flow Assurance, A part of the AIChE Spring Meeting, Houston, Texas, USA.*

Walton, I.C., 1995. Computer simulator of coiled tubing wellbore cleanouts in deviated wells recommends optimum pump rate and fluid viscosity. In *SPE Production Operations Symposium. Oklahoma City, Oklahoma, USA.*

Wang, C., Li, G. and Reynolds, A.C., 2007. Optimal well placement for production optimization. In SPE *Eastern regional meeting*, *Lexington, Kentucky, USA.*

Wang, Z.M., Li, M. and Hong, Y.K., 2009a. Effect of drillpipe rotation on borehole cleaning for extended reach well. *J. Hydrodynamics*, *21*(3), 366-372.

Wang, R.H., Cheng, R.C., Wang, H.G. and Bu, Y.H., 2009b. Numerical simulation of transient cuttings transport with foam fluid in horizontal wellbore. *J. Hydrodynamics, Ser. B*, *21*(4), 437-444.

Wang, Z., Zhai, Y., Hao, X., Guo, X. and Sun, L., 2010. Numerical simulation on three-layer dynamic cutting transport model and its application on Extended Reach Drilling. In *SPE/IADC Asia Pacific Drilling Technology Conference and Exhibition. Ho Chi Minh City, Vietnam.*

Wang, Y., Duan, M., Wang, D., Liu, J. and Dong, Y., 2011. A Model for Deepwater Floating Platforms Selection Based on BP Artificial Neural Networks. In *The Twenty-first International Offshore and Polar Engineering Conference*, *Maui, Hawaii, USA.*

Wang, H., Echeverría-Ciaurri, D., Durlofsky, L. and Cominelli, A., 2012. Optimal well placement under uncertainty using a retrospective optimization framework. *SPE J.*, *17*(01), 112-121.

Wächter, A. and Biegler, L.T., 2005. Line search filter methods for nonlinear programming: Motivation and global convergence. *SIAM J. Optim.*, *16*(1), 1-31.

Wächter, A. and Biegler, L.T., 2006. On the implementation of an interior-point filter line-search algorithm for large-scale nonlinear programming. *Math. Prog.*, *106*(1), 25-57.

Wei, N., Meng, Y., Li, G., Wan, L., Xu, Z., Xu, X. and Zhang, Y., 2013. Cuttings transport models and experimental visualization of underbalanced horizontal drilling. *Math. Prob. in Eng.*, *2013*.

Wen, C. Y., & Yu, Y. H., 1966. Mechanics of fluidization. *Chem. Eng. Prog. Symp. Ser. 62*(1), 100–111.

Werner, B., Myrseth, V. and Saasen, A., 2017. Viscoelastic properties of drilling fluids and their influence on cuttings transport. *J. Pet. Sci. Eng.*, *156*, 845-851.

Wilson, E. and Stammler, F., 2016. Beyond extractivism and alternative cosmologies: Arctic communities and extractive industries in uncertain times. *The Extractive Ind. Soc.*, *3*(1), 1-8.

Wong, G.K., Dria, D.E., Geilikman, M.B., Stewart, D.R., 2005. Bean-up guidelines for sand-control completions. *In: SPE Annual Technical Conference and Exhibition, Dallas, Texas, USA.*

Xiaofeng, S., Kelin, W., Tie, Y., Shuai, S. and Shizhu, L., 2013a. Cuttings Transport with Gas in the Highly Deviated Horizontal Wells. *Open Fuels Energy Sci. J.*, *6*, 23-29.

Xiaofeng, S., Tie, Y., Shuai, S., Kelin, W. and Shizhu, L., 2013b. Cuttings Transport Behavior and Simulation Analysis Affected by Hole Cleaning Tool. *Open Pet. Eng. J.*, *6*, 64-68.

Xu, J., Ozbayoglu, E., Miska, S. Z., Yu, M., & Takach, N., 2013. Cuttings Transport with Foam in Highly Inclined Wells at Simulated Downhole Conditions. *Arch. Mining Sci.*, *58*(2), 481-494.

Yasari, E., Pishvaie, M.R., Khorasheh, F., Salahshoor, K. and Kharrat, R., 2013. Application of multi-criterion robust optimization in water-flooding of oil reservoir. *J. Pet. Sci. Eng.*, *109*, 1-11.

Yeten, B., Durlofsky, L.J. and Aziz, K., 2003. Optimization of nonconventional well type, location, and trajectory. *SPE J.*, *8*(03), 200-210.

Yeten, B., Castellini, A., Guyaguler, B. and Chen, W.H., 2005. A comparison study on experimental design and response surface methodologies. In *SPE Reservoir Simulation Symposium*, *Woodlands Texas, USA.*

Yeu, W.J., Katende, A., Sagala, F. and Ismail, I., 2019. Improving hole cleaning using low density polyethylene beads at different mud circulation rates in different hole angles. *J. Nat. Gas Sci. Eng.*, *61*, 333-343.

Yilmaz, D., 2012. Discrete Phase Simulations of Drilled Cuttings Transport Process in Highly Deviated Wells. *Master Dissertation, Louisiana State University, USA.*

Yow, H.N., Pitt, M.J. and Salman, A.D., 2005. Drag correlations for particles of regular shape. *Adv. Powder Technol. 16*(4), 363-372.

Ytrehus, J.D., Taghipour, A., Lund, B., Werner, B., Opedal, N., Saasen, A. and Ibragimova, Z., 2014. Experimental study of cuttings transport efficiency of water based drilling fluids. In *ASME 2014 33rd International Conference on Ocean, Offshore and Arctic Engineering. San Francisco, California, USA.*

Ytrehus, J.D., Lund, B., Taghipour, A., Kosberg, B.R., Carazza, L., Gyland, K.R. and Saasen, A., 2018. Cuttings Bed Removal in Deviated Wells. In *ASME 2018 37th International Conference on Ocean, Offshore and Arctic Engineering. Madrid, Spain*.

Zaisha, M.A.O., Chao, Y. and Kelessidis, V.C., 2012. Modeling and numerical simulation of yield viscoplastic fluid flow in concentric and eccentric annuli. *Chin. J. Chem. Eng.*, *20*(1), 191-202.

Zakerian, A., Sarafraz, S., Tabzar, A., Hemmati, N. and Shadizadeh, S.R., 2018. Numerical modeling and simulation of drilling cutting transport in horizontal wells. *J. Pet. Expl. Prod. Technol.*, *8*(2), 455-474.

Zandvliet, M., Handels, M., van Essen, G., Brouwer, R. and Jansen, J.D., 2008. Adjoint-based well-placement optimization under production constraints. *SPE J.*, *13*(04), 392-399.

Zangl, G., Graf, T. and Al-Kinani, A., 2006. Proxy modeling in production optimization. In *SPE Europec/EAGE Annual Conference and Exhibition*, *Vienna, Austria.*

Zhang, H., Liang, Y., Zhang, W., Wang, B., Yan, X. and Liao, Q., 2017. A unified MILP model for topological structure of production well gathering pipeline network. *J. Pet. Sci. Eng.*, *152*, 284-293.

Zhang, H., Liang, Y., Zhang, W., Wang, B., Yan, X. and Liao, Q., 2017. A unified MILP model for topological structure of production well gathering pipeline network. *J. Pet. Sci. Eng.*, *152*, 284-293.

Zhang, J., Luo, W., Li, C., Wan, T., Zhang, Z. and Zhou, C., 2018. Study of the cuttings transport in stable foam drilling. *Oil & Gas Science and Technology–Revue d'IFP Energies Nouvelles*, *73*, 30.

Zhang, Y., Li, X., Chen, Z., Wang, Y. and Xia, Z., 2019. Drilling Simulation in Hydrate-bearing Sediments Using a Novel Hydrate Drilling Simulator. *Energy Procedia*, *158*, 5138-5143.

Zhao, Y., Zalluhoglu, U., Marck, J., Demirer, N. and Morari, M., 2019. Model Predictive Control for Mud Motor Operation in Directional Drilling. In *2019 Am. Control Conf. (ACC)*. 5197-5202.

Zhou, J. and Nygaard, G., 2010. Control and estimation of downhole pressure in managed pressure drilling operations. In *IEEE 2010 4th International Symposium on Communications, Control and Signal Processing (ISCCSP) Limassol, Cyprus*. 1-6.

Zhou, J. and Nygaard, G., 2011. Automatic model-based control scheme for stabilizing pressure during dual-gradient drilling. *J. Proc. Control*, *21*(8), 1138-1147.

Zhou, L., Ahmed, R.M., Miska, S.Z., Takach, N.E., Yu, M. and Pickell, M.B., 2004a. Experimental study of aerated mud flows under horizontal borehole conditions. In *SPE/ICoTA Coiled Tubing Conference and Exhibition. Houston, Texas, USA.*

Zhou, L., Ahmed, R.M., Miska, S.Z., Takach, N.E., Yu, M. and Pickell, M.B., 2004b. Experimental study and modeling of cuttings transport with aerated mud in horizontal wellbore at simulated downhole conditions. In *SPE Annual Technical Conference and Exhibition. Houston, Texas, USA.*

Zhou, L., Ahmed, R.M., Miska, S.Z., Takach, N.E., Yu, M. and Saasen, A., 2005. Hydraulics of drilling with aerated muds under simulated borehole conditions. In *SPE/IADC Drilling Conference. Amsterdam, Netherlands.*

Zhou, L., 2008. Hole cleaning during underbalanced drilling in horizontal and inclined wellbore. *SPE Drill. Compl.*, *23*(03), 267-273.

Zhou, J., Stamnes, Ø.N., Aamo, O.M. and Kaasa, G.O., 2009. Pressure regulation with kick attenuation in a managed pressure drilling system. In *Proceedings of the 48th IEEE Conference on Decision and Control (CDC) held jointly with 2009 28th Chinese Control Conference*, *Shanghai, China.* 5586-5591.

Zhou, J., Nygaard, G., Godhavn, J.M., Breyholtz, Ø. and Vefring, E.H., 2010. Adaptive observer for kick detection and switched control for bottomhole pressure regulation and kick attenuation during managed pressure drilling. In *IEEE Proceedings of the 2010 Am. Control Conf.*, *Baltimore, USA.* 3765-3770.